batteries

Special Issue Reprint

Advanced Studies on High-Performance Metal-Ion Capacitors

Technologies, Systems and Applications

Edited by
Kangyu Zou, Tianjing Wu and Jiangmin Jiang

mdpi.com/journal/batteries

MDPI

Advanced Studies on High-Performance Metal-Ion Capacitors: Technologies, Systems and Applications

Advanced Studies on High-Performance Metal-Ion Capacitors: Technologies, Systems and Applications

Guest Editors

Kangyu Zou
Tianjing Wu
Jiangmin Jiang

MDPI
Basel • Beijing • Wuhan • Barcelona • Belgrade • Novi Sad • Cluj • Manchester

Guest Editors

Kangyu Zou
School of Materials Science and Engineering
Changsha University of Science and Technology
Changsha
China

Tianjing Wu
School of Chemistry
Xiangtan University
Xiangtan
China

Jiangmin Jiang
School of Materials Science and Physics
China University of Mining and Technology
Xuzhou
China

Editorial Office
MDPI AG
Grosspeteranlage 5
4052 Basel, Switzerland

This is a reprint of the Special Issue, published open access by the journal *Batteries* (ISSN 2313-0105), freely accessible at: https://www.mdpi.com/journal/batteries/special_issues/1P3BU89I8G.

For citation purposes, cite each article independently as indicated on the article page online and as indicated below:

Lastname, A.A.; Lastname, B.B. Article Title. *Journal Name* **Year**, *Volume Number*, Page Range.

ISBN 978-3-7258-6195-8 (Hbk)
ISBN 978-3-7258-6196-5 (PDF)
https://doi.org/10.3390/books978-3-7258-6196-5

Contents

batteries

Article

Biomass-Derived Carbon Materials for Advanced Metal-Ion Hybrid Supercapacitors: A Step Towards More Sustainable Energy

Syed Shaheen Shah

Department of Material Chemistry, Graduate School of Engineering, Kyoto University, Nishikyo-ku,
Kyoto 615-8520, Japan; shah.syedshaheen.78r@st.kyoto-u.ac.jp

Abstract: Modern research has made the search for high-performance, sustainable, and efficient energy storage technologies a main focus, especially in light of the growing environmental and energy-demanding issues. This review paper focuses on the pivotal role of biomass-derived carbon (BDC) materials in the development of high-performance metal-ion hybrid supercapacitors (MIHSCs), specifically targeting sodium (Na)-, potassium (K)-, aluminium (Al)-, and zinc (Zn)-ion-based systems. Due to their widespread availability, renewable nature, and exceptional physicochemical properties, BDC materials are ideal for supercapacitor electrodes, which perfectly balance environmental sustainability and technological advancement. This paper delves into the synthesis, functionalization, and structural engineering of advanced biomass-based carbon materials, highlighting the strategies to enhance their electrochemical performance. It elaborates on the unique characteristics of these carbons, such as high specific surface area, tuneable porosity, and heteroatom doping, which are pivotal in achieving superior capacitance, energy density, and cycling stability in Na-, K-, Al-, and Zn-ion hybrid supercapacitors. Furthermore, the compatibility of BDCs with metal-ion electrolytes and their role in facilitating ion transport and charge storage mechanisms are critically analysed. Novelty arises from a comprehensive comparison of these carbon materials across metal-ion systems, unveiling the synergistic effects of BDCs' structural attributes on the performance of each supercapacitor type. This review also casts light on the current challenges, such as scalability, cost-effectiveness, and performance consistency, offering insightful perspectives for future research. This review underscores the transformative potential of BDC materials in MIHSCs and paves the way for next-generation energy storage technologies that are both high-performing and ecologically friendly. It calls for continued innovation and interdisciplinary collaboration to explore these sustainable materials, thereby contributing to advancing green energy technologies.

Keywords: biomass; activated carbon; zinc-ion hybrid supercapacitor; sodium-ion hybrid supercapacitor; potassium-ion hybrid supercapacitor; aluminium-ion hybrid supercapacitor

1. Introduction

The efficient utilization of renewable energy sources, such as solar and wind, relies heavily on sustainable energy storage. Hybrid supercapacitors (HSCs) have been created to store energy using electric double-layer capacitance and Faradaic pseudocapacitance modes [1]. Even though they are used in various applications, HSCs offer a larger specific capacitance, a longer service life, and a greater power density than general batteries and double-layer capacitors [2]. Hence, their exceptional performance makes them an outstanding choice for advanced energy storage devices in the next generation [3]. Supercapacitors, sustainable energy storage options, are gaining popularity in fulfilling energy requirements and decreasing dependence on traditional energy sources [4]. Electrochemical capacitors, also known as supercapacitors, are potential alternatives or additions to batteries because of their high specific power, durability, and rapid charging and discharging capabilities [5].

These devices have many applications, from portable electronics to hybrid electric cars and power plants. When combined with fuel cells or batteries in hybrid electric vehicles, HSCs can provide the necessary energy for rapid acceleration [6]. Over the years, supercapacitors have demonstrated an existence ranging from low-scale to high-power energy storage systems. Supercapacitors are heavily influenced by the elements incorporated in preparing HSCs due to their high capacitance values [7–9]. Overall, it is essential that sustainable energy storage technologies, such as HSCs, be used to produce renewable energy because they provide good proficiency and long durability.

Metal-ion HSCs (MIHSCs) are an unequalled venture in sustainable energy storage technologies. They incorporate two distinctive types of devices: supercapacitors and batteries. MIHSCs are a hybrid of supercapacitors and batteries, with both the high power density of supercapacitors and the high energy density of batteries. Li et al. [10] explained that by incorporating supercapacitor-type and battery-type electrodes, MIHSCs inherit two charge storage mechanisms, delivering a high level of power per unit volume from the supercapacitor and a high level of energy per unit volume from the battery. In other words, MIHSCs are vital in maintaining modern devices due to their acutely growing energy demands. Moreover, it could be inferred that the hybrid device type is already quite promising in energy storage technologies that can satiate the rapid increase in energy needs [11]. They are essential in maintaining energy storage because batteries and supercapacitors can be used in a hybrid configuration since MIHSCs combine supercapacitors' long-cycle stability with batteries' inherent disadvantages [12,13]. Furthermore, these devices are instrumental in refining energy storage. They pave the way for achieving equilibrium in energy utilization in density and power. Their use in energy storage allows for wide operating potential windows (OPWs), high energy, safer application, and high power density; thus, MIHSCs show promising potential as a leading contender for the future generation of storage devices [14,15].

MIHSCs, comprising zinc-, sodium-, potassium-, and aluminium-ion HSCs, are differentiated based on efficiency and performance. Zinc-ion HSCs (ZIHSCs) are a potential form of energy storage which possess both the large storage capacity of zinc-ion batteries and the high power of a supercapacitor; high energy/power density is suitable for effective and consistent energy storage. ZIHSCs were presented as having better initial and first-cycle capacity retention [16,17]. Sodium-ion HSCs (NIHSCs) are new alloying-based MIHSCs fabricated by overcoming sodium-ion and lithium-ion devices' explosive and toxic drawbacks. The NIHSCs are structurally proven to occupy the neutralizing position with the best energy and power density ratio. However, high-power alkalis have recently gained much attention since the breakthrough of ion batteries with sodium and potassium [18,19]. Potassium-ion HSCs (KIHSCs) exhibit a significant ability to maintain their capacity over multiple cycles. KIHSCs have the most reasonable energy density of 58.2 Wh/kg with exceptional cycling durability [19]. Aluminium-ion HSCs (AIHSCs) made entirely from nitrogen-doped carbon spheres with a hierarchical porous hollow structure exhibit much better performance [20]. AIHSCs were thus developed to have drastically superior energy and power densities and show great potential for electrochemical performance [21]. Therefore, these MIHSCs are optimal for energy storage systems fulfilling requirements.

Biomass-derived carbon (BDC) materials are essential for improving the efficiency and performance of MIHSCs. Carbon materials possess numerous benefits, such as cost-effectiveness, environmental friendliness, and sustainability, making them highly appealing for energy conversion and storage. BDC materials provide multiple characteristics that render them highly suitable for enhancing the electrochemical efficiency of supercapacitors [22–24]. The inherent characteristics of these carbon compounds encompass a substantial specific surface area (SSA), commendable electrical conductivity, and adjustable porosity. The efficiency of devices, especially MIHSCs, can be enhanced by utilizing BDC materials. Specifically, in a ZIHSC [25], BDC materials could function as high-performance electrode materials. Such materials offer a high SSA that ensures sufficient charge storage and an overall improvement in the capacitive behaviour of such devices. Utilizing BDC materials in a NIHSC [24] could also realize high energy and power density. For KIHSCs, BDC materials could enhance capacity retention and cycling stability [26]. Lastly, these materials could improve ion adsorption and mobility in AIHSCs, increasing their energy and power density [27]. BDC materials, therefore, present a sustainable way of integrating high performance into MIHSCs. The unique natural properties of this type of carbon make it suitable for enhancing energy storage in these supercapacitors, which would, therefore, find an extensive range of applications in the current shift to sustainability.

This review study thoroughly examines using carbon materials produced from biomass to develop high-performance MIHSCs. The focus is primarily on sodium-, potassium-, aluminium-, and zinc-ion-based systems. BDC compounds are highlighted for their abundant availability, renewable nature, and exceptional physicochemical properties. These materials are considered excellent choices for supercapacitor electrodes, as they effectively combine environmental sustainability with technical progress. This paper explores creating, modifying, and designing the structure of these materials, focusing on their significant SSA, adjustable porosity, and the introduction of diverse elements, which are crucial for gaining excellent electrochemical performance in energy storage systems. An important innovation is the thorough comparison of these carbon materials in various metal-ion systems, revealing the combined effects of their structural characteristics on each type of supercapacitor. This review also discusses the difficulties of scalability and maintaining consistent performance and provides valuable insights for improving sustainable energy storage technologies. It highlights the potential of using BDC materials to develop advanced MIHSCs.

2. Basic Principles of MIHSCs

Capacitors, batteries, and HSCs are three energy storage technologies with unique attributes. Capacitors, specifically electrolytic capacitors, are efficient energy storage devices with notably high power capability and cyclic life [28]. They offer unprecedented ultrahigh power density and charge–discharge speed advantages, outperforming chemical batteries and electrochemical supercapacitors [29]. In contrast, batteries have notably high energy densities and are known for storing large amounts of energy. Various types of batteries are utilized in several industries, including portable electronic devices, electric cars, and large-scale electrical storage at power stations [30]. They use chemical reactions to store significantly more energy than capacitors, while their power capabilities are considerably lower than those of capacitance devices. Supercapacitors, alternatively called electrical double-layer capacitors [31], are rechargeable energy storage approaches with capacitors' and batteries' characteristics. Such power and energy delivery within traditional capacitors and batteries lend supercapacitors unique characteristics that make them promising energy storage device candidates [32]. Supercapacitors have a significantly greater power density than lithium-ion batteries but are behind these in energy density [12,33]. HSCs, specifically MIHSCs [16], combine the best of both worlds by providing energy and power density superior to capacitors or batteries. The devices consist of a battery-type electrode and a capacitive electrode, giving potential avenues for enhancing energy storage systems in the future [14]. Energy storage devices can be categorized based on the area in which they excel, with capacitors having superior power density and cyclic life, batteries having high energy density, supercapacitors offering power and many cycles, and hybrid capacitors having both exceptional power and energy density.

MIHSCs represent a significant advancement in energy storage technology since they effectively merge the advantages of batteries and supercapacitors for efficient energy storage applications. These devices are believed to enhance both unique power and energy densities [12]. MIHSCs leverage the advantageous features of both battery-type and capacitive electrodes. This allows them to achieve a high energy density similar to batteries and a high power density comparable to supercapacitors [16]. A diverse array of metal oxide/hydroxide materials can unite to undermine the integrity of the material, exhibiting a shift in valence at different potentials, which is incorporated to enhance the efficiency of HSCs [34]. Different MIHSCs, including LIC and NHC, have distinct properties and performances [35]. Coating capacitor-type and active battery-type material for pseudocapacitive reactions is the standard format in which HSCs use more of what works well in the performance [36]. Batteries and supercapacitors are then integrated to achieve optimal performance in pseudocapacitive reactions, such as the features of battery-type material [37]. Bunker and his colleague's work on materials such as ZHSCs and PIHCs attempts to understand a battery that delivers optimal functionality [21,38]. Furthermore, researchers have created multivalent-ion HSCs to attain elevated energy and power densities [39]. MIHSCs constitute a significant advancement in energy storage technology that combines the benefits of batteries and supercapacitors. These devices utilize a range of metal ions and electrode materials to enhance power and energy density, making them a promising alternative for the future of energy storage.

MIHSCs integrate battery-type and capacitive electrodes to achieve high energy density, fast energy discharge, and extended lifespan [40]. The process of charging and discharging between the two electrodes exhibits significant differences. During the charging process, ions are stored in the electrolyte on the electrode's surface, forming an electric double layer in electrodes similar to supercapacitors [41]. For a battery-type electrode, ions are propelled into an electrode material via a redox process. The charging process of MIHSCs commences by applying a voltage to the device, enabling the ions in the electrolyte to propel themselves towards the electrode's surface through different methods. Electrons are generated via intermediary electrodes [42] or redox reactions [43]. Charging refers to the input of electric current retained within the device and availed during discharge. In this regard, discharging involves the removal of stored charge as the ions migrate back into the composition from the negatrode and positrode.

Consequently, a current is produced and can drive electrically driven devices [44]. The working principles of MIHSCs are the primary determinants of efficiency when measuring their performance. The device can produce a high power output and store a significant amount of charge throughout multiple life cycles due to the integration of supercapacitors and battery technologies [45]. The choice of electrodes, the electrolyte composition, and the charging approach determine the overall efficiency [12]. Highly appropriate charge–discharge operations are crucial to fully realizing sophisticated energy storage devices' energy storage and distribution functionalities. MIHSCs exploit capacitive and battery-type securities as electrodes; hence, they avail the merged properties of supercapacitors and batteries. Battery-type securities undertake redox responses, with capacitive securities acting as an electrochemical double layer or pseudocapacitors during charging and discharging, as demonstrated in Figure 1a,b. Therefore, when designing MIHSCs, ensuring security, including the battery, is essential [46,47].

Carbon-based zinc HSCs' energy storage and release mechanism involves multiple processes. The charge and discharge processes are enabled by the reversible deposition and removal of Zn/Zn^{2+} on the zinc metal electrode during charge and discharge, respectively (Equation (1)). However, the mechanism of the carbon negatrode is more complex. Some researchers believe that the Zn^{2+} ions' adsorption/desorption on the carbon surface is a critical component of the capacity (Equation (2)) [48,49]. In contrast, others propose that anions, such as sulfate ($SO_4{}^{2-}$), also play a substantial role in the energy storage process (Equation (3)) [50]. The behaviour of these negatively charged ions in the electric double layer is contingent upon the carbon material's operating voltage and zero charge potential. In addition to physical adsorption/desorption, chemical adsorption/desorption can occur, especially in carbon materials doped with heteroatoms such as oxygen and nitrogen. This leads to the generation of extra pseudocapacitance (Equations (4) and (5)) [51].

Zn positrode:

$$\mathrm{Zn}^{2+} + 2\mathrm{e}^- \leftrightarrow \mathrm{Zn}^{2+} \tag{1}$$

Carbon-based negatrode:

i. Process of physical adsorption or desorption

$$C + X^- \leftrightarrow C \parallel X^- \tag{2}$$

$$C + Zn^{2+} \leftrightarrow C \parallel Zn^{2+} \tag{3}$$

Here, C stands for the carbon, while X^- symbolizes the electrolyte anion.

ii. Process of chemical adsorption or desorption

$$C \cdots O + Zn^{2+}/H^+ + 2e^- \leftrightarrow C \cdots O \cdots Zn/C \cdots O \cdots H \tag{4}$$

$$N \cdots O + Zn^{2+}/H^+ + 2e^- \leftrightarrow N \cdots O \cdots Zn/C \cdots O \cdots H \tag{5}$$

Here, $C \cdots O$ represents oxygen-containing functional groups on the carbon material, while $N \cdots O$ denotes nitrogen-containing functional groups. These groups play roles in the chemical processes occurring on carbon-based electrodes.

Carbon-based MIHSCs have demonstrated exceptional performance, which promises to transform future energy storage. This technology exhibits a strong combination of high energy density, rapid charge–discharge rate, and excellent cycle life. It is a significant competitor in multiple industries, such as portable devices, electric cars, and renewable energy systems.

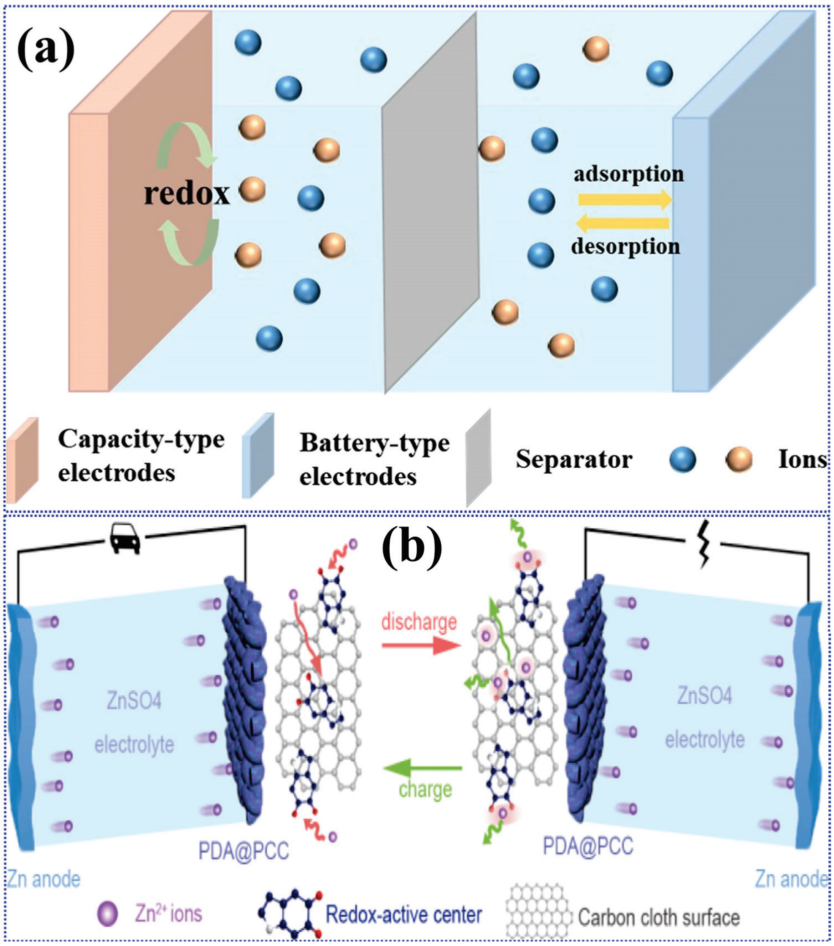

Figure 1. (**a**) A schematic representation for an MIHSC consisting of battery-type and capacitor-type electrodes. Reproduced with permission from Ref. [46]. Reproduced under the term CC BY 4.0. Copyright 2024, Fan et al., Springer Nature. (**b**) A specific charge–discharge demonstration of a ZIHSC using a carbon-based negatrode. Reproduced with permission from Ref. [47]. Copyright 2020, American Chemical Society.

3. Synthesis of BDC Materials for MIHSCs

Several essential techniques and aspects are involved in synthesizing BDC materials for MIHSCs to improve their electrochemical performance. Pyrolysis is the most commonly used technique for converting biomass into carbon materials at high temperatures without oxygen to produce porous carbon structures suitable for energy storage applications [52]. Hydrothermal carbonization is another critical technique for converting biomass into carbon at high temperatures and pressure in water, resulting in unique properties of carbon materials [53]. Template methods are also used to control the morphology and porosity of BDC materials, which involves sacrificing templates to form specific structuring in the synthesized materials [54]. Activation techniques, such as chemical or physical methods, are mainly used to increase the SSA and porosity of carbon compounds derived from biomass sources. While these alterations directly enhance the SSA and porosity, they also indirectly improve the electrochemical performance. This is because a larger surface area and enhanced porosity enable more efficient movement of ions and easier access to the electroactive sites. This can result in a noticeable improvement in conductivity during operation [55]. Alloying or doping bio-based carbons with heteroatoms such as nitrogen or phosphorus enhances conductivity and produces the appropriate materials for supercapacitors [56]. The porosity development of BDC materials is critical to maximizing energy storage capacity. Surface functionalization methods include surface chemistry modification for improved interaction with various electrolytes that contribute generously to the supercapacitors' electrochemical performance [57]. The performance qualities of bio-based carbons are influenced by their electrochemical properties, including capacitance and cyclic stability. These features are considered while choosing appropriate synthesis methods [58]. Figure 2a depicts the essential electrode materials for MIHSCs, with the electrolyte playing a critical role in charging the contact between the electrode and the electrolyte [59]. Research on electrode materials aims to enhance long-term charge propagation and stability in MIHSCs by optimizing pore size and distribution. Similarly, Figure 2b showcases a range of carbon-based materials employed in supercapacitive storage systems, highlighting their distinct attributes [60]. The synthesis of BDC materials for MIHSCs involves critical techniques, pyrolysis, hydrothermal carbonization, template methods, activation techniques, heteroatom doping, porosity development, surface functionalization, and other processes to ensure proper suitability for supercapacitors.

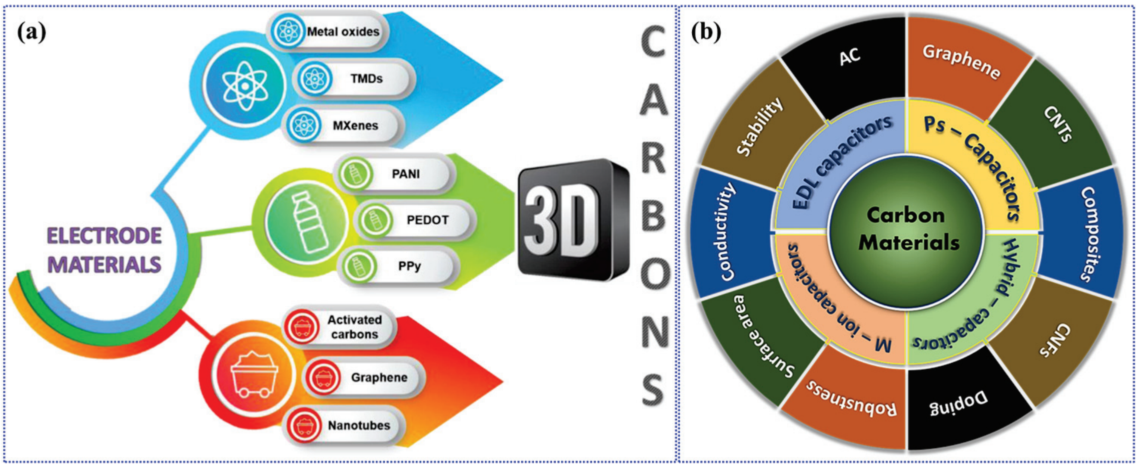

Figure 2. (**a**) Segmentation of electrode materials for MIHSCs. Reproduced with permission from Ref. [59]. Reproduced under the term CC BY 4.0. Copyright 2020, Galek et al., Frontiers. (**b**) Schematic representation for various carbon-based materials used as electrodes in different supercapacitive storage systems. Reproduced with permission from Ref. [60]. Reproduced under the term CC BY 4.0. Copyright 2022, Olabi et al., MDPI.

3.1. Synthesis of BDC Materials for ZIHSCs

BDC materials have attracted considerable interest because of their varied structural characteristics and possible uses in energy storage systems, particularly in synthesizing ZIHSCs. These materials offer renewability, sustainability, and cost-effectiveness advantages, making them attractive for various electrochemical applications [58,61]. BDC materials' structural diversity, porosity, and surface heteroatom doping have significantly impacted their performance in supercapacitors and other energy storage systems [61]. Additionally, synthesizing activated carbon (AC) from lignocellulosic biomass via chemical activation is promising for obtaining suitable precursors for energy storage applications [62]. Furthermore, incorporating self-doped heteroatoms in biomass-derived ACs has enhanced their electrochemical performance, laying a foundation for their supercapacitor application [63]. The potential of BDC materials in synthesizing ZIHSCs has been further supported by developing novel electrode materials and electrolytes. For instance, combining a zinc-activated positrode and a BDC negatrode has been explored, leading to the assembly of an aqueous ZIHSC with promising performance [16,64,65].

Moreover, using hydrogel electrolytes based on naturally abundant cellulose has been identified as an ideal approach for constructing flexible solid-state ZIHSCs, aligning with the principles of resource renewability and environmental sustainability [66]. Furthermore, the study of hollow mesoporous carbon spheres as electrode materials for symmetrical and aqueous ZIHSCs has shown promise for developing high-performance energy storage devices [67]. BDC materials provide a flexible foundation for creating electrode materials and electrolytes, which allows for the advancement of high-performance ZIHSCs. Due to their varied structure, ability to hold substances, the introduction of different elements on their surface, ability to be replenished, and ability to be maintained over time, these materials are appealing options for meeting the increasing need for effective energy storage solutions [68,69].

Samage et al. [70] explored the transformation of *Solanum melongena* (SM), an agro-waste, into a self-doped carbon material suitable for symmetric supercapacitors and ZIHSCs through a one-step pyrolysis process. Initially, the SM was washed to remove impurities, chopped into small pieces, and sun-dried before being crushed into a fine powder, as shown in Figure 3a. The pyrolysis process was carried out in a nitrogen atmosphere that does not react with the materials. The temperature was increased gradually at a rate of 5 °C per minute, reaching 700 °C, 800 °C, and 900 °C successively. The pyrolysis process lasted for a total of 3 h. After the pyrolysis process, the carbonized samples were subjected to a washing step using 0.5 M HCl. They were then rinsed with distilled water until the pH became neutral and dried at 80 °C for 12 h. The resulting SM-derived carbon (SMC) exhibited a three-dimensional porous structure with uneven flake-like shapes, with SMC-700 showing a more hydrophilic nature than SMC-800 and SMC-900. Surface morphology examined through FESEM revealed the formation of porous structures at 700 °C and 800 °C, while 900 °C samples showed pore structure collapsing due to aggregated carbon, which undergoes a process where it transforms into thick layers resembling flakes. The nitrogen sorption isotherms revealed that SMC-800 had a significant SSA of 686.29 m^2/g, mainly attributed to micropores and mesopores, resulting in a high porosity. The iron content in the precursor was used strategically for graphitization, converting amorphous carbon into graphitic nanostructures during pyrolysis.

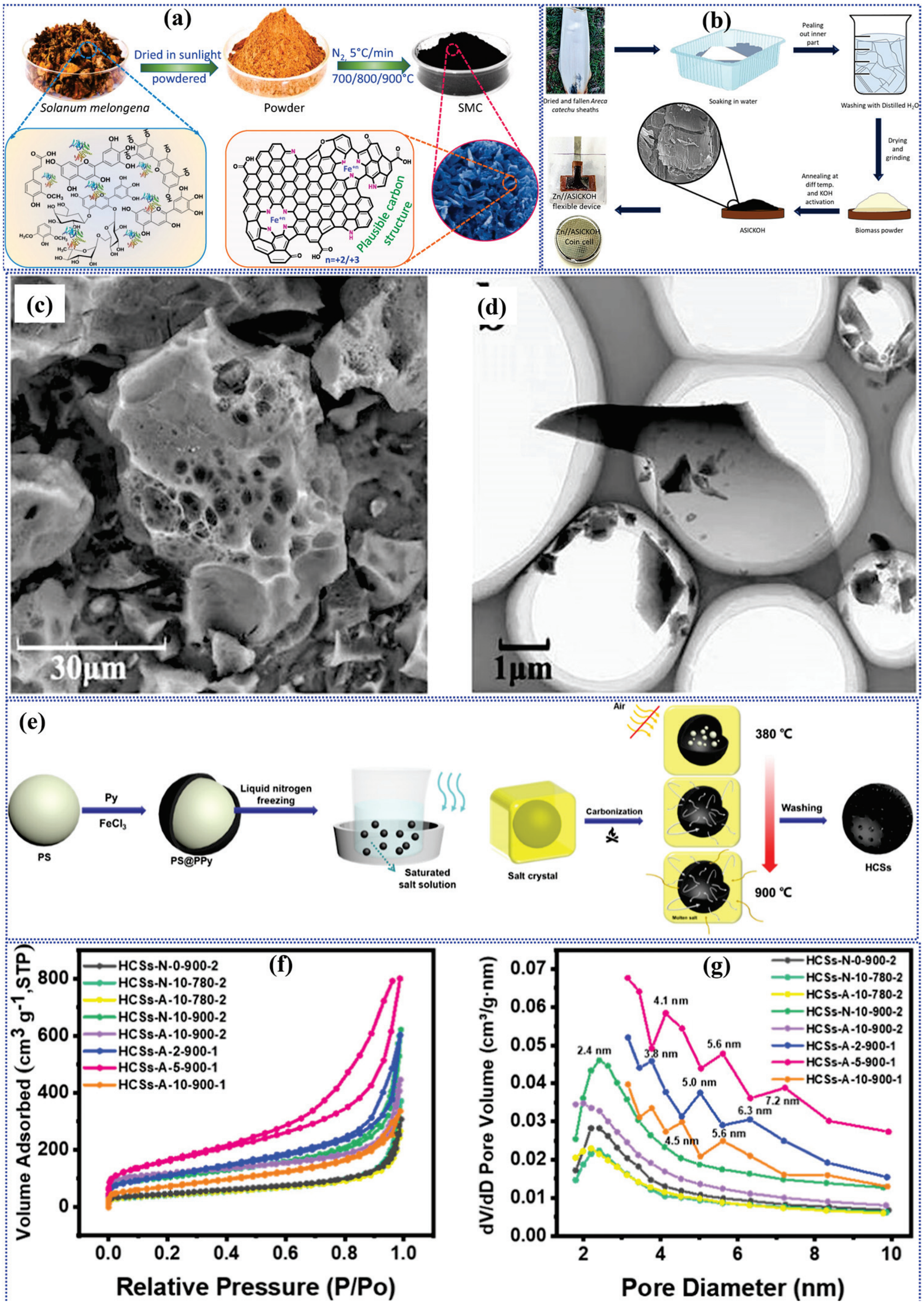

Figure 3. (**a**) A diagram illustrating the process of preparing the self-doped SMC. Reproduced with permission from Ref. [70]. Copyright 2024, Elsevier. (**b**) Diagram showing the process for synthesizing an AC from Areca Catechu sheaths, along with its application in ZIHSCs in coin and pouch cell formats. Reproduced with permission from Ref. [71]. Copyright 2022, American Chemical Society. (**c**) FESEM and (**d**) TEM micrographs of the N/S-AC. Reproduced with permission from Ref. [72]. Copyright 2023, American Chemical Society. (**e**) Diagram illustrating the process of preparing HCS. (**f**) Nitrogen adsorption/desorption isotherms and (**g**) pore size distribution of the HCSs under different circumstances. Reproduced with permission from Ref. [73]. Copyright 2024, American Chemical Society.

Naik et al. [71] investigated the production of high-performance flexible ZIHSCs using carbon sheets produced from agricultural waste. The carbon material is derived from *Areca Catechu sheaths*, an abundant agricultural waste, through a multi-step process. As demonstrated in Figure 3b, the synthesis begins with collecting dried sheaths from a local farm, washing them, and soaking them in water to remove the inner part. After peeling, the inner section is dehydrated, pulverized into a fine powder, and subjected to annealing in a tubular furnace at temperatures between 700 and 900 °C for 3 h while exposed to a nitrogen flow. Post-carbonization, the carbon materials undergo a washing procedure using a solution of 1 M HCl and a mixture of ethanol and water. Subsequently, they are dried at 80 °C for one night. The carbon obtained at a temperature of 900 °C exhibited superior performance and was subsequently subjected to KOH activation, leading to KOH-AC formation. The carbon compounds demonstrate a significant SSA, with KOH-AC boasting a value of 2760 m^2/g. The enhanced SSA and reduced pore diameter in KOH-AC contribute to its improved electrochemical performance.

Lignin, a significant biomass constituent, produces nitrogen and sulfur co-doped hierarchical porous carbon (N/S-AC) materials for high-performance ZIHSCs [72]. The preparation entails a dual-phase procedure: charring and activation using co-doping. The process involves combining lignin with urea and thiourea to provide nitrogen and sulfur, subjecting the mixture to carbonization at a temperature of 750 °C. As a result, nitrogen and sulfur co-doped activated carbon is formed. The materials possess a hierarchical pore structure, which is essential for offering active sites with a high SSA and an appropriate distribution of pore sizes. The FESEM image (Figure 3c) reveals that the N/S-AC has micrometre-sized particles with a porous structure, while TEM analysis (Figure 3d) confirms an interconnected porous nature. The BET SSA for the N/S-AC material is estimated at 2773.02 m^2/g, demonstrating significant porosity. Additionally, the doped heteroatoms contribute to adjusting the pore structure and increasing surface wettability, providing enhanced conductivity and pseudocapacitance, making them ideal for high-performance ZIHSCs.

Zhao et al. [73] proposed a sustainable technique for producing hierarchically porous hollow carbon spheres (HCSs) as negatrode materials in ZIHSCs. The procedure entails the pyrolysis of polystyrene–polypyrrole nanoparticles within a sodium chloride confinement, as shown in Figure 3e. This synthesis is performed in a single vessel, in the presence of air, eliminating the requirement to use inert gas to protect the reaction. The HCSs obtained display a hierarchical pore structure with a significant SSA of 578.2 m^2/g. They are also doped with 2.6 at.% oxygen and 5.6 at.% of nitrogen. Figure 3f,g display the N_2 adsorption/desorption isotherms and the related pore size distribution of the HCSs under different circumstances. The carbon spheres' form and structure remain intact throughout the pyrolysis process, and their porous nature enhances their electrochemical properties. Du et al. [74] proposed a technique for creating a two-dimensional (2D) porous carbon matrix co-doped with nitrogen and oxygen. This matrix is synthesized using biomass generated from yeast cell walls. The synthesis involves a molten salt method, where yeast cell walls are mixed with a urea solution, freeze-dried to form precursors, and heated at 800 °C in an air atmosphere with NaCl and KCl. The resulting material exhibits a 2D lamellar structure, with its porous nature further enhanced by the urea decomposition, which introduces micro- and mesopores into the carbon matrix. The material, known as NAC-20, possesses a significant SSA of 368.63 m^2/g. It is composed of a carbon structure that has been co-doped with nitrogen (6.03%) and oxygen (9.96%). This co-doping enhances the material's electrical conductivity and wettability. Several BDCs have been synthesized and utilized in ZIHSC configurations. Biomass-based nitrogen–oxygen co-doped carbons have exhibited high SSAs, heteroatom doping, and porous morphologies contributing to the performance of these electrodes. Their characteristic properties and performance capabilities, including morphology and SSA, are listed in Table 1. Thus, it is clear from the literature that biomass-based carbons with improved morphologies, porous structures, and enhanced SSAs were addressed to permit effective ZIHSCs. The hierarchical pores and substantial heteroatom doping of catalytic zinc ions may improve these devices' specific capacitance, energy, cyclability, and power.

3.2. Synthesis of BDC Materials for NIHSCs

BDC materials have attracted considerable interest for their possible use in NIHSCs due to their capacity to be renewed, their sustainability, and their cost-effectiveness [23,75,76]. These materials have been investigated as potential electrode materials for high-energy NIHSCs, showing promising electrochemical performance [23]. BDC materials' inherent structural benefits, cost-effectiveness, and renewability make them highly appealing for sodium-ion energy storage systems [76]. Moreover, introducing heteroatoms into BDC materials increases the interlayer distance, enhancing the efficiency of transporting and storing sodium ions. As a result, sodium-ion batteries exhibit exceptional performance at high rates [61]. The synthesis of BDC materials has been a subject of interest, with research focusing on tailoring their structure to enhance their performance in NIHSCs. For instance, hierarchically porous carbon derived from shiitake mushrooms has been investigated for capacitive energy storage, demonstrating the potential for BDC materials in energy storage applications [77].

Furthermore, the favourable tubular composition of BDC has been identified as a possible positrode option for sodium-ion batteries, thanks to its abundant availability, affordable price, and sustainable nature [78]. In addition, there have been new developments in energy storage using NIHSCs and ZIHSCs, revealing the potential of biomass-derived materials to meet energy storage requirements [18]. BDC materials show significant potential for NIHSCs, providing a viable and economical option for energy storage applications. These materials' diverse structure and electrochemical activity, combined with continuing research on their synthesis and performance improvement, make them viable contenders for meeting the increasing need for effective sodium-ion energy storage solutions.

The research works by Niu et al. [79] mainly focused on synthesizing two types of BDC materials using gelatine and phytic acid as precursors, as demonstrated in Figure 4a. The synthesis was carried out using sustainable concepts, including non-toxic precursors, which are readily available, low in cost, and ecologically friendly processes. The synthesis also included the utilization of physisorption, nanostructure engineering, and heteroatom doping, particularly phosphorus and nitrogen, to enhance the efficiency of carbon materials. P- and N-doped networked carbon nanosheets with hierarchical porosity were formed. They exhibited porous nanosheet networks synthesized directly by KCl/ice as a dual template or KOH for microporosity. The materials illustrated several morphologic features, such as nanosheet networks and a high SSA, essential for their application as electrodes in NIHSCs. Guo et al. [80] investigated the sustainable fabrication of dual (N, O)-doped biocarbon nanosheets from marine biomass. As described in Figure 4b, the direct pyrolysis of cuttlebones, along with the air oxidation activation approach, allows for a precise decrease in the thickness of carbon sheets from 35 to 5 nm. Consequently, this leads to the formation of a distinct hierarchical porous structure characterized by enhanced SSA and porosity and an increase in N-doping content from 7.5% to 13.9% at the atomic level. The controlled N-doping content of the nanosheets was independently monitored by the new role of air oxidation activation in regulating heteroatom content in the carbon matrix, ensuring novel biocarbon nanosheets with significant nitrogen and oxygen doping in the carbon matrix. The dual-doped structure provides improved conductivity and additional charge storage.

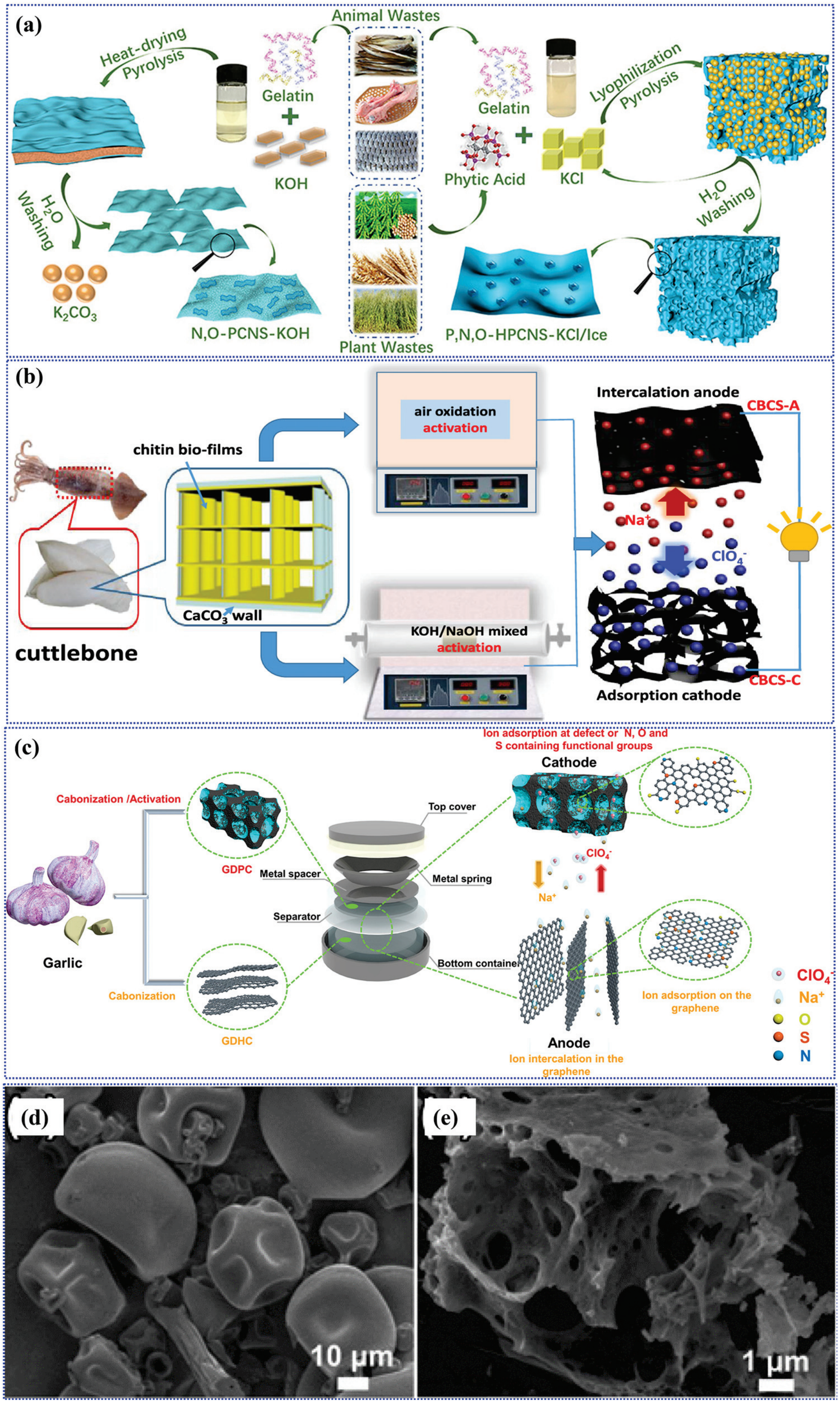

Figure 4. (**a**) A diagram illustrating the synthesis of interconnected carbon nanosheets with hierarchical porosity, incorporating phosphorus (P) and nitrogen (N) dopants. This synthesis involves dual KCl templates and ice (P, N-HPCNS-KCl/Ice). Reproduced with permission from Ref. [79]. Copyright 2020, American Chemical Society. (**b**) The diagram illustrates the synthesis process of the material and the corresponding charge storage processes at the positrode and negatrode in a NIHSC. Reproduced

with permission from Ref. [80]. Copyright 2018, American Chemical Society. (**c**) A scheme outlining the GDHC and GDPC preparation process and the mechanisms underlying sodium-ion storage in NIHSCs. Reproduced with permission from Ref. [81]. Copyright 2019, American Chemical Society. (**d**,**e**) FESEM micrographs of the PCNS at different magnifications. Reproduced with permission from Ref. [82]. Copyright 2020, Elsevier.

Liu et al. [81] examined a NIHSC made from carbon compounds obtained from garlic. The synthesis (Figure 4c) involves two methods: high-temperature pyrolysis at 1100 °C to create a durable carbon positrode, referred to as GDHC, and carbonization tailored by KOH activation to generate a porous carbon negatrode, referred to as GDPC. The GDHC positrode demonstrates a pseudo-graphitic arrangement characterized by an interlayer distance ranging from 0.365 to 0.376 nm. Conversely, GDPC possesses a highly permeable structure, with an SSA measuring 1682 m^2/g. The carbon material structure is assessed using scanning electron microscopy, which identifies the block-like morphology of GDHC and the porous structure of GDPC. In addition, XRD and Raman spectra provide evidence of a well-organized structure and the presence of graphite. Zhang et al. [82] studied fabricating a three-dimensional porous carbon nanosheet (PCNS) utilizing soy protein and zinc nitrate. The synthesis involves using a chemical gas expansion approach followed by calcination to produce a three-dimensional PCNS material doped with nitrogen and sulfur. The resulting PCNS has a hierarchical porous structure characterized by a significant abundance of micropores and mesopores, as revealed in Figure 4d,e. The PCNS exhibits an SSA of ~516.6 m^2/g. The carbon compounds exhibit an interlayer spacing of 0.385 nm, surpassing that of graphite. This higher spacing aids in the process of Na^+ intercalation and deintercalation. The result showcases a distinctive linked structure of carbon nanosheets, which offer abundant pathways for ion transport and improve its ability to store salt. Zhang et al. [83] examined the production of rigid carbon material from lotus stems. The synthesis entails subjecting the lotus stems to carbonization at several temperatures, namely 1200, 1400, and 1600 °C. The resultant materials, LS1200, LS1400, and LS1600, maintain a porous structure with a hierarchical channel array inherited from the lotus stems. FESEM and TEM investigations demonstrate that greater carbonization temperatures result in an elevated graphitization degree and a decreased tube wall thickness. The materials exhibit d_{002} spacings of 3.69 Å, 3.68 Å, and 3.61 Å, corresponding to LS1200, LS1400, and LS1600, respectively. These values indicate different levels of graphitic ordering. The carbons have a relatively low SSA ranging from 23.73 to 25.81 m^2/g. This SSA gradually decreases as the carbonization temperature increases. Several more carbon materials generated from biomass, characterized by their unique shapes, porous architectures, and large SSA, have greatly improved the efficiency of NIHSCs. The presence of a distinct microstructure, which includes both hierarchical porosity and doped structures, enables enhanced ion transport and charge storage capabilities. These supercapacitors have remarkable electrochemical properties, including a high capacitance, energy density, power density, and great cycle stability. All of these factors are thoroughly presented in Table 1.

3.3. Synthesis of BDC Materials for AIHSCs

BDC materials are considered promising options for developing AIHSCs because of their capacity to be renewed, their sustainability, and their environmentally beneficial characteristics [61,84]. These materials provide a viable and long-lasting option for storing energy, in line with the ideals of using renewable resources and promoting environmental sustainability. BDC materials' structural diversities and synthesis methods have been demonstrated to significantly enhance their performance in supercapacitors [61,84]. An example is using a nitrogen-doped carbon nanofiber network obtained from biomass as a template to decorate ultrathin nickel–cobalt-layered double hydroxide nanosheets [52]. This demonstrates the high performance of the nanosheets as an electrode for an asymmetric supercapacitor [25]. Furthermore, using biomass straw-derived porous carbon to produce supercapacitors through ball milling has attracted interest because of its renewable nature, abundant availability, affordability, and positive environmental impact [85]. Moreover, researchers have investigated the various structural variations in BDC materials for their potential uses in energy storage, focusing on the significance of their porous nature and the introduction of heteroatoms on their surfaces [61]. The synthesis methods of BDC materials are a subject of interest, with research focusing on tailoring their structure to enhance their performance in AIHSCs. These materials' renewable and eco-friendly characteristics and their wide range of structures make them appealing for meeting energy storage requirements, especially in AIHSCs. Using BDC materials in AIHSCs has significant potential for creating long-lasting and effective energy storage solutions. BDC materials provide a sustainable and cost-effective framework for creating AIHSCs. Their structural diversity and capacity to be renewed make them excellent options for meeting the increasing need for efficient energy storage solutions.

The research reported by Feng et al. [86] presents a sustainable and solvent-free technique for producing polymer spheres using m-phenylenediamine and hexamethylenetetramine (HMTA), with Pluronic F127 serving as a guiding agent for the structure, as demonstrated in Figure 5a. The combination is subjected to a temperature of 160 °C, initiating the polymerization process of MPF resin spheres. Subsequently, these spheres are subjected to a temperature of 600 °C, converting them into porous carbon spheres (PCSs). The PCSs possess a significant SSA of 3115 m^2/g and a 3.05 cm^3/g pore volume. The FESEM study (Figure 5b,c) reveals that the resin spheres maintain a spherical shape throughout the activation and carbonization techniques. Figure 5d displays the solid-state 13C NMR spectrum, which reveals a peak at 18 ppm for methyl and methylene. The 70, 73, and 75 ppm peaks show bonding between carbon and oxygen. A series of distinct peaks (104, 113, 129, and 147 ppm) associated with different carbon environments in the benzene ring are produced by the chemical shift over 100 ppm. Figure 5e displays the FTIR spectra of MPF resin spheres, revealing aromatic, methylene, amino, and hydroxyl functional groups. The FTIR data corroborate the atomic structure of the MPF resin. According to NMR and FTIR investigations, the m-phenylenediamine and formaldehyde derived from the breakdown of HMTA polymerize almost entirely; full polymerization results in volumetric productivity and ultrahigh yield. The carbon material obtained has a hierarchical structure containing micropores and mesopores, making it well suited for energy storage.

Seon et al. [87] examined the production of AIHSCs that incorporate a battery-like aluminium positrode with a capacitor-like graphene negatrode. They employed an ionic liquid, namely 1-ethyl-3-methylimidazolium chloride (EMImCl), and aluminium chloride ($AlCl_3$) as the electrolyte. The investigation is focused on two surface treatment approaches, electropolishing and electrodeposition, to improve the electrochemical performance of the aluminium positrode. The aluminium positrode, formed by electrodeposition on a molybdenum foil substrate, has a dendritic structure and a significant SSA. The presence of roughness and dendritic development improves the electrochemical activity of the material, resulting in higher efficiency in storing Al^{3+} ions. The XPS and GIXRD analysis reveals a reduction in the thickness of oxide layers and the presence of Al–OH species, which contribute to the formation of redox-active sites.

Lei et al. [88] reported the development and production of AIHSCs with a nitrogen-doped graphene negatrode, aluminium positrode, and [EMIm]Cl and $AlCl_3$ electrolyte with high capacitance. A layer of nitrogen-doped graphene was applied to a tantalum foil, creating a flexible negatrode with a nitrogen concentration of 3–5% by weight. Doping alters the arrangement of energy levels in the band structure, amplifies the ability of graphene to conduct electricity, and boosts its ability to store electrical charge. The FESEM study revealed crumpled graphene layers stacked on each other, resulting in a large SSA that facilitates electrochemical reactions. Sun et al. [89] presented using a nitrogen-doped micro-mesoporous carbon sphere (NCS) as a negatrode material in aluminium-based HSCs. The NCS was produced by combining phenolic resin with melamine in a 1:1 mass ratio, followed by carbonization at 600 °C in nitrogen. Subsequently, the carbon precursor was mixed with KOH and heated at 800 °C, forming a porous configuration. The SESEM study indicated the presence of round particles with sizes ranging from 0.1 to 1 µm. TEM demonstrated that these particles have an amorphous structure. The NCS has a BET SSA of 3078 m^2/g, considerably greater than the 506 m^2/g of the NC precursor containing nitrogen. This difference allows for more adsorption sites and facilitates more efficient ion diffusion.

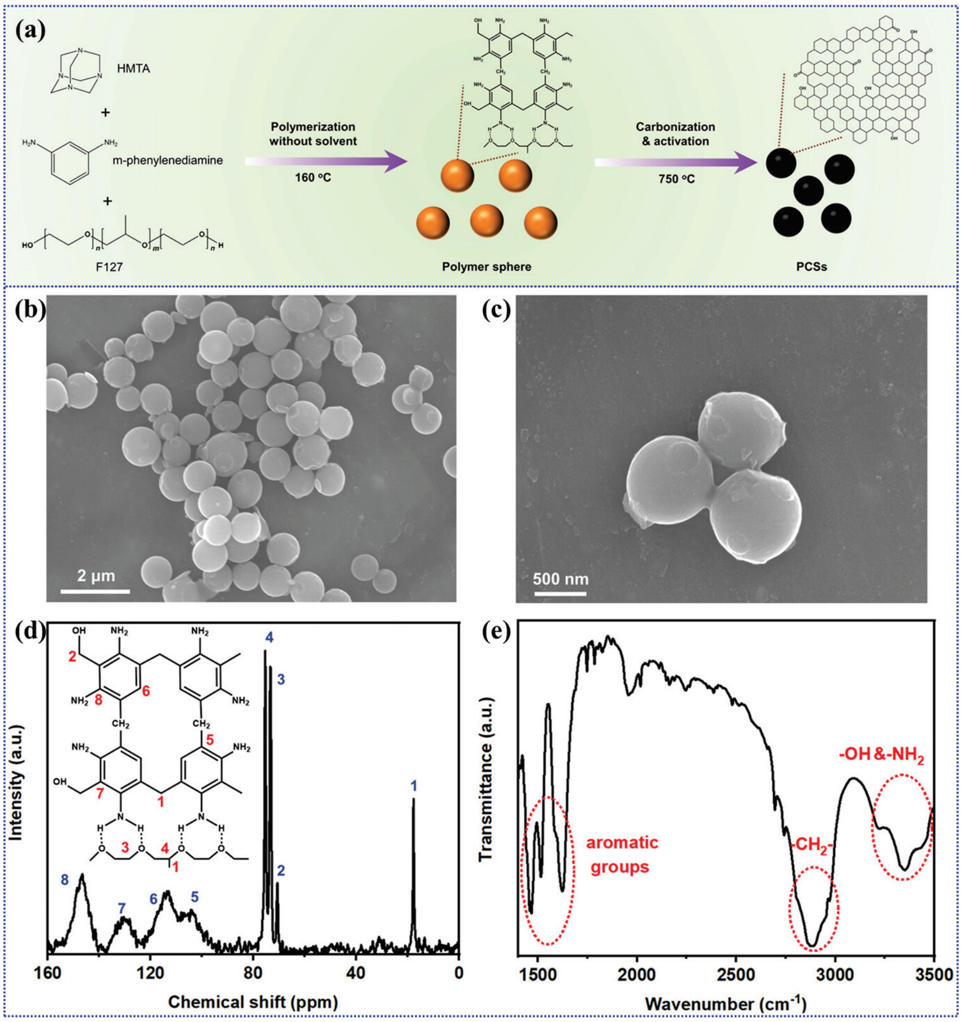

Figure 5. (**a**) The solvent-free synthesis method for MPF polymer spheres and PCSs is illustrated schematically. Morphological and structural characterization of MPF resin spheres; (**b**) low- and (**c**) high-magnification FESEM micrographs; (**d**) solid-state 13C NMR spectrum; and (**e**) FTIR spectrum. Reproduced with permission from Ref. [86]. Copyright 2023, Wiley.

Optimizing the synthesis parameters during the carbon generation from biomass is essential for improving the efficiency of AIHSCs. BDC materials provide a sustainable and environmentally friendly option for producing electrodes, including distinctive structures that may be fine-tuned to achieve exceptional electrochemical capabilities. Research emphasizes the importance of various parameters, including SSA, porosity, nitrogen doping, and the existence of electrochemically active metals in carbons generated from biomass [90–92]. These properties can all be affected by the procedure used for synthesis. Researchers may customize the characteristics of BDCs for supercapacitor applications by precisely controlling culture conditions, nutrient concentrations, and activation methods. This enables them to attain a high specific capacitance, exceptional cycle stability, and enhanced energy storage capacities. Various essential parameters for producing BDCs for AIHSCs are tabulated in Table 1.

3.4. Synthesis of BDC Materials for KIHSCs

BDC materials have garnered considerable attention in the field of KIHSCs due to their renewable nature, sustainability, and promise for efficient energy storage applications [93,94]. These materials offer a sustainable and cost-effective energy storage alternative, aligning with resource renewability and environmental sustainability principles. BDC materials' synthesis processes and structural design have been demonstrated to be significantly improved [93–95]. An example is the deliberate arrangement of well-distributed, extremely thin MoS_2 nanosheets within a hollow carbon structure, showing rapid potassium storage. This emphasizes the promise of BDC materials in KIHSCs [96]. Furthermore, the recent advancements and prospects of biomass-derived hierarchically porous carbon have been examined, focusing on the significance of developing and fabricating these materials for supercapacitor applications, specifically KIHSCs [94]. Using BDC materials in KIHSCs has significant potential for creating sustainable and highly effective energy storage solutions. The SSA, distribution of pore sizes, and ultimate electrochemical performance of the carbon materials are determined by the type of biomass precursor used and the activation processes employed. This emphasizes the significance of synthesis methods in customizing the properties of these materials for KIHSCs. Moreover, the recent advancements in creating and using hybrid electrodes made from biomass have given us valuable knowledge about the electrochemical properties of these materials and the ways they store ions in various types of batteries, such as potassium-ion batteries. This highlights the potential of BDC materials in KIHSCs [97]. BDC materials offer a sustainable and cost-effective platform for developing KIHSCs, with their structural diversity and renewability positioning them as valuable candidates for addressing the increasing need for effective energy storage technologies.

Graphene-like AC nanosheets and hard carbon (HC), two different carbon compounds made from almond shells, were synthesized according to Pham et al. [98]. The production of the HC involves a straightforward carbonization procedure at various temperatures, whereas the AC is generated by chemically activating it with KOH as the activating agent. An analysis of the structural properties of the materials shows that the hard carbon has a notable distance between its layers, which is advantageous for the process of potassium-ion (de)intercalation. The AC nanosheets possess a high SSA and an intricate porous structure. These observations, along with the analysis of the structure and chemistry, suggest that both HC and AC possess qualities that make them appropriate for storing potassium ions. A schematic representation for the dual-carbon KIHSCs using carbon nanosheet negatrodes derived from biomass and similar to graphene is shown in Figure 6a. Chen et al. [99] presented an innovative "plains–hills" model of carbon structure for producing electrode materials inspired by a lotus leaf's surface structure. This design comprises ultrathin carbon nanosheets, also known as "plains", which are formed with multiple lumps, referred to as "hills", (Figure 6b) using a one-step pyrolysis method. The synthesis entails utilizing $CaCl_2$ as a dual-purpose compound, complexing agent, and oxygen scavenger in a Ca^{2+}-bio gel, as demonstrated in Figure 6c. This structure integrates an unstacked nanosheet with different levels of imperfections, achieving a harmonious balance between pseudocapacitance and conductivity. The carbon materials obtained exhibit a balanced combination of high pseudocapacitance and conductivity. They have an SSA of 581 m^2/g and a drop in oxygen doping from 24.9% to 12.3%. This reduction contributes to the presence of both ordered and amorphous carbon structures.

Huang et al. [100] outlined a single-step calcination technique for converting mango seed husk into BDC doped with nitrogen and oxygen (NOHC). This material is intended to be a positrode KIHSC. The NOHC materials that have been synthesized exhibit a significant level of graphitization, with interlayer spacings that vary between 0.39 and 0.38 nm in correlation with increasing temperature. The materials demonstrate a BET SSA of up to

489.4 m^2/g, suggesting a porous structure advantageous for capacitive charge storage. A combination of rod- and sheet-like structures characterizes the shape of the NOHC. Doped nitrogen and oxygen are included to enhance the electronic conductivity and create active spots.

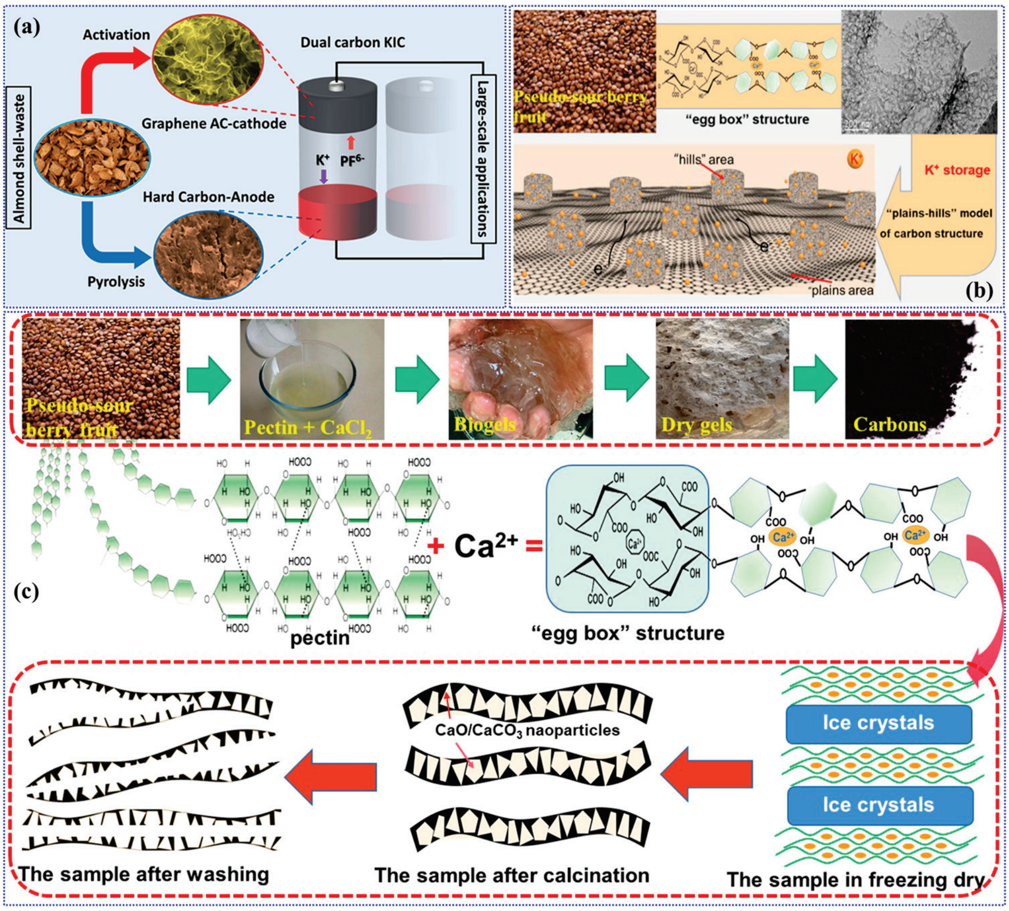

Figure 6. (**a**) Dual-carbon KIHSCs using carbon nanosheet negatrodes derived from biomass and similar to graphene. Reproduced with permission from Ref. [98]. Copyright 2020, American Chemical Society. (**b**) A graphical representation for the K^+-ion storage in BDC materials. (**c**) A graphical depiction of the CACF samples' synthesis protocol. Reproduced with permission from Ref. [99]. Copyright 2021, American Chemical Society.

Developing efficient synthesis techniques for carbon produced from biomass is crucial in determining the optimal performance of HSCs that use potassium ions. Supercapacitors have attracted significant attention because of their remarkable power density, long cycle life, and ecologically sustainable characteristics. However, the properties of the carbon compounds used as the electrode material significantly impact the device's performance. BDC is an ideal substitute for carbon since it is naturally abundant, inexpensive, and environmentally friendly. The synthesis techniques used to produce carbon, such as carbonization and activation processes, significantly impact its structure and other properties, thus affecting the performance of supercapacitors. The optimization of KIHSCs can be influenced by various parameters, as indicated in Table 1. The criteria encompass SSA, pore size distribution, surface functional groups, electrical conductivity, and other aspects, such as element content, which will be elaborated on later. Scientists can customize the carbon material by optimizing the synthesis technique to improve its capacitive behaviour, ion transport kinetics, and other energy-related characteristics. Thus, to enhance the above procedures, researchers can utilize several precursors and employ varied carbonization temperatures, activation methods, and post-treatment strategies.

Table 1. Synthetic protocols for preparing BDC materials in high-performance MIHSCs.

Biomass Source	Carbon Preparation Protocols	Morphology	SSA (m^2/g)	Ref.
Solanum melongena	Pyrolysis; 700, 800, and 900 °C; N_2 gas	Irregular flake-like 3D porous structure	574.34, 686.29, and 239.16	[70]
Areca Catechu sheaths	Pyrolysis; KOH activation; 900 °C; N_2 gas	Porous nanosheet	2760	[71]
Lignin	Pyrolysis; KOH activation; 750 °C; N_2 gas	Particles with a porous structure	2773.02	[72]
Salt crystals	Carbonization; $FeCl_3$ activation; 900 °C; N_2 gas	Hierarchically porous hollow spheres	578.2	[73]
Recycled yeast cell wall	Carbonization, NaCl/KCl activation, 800 °C; air	2D lamellar structure	368.63	[74]
Ipomoea carnea leaves	Carbonized; KOH activation; 900 °C; N_2 gas	Transparent spheres	736.7	[101]
Resorcinol–furfural resin	Carbonization, KOH activation, 900 °C, N_2 gas	3D hierarchical porous structure	1350	[102]
Anhydrous glucose	Pyrolysis; magnesium oxide and potassium bicarbonate activation; 750 °C; Ar gas	3D honeycomb-like structure with interconnected pores	2265	[103]
Sodium lignosulfonate	Carbonization; KOH activation; 900 °C; N_2 gas	Hierarchical porous structure	2460	[104]
Tannin	Pyrolysis; 800 °C; N_2 gas	Hierarchical micro- and mesoporous structure	967	[105]
Pine needles	Carbonization; KOH activation; 800 °C; Ar gas	Microporous structures with interconnected pores and channels	2493.4	[106]
Zeolitic imidazolate framework	Carbonization; thiourea mixing; 800 °C; Ar gas	Cubic porous structure	677.2	[107]
Fallen autumn leaves	Carbonization; KOH activation; 950 °C; N_2 gas	Amorphous and porous structures, with minor graphitic flakes	2114	[108]
Osmanthus flowers	Freeze drying; carbonization; 800 °C; Ar gas	Foamy-like structure with hierarchical pores	690.3	[109]
Aerial roots of Ficus macrocarpa	Pyrolysis; $KHCO_3$ activation; 900 °C; N_2 gas	Hierarchical porous nanosheet structure	1454.7	[110]
Gelatine/phytic acid	Pyrolysis; KOH/$KHCO_3$ activation; 900 °C; N_2 gas	Ultrathin and small nanosheets	1911	[79]
Marine biomass	Carbonization; 600 °C; N_2 gas	Porous nanosheets	1489	[80]
Garlic	Pyrolysis; KOH activation; 1100 °C; N_2 gas	Blocky morphology	1682	[81]
Soy protein	Pyrolysis; zinc nitrate activation; 700 °C; Ar gas	Hierarchical porous structure with abundant micropores and mesopores	516.6	[82]
Lotus stems	Carbonization; 1200, 1400, and 1600 °C; Ar gas	Turbostratic graphitic structure	25.81, 24.37, and 23.73	[83]
Apricot shell	Pyrolysis; 900, 1100, 1300, and 1500 °C; H_2/Ar atmosphere	Porous structure with well-connected porous network	2.7 to 56.7	[111]
Mango peels	Carbonization; sulfur and hexamethylenetetramine mixing; 1000 °C/800 °C; Ar gas	Porous flake-like morphology	1079.88	[112]

Table 1. *Cont.*

Biomass Source	Carbon Preparation Protocols	Morphology	SSA (m^2/g)	Ref.
Agricultural wastes, specifically peanut shell, wheat straw, rice straw, corn stalk, cotton stalk, and soybean stalk	Hydrothermal reaction with H_2SO_4 aqueous solution and subsequent chemical activation with KOH at 800 °C; Ar atmosphere	Porous sheet structure with interconnected macropores, mesopores, and micropores	534.3 to 1994.2	[113]
Cassava peel	Pre-carbonization 350 °C; KOH activation at 600 °C; Ar atmosphere	Slit-type pores and a highly disordered structure	1032	[114]
Corn silk	Pre-carbonization at 350 °C; KOH activation; carbonization at 800 °C; Ar atmosphere	Microporous nanosheets	2550	[115]
Sugarcane bagasse	$NaH_2PO_2{\cdot}2H_2O$ and melamine dispersion; hydrothermal reaction at 180 °C for 24 h; KOH activation; carbonization; 700 °C; Ar atmosphere	3D interconnected hierarchical porous structure	2803.2	[116]
m-phenylenediamine-formaldehyde resin	Carbonization; KOH activation; 750 °C; Ar atmosphere	Spherical morphology	3115	[86]
Graphene	...	Nanosheets	2675	[87]
Nitrogen-doped graphene derived from a synthetic approach	...	Wrinkled and overlapping morphology with a few layers	...	[88]
Phenol resin and melamine	Pre-carbonized at 600 °C; KOH activation at 800 °C; N_2 environment	Spherical particles	3078	[89]
Almond shells	Carbonization; KOH activation; 1100 °C; N_2 environment	Sheetlike nanostructures	127	[98]
Sour berry fruits	Freeze drying, $CaCl_2$ curing; bio gel and dry gel production; acid treatment	Nanoflakes	581	[99]
Mango seed shuck	Carbonization; 900, 1100, and 1300 °C; Ar atmosphere	Rod- or sheet-shaped feature	489.4, 383.2, and 319.1	[100]
Petroleum pitch	Pyrolysis; $KHCO_3$ activation; 800 °C; inert atmosphere	Cross-linked nanosheets	48.8	[117]
Gpositroderma lucidum spores	Carbonization at 850 °C; mixing with diethylene triamine and ammonium molybdate tetrahydrate; hydrothermal reaction at 200 °C; pyrolysis at 850 °C; N_2 atmosphere	Porous cage-like structure with double walls and a 3D network of interconnected carbon structures	217	[118]
Potato	Two-step carbonization; pre-pyrolysed at 500 °C; carbonization at various temperatures (900 °C, 1000 °C, and 1100 °C); Ar atmosphere	Mesoporous	620.77, 531.67, and 325.73	[119]
Hemp stalk core	Carbonization; 800 °C; N_2 atmosphere	Honeycomb-like structure	1185.3	[120]
Walnut septum	Pyrolysis; urea activation, 800 °C; N_2 atmosphere	Tubular cellular structure	176.9	[121]

4. Application of BDCs in MIHSCs

Carbon materials derived from biomass have emerged as potential candidates for MIHSCs, especially in the case of zinc and other moieties, namely sodium, potassium, and AIHSCs. This approach is attractive, as using such precursors would be sustainable and relatively cheaper than other biomass-based energy storage materials. Carbon materials can be prepared from biomass using pyrolysis, hydrothermal carbonization, or activation methods to obtain porous carbons with desired properties as a supercapacitor electrode [105,122,123]. Since the initiation of research on MIHSCs, scientists have investigated many types of electrode materials [124]. Figure 7a illustrates the configuration of these capacitors, emphasizing the primary materials employed for electrodes. The positrode materials are classified into various groups, including carbon-based materials, titanium-based compounds, niobium pentoxide (Nb_2O_5), and other transition metal compounds such as molybdenum, tungsten, and vanadium. Scientists have also employed various methods to customize and optimize the active substances to improve the rate capability, prolong the lifespan, and increase the capacity of the capacitors, as shown in Figure 7b. The following discussion will explore the progress in developing practical positrode materials, organized by their respective types. Among various MIHSCs, biomass-based carbon materials are most commonly used in ZIHSCs. Prior research has demonstrated that using carbon derived from biomass can enhance the energy storage capacity of ZIHSCs, resulting in improved gravimetric and volumetric energy density [21,76,125]. Hierarchical carbon structures prepared from biomass have mainly been effective in increasing the energy storage of ZIHSCs. Moreover, the nitrogen doping of biomass-originated carbon can facilitate the performance of potassium supercapacitors, thus suggesting new possibilities for the applications of advanced energy storage solutions. Additionally, sodium and AIHSC applications have been investigated using BDC materials. These materials enabled relatively high energy storage for the sodium battery to develop a sustainable energy storage solution. Biomass-originated carbons are still being studied in AIHSCs to improve energy retention performance and energy density without volume expansion, as previously reported in the field. The possible designs and study suggest a sustainable and flexible approach to MIHSCs using biomass-based carbon material.

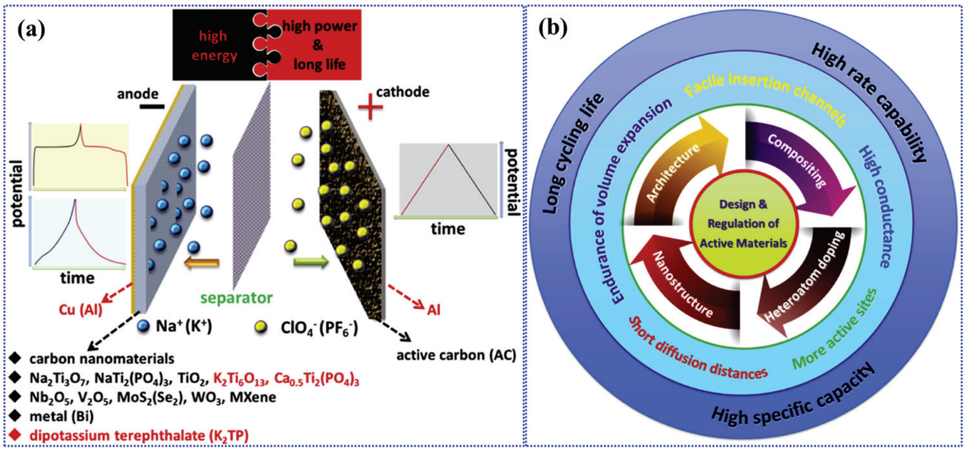

Figure 7. (**a**) Structural diagram of an MIHSC, illustrating the key components and materials. (**b**) Illustration of various strategies employed in designing and optimizing electrode materials for enhanced performance. Reproduced with permission from Ref. [124]. Copyright 2019, Elsevier.

The overall performance of MIHSCs is substantially influenced by the interaction of electrolyte volume, electrode mass, and surface area, which are essential considerations. The electrolyte volume impacts the quantity of charge that may be stored, where a smaller volume may result in a greater energy density [126]. MIHSCs can increase the device's energy density by reducing the electrolyte's total volume. In addition, selecting electrolytes such as water-in-salt electrolytes can significantly impact the performance of these supercapacitors [127]. The mass of the electrode is a crucial factor affecting MIHSCs' performance. High capacitance, cycle life, and operating voltage require optimal electrode mass ratios [128]. The electrode material's mass directly impacts the MIHSCs' charge storage capacity, affecting energy density [128]. In addition, the electrode material should possess a high surface area relative to its volume or mass to improve its performance [129]. The electrochemical performance of MIHSCs is significantly influenced by surface area. Maximizing the electrochemical double-layer capacitance and pseudocapacitance requires a large surface area for the electrodes, which leads to enhanced performance [130]. BDCs with mesopores are preferred for MIHSCs because of their expansive specific surface area and appropriate distribution of pore sizes, which enhance their overall performance. Additionally, it is essential to develop electrode materials that possess significant active surface areas and facilitate rapid ion transfer to attain superior energy density and rate capability in supercapacitors. Overall, the performance of MIHSCs is influenced by the synergistic interaction of electrolyte volume, electrode mass, and surface area. By optimizing these characteristics, it is possible to improve the energy density, power density, and cycling stability of these sophisticated energy storage devices.

4.1. ZIHSCs

BDC materials are considered suitable candidates for optimizing the performance of ZIHSCs. BDC materials are recognized for their ability to have a regulated microstructure with a large SSA. Due to their environmentally benign nature, they are considered a desirable choice for creating energy storage systems [131]. In this case, the application of BDC materials in ZIHSCs is addressed to assess the opportunity to improve the power capability of these supercapacitors. Porous carbon compounds derived from biomass are commonly recognized as superior electrodes for charge storage devices, such as supercapacitors, owing to their affordability and resilience. These materials have proven to be highly efficient in tackling energy storage and conversion challenges [23,132].

Consequently, implementing BDC materials in ZHSCs is aligned with the sustainable strategy. It provides a direction for one of the various commercial implementations to develop high-efficiency energy storage systems. Additionally, the negatrode material for ZIHSCs is critical to the carbon-based material's structural characteristics and electrochemical performance. Recent research analysed the influence of carbon materials, including AC, N-doped AC, graphene oxide, and carbon nanotube, on the development of ZIHSCs, focusing on the role of carbon materials in high-efficiency and -power functionality [133,134]. By incorporating the unique qualities offered by BDC materials, particularly the large SSA and regulated porosity, enhancing the energy density and power density of ZIHSCs is necessary to assure the practicality of high-power applications. This type of development collaborates with high-performance ZIHSCs for the marketable implementation of zinc-ion batteries due to the opportunity to provide high-efficiency, sustainable energy storage systems.

The ZIHSCs were created using the SMC as the negatrode, commercial zinc foil as the positrode, and a 2 M $ZnSO_4 \cdot 7H_2O$ solution as the electrolyte, with a Whatman filter paper as the separator, as shown in Figure 8a [70]. The electrochemical studies indicated the potential for energy storage applications. The specific capacitance, energy, and power for SMC-800-based ZIHSCs were 313.08 F/g, 141.35 Wh/kg, and 6935.38 W/kg, respectively. The ZIHSC devices exhibited excellent cyclic stability, losing only 1.92% over 20,000 GCD cycles at 4 A/g. The symmetric supercapacitors fabricated using produced carbon samples with 6 M KOH delivered high specific capacitance, with SMC-800 achieving the best performance. The symmetric supercapacitor with SMC-800 demonstrated a high specific capacitance of 154.64 F/g at 0.1 A/g and excellent stability with over 99% retention after 50,000 GCD cycles at 10 A/g. These results suggest that the developed BDC materials suit high-performance energy storage applications in ZIHSCs. The flexible ZIHSC was fabricated with KOH-AC as the positrode electrode and metallic zinc as the negatrode [71]. The positrode in the coin cell format was formed by depositing the active material slurry onto a pre-cut titanium foil using drop-casting, followed by drying in an oven. The electrolyte employed was a zinc sulfate solution with a concentration of 1 Molar. The ZIHSC with the KOH-AC positrode exhibited a notable specific capacitance, reaching 208 F/g at a current density of 0.1 A/g. Additionally, it demonstrated exceptional rate capability, maintaining 84.5% of its capacitance after undergoing 10,000 cycles at a 5 A/g current density. Figure 8b displays the CV curves of ZIHSC utilizing Areca catechu sheath-derived AC, together with the background information, which includes a digital image of the sandwich-type pouch cell architecture. A laser-scribed carbon pattern on a polyimide sheet was used as the current collector for both the positrode and negatrode in order to create a flexible pouch cell. This design showcased excellent flexibility and stability when subjected to mechanical stress. Under bending conditions, the flexible device exhibits an energy density of 32.6 $\mu Wh/cm^2$ and a high power density of ~2 W/cm^2. The electrochemical tests suggest that BDC sheets derived from agricultural waste show great potential for high-performance ZIHSCs, providing both sustainability and cost-effectiveness in energy storage applications.

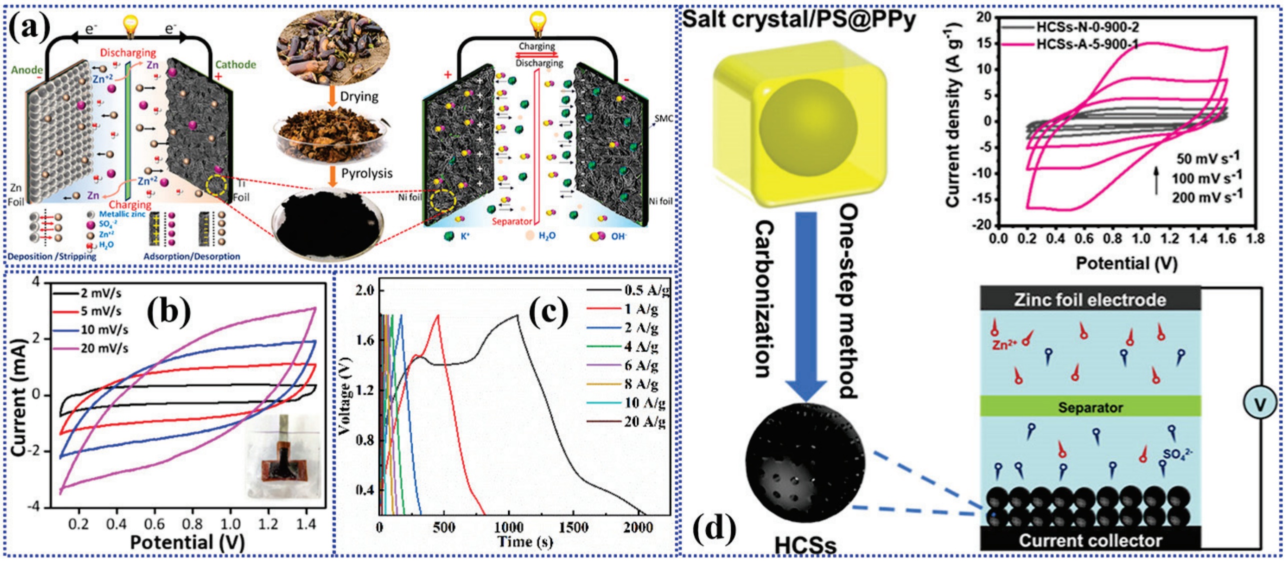

Figure 8. (**a**) The diagram illustrates the process of creating a ZIHSC utilizing SMC as the positrode. Reproduced with permission from Ref. [70]. Copyright 2024, Elsevier. (**b**) CV curves of ZIHSC using Areca catechu sheath-derived AC; the background includes a digital image of the sandwich-type pouch cell configuration. Reproduced with permission from Ref. [71]. Copyright 2022, American Chemical Society. (**c**) The GCD profiles of the N/S-AC-based ZIHSC at various current densities. Reproduced with permission from Ref. [72]. Copyright 2023, American Chemical Society. (**d**) Schematic representation of the HCSs' synthesis and their electrochemical performance in ZIHSCs. Reproduced with permission from Ref. [73]. Copyright 2024, American Chemical Society.

The synthesized N/S-AC materials were used to fabricate the ZIHSC with a carbon negatrode and zinc foil positrode, employing 2 M $ZnSO_4$ aqueous electrolyte [72]. The electrochemical results (Figure 8c) designate that the specific capacitance for the N/S-AC-based ZIHSCs reached 307 F/g at 0.5 A/g, demonstrating an excellent capacity retention of 99.72% after 20,000 cycles at 10 A/g. The achieved energy density was 108.8 Wh/kg, whereas the achieved power density was 115,200 W/kg. The exceptional electrochemical capabilities of this material can be attributed to the combined effects of nitrogen and sulfur doping, as well as the hierarchical porous structure. Moreover, the manufacturing procedure enables the creation of a significant quantity of BDC materials, demonstrating the capacity of these materials for creating high-performance ZIHSCs on a wide scale.

Zhao et al. [73] created ZIHSCs by using the manufactured HCSs as negative electrodes, zinc foil as the positrode, and a 2 M $ZnSO_4$ electrolyte, as shown in Figure 8d. The ZISCs based on HCSs-A-5-900-1 had a specific capacitance of 108 F/g at a current density of 0.2 A/g. They also had an energy density of 26.2 Wh/kg and a power density of 140.1 W/kg. In addition, the supercapacitors demonstrated remarkable cycling stability, maintaining 65% of their capacity after undergoing 5000 cycles. The ZIHSCs exhibited a significant capacitive-controlled storage level, contributing to their exceptional electrochemical performance. The hierarchical porosity and doping levels of the HCSs are essential factors that significantly contribute to their performance, rendering these carbon materials highly favourable for energy storage applications. Du et al. [74] demonstrated the electrochemical performance of the synthesized carbon matrix by constructing ZIHSCs using NAC-20 as the negatrode, zinc flakes as the positrode, and a 2 M $ZnSO_4$ electrolyte. The ZIHSCs showed a capacitance of 191.1 F/g at 0.5 A/g, a stable cycle life of over 10,000 cycles, and a 103% capacity retention. Additionally, these supercapacitors achieved an energy density of 37 Wh/kg at a power density of 91 W/kg. Combining a high SSA, porous structure, and heteroatom doping contributes to this remarkable performance, allowing ZIHSCs assembled with NAC-20 to store energy effectively and light up a red LED for nearly 5 min, demonstrating their practical application. Several different BDCs have been used as electrodes in ZIHSCs, significantly increasing their performance. Nitrogen–oxygen co-doped carbon obtained from yeast cell walls and other feedstock demonstrated exceptional electrochemical characteristics. There has been a notable increase in interest in electrochemical energy storage in recent years, with a specific emphasis on ZIHSCs. These investigations have been conducted to explore the use of BDC materials. These materials are valued for their sustainability, cost-effectiveness, and ecologically favourable properties. These materials have shown great potential in improving the electrochemical performance of ZIHSCs through several methods, such as maximizing surface area, porosity, and electrical conductivity [134–141]. Various studies have examined ZIHSCs using BDCs derived from hemp biomass [142], glutinous rice [143], platanus achene fruits [144], pyrolytic carbon black and critical PANI [145], metal organic frameworks (MOFs) [146,147], carp scales [148], green cokes [149], bamboo [150,151], rice husk [152], heavy fraction of bio-oil [153], yeast [154], by-product of traditional Chinese medicine [155], wood [156], lignin [157,158], corncob cellulose [159], heavy bio-oil [160], and sugarcane [161]. The wide variety of BDCs, each with their own unique structure and electrochemical properties, has played a significant role in the progress of ZIHSCs. Their utilization has resulted in significant enhancements in performance indicators, including specific capacitance, energy density, power density, and cycling stability, establishing their position in the future of sustainable energy storage technologies. Several important performance metrics from the experimental results of these carbonaceous materials are presented in Table 2, revealing their ability to drive ZIHSCs to the next level.

4.2. NIHSCs

BDC materials have emerged as potential materials for enhancing the efficiency of NIHSCs in recent years. BDC materials are affordable and eco-friendly alternatives that are extensively used to improve the efficiency of SIHSCs. Moreover, these materials possess other distinctive characteristics compared to conventional carbon, such as large interlayer spaces, disorderly carbon structures, and more active functional groups that ensure better charge storage than conventional carbon [94,162]. The commercial potential of BDC materials in supercapacitors arises from the diverse structure and superior properties of these materials. They fit the supercapacitor performance property and tailored structure. It is feasible to enhance the energy density, power density, and cycling stability of BDC materials used in supercapacitors. Therefore, their commercial potential in the commercial sector plays a natural role in producing sodium-ion batteries for industrial applications. Their eco-friendly nature and sources, coupled with their versatile high-performance structure moulded by nature, make BDCs promising candidates for sustainable energy storage in the sodium-ion battery industry [76]. The progress in research on BDC materials for sodium-ion energy storage devices indicates their potential for innovation and collaborative development in supercapacitors.

Table 2. A summary of electrochemical performance for the BDC materials in high-performance MIHSCs.

Positrode	Negatrode	Electrolyte	HSC Type	Specific Capacitance (F/g) @ Current Density (A/g)	Energy Density (Wh/kg) @ Power Density (W/kg)	Capacitance Retention (% @ No. of Cycles)	Ref.
SMC	Zn foil	2 M $ZnSO_4{\cdot}7H_2O$	ZIHSC	313.08 @ 0.1	141.35 @ 6935.38	99 @ 50,000	[70]
KOH-AC	Zn foil	1 M $ZnSO_4$	ZIHSC	208 @ 0.1	52 @ 1906.4	84.5 @ 10,000	[71]
N/S-AC	Zn foil	2 M $ZnSO_4$	ZIHSC	307 @ 0.5	108.8 @ 115,200	99.72 @ 20,000	[72]
HCSs	Zn foil	2 M $ZnSO_4$	ZIHSC	108.7 @ 0.2	26.2 @ 140.1	65 @ 5000	[73]
NAC	Zin sheet	2 M $ZnSO_4$	ZIHSC	191.1 @ 0.5	37 @ 91	103 @ 10,000	[74]
ICF	Zn foil	1 M $ZnSO_4/MnSO_4$	ZIHSC	168 @ 1	39.7 @ 9000	79.5 @ 5000	[101]
Porous carbon	Zn foil	2 M $ZnSO_4$	ZIHSC	291 @ 0.1	79 @ 391	96 @ 50,000	[102]
HHPC	Zn foil	2 M $ZnSO_4$	ZIHSC	147 mAh/g @ 0.2	117.6 @ 160	88 @ 20,000	[103]
LHPC	Zinc metal	1 M $ZnSO_4$	ZIHSC	298 @ 0.1	135 @ 101	97 @ 8000	[104]
TOMC	Zn foil	2 M $ZnSO_4$	ZIHSC	331.2 @ 0.2	148.9 @ 180	85.7 @ 10,000	[105]
PNMNC	Zn foil	1 M $ZnSO_4$	ZIHSC	472.5 @ 0.1	39.7 @ 9000	97.1 @ 10,000	[106]
S, N-CNC	Zn foil	2 M $ZnSO_4$	ZIHSC	331 @ 1	148.9 @ 900	70 @ 10,000	[107]
AC650	Zn foil	2 M $ZnSO_4$	ZIHSC	95 @ 0.1	86 @ 210	73 @ 10,000	[108]
NPFC700	Zn foil	1 M $Zn(CF_3SO_3)_2$	ZIHSC	207.9 @ 0.1	85.7 @ 15.4	97.4 @ 20,000	[109]
FHPCNSs-800	Zn foil	2 M $ZnSO_4$	ZIHSC	220.1 mAh/g @ 0.2	181.6 @ 165	100 @ 30,000	[110]
P,N-HPCNS-KCl/Ice	HPCB-KOH	1 M $NaClO_4$	NIHSC	119 mAh/g @ 0.035	135.3 @ 30	88.6 @ 8000	[79]
CBCS-A3	CBCS-C	1 M $NaClO_4$	NIHSC	640 mAh/g @ 0.1	36,000 @ 53,000	90.5 @ 8000	[80]
GDHC	GDPC	1 M $NaClO_4$	NIHSC	260 mAh/g @ 0.05	156 @ 355	73 @ 10,000	[81]
PCN	HPC	1 M $NaClO_4$	NIHSC	205 mAh/g @ 0.5	119 @ 200	82 @ 8000	[82]
LS1400	Sodium foil	1 M $NaClO_4$	NIHSC	350 mAh/g @ 0.1	. . .	94 @ 450	[83]
HASH	HASH	1 M $NaClO_4$	NIHSC	400 mAh/g @ 0.1	. . .	91.7, 500	[111]
NS-MPC	Na-metal foil	1 M $NaClO_4$	NIHSC	765 mAh/g @ 0.1	. . .	52 @ 2500	[112]
BDC	$Na_2Ti_{2.97}Nb_{0.03}O_7$	1 M $NaClO_4$	NIHSC	60.5 @ 0.2	169.4 @ 120.5	83.8 @ 500	[113]
CAC	CAC	1 M $NaClO_4$	NIHSC	247 @ 0.5	160 @ 425	100 @ 10,000	[114]
CSC	CSC	1 M $NaClO_4$	NIHSC	126 @ 0.3	116 @ 1560	68 @ 300	[115]
SBNPK	SBNPK	1 M $NaClO_4$	NIHSC	356.4 @ 1	6.5 @ 251.9	96.5 @ 20,000	[116]
PCSs	Al foil	$EMIMAlCl_4$ (1-ethyl-3-methylimidazolium tetrachloroaluminate)	AIHSC	200 mAh/g @ 0.100	220 @ 900	80 @ 1500	[86]
Graphene	Al foil	EMImCl and $AlCl_3$	AIHSC	211 @ 3	51 @ 3390	87 @ 5000	[87]
Nitrogen-doped graphene	Al foil	EMImCl and $AlCl_3$	AIHSC	240 @ 0.1	. . .	90 @ 2000	[88]
NCS	Al foil	EMImCl and $AlCl_3$	AIHSC	224 mAh/g @ 0.3	. . .	100 @ 35,000	[89]
AS-AC	AS-HC	1 M KPF_6	KIHSC	88 @ 0.053	105 @ 250	96 @ 10,000	[98]
CACF	CACF	1 M potassium bis(fluorosulfonyl)imide (KFSI)	KIHSC	350 mAh/g @ 0.1	178.4 @ 1115	75.2 @ 10,000	[99]
NOHC	Hard carbon	0.8 M KPF_6	KIHSC	186.3 mAh/g @ 0.1	68 @ 2000	80 @ 1000	[100]
ACNs	SCNs	0.8 M KPF_6	KIHSC	89.1 @ 0.1	124.0 @ 198.9	89.4 2 @ 9000	[117]
NOBC	Potassium disk	1 M KPF_6	KIHSC	251.2 mAh/g @ 0.5	. . .	77.74 @ 2000	[118]
PBPC	Potassium metal	3 M potassium bis(fluoro-slufonyl)imide (KFSI)	KIHSC	248 mAh/g @ 0.1	. . .	87.5 @ 400	[119]
N-CHC	N-CHC	1 M KPF_6	KIHSC	42.4 mAh/g @ 0.3	27.36 @ 203.4	91 @ 600	[120]
NHPC	NHPC	0.8 M KPF_6	KIHSC	263.6 mAh/g @ 0.1	. . .	84 @ 1000	[121]

Marine-biomass-derived porous carbon nanosheets (CBCS-A3) served as the positrodes in NIHSCs [80]. As demonstrated in Figure 9a, the CBCS-A3 positrode showed an outstanding capacity of 640 mAh/g at 0.1 A/g, and it showed state-of-the-art Na^+ storage performance, which is very close to the same performance of lithium-ion storage in similar materials. Furthermore, devices showed high cycling retention, retaining 270 mAh/g and 138 mAh/g after ten thousand cycles at 2 A/g and 10 A/g, respectively. The NIHSCs which used a CBCS-A3 positrode and a CBC-C negatrode displayed an excellent combination of energy–power densities at 5 A/g, 36 Wh/kg at 53,000 W/kg, and retained 90.5% capacitance retention after 8000 cycles. This research demonstrates the applicability of BDC materials for enhanced Na-ion storage and extensive energy. Niu et al. [79] obtained carbon materials from biomass and implemented them as electrode materials in NIHSCs. Specifically, the P- and N-doped and N-doped BDCs acted as the negatrode and positrode, respectively. The supercapacitors demonstrated excellent electrochemical performance, as demonstrated by the GCD profiles in Figure 9b,c, combining a high energy density (135.3 Wh/kg) with high power density (16.1 kW/kg), and outstanding long-term stability, retaining 88.6% of the initial capacity even after 8000 cycles. These results can be explained by the unique structural features of carbon materials, comprising hierarchical porosity and heteroatom doping. These features enabled the supercapacitors to maintain excellent kinetic compatibility between the negatrode and positrode. Therefore, utilizing carbon materials obtained from renewable biomass sources in sophisticated energy systems is extremely advantageous because of their sustainable production and exceptional electrochemical capabilities. A NIHSC was made using a GDHC positrode and a GDPC negatrode, with the electrodes having a 1:1 mass ratio [81]. The developed NIHSC performed excellently in a wide (4 V) operating potential window, as shown in Figure 9d. The capacitor has an energy density range of 31 to 156 Wh/kg and a power density range of 355 to 38,910 W/kg. In addition, the capacitor exhibits remarkable cycling stability (Figure 9e), maintaining 73% of its original capacity after undergoing 10,000 cycles at a 30 A/g current density. The capacitance decline shown in Figure 9e is mainly ascribed to the interconnected phenomena that affect the electrochemical performance and durability of the electrode materials in NIHSCs. One of the most important factors is the creation and continuous development of the Solid Electrolyte Interface (SEI). Although initially advantageous in stabilizing electrochemical reactions at the interface, the passivating layer can gradually thicken and lose conductivity, hindering ion movement and causing capacity degradation. Simultaneously, the electrode material undergoes mechanical degradation due to the stress caused by volumetric changes during ion insertion and extraction. This degradation leads to the loss of electrical contact and active material from the structure of the electrode. In addition, the frequent insertion of ions can lead to the blockage of pores and the formation of a protective layer on the electrodes, resulting in a significant decrease in the accessible surface area for ion storage and a reduction in the overall capacitance. The decline is worsened by the decomposition of electrolytes, which results in the creation of non-conductive deposits on the surfaces of electrodes, further impeding the movement of ions. The combined impacts lead to a gradual decrease in the capacitor's capacity to hold charge. This requires sophisticated material designs and engineering techniques to improve the strength of the structure, optimize the interaction between the electrolyte and electrode, and maintain consistent electrochemical performance over long periods of use. It is essential to tackle these problems to enhance the longevity and effectiveness of sodium-ion capacitors in real-world use. The electrochemical performance of the NIHSC showcases the potential of carbon materials derived from biomass in the advancement of sustainable and high-performance energy storage systems. This study focuses on the synthesis technique of carbon materials and their efficient utilization in developing high-performance NIHSCs.

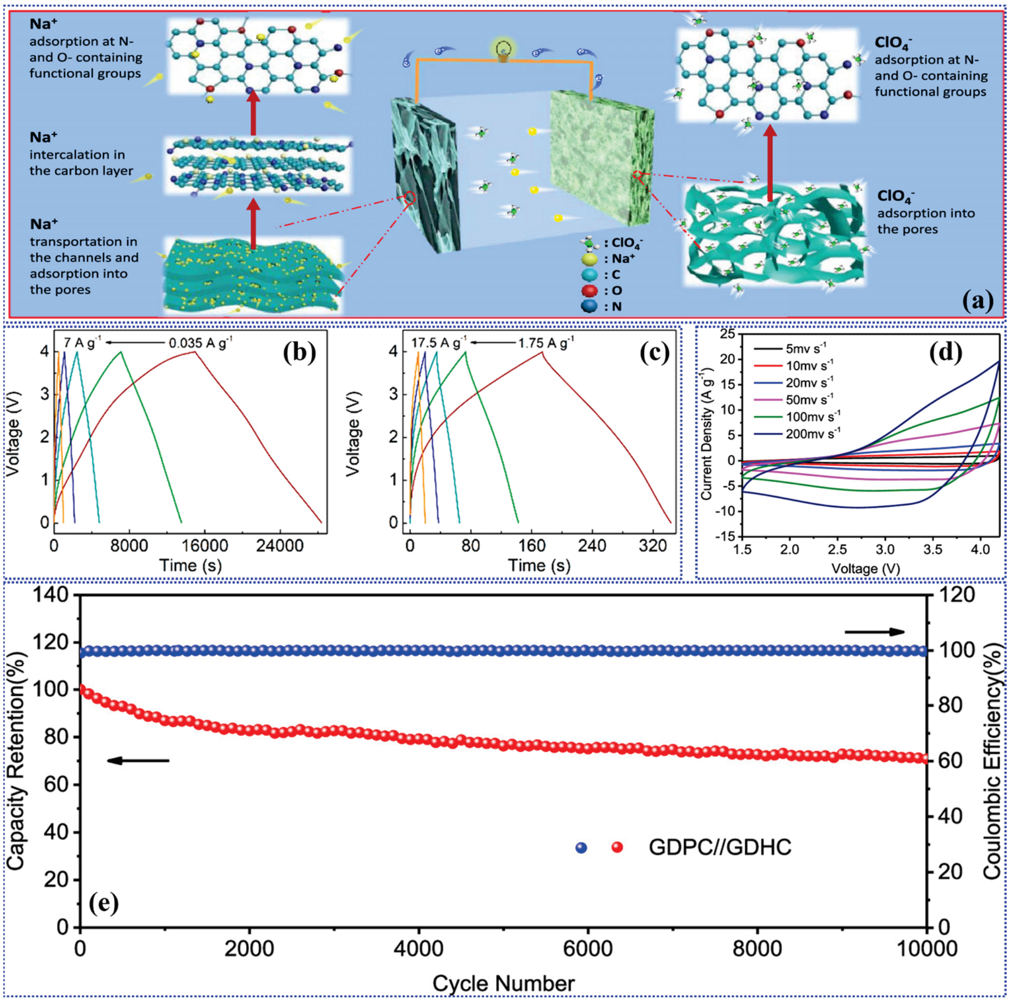

Figure 9. (**a**) Schematic depiction of the charge storage techniques employed in the NIHSC. Reproduced with permission from Ref. [80]. Copyright 2018, American Chemical Society. (**b**,**c**) GCD profiles at different current densities for the BDC-based NIHSC. Reproduced with permission from Ref. [79]. Copyright 2020, American Chemical Society. (**d**) CV curves at various scan rates and (**e**) cyclic stability and Coulombic efficiency for 10,000 GCD cycles of the GDPC//GDHC NIHSC. Reproduced with permission from Ref. [81]. Copyright 2019, American Chemical Society.

The PCNS functions as the positrode in NIHSCs in conjunction with a negatrode made of hierarchically porous carbon with capacitive properties [82]. The supercapacitor exhibits an energy density of 119 Wh/kg when subjected to a power density of 200 W/kg and a lower energy density of 53 Wh/kg when subjected to a higher power density of 20 kW/kg. Furthermore, it maintains 82% of its capacity after undergoing 8000 cycles at a current density of 5 A/g, demonstrating exceptional cycling stability. The outstanding performance of these devices may be due to the synergistic coupling of a battery-type positrode and a capacitive-type negatrode, which leads to a device with high energy and power density. This work highlights the capacity of carbon materials obtained from biomass to be used in sodium-ion storage systems that are both sustainable and high-performing. The created carbon compounds were evaluated as positrodes in NIHSCs [83]. When exposed to a current density of 100 mA/g, the LS1400 material exhibits a substantial reversible 350 mAh/g capacity. Additionally, it exhibits a plateau capacity of 250 mAh/g, indicating its possible suitability as a material for positrodes. The material has remarkable cycling stability, retaining 94% of its initial capacity after surviving 450 cycles at a current density of 100 mA/g. The EIS analysis showed that LS1400 has a lower charge transfer resistance and improved Na^+ diffusion kinetics compared to LS1200 and LS1600. The sodium storage method entails the adsorption of Na^+ ions in regions with imperfections, the insertion of Na^+ ions between graphite layers, and the deposition of Na metal in confined pores [163]. The LS1400 version exhibits a significant proportion of closed pores, considerably enhancing its plateau capacity. This study highlights the ability of hard carbons derived from lotus stems to serve as high-performance positrode materials for nonaqueous NIHSCs. Several alternative carbon compounds from biomass have been used as electrodes in NIHSCs, showcasing their capability in advanced energy storage technologies [164–168]. These materials, obtained from natural sources including lotus stems, marine biomass, and other plant-based precursors, display various shapes, layered porosity, and doping characteristics that enhance their exceptional electrochemical capabilities. The progress in SIHSCs has received significant attention in recent years due to their promise as affordable and environmentally friendly energy storage options [78,79,169–172]. As a result of this interest, several studies have been conducted on utilizing BDC materials obtained from various biomasses. These studies aim to exploit these materials' renewable, environmentally benign, and economically advantageous properties. These materials have demonstrated considerable potential in enhancing the electrochemical efficiency of SIHSCs by optimizing variables such as the specific surface area, porosity, and electrical conductivity [173,174]. Several types of biomasses, including carrageenan [175], jute [176], cork [177], sodium lauryl sulfate/PANI [178], peanut shell [179], MOFs [180], sucrose [181], spring onion [182], rice husk [183], wheat bran [184], and recycled olive pits [185], have been documented as suitable sources for synthesizing BDCs for SIHSCs. The wide variety of carbon compounds obtained from biomass and their specific structural and electrochemical properties have played a crucial role in the progress in SIHSCs. Their utilization has resulted in significant enhancements in performance indicators, including the specific capacitance, energy density, power density, and cycling stability, consequently reinforcing their position in the future of sustainable energy storage solutions. Their performance, including important factors such as capacitance, cycle stability, and energy and power density, is outlined in Table 2.

4.3. AIHSCs

BDC materials have proven to be a capable solution to boost the AIHSCs' performance. These materials, which are well known for their sustainability and low cost, have remarkably supported the efficiency of AIHSCs. The unique characteristics of BDC, including hierarchical porous structures, nitrogen doping, and high SSAs, facilitate excellent charge storage and improved electrochemical performance of AIHSCs [186]. The materials used in BDC have shown exceptional energy density, power density, and cycling stability. This makes them very appropriate for commercial application in aluminium-ion batteries for AIHSCs [187]. The application of BDC materials in AIHSCs is commercially applicable due to their structural flexibility and excellent electrochemical characteristics. The technology, therefore, comes with customization design and performance qualities required for high-performance supercapacitors. BDC materials help to improve the overall performance and efficiency of AIHSCs, making them commercially viable in the aluminium-ion battery industry. The materials' contributions are based on their renewable, abundant, and non-toxic nature and adjustable features. These qualities make them highly suitable for sustainable energy storage solutions in the aluminium-ion battery industry [187]. The existing research and applications regarding BDC for aluminium-ion energy storage solutions can potentially drive real-world applications and innovation in high-performance energy systems.

Feng et al. [86] reported an AIHSC composed of a PCS negatrode, an aluminium positrode, and an ionic liquid electrolyte called $EMIMAlCl_4$. The AIHSC device and its accompanying electrochemical performances are depicted Figure 10a–h. The PCS negatrode, utilizing a double-layer capacitive process, demonstrates a consistent and reliable charge storage mechanism. It has a specific capacity of around 200 milliampere-hours per gram at a current density of 100 milliamperes per gram. The device's electrochemical performance is characterized by quasi-rectangular cyclic voltammetry profiles, which indicate its capacitive nature. The PCS negatrode exhibits remarkable rate capabilities, maintaining approximately 80% capacity retention even at a current density of 2500 mA/g. Extended cycling investigations have demonstrated that the material's capacity reaches 150 mAh/g after undergoing 1500 cycles at a current density of 2000 mA/g. At a temperature of 50 °C, the supercapacitor achieves an energy density of 220 Wh/kg and a power density of 9 kW/kg, outperforming other aluminium-based energy storage devices in terms of both energy and power capabilities. Additionally, it has a lifespan of over 1000 cycles.

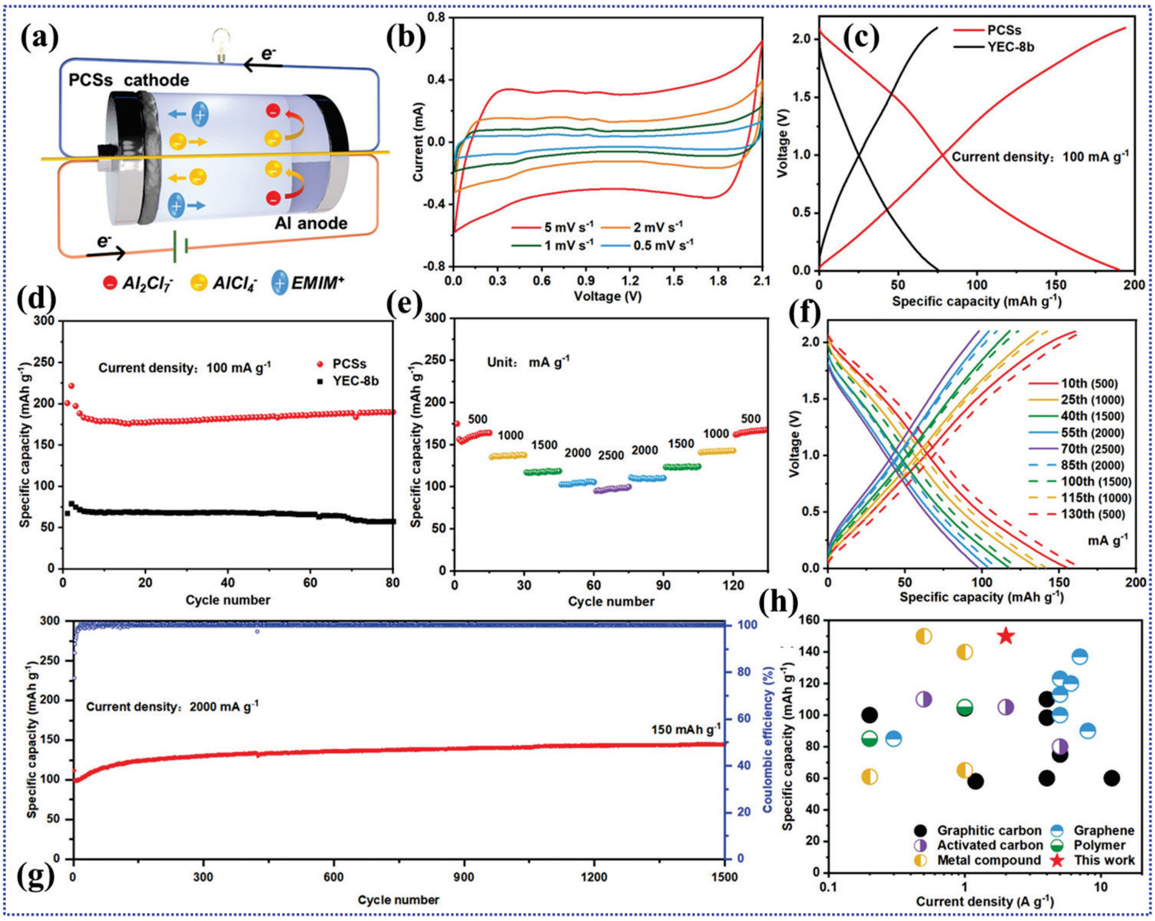

Figure 10. Electrochemical performance evaluation of AIHSC based on PCSs at 25 °C. (**a**) Schematic depiction of the rechargeable AIHSC working mechanism, (**b**) CV profiles observed at diverse scan rates, (**c**) GCD curves for PCSs and YEC-8b at 100 mA/g, (**d**) cycling stability comparison between PCSs and YEC-8b at 100 mA/g, (**e**) rate performance analysis and (**f**) corresponding GCD curves for PCSs at numerous current densities, (**g**) long-term cycling stability and Coulombic efficiency observed at 2000 mA/g, and (**h**) specific capacity comparison of Al-based AIHSCs with a cycle life exceeding 1000 cycles. Reproduced with permission from Ref. [86]. Copyright 2023, Wiley.

Soen et al. [87] demonstrated an AIHSC that has favourable electrochemical characteristics. The AIHSC produced using electrodeposition has a specific capacitance of 211 F/g, surpassing the electropolished counterpart by 20%. The ASC also exhibits an energy density of 151 Wh/kg at a power density of 3390 W/kg and maintains 70% of its capacitance even at a current density of 20 A/g, demonstrating exceptional rate capability. The device retains 87% of its capacity after completing 5000 cycles. The extraordinary performance may be attributed to the reduced resistance to charge transfer, the irregular and branching structure, and areas with elevated surface energy. This study demonstrates that using a surface treatment for aluminium electrodes can significantly enhance the performance of AIHSCs, rendering them a viable option for advanced energy storage devices in the future. Lie et al. [88] reported an HSC composed of an aluminium positrode, a graphene negatrode, and an ionic liquid electrolyte. It has a specific discharge capacitance of 240 F/g at a current density of 0.1 A/g and a Coulombic efficiency of 90%. After undergoing 1000 cycles at a current density of 0.3 A/g, the device exhibits a capacitance of 254 F/g. Furthermore, after 2000 cycles at a current density of 2.0 A/g, the capacitance decreases to 130 F/g. These results indicate that the device has excellent cyclic stability and achieves almost 100% Coulombic efficiency. The electrochemical impedance spectrum indicates a charge transfer resistance of 13.15 Ω, a series resistance of 3.82 Ω, and a dispersed resistance of 6.36 Ω. The primary energy storage mechanism in this case comprises the combination of electric double-layer capacitance resulting from the adsorption and desorption of $AlCl^{4-}$ ions, as well as weak intercalation and deintercalation in nitrogen-doped graphene. This makes it a desirable option for high-performance supercapacitors. Sun et al. [89] developed an AIHSC composed of a positrode made of aluminium foil, a negatrode made of NCS, and an electrolyte made of 1-ethyl-3-methylimidazolium chloride ([EMIm]Cl) and $AlCl_3$. The device demonstrates non-ideal rectangular CV curves and achieves a high specific discharge capacitance of 224 mAh/g at a current density of 0.300 A/g, while maintaining a Coulombic efficiency of 98%. The NCS negatrode exhibits outstanding cycling performance, with a 114 mAh/g capacity at 10 A/g even after undergoing 35,000 cycles. Electrochemical impedance spectroscopy revealed a progressive reduction in charge transfer resistance throughout cycling, resulting in consistent and reliable performance. The Al-HSC exhibits a blend of battery-like and capacitor-like properties, making it a very promising energy storage device. It provides fast charge–discharge cycles and maintains long-term stability.

Using the most suitable carbon materials obtained from biomass can significantly improve the efficiency of AIHSCs, enhancing their electrochemical performance. BDC materials, such as corn wastes, corn cob, jute sticks, corn silk, sulfur-doped carbon, nitrogen-doped carbon, and porous carbon sheets, possess distinctive characteristics such as a high SSA, hierarchical porous structures, and diverse elemental distributions [188–192]. These characteristics render them very well suited for utilization as electrode materials. The materials exhibit outstanding electrochemical performance, characterized by a high specific capacitance, enhanced energy densities, and excellent cycling stability. The qualities listed in Table 2 are essential for improving the overall efficiency of supercapacitors. By carefully selecting and optimising carbon materials derived from biomass, it is possible to tailor the electrochemical properties of AIHSCs, leading to improved performance and long-lasting durability for energy storage.

4.4. KIHSCs

BDC materials significantly improve the efficiency of KIHSCs. Biomass-derived materials have advantages such as hierarchical porous structures with nitrogen doping and high SSA. Rich nitrogen doping and defects with BDC gain due to these parameters exhibit high SSA and other features favourable to electrochemical energy storage. This means that a KIHSC has a larger charge storage capability [193]. According to the mentioned benefits, BDC materials can significantly enhance the energy and power density and the cyclic stability of KIHSCs. They possess great commercial potential in the potassium-ion battery field. BDC materials' structural and electrochemical properties prove their high commercial acumen. Strong structural characteristics and additional electrochemical properties are available. Two advantages are critical to the success of supercapacitors with high performance: they are highly effective and environmentally friendly. Unique materials are appreciated because of their design characteristics and possibilities for developing high-performance supercapacitors [94], a good choice for scaling KIHSCs for commercial application in the potassium-ion battery market.

The unique structural characteristics and cost-effectiveness of porous carbons derived from biomass make them promising electrode materials for KIHSCs. BDCs possess many advantageous properties that make them suitable for KIHSC applications. A substantial SSA and an intricate pore structure comprising micropores, mesopores, and macropores facilitate the efficient migration of ions and provide abundant active sites for storing potassium ions. Heteroatom doping involves the introduction of heteroatoms, such as nitrogen, oxygen, and sulfur, into carbon materials derived from biomass [194]. This process can improve the capacity of the carbons to be wetted and conduct electricity, resulting in enhanced electrochemical performance. Tuneable surface chemistry refers to the ability to modify the chemical properties of BDCs by choosing specific biomass precursors and activation procedures. This allows for the enhancement of the potassium-ion storage capacity. KIHSCs, utilizing porous carbon electrodes generated from biomass, have exhibited encouraging electrochemical characteristics [99]. The high specific capacitance values, often exceeding 300 F/g, are attributed to the hierarchical pore structure and the incorporation of heteroatom doping. The exceptional rate capacity of the material is attributed to its linked pore network and strong electrical conductivity, which enable fast ion transport and consequently lead to outstanding rate capability and high power density. The robust carbon structure and uniform surface chemistry of carbons derived from biomass ensure exceptional stability after several charge–discharge cycles [195]. Although biomass-derived porous carbons have demonstrated encouraging outcomes in KIHSCs, some obstacles still need to be addressed. Additional investigation is required to enhance the pores' configuration and the surface's chemical composition to achieve the highest possible efficiency in storing and transporting potassium ions. To improve the energy density of KIHSCs, one can utilize strategies like incorporating battery-type materials or integrating pseudocapacitive materials. In order to make biomass-derived porous carbons commercially feasible, it is crucial to develop synthesis methods that are both scalable and cost-effective. Porous carbons generated from biomass provide a sustainable and cost-effective alternative for KIHSCs. There is potential for enhancing their performance by optimizing material design and synthesis.

Using AS-HC as the negatrode and AS-AC as the positrode in a potassium-based electrolyte, a KIHSC was created, as shown in Figure 11a [98]. The device has a remarkable electrochemical performance, as demonstrated in Figure 11b–d, with a specific energy of 105 Wh/kg and no capacitance degradation after 10,000 cycles, indicating exceptional cycling stability. The AC electrode exhibits a dual electrical layer capacitance characteristic and supplementary pseudocapacitive peaks, which augment the device's overall performance. The specific discharge capacity of the AS-HC electrode reaches a stable state after a few cycles, suggesting that potassium storage is reversible and plays a role in the device's high Coulombic efficiency and structural stability.

Chen et al. [99] constructed a KIHSC using plains–hills carbon as the positrode and negatrode. The device exhibits a reversible capacity of 147.2 mAh/g at a current density of 10 A/g after undergoing 5000 cycles, indicating excellent stability. CV and GCD experiments were used to evaluate the electrode's performance, demonstrating an energy density of 178.4 Wh/kg at a power density of 1115 W/kg. The KIHSC exhibits remarkable cycling performance, maintaining 75.2% of its capacity after 10,000 cycles. Its ideal blend of conductivity and pseudocapacitance accounts for the device's outstanding performance, making it an extremely advanced electrode material for potassium ion storage. A KIHSC device was constructed using the NOHC as the positrode and AC as the negatrode [100]. The device exhibits an initial reversible capacity of 186.3 mAh/g and maintains 93.5% of its capacity after undergoing 500 cycles at a current density of 0.1 A/g, thus displaying exceptional cycle stability. Furthermore, the device demonstrates an energy density of 68 Wh/kg at a power density of 2000 W/kh and sustains an 80% capacity retention after 1000 cycles at a current of 1 ampere per gram. The NOHC's structure and the development of a stable SEI layer during cycling enable a combination of K-ion intercalation and capacitive processes that contribute to the system's performance. Ultimately, while improving the synthesis methods, it is equally important to conduct electrochemical analysis on biomass-generated carbon to achieve optimal performance in KIHSCs. Electrochemical characterization techniques are crucial for comprehending the carbon material's charge storage mechanisms, kinetics, and overall electrochemical behaviour when exposed to potassium ions.

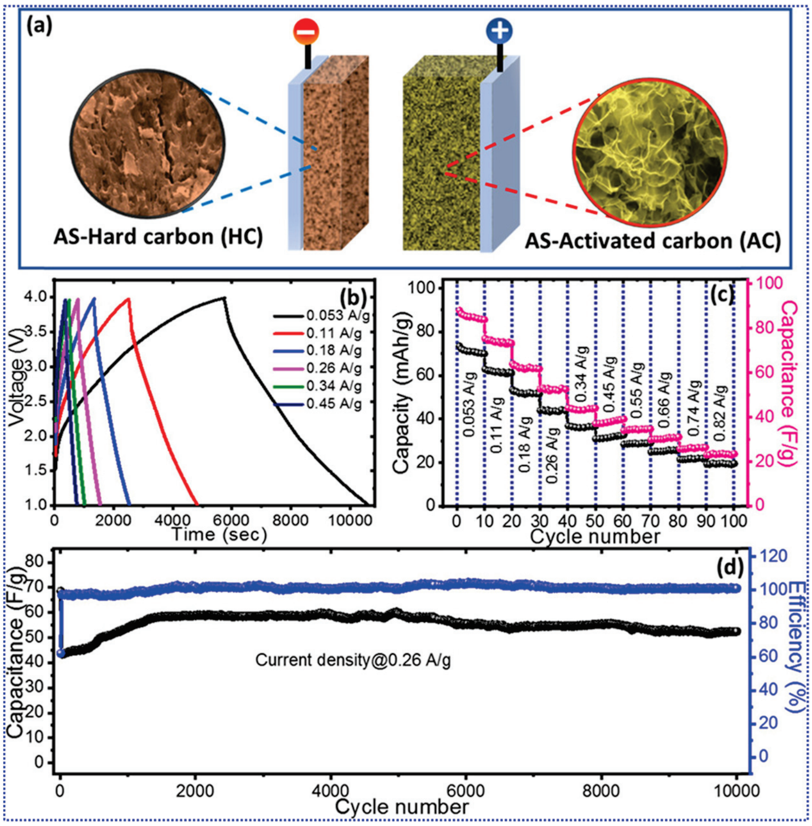

Figure 11. The complete cell KIHSC electrochemical performances of the HC-1000/AC-800: (**a**) a schematic representation of the KIHSC complete cell, (**b**) GCD profiles recorded at various current densities, (**c**) specific capacity and specific capacitance variation with several cycles at various current densities, and (**d**) cyclic stability of the full cell with corresponding Coulombic efficiency over 10,000 cycles. Reproduced with permission from Ref. [98]. Copyright 2020, American Chemical Society.

The field of energy storage has seen significant progress in the development of KIHSCs in recent years. The increasing interest in BDC compounds has led to several studies exploring their use, taking advantage of their sustainable, cost-effective, and environmentally beneficial properties. These materials have shown significant promise in improving the electrochemical performance of KIHSCs by optimizing variables such as specific surface area, porosity, and electrical conductivity [196–200]. Multiple prominent research studies have shown the utilization of different carbon materials derived from agaric [201], ganoderma lucidum [202], coffee grounds [203], rapeseed meal [204], lignin [205], and 2D tremella [206] for KIHSCs. The wide variety of carbon compounds obtained from biomass, each with its unique structure and electrochemical properties, has significantly contributed to the progress in potassium-ion hybrid supercapacitors (KIHSCs). Their utilization has resulted in significant enhancements in performance measures, including the specific capacitance, energy density, power density, and cycling stability, consequently confirming their position in the future of sustainable energy storage technologies. Table 2 presents a concise overview of the different electrochemical parameters required to evaluate the effectiveness of BDC in KIHSCs. Specific capacitance, rate capability, cycling stability, charge transfer resistance, and diffusion coefficients are crucial in optimizing electrochemical characterization techniques. The optimization of electrochemical characterization processes involves the utilization of many methods, including CV, GCD experiments, and EIS. Surface characterization techniques offer additional information about electrochemical behaviour, particularly in situ approaches. This information allows researchers to discover limitations and optimize the carbon material. Through meticulous analysis of the electrochemical data, researchers can gain insights into the ion transport pathways, kinetics of charge storage, and the impact of functional surface groups on the electrochemical performance. This comprehension can improve the synthesis processes, electrode manufacturing procedures, and electrolyte compositions, boosting the energy storage capacity and lifespan of KIHSCs. Optimizing electrochemical characterization techniques is crucial for establishing correlations between structure and properties and constructing prediction models for carbon derived from biomass. Predictive models can direct and expedite the logical creation of carbon materials for certain uses, advancing high-efficiency and financially feasible energy storage technologies.

5. Various Factors Affecting the Electrochemical Behaviour of BDC-Based MIHSCs

BDC electrodes possess numerous advantages compared to alternative carbon-based electrodes for MIHSCs. The advantages encompass heightened electrical conductivity, enhanced surface wettability, the induction of pseudocapacitance, expedited charge transfer, and facilitated reactions at the electrode/electrolyte interface [207]. BDC materials provide both sustainability and cost-effectiveness, rendering them a compelling choice for supercapacitor electrodes. They have a structure that allows for the passage of substances through small holes, a high ability to store electrical charge per unit mass, and the ability to remain stable over time. These properties make them better than many other carbon-based materials used in MIHSCs [208]. Lignin/cellulose nanofibers from biomass exhibit potential as electrode materials because of their exceptional durability, favourable electronic conductivity, and porous structure [209]. Moreover, carbon compounds obtained from biomass, which are renewable, have shown considerable promise in improving the performance of electrodes for MIHSCs [84]. Porous BDCs, which can be tailored to have specific nano/microstructures, are attracting interest due to their high effectiveness and cost-effectiveness as materials for supercapacitor electrodes [210]. The use of biomass-generated carbon can result in various electrochemical characteristics, including specific capacitance and surface area, due to its varied internal structure [211]. BDC materials have distinctive characteristics, such as a highly developed porous structure, a substantial specific surface area, and excellent electrical conductivity. These attributes render them highly favourable as electrode materials for supercapacitors with exceptional performance capabilities [212]. Electrodes made from BDCs provide a sustainable, economically viable, and highly effective alternative for supercapacitors. Their distinctive qualities and benefits have led to their growing popularity in energy storage.

Several vital parameters that control the electrochemical behaviour of BDC-based MIHSCs for energy storage are tabulated in Table 3. Electrolyte choice, OPW range, and electrode material qualities are essential. Supercapacitors' ion transport efficiency depends on electrolyte choice. The electrolyte must promote fast ion movement and chemical stability within the device's working voltage range. BDCs, which frequently incorporate inherent functional groups derived from natural doping elements such as nitrogen, sulfur, and phosphorus, exhibit distinct interactions with electrolyte ions, influencing charge storage. Given the complex surface chemistry of BDCs, electrolyte stability and conductivity are crucial. These electrodes could use electrolytes with higher ionic conductivity to maximize their porous structure. The OPW determines the voltage range, which affects supercapacitor energy and power density. BDCs can withstand higher voltages due to their surface chemistries and structural stability. This trait may improve energy storage. However, deviating from the constant voltage range may cause rapid material degradation. Biomass carbons may have inherent heteroatoms that affect voltage range stability, supercapacitor lifetime, and efficiency. This depends on how heteroatoms interact with the electrolyte. BDC electrodes have many advantages over carbon-based electrodes. BDC electrodes are more sustainable since they use renewable resources. This reduces the environmental effect of electrode material manufacture and promotes sustainability. Bio-wastes minimize material costs compared to conventional electrodes that use expensive processed carbons or synthetic precursors. High porosity in BDCs helps MIHSCs store more ions. This structural benefit is achieved without activation or templating, which traditional carbon composites require. BDCs store energy using pseudocapacitance mechanisms due to their heteroatoms. This increases energy storage capacities beyond double-layer capacitance. Supercapacitors can be customized and function better by changing electrode properties like conductivity and wettability using physical or chemical approaches. A number of biomass types can be used to make carbons with customized supercapacitor characteristics. Customization is harder with standard carbon sources. In addition, BDCs are thermally stable, ensuring constant performance across all operational temperatures. This is essential for energy storage applications that need durability. Carbon electrodes made from biomass are a sustainable energy storage solution. They have enhanced performance and are cost-effective and adaptable for supercapacitor applications. These advantages make them attractive alternatives to carbon-based electrodes, which are often limited by their environmental impact, high cost, and inflexibility.

Table 3. Merits of BDC electrodes compared with other types of carbon-based electrodes used in MIHSCs.

Feature	BDC Electrodes	Traditional Carbon-Based Electrodes
Sustainability	Produced from renewable materials, rendering them ecologically sound and enduring.	Frequently obtained from finite resources or artificial methods, which might result in a greater ecological footprint.
Cost	The cost is typically cheaper because waste or natural by-products are utilized, decreasing material prices.	Usually, the higher cost is a result of utilizing new or artificial materials.
Porous structure	The material has inherent high porosity, which results in a diverse range of pore diameters. This characteristic significantly improves its ability to store ions.	Porosity must be deliberately designed and controlled, often necessitating the use of supplementary processing procedures.
Natural doping	Includes inherent heteroatoms like nitrogen, sulfur, and phosphorus, improving electrochemical performance by increasing pseudocapacitance.	Doping necessitates the use of further chemical processing to insert heteroatoms, hence augmenting the intricacy and expense.
Modification flexibility	Can be readily adjusted through physical or chemical activation to customize characteristics such as surface area and conductivity.	Modifying synthetic or processed carbon materials is feasible, but their inherent qualities frequently limit flexibility.
Unique chemistries	The electrode characteristics can be modified to suit individual applications, as they vary greatly depending on the type of biomass used.	Typically uniform, with minimal variation in electrochemical characteristics until intentionally modified.
Thermal stability	Excellent thermal stability is advantageous for preserving performance over various temperature conditions.	The thermal stability of a material can vary and is influenced by the precursor and the procedure used to create it. Achieving consistent thermal stability may necessitate strict management.
Renewable production	The production cycle can be included in a sustainable bio-waste usage loop, fostering a circular economy.	Typically, it depends on industrial operations not included in a renewable cycle, with a greater emphasis on extracting resources.

5.1. Effect of Electrolytes on the Electrochemical Behaviour of BDC Electrodes

Electrolytes have a crucial role in determining the electrochemical characteristics of BDCs in MIHSCs. The selection of electrolytes substantially influences the performance of the supercapacitor system. Yoo et al. [126] showed that newly created nonaqueous electrolytes containing bis(trifluoromethylsulfonyl)imide salts allowed reversible deposition on metal positrodes and reversible adsorption on an AC negatrode. This led to the development of MIHSCs. Momodu et al. [213] highlighted the significance of electrolytes by demonstrating that gel-based electrolytes had exceptional stability and distinctive recuperative properties. This suggests that gel electrolytes formed from plant biomass can be effectively utilized in supercapacitor devices. In their study, Zhu et al. [214] emphasized that carbon-based supercapacitors demonstrated significant gravimetric capacitance and energy density while using organic and ionic liquid electrolytes. This highlights the importance of choosing the proper electrolyte to improve the electrochemical performance of carbon electrodes generated from biomass. In addition, Li et al. [215] examined progress in electrode materials and electrolyte innovation for lithium-ion capacitors, highlighting the pivotal significance of electrolytes in energy storage devices. In addition, Biswal et al. [216] reported that carbon electrodes displayed almost perfect capacitive behaviour with minimal ionic resistance, highlighting the significance of the rapid diffusion of electrolyte ions into the porous network for effective supercapacitor functioning. Figure 12a depicts the intricate ecology of electrode materials and electrolytes in MIHSCs, highlighting the importance of selecting the proper electrolyte to enhance performance. These findings emphasize the crucial importance of electrolytes in controlling the electrochemical properties of BDCs for MIHSCs.

Han et al. [127] showed that water-in-salt electrolytes based on acetate successfully enhanced the performance of ZIHSCs. These electrolytes exhibited excellent reversibility and stability during zinc plating and stripping. Choosing the appropriate electrolyte composition is crucial for maintaining the durability and effectiveness of the supercapacitor device. In addition, Zhang et al. [217] emphasized the significance of the electrolyte mixture in improving the electrochemical efficiency of ZIHSCs. The study demonstrated that using a particular electrolyte mixture enhanced electrochemical performance by substituting the bound water within the solvation structure. This substitution led to an improvement in the solvation structure, ultimately resulting in superior overall performance. This highlights the electrolyte composition's significance in enhancing the supercapacitor device's electrochemical performance. In addition, Eskusson et al. [218] examined the electrochemical characteristics of different aqueous electrolytes in ZIHSCs. The study compared several electrolytes and their effects on the electrochemical properties of the supercapacitor device. A comprehensive understanding of the interactions between electrolytes and electrodes is essential for optimal performance and durability in ZIHSCs. Ultimately, selecting electrolytes plays a crucial role in influencing the electrochemical characteristics and overall efficiency of BDC electrodes in ZIHSCs. Optimizing the electrolyte composition can improve the supercapacitor system's efficiency, stability, and durability, enhancing energy storage capacity.

Shao et al. [219] highlighted the significance of asymmetric supercapacitors in extending the voltage range beyond the point when electrolytes break down due to thermodynamic factors. This offers a solution to the energy storage constraints faced by symmetric supercapacitors. This emphasizes the importance of considering the compatibility of electrolytes and electrode materials to improve the overall performance of supercapacitors. Moreover, Simon and Gogotsi [220] emphasized that combining appropriate electrode materials with the proper electrolyte can augment the supercapacitor system's energy storage capacity and power. It is crucial to recognize that there is no flawless active substance, and the choice of electrolyte should align with specific performance goals. Comprehending the interplay between electrode materials and electrolytes is essential for attaining optimal electrochemical performance in NIHSCs. In addition, Maurya et al. [221] examined the configuration of NIHSCs, highlighting the importance of the three constituents, i.e., positrode, negatrode, and electrolyte, which resemble those found in batteries. This highlights the need for electrolytes that can fulfil the specific demands of NIHSCs. By carefully choosing and designing electrolytes, it is possible to improve the electrochemical efficiency and longevity of carbon electrodes generated from biomass in NIHSCs. Ultimately, the selection of electrolyte composition has a substantial impact on the electrochemical characteristics and overall efficacy of BDC electrodes in NIHSCs. By integrating findings from studies on asymmetric supercapacitors, electrode–electrolyte compatibility, and NIHSCs design, it is possible to enhance the efficiency and performance of supercapacitor systems for energy storage purposes. MIHSC applications make use of different types of aqueous electrolytes, including acidic, basic, and neutral solutions, as shown in Figure 12b.

The electrolyte's composition is vital for maximizing the performance and efficiency of the supercapacitor system. Dubal et al. [222] stressed the significance of creating a streamlined pathway for electron transport and ensuring optimal electrolyte access to the electrochemically active materials in carbon fibres. They underscored the importance of electrolyte permeability and connectivity within the electrode structure. In addition, Tomboc et al. [223] examined the energy storage mechanisms in supercapacitors, specifically emphasizing ion adsorption at the interface between the electrode and electrolyte (electric double-layer capacitance) and faradaic processes that involve electron transfer through oxidation/reduction reactions (pseudocapacitance). Comprehending these principles is essential for choosing electrolytes that can efficiently facilitate both forms of energy storage processes in AIHSCs. In addition, Kim et al. [224] showed that electric double-layer capacitors store charges by physically adsorbing electrolyte ions onto porous carbon electrodes, highlighting the significance of the electrode–electrolyte interface in the performance of supercapacitors. This emphasizes the need to ensure that the electrolyte is compatible with the electrode material in order to achieve efficient charge storage and transfer in AIHSCs. Ultimately, the choice of the correct electrolyte composition is crucial for controlling the electrochemical characteristics and overall efficiency of BDC electrodes in AIHSCs. By incorporating findings from studies on electron transport pathways, energy storage processes, and electrode–electrolyte interactions, it is feasible to improve the efficiency and functionality of supercapacitor devices used for energy storage purposes.

Dubal et al. [222] stressed the significance of creating a streamlined pathway for electron transport and ensuring that the electrolyte can effectively reach the electrochemically active materials in carbon fibres. They highlighted the importance of having good electrolyte permeability and connectivity within the electrode structure to improve the overall electrochemical performance. In addition, Kim et al. [224] explained how electric double-layer capacitors store charges utilizing the physisorption of electrolyte ions onto BDC electrodes. This highlights the importance of the interface between the electrode and electrolyte in determining the performance of supercapacitors. It emphasizes the need to use electrolytes compatible with the electrode material to achieve efficient storage and charge transfer in KIHSCs. Figure 12c illustrates the many energy storage technologies, including MIHSCs, and emphasizes the strategic integration of specific electrolytes to enhance performance. Stressing the importance of electrolyte selection [225], this study demonstrates how particular electrolytes utilized in BDC electrodes directly influence the efficiency and efficacy of MIHSCs in different applications. Choosing electrolyte composition is crucial for controlling BDC electrodes' electrochemical characteristics and overall efficiency in KIHSCs. By incorporating findings from studies on electron transport pathways, energy storage processes, and electrode–electrolyte interactions, it is feasible to enhance the efficiency and usefulness of supercapacitor systems for energy storage purposes.

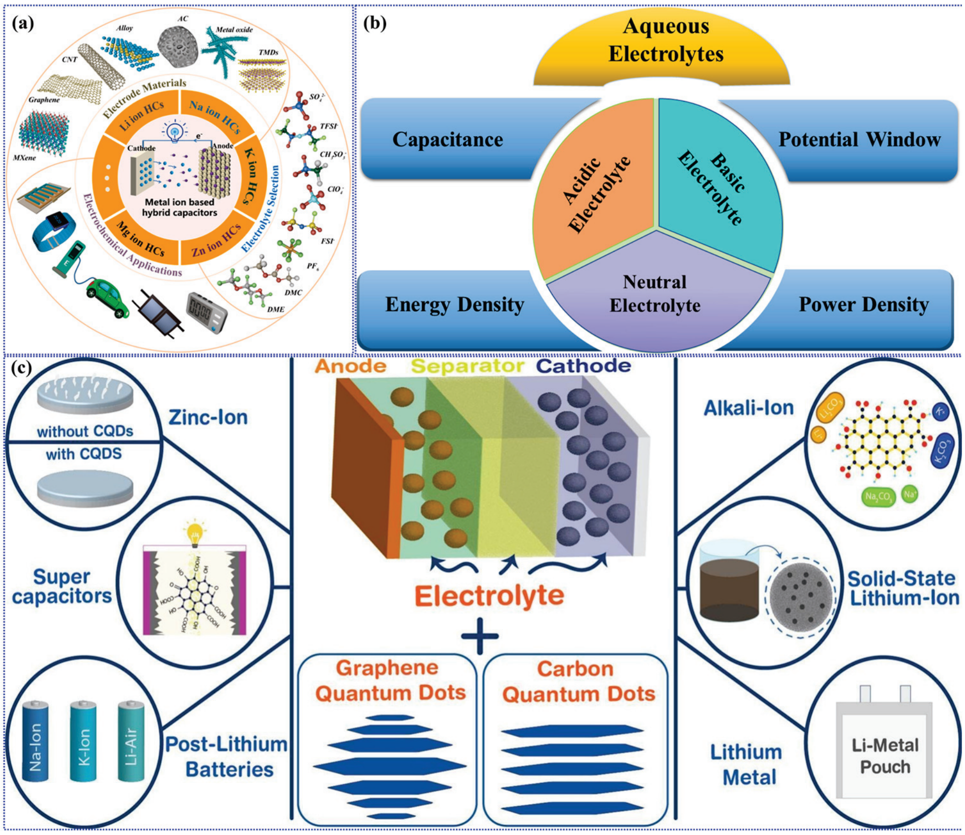

Figure 12. (**a**) Exploration of materials and electrolytes for MIHSCs. Reproduced with permission from Ref. [226]. Copyright 2021, Elsevier. (**b**) The impact of aqueous electrolytes on the efficiency of MIHSCs. Reproduced with permission from Ref. [227]. Copyright 2020, Elsevier. (**c**) Schematic representation of the effect of electrolytes on carbon-based electrodes in MIHSCs. Reproduced with permission from Ref. [225]. Reproduced under the term CC BY 4.0. Copyright 2024, Shaker et al., Elsevier.

5.2. Advancements in High-OPW MIHSCs

The energy density and overall performance of MIHSCs are greatly affected by a high OPW, making it a crucial aspect of these energy storage devices. Maximizing the OPW in such systems is essential for augmenting their capabilities. A practical approach to increase the OPWs in MIHSCs is utilizing electrode materials that can function efficiently at higher potentials. For instance, using materials such as BDCs and MoO_2 with a more significant work function can aid in advancing high-voltage supercapacitors [228]. By incorporating materials like silicene into MIHSCs, it is possible to create devices with a broad range of OPWs, reaching up to 3 V [229]. This allows for higher energy and power densities in the MIHSCs. Moreover, the configuration of asymmetrical MIHSCs using BDCs can also enhance the OPWs. By manipulating electrode work functions and utilising specific electrode combinations, it is possible to fabricate high-voltage asymmetric MIHSCs that exhibit improved performance [228]. Furthermore, sophisticated electrode materials such as highly porous BDCs and metallic nanosheets can provide exceptional energy storage capabilities at increased OPWs, highlighting the need to select appropriate materials to achieve high supercapacitor OPWs [230]. Ultimately, high OPWs in MIHSCs are of utmost importance, as they are directly correlated with these devices' energy density and overall efficiency. Employing suitable electrode materials, implementing asymmetric configurations, and integrating novel substances such as silicene and metallic nanosheets makes it feasible to enhance the voltage in MIHSCs, thus unleashing their complete energy storage capacity.

High-voltage aqueous ZIHSCs are a noteworthy advancement in energy storage. They offer improved safety features and higher energy densities compared to conventional systems. The ability to attain elevated operational voltages is dependent on the inventive restructuring of the hydrogen bond network in the electrolyte, which is assisted by the use of co-solvents such as polyethylene glycol and N, N-dimethylformamide [231]. These co-solvents alter the structure of the hydrogen bonds, which decreases the movement and reactivity of water molecules. As a result, the electrolyte can withstand greater OPWs up to 4.27 V without breaking down. This method avoids the usual problems with water-based systems and takes advantage of the natural safety and environmental advantages of electrolytes based on water. This opens up the possibility of developing ZIHSCs in the future which have far better energy storage capacity. The advancement of high-voltage KIHSCs represents a crucial breakthrough in energy storage technology, providing a combination of high power and energy density essential for various applications [232]. These KIHSCs achieve high OPWs by exploiting the distinctive characteristics of potassium ions, such as their larger size and lower solvation energy than lithium and sodium. This enables easier removal of solvent molecules and faster movement of ions during ion insertion and removal processes. The lower typical electrode potential of potassium in electrolytes such as propylene carbonate is also a contributing factor to the high voltage capability of these devices. The reduced potential and the creation of robust electrochemical interfaces enable potassium-ion supercapacitors to function effectively at higher voltages. This maximizes energy density and improves the overall performance and efficiency of the MIHSCs.

5.3. Theoretical Calculations: Insights into Energy Storage Mechanisms in MIHSCs

Theoretical calculations are crucial for comprehending the energy storage mechanisms of MIHSCs. By employing density functional theory (DFT) calculations, researchers can obtain valuable information regarding charge separation mechanisms and the efficient confinement of precursors inside these systems [233,234]. The characteristics of metal-based hydroxides have been investigated using DFT calculations. These calculations have also been used to examine how the incorporation of transition metal ions and lattice defects affects the electronic properties of these hydroxides [235]. In addition, DFT has played a crucial role in comparing the characteristics of several polypyridyl dyes based on metal ions for dye-sensitized solar cells [236]. MIHSCs are a form of energy storage device that combines battery-like electrodes with capacitive electrodes. They have shown great potential in high energy and remarkable power densities [16]. Hybrid supercapacitors exhibit superior energy density compared to conventional electric double-layer capacitors and effectively surpass the power density constraints of batteries [52,237,238]. MIHSCs, specifically ZIHSCs, are recognized for their exceptional safety, impressive energy and power outputs, long-lasting performance, and cost-efficiency [106]. These devices combine the benefits of zinc-ion batteries, which have high energy density, with supercapacitors, which have excellent power density and cycle stability [14]. Zinc metal positrodes have generated considerable interest in energy storage systems due to their inherent advantages, leading to the development of aqueous ZIHSCs [38]. DFT simulations provide valuable insights into the energy storage mechanisms in MIHSCs, which contribute to developing high-performance energy storage devices with improved energy and power densities.

Recent advancements in DFT calculations have shed light on the energy barriers involved in the adsorption and desorption of Zn^{2+} ions on doped carbon electrodes, which is crucial for optimizing the chemisorption kinetics in ZIHSCs [239]. The addition of nitrogen and sulfur heteroatoms to the carbon structure considerably impacts the energy barriers, leading to improved electrochemical performance. DFT investigations reveal that the adsorption of Zn^{2+} ions commences by their contact with the oxygen sites of hydroxyl groups. This interaction leads to the breaking of O-H bonds and the subsequent creation of C-O-Zn bonds, accompanied by the release of H^+ ions. The significance of this sequence is in its ability to determine the chemisorption kinetics, which directly impact the performance of ZIHSCs. The computational analysis in Figure 13a,b reveals that the energy barrier for this process is significantly reduced when N/S co-doping is present, measuring at 1.17 eV, in contrast to 1.91 eV for N-doped alone and 3.21 eV for undoped electrodes. Incorporating N/S co-doping decreases the energy barriers, resulting in faster adsorption and improved ion exchange reversibility and efficiency at the electrode interface during charge–discharge cycles. The findings have significant ramifications, indicating that by strategically adding N and S heteroatoms to the electrode material of ZIHSCs, these capacitors' energy storage capacity and cycling stability can be significantly improved. Reducing energy barriers enables faster and more effective ion adsorption and desorption, which is crucial for high-performance supercapacitors that achieve rapid energy delivery and high power densities. Therefore, combining N/S co-doping is essential to improve future supercapacitors' design and functional capabilities, making them more efficient and long-lasting.

DFT computations are essential in studying and improving ion diffusion pathways within positrode materials in NIHSCs. These calculations play a crucial role in determining the energy barriers related to the movement of sodium ions. These barriers are essential factors that affect the electrochemical performance of supercapacitors. DFT is used to analyse and understand how changes in the structure and composition of the positrode might improve ion transport and increase the device's overall efficiency [240]. This is conducted by comparing the diffusion barriers in different materials or modified structures. A detailed analysis of the obstacles that hinder the movement of sodium ions in two different situations involving electrodes made of manganese oxide (MnO) is depicted in Figure 13c–g. The initial scenario investigates the diffusion of sodium ions across the main body of cubic MnO. In this process, ions move by directly jumping between interstitial sites. This process does not entail the displacement of lattice atoms, but it does exhibit a relatively high energy barrier, which suggests that ion transport occurs at a slower rate. The second scenario examines the diffusion of sodium ions at the interface between Mn and Na_2O, a crucial region for enhancing ion transport. The interface reduces the energy needed for Na ions to move, making them more mobile than their movement through the more significant MnO material. The decrease in energy barriers at the interface can be ascribed to the distinctive structural and electrical interactions that occur, facilitating the migration of Na ions across the electrode. The insights obtained from DFT calculations are crucial and show that by strategically manipulating the interfaces in positrode materials, we may significantly influence the performance of NIHSCs. Reducing the obstacles to the movement of ions at essential points, like the interface between manganese and sodium oxide, makes it feasible to raise the speed at which ions are transported. This, in turn, can lead to improved performance regarding the rate at which the supercapacitor can charge and discharge and its overall efficiency. This research enhances our comprehension of material behaviours at the atomic scale and guides the future development and creation of advanced electrode materials for improved energy storage technologies.

DFT simulations have played a crucial role in understanding the adsorption process on heteroatom-doped carbon negatrodes in AIHSCs [241]. These theoretical insights are essential for developing negatrodes with the most efficient energy storage capacities. The DFT simulations were used to study the interaction between the $[AlCl_4]^-$ moieties and the nitrogen and sulfur co-doped carbon negatrode (N,S-C). The DFT analysis demonstrates that adding nitrogen and sulfur to the carbon structure dramatically improves the adsorption potency of $[AlCl_4]^-$ ions. The improvement is due to the distinctive electronic characteristics provided by the N and S dopants, which alter the electronic surroundings of the carbon structure, thereby enabling more robust and more enduring interactions with the $[AlCl_4]^-$ ions. Specifically, graphitic and pyridinic nitrogen sites were discovered to enhance adsorption energies, suggesting a more advantageous adsorption situation than carbon that is not doped. The computational findings provide a crucial explanation for the experimental data on the enhanced capacitance and cycling stability of the N,S-doped carbon negatrodes in AIHSCs. DFT's predictive and explanatory power concerning the impact of heteroatom doping on adsorption characteristics highlights its usefulness in advancing energy storage materials. The combination of theoretical predictions and experimental advancements offers a strong foundation for improving the efficiency of aluminium-ion batteries and supercapacitors.

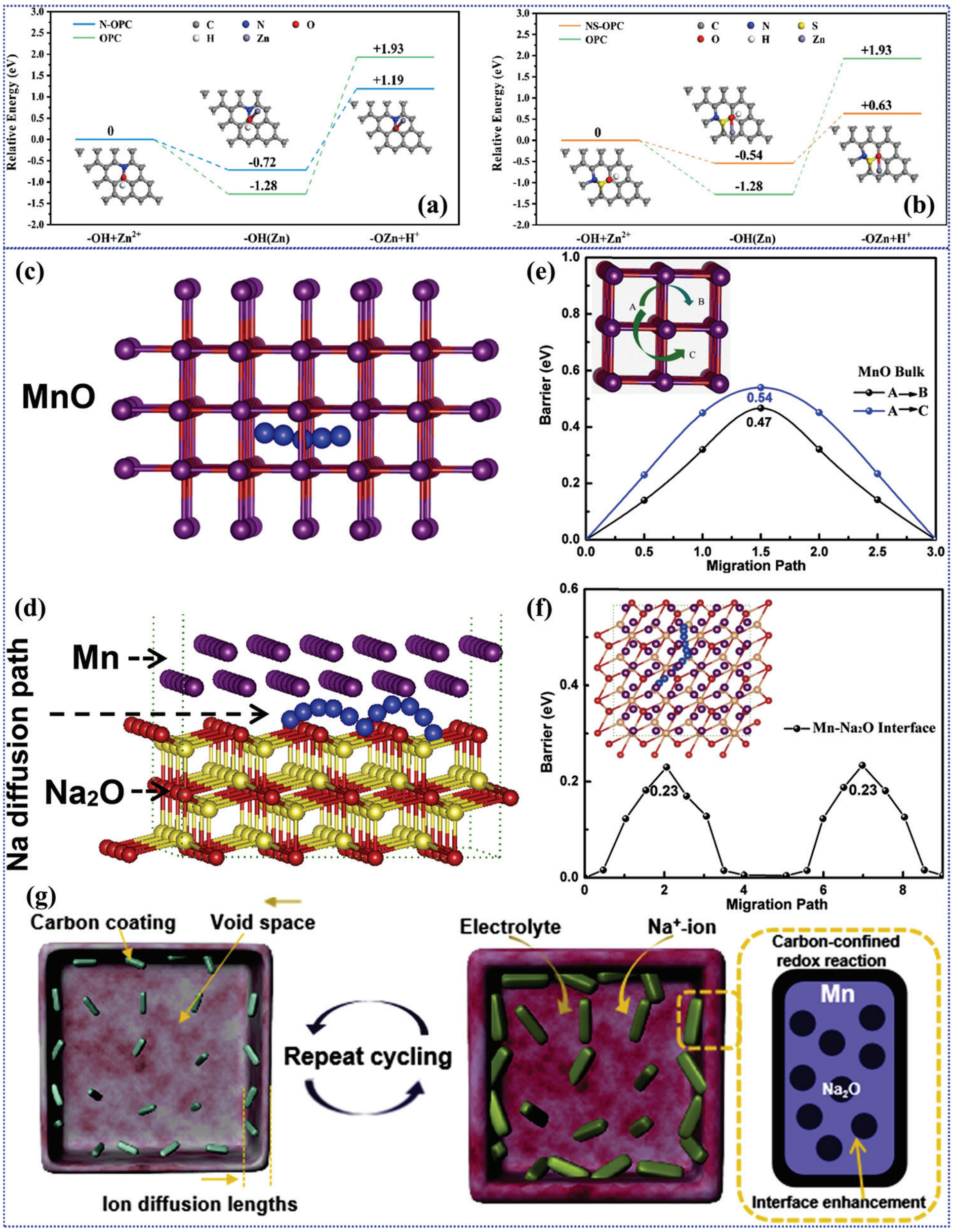

Figure 13. (**a**,**b**) Variations in the relative energy levels during the chemisorption process for ZIHSCs. Reproduced with permission from Ref. [239]. Copyright 2023, American Chemical Society. Atomic structures of various models and distinct Na diffusion pathways in (**c**) MnO and (**d**) Mn/Na_2O interface. Diffusion energy barriers for Na atoms are shown for (**e**) MnO bulk and (**f**) Mn/Na_2O interface. (**g**) Diagram illustrating the energy storage mechanisms for the MnO@HCNb electrode. Reproduced with permission from Ref. [240]. Copyright 2020, Elsevier.

DFT calculations provide valuable insights into the interactions at the interface and the mechanisms of charge transport in the electrode materials of KIHSCs [242]. These calculations have a substantial impact on the electrochemical performance of the supercapacitors. More precisely, bonding polyaniline (PANI) with molybdenum disulfide (MoS_2) promotes improved reaction speed, essential for adequate energy storage. DFT investigations demonstrate that incorporating PANI into the MoS_2 layers substantially reduces the barrier for K^+ diffusion. This indicates that the molecular-level hybridization reinforces the material's structural integrity and improves its electrical conductivity. This alteration leads to an electronic structure that is easier to access and facilitates faster and more efficient ion transport. The formation of covalent connections between PANI and MoS_2 establishes novel routes for electron transmission, reducing the energy obstacles linked to the insertion and removal of potassium ions in the charge–discharge procedures. Theoretical findings highlight the potential of employing organic–inorganic hybrid materials in supercapacitors to overcome the constraints imposed by conventional electrode materials. These hybrids can lower energy barriers and improve the movement of ions. As a result, they can attain a high capacitance and maintain excellent cycling stability. This makes them well suited for energy storage applications that require high performance. The findings obtained from DFT calculations play a vital role in directing the manufacture and enhancement of electrode materials to use these favourable characteristics fully.

6. Challenges and Future Research Perspectives

BDC materials are promising for high-performance MIHSCs, primarily due to their sustainable nature, widespread availability, and affordability. These materials exhibit significant attributes, including structural diversity, porousness, and heteroatom doping, greatly enhancing their electrochemical performance. This review thoroughly examines these characteristics and the obstacles that must be overcome for practical supercapacitor use. A major challenge lies in synthesizing BDC compounds with consistent and optimal structures for energy storage. The intricate chemical composition of biomasses hinders the continuous production of carbon nanotube fibres. Additionally, generating high-performance shape-memory carbon aerogels from biomass is a difficult task. To tackle these problems, several techniques have been suggested, such as altering the distance between layers in carbon materials, which can improve ion movement and storage. Incorporating nitrogen, phosphorus, and sulfur directly into the carbon structure enhances conductivity and electrochemical activity. Introducing multiple heteroatoms simultaneously generates a synergistic effect, improving overall supercapacitor performance.

BDC compounds also show promise as raw materials for metal-ion batteries, contributing to developing materials for such batteries. However, obstacles such as insufficient electrochemical storage capacity render BDCs unsuitable for battery applications. Efforts to enhance specific capacity and lifespan are necessary to make them viable for battery use. The complex structure of biomass precursors also hinders the continuous production of carbon nanotube fibres and shape-memory carbon aerogels, which are essential for battery applications. Several methodologies have been proposed to address these issues, such as biomass-derived nitrogen-doped porous carbons, which can replace noble metal catalysts in metal-ion batteries, improving battery performance. Improving electrode design, refining electrolyte composition, and innovating new energy storage mechanisms are crucial for progressing BDCs in MIHSCs. A deeper understanding of the correlation between the composition and characteristics of carbon compounds obtained from biomass will guide research focused on specific synthesis techniques, such as interlayer modulation and self-doping, to produce tailor-made materials with improved performance.

Advances in BDC materials for high-performance MIHSCs include electrode materials with high energy densities and mechanical stability, which are crucial for large-scale production. Surface engineering is vital for enhancing charge–discharge capabilities and maintaining consistent performance across multiple cycles, which is essential for industrial-scale applications. Encasing metal nanoparticles with metal oxides within zeolitic imidazolate frameworks can improve the performance of carbon materials for energy storage. Further enhancing capacitance is possible by using high-mass-loading biomass-based porous carbon electrodes.

BDCs have garnered considerable interest in advanced MIHSCs because of their notable characteristics, such as large surface area, conductivity, and cost-effectiveness [243].

Recent studies have investigated different types of carbon materials, such as nanoporous carbon, graphene, carbon nanosheets, and carbon aerogels obtained from sustainable sources like bagasse. These studies have shown that these materials can be inexpensive and effective electrode materials for supercapacitors [244,245]. Moreover, combining MOFs and conductive materials such as polypyrrole has been recognized as a method to improve the capacitance properties of supercapacitors, effectively resolving concerns regarding inadequate electrical conductivity [246–248]. In addition, the progress in creating all-carbon hybrids, specifically rGO/CNF nanostructures, has demonstrated encouraging outcomes in attaining superior charging and discharging abilities for supercapacitor electrodes [249]. Researchers have explored using carbon materials and transition metal compounds to improve electrode materials for KIHSCs to achieve higher power and energy density in advanced metal-ion hybrid supercapacitors [12]. In addition, the use of yolk–shell-structured nickel cobalt sulfide and CNT composites has demonstrated excellent performance in hybrid supercapacitors, emphasizing the significance of carbon materials as key electrode components [250]. The development of MIHSCs has enabled the creation of energy storage devices that combine the advantages of batteries and supercapacitors. These devices offer large energy storage capacity, fast charge–discharge rates, and an extended cycle life [18,41]. These advancements highlight the potential of carbon materials sourced from biomass to influence the future of MIHSCs. They offer a sustainable and efficient alternative for energy storage applications.

The ongoing exploration of BDC compounds for energy storage indicates a promising future. Techniques such as co-incorporating phosphorus and boron can significantly prolong supercapacitors' lifespan, making them more suitable for practical applications. These materials can become ideal for commercial use by creating scalable and economical synthesis methods and advancing material design and performance. The challenges and outlook for using BDC materials in high-performance MIHSCs must address structural, functional, and material difficulties. Advanced synthesis methods, innovative design strategies, and a thorough study of structure–property relationships are essential for the progress of these materials in energy storage. Tackling these challenges will allow BDC materials to substantially contribute to advancing sustainable and high-performance energy storage systems.

7. Conclusions

This review study thoroughly examines the crucial significance of BDC materials in advancing the exceptional performance of MIHSCs. This paper concentrates explicitly on systems based on sodium, potassium, and zinc ions. These materials are highlighted for their plentiful supply, capacity to be renewed, and remarkable physical and chemical qualities, making them ideal for energy storage applications. This review extensively examines the process of creating, modifying, and structurally enhancing carbon materials obtained from biomass. It highlights the significance of their large SSA, adjustable porosity, and introduction of heteroatoms in enhancing their electrochemical capabilities. This study explores many methods of creating carbon materials from biomass, such as pyrolysis, hydrothermal carbonization, and activation procedures. These processes make materials with various structural properties and regulated shapes. These techniques facilitate the production of carbon materials with hierarchical porous architectures and tailored surface chemistry, rendering them appropriate for MIHSCs. This review analyses the electrochemical characteristics of carbon materials obtained from biomass in various MIHSCs. It showcases their capacity to attain high capacitance, energy density, and cycling stability. This research emphasizes the suitability of BDCs with metal-ion electrolytes, their function in aiding ion transport, and the mechanisms underlying their ability to store charges. This study discusses the practical uses of BDC materials in sodium, potassium, aluminium, and ZIHSCs. It highlights how these materials can improve the performance of these systems. The analysis of several metal-ion systems demonstrates the benefits of BDCs' structural characteristics for each form of supercapacitor. This review examines the present obstacles in developing carbon materials produced from biomass for supercapacitors, encompassing scalability, cost-effectiveness, and performance consistency.

Additionally, it provides valuable insights for future studies, including enhancing the synthesis procedures, optimizing the structural configuration, and investigating novel energy storage mechanisms. This research highlights the significant impact of BDC materials in MIHSCs, which can lead to the development of environmentally friendly and efficient energy storage systems. This review is unusual because it comprehensively compares carbon compounds obtained from biomass in various metal-ion systems. It uncovers the distinct contributions of these materials to different types of supercapacitors. This comparison offers vital insights into the structural characteristics that improve electrochemical performance, influencing the advancement of sustainable energy storage solutions. This paper incorporates the latest developments in the field, emphasizing the breakthroughs in creating carbon materials from biomass and their usage in MIHSCs. The statement underscores the importance of ongoing innovation and interdisciplinary cooperation in investigating these sustainable materials better. This will help advance green energy technologies and harmoniously balance environmental sustainability and technical advancement. Overall, this review paper offers an in-depth examination of carbon materials produced from biomass in MIHSCs with exceptional performance. This study emphasizes the capacity of these materials to bring about significant changes, tackles existing obstacles, and provides insights for future investigations, thereby promoting the progress of sustainable energy storage technologies.

Funding: This work is supported by the Japan Society for the Promotion of Science (JSPS) through KAKENHI Grant Number 22F22336.

Institutional Review Board Statement: Not applicable.

Informed Consent Statement: Not applicable.

Data Availability Statement: Data are contained within this article.

Acknowledgments: The author acknowledges the support of the Japan Society for the Promotion of Science (JSPS) for the postdoctoral fellowship.

Conflicts of Interest: The author declares no conflicts of interest.

References

1. Guo, H.; Qiao, M.; Yan, J.; Jiang, L.; Yu, J.; Li, J.; Deng, S.; Qu, L. Fabrication of Hybrid Supercapacitor by $MoCl_5$ Precursor-Assisted Carbonization with Ultrafast Laser for Improved Capacitance Performance. *Adv. Funct. Mater.* **2023**, *33*, 2213514. [CrossRef]
2. Han, X.; Wang, B.; Yang, C.; Meng, G.; Zhao, R.; Hu, Q.; Triana, O.; Iqbal, M.; Li, Y.; Han, A.; et al. Inductive Effect in Mn-Doped NiO Nanosheet Arrays for Enhanced Capacitive and Highly Stable Hybrid Supercapacitor. *ACS Appl. Energy Mater.* **2019**, *2*, 2072–2079. [CrossRef]
3. Lee, S.-H.; Kim, J.H.; Yoon, J.-R. Laser Scribed Graphene Cathode for Next Generation of High Performance Hybrid Supercapacitors. *Sci. Rep.* **2018**, *8*, 8179. [CrossRef]
4. Larcher, D.; Tarascon, J.-M. Towards Greener and More Sustainable Batteries for Electrical Energy Storage. *Nat. Chem.* **2015**, *7*, 19–29. [CrossRef]
5. Zhai, Y.; Dou, Y.; Zhao, D.; Fulvio, P.F.; Mayes, R.T.; Dai, S. Carbon Materials for Chemical Capacitive Energy Storage. *Adv. Mater.* **2011**, *23*, 4828–4850. [CrossRef] [PubMed]
6. Zhang, X.; Hou, L.; Ciesielski, A.; Samorì, P. 2D Materials Beyond Graphene for High-Performance Energy Storage Applications. *Adv. Energy Mater.* **2016**, *6*, 1600671. [CrossRef]
7. Mondal, M.; Goswami, D.K.; Bhattacharyya, T.K. High-Performing Asymmetric 2 V Supercapacitor Assembled with Leucine-Capped RGO-α-Fe_2O_3 as Anode and PANI Decorated MwCNT-V_2O_5 as Cathode. *J. Electrochem. Soc.* **2023**, *170*, 110521. [CrossRef]
8. Li, J.; Zhu, J.; Dong, Z.; Wu, Q. Nanomaterials Derived from a Template Method for Supercapacitor Applications. *ChemistrySelect* **2023**, *8*, e202204487. [CrossRef]
9. Genc, R.; Alas, M.O.; Harputlu, E.; Repp, S.; Kremer, N.; Castellano, M.; Colak, S.G.; Ocakoglu, K.; Erdem, E. High-Capacitance Hybrid Supercapacitor Based on Multi-Colored Fluorescent Carbon-Dots. *Sci. Rep.* **2017**, *7*, 11222. [CrossRef]

10. Li, S.; Chen, W.; Huang, X.; Ding, L.; Ren, Y.; Xu, M.; Zhu, J.; Miao, Z.; Liu, H. Enabling Wasted A4 Papers as a Promising Carbon Source to Construct Partially Graphitic Hierarchical Porous Carbon for High-Performance Aqueous Zn-Ion Storage. *ACS Appl. Mater. Interfaces* **2024**, *16*, 10126–10137. [CrossRef]
11. Díez, N.; Sevilla, M. Hybrid Metal-Ion Capacitors Based on Carbon Nanospheres. *ChemElectroChem* **2024**, *11*, e202300475. [CrossRef]
12. Wang, Z.; Hong, P.; Zhao, H.; Lei, Y. Recent Developments and Future Prospects of Transition Metal Compounds as Electrode Materials for Potassium-Ion Hybrid Capacitors. *Adv. Mater. Technol.* **2023**, *8*, 2200515. [CrossRef]
13. Gao, Q.; Li, P.; Ding, S.; He, H.; Cai, M.; Ning, X.; Cai, Y.; Zhang, M. Cu2Se-ZnSe Heterojunction Encapsulated in Carbon Fibers for High-Capacity Anodes of Sodium-Ion Batteries. *Ionics* **2020**, *26*, 5525–5533. [CrossRef]
14. Tang, H.; Yao, J.; Zhu, Y. Recent Developments and Future Prospects for Zinc-Ion Hybrid Capacitors: A Review. *Adv. Energy Mater.* **2021**, *11*, 2003994. [CrossRef]
15. Zeng, F.; Gong, X.; Xu, Z.; Du, Z.; Xu, J.; Deng, T.; Wang, D.; Zeng, Y.; Yu, S.; Meng, Z.; et al. A New Selection Criterion for Voltage Windows of Aqueous Zinc Ion Hybrid Capacitors: Achieving a Balance between Energy Density and Cycle Stability. *J. Mater. Chem. A* **2023**, *11*, 26698–26706. [CrossRef]
16. Shang, K.; Liu, Y.; Cai, P.; Li, K.; Wen, Z. N, P, and S Co-Doped 3D Porous Carbon-Architectured Cathode for High-Performance Zn-Ion Hybrid Capacitors. *J. Mater. Chem. A* **2022**, *10*, 6489–6498. [CrossRef]
17. Zheng, H.; Zhou, H.; Zheng, B.; Wei, C.; Ma, A.; Jin, X.; Chen, W.; Liu, H. Stable Flexible Electronic Devices under Harsh Conditions Enabled by Double-Network Hydrogels Containing Binary Cations. *ACS Appl. Mater. Interfaces* **2024**, *16*, 7768–7779. [CrossRef]
18. Shaikh, N.S.; Lokhande, V.C.; Praserthdam, S.; Lokhande, C.D.; Ezema, F.I.; Salunkhe, D.J.; Shaikh, J.S.; Kanjanaboos, P. Recent Advancements in Energy Storage Based on Sodium Ion and Zinc Ion Hybrid Supercapacitors. *Energy Fuels* **2021**, *35*, 14241–14264. [CrossRef]
19. Dong, S.; Li, Z.; Xing, Z.; Wu, X.; Ji, X.; Zhang, X. Novel Potassium-Ion Hybrid Capacitor Based on an Anode of $K_2Ti_6O_{13}$ Microscaffolds. *ACS Appl. Mater. Interfaces* **2018**, *10*, 15542–15547. [CrossRef]
20. Qiu, D.; Guan, J.; Li, M.; Kang, C.; Wei, J.; Li, Y.; Xie, Z.; Wang, F.; Yang, R. Kinetics Enhanced Nitrogen-Doped Hierarchical Porous Hollow Carbon Spheres Boosting Advanced Potassium-Ion Hybrid Capacitors. *Adv. Funct. Mater.* **2019**, *29*, 1903496. [CrossRef]
21. Ruan, J.; Mo, F.; Chen, Z.; Liu, M.; Zheng, S.; Wu, R.; Fang, F.; Song, Y.; Sun, D. Rational Construction of Nitrogen-Doped Hierarchical Dual-Carbon for Advanced Potassium-Ion Hybrid Capacitors. *Adv. Energy Mater.* **2020**, *10*, 1904045. [CrossRef]
22. Buliyaminu, I.A.; Aziz, M.A.; Shah, S.S.; Mohamedkhair, A.K.; Yamani, Z.H. Preparation of Nano-Co_3O_4-Coated Albizia Procera-Derived Carbon by Direct Thermal Decomposition Method for Electrochemical Water Oxidation. *Arab. J. Chem.* **2020**, *13*, 4785–4796. [CrossRef]
23. Natarajan, S.; Lee, Y.; Aravindan, V. Biomass-Derived Carbon Materials as Prospective Electrodes for High-Energy Lithium- and Sodium-Ion Capacitors. *Chem. Asian J.* **2019**, *14*, 936–951. [CrossRef] [PubMed]
24. Shah, S.S.; Qasem, M.A.A.; Berni, R.; Del Casino, C.; Cai, G.; Contal, S.; Ahmad, I.; Siddiqui, K.S.; Gatti, E.; Predieri, S.; et al. Physico-Chemical Properties and Toxicological Effects on Plant and Algal Models of Carbon Nanosheets from a Nettle Fibre Clone. *Sci. Rep.* **2021**, *11*, 6945. [CrossRef] [PubMed]
25. Lai, F.; Miao, Y.-E.; Zuo, L.; Lu, H.; Huang, Y.; Liu, T. Biomass-Derived Nitrogen-Doped Carbon Nanofiber Network: A Facile Template for Decoration of Ultrathin Nickel-Cobalt Layered Double Hydroxide Nanosheets as High-Performance Asymmetric Supercapacitor Electrode. *Small* **2016**, *12*, 3235–3244. [CrossRef] [PubMed]
26. Wang, Q.; Qin, B.; Qu, C.; Wang, B.; Duan, H.; Cao, Q.; Li, H.; Qi, J. Synthesis of Hierarchical Porous Carbon from Bio-Oil for Supercapacitor Application. *Energy Fuels* **2023**, *37*, 16970–16978. [CrossRef]
27. Wang, T.; Hu, S.; Yu, W.; Hu, Y.; Yan, S.; Wang, M.; Zhao, W.; Xu, J.; Zhang, J. Biologically Inspired Small Herbal Biomolecules and Biomass Carbon for High-Performance Supercapacitors. *ACS Appl. Energy Mater.* **2023**, *6*, 2347–2357. [CrossRef]
28. Zhou, Y.; Parker, C.B.; Joshi, P.; Naskar, A.K.; Glass, J.T.; Cao, C. 4D Printing of Stretchable Supercapacitors via Hybrid Composite Materials. *Adv. Mater. Technol.* **2021**, *6*, 2001055. [CrossRef]
29. Liu, H.; Yao, M.; Yao, X. Improving Energy Density of Crystalline–Amorphous Multilayer Films Deposited on Ti Foils by Structural Modulation. *J. Am. Ceram. Soc.* **2021**, *104*, 1379–1390. [CrossRef]
30. Choi, N.; Chen, Z.; Freunberger, S.A.; Ji, X.; Sun, Y.; Amine, K.; Yushin, G.; Nazar, L.F.; Cho, J.; Bruce, P.G. Challenges Facing Lithium Batteries and Electrical Double-Layer Capacitors. *Angew. Chem. Int. Ed.* **2012**, *51*, 9994–10024. [CrossRef]
31. He, M.; Fic, K.; Frąckowiak, E.; Novák, P.; Berg, E.J. Towards More Durable Electrochemical Capacitors by Elucidating the Ageing Mechanisms under Different Testing Procedures. *ChemElectroChem* **2019**, *6*, 566–573. [CrossRef]
32. Wu, Z.; Parvez, K.; Feng, X.; Müllen, K. Graphene-Based in-Plane Micro-Supercapacitors with High Power and Energy Densities. *Nat. Commun.* **2013**, *4*, 2487. [CrossRef]
33. Kandambeth, S.; Jia, J.; Wu, H.; Kale, V.S.; Parvatkar, P.T.; Czaban-Jóźwiak, J.; Zhou, S.; Xu, X.; Ameur, Z.O.; Abou-Hamad, E.; et al. Covalent Organic Frameworks as Negative Electrodes for High-Performance Asymmetric Supercapacitors. *Adv. Energy Mater.* **2020**, *10*, 2001673. [CrossRef]
34. Nguyen, T.; Montemor, M.d.F. Metal Oxide and Hydroxide–Based Aqueous Supercapacitors: From Charge Storage Mechanisms and Functional Electrode Engineering to Need-Tailored Devices. *Adv. Sci.* **2019**, *6*, 1801797. [CrossRef] [PubMed]

35. Naoi, K.; Ishimoto, S.; Miyamoto, J.; Naoi, W. Second Generation 'Nanohybrid Supercapacitor': Evolution of Capacitive Energy Storage Devices. *Energy Environ. Sci.* **2012**, *5*, 9363–9373. [CrossRef]
36. Guo, Q.; Liu, J.; Bai, C.; Chen, N.; Qu, L. 2D Silicene Nanosheets for High-Performance Zinc-Ion Hybrid Capacitor Application. *ACS Nano* **2021**, *15*, 16533–16541. [CrossRef]
37. Xia, L.; Tang, B.; Wei, J.; Zhou, Z. Recent Advances in Alkali Metal-Ion Hybrid Supercapacitors. *Batter. Supercaps* **2021**, *4*, 1108–1121. [CrossRef]
38. Wang, Q.; Wang, S.; Li, J.; Ruan, L.; Wei, N.; Huang, L.; Dong, Z.; Cheng, Q.; Xiong, Y.; Zeng, W. A Novel Aqueous Zinc-Ion Hybrid Supercapacitor Based on TiS_2 (De)Intercalation Battery-Type Anode. *Adv. Electron. Mater.* **2020**, *6*, 2000388. [CrossRef]
39. Liu, Y.; Zhang, Y.; Sun, Z.; Cheng, S.; Cui, P.; Wu, Y.; Zhang, J.; Fu, J.; Xie, E. New Insight into the Mechanism of Multivalent Ion Hybrid Supercapacitor: From the Effect of Potential Window Viewpoint. *Small* **2020**, *16*, 2003403. [CrossRef] [PubMed]
40. Wang, H.; Zhu, C.; Chao, D.; Yan, Q.; Fan, H.J. Nonaqueous Hybrid Lithium-Ion and Sodium-Ion Capacitors. *Adv. Mater.* **2017**, *29*, 1702093. [CrossRef]
41. Ma, Y.; Chang, H.; Zhang, M.; Chen, Y. Graphene-Based Materials for Lithium-Ion Hybrid Supercapacitors. *Adv. Mater.* **2015**, *27*, 5296–5308. [CrossRef]
42. Zuo, W.; Li, R.; Zhou, C.; Li, Y.; Xia, J.; Liu, J. Battery-Supercapacitor Hybrid Devices: Recent Progress and Future Prospects. *Adv. Sci.* **2017**, *4*, 1600539. [CrossRef] [PubMed]
43. Peng, L.; Peng, X.; Liu, B.; Wu, C.; Xie, Y.; Yu, G. Ultrathin Two-Dimensional MnO_2/Graphene Hybrid Nanostructures for High-Performance, Flexible Planar Supercapacitors. *Nano Lett.* **2013**, *13*, 2151–2157. [CrossRef]
44. Karri, S.N.; Ega, S.P.; Perupogu, V.; Srinivasan, P. Enhancing the Electrochemical Performance of Polyaniline Using Fly Ash of Coal Waste for Supercapacitor Application. *ChemistrySelect* **2021**, *6*, 2576–2589. [CrossRef]
45. Unnikrishnan, B.; Wu, C.-W.; Chen, I.-W.P.; Chang, H.-T.; Lin, C.-H.; Huang, C.-C. Carbon Dot-Mediated Synthesis of Manganese Oxide Decorated Graphene Nanosheets for Supercapacitor Application. *ACS Sustain. Chem. Eng.* **2016**, *4*, 3008–3016. [CrossRef]
46. Fan, W.; Wang, F.; Xiong, X.; Song, B.; Wang, T.; Cheng, X.; Zhu, Z.; He, J.; Liu, Y.; Wu, Y. Recent Advances in Functional Materials and Devices for Zn-Ion Hybrid Supercapacitors. *NPG Asia Mater.* **2024**, *16*, 18. [CrossRef]
47. Huang, C.; Zhao, X.; Xu, Y.; Zhang, Y.; Yang, Y.; Hu, A.; Tang, Q.; Song, X.; Jiang, C.; Chen, X. Sewable and Cuttable Flexible Zinc-Ion Hybrid Supercapacitor Using a Polydopamine/Carbon Cloth-Based Cathode. *ACS Sustain. Chem. Eng.* **2020**, *8*, 16028–16036. [CrossRef]
48. Zhang, H.; Liu, Q.; Fang, Y.; Teng, C.; Liu, X.; Fang, P.; Tong, Y.; Lu, X. Boosting Zn-Ion Energy Storage Capability of Hierarchically Porous Carbon by Promoting Chemical Adsorption. *Adv. Mater.* **2019**, *31*, 1904948. [CrossRef] [PubMed]
49. Zheng, Y.; Zhao, W.; Jia, D.; Liu, Y.; Cui, L.; Wei, D.; Zheng, R.; Liu, J. Porous Carbon Prepared via Combustion and Acid Treatment as Flexible Zinc-Ion Capacitor Electrode Material. *Chem. Eng. J.* **2020**, *387*, 124161. [CrossRef]
50. Li, Z.; Chen, D.; An, Y.; Chen, C.; Wu, L.; Chen, Z.; Sun, Y.; Zhang, X. Flexible and Anti-Freezing Quasi-Solid-State Zinc Ion Hybrid Supercapacitors Based on Pencil Shavings Derived Porous Carbon. *Energy Storage Mater.* **2020**, *28*, 307–314. [CrossRef]
51. Yin, J.; Zhang, W.; Wang, W.; Alhebshi, N.A.; Salah, N.; Alshareef, H.N. Electrochemical Zinc Ion Capacitors Enhanced by Redox Reactions of Porous Carbon Cathodes. *Adv. Energy Mater.* **2020**, *10*, 2001705. [CrossRef]
52. Shah, S.S.; Aziz, M.A.; Ali, M.; Hakeem, A.S.; Yamani, Z.H. Advanced High-Energy All-Solid-State Hybrid Supercapacitor with Nickel-Cobalt-Layered Double Hydroxide Nanoflowers Supported on Jute Stick-Derived Activated Carbon Nanosheets. *Small* **2023**, 2306665. [CrossRef]
53. Wang, R.; Han, M.; Zhao, Q.; Ren, Z.; Guo, X.; Xu, C.; Hu, N.; Lu, L. Hydrothermal Synthesis of Nanostructured Graphene/Polyaniline Composites as High-Capacitance Electrode Materials for Supercapacitors. *Sci. Rep.* **2017**, *7*, 44562. [CrossRef]
54. Young, C.; Park, T.; Yi, J.W.; Kim, J.; Hossain, M.S.A.; Kaneti, Y.V.; Yamauchi, Y. Advanced Functional Carbons and Their Hybrid Nanoarchitectures towards Supercapacitor Applications. *ChemSusChem* **2018**, *11*, 3546–3558. [CrossRef]
55. Abouelamaiem, D.I.; He, G.; Parkin, I.; Neville, T.P.; Jorge, A.B.; Ji, S.; Wang, R.; Titirici, M.-M.; Shearing, P.R.; Brett, D.J.L. Synergistic Relationship between the Three-Dimensional Nanostructure and Electrochemical Performance in Biocarbon Supercapacitor Electrode Materials. *Sustain. Energy Fuels* **2018**, *2*, 772–785. [CrossRef]
56. Wang, K.; Zhang, Z.; Sun, Q.; Wang, P.; Li, Y. Durian Shell-Derived N, O, P-Doped Activated Porous Carbon Materials and Their Electrochemical Performance in Supercapacitor. *J. Mater. Sci.* **2020**, *55*, 10142–10154. [CrossRef]
57. Liu, B.; Zhang, X.; Tian, D.; Li, Q.; Zhong, M.; Chen, S.; Hu, C.; Ji, H. In Situ Growth of Oriented Polyaniline Nanorod Arrays on the Graphite Flake for High-Performance Supercapacitors. *ACS Omega* **2020**, *5*, 32395–32402. [CrossRef]
58. Mehmandoust, M.; Li, G.; Erk, N. Biomass-Derived Carbon Materials as an Emerging Platform for Advanced Electrochemical Sensors: Recent Advances and Future Perspectives. *Ind. Eng. Chem. Res.* **2023**, *62*, 4628–4635. [CrossRef]
59. Galek, P.; Mackowiak, A.; Bujewska, P.; Fic, K. Three-Dimensional Architectures in Electrochemical Capacitor Applications—Insights, Opinions, and Perspectives. *Front. Energy Res.* **2020**, *8*, 139. [CrossRef]
60. Olabi, A.G.; Abbas, Q.; Abdelkareem, M.A.; Alami, A.H.; Mirzaeian, M.; Sayed, E.T. Carbon-Based Materials for Supercapacitors: Recent Progress, Challenges and Barriers. *Batteries* **2022**, *9*, 19. [CrossRef]
61. Jiang, L.; Sheng, L.; Fan, Z. Biomass-Derived Carbon Materials with Structural Diversities and Their Applications in Energy Storage. *Sci. China Mater.* **2018**, *61*, 133–158. [CrossRef]

62. Falco, C.; Marco-Lozar, J.P.; Salinas-Torres, D.; Morallón, E.; Cazorla-Amorós, D.; Titirici, M.M.; Lozano-Castelló, D. Tailoring the Porosity of Chemically Activated Hydrothermal Carbons: Influence of the Precursor and Hydrothermal Carbonization Temperature. *Carbon* **2013**, *62*, 346–355. [CrossRef]
63. Chen, D.; Yang, L.; Li, J.; Wu, Q. Effect of Self-Doped Heteroatoms in Biomass-Derived Activated Carbon for Supercapacitor Applications. *ChemistrySelect* **2019**, *4*, 1586–1595. [CrossRef]
64. Guo, D.; Li, Z.; Wang, D.; Sun, M.; Wang, H. Design and Synthesis of Zinc-Activated $Co_xNi_{2-x}P$/Graphene Anode for High-Performance Zinc Ion Storage Device. *ChemSusChem* **2021**, *14*, 2205–2215. [CrossRef]
65. Yang, J.; Bissett, M.A.; Dryfe, R.A.W. Investigation of Voltage Range and Self-Discharge in Aqueous Zinc-Ion Hybrid Supercapacitors. *ChemSusChem* **2021**, *14*, 1700–1709. [CrossRef]
66. Lu, J.; Lin, X.; Wang, S.; Xu, X.; Zhou, Y.; Zhang, Y.; Li, Q.; Liu, H. High Ionic Conductivity and Toughness Hydrogel Electrolyte for High-Performance Flexible Solid-State Zinc-Ion Hybrid Supercapacitors Enabled by Cellulose-Bentonite Coordination Interactions. *Green Chem.* **2023**, *25*, 1635–1646. [CrossRef]
67. Chen, S.; Yang, G.; Zhao, X.; Wang, N.; Luo, T.; Chen, X.; Wu, T.; Jiang, S.; van Aken, P.A.; Qu, S.; et al. Hollow Mesoporous Carbon Spheres for High Performance Symmetrical and Aqueous Zinc-Ion Hybrid Supercapacitor. *Front. Chem.* **2020**, *8*, 663. [CrossRef]
68. Chang, H.; Khan, I.; Yuan, A.; Khan, S.; Sadiq, S.; Khan, A.; Shah, S.A.; Chen, L.; Humayun, M.; Usman, M. Polyarylimide-Based COF/MOF Nanoparticle Hybrids for CO_2 Conversion, Hydrogen Generation, and Organic Pollutant Degradation. *ACS Appl. Nano Mater.* **2024**, *7*, 10451–10465. [CrossRef]
69. Shah, S.A.; Khan, I.; Yuan, A. MoS_2 as a Co-Catalyst for Photocatalytic Hydrogen Production: A Mini Review. *Molecules* **2022**, *27*, 3289. [CrossRef]
70. Samage, A.; Halakarni, M.; Yoon, H.; Sanna Kotrappanavar, N. Sustainable Conversion of Agricultural Biomass Waste into Electrode Materials with Enhanced Energy Density for Aqueous Zinc-Ion Hybrid Capacitors. *Carbon* **2024**, *219*, 118774. [CrossRef]
71. Naik, P.B.; Yadav, P.; Nagaraj, R.; Puttaswamy, R.; Beere, H.K.; Maiti, U.N.; Mondal, C.; Sanna Kotrappanavar, N.; Ghosh, D. Developing High-Performance Flexible Zinc Ion Capacitors from Agricultural Waste-Derived Carbon Sheets. *ACS Sustain. Chem. Eng.* **2022**, *10*, 1471–1481. [CrossRef]
72. Li, S.; Luo, X.; Xiao, H.; Li, D.; Chen, Y. Nitrogen and Sulfur Codoped Hierarchical Porous Carbon Derived from Lignin for High-Performance Zinc Ion Capacitors. *ACS Appl. Energy Mater.* **2023**, *6*, 6700–6711. [CrossRef]
73. Zhao, X.; Hong, R.; Lu, R.; Chen, Y.; Yang, X. Sustainable Synthesis of Hierarchically Porous Hollow Carbon Spheres for Enhanced Zinc-Ion Hybrid Supercapacitors. *ACS Appl. Energy Mater.* **2024**, *7*, 931–940. [CrossRef]
74. Du, X.; Ma, Y.; Xie, X.; Jiang, H.; Sun, X.; Yang, X.; Zhang, Y.; Hou, C.; Du, W. Preparation of Two-Dimensional Porous Nitrogen-oxygen Co-Doped Recycled Yeast Cell Wall Derived-carbon Matrix for High-Performance Zinc Ion Supercapacitors. *J. Energy Storage* **2024**, *82*, 110428. [CrossRef]
75. Wang, J.; Nie, P.; Ding, B.; Dong, S.; Hao, X.; Dou, H.; Zhang, X. Biomass Derived Carbon for Energy Storage Devices. *J. Mater. Chem. A* **2017**, *5*, 2411–2428. [CrossRef]
76. Yan, M.; Qin, Y.; Wang, L.; Song, M.; Han, D.; Jin, Q.; Zhao, S.; Zhao, M.; Li, Z.; Wang, X.; et al. Recent Advances in Biomass-Derived Carbon Materials for Sodium-Ion Energy Storage Devices. *Nanomaterials* **2022**, *12*, 930. [CrossRef]
77. Cheng, P.; Gao, S.; Zang, P.; Yang, X.; Bai, Y.; Xu, H.; Liu, Z.; Lei, Z. Hierarchically Porous Carbon by Activation of Shiitake Mushroom for Capacitive Energy Storage. *Carbon* **2015**, *93*, 315–324. [CrossRef]
78. Liu, H.; Liu, H.; Di, S.; Zhai, B.; Li, L.; Wang, S. Advantageous Tubular Structure of Biomass-Derived Carbon for High-Performance Sodium Storage. *ACS Appl. Energy Mater.* **2021**, *4*, 4955–4965. [CrossRef]
79. Niu, J.; Guan, J.; Dou, M.; Zhang, Z.; Kong, J.; Wang, F. Sustainable Synthesis of Biomass-Derived Carbon Electrodes with Hybrid Energy-Storage Behaviors for Use in High-Performance Na-Ion Capacitors. *ACS Appl. Energy Mater.* **2020**, *3*, 2478–2489. [CrossRef]
80. Guo, Y.; Liu, W.; Wu, R.; Sun, L.; Zhang, Y.; Cui, Y.; Liu, S.; Wang, H.; Shan, B. Marine-Biomass-Derived Porous Carbon Sheets with a Tunable N-Doping Content for Superior Sodium-Ion Storage. *ACS Appl. Mater. Interfaces* **2018**, *10*, 38376–38386. [CrossRef]
81. Liu, H.; Liu, X.; Wang, H.; Zheng, Y.; Zhang, H.; Shi, J.; Liu, W.; Huang, M.; Kan, J.; Zhao, X.; et al. High-Performance Sodium-Ion Capacitor Constructed by Well-Matched Dual-Carbon Electrodes from a Single Biomass. *ACS Sustain. Chem. Eng.* **2019**, *7*, 12188–12199. [CrossRef]
82. Zhang, L.; Sun, J.; Zhao, H.; Sun, Y.; Dai, L.; Yao, F.; Fu, Y.; Zhu, J. Gas Expansion-Assisted Preparation of 3D Porous Carbon Nanosheet for High-Performance Sodium Ion Hybrid Capacitor. *J. Power Sources* **2020**, *475*, 228679. [CrossRef]
83. Zhang, N.; Liu, Q.; Chen, W.; Wan, M.; Li, X.; Wang, L.; Xue, L.; Zhang, W. High Capacity Hard Carbon Derived from Lotus Stem as Anode for Sodium Ion Batteries. *J. Power Sources* **2018**, *378*, 331–337. [CrossRef]
84. Gao, Z.; Zhang, Y.; Song, N.; Li, X. Biomass-Derived Renewable Carbon Materials for Electrochemical Energy Storage. *Mater. Res. Lett.* **2017**, *5*, 69–88. [CrossRef]
85. Jiang, B.; Cao, L.; Yuan, Q.; Ma, Z.; Huang, Z.; Lin, Z.; Zhang, P. Biomass Straw-Derived Porous Carbon Synthesized for Supercapacitor by Ball Milling. *Materials* **2022**, *15*, 924. [CrossRef] [PubMed]
86. Feng, S.; Xing, L.; Li, K.; Wang, H.; An, Q.; Zhou, L.; Mai, L. Solvent-Free Synthesis of Polymer Spheres and the Activation to Porous Carbon Spheres for Advanced Aluminum-Ion Hybrid Capacitors. *Small Methods* **2023**, *7*, 2300150. [CrossRef]

87. Seon, E.; Jang, S.; Raj, M.R.; Tak, Y.; Lee, G. Ultrahigh Energy Density and Long-Life Cyclic Stability of Surface-Treated Aluminum-Ion Supercapacitors. *ACS Appl. Mater. Interfaces* **2022**, *14*, 45059–45072. [CrossRef] [PubMed]
88. Lei, H.; Tu, J.; Tian, D.; Jiao, S. A Nitrogen-Doped Graphene Cathode for High-Capacitance Aluminum-Ion Hybrid Supercapacitors. *New J. Chem.* **2018**, *42*, 15684–15691. [CrossRef]
89. Sun, W.; Xing, L.; Zhang, B.; Shi, W.; Ren, J.; Zhang, X.; Xiong, F.; An, Q. Ultra-High-Performance Aluminum-Based Hybrid Supercapacitors Prepared for Nitrogen-Doped Micro-Mesoporous Carbon Sphere. *J. Power Sources* **2023**, *571*, 233052. [CrossRef]
90. Zhang, K.; Liu, M.; Si, M.; Wang, Z.; Zhuo, S.; Chai, L.; Shi, Y. Polyhydroxyalkanoate-Modified Bacterium Regulates Biomass Structure and Promotes Synthesis of Carbon Materials for High-Performance Supercapacitors. *ChemSusChem* **2019**, *12*, 1732–1742. [CrossRef]
91. Feng, T.; Wang, S.; Hua, Y.; Zhou, P.; Liu, G.; Ji, K.; Lin, Z.; Shi, S.; Jiang, X.; Zhang, R. Synthesis of Biomass-Derived N,O-Codoped Hierarchical Porous Carbon with Large Surface Area for High-Performance Supercapacitor. *J. Energy Storage* **2021**, *44*, 103286. [CrossRef]
92. Shah, S.S.; Aziz, M.A.; Yamani, Z.H. Recent Progress in Carbonaceous and Redox-Active Nanoarchitectures for Hybrid Supercapacitors: Performance Evaluation, Challenges, and Future Prospects. *Chem. Rec.* **2022**, *22*, e202200018. [CrossRef] [PubMed]
93. Sudhan, N.; Subramani, K.; Karnan, M.; Ilayaraja, N.; Sathish, M. Biomass-Derived Activated Porous Carbon from Rice Straw for a High-Energy Symmetric Supercapacitor in Aqueous and Non-Aqueous Electrolytes. *Energy Fuels* **2017**, *31*, 977–985. [CrossRef]
94. Yin, Y.; Liu, Q.; Zhao, Y.; Chen, T.; Wang, J.; Gui, L.; Lu, C. Recent Progress and Future Directions of Biomass-Derived Hierarchical Porous Carbon: Designing, Preparation, and Supercapacitor Applications. *Energy Fuels* **2023**, *37*, 3523–3554. [CrossRef]
95. Zhang, W.; Yin, J.; Wang, C.; Zhao, L.; Jian, W.; Lu, K.; Lin, H.; Qiu, X.; Alshareef, H.N. Lignin Derived Porous Carbons: Synthesis Methods and Supercapacitor Applications. *Small Methods* **2021**, *5*, 2100896. [CrossRef]
96. Cui, Y.; Liu, W.; Feng, W.; Zhang, Y.; Du, Y.; Liu, S.; Wang, H.; Chen, M.; Zhou, J. Controlled Design of Well-Dispersed Ultrathin MoS 2 Nanosheets inside Hollow Carbon Skeleton: Toward Fast Potassium Storage by Constructing Spacious "Houses" for K Ions. *Adv. Funct. Mater.* **2020**, *30*, 1908755. [CrossRef]
97. Baskar, A.V.; Singh, G.; Ruban, A.M.; Davidraj, J.M.; Bahadur, R.; Sooriyakumar, P.; Kumar, P.; Karakoti, A.; Yi, J.; Vinu, A. Recent Progress in Synthesis and Application of Biomass-Based Hybrid Electrodes for Rechargeable Batteries. *Adv. Funct. Mater.* **2023**, *33*, 2208349. [CrossRef]
98. Pham, H.D.; Mahale, K.; Hoang, T.M.L.; Mundree, S.G.; Gomez-Romero, P.; Dubal, D.P. Dual Carbon Potassium-Ion Capacitors: Biomass-Derived Graphene-like Carbon Nanosheet Cathodes. *ACS Appl. Mater. Interfaces* **2020**, *12*, 48518–48525. [CrossRef]
99. Chen, M.; Liu, W.; Du, Y.; Cui, Y.; Feng, W.; Zhou, J.; Gao, X.; Wang, T.; Liu, S.; Jin, Y. "Plains–Hills": A New Model to Design Biomass-Derived Carbon Electrode Materials for High-Performance Potassium Ion Hybrid Supercapacitors. *ACS Sustain. Chem. Eng.* **2021**, *9*, 3931–3941. [CrossRef]
100. Huang, F.; Liu, W.; Wang, Q.; Wang, F.; Yao, Q.; Yan, D.; Xu, H.; Xia, B.Y.; Deng, J. Natural N/O-Doped Hard Carbon for High Performance K-Ion Hybrid Capacitors. *Electrochim. Acta* **2020**, *354*, 136701. [CrossRef]
101. Rajkumar, P.; Thirumal, V.; Radhika, G.; Gnanamuthu, R.M.; Subadevi, R.; Sivakumar, M.; Yoo, K.; Kim, J. Eco-Friendly Production of Carbon Electrode from Biomass for High Performance Lithium and Zinc Ion Capacitors with Hybrid Energy Storage Characteristics. *Mater. Lett.* **2024**, *354*, 135320. [CrossRef]
102. Tian, Z.; Yang, C.; Zhang, C.; Han, X.; Han, J.; Liu, K.; He, S.; Duan, G.; Jian, S.; Hu, J.; et al. In-Situ Activation of Resorcinol-Furfural Resin Derived Hierarchical Porous Carbon for Supercapacitors and Zinc-Ion Hybrid Capacitors. *J. Energy Storage* **2024**, *85*, 111130. [CrossRef]
103. Chen, G.; Hu, Z.; Pan, Z.; Wang, D. Design of Honeycomb-like Hierarchically Porous Carbons with Engineered Mesoporosity for Aqueous Zinc-Ion Hybrid Supercapacitors Applications. *J. Energy Storage* **2021**, *38*, 102534. [CrossRef]
104. Zhao, L.; Jian, W.; Zhang, X.; Wen, F.; Zhu, J.; Huang, S.; Yin, J.; Lu, K.; Zhou, M.; Zhang, W.; et al. Multi-Scale Self-Templating Synthesis Strategy of Lignin-Derived Hierarchical Porous Carbons toward High-Performance Zinc Ion Hybrid Supercapacitors. *J. Energy Storage* **2022**, *53*, 105095. [CrossRef]
105. Yu, H.; Chen, X.; Zhou, J.; Wang, H. Tannin-Derived Ordered Mesoporous Carbon Cathode for Zn-Ion Hybrid Supercapacitor with Remarkable Energy Density. *Ind. Eng. Chem. Res.* **2023**, *62*, 62–71. [CrossRef]
106. Zheng, J.; Song, Q.; Qi, Y.; Leng, H.; Zhou, W.; Li, S.; Qiu, J. N, O Co-Doped Porous Carbon Derived from Pine Needles for Zinc-Ion Hybrid Supercapacitors. *New J. Chem.* **2023**, *47*, 9692–9700. [CrossRef]
107. Gupta, H.; Dahiya, Y.; Rathore, H.K.; Awasthi, K.; Kumar, M.; Sarkar, D. Energy-Dense Zinc Ion Hybrid Supercapacitors with S, N Dual-Doped Porous Carbon Nanocube Based Cathodes. *ACS Appl. Mater. Interfaces* **2023**, *15*, 42685–42696. [CrossRef] [PubMed]
108. Sielicki, K.; Maślana, K.; Mijowska, E. Fallen Autumn Leaves—The Source of Highly Porous Carbon for Zn-Ion Hybrid Supercapacitors. *Diam. Relat. Mater.* **2024**, *144*, 111021. [CrossRef]
109. Wei, F.; Wei, Y.; Wang, J.; Han, M.; Lv, Y. N, P Dual Doped Foamy-like Carbons with Abundant Defect Sites for Zinc Ion Hybrid Capacitors. *Chem. Eng. J.* **2022**, *450*, 137919. [CrossRef]
110. Wang, H.; Chen, X.; Zhang, J.; Yuan, Z.; Ye, P.; Shen, J.; Zhong, Y.; Hu, Y. Unveiling the Cooperative Roles of Pyrrolic-N and Carboxyl Groups in Biomass-Derived Hierarchical Porous Carbon Nanosheets for High Energy-Power Zn-Ion Hybrid Supercapacitors. *Appl. Surf. Sci.* **2022**, *598*, 153819. [CrossRef]
111. Zhu, Y.; Chen, M.; Li, Q.; Yuan, C.; Wang, C. A Porous Biomass-Derived Anode for High-Performance Sodium-Ion Batteries. *Carbon* **2018**, *129*, 695–701. [CrossRef]

112. Muruganantham, R.; Wang, F.-M.; Liu, W.-R. A Green Route N, S-Doped Hard Carbon Derived from Fruit-Peel Biomass Waste as an Anode Material for Rechargeable Sodium-Ion Storage Applications. *Electrochim. Acta* **2022**, *424*, 140573. [CrossRef]
113. Chen, J.; Zhou, X.; Mei, C.; Xu, J.; Zhou, S.; Wong, C.-P. Evaluating Biomass-Derived Hierarchically Porous Carbon as the Positive Electrode Material for Hybrid Na-Ion Capacitors. *J. Power Sources* **2017**, *342*, 48–55. [CrossRef]
114. Ragul, S.; Sujithkrishnan, E.; Elumalai, P. Inherent Heteroatom-Enriched Amorphous Carbon as High-Performance Electrode for Sodium-Ion Battery and Sodium-Ion Ultracapacitor. *Energy Fuels* **2022**, *36*, 15221–15233. [CrossRef]
115. Vadivazhagan, M.; Parameswaran, P.; Mani, U.; Nallathamby, K. Waste-Driven Bio-Carbon Electrode Material for Na-Ion Storage Applications. *ACS Sustain. Chem. Eng.* **2018**, *6*, 13915–13923. [CrossRef]
116. Zou, X.; Dong, C.; Jin, Y.; Wang, D.; Li, L.; Wu, S.; Xu, Z.; Chen, Y.; Li, Z.; Yang, H. Engineering of N, P Co-Doped Hierarchical Porous Carbon from Sugarcane Bagasse for High-Performance Supercapacitors and Sodium Ion Batteries. *Colloids Surf. A Physicochem. Eng. Asp.* **2023**, *672*, 131715. [CrossRef]
117. Wu, C.; Xu, Q.; Ning, H.; Zhao, Y.; Guo, S.; Sun, X.; Wang, Y.; Hu, H.; Wu, M. Petroleum Pitch Derived Carbon as Both Cathode and Anode Materials for Advanced Potassium-Ion Hybrid Capacitors. *Carbon* **2022**, *196*, 727–735. [CrossRef]
118. Yang, M.; Kong, Q.; Feng, W.; Yao, W. N/O Double-Doped Biomass Hard Carbon Material Realizes Fast and Stable Potassium Ion Storage. *Carbon* **2021**, *176*, 71–82. [CrossRef]
119. Cao, W.; Zhang, E.; Wang, J.; Liu, Z.; Ge, J.; Yu, X.; Yang, H.; Lu, B. Potato Derived Biomass Porous Carbon as Anode for Potassium Ion Batteries. *Electrochim. Acta* **2019**, *293*, 364–370. [CrossRef]
120. Wang, P.; Gong, Z.; Ye, K.; Gao, Y.; Zhu, K.; Yan, J.; Wang, G.; Cao, D. N-Rich Biomass Carbon Derived from Hemp as a Full Carbon-Based Potassium Ion Hybrid Capacitor Anode. *Appl. Surf. Sci.* **2021**, *553*, 149569. [CrossRef]
121. Gao, C.; Wang, Q.; Luo, S.; Wang, Z.; Zhang, Y.; Liu, Y.; Hao, A.; Guo, R. High Performance Potassium-Ion Battery Anode Based on Biomorphic N-Doped Carbon Derived from Walnut Septum. *J. Power Sources* **2019**, *415*, 165–171. [CrossRef]
122. Gong, Y.; Fu, D.; Fan, M.; Zheng, S.; Xue, Y. Multilayer Core–Sheath Wires with Radially Aligned N-Doped Carbon Nanohole Arrays for Boosting Energy Storage in Zinc-Ion Hybrid Supercapacitors. *ACS Appl. Mater. Interfaces* **2024**, *16*, 4793–4802. [CrossRef] [PubMed]
123. Sun, Z.; Jiao, X.; Chu, S.; Li, Z. Low-cost Porous Carbon Materials Prepared from Peanut Red Peels for Novel Zinc-ion Hybrid Capacitors. *ChemistrySelect* **2023**, *8*, e202304071. [CrossRef]
124. Chen, J.; Yang, B.; Liu, B.; Lang, J.; Yan, X. Recent Advances in Anode Materials for Sodium- and Potassium-Ion Hybrid Capacitors. *Curr. Opin. Electrochem.* **2019**, *18*, 1–8. [CrossRef]
125. Zeng, Z.; Mao, Y.; Hu, Z.; Chen, K.; Huang, Q.; Song, Y.; Wu, Z.; Zhang, P.; Chen, T.; Guo, X. Research Progress and Commercialization of Biologically Derived Hard Carbon Anode Materials for Sodium-Ion Batteries. *Ind. Eng. Chem. Res.* **2023**, *62*, 15343–15359. [CrossRef]
126. Yoo, H.D.; Han, S.-D.; Bayliss, R.D.; Gewirth, A.A.; Genorio, B.; Rajput, N.N.; Persson, K.A.; Burrell, A.K.; Cabana, J. "Rocking-Chair"—Type Metal Hybrid Supercapacitors. *ACS Appl. Mater. Interfaces* **2016**, *8*, 30853–30862. [CrossRef]
127. Han, J.; Mariani, A.; Zarrabeitia, M.; Jusys, Z.; Behm, R.J.; Varzi, A.; Passerini, S. Zinc-Ion Hybrid Supercapacitors Employing Acetate-Based Water-in-Salt Electrolytes. *Small* **2022**, *18*, 2201563. [CrossRef]
128. Varanasi, S.R.; Bhatia, S.K. Optimal Electrode Mass Ratio in Nanoporous Carbon Electrochemical Supercapacitors. *J. Phys. Chem. C* **2016**, *120*, 27925–27933. [CrossRef]
129. Cho, S.; Lim, J.; Seo, Y. Flexible Solid Supercapacitors of Novel Nanostructured Electrodes Outperform Most Supercapacitors. *ACS Omega* **2022**, *7*, 37825–37833. [CrossRef]
130. Cherusseri, J.; Sambath Kumar, K.; Choudhary, N.; Nagaiah, N.; Jung, Y.; Roy, T.; Thomas, J. Novel Mesoporous Electrode Materials for Symmetric, Asymmetric and Hybrid Supercapacitors. *Nanotechnology* **2019**, *30*, 202001. [CrossRef]
131. Wang, J.; Kaskel, S. KOH Activation of Carbon-Based Materials for Energy Storage. *J. Mater. Chem.* **2012**, *22*, 23710–23725. [CrossRef]
132. Ahmad, S.; Hussain, A.; Mian, S.A.; Rahman, G.; Ali, S.; Jang, J. Sensing and Conversion of Carbon Dioxide to Methanol Using Ag-Decorated Zinc Oxide Nanocatalyst. *Mater. Adv.* **2024**, *5*, 1119–1129. [CrossRef]
133. Wang, Z.; Zhang, M.; Ma, W.; Zhu, J.; Song, W. Application of Carbon Materials in Aqueous Zinc Ion Energy Storage Devices. *Small* **2021**, *17*, 2100219. [CrossRef]
134. Javed, M.S.; Asim, S.; Najam, T.; Khalid, M.; Hussain, I.; Ahmad, A.; Assiri, M.A.; Han, W. Recent Progress in Flexible Zn-ion Hybrid Supercapacitors: Fundamentals, Fabrication Designs, and Applications. *Carbon Energy* **2023**, *5*, e271. [CrossRef]
135. Yu, J.; Wang, L.; Peng, J.; Jia, X.; Zhou, L.; Yang, N.; Li, L. O-Doped Porous Carbon Derived from Biomass Waste for High-Performance Zinc-Ion Hybrid Supercapacitors. *Ionics (Kiel)* **2021**, *27*, 4495–4505. [CrossRef]
136. Amiri, A.; Swart, E.N.; Polycarpou, A.A. Recent Advances in Electrochemically-Efficient Materials for Zinc-Ion Hybrid Supercapacitors. *Renew. Sustain. Energy Rev.* **2021**, *148*, 111288. [CrossRef]
137. Hou, X.; Ren, P.; Tian, W.; Xue, R.; Fan, B.; Ren, F.; Jin, Y. High-Performance Zn-Ion Hybrid Supercapacitors Based on Biomass-Derived Hierarchical Porous Carbon through Template-Activated Bifunctional Induced and Ice-Crystal Assisted Strategy. *J. Power Sources* **2024**, *603*, 234408. [CrossRef]
138. Zhou, S.; Li, C.; Gao, G.; Fan, H.; Hu, X. Bio-Based Resins with Tannin and Hydroxymethylfurfural Derived High-Yield Carbon for Zn-Ion Hybrid Supercapacitors. *J. Clean. Prod.* **2023**, *389*, 136067. [CrossRef]

139. Zhang, W.; Yin, J.; Jian, W.; Wu, Y.; Chen, L.; Sun, M.; Schwingenschlögl, U.; Qiu, X.; Alshareef, H.N. Supermolecule-Mediated Defect Engineering of Porous Carbons for Zinc-Ion Hybrid Capacitors. *Nano Energy* **2022**, *103*, 107827. [CrossRef]
140. Ma, Y.; Hou, C.; Kimura, H.; Xie, X.; Jiang, H.; Sun, X.; Yang, X.; Zhang, Y.; Du, W. Recent Advances in the Application of Carbon-Based Electrode Materials for High-Performance Zinc Ion Capacitors: A Mini Review. *Adv. Compos. Hybrid Mater.* **2023**, *6*, 59. [CrossRef]
141. Li, Y.; Zhang, X.; Lu, T.; Zhang, Y.; Li, X.; Yu, D.; Zhao, G. Boosting the Capacitance of Aqueous Zinc-Ion Hybrid Capacitors by Engineering Hierarchical Porous Carbon Architecture. *Batteries* **2023**, *9*, 429. [CrossRef]
142. Tekin, B.; Topcu, Y. Novel Hemp Biomass-Derived Activated Carbon as Cathode Material for Aqueous Zinc-Ion Hybrid Supercapacitors: Synthesis, Characterization, and Electrochemical Performance. *J. Energy Storage* **2024**, *77*, 109879. [CrossRef]
143. Yao, L.; Jiang, J.; Peng, H.; Yang, H.; Liu, S.; Wen, X.; Cai, P.; Zou, Y.; Zhang, H.; Xu, F.; et al. Glutinous Rice-Derived Carbon Material for High-Performance Zinc-Ion Hybrid Supercapacitors. *J. Energy Storage* **2023**, *58*, 106378. [CrossRef]
144. Yuksel, R.; Karakehya, N. High Energy Density Biomass-Derived Activated Carbon Materials for Sustainable Energy Storage. *Carbon* **2024**, *221*, 118934. [CrossRef]
145. Jiang, G.; Chen, M.; Sun, Y.; Pan, J. Dual N-Doped Porous Carbon Derived from Pyrolytic Carbon Black and Critical PANIs Constructing High-Performance Zn Ion Hybrid Supercapacitor. *J. Energy Storage* **2023**, *63*, 106955. [CrossRef]
146. Wang, D.; Li, Z.; Guo, D.; Sun, M. Metal-Organic Framework Derived Zinc and Nitrogen Co-Doped Porous Carbon Materials for High Performance Zinc-Ion Hybrid Supercapacitors. *Electrochim. Acta* **2022**, *427*, 140854. [CrossRef]
147. Jia, D.; Shen, Z.; Zhou, W.; Li, Y.; He, J.; Jiang, L.; Wei, Y.; He, X. Ultrahigh N-Doped Carbon with Hierarchical Porous Structure Derived from Metal-Organic Framework for High-Performance Zinc Ion Hybrid Capacitors. *Chem. Eng. J.* **2024**, *485*, 149820. [CrossRef]
148. Liu, H.; Chen, W.; Peng, H.; Huang, X.; Li, S.; Jiang, L.; Zheng, M.; Xu, M.; Zhu, J. Bioinspired Design of Graphene-Based N/O Self-Doped Nanoporous Carbon from Carp Scales for Advanced Zn-Ion Hybrid Supercapacitors. *Electrochim. Acta* **2022**, *434*, 141312. [CrossRef]
149. Zhang, X.; Tian, X.; Song, Y.; Wu, J.; Yang, T.; Liu, Z. High-Performance Activated Carbon Cathodes from Green Cokes for Zn-Ion Hybrid Supercapacitors. *Fuel* **2022**, *310*, 122485. [CrossRef]
150. Wang, J.; Huang, Y.; Han, X.; Li, Z.; Zhang, S.; Zong, M. A Flexible Zinc-Ion Hybrid Supercapacitor Constructed by Porous Carbon with Controllable Structure. *Appl. Surf. Sci.* **2022**, *579*, 152247. [CrossRef]
151. Zhang, X.; Zhang, Y.; Zhang, H.; Zhang, Y.; Ma, Z.; Sun, L. Zinc-ion Hybrid Capacitor with High Energy Density Constructed by Bamboo Shavings Derived Spongy-like Porous Carbon. *ChemistrySelect* **2021**, *6*, 6937–6943. [CrossRef]
152. Liu, Y.; Tan, H.; Tan, Z.; Cheng, X. Rice Husk-Derived Carbon Materials for Aqueous Zn-Ion Hybrid Supercapacitors. *Appl. Surf. Sci.* **2023**, *608*, 155215. [CrossRef]
153. Fan, H.; Zhou, S.; Li, Q.; Gao, G.; Wang, Y.; He, F.; Hu, G.; Hu, X. Hydrogen-Bonded Frameworks Crystals-Assisted Synthesis of Flower-like Carbon Materials with Penetrable Meso/Macropores from Heavy Fraction of Bio-Oil for Zn-Ion Hybrid Supercapacitors. *J. Colloid Interface Sci.* **2021**, *600*, 681–690. [CrossRef] [PubMed]
154. Dang, Z.; Li, X.; Li, Y.; Dong, L. Heteroatom-Rich Carbon Cathodes toward High-Performance Flexible Zinc-Ion Hybrid Supercapacitors. *J. Colloid Interface Sci.* **2023**, *644*, 221–229. [CrossRef] [PubMed]
155. Song, B.; Liu, Q.; Shi, F.; Xue, T.; Yang, C.; Zang, L. Porous Carbon Derived from a By-Product of Traditional Chinese Medicine for High-Performance Aqueous Zinc-Ion Hybrid Supercapacitors. *Diam. Relat. Mater.* **2024**, *142*, 110785. [CrossRef]
156. Lou, G.; Pei, G.; Wu, Y.; Lu, Y.; Wu, Y.; Zhu, X.; Pang, Y.; Shen, Z.; Wu, Q.; Fu, S.; et al. Combustion Conversion of Wood to N, O Co-Doped 2D Carbon Nanosheets for Zinc-Ion Hybrid Supercapacitors. *Chem. Eng. J.* **2021**, *413*, 127502. [CrossRef]
157. Liu, H.; Chen, H.; Shi, K.; Zhang, F.; Xiao, S.; Huang, L.; Zhu, H. Lignin-Derived Porous Carbon for Zinc-Ion Hybrid Capacitor. *Ind. Crops Prod.* **2022**, *187*, 115519. [CrossRef]
158. Xue, B.; Liu, C.; Wang, X.; Feng, Y.; Xu, J.; Gong, F.; Xiao, R. Urea-Boosted Gas-Exfoliation Synthesis of Lignin-Derived Porous Carbon for Zinc Ion Hybrid Supercapacitors. *Chem. Eng. J.* **2024**, *480*, 147994. [CrossRef]
159. Yang, S.; Cui, Y.; Yang, G.; Zhao, S.; Wang, J.; Zhao, D.; Yang, C.; Wang, X.; Cao, B. $ZnCl_2$ Induced Hierarchical Porous Carbon for Zinc-Ion Hybrid Supercapacitors. *J. Power Sources* **2023**, *554*, 232347. [CrossRef]
160. Xue, B.; Xu, J.; Xiao, R. Ice Template-Assisting Activation Strategy to Prepare Biomass-Derived Porous Carbon Cages for High-Performance Zn-Ion Hybrid Supercapacitors. *Chem. Eng. J.* **2023**, *454*, 140192. [CrossRef]
161. Liu, H.; Li, S.; Huang, X.; Chen, W.; Xu, M.; Ren, Y.; Zhang, R.; Miao, Z.; Zhu, J. High Energy-Power Zinc-Ion Hybrid Supercapacitors Achieved by 3D Channels Enriched Biomass-Derived N/O Co-Doped 2D Arcuate Carbon Nanosheets. *Mater. Today Chem.* **2023**, *29*, 101476. [CrossRef]
162. Muruganantham, R.; Wang, F.-M.; Yuwono, R.A.; Sabugaa, M.; Liu, W.-R. Biomass Feedstock of Waste Mango-Peel-Derived Porous Hard Carbon for Sustainable High-Performance Lithium-Ion Energy Storage Devices. *Energy Fuels* **2021**, *35*, 10878–10889. [CrossRef]
163. Ding, J.; Li, Z.; Cui, K.; Boyer, S.; Karpuzov, D.; Mitlin, D. Heteroatom Enhanced Sodium Ion Capacity and Rate Capability in a Hydrogel Derived Carbon Give Record Performance in a Hybrid Ion Capacitor. *Nano Energy* **2016**, *23*, 129–137. [CrossRef]
164. Liao, K.; Wang, H.; Wang, L.; Xu, D.; Wu, M.; Wang, R.; He, B.; Gong, Y.; Hu, X. A High-Energy Sodium-Ion Capacitor Enabled by a Nitrogen/Sulfur Co-Doped Hollow Carbon Nanofiber Anode and an Activated Carbon Cathode. *Nanoscale Adv.* **2019**, *1*, 746–756. [CrossRef]

165. Hong, K.; Qie, L.; Zeng, R.; Yi, Z.; Zhang, W.; Wang, D.; Yin, W.; Wu, C.; Fan, Q.; Zhang, W.; et al. Biomass Derived Hard Carbon Used as a High Performance Anode Material for Sodium Ion Batteries. *J. Mater. Chem. A* **2014**, *2*, 12733–12738. [CrossRef]
166. Liu, L.; Sun, X.; Dong, Y.; Wang, D.; Wang, Z.; Jiang, Z.; Li, A.; Chen, X.; Song, H. N-Doped Hierarchical Porous Hollow Carbon Spheres with Multi-Cavities for High Performance Na-Ion Storage. *J. Power Sources* **2021**, *506*, 230170. [CrossRef]
167. Han, P.; Han, X.; Yao, J.; Zhang, L.; Cao, X.; Huang, C.; Cui, G. High Energy Density Sodium-Ion Capacitors through Co-Intercalation Mechanism in Diglyme-Based Electrolyte System. *J. Power Sources* **2015**, *297*, 457–463. [CrossRef]
168. Ghanem, A.S.; Ba-Shammakh, M.; Usman, M.; Khan, M.F.; Dafallah, H.; Habib, M.A.M.; Al-Maythalony, B.A. High Gas Permselectivity in ZIF-302/Polyimide Self-consistent Mixed-matrix Membrane. *J. Appl. Polym. Sci.* **2020**, *137*, 48513. [CrossRef]
169. Xiang, A.; Shi, D.; Chen, P.; Li, Z.; Tu, Q.; Liu, D.; Zhang, X.; Lu, J.; Jiang, Y.; Yang, Z.; et al. $Na_4Fe_3(PO_4)_2(P_2O_7)$@C/$Ti_3C_2T_x$ Hybrid Cathode Materials with Enhanced Performances for Sodium-Ion Batteries. *Batteries* **2024**, *10*, 121. [CrossRef]
170. Thirumal, V.; Sreekanth, T.V.M.; Yoo, K.; Kim, J. Biomass-Derived Hard Carbon and Nitrogen-Sulfur Co-Doped Graphene for High-Performance Symmetric Sodium Ion Capacitor Devices. *Energies* **2023**, *16*, 802. [CrossRef]
171. Zhu, J.; Roscow, J.; Chandrasekaran, S.; Deng, L.; Zhang, P.; He, T.; Wang, K.; Huang, L. Biomass-Derived Carbons for Sodium-Ion Batteries and Sodium-Ion Capacitors. *ChemSusChem* **2020**, *13*, 1275–1295. [CrossRef]
172. Thangavel, R.; Kannan, A.G.; Ponraj, R.; Yoon, G.; Aravindan, V.; Kim, D.-W.; Kang, K.; Yoon, W.-S.; Lee, Y.-S. Surface Enriched Graphene Hollow Spheres towards Building Ultra-High Power Sodium-Ion Capacitor with Long Durability. *Energy Storage Mater.* **2020**, *25*, 702–713. [CrossRef]
173. Panda, M.R.; Kathribail, A.R.; Modak, B.; Sau, S.; Dutta, D.P.; Mitra, S. Electrochemical Properties of Biomass-Derived Carbon and Its Composite along with $Na_2Ti_3O_7$ as Potential High-Performance Anodes for Na-Ion and Li-Ion Batteries. *Electrochim. Acta* **2021**, *392*, 139026. [CrossRef]
174. Wang, H.; Yu, W.; Shi, J.; Mao, N.; Chen, S.; Liu, W. Biomass Derived Hierarchical Porous Carbons as High-Performance Anodes for Sodium-Ion Batteries. *Electrochim. Acta* **2016**, *188*, 103–110. [CrossRef]
175. Dong, G.; Wang, H.; Liu, W.; Shi, J.; Sun, S.; Li, D.; Zhang, H.; Yang, Y.; Cui, Y. Nitrate Salt Assisted Fabrication of Highly N-Doped Carbons for High-Performance Sodium Ion Capacitors. *ACS Appl. Energy Mater.* **2018**, *1*, 5636–5645. [CrossRef]
176. Nagmani; Satpathy, B.K.; Singh, A.K.; Pradhan, D.; Puravankara, S. Utilization of Single Biomass-Derived Micro-Mesoporous Carbon for Dual-Carbon Symmetric and Hybrid Sodium-Ion Capacitors. *New J. Chem.* **2023**, *47*, 12658–12669. [CrossRef]
177. Casal, M.D.; Díez, N.; Payá, S.; Sevilla, M. Cork-Derived Carbon Sheets for High-Performance Na-Ion Capacitors. *ACS Appl. Energy Mater.* **2023**, *6*, 8120–8131. [CrossRef]
178. Liu, H.; Jia, M.; Sun, N.; Cao, B.; Chen, R.; Zhu, Q.; Wu, F.; Qiao, N.; Xu, B. Nitrogen-Rich Mesoporous Carbon as Anode Material for High-Performance Sodium-Ion Batteries. *ACS Appl. Mater. Interfaces* **2015**, *7*, 27124–27130. [CrossRef]
179. Ding, J.; Wang, H.; Li, Z.; Cui, K.; Karpuzov, D.; Tan, X.; Kohandehghan, A.; Mitlin, D. Peanut Shell Hybrid Sodium Ion Capacitor with Extreme Energy–Power Rivals Lithium Ion Capacitors. *Energy Environ. Sci.* **2015**, *8*, 941–955. [CrossRef]
180. Shi, X.; Yu, J.; Liu, Q.; Shao, L.; Cai, J.; Sun, Z. Metal-Organic-Framework-Derived Multi-Heteroatom Doped Cu1.8Se/C Composites for High-Performance Na-Ion Hybrid Capacitor. *Sustain. Mater. Technol.* **2021**, *28*, e00275. [CrossRef]
181. Yan, R.; Leus, K.; Hofmann, J.P.; Antonietti, M.; Oschatz, M. Porous Nitrogen-Doped Carbon/Carbon Nanocomposite Electrodes Enable Sodium Ion Capacitors with High Capacity and Rate Capability. *Nano Energy* **2020**, *67*, 104240. [CrossRef]
182. Zhao, G.; Yu, D.; Zhang, H.; Sun, F.; Li, J.; Zhu, L.; Sun, L.; Yu, M.; Besenbacher, F.; Sun, Y. Sulphur-Doped Carbon Nanosheets Derived from Biomass as High-Performance Anode Materials for Sodium-Ion Batteries. *Nano Energy* **2020**, *67*, 104219. [CrossRef]
183. Li, L.; Sun, M.; Xu, Z.; Wang, Z.; Liu, K.; Chen, Y.; Wang, Z.; Chen, H.; Yang, H. Hierarchical Porous Hard Carbon Derived from Rice Husks for High-Performance Sodium Ion Storage. *Colloids Surf. A Physicochem. Eng. Asp.* **2023**, *661*, 130927. [CrossRef]
184. Zhang, L.; Wang, Y.; Yang, S.; Zhao, G.; Han, L.; Li, Y.; Zhu, G. Biomass-Derived S, P, Cl Tri-Doped Porous Carbon for High-Performance Supercapacitor. *Diam. Relat. Mater.* **2022**, *126*, 109061. [CrossRef]
185. Ajuria, J.; Redondo, E.; Arnaiz, M.; Mysyk, R.; Rojo, T.; Goikolea, E. Lithium and Sodium Ion Capacitors with High Energy and Power Densities Based on Carbons from Recycled Olive Pits. *J. Power Sources* **2017**, *359*, 17–26. [CrossRef]
186. Dos Reis, G.S.; Petnikota, S.; Subramaniyam, C.M.; de Oliveira, H.P.; Larsson, S.; Thyrel, M.; Lassi, U.; García Alvarado, F. Sustainable Biomass-Derived Carbon Electrodes for Potassium and Aluminum Batteries: Conceptualizing the Key Parameters for Improved Performance. *Nanomaterials* **2023**, *13*, 765. [CrossRef]
187. Li, B.; Dai, F.; Xiao, Q.; Yang, L.; Shen, J.; Zhang, C.; Cai, M. Activated Carbon from Biomass Transfer for High-Energy Density Lithium-Ion Supercapacitors. *Adv. Energy Mater.* **2016**, *6*, 1600802. [CrossRef]
188. Xie, K.; Zhang, W.; Ren, K.; Zhu, E.; Lu, J.; Chen, J.; Yin, P.; Yang, L.; Guan, X.; Wang, G. Electrochemical Performance of Corn Waste Derived Carbon Electrodes Based on the Intrinsic Biomass Properties. *Materials* **2023**, *16*, 5022. [CrossRef]
189. Nayem, S.M.A.; Islam, S.; Shah, S.S.; Sultana, N.; Mahfoz, W.; Ahammad, A.J.S.; Aziz, A. Biomass Based S-doped Carbon for Supercapacitor Application. In *Biomass-Based Supercapacitors*; Wiley: Hoboken, NJ, USA, 2023; pp. 315–327.
190. Wei, X.; Qiu, B.; Xu, L.; Qin, Q.; Zhang, W.; Liu, Z.; Wei, F.; Lv, Y. High Performance Hierarchical Porous Carbon Derived from Waste Shrimp Shell for Supercapacitor Electrodes. *J. Energy Storage* **2023**, *62*, 106900. [CrossRef]
191. Zeng, Y.; Zhao, W.; Li, X.; Chen, X.; Song, J.; Wu, X.; Huang, Z. Biomass Waste Derived Heteroatom Doping Porous Carbon Sheets for High Performance Supercapacitor. *Mater. Today Commun.* **2023**, *36*, 106623. [CrossRef]
192. Wahed, F.; Shah, S.S.; Hayat, K.; Shah, S.K.; Aziz, M.A. Conduction Mechanisms and Thermoelectric Applications of La1-XSrxCoO_3 Nanofibers. *J. Mater. Sci.* **2022**, *57*, 8828–8844. [CrossRef]

193. Hou, J.; Cao, C.; Idrees, F.; Ma, X. Hierarchical Porous Nitrogen-Doped Carbon Nanosheets Derived from Silk for Ultrahigh-Capacity Battery Anodes and Supercapacitors. *ACS Nano* **2015**, *9*, 2556–2564. [CrossRef]
194. Shen, Y.; Zhu, Y. One-Pot Synthesis of Biomass-Derived Porous Carbons for Multipurpose Energy Applications. *J. Mater. Chem. A* **2024**, *12*, 6211–6242. [CrossRef]
195. Li, Z.; Guo, D.; Liu, Y.; Wang, H.; Wang, L. Recent Advances and Challenges in Biomass-Derived Porous Carbon Nanomaterials for Supercapacitors. *Chem. Eng. J.* **2020**, *397*, 125418. [CrossRef]
196. Qian, Y.; Wu, B.; Li, Y.; Pan, Z.; Tian, J.; Lin, N.; Qian, Y. Pressure-Dependent Self-Template Pyrolysis Modulates the Porosity and Surface Chemical Configuration of Carbon for Potassium Ion Hybrid Capacitors. *Chem. Eng. J.* **2023**, *451*, 138579. [CrossRef]
197. Zhao, L.; Sun, S.; Lin, J.; Zhong, L.; Chen, L.; Guo, J.; Yin, J.; Alshareef, H.N.; Qiu, X.; Zhang, W. Defect Engineering of Disordered Carbon Anodes with Ultra-High Heteroatom Doping Through a Supermolecule-Mediated Strategy for Potassium-Ion Hybrid Capacitors. *Nano-Micro Lett.* **2023**, *15*, 41. [CrossRef]
198. Pan, Z.; Qian, Y.; Li, Y.; Xie, X.; Lin, N.; Qian, Y. Novel Bilayer-Shelled N, O-Doped Hollow Porous Carbon Microspheres as High Performance Anode for Potassium-Ion Hybrid Capacitors. *Nano-Micro Lett.* **2023**, *15*, 151. [CrossRef]
199. Gao, Q.; Li, T.; Liu, C.; Sun, J.; Liu, Y.; Hou, L.; Yuan, C. Hierarchically Porous N-Doped Carbon Framework with Enlarged Interlayer Spacing as Dual-Carbon Electrodes for Potassium Ion Hybrid Capacitors. *Carbon Neutrality* **2023**, *2*, 18. [CrossRef]
200. Yvenat, M.-E.; Chavillon, B.; Mayousse, E.; Perdu, F.; Azaïs, P. Development of an Adequate Formation Protocol for a Non-Aqueous Potassium-Ion Hybrid Supercapacitor (KIC) through the Study of the Cell Swelling Phenomenon. *Batteries* **2022**, *8*, 135. [CrossRef]
201. Zhu, L.; Zhang, Z.; Luo, J.; Zhang, H.; Qu, Y.; Yang, Z. Self-Templated Synthesis of Hollow Hierarchical Porous Olive-like Carbon toward Universal High-Performance Alkali (Li, Na, K)-Ion Storage. *Carbon* **2021**, *174*, 317–324. [CrossRef]
202. Yang, M.; Dai, J.; He, M.; Duan, T.; Yao, W. Biomass-Derived Carbon from Ganoderma Lucidum Spore as a Promising Anode Material for Rapid Potassium-Ion Storage. *J. Colloid Interface Sci.* **2020**, *567*, 256–263. [CrossRef] [PubMed]
203. Cao, B.; Gao, S.; Ma, Y.; Zhang, D.; Guo, Z.; Du, M.; Xin, Z.; Zhou, C.; Liu, H. Biomass-Derived Carbon-Sulfur Hybrids Boosting Electrochemical Kinetics to Achieve High Potassium Storage Performance. *J. Colloid Interface Sci.* **2024**, *661*, 598–605. [CrossRef] [PubMed]
204. Lu, S.; Xiao, Q.; Yang, W.; Wang, X.; Guo, T.; Xie, Q.; Ruan, Y. Multi-Heteroatom-Doped Porous Carbon with High Surface Adsorption Energy of Potassium Derived from Biomass Waste for High-Performance Supercapacitors. *Int. J. Biol. Macromol.* **2024**, *258*, 128794. [CrossRef] [PubMed]
205. Zhong, L.; Qiu, X.; Yang, S.; Sun, S.; Chen, L.; Zhang, W. Supermolecule-Regulated Synthesis Strategy of General Biomass-Derived Highly Nitrogen-Doped Carbons toward Potassium-Ion Hybrid Capacitors with Enhanced Performances. *Energy Storage Mater.* **2023**, *61*, 102887. [CrossRef]
206. Zhu, L.; Zhang, Z.; Zhang, H.; Wang, Y.; Luo, J.; Yu, J.; Qu, Y.; Yang, Z. Tunable 2D Tremella-Derived Carbon Nanosheets with Enhanced Pseudocapacitance Behavior for Ultrafast Potassium-Ion Storage. *Sci. China Technol. Sci.* **2021**, *64*, 2047–2056. [CrossRef]
207. Hu, W.; Xiang, R.; Lin, J.; Cheng, Y.; Lu, C. Lignocellulosic Biomass-Derived Carbon Electrodes for Flexible Supercapacitors: An Overview. *Materials* **2021**, *14*, 4571. [CrossRef]
208. Xie, K.; Qin, X.; Wang, X.; Wang, Y.; Tao, H.; Wu, Q.; Yang, L.; Hu, Z. Carbon Nanocages as Supercapacitor Electrode Materials. *Adv. Mater.* **2012**, *24*, 347–352. [CrossRef]
209. Adam, A.A.; Ojur Dennis, J.; Al-Hadeethi, Y.; Mkawi, E.M.; Abubakar Abdulkadir, B.; Usman, F.; Mudassir Hassan, Y.; Wadi, I.A.; Sani, M. State of the Art and New Directions on Electrospun Lignin/Cellulose Nanofibers for Supercapacitor Application: A Systematic Literature Review. *Polymers* **2020**, *12*, 2884. [CrossRef]
210. Yang, X.; Lv, T.; Qiu, J. High Mass-Loading Biomass-Based Porous Carbon Electrodes for Supercapacitors: Review and Perspectives. *Small* **2023**, *19*, 2300336. [CrossRef]
211. Zhang, M.; Peng, L. Research Progress of Biomass-Derived Carbon for the Supercapacitors. *Mater. Res. Express* **2024**, *11*, 012004. [CrossRef]
212. Lu, Q.; Zhou, S.; Zhang, Y.; Chen, M.; Li, B.; Wei, H.; Zhang, D.; Zhang, J.; Liu, Q. Nanoporous Carbon Derived from Green Material by an Ordered Activation Method and Its High Capacitance for Energy Storage. *Nanomaterials* **2020**, *10*, 1058. [CrossRef] [PubMed]
213. Momodu, D.; Bello, A.; Oyedotun, K.; Ochai-Ejeh, F.; Dangbegnon, J.; Madito, M.; Manyala, N. Enhanced Electrochemical Response of Activated Carbon Nanostructures from Tree-Bark Biomass Waste in Polymer-Gel Active Electrolytes. *RSC Adv.* **2017**, *7*, 37286–37295. [CrossRef]
214. Zhu, Y.; Murali, S.; Stoller, M.D.; Ganesh, K.J.; Cai, W.; Ferreira, P.J.; Pirkle, A.; Wallace, R.M.; Cychosz, K.A.; Thommes, M.; et al. Carbon-Based Supercapacitors Produced by Activation of Graphene. *Science* **2011**, *332*, 1537–1541. [CrossRef] [PubMed]
215. Li, B.; Zheng, J.; Zhang, H.; Jin, L.; Yang, D.; Lv, H.; Shen, C.; Shellikeri, A.; Zheng, Y.; Gong, R.; et al. Electrode Materials, Electrolytes, and Challenges in Nonaqueous Lithium-Ion Capacitors. *Adv. Mater.* **2018**, *30*, 1705670. [CrossRef]
216. Biswal, M.; Banerjee, A.; Deo, M.; Ogale, S. From Dead Leaves to High Energy Density Supercapacitors. *Energy Environ. Sci.* **2013**, *6*, 1249–1259. [CrossRef]
217. Zhang, Q.; Yuan, M.; Liu, L.; Li, S.; Chen, X.; Liu, J.; Pang, X.; Wang, X. Study of Zinc Diffusion Based on S, N-Codoped Honeycomb Carbon Cathodes for High-Performance Zinc-Ion Capacitors. *Langmuir* **2024**, *40*, 5326–5337. [CrossRef] [PubMed]

218. Eskusson, J.; Thomberg, T.; Lust, E.; Jänes, A. Electrochemical Characteristics of Zn-Ion Hybrid Supercapacitors Based on Aqueous Solution of Different Electrolytes. *J. Electrochem. Soc.* **2022**, *169*, 020512. [CrossRef]
219. Shao, Y.; El-Kady, M.F.; Sun, J.; Li, Y.; Zhang, Q.; Zhu, M.; Wang, H.; Dunn, B.; Kaner, R.B. Design and Mechanisms of Asymmetric Supercapacitors. *Chem. Rev.* **2018**, *118*, 9233–9280. [CrossRef]
220. Simon, P.; Gogotsi, Y. Capacitive Energy Storage in Nanostructured Carbon-Electrolyte Systems. *Acc. Chem. Res.* **2013**, *46*, 1094–1103. [CrossRef]
221. Maurya, D.K.; Murugadoss, V.; Guo, Z.; Angaiah, S. Designing $Na_2Zn_2TeO_6$-Embedded 3D-Nanofibrous Poly(Vinylidenefluoride)-Co-Hexafluoropropylene-Based Nanohybrid Electrolyte via Electrospinning for Durable Sodium-Ion Capacitors. *ACS Appl. Energy Mater.* **2021**, *4*, 8475–8487. [CrossRef]
222. Dubal, D.P.; Ayyad, O.; Ruiz, V.; Gómez-Romero, P. Hybrid Energy Storage: The Merging of Battery and Supercapacitor Chemistries. *Chem. Soc. Rev.* **2015**, *44*, 1777–1790. [CrossRef] [PubMed]
223. Tomboc, G.M.; Tesfaye Gadisa, B.; Jun, M.; Chaudhari, N.K.; Kim, H.; Lee, K. Carbon Transition-metal Oxide Electrodes: Understanding the Role of Surface Engineering for High Energy Density Supercapacitors. *Chem.—Asian J.* **2020**, *15*, 1628–1647. [CrossRef] [PubMed]
224. Kim, T.; Jung, G.; Yoo, S.; Suh, K.S.; Ruoff, R.S. Activated Graphene-Based Carbons as Supercapacitor Electrodes with Macro- and Mesopores. *ACS Nano* **2013**, *7*, 6899–6905. [CrossRef] [PubMed]
225. Shaker, M.; Ng, S.; Sadeghi Ghazvini, A.A.; Javanmardi, S.; Gaho, M.A.; Jin, Z.; Ge, Q. Carbon/Graphene Quantum Dots as Electrolyte Additives for Batteries and Supercapacitors: A Review. *J. Energy Storage* **2024**, *85*, 111040. [CrossRef]
226. Liu, X.; Sun, Y.; Tong, Y.; Wang, X.; Zheng, J.; Wu, Y.; Li, H.; Niu, L.; Hou, Y. Exploration in Materials, Electrolytes and Performance towards Metal Ion (Li, Na, K, Zn and Mg)-Based Hybrid Capacitors: A Review. *Nano Energy* **2021**, *86*, 106070. [CrossRef]
227. Iqbal, M.Z.; Zakar, S.; Haider, S.S. Role of Aqueous Electrolytes on the Performance of Electrochemical Energy Storage Device. *J. Electroanal. Chem.* **2020**, *858*, 113793. [CrossRef]
228. Kumar, K.S.; Pandey, D.; Thomas, J. High Voltage Asymmetric Supercapacitors Developed by Engineering Electrode Work Functions. *ACS Energy Lett.* **2021**, *6*, 3590–3599. [CrossRef]
229. Guo, Q.; Bai, C.; Gao, C.; Chen, N.; Qu, L. Two Dimensional Silicene Nanosheets: A New Choice of Electrode Material for High-Performance Supercapacitor. *ACS Appl. Mater. Interfaces* **2022**, *14*, 39014–39021. [CrossRef] [PubMed]
230. Wan, F.; Wang, X.; Tang, C.; Jiang, C.; Wang, W.; Li, B.; Zhang, Y.; Zhu, X. Metallic 1T-MoS_2 Coupled with MXene towards Ultra-High Rate-Capabilities for Supercapacitors. *J. Mater. Chem. A* **2022**, *10*, 12258–12268. [CrossRef]
231. Hu, Z.; Song, Z.; Huang, Z.; Tao, S.; Song, B.; Cao, Z.; Hu, X.; Wu, J.; Li, F.; Deng, W.; et al. Reconstructing Hydrogen Bond Network Enables High Voltage Aqueous Zinc-Ion Supercapacitors. *Angew. Chem.* **2023**, *135*, e202309601. [CrossRef]
232. Komaba, S.; Hasegawa, T.; Dahbi, M.; Kubota, K. Potassium Intercalation into Graphite to Realize High-Voltage/High-Power Potassium-Ion Batteries and Potassium-Ion Capacitors. *Electrochem. Commun.* **2015**, *60*, 172–175. [CrossRef]
233. Zhang, F.; Dong, H.; Li, Y.; Fu, D.; Yang, L.; Shang, Y.; Li, Q.; Shao, Y.; Gang, W.; Ding, T.; et al. In Situ Metal-Oxygen-Hydrogen Modified B-Tio_2@Co_2 P-X S-Scheme Heterojunction Effectively Enhanced Charge Separation for Photo-assisted Uranium Reduction. *Adv. Sci.* **2024**, *11*, 2305439. [CrossRef] [PubMed]
234. Huang, Z.; Wang, T.; Song, H.; Li, X.; Liang, G.; Wang, D.; Yang, Q.; Chen, Z.; Ma, L.; Liu, Z.; et al. Effects of Anion Carriers on Capacitance and Self-Discharge Behaviors of Zinc Ion Capacitors. *Angew. Chem.* **2021**, *133*, 1024–1034. [CrossRef]
235. Li, X.; Chen, F.; Zhao, B.; Zhang, S.; Zheng, X.; Wang, Y.; Jin, X.; Dai, C.; Wang, J.; Xie, J.; et al. Ultrafast Synthesis of Metal-Layered Hydroxides in a Dozen Seconds for High-Performance Aqueous Zn (Micro-) Battery. *Nano-Micro Lett.* **2023**, *15*, 32. [CrossRef] [PubMed]
236. Sen, A.; Groß, A. Promising Sensitizers for Dye Sensitized Solar Cells: A Comparison of Ru(II) with Other Earth's Scarce and Abundant Metal Polypyridine Complexes. *Int. J. Quantum Chem.* **2019**, *119*, e25963. [CrossRef]
237. dos Santos Junior, G.A.; Fortunato, V.D.S.; Bastos, G.A.A.; Silva, G.G.; Ortega, P.F.R.; Lavall, R.L. High-Performance Lithium-Ion Hybrid Supercapacitors Based on Lithium Salt/Imidazolium Ionic Liquid Electrolytes and Ni-Doped $LiMn_2O_4$ Cathode Materials. *ACS Appl. Energy Mater.* **2020**, *3*, 9028–9039. [CrossRef]
238. Shah, S.S.; Aziz, M.A.; Cevik, E.; Ali, M.; Gunday, S.T.; Bozkurt, A.; Yamani, Z.H. Sulfur Nano-Confinement in Hierarchically Porous Jute Derived Activated Carbon towards High-Performance Supercapacitor: Experimental and Theoretical Insights. *J. Energy Storage* **2022**, *56*, 105944. [CrossRef]
239. Yu, J.; Jia, X.; Peng, J.; Meng, B.; Wei, Y.; Hou, X.; Zhao, J.; Yang, N.; Xie, K.; Chu, D.; et al. Synergistic Effect of Nitrogen–Sulfur Codoping on Honeycomb-like Carbon-Based High-Energy-Density Zinc-Ion Hybrid Supercapacitors. *ACS Appl. Energy Mater.* **2023**, *6*, 2728–2738. [CrossRef]
240. Qin, J.; Sari, H.M.K.; Wang, X.; Yang, H.; Zhang, J.; Li, X. Controlled Design of Metal Oxide-Based (Mn^{2+}/Nb^{5+}) Anodes for Superior Sodium-Ion Hybrid Supercapacitors: Synergistic Mechanisms of Hybrid Ion Storage. *Nano Energy* **2020**, *71*, 104594. [CrossRef]
241. Li, J.; El-Demellawi, J.K.; Sheng, G.; Björk, J.; Zeng, F.; Zhou, J.; Liao, X.; Wu, J.; Rosen, J.; Liu, X.; et al. Pseudocapacitive Heteroatom-Doped Carbon Cathode for Aluminum-Ion Batteries with Ultrahigh Reversible Stability. *Energy Environ. Mater.* **2024**, e12733. [CrossRef]
242. Chen, J.; Liu, B.; Cai, H.; Liu, S.; Yamauchi, Y.; Jun, S.C. Covalently Interlayer-Confined Organic–Inorganic Heterostructures for Aqueous Potassium Ion Supercapacitors. *Small* **2023**, *19*, 2204275. [CrossRef] [PubMed]

243. Huang, J.; Sumpter, B.G.; Meunier, V. A Universal Model for Nanoporous Carbon Supercapacitors Applicable to Diverse Pore Regimes, Carbon Materials, and Electrolytes. *Chem.—Eur. J.* **2008**, *14*, 6614–6626. [CrossRef] [PubMed]
244. Han, C.; Wang, X.; Peng, J.; Xia, Q.; Chou, S.; Cheng, G.; Huang, Z.; Li, W. Recent Progress on Two-Dimensional Carbon Materials for Emerging Post-Lithium (Na^+, K^+, Zn^{2+}) Hybrid Supercapacitors. *Polymers* **2021**, *13*, 2137. [CrossRef] [PubMed]
245. Hao, P.; Zhao, Z.; Tian, J.; Li, H.; Sang, Y.; Yu, G.; Cai, H.; Liu, H.; Wong, C.P.; Umar, A. Hierarchical Porous Carbon Aerogel Derived from Bagasse for High Performance Supercapacitor Electrode. *Nanoscale* **2014**, *6*, 12120–12129. [CrossRef] [PubMed]
246. Xu, X.; Tang, J.; Qian, H.; Hou, S.; Bando, Y.; Hossain, M.S.A.; Pan, L.; Yamauchi, Y. Three-Dimensional Networked Metal–Organic Frameworks with Conductive Polypyrrole Tubes for Flexible Supercapacitors. *ACS Appl. Mater. Interfaces* **2017**, *9*, 38737–38744. [CrossRef]
247. Khan, A.; Sadiq, S.; Khan, I.; Humayun, M.; Jiyuan, G.; Usman, M.; Khan, A.; Khan, S.; Alanazi, A.F.; Bououdina, M. Preparation of Visible-Light Active MOFs-Perovskites (ZIF-67/$LaFeO_3$) Nanocatalysts for Exceptional CO_2 Conversion, Organic Pollutants and Antibiotics Degradation. *Heliyon* **2024**, *10*, e27378. [CrossRef] [PubMed]
248. Sadiq, S.; Khan, S.; Khan, I.; Khan, A.; Humayun, M.; Wu, P.; Usman, M.; Khan, A.; Alanazi, A.F.; Bououdina, M. A Critical Review on Metal-Organic Frameworks (MOFs) Based Nanomaterials for Biomedical Applications: Designing, Recent Trends, Challenges, and Prospects. *Heliyon* **2024**, *10*, e25521. [CrossRef] [PubMed]
249. Yuksel, R.; Yarar Kaplan, B.; Bicer, E.; Yurum, A.; Alkan Gursel, S.; Unalan, H.E. All-Carbon Hybrids for High Performance Supercapacitors. *Int. J. Energy Res.* **2018**, *42*, 3575–3587. [CrossRef]
250. Deng, Y.; Wang, X.; Wang, Z.; Wang, X.; Li, Z.; Wang, L.; Zhou, C.; Chen, D.; Luo, Y. Yolk–Shell Structured Nickel Cobalt Sulfide and Carbon Nanotube Composite for High-Performance Hybrid Supercapacitors. *Energy Fuels* **2021**, *35*, 5342–5351. [CrossRef]

batteries

MDPI

Article

Anion Intercalation/De-Intercalation Mechanism Enabling High Energy and Power Densities of Lithium-Ion Capacitors

Yang Zhang, Junquan Lao and Ping Xiao *

Department of Materials, Henry Royce Institute, University of Manchester, Manchester M13 9PL, UK;
yang.zhang-26@postgrad.manchester.ac.uk (Y.Z.); junquan.lao@manchester.ac.uk (J.L.)
* Correspondence: p.xiao@manchester.ac.uk

Abstract: The growing demands for electrochemical energy storage systems is driving the exploration of novel devices, with lithium-ion capacitors (LICs) emerging as a promising strategy to achieve both high energy density and fast charge capability. However, the low capacitance of commercial activated carbon (AC) cathode based on anion absorption/desorption limits LIC applications. Herein, commercial graphite is proposed as the cathode to construct an innovative AC (−)//graphite (+) system. The graphite cathode functions as anion hosting, allowing reversible intercalation/de-intercalation of anions into/from its interlayers. The as-designed AC (−)//graphite (+) full cell achieves stable cycling with 90.6% capacity retention after 200 cycles at 0.1 A g^{-1} and a prolonged lifespan with 87.5% capacity retention after 5000 cycles at 0.5 A g^{-1} with the upper cut-off voltage of 5.0 V, yielding a high average Coulombic efficiency (CE) of 99.3%. Moreover, the full cell exhibits a high energy density (>200 Wh kg^{-1}) and power density of 7.7 kW kg^{-1} (calculated based on active mass in both electrodes). These performances exceed most LICs based on anions absorption/desorption on the surface of AC cathodes. This work explores an effective electrode revolution with the assistance of anion intercalation/de-intercalation chemistry for developing novel LICs with high energy and power densities.

Keywords: lithium-ion capacitor; hybrid dual-ion system; graphite cathode; anion intercalation/de-intercalation; energy density

---

1. Introduction

Addressing the increasing global energy demands requires advancements in electrochemical devices, given their wide-ranging applications from portable electronics to electric transportation to the integration of renewable energy sources for powering the electrical grid [1,2]. Lithium-ion batteries (LIBs) have emerged as the predominant energy storage and conversion device owing to its high energy density (>300 Wh kg^{-1}), yet the lower power density remains a notable challenge [3,4]. In comparison to extensively researched LIBs, supercapacitors (electrical double-layer capacitors) typically consist of a symmetrical structure composed of high surface area carbon materials such as activated carbon (AC). This configuration facilitates rapid energy storage through ion adsorption/desorption on the surface of the AC, consequently achieving high power density and a long cycling life, but their practical application is limited by lower energy density (<10 Wh kg^{-1}) [5]. Therefore, there is a strong appeal for innovative electrochemical energy storage and conversion devices that integrate the merits of both batteries (high energy density) and supercapacitors (high power density).

Lithium-ion capacitors (LICs), utilising a battery-type anode (graphite or $Li_4Ti_5O_{12}$) driven by Faraday reactions (mainly intercalation/deintercalation behaviour) and a capacitor-type cathode operating on non-Faraday reactions (absorption/desorption behaviour), have been developed to achieve enhanced energy density (20–146 Wh kg^{-1}) [6]. However, the energy density of commercial AC cathode-based LICs via anion absorption/desorption behaviour during charging/discharging processes is constrained by the limitation of low capacitance and low stable working voltage (<4.6 V versus Li/Li^+) [7–9]. Building upon this foundation, considerable efforts have been made, encompassing the exploration of high-capacitance electrode materials, surpassing commercial AC to construct high-voltage devices [10,11].

Graphite, consisting of stacked layers of graphene held together by weak van der Waals force, has the capability to electrochemically accommodate charge carriers. The graphite can form acceptor-type graphite interphase compounds (GICs) by stabilising additional holes in its bonding π-band, allowing for the intercalation/de-intercalation of anions. Typically, the charge-transfer reaction with the intercalation/de-intercalation of anions is exhibited as Equation (1) [12].

$$C + xA^- \leftrightarrow A_xC + xe^- \quad (1)$$

The graphite cathode demonstrates favourable operation at a high upper cut-off voltage of 5.3 V, yielding a medium voltage of around 4.6 V, which is significant compared to most cathode materials. The high working voltage ensures a potentially high energy density. Typically, graphite cathode is coupled with graphite anode to construct dual-graphite batteries. However, the dual-graphite batteries face challenges, including a limited rate capability and, particularly, a short cycle life. These issues are primarily due to the insufficient reaction kinetics of the graphite anode, which experiences inevitable capacity decay with increasing the current density up to 300 mA g^{-1} [13]. In contrast, the graphite cathode is expected to exhibit superior rate performance, capable of sustaining a stable capacity close to its theoretical value of approximately 100 mAh g^{-1} even at a high current density up to 2 A g^{-1} [14]. Remarkably, the high operating voltage and excellent rate performance of the graphite cathode contribute to maximising the advantages of LICs incorporating an AC anode, especially in terms of rapid and stable charge storage. This suggests promising potential for developing innovative high-energy and high-power LICs based on anion intercalation chemistry. However, this novel construction is still in the early stages of research, with limited studies primarily focusing on the low voltage range (0–4.5 V), demonstrating low energy density (<100 Wh kg^{-1}) [15–17]. Therefore, optimising and matching the graphite cathode and electrolyte to unlock performance at higher voltages and achieve a prolonged cyclic life is of great significance. Furthermore, there is substantial room for improvement in the fundamental and technical principles of this system, as well as in the exploration of its working mechanisms.

Herein, we propose the construction of novel LICs featuring an AC anode and graphite cathode in a standard concentration electrolyte (1M $LiPF_6$ EMC), employing the combination of cation absorption/desorption and anion intercalation/de-intercalation chemistry. The as-prepared AC (−)//graphite (+) full cell is operated at a high voltage range of 2.0–5.0 V, with a medium voltage above 4.2 V at the current density of 0.1 A g^{-1}. As expected, excellent cyclic stability (90.6% capacity retention after 200 cycles at 0.1 A g^{-1}) and long-term cycle life (87.5% capacity retention after 5000 cycles at 0.5 A g^{-1} with an average CE of 99.3%) can be achieved in the AC (−)//graphite (+) full cell. Notably, a high energy density of 204 Wh kg^{-1} (calculated on the active mass of both electrodes) is achieved. This exploration sheds light on the construction of novel LICs based on graphite cathode and demonstrates the potential to achieve electrochemical systems with high-performance energy storage capability through the assistance of anion intercalation chemistry.

2. Materials and Methods

2.1. Materials

Electrolyte: 1M $LiPF_6$ EC/EMC (1:1, vol.) and 1M $LiPF_6$ EMC were produced from Merck Life Science UK Limited. SLP50, SP1, and SFG6L graphite and Super P carbon black were sourced from IMERYS Graphite & Carbon (Switzerland). Lithium metal foil with a diameter of 16 mm and a thickness of 0.025 cm, along with polypropylene (PP) separator film, were obtained from Xiamen TOB New Energy Technology Co., Ltd (China). Sodium alginate (NaAl) was a product of MP Biomedicals. Commercial Ketjen Black (KB) was purchased from Shandong Gelon Lib Co., Limited (China). The glass fibre membrane separator (MG 160) was acquired from Fisher Scientific UK Ltd. Commercial TF-B520 activated carbon was supplied by MTI Corporation (UK). All chemicals were used directly without undergoing any additional purification processes.

2.2. Experimental Procedures

2.2.1. Graphite and Activated Carbon Electrode Preparation

For preparation of the graphite and activated carbon electrode, SLP50 graphite, Ketjen Black, and sodium alginate (NaAl) binder were first mixed by deionised water using a speed mixer (SpeedMixer DAC 600.2, Artisan technology group, USA) in a mass ratio of 8:1:1. The homogeneous slurry was then cast onto carbon-coated Al foil as the current collector, and the electrode was dried in a vacuum oven at 80 °C overnight. The electrode discs of 12 mm in diameter with a mass loading of 1.8–2.2 mg were cut. The TF-B520 activated carbon electrode was prepared using CMC binder and carbon black (Super P) in a mass ratio of 7:1.5:1.5. The CMC binder was first dissolved by deionised water, and then, activated carbon and carbon black were added to form a homogeneous slurry. The paste was coated on the Cu foil, and the desired electrode (diameter of 15 mm) was obtained after drying at 80 °C overnight. The mass ratio between graphite and the activated carbon electrode was 2:1 in this work.

2.2.2. Cell Assembly and Electrochemical Testing of the Li//AC, Li//Graphite Half Cell, and AC (−)//Graphite (+) Cells

Cell assembly: The CR2032-type coin cells were used to assemble cells, while AC or graphite with the electrode and lithium metal (diameter 16 mm) was served as the counter/reference electrode, and the polypropylene separator film or glass fibre (diameter 18 mm) was used as the separator. The electrolytes for Li//AC and Li//graphite half cells were 1M $LiPF_6$ EC/EMC (1:1, vol.) and 1M $LiPF_6$ EMC (~120 µL), respectively. For the assembly of AC (−)//graphite (+) cells, the AC anode was first discharged/charged for 5 cycles in Li//AC half cells within 0.01–3.0 V at 100 mA g^{-1}, then discharged to 0.01 V to the pre-lithiate. In the meantime, the graphite cathode was pre-cycled for 5 charge/discharge processes in Li//graphite half cells within 3.0–5.0 V at 100 mA g^{-1}, then stopped at the upper cut-off voltage of 5.0 V. The coin cell configuration is displayed in Figure S1 (Supplementary Materials). The pre-prepared AC anode and graphite cathode were then assembled in a coin cell with a glass fibre separator, and the amount of electrolyte was ~150 µL. The assembly of coin cells was conducted in the glovebox with $O_2 < 0.5$ ppm and $H_2O < 0.5$ ppm.

Electrochemical performance measurements: The galvanostatic charge/discharge test was performed with the NEWARE test system (BTS9000, Shenzhen, China), and the voltage ranges for the Li//AC, Li//graphite, and AC (−)//graphite (+) cells were 0.01–3.0 V, 3.0–5.0 V, and 2.0–5.0 V, respectively. Cyclic voltammetry (CV) was measured with the electrochemical workstation (VersaSTAT 4 Potentiostat Galvanostat, Ametek scientific instruments, USA).

2.2.3. Materials Characterisations

The morphologies of pristine graphite and activated carbon were examined by scanning electron microscope (SEM; TESCAN MIRA3 SC + OI EDS). The transmission electron microscope (TEM) images were acquired by Talos™ F200X TEM. X-ray diffraction (XRD) was conducted with an X-ray diffractometer (Powder X-ray Diffraction Phillips X'Pert) using Cu-Kα radiation at a wavelength of 0.15418 nm (V = 30 kV, I = 25 mA). Raman measurement was carried out by a Renishaw inVia Reflex Raman microscope. The surface area was analysed by acquiring nitrogen absorption/desorption isotherms using the Brunauer–Emmett–Teller (BET) method on a Surface Area Analyzer—Quadrasorb Evo.

3. Results and Discussion

3.1. Half Cell Investigations

3.1.1. Li//Graphite Half Cell via Anion Intercalation/De-Intercalation

Figure 1a shows the XRD pattern of SLP50 graphite, in which a strong peak located at 26.35° is observed. This reflection can be associated with the crystallographic (002) plane of graphite. The Raman spectrum of SLP50 graphite is exhibited in Figure 1b, appearing in three peaks positioned at 1335, 1580, and 2686 cm^{-1}, which correspond to the D band, G band, and 2D band, respectively. The G band is the specific reflection for sp^2 carbon networks, while the D band is the defect-induced Raman feature. The ratio of intensity I_D/I_G for the D and G bands is normally used for predicting the defect quantity and degree of graphitisation. The I_D/I_G for SLP50 graphite was calculated to be 0.256, suggesting few defects in the well-ordered graphitic structures. Figure 1c is the N_2 adsorption/desorption isotherms, revealing the BET surface area for SLP50 graphite to be 2.6 m^2/g. This relatively small surface suggests limited porosity or specific surface features. The pore size distribution is exhibited in Figure S2 (Supplementary Materials), indicating the presence of a small quantity of pores. The SEM technique was further employed to gain a more comprehensive understanding of the surface feature and morphology of SLP50 graphite. The SEM images are depicted in Figure 1d–f, and flake-shaped graphitic particles with a thickness of ~2 μm are observed, while the particle size distribution is mainly between the range of ~20 to 50 μm. Furthermore, the high-resolution TEM images are listed in Figure 1g,h, revealing detailed insights into the crystalline structure. The lattice distance for the (002) plane of SLP50 graphite was analysed to be ~0.338–0.346 nm, offers a suitable interlayer spacing that can effectively accommodate the intercalation of anions.

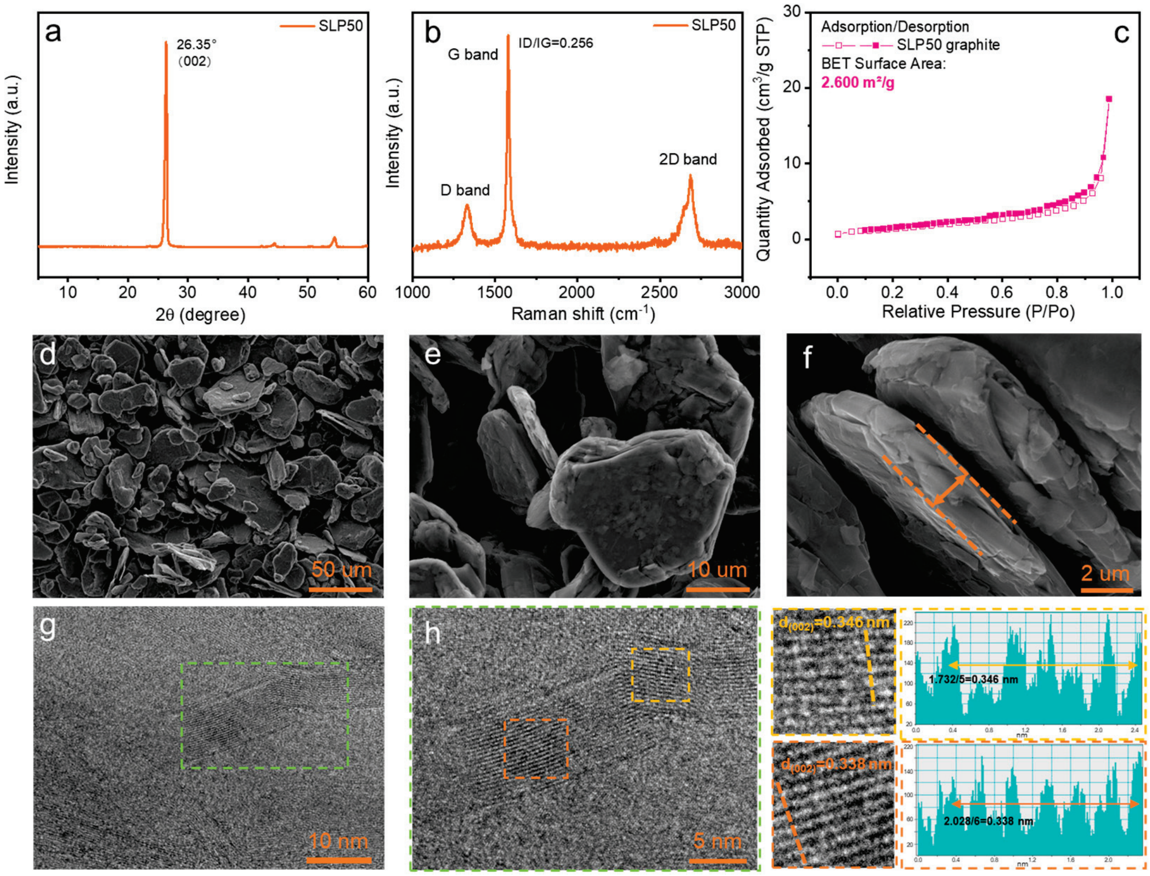

Figure 1. Characterisation of SLP50 graphite: (**a**) XRD; (**b**) Raman; (**c**) N_2 adsorption/desorption isotherm; (**d**–**f**) SEM images; (**g**,**h**) high-resolution TEM images.

Figure 2 displays the testing results of electrochemical PF_6^- anion intercalation into SLP50 graphite in the Li//graphite half cells based on 1M $LiPF_6$ EMC electrolyte. The PF_6^- anion intercalation/de-intercalation process was first analysed at a constant current density of 100 mA g^{-1} in the voltage range of 3.0–5.0 V. The galvanostatic charge/discharge curves for the initial three cycles are exhibited in Figure 2a. The charge platforms detected in the curves are associated with the "staging" process, which are identified as four potential regions of 4.44–4.51 V (stage I), 4.51–4.74 V (stage II), 4.74–4.92 V (stage III), and 4.92–5.0 V (stage IV), reflecting that the PF_6^- anions intercalate into graphite interlayers to form graphite intercalation compounds (GICs) [18]. Meanwhile, the anion de-intercalation platforms are observed in the discharge curves, revealing a reversible PF_6^- anion intercalation/de-intercalation process. Figure 2b shows the relevant capacitance differential (dQ/dV) curves, while these specific peaks correspond to the charge/discharge plateaus in galvanostatic charge/discharge curves. The onset voltage for anion intake is around 4.44 V, and subsequent peaks confirm the occurrence of intercalation/de-intercalation processes at certain potentials. Figure 2c lists the evaluation of the specific capacity and Coulombic efficiency (CE) within 100 cycles. Importantly, a high discharge capacity of ~120 mAh g^{-1} via this anion intercalation/de-intercalation process was achieved and was extremely stable after 100 repeated charge/discharge processes. The initial CE was 40% and increased from cycle to cycle until it was stable at ~90%, and the small CE was due to the electrolyte degradation and self-discharge reactions at the high upper cut-off voltage. Figure 2d exhibits the specific capacity of Li//graphite half cells at a high current density of 500 mA g^{-1} in the voltage range of 3.0–5.0 V. The discharge capacity decreases slightly to ~100 mAh g^{-1}, and the capacity retention after 2000 cycles is 82%, indicating the great long-term cyclic stability. This excellent cyclic capability of SLP50 graphite in a standard concentration electrolyte (1M $LiPF_6$ EMC) is comparable to other reported graphite cathodes, even those using high-concentration electrolytes or ionic liquid electrolytes [19,20]. Figure 2e concludes the medium discharge voltage of the Li//graphite half cells, and the inset displays charge/discharge curves from the 100th to 2000th cycles. Notably, the medium discharge voltage was stable at ~4.5 V after 2000 cycles, indicating excellent cyclic reversibility and stability. A slight decrease in the charge/discharge plateau voltage during the cycles further demonstrates less polarisation in the cell. Figure 2f presents the charge/discharge capacities of the Li//graphite half cells at different current densities. At the current densities of 0.1, 0.2, 0.4, 0.8, and 1.0 A g^{-1}, the discharge capacities of the cell were around 100 mAh g^{-1}, respectively, indicating great applicability with the current increasing. Figure S3 (Supplementary Materials) shows the cyclic voltammetry curves of the Li//graphite half cells at different scan rates, where the primary oxidation/reduction peaks are observed and retained well when the scan rate changes, revealing good reversibility of the electrode reaction. In addition, the capacity decayed to 75 mAh g^{-1} and then fell to 70 mAh g^{-1} when the current density increased to 1.5 and 2.0 A g^{-1}. This decrease in capacity under high current conditions is a consequence of larger concentration polarisation, hindering the electrode reactions and the effective capacity. Figure 2g shows the charge/discharge curves of the cell at different current densities. Correspondingly, the voltage hypothesis phenomenon was observed in the charge/discharge curves as the current densities increased, suggesting there was a noticeable deviation in the voltage behaviour. Notably, the discharge capacity was recovered to 100 mAh g^{-1} when the current density was reversed to 1.0 A g^{-1}, revealing a good reversibility of the Li//graphite cell. Moreover, the medium voltage and onset voltage for anion intercalation into graphite interlayers at different current densities are compared in Figure 2h. It is observed that the medium voltage was reversibly resumed to 4.51 V when the current density returned from 2 A g^{-1} to 0.1 A g^{-1}, suggesting good reversibility of the cell. The onset voltage for anion intercalation kept increasing when the current density was increased, which most likely contributed to the higher activation barrier resulting from the sluggish kinetic movement of PF_6^- at the large current condition [21]. These results demonstrate the effective intercalation and de-intercalation of PF_6^- anions in SLP50 graphite, suggesting the potential for the construction of a high-performance full-cell system.

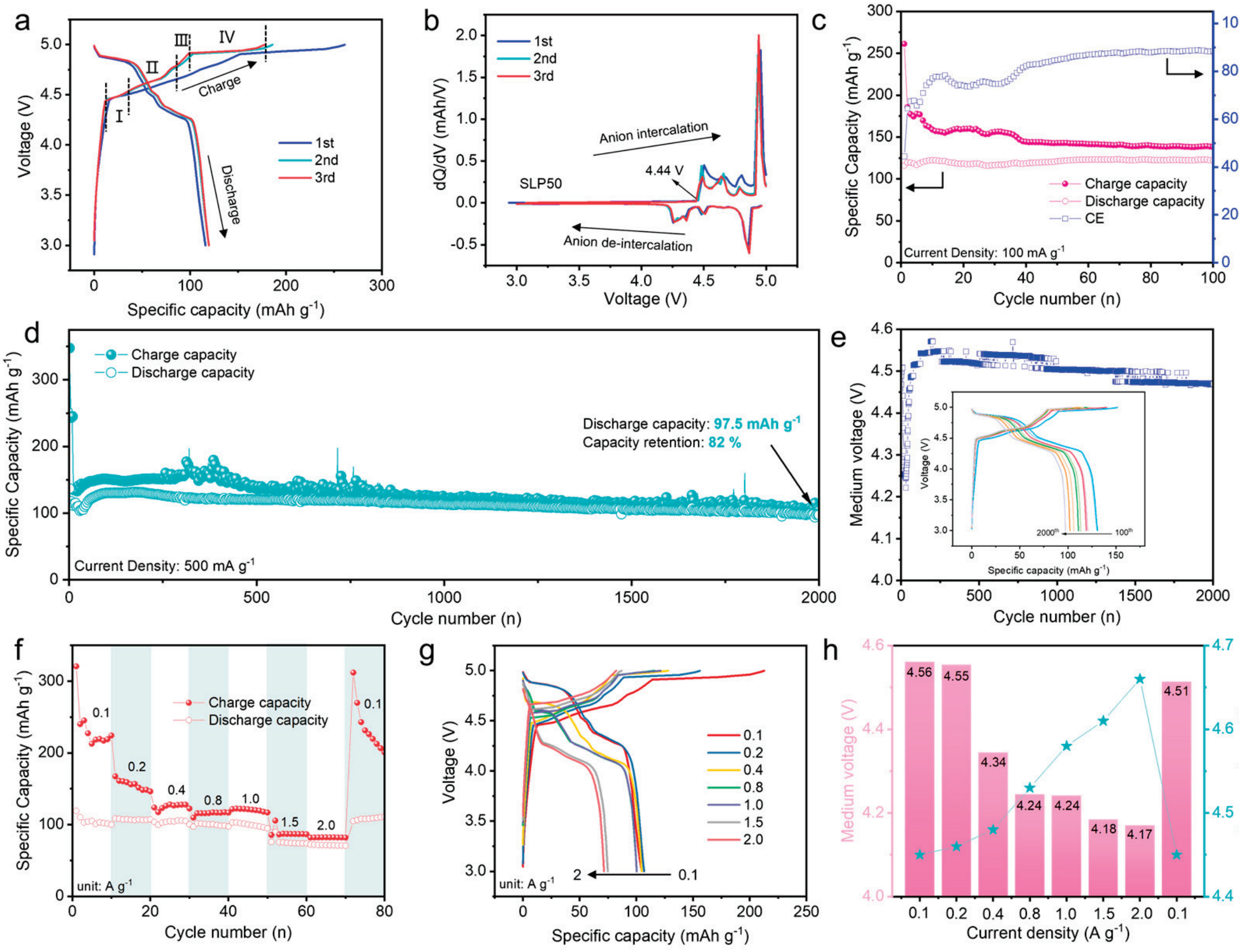

Figure 2. Electrochemical performances of Li//graphite half cells in 1M $LiPF_6$ EMC electrolytes. (**a**) Galvanostatic charge/discharge curves for the initial three cycles and (**b**) relevant initial three capacitance differential (dQ/dV) curves; (**c**) charge/discharge capacities and Coulombic efficiency at the current density of 100 mA g^{-1} within 100 cycles; (**d**) charge/discharge capacities at the current density of 500 mA g^{-1} within 2000 cycles; (**e**) medium voltage at different cycles, and the inset is the charge/discharge curves at the 100th–2000th cycles; (**f**) charge discharge capacities of the cells under various current densities from 0.1 to 2.0 A g^{-1}; (**g**) relevant charge/discharge curves; (**h**) medium and onset voltage comparisons under different current densities.

3.1.2. Li//AC Half Cells via Li^+ Adsorption/Desorption

The crystallinity of TF-B520 activated carbon (AC) was conducted using XRD, and the pattern is exhibited in Figure 3a. The absence of a diffraction peak for the reflection of the graphite (002) plane is attributed to the lack of a well-defined long-range order in the arrangement of the carbon atom [22]. The broad and weak peak around 43° is observed in the spectrum, corresponding to the diffraction of the (100) plane, while the low intensity of the diffraction peak demonstrates the amorphous structures [23]. Figure 3b displays the Raman spectra of AC, while the D band (1345.7 cm^{-1}) and G band (1598.5 cm^{-1}) are clearly observed. The ID/IG was calculated as 0.93, indicating lower fractions of the graphitic region and the disordered nature of the carbon matrix. According to the N_2 adsorption/desorption curves in Figure 3c, the BET surface area value for AC was measured to be 911.75 m^2/g, which is much larger than that of SLP50 graphite. The pore size distribution, shown in Figure S4 (Supplementary Materials), highlights a prominent microporous structure with a pore size ranging from 0.5 to 0.8 nm. A larger surface area implies more adsorption sites, thus conferring a higher adsorption capacity. This facilitates rapid adsorption and desorption of ions on the AC electrode surface. Figure 3d,e show the SEM images of the AC, and the size is mainly distributed in the range of 5–10 µm. Figure 3f illustrates the TEM image of the AC, revealing disordered microstructures characteristic of amorphous carbon.

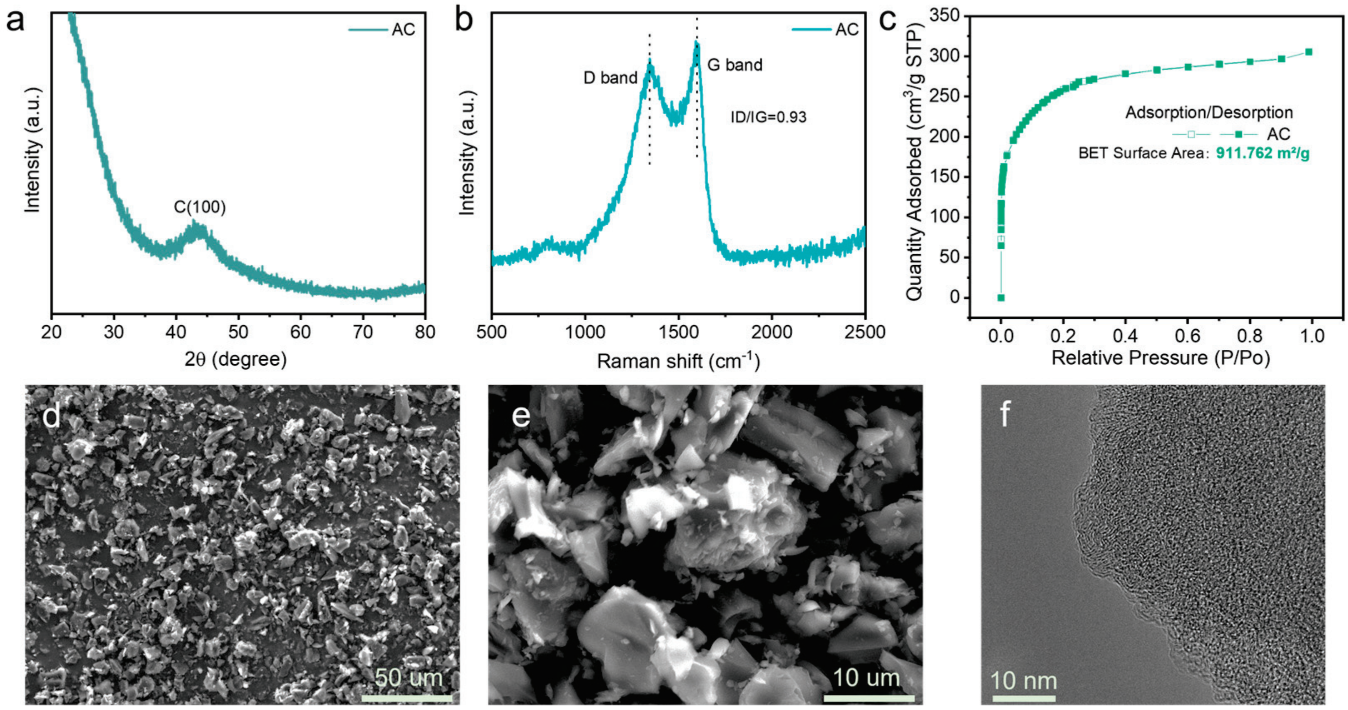

Figure 3. Characterisation of TF-B520 activated carbon: (**a**) XRD; (**b**) Raman; (**c**) N_2 adsorption/desorption isotherm; (**d**,**e**) SEM images; (**f**) high-resolution TEM image.

The electrochemical performances of the AC electrode were investigated in Li//AC half cells with the electrolyte of 1M $LiPF_6$ EC/EMC (vol. 1:1). Figure 4a displays the initial five galvanostatic charge/discharge curves for the AC electrode at the current density of 100 mA g^{-1} between the voltage range of 0.01–3.0 V. The first discharge capacity was found to be 1200 mAh g^{-1}, which reduced to ~300 mAh g^{-1} in the second cycle and was stable for five cycles. The long plateau in the first cycle is attributed to the formation of a solid electrolyte interphase (SEI) film on the AC electrode surface. Figure 4b illustrates the specific charge/discharge capacities and CE of the cell at 100 mA g^{-1} in different cycles. The discharge capacity was kept at ~260 mAh g^{-1} after 200 repeated charge/discharge processes, indicating an excellent cyclic stability. Figure 4c shows the charge/discharge capacities and CE of the cell at a large current density of 500 mA g^{-1} after the initial 10 formation cycles at 100 mA g^{-1}. The capacity was maintained above 200 mAh g^{-1} after 1000 cycles, yielding a CE near 99.7%. Notably, a good cyclic capability was confirmed by the overlapped charge/discharge curves of the cells at different cycles from the 100th to 1000th (Figure 4d). CV analysis of the Li//AC cell was first conducted at the scan rate of 0.1 mV s^{-1}, and the initial four cycle CV curves are exhibited in Figure 4e. It is obvious that the typical broad peak between 0.5 and 1.0 V is observed for each cycle, probably due to a formation of the SEI layer on the AC electrode surface. The strong current drop below the voltage of 0.5 V is associated with the reaction between Li^+ and the AC electrode. Furthermore, the CV analysis at various scan rates (0.2, 0.5, 0.8, 1.0, and 2.0 mV s^{-1}) was carried out to investigate the electrochemical dynamic behaviour of the electrode, and the curves are depicted in Figure 4f. As the scan rate increases, the peak intensity of the electrode reaction rises, resulting from an augmented electrochemical reaction rate. Notably, according to previous reports, the electrochemical storage behaviour can be specified by the equations as follows [24–26]:

$$i = av^b \tag{2}$$

$$\log(i) = \mathrm{b}\log(v) + \log a \tag{3}$$

$$i = k_1 v + k_2 v^{1/2} \tag{4}$$

$$i/v^{1/2} = k_1 v^{1/2} + k_2 \tag{5}$$

where i is the current, v is the scan rate, and a and b are the variable parameters. The b-value, determined from the slop of log(i) versus log(v) plot, approaches 0.5 when diffusion-controlled behaviours are predominant. Conversely, a b-value close to 1.0 signifies the dominance of pseudocapacitive contributions. Figure 4g shows the fitted relationship between log(i) and log(v) of the AC electrode at different voltages. The corresponding b-values when discharged to 1.0 and 0.8 V and charged to 0.8 and 1.0 V are calculated to be 0.92, 0.86, 0.96, and 1.0, respectively. The b-value approaching 1 indicates the surface-induced capacitive behaviour of the AC electrode, revealing efficient electrode reaction kinetics. Based on Equations (4) and (5), the current (i) is expressed as the sum of k_1v and $k_2v^{1/2}$ at specific voltages corresponding to the capacitive behaviour and diffusion-controlled behaviour, respectively. The value of k_1 can be determined by plotting the curve with $i/v^{1/2}$ versus $v^{1/2}$, and the capacitive contribution is the value of k_1v. Figure 4h quantitatively analyses the surface-dominated contribution, revealing that 65.45% of the whole capacity belongs to the non-diffusion controlled capacity at the scan rate of 2 mV s^{-1}. Clearly, it is found that the diffusion-controlled behaviours mainly contribute to the whole discharge capacity in the reduction range between 0.75 and 0.01 V, suggesting a Li^+ intake process occurring on the electrode at low voltage. This behaviour is similar to that of previously reported electrode materials [27,28]. Moreover, as shown in Figure 4i, the percentage for capacitive contributions of the AC electrode exhibits an increasing trend when the scan rate rises, disclosing the more dominated capacitive behaviour at high rates.

3.2. AC (−)//Graphite (+) Full-Cell Investigations

3.2.1. Cell Configuration

The full-cell configuration of AC (−)//graphite (+) is achieved by employing an AC anode and graphite cathode. Scheme 1 illustrates a comparison of the three capacitors mentioned above (supercapacitor, conventional LICs with an AC cathode, and LICs with a graphite cathode). In these novel LICs with a graphite cathode, PF_6^- anions are forced to intercalate into graphite interlayers during the charging process, while Li^+ ions are absorbed onto the AC surface. Conversely, during the discharging process, PF_6^- anions and Li^+ ions are released and return to the electrolyte. Here, a pre-lithiation process is necessary for the AC anode to enhance the availability of Li^+ ions for charge storage and facilitate the effective formation of SEI film. The charge/discharge curves for the pre-lithiation process of the AC anode are displayed in Figure S5a (Supplementary Materials). Additionally, a pre-cycle treatment is applied to the graphite cathode to activate the anion intercalation pathways, with the charge/discharge curves of the Li//graphite half cells shown in Figure S5b (Supplementary Materials). The AC and graphite electrodes are fully discharged and fully charged to 0.01 V and 5 V, respectively, allowing for Li^+ absorption and PF_6^- anions intercalation, before being used to assemble the full cell.

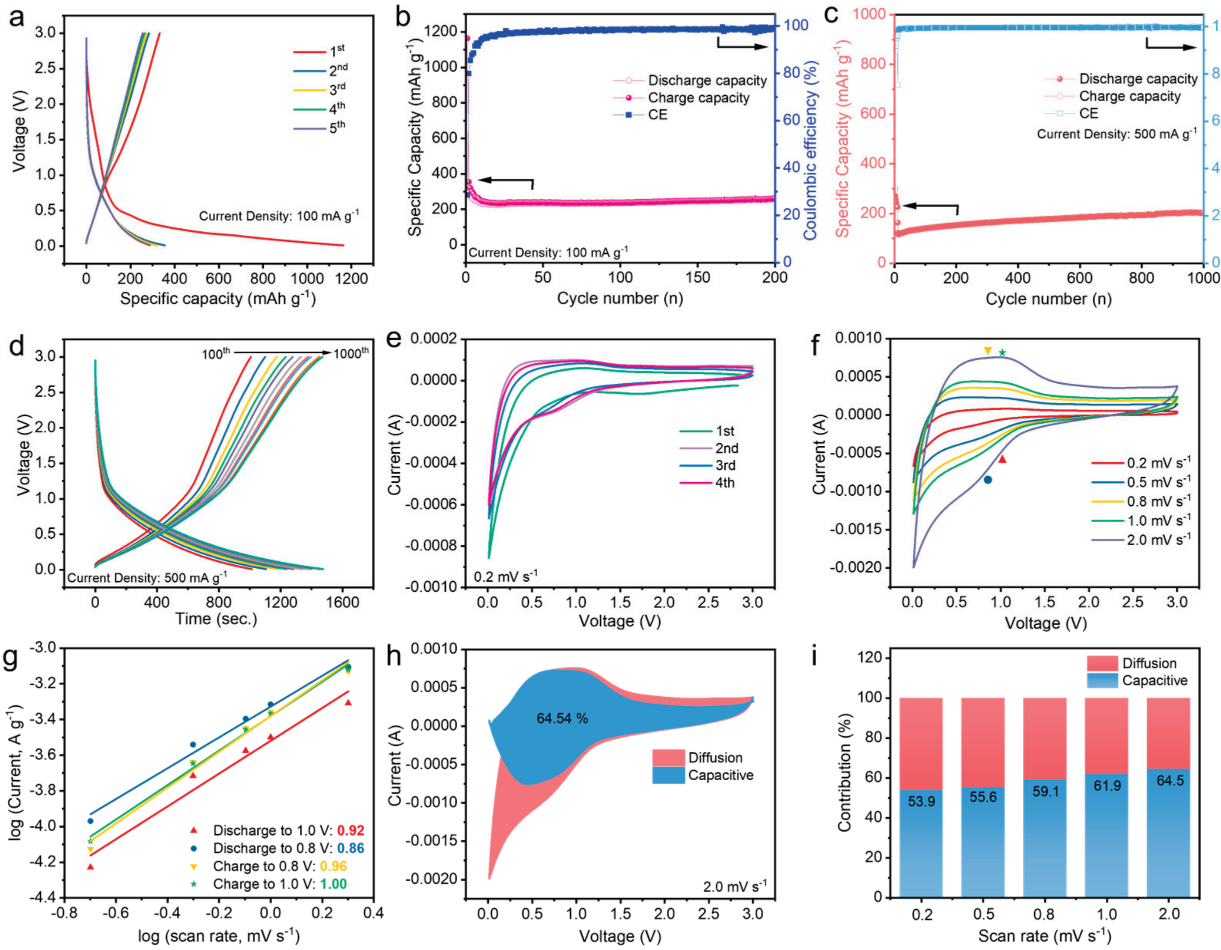

Figure 4. Electrochemical performances of Li//AC half cells in 1M $LiPF_6$ EC/EMC (vol. 1:1) electrolytes. (**a**) Galvanostatic charge/discharge curves for the initial five cycles, and (**b**) charge/discharge capacities and Coulombic efficiency at the current density of 100 mA g^{-1} within 200 cycles; (**c**) charge/discharge capacities at the current density of 500 mA g^{-1} within 1000 cycles, and (**d**) relevant charge/discharge curves at different cycles; (**e**) initial four CV curves at the scan rate of 0.1 mV s^{-1}; (**f**) CV curves at various scan rates of 0.2, 0.5, 0.8, 1.0, and 2.0 mV s^{-1}; (**g**) the linear relation between log(i) and log(v); (**h**) pseudocapacitive contributions (blue) and diffusion-controlled contributions (pink) at the scan rate of 2.0 mV s^{-1}; (**i**) ratios of capacitive and diffusion charge storage to the total charge storage at different scan rates.

3.2.2. Electrochemical Performances

The electrochemical performance of AC (−)//graphite (+) full cells was first investigated by the galvanostatic charge/discharge test. Figure 5a displays the initial five charge/discharge curves of the cell at the current density of 100 mA g^{-1} with the voltage range between 2.0 and 5.0 V. It is clear that the voltage plateaus corresponding to the anion intercalation behaviour are observed. The charge capacity of the first cycle reaches 90 mAh g^{-1}, but the first discharge capacity is lower than 50 mAh g^{-1}, yielding an initial CE of 50%. The lower CE in the first cycle is probably associated with the parasitic reactions, such as the electrolyte decomposition and self-discharge behaviour. Notably, the subsequent curves are overlapped well, which demonstrates the excellent cyclic reversibility and stability. Correspondingly, the initial five dQ/dV curves are exhibited in Figure 5b, while the peaks are attributed to the plateaus in the charge/discharge curves. The onset voltage for anion intercalation in the first cycle is 3.95 V, and the voltage decreases to 3.81 V in the second cycle and 3.76 V for subsequent cycles. The shift in the onset voltage indicates that the first uptake of anions into graphite interlayers needs to overcome the activation barrier to open the interlayer gaps [21,29,30]. This onset shift is also observed in CV curves of the cell at the scan rate of 0.2 mV s^{-1} (Figure S6a, Supplementary Materials). Meanwhile, the specific peaks observed in the CV curves are associated with the anion intercalation/de-intercalation behaviours. Moreover, Figure S6b (Supplementary Materials) exhibits CV curves at various scan rates from 0.2 to 2.0 mV s^{-1}, and good reversibility of the cell is demonstrated. Figure 5c exhibits the charge/discharge capacities and relevant CE of the AC (−)//graphite (+) cell at the current density of 100 mA g^{-1} between the voltage range of 2.0–5.0 V within the 200 cycles. The discharge capacity of 45 mAh g^{-1} is delivered after 200 repeated charge/discharge processes, yielding a CE of 91.4%. The capacity retention of the cell is higher than 90%, demonstrating an excellent cyclic stability. The cyclic stability of the AC (−)//graphite (+) cell was further explored through the galvanostatic charge/discharge cycle at a high current density of 500 mA g^{-1}. The charge/discharge capacities and CE for 5000 cycles are exhibited in Figure 5d. Obviously, the capacity was still stable after 5000 cycles, yielding a capacity retention of 87.5% with an average CE of 99.3%. Furthermore, as shown in Figure 5e, the reversible discharge capacities of 48.7, 46.1, 41.0, 33.5, 31.4, 27.4, and 26.3 mAh g^{-1} are maintained at various current densities of 0.1, 0.2, 0.5, 0.8, 1.0, 1.5, and 2.0 A g^{-1}, respectively. Particularly, the capacity of the AC (−)//graphite (+) cell recovered to 47.6 mAh g^{-1} when the current density was switched back to the initial 0.1 A g^{-1}, exhibiting excellent rate capability and cyclic reversibility. Figure S7a (Supplementary Materials) displays the charge/discharge curves of the cell cycled at various current densities. Obviously, the discharge time reduces with the increasing current density. Figure S7b (Supplementary Materials) illustrates the medium voltage of the cell at various current densities, while the medium voltage drops from 4.2 V to 3.8 V when the current density increases from 0.1 to 2.0 A g^{-1}. This result demonstrates a high operating voltage in the AC (−)//graphite (+) full-cell system.

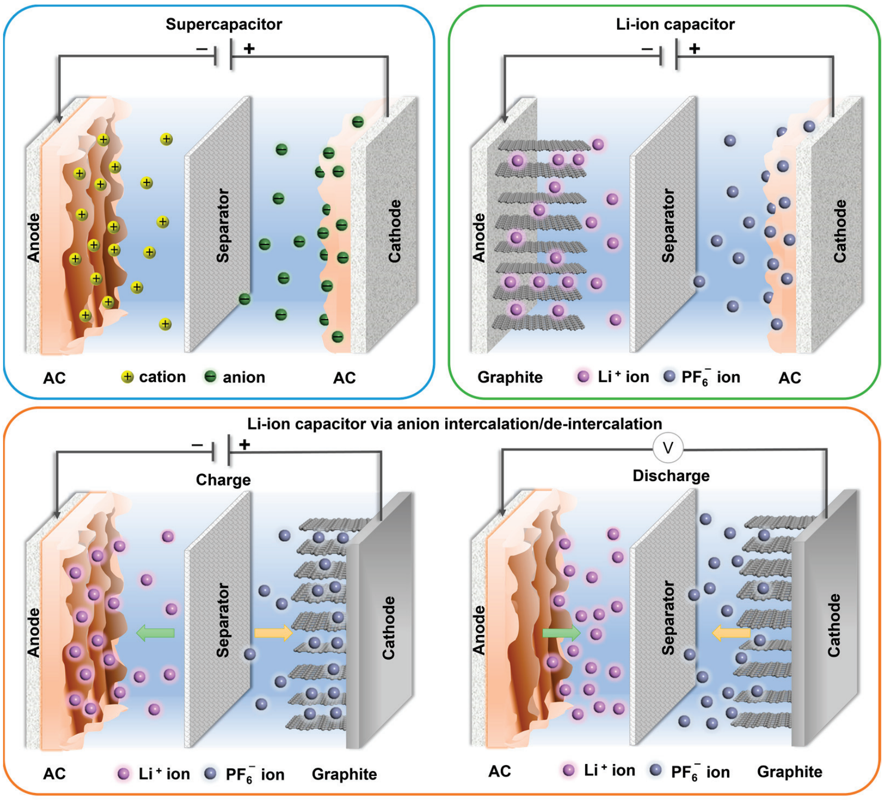

Scheme 1. The comparison among the conventional supercapacitor (AC//AC symmetric configuration), Li-ion capacitor (graphite (−)//AC (+) asymmetric configuration), and Li-ion capacitor via anion intercalation (AC (−)//graphite (+) configuration).

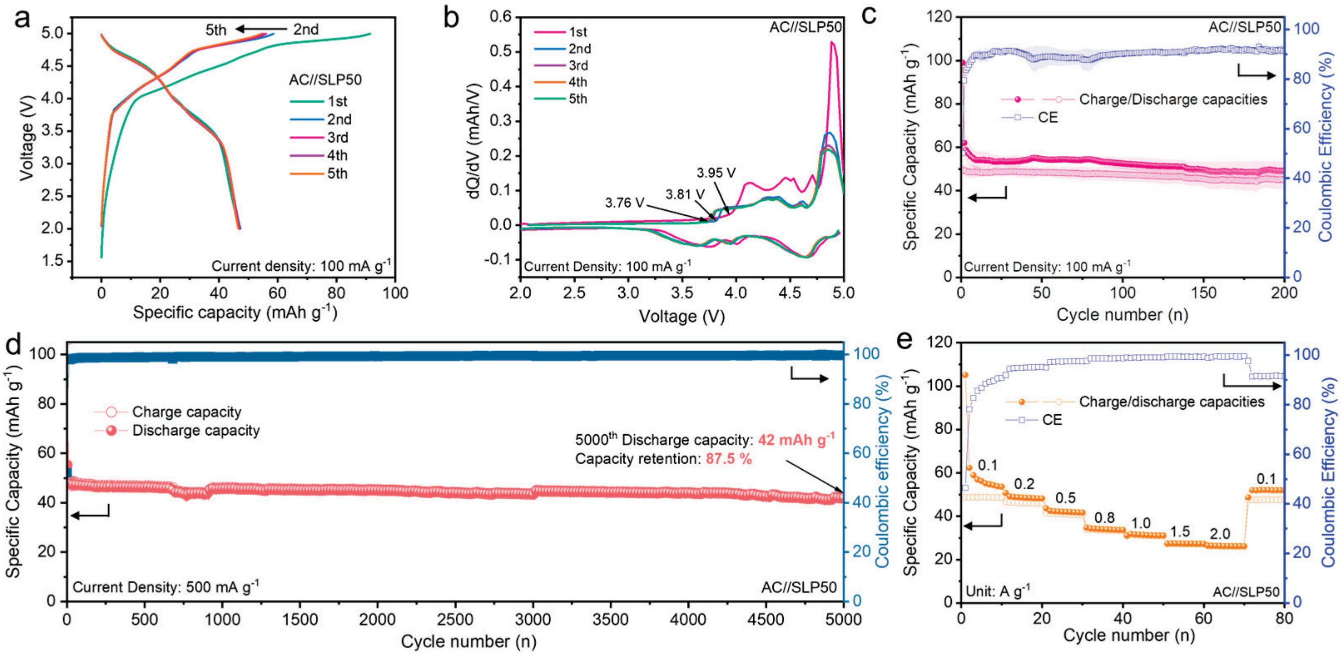

Figure 5. Electrochemical performances of the AC (−)//graphite (+) full cell in 1M $LiPF_6$ EMC electrolytes. (**a**) Galvanostatic charge/discharge curves for the initial five cycles and (**b**) relevant dQ/dV curves; (**c**) charge/discharge capacities and CE at the current density of 100 mA g^{-1} within 200 cycles; (**d**) charge/discharge capacities and CE at current density of 500 mA g^{-1} within 5000 cycles; (**e**) rate performances at different current densities of 0.1, 0.2, 0.5, 0.8, 1.0, 1.5, and 2.0 A g^{-1}.

Accordingly, the energy and power density of the AC (−)//graphite (+) full-cell system were calculated using the equations provided in the Supplementary Materials, with detailed data displayed in Table S1 (Supplementary Materials). The comparisons, shown in the Ragone plot in Figure 6a and Table S2 (Supplementary Materials), are displayed with the previously fabricated LICs. A high energy density of 204 Wh kg^{-1} (calculated based on the active mass of both electrodes) is achieved at a power density of 418 W kg^{-1}. At a high power density of 7.7 kW kg^{-1}, the AC (−)//SLP50 graphite (+) full cell delivers an energy density of 100 Wh kg^{-1}, exceeding most LICs based on anion absorption/desorption on the surface of the AC cathode [9,31–40]. Additionally, the electrochemical performance of this AC (−)//SLP50 graphite (+) full-cell system is compared to reported dual-graphite battery systems [41–50]. The comparison of the cycle life, capacity retention, and average Coulombic efficiency is presented in Figure 6b, with the detailed data summarised in Table S3. Notably, the novel AC (−)//SLP50 graphite (+) full-cell system in this work demonstrates a prolonged cycle life, along with cyclic efficiency and capacity retention comparable to those of dual-graphite batteries.

Moreover, different types of graphite, including SP1 and SFG6L, were applied as cathodes in the AC (−)//graphite (+) full-cell system. The detailed physical properties of these two graphite types are displayed in Figure S8 (Supplementary Materials). Figure S9 (Supplementary Materials) exhibits the electrochemical performance of the full cell, demonstrating a reversible and stable cyclic capability for both AC (−)//SP1 graphite (+) and AC (−)//SFG6L graphite (+) configurations. In summary, it can be concluded that various graphite cathode materials are suitable for this novel AC (−)//graphite (+) system in the electrolyte of 1 M $LiPF_6$ EMC operating at a high voltage range. This demonstrates the compatibility of graphite cathodes with anion intercalation behaviour for the improvement in the overall performances of AC-based energy storage devices. Notably, the electrochemical performance varies with different types of graphite. The potential influence of graphite properties on the overall performance of this AC (−)//graphite (+) full-cell system will be explored in our future work.

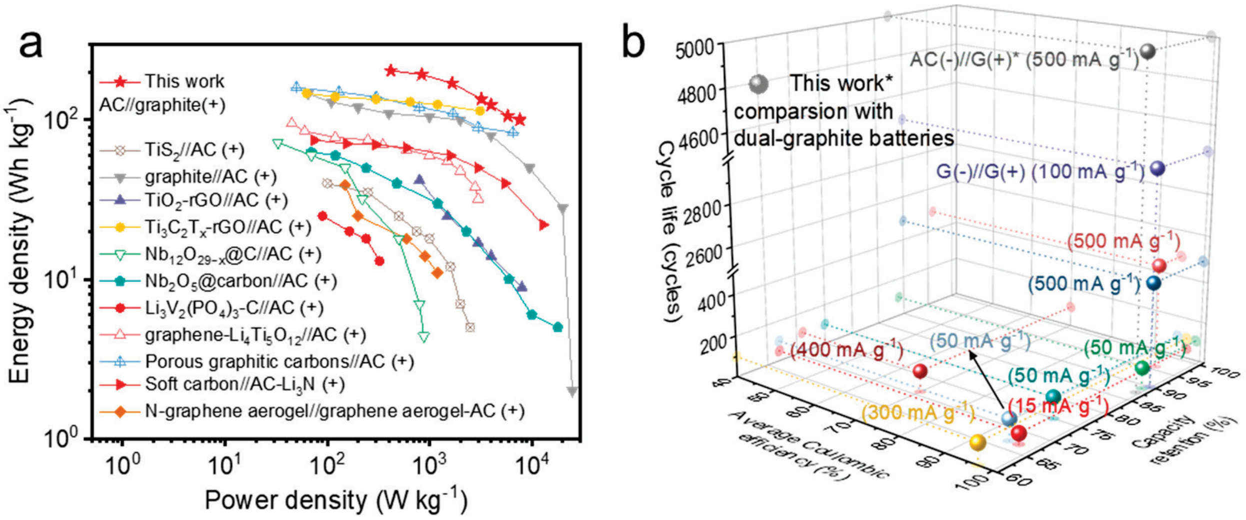

Figure 6. Comparison of performances of the AC (−)//graphite (+) full cell in this work with reported works. (**a**) Ragone plot of the AC (−)//graphite (+) full cell in this work, and comparison with previously fabricated LICs in the literature. (**b**) Cyclic performances of the AC (−)//graphite (+) full cell in this work compared with reported dual-graphite batteries.

4. Conclusions

In summary, we demonstrated graphite as the cathode material for a novel AC (−)//graphite (+) device with the assistance of anion intercalation/de-intercalation chemistry. It has been found that the graphite cathode storing an anion charge via intercalation behaviour can deliver a higher capacitance than the commercial AC based on surface adsorption. The as-designed AC (−)//graphite (+) device showed a high energy density (>200 Wh kg^{-1}) with a well-maintained power density (>7 kW kg^{-1}), surpassing most reported supercapacitors and LICs. The AC (−)//graphite (+) device was also evaluated by cyclic stability and rate capability, which achieved a high capacity retention of 87.5% after 5000 cycles at the current density of 0.5 A g^{-1}, yielding an average CE of 99.3%. Moreover, various commercial graphite with different properties were successfully applied in this AC (−)//graphite (+) system, demonstrating good compatibility. Considering the abundance, wide availability, and low cost of the commercial graphite, this work is expected to inspire the development of novel electrochemical devices with a prolonged cyclic life, high energy density, and fast energy conversion rates.

Supplementary Materials: The following supporting information can be downloaded at https://www.mdpi.com/article/10.3390/batteries10090296/s1: Figure S1. The coin cell construction for (a) Li//AC or Li//graphite half cells and (b) AC (-)//graphite (+) full cell. Figure S2. Pore size distribution of SLP50 graphite. Figure S3. The cyclic voltammetry curves of the Li//graphite half cells at different scan rates. Figure S4. Pore size distribution of TF-B520 activated carbon. Figure S5. (a) The charge/discharge curves for (a) the pre-lithiation process of Li//AC half cells, and (b) the pre-cycle treatment of Li//graphite half cells. Figure S6. (a) Initial three CV curves of the AC (-)//SLP50 (+) full cell at the scan rate of 0.1 mV s^{-1}, and (b) CV curves of the cell at different scan rates. Figure S7. (a) Charge/discharge curves of the AC (-)//SLP50 (+) full cell cycled at various current densities. (b) Medium voltage of the cell at various current densities. Table S1. Energy density and power density of the AC (-)//SLP50 graphite (+) full cell. Table S2. Comparison of the energy and power densities of the AC (-)//SLP50 graphite (+) full cell with reported AC cathode-based LICs. Table S3. Comparison of the electrochemical performance of the AC (-)//SLP50 graphite (+) full cell with reported dual-graphite batteries (G(-)//G(+)). Figure S8. (a,b) SEM images and (c) Raman spectrum of SP1 graphite, and (d,e) SEM images and (f) Raman spectrum of SFG6L graphite. Figure S9. (a) Charge/discharge capacities and CE at current density of 100 mA g^{-1} within 500 cycles, (b) rate performance at various current densities, and (c) charge/discharge capacities and CE at current density of 500 mA g^{-1} within 3000 cycles of AC (-)//SP1 (+) and AC (-)//SFG6L (+) full cells.

Author Contributions: Y.Z.: Conceptualisation, Methodology, Validation, Formal analysis, Investigation, Data curation, and Writing—original draft. J.L.: Formal analysis and Investigation. P.X.: Resources, Writing—review and editing, Supervision, and Project administration. All authors have read and agreed to the published version of the manuscript.

Funding: This work was supported by the China Scholarship Council/University of Manchester award. Ping Xiao acknowledges financial support from the Royal Academy of Engineering and Rolls-Royce for appointment of the Rolls-Royce/Royal Academy of Engineering Research Chair in Advanced Coating Technology.

Data Availability Statement: Data will be made available on request.

Conflicts of Interest: The authors declare that they have no known competing financial interests or personal relationships that could have appeared to influence the work reported in this paper.

References

1. Zou, K.; Deng, W.; Silvester, D.S.; Zou, G.; Hou, H.; Banks, C.E.; Li, L.; Hu, J.; Ji, X. Carbonyl Chemistry for Advanced Electrochemical Energy Storage Systems. *ACS Nano* **2024**, *18*, 19950–20000. [CrossRef]
2. Liu, J.; Wang, J.; Xu, C.; Jiang, H.; Li, C.; Zhang, L.; Lin, J.; Shen, Z.X. Advanced Energy Storage Devices: Basic Principles, Analytical Methods, and Rational Materials Design. *Adv. Sci.* **2018**, *5*, 1700322. [CrossRef] [PubMed]
3. Zou, K.; Jiang, M.; Ning, T.; Tan, L.; Zheng, J.; Wang, J.; Ji, X.; Li, L. Thermodynamics-directed bulk/grain-boundary engineering for superior electrochemical durability of Ni-rich cathode. *J. Energy Chem.* **2024**, *97*, 321–331. [CrossRef]
4. Khan, F.M.N.U.; Rasul, M.G.; Sayem, A.S.M.; Mandal, N. Maximizing energy density of lithium-ion batteries for electric vehicles: A critical review. *Energy Rep.* **2023**, *9*, 11–21. [CrossRef]
5. Divya, M.L.; Natarajan, S.; Lee, Y.S.; Aravindan, V. Biomass-Derived Carbon: A Value-Added Journey Towards Constructing High-Energy Supercapacitors in an Asymmetric Fashion. *ChemSusChem* **2019**, *12*, 4353–4382. [CrossRef]
6. Wang, G.; Oswald, S.; Löffler, M.; Müllen, K.; Feng, X. Beyond Activated Carbon: Graphite-Cathode-Derived Li-Ion Pseudocapacitors with High Energy and High Power Densities. *Adv. Mater.* **2019**, *31*, 1807712. [CrossRef]
7. Zhang, S.; Li, C.; Zhang, X.; Sun, X.; Wang, K.; Ma, Y. High Performance Lithium-Ion Hybrid Capacitors Employing Fe_3O_4-Graphene Composite Anode and Activated Carbon Cathode. *ACS Appl. Mater. Interfaces* **2017**, *9*, 17136–17144. [CrossRef]
8. Eleri, O.E.; Lou, F.; Yu, Z. Lithium-Ion Capacitors: A Review of Strategies toward Enhancing the Performance of the Activated Carbon Cathode. *Batteries* **2023**, *9*, 533. [CrossRef]
9. Khomenko, V.; Raymundo-Piñero, E.; Béguin, F. High-energy density graphite/AC capacitor in organic electrolyte. *J. Power Sources* **2008**, *177*, 643–651. [CrossRef]
10. Sun, H.; Mei, L.; Liang, J.; Zhao, Z.; Lee, C.; Fei, H.; Ding, M.; Lau, J.; Li, M.; Wang, C.; et al. Three-dimensional holey-graphene/niobia composite architectures for ultrahigh-rate energy storage. *Science* **2017**, *356*, 599–604. [CrossRef]
11. Kim, H.S.; Cook, J.B.; Lin, H.; Ko, J.S.; Tolbert, S.H.; Ozolins, V.; Dunn, B. Oxygen vacancies enhance pseudocapacitive charge storage properties of MoO_{3-x}. *Nat. Mater.* **2017**, *16*, 454–462. [CrossRef] [PubMed]
12. Zhang, L.; Wang, H.; Zhang, X.; Tang, Y. A Review of Emerging Dual-Ion Batteries: Fundamentals and Recent Advances. *Adv. Funct. Mater.* **2021**, *31*, 2010958. [CrossRef]
13. Xiang, W.; Chen, M.; Zhou, X.; Chen, J.; Huang, H.; Sun, Z.; Lu, Y.; Zhang, G.; Wen, X.; Li, W. Highly Enforced Rate Capability of a Graphite Anode via Interphase Chemistry Tailoring Based on an Electrolyte Additive. *J. Phys. Chem. Lett.* **2022**, *13*, 5151–5159. [CrossRef]
14. Wang, G.; Yu, M.; Wang, J.; Li, D.; Tan, D.; Löffler, M.; Zhuang, X.; Müllen, K.; Feng, X. Self-Activating, Capacitive Anion Intercalation Enables High-Power Graphite Cathodes. *Adv. Mater.* **2018**, *30*, 1800533. [CrossRef]
15. Gao, J.; Tian, S.; Qi, L.; Yoshio, M.; Wang, H. Hexafluorophosphate intercalation into graphite electrode from gamma-butyrolactone solutions in activated carbon/graphite capacitors. *J. Power Sources* **2015**, *297*, 121–126. [CrossRef]
16. Yoshio, M.; Nakamura, H.; Wang, H. Novel megalo-capacitance capacitor based on graphitic carbon cathode. *Electrochem. Solid-State Lett.* **2006**, *9*, 561–563. [CrossRef]
17. Rajalekshmi, A.R.; Divya, M.L.; Lee, Y.S.; Aravindan, V. High-performance Li-ion capacitor via anion-intercalation process. *Batter. Energy* **2022**, *1*, 20210005. [CrossRef]
18. Ji, B.; Zhang, F.; Song, X.; Tang, Y. A Novel Potassium-Ion-Based Dual-Ion Battery. *Adv. Mater.* **2017**, *29*, 1700519. [CrossRef]
19. Beltrop, K.; Qi, X.; Hering, T.; Röser, S.; Winter, M.; Placke, T. Enabling bis(fluorosulfonyl)imide-based ionic liquid electrolytes for application in dual-ion batteries. *J. Power Sources* **2018**, *373*, 193–202. [CrossRef]
20. Wu, L.N.; Peng, J.; Sun, Y.K.; Han, F.M.; Wen, Y.F.; Shi, C.G.; Fan, J.J.; Huang, L.; Li, J.T.; Sun, S.G. High-Energy Density Li metal Dual-Ion Battery with a Lithium Nitrate-Modified Carbonate-Based Electrolyte. *ACS Appl. Mater. Interfaces* **2019**, *11*, 18504–18510. [CrossRef]

21. Placke, T.; Fromm, O.; Lux, S.F.; Bieker, P.; Rothermel, S.; Meyer, H.-W.; Passerini, S.; Winter, M. Reversible Intercalation of Bis(trifluoromethanesulfonyl)imide Anions from an Ionic Liquid Electrolyte into Graphite for High Performance Dual-Ion Cells. *J. Electrochem. Soc.* **2012**, *159*, A1755–A1765. [CrossRef]
22. Luo, X.F.; Yang, C.H.; Peng, Y.Y.; Pu, N.W.; Der Ger, M.; Hsieh, C.T.; Chang, J.K. Graphene nanosheets, carbon nanotubes, graphite, and activated carbon as anode materials for sodium-ion batteries. *J. Mater. Chem. A* **2015**, *3*, 10320–10326. [CrossRef]
23. Zięzio, M.; Charmas, B.; Jedynak, K.; Hawryluk, M.; Kucio, K. Preparation and characterization of activated carbons obtained from the waste materials impregnated with phosphoric acid(V). *Appl. Nanosci.* **2020**, *10*, 4703–4716. [CrossRef]
24. Zou, K.; Cai, P.; Liu, C.; Li, J.; Gao, X.; Xu, L.; Zou, G.; Hou, H.; Liu, Z.; Ji, X. A kinetically well-matched full-carbon sodium-ion capacitor. *J. Mater. Chem. A* **2019**, *7*, 13540–13549. [CrossRef]
25. Ge, P.; Li, S.; Xu, L.; Zou, K.; Gao, X.; Cao, X.; Zou, G.; Hou, H.; Ji, X. Hierarchical Hollow-Microsphere Metal–Selenide@Carbon Composites with Rational Surface Engineering for Advanced Sodium Storage. *Adv. Energy Mater.* **2019**, *9*, 1803035. [CrossRef]
26. Tan, L.; Huang, X.; Yin, T.; Guo, Y.; Ning, T.; Mei, Y.; Zou, K.; Li, L.; Ji, X.; Zou, G. A 5 V ultrahigh energy density lithium metal capacitor enabled by the fluorinated electrolyte. *Energy Storage Mater.* **2024**, *71*, 103692. [CrossRef]
27. Tan, X.; Zhang, F.; Chen, D.; Wang, P.; Liu, Y.; Meng, C.; Zhang, Y. Modulating NH4+ in vanadium oxide framework for high-efficient aqueous NH_4^+ storage. *Chem. Eng. J.* **2024**, *489*, 151119. [CrossRef]
28. Sun, L.; Zhang, Y.; Si, H.; Zhang, Y.; Liu, J.; Liu, J.; Zhang, Y. TiO_2-modified red phosphorus nanosheets entangled in carbon nanotubes for high performance lithium ion batteries. *Electrochim. Acta* **2019**, *297*, 319–327. [CrossRef]
29. Balabajew, M.; Reinhardt, H.; Bock, N.; Duchardt, M.; Kachel, S.; Hampp, N.; Roling, B. In-Situ Raman Study of the Intercalation of Bis(trifluoromethylsulfonyl)imid Ions into Graphite inside a Dual-Ion Cell. *Electrochim. Acta* **2016**, *211*, 679–688. [CrossRef]
30. Lu, Y.; Zhang, D.; Wang, L.; Xu, M.; Song, J.; Goodenough, J.B. Electrochemical Behavior of a Graphite Electrode Prepared by Anodic Electrophoretic Deposition. *J. Electrochem. Soc.* **2012**, *159*, A321–A324. [CrossRef]
31. Satish, R.; Aravindan, V.; Ling, W.C.; Madhavi, S. Carbon-coated $Li_3V_2(PO_4)_3$ as insertion type electrode for lithium-ion hybrid electrochemical capacitors: An evaluation of anode and cathodic performance. *J. Power Sources* **2015**, *281*, 310–317. [CrossRef]
32. Kim, H.; Cho, M.Y.; Kim, M.H.; Park, K.Y.; Gwon, H.; Lee, Y.; Roh, K.C.; Kang, K. A novel high-energy hybrid supercapacitor with an anatase TiO_2-reduced graphene oxide anode and an activated carbon cathode. *Adv. Energy Mater.* **2013**, *3*, 1500–1506. [CrossRef]
33. Leng, K.; Zhang, F.; Zhang, L.; Zhang, T.; Wu, Y.; Lu, Y.; Huang, Y.; Chen, Y. Graphene-based Li-ion hybrid supercapacitors with ultrahigh performance. *Nano Res.* **2013**, *6*, 581–592. [CrossRef]
34. Li, G.; Yin, Z.; Guo, H.; Wang, Z.; Yan, G.; Yang, Z.; Liu, Y.; Ji, X.; Wang, J. Metalorganic Quantum Dots and Their Graphene-Like Derivative Porous Graphitic Carbon for Advanced Lithium-Ion Hybrid Supercapacitor. *Adv. Energy Mater.* **2019**, *9*, 1802878. [CrossRef]
35. Wang, X.; Wang, Z.; Zhang, X.; Peng, H.; Xin, G.; Lu, C.; Zhong, Y.; Wang, G.; Zhang, Y. Nitrogen-Doped Defective Graphene Aerogel as Anode for all Graphene-Based Lithium Ion Capacitor. *ChemistrySelect* **2017**, *2*, 8436–8445. [CrossRef]
36. Lim, E.; Jo, C.; Kim, H.; Kim, M.H.; Mun, Y.; Chun, J.; Ye, Y.; Hwang, J.; Ha, K.S.; Roh, K.C.; et al. Facile Synthesis of Nb_2O_5@Carbon Core-Shell Nanocrystals with Controlled Crystalline Structure for High-Power Anodes in Hybrid Supercapacitors. *ACS Nano* **2015**, *9*, 7497–7505. [CrossRef] [PubMed]
37. Chaturvedi, A.; Hu, P.; Aravindan, V.; Kloc, C.; Madhavi, S. Unveiling two-dimensional TiS_2 as an insertion host for the construction of high energy Li-ion capacitors. *J. Mater. Chem. A* **2017**, *5*, 9177–9181. [CrossRef]
38. Sun, C.; Zhang, X.; Li, C.; Wang, K.; Sun, X.; Ma, Y. High-efficiency sacrificial prelithiation of lithium-ion capacitors with superior energy-storage performance. *Energy Storage Mater.* **2020**, *24*, 160–166. [CrossRef]
39. Yi, S.; Wang, L.; Zhang, X.; Li, C.; Liu, W.; Wang, K.; Sun, X.; Xu, Y.; Yang, Z.; Cao, Y.; et al. Cationic intermediates assisted self-assembly two-dimensional $Ti_3C_2T_x$/rGO hybrid nanoflakes for advanced lithium-ion capacitors. *Sci. Bull.* **2021**, *66*, 914–924. [CrossRef]
40. Liu, C.; Wang, B.; Xu, L.; Zou, K.; Deng, W.; Hou, H.; Zou, G.; Ji, X. Novel Nonstoichiometric Niobium Oxide Anode Material with Rich Oxygen Vacancies for Advanced Lithium-Ion Capacitors. *ACS Appl. Mater. Interfaces* **2023**, *15*, 5387–5398. [CrossRef]
41. Wang, G.; Wang, F.; Zhang, P.; Zhang, J.; Zhang, T.; Müllen, K.; Feng, X. Polarity-Switchable Symmetric Graphite Batteries with High Energy and High Power Densities. *Adv. Mater.* **2018**, *30*, 1802949. [CrossRef] [PubMed]
42. Wrogemann, J.M.; Haneke, L.; Ramireddy, T.; Frerichs, J.E.; Sultana, I.; Chen, Y.I.; Brink, F.; Hansen, M.R.; Winter, M.; Glushenkov, A.M.; et al. Advanced Dual-Ion Batteries with High-Capacity Negative Electrodes Incorporating Black Phosphorus. *Adv. Sci.* **2022**, *9*, 2201116. [CrossRef]
43. Rothermel, S.; Meister, P.; Schmuelling, G.; Fromm, O.; Meyer, H.-W.W.; Nowak, S.; Winter, M.; Placke, T. Dual-graphite cells based on the reversible intercalation of bis(trifluoromethanesulfonyl)imide anions from an ionic liquid electrolyte. *Energy Environ. Sci.* **2014**, *7*, 3412–3423. [CrossRef]
44. Read, J.A.; Cresce, A.V.; Ervin, M.H.; Xu, K. Dual-graphite chemistry enabled by a high voltage electrolyte. *Energy Environ. Sci.* **2014**, *7*, 617–620. [CrossRef]
45. Qiao, Y.; Jiang, K.; Li, X.; Deng, H.; He, Y.; Chang, Z.; Wu, S.; Guo, S.; Zhou, H. A Hybrid Electrolytes Design for Capacity-Equivalent Dual-Graphite Battery with Superior Long-Term Cycle Life. *Adv. Energy Mater.* **2018**, *8*, 1801120. [CrossRef]
46. Heckmann, A.; Thienenkamp, J.; Beltrop, K.; Winter, M.; Brunklaus, G.; Placke, T. Towards high-performance dual-graphite batteries using highly concentrated organic electrolytes. *Electrochim. Acta* **2018**, *260*, 514–525. [CrossRef]

47. Wang, A.; Yuan, W.; Fan, J.; Li, L. A Dual-graphite Battery with Pure 1-Butyl-1-methylpyrrolidinium bis(trifluoromethylsulfonyl) Imide as the Electrolyte. *Energy Technol.* **2018**, *6*, 2172–2178. [CrossRef]
48. Huang, Y.; Xiao, R.; Ma, Z.; Zhu, W. Developing Dual-Graphite Batteries with Pure 1-Ethyl-3-methylimidazolium Trifluoromethanesulfonate Ionic Liquid as the Electrolyte. *ChemElectroChem* **2019**, *6*, 4681–4688. [CrossRef]
49. Ghosh, S.; Sarma, D.; Mahata, A.; Martha, S.K. Differences between cation and anion storage electrochemistry of graphite and its impact on dual graphite battery. *J. Power Sources* **2024**, *589*, 233721. [CrossRef]
50. Zhang, L.; Wang, H. Dual-Graphite Batteries with Flame-Retardant Electrolyte Solutions. *ChemElectroChem* **2019**, *6*, 4637–4644. [CrossRef]

batteries

MDPI

Article

One-Step Hydrothermally Synthesized $Ni_{11}(HPO_3)_8(OH)_6/Co_3(HPO_4)_2(OH)_2$ Heterostructure with Enhanced Rate Performance for Hybrid Supercapacitor Applications

Mingjun Jing [1,*], Kaige Long [1], Rui Liu [1], Xingyu Wang [1], Tianjing Wu [1], Yirong Zhu [2,*], Lijie Liu [3], Sheng Zhang [4], Yang Zhang [5] and Cheng Liu [6]

[1] The College of Chemistry, Xiangtan University, Xiangtan 411105, China
[2] College of Materials and Advanced Manufacturing, Hunan University of Technology, Zhuzhou 412007, China
[3] College of Science, Henan Agricultural University, 63 Agricultural Road, Zhengzhou 450002, China
[4] Institute of Nanoscience and Engineering, Henan University, Kaifeng 475004, China
[5] Department of Materials, Henry Royce Institute, University of Manchester, Manchester M13 9PL, UK; yang.zhang-26@postgrad.manchester.ac.uk
[6] Institut de Ciència de Materials de Barcelona (ICMAB), CSIC, Campus UAB, 08193 Bellaterra, Spain
* Correspondence: jingmingjun@xtu.edu.cn (M.J.); zhuyirong@hut.edu.cn (Y.Z.)

Abstract: Transition metal phosphate is the prospective electrode material for supercapacitors (SCs). It has an open frame construction with spacious cavities and wide aisles, resulting in excellent electric storage capacity. However, the inferior rate behavior and cycling stability of transition metal phosphate materials in alkaline environments pose significant barriers to their application in SCs. Herein, $Ni_{11}(HPO_3)_8(OH)_6/Co_3(HPO_4)_2(OH)_2$ heterostructured materials synthesized through a one-step hydrothermal process exhibiting remarkable rate capability coupled with exceptional cycling endurance. $Ni_{11}(HPO_3)_8(OH)_6/Co_3(HPO_4)_2(OH)_2$ samples exhibit a micron-scale structure composed of sheet-like compositions and unique pore structure. The multistage pore structure is favorable for promoting the diffusion of protons and ions, enhancing the sample's electrochemical storage capacity. Upon conducting electrochemical tests, it was observed that $Ni_{11}(HPO_3)_8(OH)_6/Co_3(HPO_4)_2(OH)_2$ composite electrode surpassed both the standalone $Ni_{11}(HPO_3)_8(OH)_6$ and $Co_3(HPO_4)_2(OH)_2$ electrode, achieving a remarkable specific capacity of 163 mAh g^{-1} with exceptional stability and efficiency at 1 A g^{-1}. Notably, this electrode also exhibits superior rate performance, maintaining 82.5% and 71% of its original full capacity even at 50 A g^{-1} and 100 A g^{-1}, respectively. Furthermore, it demonstrates superior stability in cycling, retaining a capacity of 92.7% at 10 A g^{-1} after 5000 cycles. Moreover, $Ni_{11}(HPO_3)_8(OH)_6/Co_3(HPO_4)_2(OH)_2$ and porous carbon (PC) were assembled into a hybrid supercapacitor (HSC). Electrochemical tests reveal an impressive power density of up to 36 kW kg^{-1} and an exceptional energy density of up to 47.4 Wh kg^{-1} for the HSC. Moreover, $Ni_{11}(HPO_3)_8(OH)_6/Co_3(HPO_4)_2(OH)_2$//PC HSC exhibits robust capacity retention stability of 92.9% after enduring 10,000 cycles at 3 A g^{-1}, demonstrating its remarkable durability. This work imparts viewpoints into the design of transition metal phosphate heterostructured materials.

Keywords: high-rate performance; hybrid supercapacitor; nickel cobalt phosphate; heterostructure

1. Introduction

As electrochemical energy storage technologies evolve, supercapacitors (SCs) have distinguished themselves among various storage devices because of their environmental friendliness, fast discharging and charging rates, lengthy lifespan, and superior safety features [1–3]. Nevertheless, despite these numerous advantages, there remains a substantial gap between the energy density of SCs and the requirements of commercial applications. Researchers have proposed a feasible approach in the form of a hybrid supercapacitor (HSC) [4,5]. HSC exhibits an exceptional combination of high energy density alongside robust power density, offering a unique balance in performance [6,7]. The performance of HSC is contingent upon the electrode material utilized. However, conventional cathode materials with a battery type exhibit slow ionic kinetics, while capacitive cathode materials display fast kinetic behavior, rendering it challenging to achieve a suitable match between the two kinetic behaviors [8,9]. In response to the issue, further investigations have revealed that oxides, hydroxides, sulfides, phosphides, and phosphates are all suitable cathode materials for HSC [10–16]. Therefore, developing cathode materials that possess enhanced high kinetics and durability can have a positive effect on overcoming current challenges.

Among various materials, transition metal phosphates have recently attracted much attention, mainly because of their unique properties as both transition metal oxides and transition metal phosphides. This mixture of properties gives them excellent electrochemical performance and high chemical stability [17–19]. Besides, it also has an open structural framework and rich redox behavior, which makes it exhibit excellent energy storage capacity [20,21]. For example, the specific capacitance for $Ni_3P_2O_8$ at 0.5 A g^{-1} is 1464 F g^{-1} [22]. This measured specific capacitance for $Co_{11}(HPO_3)_8(OH)_6$ at 0.5 A g^{-1} is 1200 F g^{-1} [23]. Therefore, transition metal phosphates are more attractive when choosing materials for electrodes. Compared with other metal phosphates that have been extensively studied, nickel-based phosphates have a high specific capacitance [24,25]. However, their poor rate behaviors and cyclic stability in alkaline electrolytes limit their large-scale application.

Researchers have implemented various strategies to address the issue, including refining the morphology of materials, constructing a suitable pore structure, designing composite materials and so on [17,26]. For example, an ultra-thin nanosheet-based nickel phosphate lamellar structure attained at 2.0 A g^{-1} current conditions the remarkable specific capacity of 131.6 mAh g^{-1} [27]. $Ni_3(PO_4)_2$/GF composite nanostructures were prepared, demonstrating a capacitance of 48 mAh g^{-1} at 0.5 A g^{-1} current conditions [28]. While these materials display favorable electrochemical characteristics, there is a continued necessity to identify straightforward and efficacious methodologies for improving nickel-based phosphate rate properties and cycling stability. However, constructing a heterostructure has attracted much attention as a novel approach to creating materials with unique interfaces, elastic structures, and synergistic effects that enhance SCs energy/power density [29–31]. Meanwhile, embedding an internal electric field across the interfaces of heterogeneous structures can potentially expedite ion diffusion, enhancing overall ion transport efficiency [32].

Moreover, the reallocation of charge within the heterostructure components fosters the creation of additional energetic storage sites, enhancing the electrode's reversible capacity and optimizing its energy storage performance [33]. Hence, rationally designed combinations of two materials in heterostructures may yield unprecedented performance due to the complementary effects of different materials. Although previous studies have achieved enhanced electrochemical performance by constructing heterostructures with different components, the synthesis process is complicated. For instance, the amorphous/crystalline nickel manganese phosphate octahydrate heterostructured samples were obtained solely through a hydrothermal process with subsequent annealing in argon gas, demonstrating a specific capacitance of 2351.6 F g^{-1} at 1 A g^{-1} [34]. This specific capacity for $Fe_{0.4}Co_{0.6}Se_2$@NiCo-P heterostructured materials was prepared using the two-step electrodeposition method at 1 A g^{-1} with a current condition of 202.3 mAh g^{-1} [35]. Reports on the simple and rapid synthesis of nickel-based metallic phosphate heterostructured materials are scarce. Therefore, it is worthwhile to explore a simple approach to construct a heterostructure of transition metal phosphates.

Herein, the $Ni_{11}(HPO_3)_8(OH)_6/Co_3(HPO_4)_2(OH)_2$ heterojunction composites were synthesized through a straightforward one-step hydrothermal process, utilizing red phosphorus (RP) as the phosphorous source. This heterostructure effectively has optimized its electronic structure. The redistribution of charges in the heterostructure will induce a greater number of active sites to participate in energy storage, improving the capacity performance of the electrodes. A further examination and analysis of the composition, properties, and structure of the materials is carried out through a series of physical characterization and electrochemical tests. Electrochemical assessments indicate that the $Ni_{11}(HPO_3)_8(OH)_6/Co_3(HPO_4)_2(OH)_2$ composite electrode boasts enhanced specific capacitance, exceptional rate performance (the capacity retention attains 82.5% and 71%, respectively, when operated at 50 A g^{-1} and 100 A g^{-1} current densities), and impressive recycling capacity. Furthermore, the HSC configured with $Ni_{11}(HPO_3)_8(OH)_6/Co_3(HPO_4)_2(OH)_2$ and porous carbon (PC) demonstrates outstanding energy/power density and robust cycling endurance. The work gives a practical and effective generalized approach for the preparation of metal-phosphate heterostructured materials.

2. Experimental Section

2.1. Chemicals and Materials

Red phosphorus (RP, AR), nickel nitrate hexahydrate ($Ni(NO_3)_2{\cdot}6H_2O$, AR), potassium hydroxide (KOH, AR), cobalt nitrate hexahydrate ($Co(NO_3)_2{\cdot}6H_2O$, AR), ammonia ($NH_3{\cdot}H_2O$, AR), and anhydrous ethanol (C_2H_5OH, AR) were sourced from Sinopharm Chemical Reagent Co. Ltd. (Shanghai, China) Acetylene black (C, AR) was procured from Shenzhen Kejing Zhida Technology Co., Shenzhen, China, porous carbon (PC, 2 nm) was obtained from Xianfeng Nanomaterials Technology Co., Ltd., Nanjing, China, polytetrafluoroethylene (PTFE, 60%) was acquired from Daikin, Japan, N-methylpyrrolidone (NMP, battery grade) was purchased from Shenzhen Kejing Zhi Technology Co., Ltd., Shenzhen, China. And Nickel foam was obtained from Changde Liyuan New Material Co., Changde, China.

2.2. Synthesis of $Ni_{11}(HPO_3)_8(OH)_6$ Cathode Material

After dissolving 0.67 mmol of $Ni(NO_3)_2{\cdot}6H_2O$ into 50 mL distilled water, 103.75 mg of RP was added and magnetically mixed at 30 min for the solution of deep red color. Then, $NH_3{\cdot}H_2O$ was dropped into this solution with the pH adjusted to 8–9. The final solution was moved to the hydrothermal kettle heated to 180 °C and held for 12 h. This reacted solution was naturally cooled to ambient temperature, and the resulting precipitated samples were fully centrifuged alternately into distilled water and subsequently into ethanol to separate any unreacted residue and dried at the temperature of 50 °C, lasting for a period of 12 h to obtain the $Ni_{11}(HPO_3)_8(OH)_6$ product.

2.3. Synthesis of $Ni_{11}(HPO_3)_8(OH)_6/Co_3(HPO_4)_2(OH)_2$ Heterojunction Composites

After dissolving 0.67 mmol $Ni(NO_3)_2{\cdot}6H_2O$ and 0.67 mmol $Co(NO_3)_2{\cdot}6H_2O$ into 50 mL of distilled water, 103.75 mg of RP was added and magnetically mixed at 30 min for the solution of deep red color. Then, $NH_3{\cdot}H_2O$ was dropped into this solution with pH adjusted to 8–9. The final solution was moved to the hydrothermal kettle heated to 180 °C and held for 12 h. This reacted solution was naturally cooled to ambient temperature, and resulting precipitated samples were fully centrifuged alternately with distilled water and ethanol to separate any unreacted residue and dried at the temperature of 50 °C, lasting for a period of 12 h to afford the $Ni_{11}(HPO_3)_8(OH)_6/Co_3(HPO_4)_2(OH)_2$ product.

2.4. Material Characteristics

The physical properties of the studied materials were analyzed using a Rigaku D/max 2550 VB^+ X-ray diffractometer. The physical and structural properties of materials, such as elemental composition, valence states, etc., were studied in depth using an ESCALab 250 X-ray photoelectron spectrometer with Thermo K-Alpha as a light source. The prepared samples were analyzed in detail for morphology, composition, and microstructure using FESEM with Signa 500. The morphological characteristics and the intricate microstructural features of the samples were thoroughly investigated using the advanced Titan G2 60–300 TEM. Pore sizing and the surface characteristics of materials were analyzed using a specific surface analyzer of Micrometrics ASAP 2020.

2.5. Electrochemical Tests

These working electrodes were produced by combining the $Ni_{11}(HPO_3)_8(OH)_6/Co_3(HPO_4)_2(OH)_2$ sample with acetylene black, serving as a conductive agent, and polytetrafluoroethylene (PTFE), acting as a binder, in a 7:2:1 ratio within an n-methyl-2-pyrrolidinone solution, which served as the dispersant. After mixing, preparation of the paste was uniformly applied to a cleaning nickel foam (collector) and dried in a vacuum oven. Finally, nickel foam was squeezed into working electrodes using a powder press at 10 MPa. The loading of $Ni_{11}(HPO_3)_8(OH)_6/Co_3(HPO_4)_2(OH)_2$ is ~1 mg cm^{-2}. The CHI 760E electrochemical workstation was used for all electrochemical tests. Therein, the Hg/HgO electrode was used as the reference electrode and the platinum sheet electrode was used as the counter electrode. The cyclic voltammetry (CV) test, alternating current impedance test (EIS), and constant current charge/discharge test (GCD) were used to analyze the electrochemical properties of electrodes. CV curves were acquired over a voltage range of 0~0.6 V, EIS was performed over a frequency range of 100 kHz to 0.01 Hz, and the GCD tests were performed over a potential range of 0~0.55 V.

In addition, HSCs were assembled and used to test their potential for practical applications. The HSC was assembled utilizing $Ni_{11}(HPO_3)_8(OH)_6/Co_3(HPO_4)_2(OH)_2$ as a cathode, PC as an anode, 2 mol L^{-1} KOH as an electrolyte, and NKK as the separator in a 2016-type coin cell configuration. To maintain charge equilibrium between the positive and negative components in the HSC, the optimal mass ratio of these two electrodes can be determined using the formula: $m^+/m^- = (C^- \times \Delta V^-)/(C^+ \times \Delta V^+)$, where + and − symbols represent the cathode and anode, respectively, while C and ΔV signify capacity and voltage range, respectively.

3. Results and Discussion

3.1. The Characterizations of Morphology, Composition, and Structure

Figure 1 presents the schematic for the preparation of $Ni_{11}(HPO_3)_8(OH)_6$ and $Ni_{11}(HPO_3)_8(OH)_6/Co_3(HPO_4)_2(OH)_2$ composites using a one-step hydrothermal process. First, $Ni_{11}(HPO_3)_8(OH)_6$ material is prepared using red phosphorus as a phosphorus source through the hydrothermal method. To elevate both the specific capacity and cycling stability, the $Ni_{11}(HPO_3)_8(OH)_6$ material has been further improved by constructing a heterostructure. Cobalt metal salt, nickel metal salt, RP, and $NH_3{\cdot}H_2O$ are thoroughly mixed, and the $Ni_{11}(HPO_3)_8(OH)_6/Co_3(HPO_4)_2(OH)_2$ product with micrometer structure of flake composition is obtained by a simple hydrothermal method (hydrothermal reaction at 180 °C in a hydrothermal autoclave for 12 h) and centrifugal drying. It is noteworthy that the $Ni_{11}(HPO_3)_8(OH)_6/Co_3(HPO_4)_2(OH)_2$ composites show a significant change in morphology compared with $Ni_{11}(HPO_3)_8(OH)_6$, and their regular lamellar composition structure enhances the energy storage capacity because it enlarges the specific surface area, providing lots of active sites. The $Ni_{11}(HPO_3)_8(OH)_6/Co_3(HPO_4)_2(OH)_2$ sample is synthesized as follows:

$$Co^{2+} + Ni^{2+} + 4OH^- \rightarrow Co(OH)_2 + Ni(OH)_2 \tag{1}$$

$$\begin{gathered} 33Ni(OH)_2 + 9Co(OH)_2 + 64P + 36H_2O \\ \rightarrow 3Ni_{11}(HPO_3)_8(OH)_6/Co_3(HPO_4)_2(OH)_2 + 34PH_3 \end{gathered} \tag{2}$$

As depicted in Figure 2a, the crystalline nature and structural configuration of the $Ni_{11}(HPO_3)_8(OH)_6/Co_3(HPO_4)_2(OH)_2$ specimen were characterized using XRD. The XRD diffraction peaks of $Ni_{11}(HPO_3)_8(OH)_6/Co_3(HPO_4)_2(OH)_2$ sample correspond to the standard cards of $Ni_{11}(HPO_3)_8(OH)_6$ (JCPDS No. 81-1065) and $Co_3(HPO_4)_2(OH)_2$ (JCPDS No. 80-1996). This suggests that the obtained material is a $Ni_{11}(HPO_3)_8(OH)_6/Co_3(HPO_4)_2(OH)_2$ heterogeneous structure. The XPS conducted on $Ni_{11}(HPO_3)_8(OH)_6/Co_3(HPO_4)_2(OH)_2$ sample offered detailed insights into its valence states and surface chemical composition. As illustrated in Figure 2b, the broad XPS spectrum validates the presence of Co, Ni, P, C, and O, confirming the purity of the specimen without any discernible traces of unintended elements beyond these constituents. Ni 2p spectroscopy with high resolution (Figure 2c) displays two peaks situated at 856.67 eV and 874.52 eV, corresponding to Ni $2p_{3/2}$ and Ni $2p_{1/2}$, respectively. Each of these main signals is accompanied by a satellite peak [36,37]. This matches well with the electronic state of Ni^{2+}. Co 2p spectroscopy with high resolution depicted in Figure 2d reveals two distinct peaks at 781.79 eV and 797.83 eV, which are indicative of Co $2p_{3/2}$ and Co $2p_{1/2}$ orbitals. This spectral signature confirms the existence of Co^{2+} ions within the system. The high-resolution P 2p spectra (Figure 2e) displays this peak at 133.4 eV attributable to P 2p, indicating the presence of $(PO_4)^{3-}$ on the $Ni_{11}(HPO_3)_8(OH)_6/Co_3(HPO_4)_2(OH)_2$ surface [38]. The $(PO_4)^{3-}$ form improves the surface activity on $Ni_{11}(HPO_3)_8(OH)_6/Co_3(HPO_4)_2(OH)_2$. This is consistent with the composition in $Ni_{11}(HPO_3)_8(OH)_6/Co_3(HPO_4)_2(OH)_2$ according to the above tests.

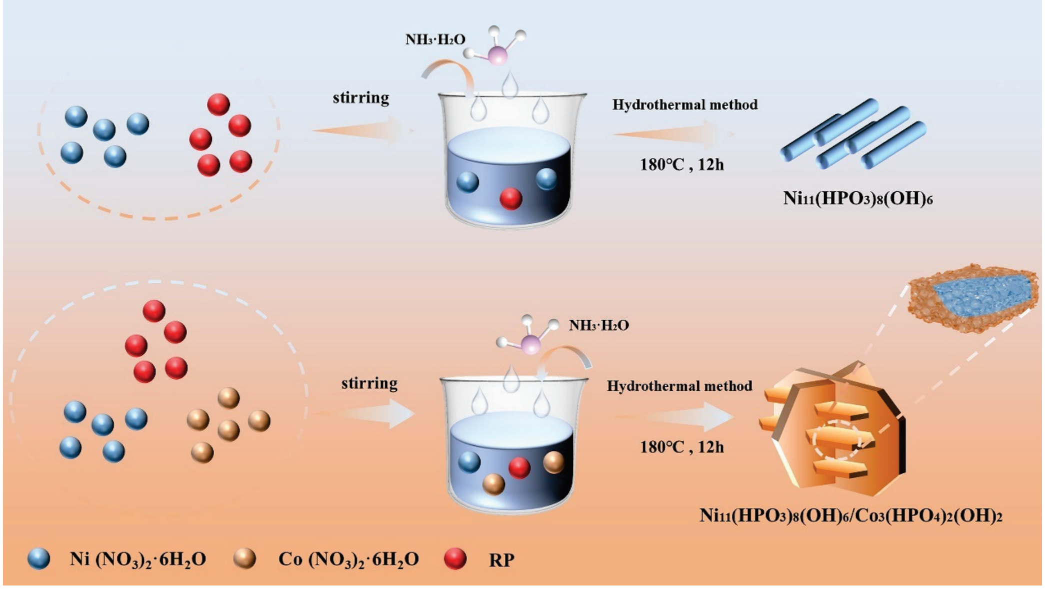

Figure 1. The schematic illustration for hydrothermal preparation of the $Ni_{11}(HPO_3)_8(OH)_6$ and $Ni_{11}(HPO_3)_8(OH)_6/Co_3(HPO_4)_2(OH)_2$ samples.

The N_2 adsorption/desorption test of the $Ni_{11}(HPO_3)_8(OH)_6/Co_3(HPO_4)_2(OH)_2$ heterogeneous structural material is shown in Figure 2f. The $Ni_{11}(HPO_3)_8(OH)_6/Co_3(HPO_4)_2(OH)_2$ material displays a clear hysteresis ring in the adsorption and desorption isotherms and a type IV isotherm, indicating the existence of their mesoporous structure in $Ni_{11}(HPO_3)_8(OH)_6/Co_3(HPO_4)_2(OH)_2$. At higher pressures ($P/P_0 > 0.9$), N_2 adsorption increased rapidly, indicating the existence of microporous structures. The specific surface area of BET for the $Ni_{11}(HPO_3)_8(OH)_6/Co_3(HPO_4)_2(OH)_2$ material is measured to be 43.2 $m^2\ g^{-1}$. For the $Ni_{11}(HPO_3)_8(OH)_6/Co_3(HPO_4)_2(OH)_2$ samples, the pore structure is analyzed by BJH. The $Ni_{11}(HPO_3)_8(OH)_6/Co_3(HPO_4)_2(OH)_2$ sample exhibits a distinctive hierarchical pore structure, further illuminated by its pore size distribution. This primarily comprises 4 nm mesopores, accompanied by a minimal presence of macropores. The $Ni_{11}(HPO_3)_8(OH)_6/Co_3(HPO_4)_2(OH)_2$ material's unique pore structure, featuring a dominance of mesopores and a small fraction of macropores, could boost electrochemical energy storage efficiency by facilitating proton and ion diffusion.

Morphology and microstructure are observed for $Ni_{11}(HPO_3)_8(OH)_6$ and $Ni_{11}(HPO_3)_8(OH)_6/Co_3(HPO_4)_2(OH)_2$ samples using FESEM. As depicted in Figure 3a–d, the findings demonstrate that the synthesized samples all display a uniform and regular morphology. The $Ni_{11}(HPO_3)_8(OH)_6$ sample displays a rod shape with a diameter of around 300 nm. In contrast, the $Ni_{11}(HPO_3)_8(OH)_6/Co_3(HPO_4)_2(OH)_2$ samples exhibit notable alterations. In particular, the $Ni_{11}(HPO_3)_8(OH)_6/Co_3(HPO_4)_2(OH)_2$ samples display a micrometer-scale structure comprising flake-like units with an overall size of approximately 9 µm. The EDS and elemental distribution of $Ni_{11}(HPO_3)_8(OH)_6$ are signaled in Figure 3e,f. EDS pattern (Figure 3g) reveals that the $Ni_{11}(HPO_3)_8(OH)_6/Co_3(HPO_4)_2(OH)_2$ material is consisted of Ni, Co, and P. In the atomic ratio of Ni, Co, and P, the approximate ratio is 3:11:10. Figure 3h provides further evidence that the elements Ni, Co and P have a single-form distribution over the structure. According to the above data, the prepared $Ni_{11}(HPO_3)_8(OH)_6/Co_3(HPO_4)_2(OH)_2$ material has the outstanding advantages of micrometer structure with lamellar composition, high specific surface area and abundant number of mesopores/macropores. Its rich active sites and unique hierarchical pore structure offer the possibility to realize electrochemical properties for the $Ni_{11}(HPO_3)_8(OH)_6/Co_3(HPO_4)_2(OH)_2$ electrode materials, such as high kinetics and high stability.

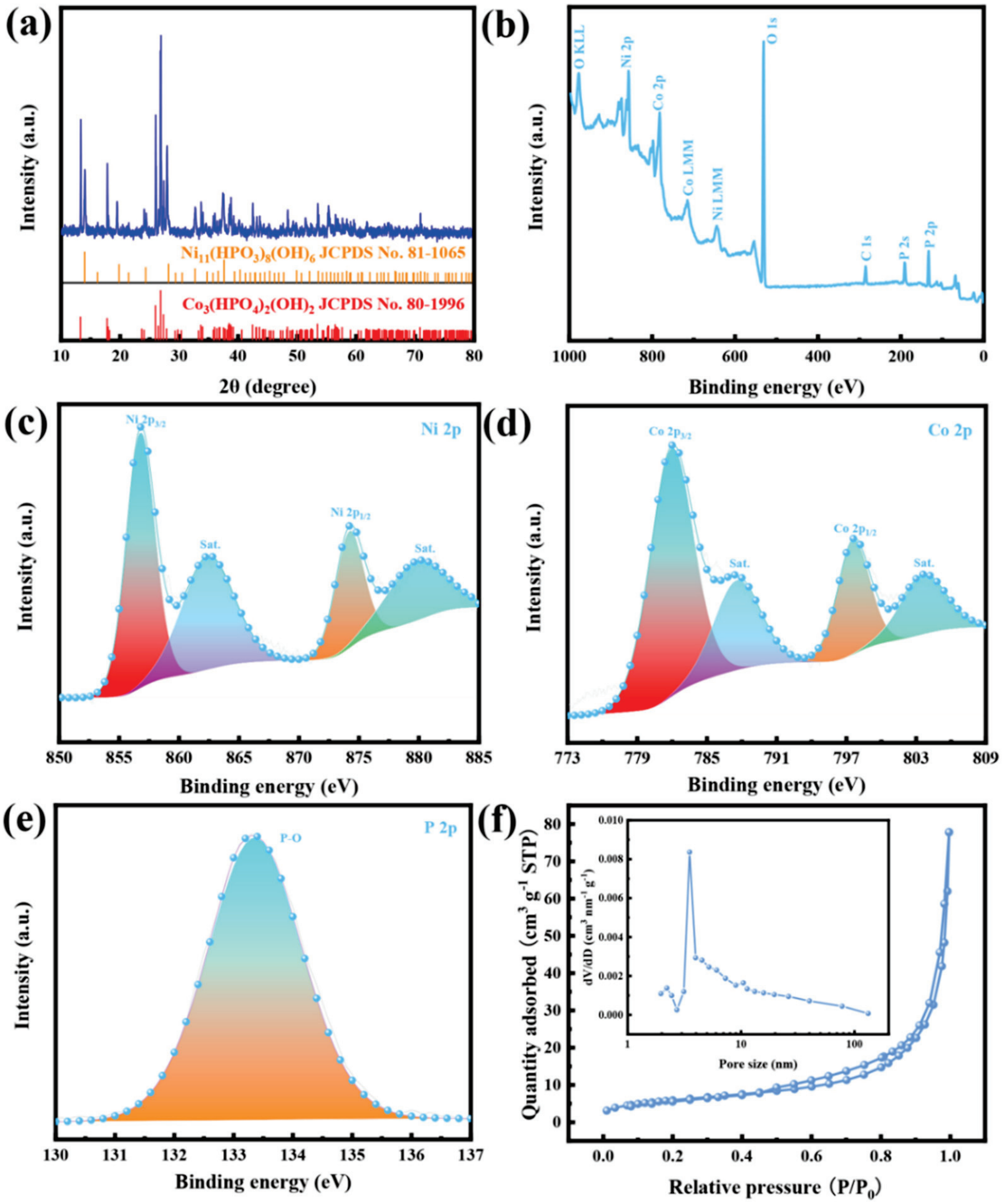

Figure 2. Characterization of $Ni_{11}(HPO_3)_8(OH)_6/Co_3(HPO_4)_2(OH)_2$ samples: (**a**) XRD plots; (**b**–**e**) XPS spectrum; (**f**) pore distribution (insert) and sorption–desorption isotherms curves of N_2.

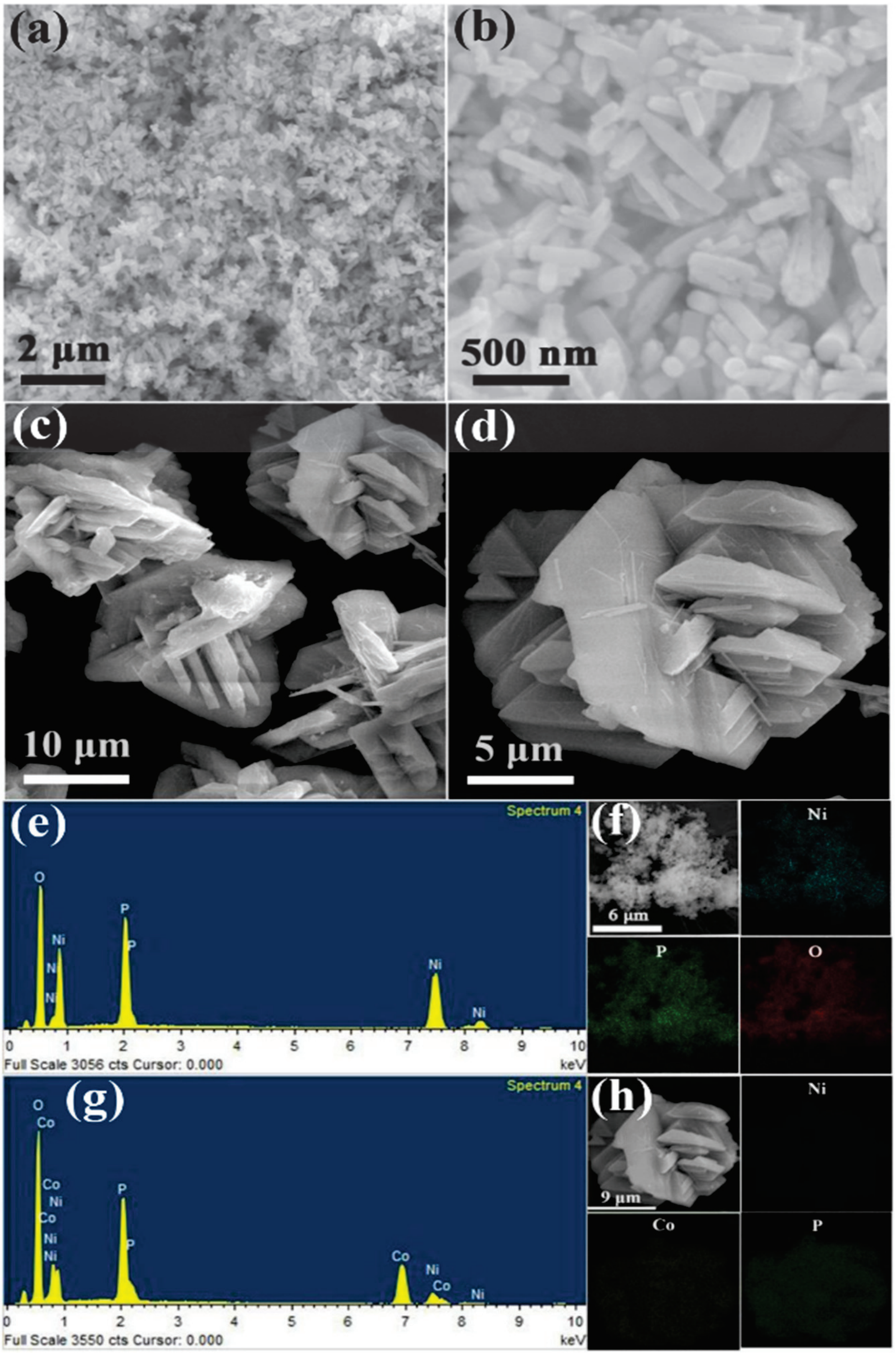

Figure 3. (**a**,**b**) FESEM images for $Ni_{11}(HPO_3)_8(OH)_6$ at different magnifications. (**c**,**d**) FESEM images for $Ni_{11}(HPO_3)_8(OH)_6/Co_3(HPO_4)_2(OH)_2$ samples with different magnifications. (**e**,**f**) EDS and elemental mappings for $Ni_{11}(HPO_3)_8(OH)_6$. (**g**,**h**) EDS and elemental mappings for the $Ni_{11}(HPO_3)_8(OH)_6/Co_3(HPO_4)_2(OH)_2$ samples.

3.2. The Electrochemical Performances of Samples

The CV curves for the $Ni_{11}(HPO_3)_8(OH)_6$ and $Ni_{11}(HPO_3)_8(OH)_6/Co_3(HPO_4)_2(OH)_2$ electrodes at 2 mV s^{-1} are presented in Figure 4a. These CV curves display clear redox peaks, demonstrating typical Faraday characteristics. The equations for the redox reactions could be as follows:

$$\begin{gathered}\mathrm{Ni_{11}(HPO_3)_8(OH)_6/Co_3(HPO_4)_2(OH)_2 + 14OH^- \leftrightarrow} \\ \mathrm{Ni_{11}(HPO_3)_8(OH)_{17} + Co_3(HPO_4)_2(OH)_5 + 14e^-}\end{gathered} \tag{3}$$

$$\begin{gathered}\mathrm{Ni_{11}(HPO_3)_8(OH)_{17} + Co_3(HPO_4)(OH)_5 + 14OH^- \leftrightarrow} \\ \mathrm{Co_3(HPO_4)(O)_4 + Ni_{11}(HPO_3)_8(O)_{14} + 18H_2O + 14e^-}\end{gathered} \tag{4}$$

Meanwhile, the $Ni_{11}(HPO_3)_8(OH)_6/Co_3(HPO_4)_2(OH)_2$ electrode displays a greater area of integration compared to the CV curve for the $Ni_{11}(HPO_3)_8(OH)_6$ electrode, indicating the $Ni_{11}(HPO_3)_8(OH)_6/Co_3(HPO_4)_2(OH)_2$ electrode possesses larger specific capacitance. Comparison is made between two electrodes with GCD curves between 0 and 0.55 V at 1 A g^{-1} is shown in Figure 4b. Compared to the $Ni_{11}(HPO_3)_8(OH)_6$ electrode, the $Ni_{11}(HPO_3)_8(OH)_6/Co_3(HPO_4)_2(OH)_2$ electrodes demonstrated superior symmetry in their charge-discharge profiles, longer discharge durations, and a broader voltage plateau. These phenomena indicate that the $Ni_{11}(HPO_3)_8(OH)_6/Co_3(HPO_4)_2(OH)_2$ electrode possesses greater capacity scalability and higher charge conversion efficiency. This specific capacity for the $Ni_{11}(HPO_3)_8(OH)_6/Co_3(HPO_4)_2(OH)_2$ electrode is determined to be 163.2 mAh g^{-1}, representing a significant increase compared to 79.4 mAh g^{-1} exhibited by the $Ni_{11}(HPO_3)_8(OH)_6$ electrode. The GCD curves (Figure 4c,d) for the $Ni_{11}(HPO_3)_8(OH)_6$ and $Ni_{11}(HPO_3)_8(OH)_6/Co_3(HPO_4)_2(OH)_2$ electrodes show non-linear charge/discharge profiles featuring distinct plateaus, attributable to reversible faraday redox reactions occurring both on the surface and within the electrodes. This further demonstrates their excellent Faraday cell performance. The specific capacities for the $Ni_{11}(HPO_3)_8(OH)_6/Co_3(HPO_4)_2(OH)_2$ electrodes were 163.2, 161.9, 161.4, 160, 158.3, 150, 134.6, and 115.9 mAh g^{-1} at 1, 2, 3, 5, 10, 20, 50, and 100 A g^{-1}, respectively, and those of $Ni_{11}(HPO_3)_8(OH)_6$ electrode are 79.4, 78.2, 77.6, 76.9, 76.2, 73.3, 65.3 and 54.8 mAh g^{-1}. The capacity retention for the $Ni_{11}(HPO_3)_8(OH)_6/Co_3(HPO_4)_2(OH)_2$ electrodes is about 71% at 100 A g^{-1}, which exhibits a notably elevated percentage in comparison to 68.9% for $Ni_{11}(HPO_3)_8(OH)_6$ electrodes, are exhibited within Figure 4e. The $Ni_{11}(HPO_3)_8(OH)_6/Co_3(HPO_4)_2(OH)_2$ electrode exhibits high specific capacity at ultra-high current densities, establishing its excellence in practical applications as a high-rate cell-typical electrode material. As shown in Figure 4f, Cyclic stability tests of the $Ni_{11}(HPO_3)_8(OH)_6/Co_3(HPO_4)_2(OH)_2$ electrodes were conducted through cyclic discharging and charging at 10 A g^{-1}. This capacity retention of the $Ni_{11}(HPO_3)_8(OH)_6/Co_3(HPO_4)_2(OH)_2$ electrode initially increases to 119% over the first 2000 cycles due to the electrode undergoing a gradual activation process. Subsequently, the capacity retention rate declines to 110.4% and remains stable for approximately 3700 cycles. After 5000 cycles, the $Ni_{11}(HPO_3)_8(OH)_6/Co_3(HPO_4)_2(OH)_2$ electrode demonstrated remarkable cycling performance, exhibiting an initial capacity retention of 110.4% and a maximum capacity retention of 92.7%. Additionally, the $Ni_{11}(HPO_3)_8(OH)_6/Co_3(HPO_4)_2(OH)_2$ electrode exhibits a Coulombic efficiency approaching 100%. The $Ni_{11}(HPO_3)_8(OH)_6/Co_3(HPO_4)_2(OH)_2$ electrode's excellent cycling stabilization may be due to the construction of heterostructures and unique multistage pore structure, along with the -OH groups incorporated within [39].

As illustrated in Table 1, the galvanic properties for the $Ni_{11}(HPO_3)_8(OH)_6/Co_3(HPO_4)_2(OH)_2$ electrodes are in comparison with other reported metal phosphide and phosphate electrodes. From the results of the comparison, it is found that the $Ni_{11}(HPO_3)_8(OH)_6/Co_3(HPO_4)_2(OH)_2$ electrode exhibits superior rate performance compared to other already reported electrodes. Furthermore, this method of constructing heterostructures to enhance material properties electrochemically is still rarely reported.

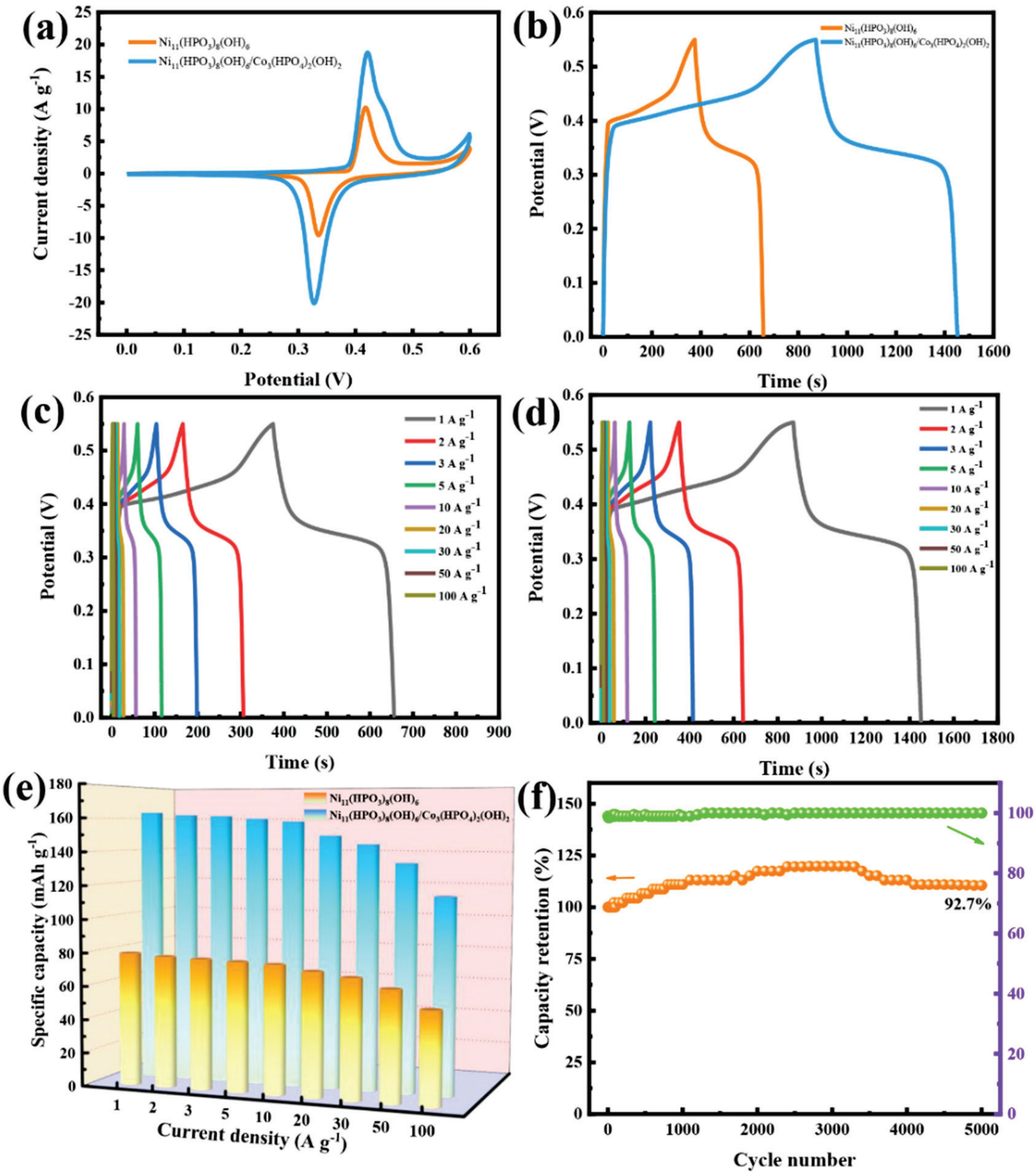

Figure 4. Electrochemical performance of the $Ni_{11}(HPO_3)_8(OH)_6$ and $Ni_{11}(HPO_3)_8(OH)_6/Co_3(HPO_4)_2(OH)_2$ electrodes in the three-electrode system: (**a**) CV curves at 2 mV s^{-1}, (**b**) GCD curves at 1 A g^{-1}. (**c**) GCD curves for the $Ni_{11}(HPO_3)_8(OH)_6$ electrode from 1 to 100 A g^{-1}. (**d**) GCD curves for the $Ni_{11}(HPO_3)_8(OH)_6/Co_3(HPO_4)_2(OH)_2$ electrode from1 to 100 A g^{-1}. (**e**) Rate performance and (**f**) cyclic stability and Coulombic efficiency for the $Ni_{11}(HPO_3)_8(OH)_6/Co_3(HPO_4)_2(OH)_2$ electrode.

Figure 5a,b presents display the CV curves for the $Ni_{11}(HPO_3)_8(OH)_6$ and $Ni_{11}(HPO_3)_8(OH)_6/Co_3(HPO_4)_2(OH)_2$ electrodes, respectively, within a range from 5 to 200mV s^{-1}. The redox peaks are visible on the CV curves, implying classical Faraday cell-type characteristics. Furthermore, the peak current distortion for electrodes is extremely small at 200 mV s^{-1}, displaying that the $Ni_{11}(HPO_3)_8(OH)_6/Co_3(HPO_4)_2(OH)_2$ electrode possesses rapid charging and discharging characteristics. Figure 5c displays the I_p-$v^{1/2}$ slopes of the oxidation peaks for the $Ni_{11}(HPO_3)_8(OH)_6$ and $Ni_{11}(HPO_3)_8(OH)_6/Co_3(HPO_4)_2(OH)_2$ electrodes, which are 17.8 and 32.1, respectively. Additionally, the I_p-$v^{1/2}$ slopes of the reduction peaks for these electrodes are −17.3 and −30.6, respectively. The two electrodes undergo a semi-quantitative analysis according to the charge storage mechanism to facilitate a deeper understanding of their electrochemical behavior, where this peak current I_p on scanning rate v is shown in the below equation: $I_p = a\,v^b$, $\log I_p = b \log v + \log a$, where the peak current denoted by the symbol I_p. The scan velocity is represented by v. Meanwhile, a and b serve as constants. Figure 5d displays the log I_p-log v fit line. The b-values for electrodes $Ni_{11}(HPO_3)_8(OH)_6$ and $Ni_{11}(HPO_3)_8(OH)_6/Co_3(HPO_4)_2(OH)_2$ are 0.7 and 0.75, respectively. Their values, ranging between 0.5 and 1, suggest a combined influence of diffusion and capacitive-controlled storage mechanisms, with capacitive control predominating. The above conclusions are subject to further verification.

Table 1. A summary of metal phosphides and phosphates used in SCs together with their corresponding electrochemical performance.

Material	Specific Capacity ($mAh\ g^{-1}$)	Rate Retention	Cyclic Property	Ref.
NiCoP/NiCo-OH	152.8 at 1 A g^{-1}	60% (1–10 A g^{-1})	88% after 1000 cycles	[40]
NiCoP	160.8 at 1 A g^{-1}	81% (1–16 A g^{-1})	/	[41]
Porous NiCoP	158.6 at 1 A g^{-1}	72.8% (1–20 A g^{-1})	72% after 3000 cycles	[42]
Ni-Co phosphate	125.8 at 1 A g^{-1}	63.4% (1–10 A g^{-1})	93% after 8000 cycles	[43]
$NH_4Co_{0.33}Ni_{0.67}PO_4 \cdot H_2O$	158 at 1.5 A g^{-1}	66% (1.5–30 A g^{-1})	57% after 1000 cycles	[44]
$Ni_xCo_{3-x}(PO_4)_2$	94.2 at 1 A g^{-1}	81.4% (1–10 A g^{-1})	85% after 1000 cycles	[45]
$Co_{0.5}Ni_{0.5}$ pyrophosphate	161 at 1.5 A g^{-1}	/	/	[46]
Cobalt-doped Ni phosphite	83.6 at 0.5 A g^{-1}	85% (0.5–5 A g^{-1})	93% after 8000 cycles	[47]
$(Ni,Co)_3(PO_4)_2 \cdot 8H_2O/(NH_4)$ $(Ni, Co)PO_4 \cdot 0.67H_2O$	141 at 0.5 A g^{-1}	88% (0.5–24 A g^{-1})	/	[48]
Ni-Co phosphate	147 at 0.2 A g^{-1}	85% (0.2–10 A g^{-1})	/	[49]
Co(P, S)/CC	101.6 at 1 A g^{-1}	56% (1–20 A g^{-1})	/	[50]
$Ni_{11}(HPO_3)_8(OH)_6/Co_3(HPO_4)_2(OH)_2$	163.2 at 1 A g^{-1}	96.9% (1–10 A g^{-1}) 91.9% (1–20 A g^{-1}) 71% (1–100 A g^{-1})	92.7% after 5000 cycles	This work

Furthermore, the diffusion-controlled/surface capacitive charge contributions can be quantified by the below equations: $I_p\ (v) = k_1 v + k_2 v^{1/2}$. Here, $k_1 v$ is for surface capacitance, and $k_2 v^{1/2}$ is for diffusion control. Figure 5e,f depicts comparative contributions of capacitive and diffusive processes in the $Ni_{11}(HPO_3)_8(OH)_6$ and $Ni_{11}(HPO_3)_8(OH)_6/Co_3(HPO_4)_2(OH)_2$ electrodes at 10 mV s^{-1}, respectively. This capacitance-controlled contribution for $Ni_{11}(HPO_3)_8(OH)_6$ is 72.1%, while that of $Ni_{11}(HPO_3)_8(OH)_6/Co_3(HPO_4)_2(OH)_2$ is 80.6%. It is reiterated that the capacitive characteristic predominates over the overall capacity of the electrodes. Figure 5g displays capacitive influences from both electrodes at varying scan velocities. These distinct capacitive behaviors of the two electrodes demonstrated an increase as the scanning velocity escalated. Moreover, the capacitive contributions of the $Ni_{11}(HPO_3)_8(OH)_6/Co_3(HPO_4)_2(OH)_2$ electrode are observed to be greater than those of the $Ni_{11}(HPO_3)_8(OH)_6$ electrode at varying scan rates. Consistent with the rate performance trend, the $Ni_{11}(HPO_3)_8(OH)_6/Co_3(HPO_4)_2(OH)_2$ electrode exhibits a dominant surface capacitance of 74.6% at 2 mV s^{-1}, indicative of its typical cell behavior under low scanning rates. The surface capacitance contribution at 100 mV s^{-1}, at 99.8%, is concordant with CV analysis outcomes. EIS tests were conducted to investigate the electrode kinetics further. Figure 5h showcases Nyquist plots for the $Ni_{11}(HPO_3)_8(OH)_6$ and $Ni_{11}(HPO_3)_8(OH)_6/Co_3(HPO_4)_2(OH)_2$ electrodes. The radius of the semicircular arc signifies the impedance to charge migration (R_{ct}), and the x-intercept represents internal resistance (R_s) in the high-frequency region. Furthermore, the $Ni_{11}(HPO_3)_8(OH)_6$ and $Ni_{11}(HPO_3)_8(OH)_6/Co_3(HPO_4)_2(OH)_2$ electrodes demonstrated a markedly low R_{ct}, indicating the process of charge translocation transpires across the electrode-electrolyte juncture. The line slope of the $Ni_{11}(HPO_3)_8(OH)_6/Co_3(HPO_4)_2(OH)_2$ electrode is closer to 90° across the lower frequency spectrum, which suggests that the $Ni_{11}(HPO_3)_8(OH)_6/Co_3(HPO_4)_2(OH)_2$ electrode exhibits greater capacitive properties. Moreover, $Ni_{11}(HPO_3)_8(OH)_6/Co_3(HPO_4)_2(OH)_2$ exhibits a more pronounced linear gradient than that observed in $Ni_{11}(HPO_3)_8(OH)_6$. The electrode's enhanced ion diffusion rate stems from the unique hierarchical porous architecture for $Ni_{11}(HPO_3)_8(OH)_6/Co_3(HPO_4)_2(OH)_2$, coupled with its superior conductivity. The EIS analysis results serve to further corroborate the assertion that the $Ni_{11}(HPO_3)_8(OH)_6/Co_3(HPO_4)_2(OH)_2$ electrode exhibits superior internal resistance and commendable reaction kinetics in comparison to the $Ni_{11}(HPO_3)_8(OH)_6$ electrode.

For evaluating the potential application for $Ni_{11}(HPO_3)_8(OH)_6/Co_3(HPO_4)_2(OH)_2$ in energy storage, the HSC was constructed in 2 mol L^{-1} KOH utilizing PC as anode and this material as a cathode. Figure 6a illustrates the total voltage window of the HSC, derived from analyzing the CV profiles for the PC and $Ni_{11}(HPO_3)_8(OH)_6/Co_3(HPO_4)_2(OH)_2$ electrodes independently at 10 mV s^{-1} in 2 mol L^{-1} KOH electrolytes. The CV curves of the PCs exhibit a rectangular shape and demonstrate excellent electric double layer (EDL) behavior. The potential ranges for the PC and $Ni_{11}(HPO_3)_8(OH)_6/Co_3(HPO_4)_2(OH)_2$ electrodes are confined to -1 to 0 V as well as 0 to 0.6 V. Figure 6b displays rectangular shape for the CV curves for $Ni_{11}(HPO_3)_8(OH)_6/Co_3(HPO_4)_2(OH)_2$//PC HSC within 2~100 mV s^{-1}, with significant redox peak characteristics within the 0~1.5 V. Meanwhile, CV curves exhibited minimal variation across varying scan rates, signifying the device's outstanding rate performance. The capacitance characteristics for the $Ni_{11}(HPO_3)_8(OH)_6/Co_3(HPO_4)_2(OH)_2$//PC HSC underwent additional examination through performing GCD tests between 2~100 A g^{-1}. Figure 6c makes known that the symmetric GCD curve of the $Ni_{11}(HPO_3)_8(OH)_6/Co_3(HPO_4)_2(OH)_2$//PC HSC shows good electrochemical reversibility. Figure 6d reveals that the $Ni_{11}(HPO_3)_8(OH)_6/Co_3(HPO_4)_2(OH)_2$//PC HSC boasts a specific capacitance value of 151.6 F g^{-1} when tested at 2 A g^{-1}, and retains a capacitance of 58.8 F g^{-1} at 100 A g^{-1}. This underscores the device's high specific capacitance, attributable to the optimal chemical composition, distinctive layered porous architecture, and exceptional electronic conductivity for the $Ni_{11}(HPO_3)_8(OH)_6/Co_3(HPO_4)_2(OH)_2$ materials. Figure 6e illustrates the Ragone diagram of the $Ni_{11}(HPO_3)_8(OH)_6/Co_3(HPO_4)_2(OH)_2$//PC HSC. The energy density for $Ni_{11}(HPO_3)_8(OH)_6/Co_3(HPO_4)_2(OH)_2$//PC HSC reaches 47.4 Wh kg^{-1} at 660 Wh kg^{-1}, and maintains 18.4 Wh kg^{-1} even at a super-high 33 kW kg^{-1}. This surpasses the energy density reported for previous cobalt-based phosphide and nickel-based phosphate HSCs. For example, $Co_3(PO_4)_2$//AC (26.66 Wh kg^{-1}/750 W kg^{-1}) [51], $Co_3(PO_4)_2 \cdot 4H_2O$/GF//C-FP (24 Wh kg^{-1}/468 W kg^{-1}) [52], $NH_4CoPO_4 \cdot H_2O$//AC (10.4 Wh kg^{-1}/141.3 W kg^{-1}) [53], NiCoP@NF//AC (27 Wh kg^{-1}/647 W kg^{-1}) [54], Ni-Co-P/PO_x//RGO(36.84 Wh kg^{-1}/727.8 W kg^{-1}) [55], $NiCoO_2$/NiCoP//AC (40.32Wh kg^{-1}/800.18 W kg^{-1}) [56], $Co_3(PO_4)_2 \cdot 8H_2O$//AC (29.29 Wh kg^{-1}/468.75 W kg^{-1}) [57]. The cycling properties for $Ni_{11}(HPO_3)_8(OH)_6/Co_3(HPO_4)_2(OH)_2$//PC HSC were examined through the implementation of cycling tests (Figure 6f). After 10,000 cycles, $Ni_{11}(HPO_3)_8(OH)_6/Co_3(HPO_4)_2(OH)_2$//PC HSC demonstrated remarkable cycling performance, exhibiting capacity retention of up to 92.9% at 3 A g^{-1}. Their feasibility in practical applications is confirmed by these test data.

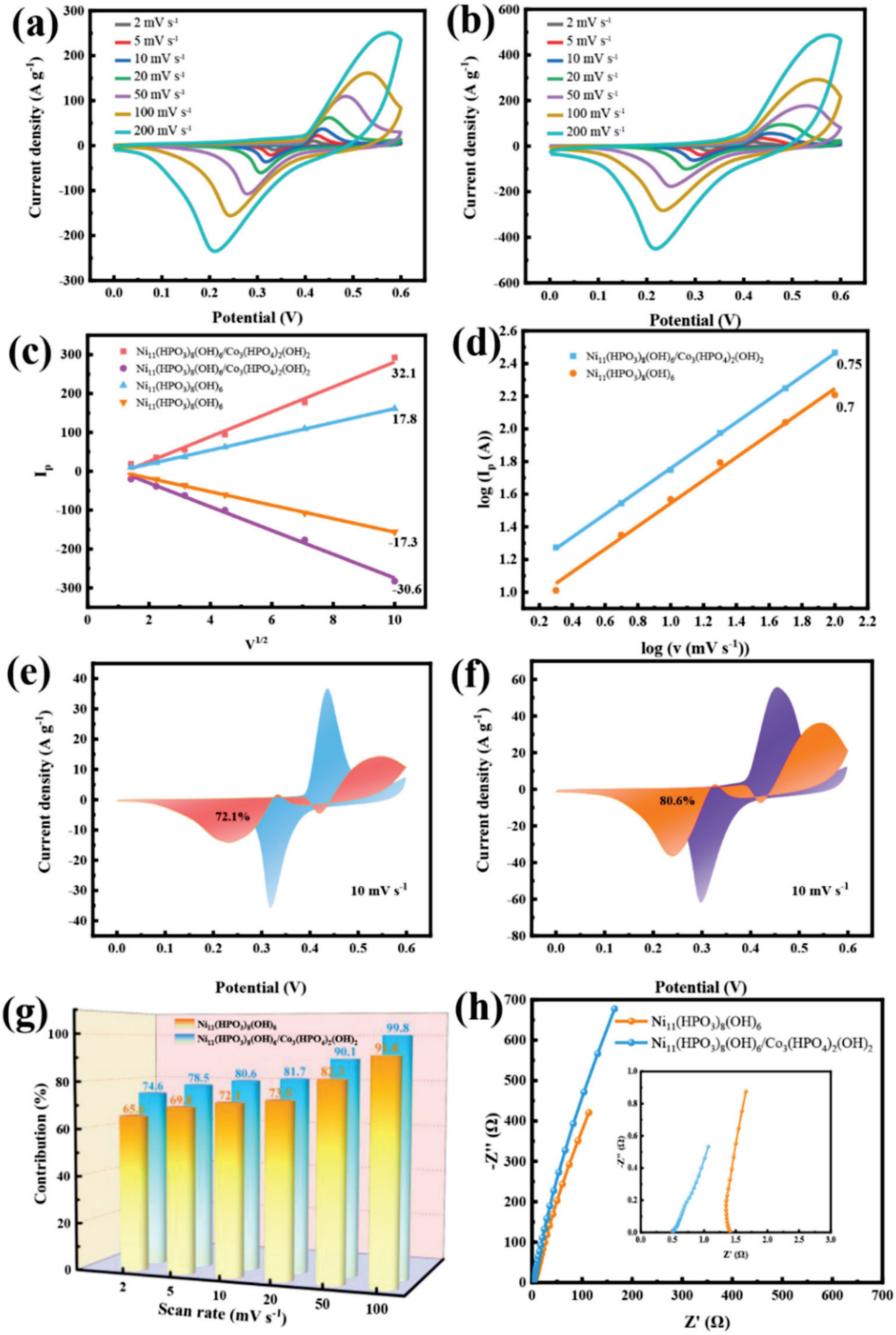

Figure 5. Electrochemical performance of the $Ni_{11}(HPO_3)_8(OH)_6$ and $Ni_{11}(HPO_3)_8(OH)_6/Co_3(HPO_4)_2(OH)_2$ electrodes: (**a**) $Ni_{11}(HPO_3)_8(OH)_6$ CV curves between 2 and 200 mV s^{-1}, (**b**) $Ni_{11}(HPO_3)_8(OH)_6/Co_3(HPO_4)_2(OH)_2$ CV curves between 2 and 200 mV s^{-1}, (**c**) linear relation of I_p-$v^{1/2}$, (**d**) log Ip-log v linear relationship, (**e**,**f**) diffusion and capacitive contributions at 10 mV s^{-1}, (**g**) capacitive contribution comparison from 2 to 100 mV s^{-1}, and (**h**) the EIS plots.

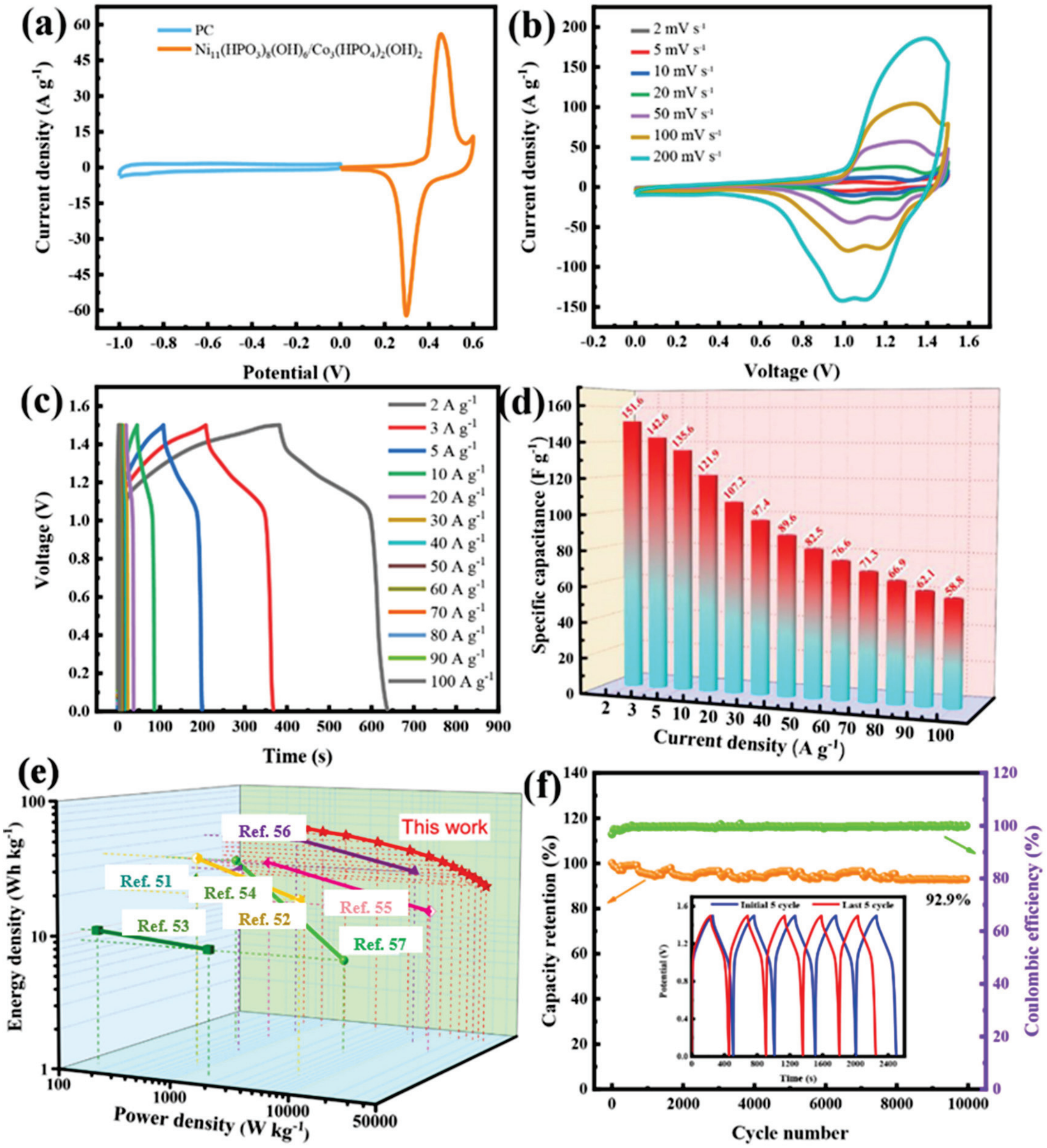

Figure 6. Electrochemical performance of $Ni_{11}(HPO_3)_8(OH)_6/Co_3(HPO_4)_2(OH)_2$//PC HSC: (**a**) CV profiles of PC and $Ni_{11}(HPO_3)_8(OH)_6/Co_3(HPO_4)_2(OH)_2$ electrodes at 10 mV s^{-1}. (**b**) CV profiles, (**c**) GCD profiles, (**d**) rate performance diagram, (**e**) Ragone plot, and (**f**) circulation characteristics and the Coulombic efficiency at 3 A g^{-1} after 10,000 cycles, inset picture shows the pre/post five GCD curves.

4. Conclusions

In summary, the $Ni_{11}(HPO_3)_8(OH)_6/Co_3(HPO_4)_2(OH)_2$ heterostructured material consisting of flakes has been synthesized through one-step hydrothermal process. Benefiting from its intricate multi-scale porosity architecture and the synergistic effect, the prepared $Ni_{11}(HPO_3)_8(OH)_6/Co_3(HPO_4)_2(OH)_2$ composite electrode demonstrates excellent cycling endurance and rate capability in alkaline conditions. Specifically, the $Ni_{11}(HPO_3)_8(OH)_6/Co_3(HPO_4)_2(OH)_2$ composite electrode exhibits superior capacity retention capabilities, with 82.5% retention at 50 A g^{-1} and 71% even at the elevated currently densities of 100 A g^{-1}. Moreover, it sustains an impressive 92.7% capacity retention after enduring 5000 cycles at 10 A g^{-1}. In addition, the $Ni_{11}(HPO_3)_8(OH)_6/Co_3(HPO_4)_2(OH)_2$//PC

HSC device showcases exceptional performance, featuring a heightened energy density of 47.4 Wh kg^{-1} alongside a superlative power density of 36 kW kg^{-1}. Notably, after enduring 10,000 cycles, it retains a good 92.9% capacity at 3 A g^{-1}. Obtained from the above data, the $Ni_{11}(HPO_3)_8(OH)_6/Co_3(HPO_4)_2(OH)_2$ heterostructured materials are likely candidates for electrode materials for high-performance HSC. Additionally, this hydrothermal synthesis method, with its low cost and simple process, provides a feasible idea for constructing phosphate heterostructured materials with excellent properties that may be applied to future storage systems.

Author Contributions: Writing—original draft preparation, K.L.; writing—review and editing, M.J., Y.Z. (Yirong Zhu) and C.L.; project administration, M.J. and Y.Z. (Yirong Zhu); formal analysis T.W. and Y.Z. (Yang Zhang); investigation, R.L. and X.W.; resources, L.L. and S.Z.; data curation, K.L. and Y.Z (Yang Zhang). All authors have read and agreed to the published version of the manuscript.

Funding: This research was funded by the Distinguished Young Scholar Fund Project of Hunan Province Natural Science Foundation (No. 2023JJ10041), the Hunan Provincial Education Office Foundation of China (No. 22A0114), the Natural Science Foundation of Henan Province (232300421228), the Topnotch Talents Program of Henan Agricultural University (30501032), and the National Natural Science Foundation of China (22305070).

Data Availability Statement: The dataset is available on request from the authors.

Conflicts of Interest: The authors declare no conflicts of interest.

References

1. Pomerantseva, E.; Bonaccorso, F.; Feng, X.; Cui, Y.; Gogotsi, Y. Energy storage: The future enabled by nanomaterials. *Science* **2019**, *366*, eaan8285. [CrossRef] [PubMed]
2. Bi, S.; Banda, H.; Chen, M.; Niu, L.; Chen, M.; Wu, T.; Wang, J.; Wang, R.; Feng, J.; Chen, T.; et al. Molecular understanding of charge storage and charging dynamics in supercapacitors with MOF electrodes and ionic liquid electrolytes. *Nat. Mater.* **2020**, *19*, 552–558. [CrossRef] [PubMed]
3. Zhang, Q.-Z.; Zhang, D.; Miao, Z.-C.; Zhang, X.-L.; Chou, S.-L. Research Progress in MnO_2–Carbon Based Supercapacitor Electrode Materials. *Small* **2018**, *14*, 1702883. [CrossRef] [PubMed]
4. Lee, J.-H.; Yang, G.; Kim, C.-H.; Mahajan, R.L.; Lee, S.-Y.; Park, S.-J. Flexible solid-state hybrid supercapacitors for the internet of everything (IoE). *Energy Environ. Sci.* **2022**, *15*, 2233–2258. [CrossRef]
5. Zhao, Z.; Ye, Y.; Zhu, W.; Xiao, L.; Deng, B.; Liu, J. Bismuth oxide nanoflake@carbon film: A free-standing battery-type electrode for aqueous sodium ion hybrid supercapacitors. *Chin. Chem. Lett.* **2018**, *29*, 629–632. [CrossRef]
6. Amiri, A.; Bruno, A.; Polycarpou, A.A. Configuration-dependent stretchable all-solid-state supercapacitors and hybrid supercapacitors. *Carbon Energy* **2023**, *5*, e320. [CrossRef]
7. Sadavar, S.; Wang, K.J.; Kang, T.; Hwang, M.; Saeed, G.; Yu, X.; Park, H.S. Anion storage for hybrid supercapacitor. *Mater. Today Energy* **2023**, *37*, 101388. [CrossRef]
8. Wang, X.; Yan, C.; Yan, J.; Sumboja, A.; Lee, P.S. Orthorhombic niobium oxide nanowires for next generation hybrid supercapacitor device. *Nano Energy* **2015**, *11*, 765–772. [CrossRef]
9. Sun, L.; Liu, Y.; Yan, M.; Yang, Q.; Liu, X.; Shi, W. Lewis acid etched $Ni_xCo_{1-x}Se_2$ derived from ZIF-L on CoO nanowires for hybrid-supercapacitors. *Chem. Eng. J.* **2022**, *431*, 133472. [CrossRef]
10. Roy, A.; Inta, H.R.; Ghosh, S.; Koppisetti, H.V.S.R.M.; Mondal, A.; Verma, B.R.; Bag, S.; Mahalingam, V. Electrochemical surface reconstruction of nickel cobalt pyrophosphate to Ni/Co-hydroxide-(oxy)hydroxide: An efficient and highly durable battery-type supercapacitor electrode material. *J. Mater. Chem. A* **2024**, *12*, 4086–4098. [CrossRef]
11. Salunkhe, R.R.; Kaneti, Y.V.; Yamauchi, Y. Metal–Organic Framework-Derived Nanoporous Metal Oxides toward Supercapacitor Applications: Progress and Prospects. *ACS Nano* **2017**, *11*, 5293–5308. [CrossRef] [PubMed]
12. Yu, X.Y.; Lou, X.W. Mixed Metal Sulfides for Electrochemical Energy Storage and Conversion. *Adv. Funct. Mater.* **2018**, *8*, 1701592. [CrossRef]
13. Zou, K.; Deng, W.; Silvester, D.S.; Zou, G.; Hou, H.; Banks, C.E.; Li, L.; Hu, J.; Ji, X. Carbonyl Chemistry for Advanced Electrochemical Energy Storage Systems. *ACS Nano* **2024**, *18*, 19950–20000. [CrossRef] [PubMed]
14. Zan, G.; Li, S.; Chen, P.; Dong, K.; Wu, Q.; Wu, T. Mesoporous Cubic Nanocages Assembled by Coupled Monolayers With 100% Theoretical Capacity and Robust Cycling. *ACS Cent. Sci.* **2024**, *10*, 1283–1294. [CrossRef]
15. Manikandan, R.; Savariraj, A.D.; Nagaraju, G.; Kale, A.M.; Puigdollers, J.; Park, H.; Kim, H.-S.; Oh, J.-M.; Raj, C.J.; Kim, B.C. Mixed-phase composites derived from cobalt terephthalate as efficient battery-type electrodes for high-performance supercapattery. *J. Mater. Sci. Technol.* **2023**, *157*, 220–233. [CrossRef]

16. Manikandan, R.; Raj, C.J.; Goli, N.; Oh, J.-M.; Kim, B.C.; Periyasamy, S.; Lee, J. Interconnected Vanadyl Pyrophosphate Nanonetworks as a Flexible Electrode for High-Voltage and Long-Life Li-Ion Supercapacitors. *Appl. Mater. Interfaces* **2023**, *15*, 25452–25461. [CrossRef]
17. Zhao, H.; Yuan, Z.-Y. Design Strategies of Transition-Metal Phosphate and Phosphonate Electrocatalysts for Energy-Related Reactions. *Chem. Eng. Sci* **2021**, *14*, 130–149. [CrossRef]
18. Cheng, Q.; Zhao, X.; Yang, G.; Mao, L.; Liao, F.; Chen, L.; He, P.; Pan, D.; Chen, S. Recent advances of metal phosphates-based electrodes for high-performance metal ion batteries. *Energy Storage Mater.* **2021**, *41*, 842–882. [CrossRef]
19. Wang, D.; Wang, Y.; Fu, Z.; Xu, Y.; Yang, L.-X.; Wang, F.; Guo, X.; Sun, W.; Yang, Z.-L. Cobalt–Nickel Phosphate Composites for the All-Phosphate Asymmetric Supercapacitor and Oxygen Evolution Reaction. *Appl. Mater. Interfaces* **2021**, *13*, 34507–34517. [CrossRef]
20. Xie, L.; Zong, Q.; Zhang, Q.; Sun, J.; Zhou, Z.; He, B.; Zhu, Z.; E, S.; Yao, Y. Hierarchical NiCoP nanosheet arrays with enhanced electrochemical properties for high-performance wearable hybrid capacitors. *J. Alloys Compd.* **2019**, *781*, 783–789. [CrossRef]
21. Fan, J.; Wu, K.; Chen, A.; Wang, M.; Xie, X.; Fan, J. Fingerprint-like NiCoP electrode material with rapid charging/discharging performance under large current density. *J. Alloys Compd.* **2022**, *902*, 163866. [CrossRef]
22. Liu, M.; Li, J.; Han, W.; Kang, L. Simple synthesis of novel phosphate electrode materials with unique microstructure and enhanced supercapacitive properties. *J. Energy Chem.* **2016**, *25*, 601–608. [CrossRef]
23. Zhang, Y.; Zheng, M.; Qu, M.; Sun, M.; Pang, H. Core–shell $Co_{11}(HPO_3)_8(OH)_6$–Co_3O_4 hybrids for high-performance flexible all-solid-state asymmetric supercapacitors. *J. Alloys Compd.* **2015**, *651*, 214–221. [CrossRef]
24. Li, X.; Elshahawy, A.M.; Guan, C.; Wang, J. Metal Phosphides and Phosphates-based Electrodes for Electrochemical Supercapacitors. *Small* **2017**, *13*, 1701530. [CrossRef] [PubMed]
25. Wang, X.; Zhai, X.; Lv, P.; Jiao, Y.; Wang, S.; Chi, J. Amorphous nickel phosphate as a high performance electrode material for supercapacitor. *Synth. Met.* **2023**, *292*, 117217. [CrossRef]
26. Zhang, Y.-N.; Su, C.-Y.; Chen, J.-L.; Huang, W.-H.; Lou, R. Recent progress of transition metal-based biomass-derived carbon composites for supercapacitor. *Rare Met.* **2023**, *42*, 769–796. [CrossRef]
27. Zhang, G.C.; Feng, M.; Li, Q.; Wang, Z.; Fang, Z.; Niu, Z.; Qu, N.; Fan, X.; Li, S.; Gu, J.; et al. High Energy Density in Combination with High Cycling Stability in Hybrid Supercapacitors. *Appl. Mater. Interfaces* **2022**, *14*, 2674–2682. [CrossRef]
28. Mirghni, A.A.; Madito, M.J.; Oyedotun, K.O.; Masikhwa, T.M.; Ndiaye, N.M.; Ray, S.J.; Manyala, N. A high energy density asymmetric supercapacitor utilizing a nickel phosphate/graphene foam composite as the cathode and carbonized iron cations adsorbed onto polyaniline as the anode. *RSC Adv.* **2018**, *8*, 11608–11621. [CrossRef]
29. Chen, G.; Yan, L.; Luo, H.; Guo, S. Nanoscale Engineering of Heterostructured Anode Materials for Boosting Lithium-Ion Storage. *Adv. Mater.* **2016**, *28*, 7580–7602. [CrossRef]
30. Lin, Y.; Sun, K.; Liu, S.; Chen, X.; Cheng, Y.; Cheong, W.-C.; Chen, Z.; Zheng, L.; Zhang, J.; Li, X.; et al. Construction of CoP/NiCoP Nanotadpoles Heterojunction Interface for Wide pH Hydrogen Evolution Electrocatalysis and Supercapacitor. *Adv. Funct. Mater.* **2019**, *9*, 1901213. [CrossRef]
31. Liu, X.; Zhu, Y.; Lu, Z.; Xiao, J.; Zou, G.; Hou, H.; Ji, X. Heterostructured flower-like NiO/Co_3O_4 microspheres modified by bifunctional carbon quantum dots as a battery-type cathode for high energy and power density hybrid supercapacitors. *Carbon Neutralization* **2023**, *2*, 721–737. [CrossRef]
32. Li, Y.; Zhang, J.; Chen, Q.; Xia, X.; Chen, M. Emerging of Heterostructure Materials in Energy Storage: A Review. *Adv. Mater.* **2021**, *33*, 2100855. [CrossRef] [PubMed]
33. Yun, X.; Lu, T.; Zhou, R.; Lu, Z.; Li, J.; Zhu, Y. Heterostructured $NiSe_2$/$CoSe_2$ hollow microspheres as battery-type cathode for hybrid supercapacitors: Electrochemical kinetics and energy storage mechanism. *Chem. Eng. J.* **2021**, *426*, 131328. [CrossRef]
34. Li, M.; Li, M.; Zhao, M.; Wu, B.; Mourdikoudis, S.; Wei, S.; Oliveira, F.M.; He, J.; Děkanovský, L.; Luxa, J.; et al. Rational design of crystalline/amorphous nickel manganese phosphate octahydrate heterostructure for high-performance aqueous and all-solid-state asymmetric supercapacitors. *Chem. Eng. J.* **2024**, *482*, 148895. [CrossRef]
35. Jiang, T.; Zhang, Y.; Du, C.; Xiao, T.; Wan, L. Two-step electrodeposition synthesis of iron cobalt selenide and nickel cobalt phosphate heterostructure for hybrid supercapacitors. *J. Colloid Interface Sci.* **2023**, *629*, 1049–1060. [CrossRef]
36. Davidson, A.; Tempere, J.F.; Che, M.; Roulet, H.; Dufour, G. Spectroscopic Studies of Nickel(II) and Nickel(III) Species Generated upon Thermal Treatments of Nickel/Ceria-Supported Materials. *J. Phys. Chem.* **1996**, *100*, 4919–4929. [CrossRef]
37. Casella, I.G.; Gatta, M. Electrochemical and XPS Characterization of Composite Modified Electrodes Obtained by Nickel Deposition on Noble Metals. *Anal. Chem.* **2000**, *72*, 2969–2975. [CrossRef]
38. Huang, J.; Xiong, Y.; Peng, Z.; Chen, L.; Wang, L.; Xu, Y.; Tan, L.; Yuan, K.; Chen, Y. A General Electrodeposition Strategy for Fabricating Ultrathin Nickel Cobalt Phosphate Nanosheets with Ultrahigh Capacity and Rate Performance. *ACS Nano* **2020**, *14*, 14201–14211. [CrossRef]
39. Dan, H.; Tao, K.; Zhou, Q.; Gong, Y.; Lin, J. Ni-Doped Cobalt Phosphite, $Co_{11}(HPO_3)_8(OH)_6$, with Different Morphologies Grown on Ni Foam Hydro(solvo)thermally for High-Performance Supercapacitor. *Appl. Mater. Interfaces* **2018**, *10*, 31340–31354. [CrossRef]
40. Li, X.; Wu, H.; Elshahawy, A.M.; Wang, L.; Pennycook, S.J.; Guan, C.; Wang, J. Cactus-Like NiCoP/NiCo-OH 3D Architecture with Tunable Composition for High-Performance Electrochemical Capacitors. *Adv. Funct. Mater.* **2018**, *28*, 1800036. [CrossRef]

41. Ding, R.; Li, X.; Shi, W.; Xu, Q.; Liu, E. One-pot solvothermal synthesis of ternary Ni-Co-P micro/nano-structured materials for high performance aqueous asymmetric supercapacitors. *Chem. Eng. J.* **2017**, *320*, 376–388. [CrossRef]
42. Hu, Y.-M.; Liu, M.-C.; Hu, Y.-X.; Yang, Q.-Q.; Kong, L.-B.; Kang, L. One-pot hydrothermal synthesis of porous nickel cobalt phosphides with high conductivity for advanced energy conversion and storage. *Electrochim. Acta* **2016**, *215*, 114–125. [CrossRef]
43. Li, B.; Gu, P.; Feng, Y.; Zhang, G.; Huang, K.; Xue, H.; Pang, H. Ultrathin Nickel–Cobalt Phosphate 2D Nanosheets for Electrochemical Energy Storage under Aqueous/Solid-State Electrolyte. *Adv. Funct. Mater.* **2017**, *27*, 1605784. [CrossRef]
44. Liang, B.; Chen, Y.; He, J.; Chen, C.; Liu, W.; He, Y.; Liu, X.; Zhang, N.; Roy, V.A.L. Controllable Fabrication and Tuned Electrochemical Performance of Potassium Co–Ni Phosphate Microplates as Electrodes in Supercapacitors. *Appl. Mater. Interfaces* **2018**, *10*, 3506–3514. [CrossRef]
45. Zhang, J.; Yang, Y.; Zhang, Z.; Xu, X.; Wang, X. Rapid synthesis of mesoporous $Ni_xCo_{3-x}(PO_4)_2$ hollow shells showing enhanced electrocatalytic and supercapacitor performance. *J. Mater. Chem. A* **2014**, *2*, 20182–20188. [CrossRef]
46. Chen, C.; Zhang, N.; He, Y.; Liang, B.; Ma, R.; Liu, X. Controllable Fabrication of Amorphous Co—Ni Pyrophosphates for Tuning Electrochemical Performance in Supercapacitors. *Appl. Mater. Interfaces* **2016**, *8*, 23114–23121. [CrossRef]
47. Li, B.; Shi, Y.; Huang, K.; Zhao, M.; Qiu, J.; Xue, H.; Pang, H. Cobalt-Doped Nickel Phosphite for High Performance of Electrochemical Energy Storage. *Small* **2018**, *14*, 1703811. [CrossRef]
48. Zhao, Y.; Chen, Z.; Xiong, D.-B.; Qiao, Y.; Tang, Y.; Gao, F. Hybridized Phosphate with Ultrathin Nanoslices and Single Crystal Microplatelets for High Performance Supercapacitors. *Sci. Rep.* **2016**, *6*, 17613. [CrossRef]
49. Tang, Y.; Liu, Z.; Guo, W.; Chen, T.; Qiao, Y.; Mu, S.; Zhao, Y.; Gao, F. Honeycomb-like mesoporous cobalt nickel phosphate nanospheres as novel materials for high performance supercapacitor. *Electrochim. Acta* **2016**, *190*, 118–125. [CrossRef]
50. Elshahawy, A.M.; Guan, C.; Li, X.; Zhang, H.; Hu, Y.; Wu, H.; Pennycook, S.J.; Wang, J. Sulfur-doped cobalt phosphide nanotube arrays for highly stable hybrid supercapacitor. *Nano Energy* **2017**, *39*, 162–171. [CrossRef]
51. Mao, H.; Zhang, F.; Liu, X.; Qiu, J.; Li, B.; Jin, Z. Synthesis of cobalt phosphate nanoflakes for high-performance flexible symmetric supercapacitors. *J. Mater. Sci. Mater. Electron.* **2018**, *29*, 16721–16729. [CrossRef]
52. Pang, H.; Wang, S.; Shao, W.; Zhao, S.; Yan, B.; Li, X.; Li, S.; Chen, J.; Du, W. Few-layered $CoHPO_4{\cdot}3H_2O$ ultrathin nanosheets for high performance of electrode materials for supercapacitors. *Nanoscale* **2013**, *5*, 5752–5757. [CrossRef] [PubMed]
53. Pang, H.; Yan, Z.; Wang, W.; Chen, J.; Zhang, J.; Zheng, H. Facile fabrication of $NH_4CoPO_4{\cdot}H_2O$ nano/microstructures and their primarily application as electrochemical supercapacitor. *Nanoscale* **2012**, *4*, 5946–5953. [CrossRef] [PubMed]
54. Lan, Y.; Zhao, H.; Zong, Y.; Li, X.; Sun, Y.; Feng, J.; Wang, Y.; Zheng, X.; Du, Y. Phosphorization boosts the capacitance of mixed metal nanosheet arrays for high performance supercapacitor electrodes. *Nanoscale* **2018**, *10*, 11775–11781. [CrossRef] [PubMed]
55. Chen, H.C.; Jiang, S.; Xu, B.; Huang, C.; Hu, Y.; Qin, Y.; He, M.; Cao, H. Sea-urchin-like nickel–cobalt phosphide/phosphate composites as advanced battery materials for hybrid supercapacitors. *J. Mater. Chem. A* **2019**, *7*, 6241–6249. [CrossRef]
56. Ning, W.-W.; Chen, L.-B.; Wei, W.-F.; Chen, Y.-J.; Zhang, X.-Y. $NiCoO_2$/NiCoP@Ni nanowire arrays: Tunable composition and unique structure design for high-performance winding asymmetric hybrid supercapacitors. *Rare Met.* **2020**, *39*, 1034–1044. [CrossRef]
57. Li, H.; Yu, H.; Zhai, J.; Sun, L.; Yang, H.; Xie, S. Self-assembled 3D cobalt phosphate octahydrate architecture for supercapacitor electrodes. *Mater. Lett.* **2015**, *152*, 25–28. [CrossRef]

batteries

MDPI

Article

Honeycomb-like N-Doped Carbon Matrix-Encapsulated $Co_{1-x}S/Co(PO_3)_2$ Heterostructures for Advanced Lithium-Ion Capacitors

Yutao Liu [1], Xiaopeng Xie [2], Zhaojia Wu [2], Tao Wen [3], Fang Zhao [4], Hao He [3], Junfei Duan [3] and Wen Wang [5,*]

[1] International Institute of Engineering, Changsha University of Science and Technology, Changsha 410114, China; 19520009053@163.com
[2] Hunan Datang Xianyi Technology Co., Ltd., Changsha 410114, China; xnhqin@126.com (X.X.); win32logon@163.com (Z.W.)
[3] Materials Science and Engineering, Changsha University of Science and Technology, Changsha 410114, China; 19108471202@163.com (T.W.); hehao0520@gmail.com (H.H.); junfei_duan@csust.edu.cn (J.D.)
[4] Guangdong Power Grid Co., Ltd., Guangzhou Power Supply Bureau, Guangzhou 510660, China; 15603072389@163.com
[5] State Key Laboratory Disaster Prevention & Reduction for Power Grid, Changsha University of Science and Technology, Changsha 410114, China
* Correspondence: wew@csust.edu.cn

Abstract: Lithium-ion capacitors (LICs) are emerging as promising hybrid energy storage devices that combine the high energy densities of lithium-ion batteries (LIBs) with high power densities of supercapacitors (SCs). Nevertheless, the development of LICs is hindered by the kinetic imbalances between battery-type anodes and capacitor-type cathodes. To address this issue, honeycomb-like N-doped carbon matrices encapsulating $Co_{1-x}S/Co(PO_3)_2$ heterostructures were prepared using a simple chemical blowing-vulcanization process followed by phosphorylation treatment ($Co_{1-x}S/Co(PO_3)_2$@NC). The $Co_{1-x}S/Co(PO_3)_2$@NC features a unique heterostructure engineered within carbon honeycomb structures, which efficiently promotes charge transfer at the interfaces, alleviates the volume expansion of Co-based materials, and accelerates reaction kinetics. The optimal $Co_{1-x}S/Co(PO_3)_2$@NC composite demonstrates a stable reversible capacity of 371.8 mAh g^{-1} after 800 cycles at 1 A g^{-1}, and exhibits an excellent rate performance of 242.9 mAh g^{-1} even at 8 A g^{-1}, alongside enhanced pseudocapacitive behavior. The assembled $Co_{1-x}S/Co(PO_3)_2$@NC//AC LIC delivers a high energy density of 90.47 Wh kg^{-1} (at 26.28 W kg^{-1}), a high power density of 504.94 W kg^{-1} (at 38.31 Wh kg^{-1}), and a remarkable cyclic stablitiy of 86.3% retention after 5000 cycles. This research is expected to provide valuable insights into the design of conversion-type electrode materials for future energy storage applications.

Keywords: metal sulfides; anode material; heterostructures; honeycomb carbons; lithium-ion capacitors

1. Introduction

Lithium-ion capacitors (LICs) are considered promising candidates in the field of electrochemical energy storage due to their hybrid energy storage capabilities, which combine the high energy characteristics of lithium-ion batteries (LIBs) with the high power densities of supercapacitors (SCs). However, the practical implementation of LICs remains challenging due to the distinct energy storage mechanisms: the high-energy anodes operate through a slower, repeated Faraday reaction of lithium ions, while the cathodes undergo rapid anion absorption and desorption [1–3].

To address this challenge, researchers have devoted significant efforts to discovering new battery-type anode materials that offer both rapid rate performance and high capacities. Among these materials, cobalt sulfides, which are typical transition metal sulfides, show promise as conversion-type anodes due to their potential application on account of their high theoretical specific capacities (590 mAh g^{-1}), weaker metal–sulfur bonds, and Co/Li_2S interfaces offering high electron transfer mobility [4,5]. However, cobalt sulfides experience significant volume expansion and contraction during repeated lithiation/delithiation cycles, leading to particles aggregation and the detrimental pulverization of electrode structures. This results in a rapid decline in rate performance, creating a mismatch with the capacitor-type cathodes in LICs. Numerous approaches have been proposed to improve reaction kinetics and structural stability, including downsizing particle size [6,7], constructing hierarchical porous structures [8,9], integrating with heteroatom-doped conductive carbonaceous materials [10–12], and fabricating heterogeneous architectures [13–15]. These approaches are expected to alleviate internal stress, increase contact with the electrolyte and shorten electronic and ionic transport pathways, enhance conductivity and maintain the integrity of the electrode materials, and regulate the electronic structure, ultimately aiming to enhance electrochemical performance, including increasing capacity, rate, and cycling stability. It is noteworthy that heterostructures composed of coupling components with large energy bandgap differences can induce a strong intrinsic electric field at the heterogeneous interfaces, thereby promoting reaction kinetics. Moreover, the as-formed heterointerfaces, characterized by abundant phase boundaries, have been shown to significantly influence rate capability and reversible capacity compared to individual components [16–18]. Recently, Dong and co-workers demonstrated that the CoS_2/Co_4S_3@NC heterogeneous composites exhibit high pseudocapacitive behavior and accelerate the diffusion rate of ions and electrons, thus improving the overall performance of the electrodes [19]. Wan and colleagues prepared a hierarchical binary metal sulfide (CoSn)S/C heterostructure, where the micro/nanostructures of (CoSn)S/C shorten the ion diffusion distance, facilitating the rapid transfer of Na^+ and enhancing the mechanical strength of the electrode [20]. Although cobalt-based sulfides play a significant role in improving the electrochemical properties of LICs, unlocking the potential of heterogeneous materials still requires a great deal of work to be explored.

Herein, honeycomb-like N-doped carbon matrices encapsulating $Co_{1-x}S/Co(PO_3)_2$ heterostructures are prepared using a simple chemical blowing-vulcanization process followed by phosphorylation treatment. The selection of $Co_{1-x}S$ and $Co(PO_3)_2$ components is based on their bandgaps, which are 0 eV for $Co_{1-x}S$ and approximately 2.6 eV for $Co(PO_3)_2$. The heterointerfaces between $Co_{1-x}S$ and $Co(PO_3)_2$ components induce an internal electric field, increasing the number of electrochemical active sites, improving electrochemical kinetics, and stabilizing the structure during the repeated charge/discharge. Additionally, the integrated honeycomb-structured N-doped carbon matrices provide physical confinement to reduce nanograins aggregation, accommodate volume expansion during repeated long cycling, and ensure the integrity of the electrode materials, resulting in a high reversible capacity. As expected, the optimal $Co_{1-x}S/Co(PO_3)_2$@NC composite demonstrates a stable reversible capacity of 371.8 mAh g^{-1} after 800 cycles at 1 A g^{-1}, and an excellent rate performance of 242.9 mAh g^{-1} even at 8 A g^{-1}, accompanied with enhanced pseudocapacitive behavior. Furthermore, the assembled $Co_{1-x}S/Co(PO_3)_2$@NC//AC LIC delivers a high energy density of 90.47 Wh kg^{-1} (at 26.28 W kg^{-1}), a high power density of 504.94 W kg^{-1} (at 38.31 Wh kg^{-1}), and a high cyclic stability of 86.3% retention after 5000 cycles.

2. Results and Discussion

The synthetic strategy for the honeycomb-like N-doped carbon matrix decorated with $Co_{1-x}S/Co(PO_3)_2$ heterostructures is schematically illustrated in Figure 1a. Initially, polyvinylpyrrolidone (PVP), serving as the carbon source, weakly coordinates with Co^{2+} to form a sol–gel coordination complex precursor [21,22]. The precursor provides physical confinement to prevent the agglomeration of $Co_{1-x}S$ nanograins during the calcination process. Subsequently, the precursor and mixed sulfur powder undergo thermal blowing-vulcanization treatment. Due to the high viscosity of molten PVP, the pyrolysis gasses (NO_2, NO, etc.) released from nitrate ions generate numerous bubbles as the temperature rises. These bubbles rapidly rupture, promoting the growth of interconnected thin carbon walls, resulting in the formation of N-doped carbon matrices decorated with cobalt sulfides that resemble a 3D honeycomb-like structure. Afterwards, $Co_{1-x}S/Co(PO_3)_2$@NC is obtained through a facile phosphorylation process of the $Co_{1-x}S$/@NC composite, yielding conformal $Co_{1-x}S/Co(PO_3)_2$ heterostructures. FESEM results from Figure 1b–d show that the as-prepared $Co(PO_3)_2$@NC, $Co_{1-x}S$@NC, and $Co_{1-x}S/Co(PO_3)_2$@NC composites exhibit a typical 3D interconnected honeycomb-like framework comprising numerous thin carbon walls with smooth surfaces. This indicates sulfides/phosphides are uniformly encapsulated within the carbon matrices. This structure facilitates electrolyte penetration and effectively mitigates the volume change in active species during repeated cycling, thereby maintaining structural stability. TEM was employed to further examine the morphology and chemical properties. As shown in Figures 1e–g and S1–S3, numerous small nanoparticles are found within the carbon matrices of all the $Co_{1-x}S/Co(PO_3)_2$@NC, $Co_{1-x}S$@NC, and $Co(PO_3)_2$@NC composites. Notably, the $Co_{1-x}S/Co(PO_3)_2$@NC contains nanoparticles with an average size of less than 5 nm, demonstrating shortened electronic and ionic transport paths and effectively relieving internal strain during the electrochemical process. The lattice spacings of 0.268 and 0.254 nm in the higher magnification image (Figure 1e,f) correspond to the (130) plane of $Co(PO_3)_2$ and the (101) plane of $Co_{1-x}S$, respectively. Similarly, the lattice spacings of 0.194 and 0.187 nm in Figure 1g correspond to the (102) plane of $Co_{1-x}S$ and the (−242) plane of $Co(PO_3)_2$, respectively, confirming the successful fabrication of heterostructures. The energy dispersive X-ray spectrometer (EDS) spectrum in Figure 1h confirmed the uniform dispersion of Co, S, P, N, and O in the carbon matrices.

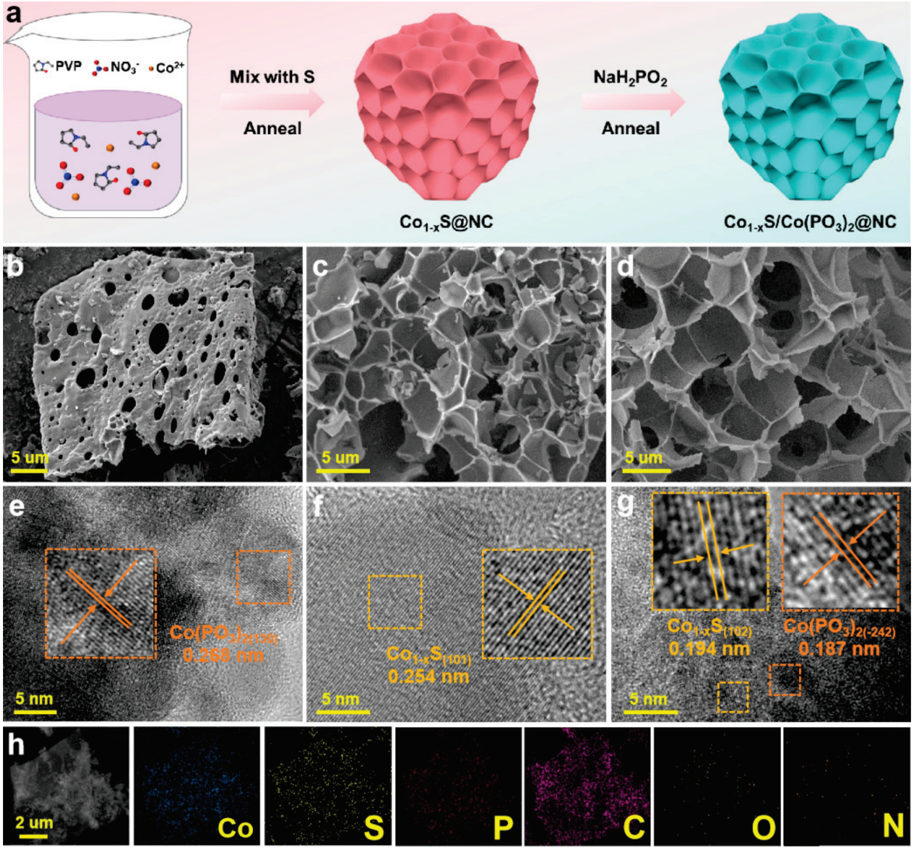

Figure 1. (**a**) Schematic illustration of synthetic process. SEM images of (**b**) $Co(PO_3)_2$@NC, (**c**) $Co_{1-x}S$@NC, and (**d**) $Co_{1-x}S/Co(PO_3)_2$@NC. HRTEM images of (**e**) $Co(PO_3)_2$@NC, (**f**) $Co_{1-x}S$@NC, and (**g**) $Co_{1-x}S/Co(PO_3)_2$@NC. (**h**) Elemental mapping of $Co_{1-x}S/Co(PO_3)_2$@NC.

The crystal structure of the synthesized materials was characterized using X-ray diffraction (XRD) patterns, as depicted in Figure 2a. The diffraction peaks of the $Co_{1-x}S/Co(PO_3)_2$@NC composites were consistently indexed to the monoclinic $Co(PO_3)_2$ phase (JCPDS No. 27-

1120) and the hexagonal $Co_{1-x}S$ phase (JCPDS No. 42-0826). For the $Co_{1-x}S$@NC and $Co(PO_3)_2$@NC composites, only single phases of $Co_{1-x}S$ and $Co(PO_3)_2$ were observed, without any impurity peaks. Moreover, the Raman spectra for three samples (Figure 2b) exhibit two prominent peaks at ~1351 and ~1371 cm^{-1}, which represent the graphitic carbon (G-band) and disordered carbon (D-band), respectively. This confirms the presence of N-doped carbon matrices. The relatively larger intensity ratio of I_D/I_G for $Co_{1-x}S/Co(PO_3)_2$@NC (0.989) implies a higher degree of structural defects compared to $Co_{1-x}S$@NC (0.973) and $Co(PO_3)_2$@NC (0.969), which is conducive for fast electron transfer [23]. Thermogravimetric analysis (TGA) was conducted to determine the contents of $Co_{1-x}S$, $Co(PO_3)_2$, and carbon in $Co_{1-x}S/Co(PO_3)_2$@NC (Figure 2c). As reported in our previous work, $Co_{1-x}S$ undergoes a multi-stage reaction involving complex oxidation processes in the air followed by carbon combustion [24,25]. The evaporation of adsorbed water accounts for the slight mass loss in the range of 50–200 °C. The oxidation of $Co_{1-x}S$ to $CoSO_4$ and Co_3O_4 is the primary cause of a notable weight loss, as well as the combustion of NC, as the temperature increases from 200 to 650 °C. Notably, the differences between the curves of $Co_{1-x}S/Co(PO_3)_2$@NC and $Co_{1-x}S$@NC are primarily attributed to the greater weight loss from NC combustions compared to the increase from oxidation of $Co_{1-x}S$. The TGA curves indicate the percentages of $Co_{1-x}S$, $Co(PO_3)_2$, and NC in $Co_{1-x}S/Co(PO_3)_2$@NC, which were 40.9 wt%, 29.4 wt%, and 29.7 wt%, respectively.

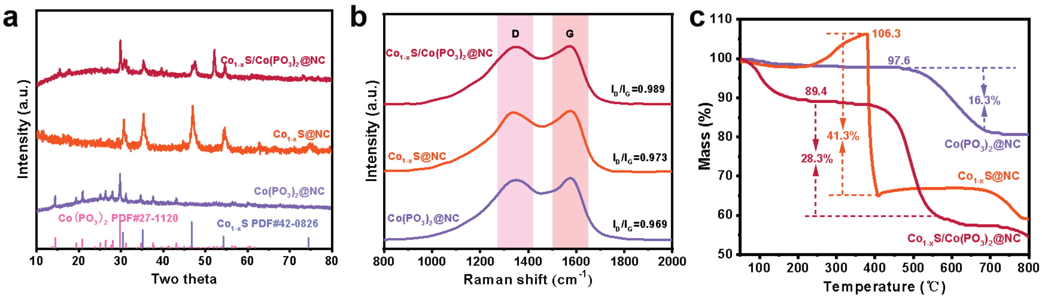

Figure 2. (**a**) XRD patterns, (**b**) Raman spectra, and (**c**) TGA curvesof $Co(PO_3)_2$@NC, $Co_{1-x}S$@NC, and $Co_{1-x}S/Co(PO_3)_2$@NC, respectively.

Furthermore, the surface chemical compositions of the three samples were analyzed using X-ray photoelectron spectroscopy (XPS) measurements. As shown in Figure 3a, elements such as cobalt, sulfur, phosphorus, oxygen, carbon, and nitrogen were clearly detected. The Co 2p high-resolution spectra, presented in Figure 3b, reveal the characteristic peaks at ~798.4 eV and ~782.6 eV, corresponding to Co $2p_{1/2}$ and Co $2p_{3/2}$ of Co^{2+}, along with their satellite peaks [26,27]. An additional set of peaks in the $Co_{1-x}S$@NC composites, located at ~793.4 eV and 778.4 eV, is associated with Co^0 and suggests that the vulcanization process of the PVP-Co^{2+} precursors is not fully completed. Figure 3c shows the S 2p spectra, where characteristic peaks at approximately 165.2 eV and 164.0 eV are associated with S $2p_{1/2}$ and S $2p_{3/2}$ of the C-S-C bond, while peaks at ~162.9 eV and ~161.8 eV correspond to S $2p_{1/2}$ and S $2p_{3/2}$ of S^{2-} [28]. Additionally, a peak at ~168.5 eV corresponds to SO_x likely due to inevitable surface oxidation. The strong chemical bonds between active species and carbon substrate are indicated by the presence of C-S-C, ensuring robust structures and excellent cycling stability during the intercalation and de-intercalation of Li^+ [29]. The characteristic peak at ~134.4 eV (Figure 3d) corresponds to P-O bonds. The C 1s peaks can be deconvoluted into three distinct peaks at ~284.8, ~285.9, and ~289.0 eV (Figure 3e), corresponding to C-C, C-N/C-O/C-S, and C=O bonds, respectively. The successful nitrogen substitution in the carbon matrix is confirmed by the presence of the C-N bond, and this is supported by the N 1s high-resolution spectra (Figure 3f). The nitrogen dopant can not only enhance interfacial wettability, create more defects and active sites, and accelerate reaction kinetics [30].

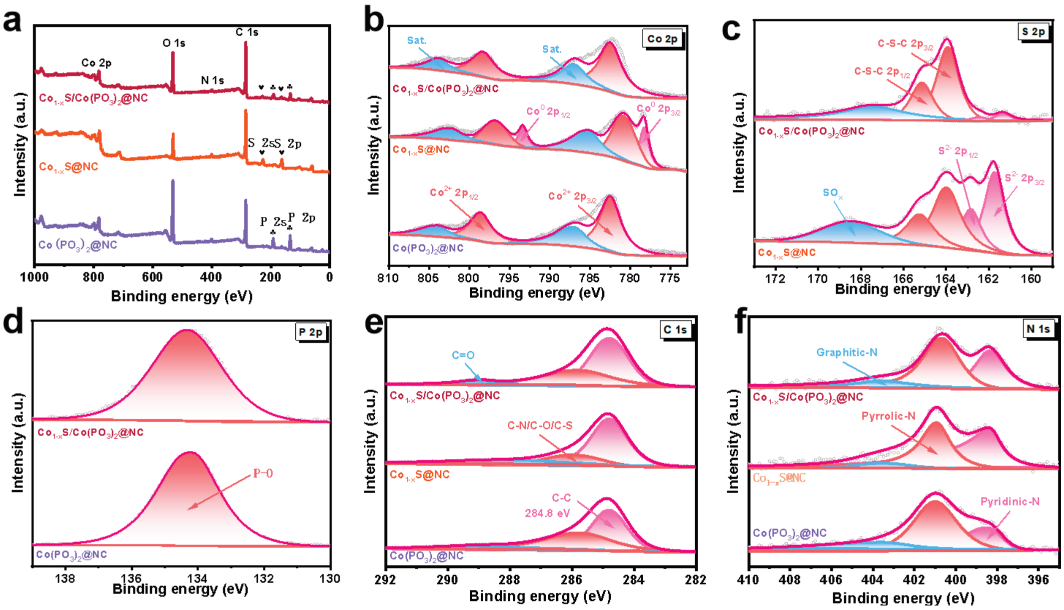

Figure 3. (**a**) The wide scan XPS of $Co(PO_3)_2$@NC, $Co_{1-x}S$@NC, and $Co_{1-x}S/Co(PO_3)_2$@NC, (**b**) Co 2p of $Co(PO_3)_2$@NC, $Co_{1-x}S$@NC, and $Co_{1-x}S/Co(PO_3)_2$@NC, (**c**) S 2p and (**d**) P 2p of $Co_{1-x}S$@NC and $Co_{1-x}S/Co(PO_3)_2$@NC, (**e**) C 1s and (**f**) N 1s of $Co_{1-x}S$@NC and $Co_{1-x}S/Co(PO_3)_2$@NC.

The Li^+ storage behavior of the $Co_{1-x}S/Co(PO_3)_2$@NC electrodes was evaluated using lithium metal as a counter electrode in an assembled 2032 coin-type half-cell. First, as shown in Figure 4a, cyclic voltammetry (CV) curves were measured at a sacn rate of 0.2 mV s^{-1}, revealing the electrochemical process over the first five cycles. In the initial cathodic scan, the sample showed significant broad peaks ~0.52 V and ~0.94 V, indicative of irreversible transformations and the formation of a solid electrolyte interface (SEI). In the subsequent scans, a set of new characteristic cathodic peaks appeared at 1.98 and 1.24 V related to the stepwise conversion reaction of $Co_{1-x}S$ into Co/Li_2S, $Co(PO_3)_2$ to CoP_2/Li_2O intermediates, and Co/Li_3P products; additionally, notable oxidation peaks were observed at 1.32, 2.05, and 2.56 V, corresponding to the oxidation reactions of Co/Li_2S to $Co_{1-x}S$ and Co/Li_3P to CoP_2 [31], which persisted in the following scans. The galvanostatic charge/discharge (GCD) profiles of the $Co_{1-x}S/Co(PO_3)_2$@NC electrode displayed initial charge/discharge capacities of 1194.0/719.1 mAh g^{-1} with an initial Coulombic efficiency of 60.2%; in subsequent cycles, the capacities remained stable over 200 cycles with Coulombic efficiency, approaching to 99.6% (Figure 4b). The cycling performance reveals that the $Co_{1-x}S/Co(PO_3)_2$@NC electrode maintains the highest reversible capacity of 643.7 mAh g^{-1} after 200 cycles at 0.2 A g^{-1}, significantly exceeding those of $Co_{1-x}S$@NC (336.5 mAh g^{-1}), $Co(PO_3)_2$@NC (274.0 mAh g^{-1}) (Figure 4c), $Co_{1-x}S/Co(PO_3)_2$@NC-1v3 (478.4 mAh g^{-1}), and $Co_{1-x}S/Co(PO_3)_2$@NC-1v8 (426.8 mAh g^{-1}) (Figure S4). The rate capability of all samples was further examined across different current densities ranging from 0.2 to 8.0 A g^{-1}. The $Co_{1-x}S/Co(PO_3)_2$@NC exhibited the best rate performance regardless of current density, with a high capacity of 642.7 mAh g^{-1} at 0.2 A g^{-1} and 242.9 mAh g^{-1} at 8.0 A g^{-1} (Figure 4d,e); the rate performance of $Co_{1-x}S/Co(PO_3)_2$@NC is superior to some previously reported cobalt sulfide-based anode materials (Figure 4f). The long-term cycling performance of $Co_{1-x}S/Co(PO_3)_2$@NC, $Co_{1-x}S$@NC, and $Co(PO_3)_2$@NC electrodes was further compared at a current density of 1 A g^{-1}. As shown in Figures 4g and S4, the $Co_{1-x}S/Co(PO_3)_2$@NC electrode delivers an obvious higher reversible capacity and improved cycling stability (371.8 mAh g^{-1} after 800 cycles), while $Co(PO_3)_2$@NC maintains a capacity of only 230.1 mAh g^{-1}, which is lower than the reversible capacity for $Co_{1-x}S/Co(PO_3)_2$@NC-1v3 and $Co_{1-x}S/Co(PO_3)_2$@NC-1v8. This difference in performance is mainly due to the synergistic effect of the heterogeneous interface and the integrated honeycomb-structured carbon, which efficiently promote charge transfer at the interfaces and accelerate the reaction kinetics, accommodate volume changes during prolonged long cycling, and ensure the structural integrity of the electrode materials.

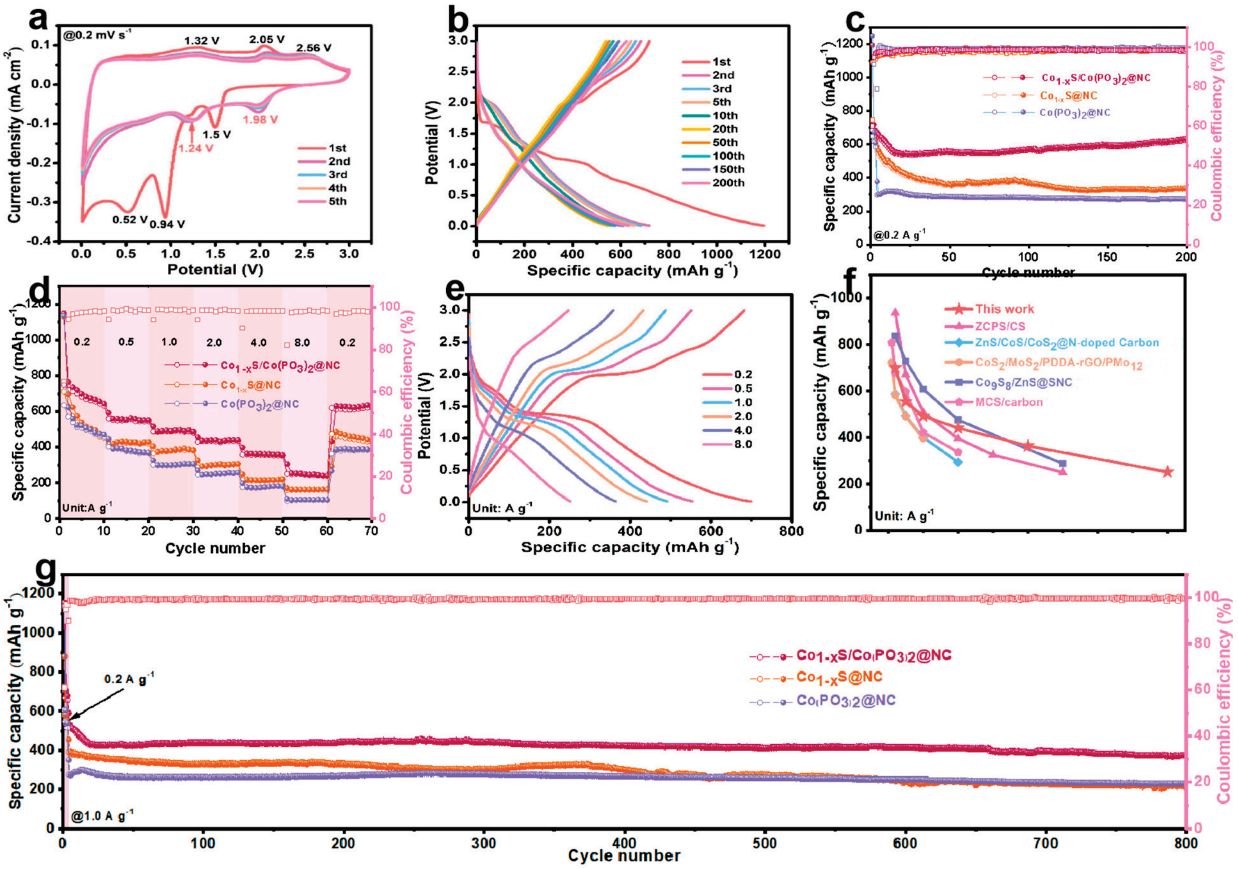

Figure 4. (**a**) The initial three CV curves of $Co_{1-x}S/Co(PO_3)_2$@NC at 0.2 mV s^{-1}, (**b**) galvanostatic charge/discharge profiles of $Co_{1-x}S/Co(PO_3)_2$@NC at 0.2 A g^{-1}, (**c**) cycling stability and coulombic efficiency at 0.2 A g^{-1} for 200 cycles, (**d**,**e**) rate capability and galvanostatic charge/discharge profiles of three samples, (**f**) corresponding comparison with reported studies, (**g**) long-term performance at 1.0 A g^{-1} for 800 cycles [32–36].

In order to assess the superior lithium storage capabilities of the $Co_{1-x}S/Co(PO_3)_2$@NC, cyclic voltammetry (CV) curves were recorded at various scanning rates, ranging from 0.1 to 5.0 mV S^{-1} (Figure 5a). As the scan rate increased, there were no discernible changes in the number or peak voltage of the observed peaks in the CV curves, indicating that $Co_{1-x}S/Co(PO_3)_2$@NC has good reversibility. It is widely accepted that the following Equation (1) could be used to explain the relationship between peak current (i) and scan rate (v):

$$i = av^{b} \tag{1}$$

where both a and b are variable parameters. The value of b can be used to diagnose whether the reaction is a diffusion-controlled reaction (for b = 0.5) or surface-controlled (for b = 1.0). As shown in Figure 5b, the b values at the $O1$ peak and $R1$ peak of the $Co_{1-x}S/Co(PO_3)_2$@NC electrodes were determined to be 0.66 and 0.67, respectively, suggesting a combination of diffusion-controlled and capacitive-controlled behaviors. Furthermore, the proportion of pseudocapacitive contribution could be quantified using the following Equation (2),

$$i = k_1 v + k_2 v^{1/2} \tag{2}$$

where $k_1 v$ and $k_2 v^{1/2}$ indicate the current response from the capacitive capacity and diffusion-controlled capacity, respectively. As shown in Figure 5c,d, the pseudocapacitive contributions of the $Co_{1-x}S/Co(PO_3)_2$@NC electrodes at the scanning rate of 2.0 mV s^{-1} were evaluated to be 70.0%. With the increase in v, the pseudocapacitive contribution gradually increases from 52.3% to 74.7%, demonstrating the important effect of the heterostructure in facilitating the electrode reaction kinetics. Figure 5e shows the Nyquist plots of three samples after three cycles at 0.1 A g^{-1}. All EIS spectra display similar characteristics, including two sections: a semicircular region at a medium- to high-frequency corresponding to R_{ct} and a linear region at low-frequency associated with Li^+ diffusion. Compared to $Co(PO_3)_2$@NC and $Co_{1-x}S$@NC, the $Co_{1-x}S/Co(PO_3)_2$@NC electrode exhibits significantly smaller R_{ct} in the medium- to high-frequency range (186 Ω compared to 304 Ω, 201 Ω), indicating that the unique heterostructures and effective particle refinement indeed enhance charge transfer and reaction kinetics. Moreover, based on the following equations related to diffusion coefficient of Li^+:

$$Z' = R_s + R_{ct} + \sigma\omega^{-1/2} \tag{3}$$

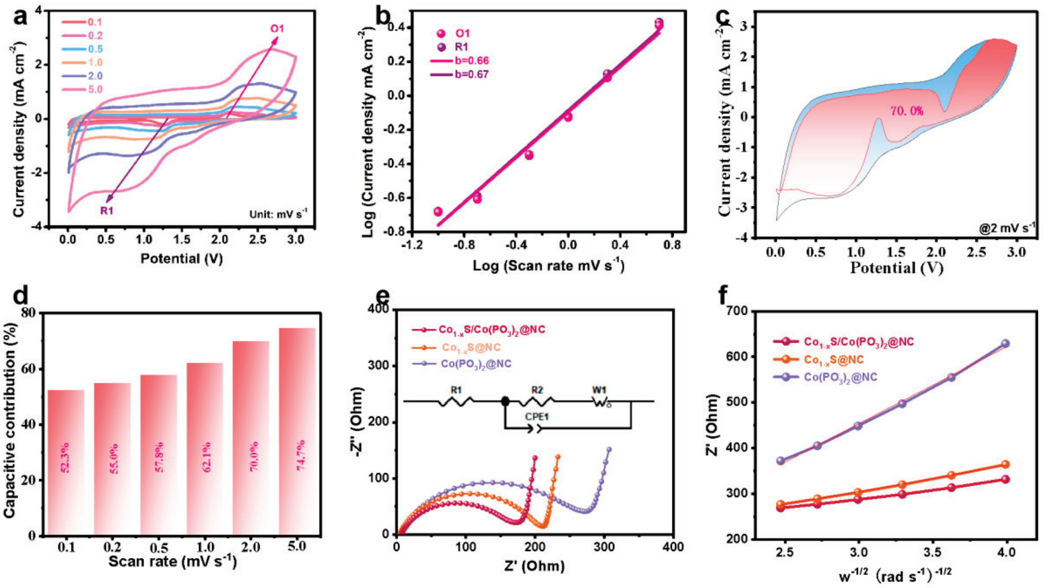

Figure 5. (**a**) CV curves at different sweep rates, (**b**) linear plot of Log *v*-Log *i*, (**c**,**d**) pseudocapacitive contribution of the $Co_{1-x}S/Co(PO_3)_2$@NC electrode at 2.0 mV s^{-1} and at different sweep rates, (**e**,**f**) Nyquist plots and the Z′ as a function of $\omega^{-1/2}$ of of $Co(PO_3)_2$@NC, $Co_{1-x}S$@NC and $Co_{1-x}S/Co(PO_3)_2$@NC.

According to Equation (3), the Warburg factor (σ) of the two electrodes was calculated based on the linear relationship between Z' and $\omega^{-1/2}$ (Figure 5f). The value of σ for the $Co_{1-x}S/Co(PO_3)_2$@NC electrode (41.0) is much lower than the $Co_{1-x}S$@NC (57.6) and $Co(PO_3)_2$@NC electrodes (168.9). As the D_{Li+} diffusion coefficient is inversely proportional to the square of the Warburg factor (σ) [3], this lower σ value indicates a faster Li^+ diffusion coefficient for the $Co_{1-x}S/Co(PO_3)_2$@NC electrode.

Considering the exceptional electrochemical performance of the $Co_{1-x}S/Co(PO_3)_2$@NC in half-cells, a prelithiated $Co_{1-x}S/Co(PO_3)_2$@NC anode and an AC cathode were combined in an optimal mass ratio of 2:1 to assemble a $Co_{1-x}S/Co(PO_3)_2$@NC@NC//AC LIC device. This device was subsequently evaluated for its electrochemical energy storage properties within a voltage window of 0–4.0 V. The working principle of the assembled LIC is illustrated in Figure 6a. During charging, Li^+ ions either intercalate into $Co_{1-x}S/Co(PO_3)_2$@NC or adsorb onto the anode surface, while PF_6^- anions are absorbed onto the AC surface. The discharge process reverses these actions. Figure 6b presents the CV curves of the LICs at scan rates of 5, 10, 20, 30, and 50 mV s^{-1}. Even at 50 mV s^{-1}, a rectangular profile is observed, indicating the capacitive behavior of the LICs [37,38]. The rate performance of the LICs was assessed under various current densities, revealing reversible capacities of 19.15 mAh g^{-1} even at 2 A g^{-1}, respectively (Figure 6c,d). The assembled optimal $Co_{1-x}S/Co(PO_3)_2$@NC//AC LIC delivers a high energy density of 90.47 Wh kg^{-1} (at 26.28 W kg^{-1}) and a high power density of 504.94 W kg^{-1} (at 38.31 Wh kg^{-1}). Furthermore, Figure 6e illustrates the long-term cycling stability of the LICs, showing a high cyclic stability of 86.3% retention after 5000 cycles at a current of 2 A g^{-1}, accompanied by a Coulombic efficiency close to 100%. The superiorities of the as-prepared $Co_{1-x}S/Co(PO_3)_2$ heterostructures were compared with the reported literature in terms of synthetic methods and electrochemical performance (Table S1). In practical applications, the LICs successfully power a light-emitting diode (LED) to illuminate a “wang” character, further demonstrating the potential of the $Co_{1-x}S/Co(PO_3)_2$ heterostructures as an electrode material for Li-ion capacitors.

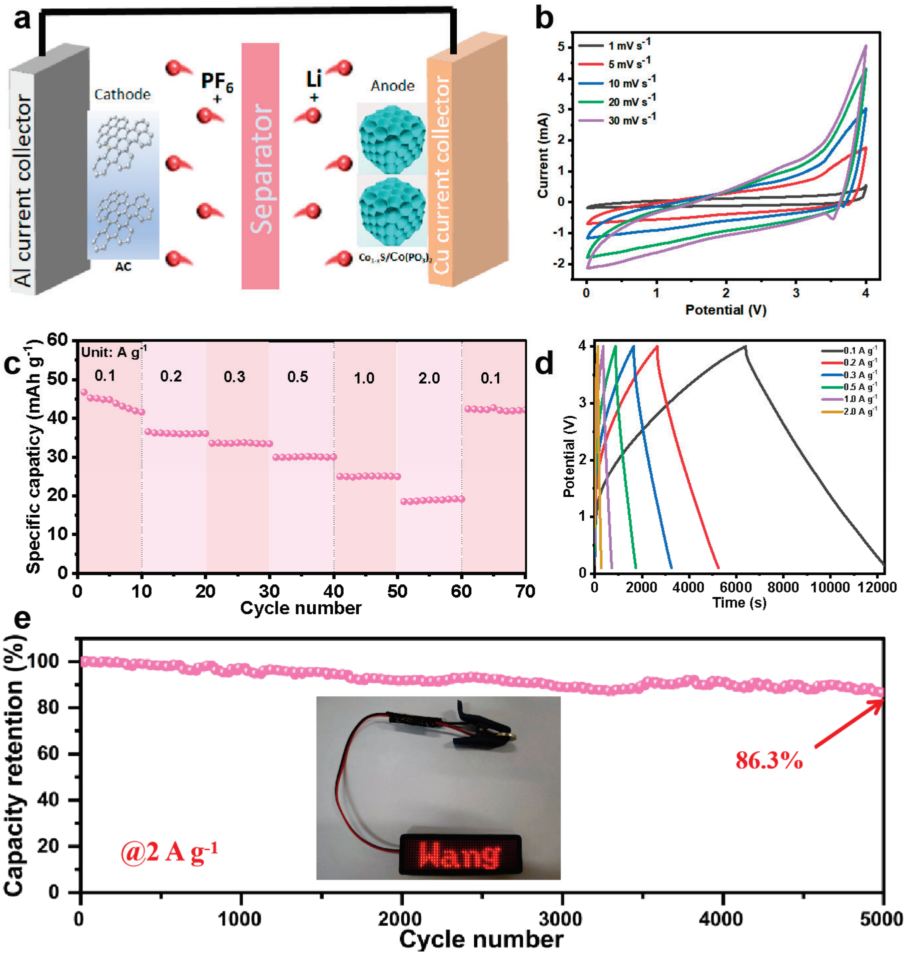

Figure 6. (**a**) Schematic illustration of the assembled $Co_{1-x}S/Co(PO_3)_2$@NC//AC LICs, (**b**) CV curves, (**c**) galvanostatic charge/discharge profiles, (**d**) rate capability, (**e**) long-term durability at 2 A/g of $Co_{1-x}S/Co(PO_3)_2$@NC//AC LICs.

3. Conclusions

In summary, we have constructed high-performance LICs using $Co_{1-x}S/Co(PO_3)_2$@NC as the anode material. This material is synthesized through the chemical blowing-vulcanization of a Co^{2+}-PVP precursor followed by phosphorylation treatment. The characteristic heterointerface and 3D honeycomb-like N-doped carbon matrix efficiently boost interfacial charge dynamics, provide spatial confinement for refined particles, and prevent structural degradation during repeated charge/discharge cycles. As a result, the optimal $Co_{1-x}S/Co(PO_3)_2$@NC composite demonstrates a stable reversible capacity of 371.8 mAh g^{-1} after 800 cycles at 1 A g^{-1}, showcasing significant pseudocapacitive contributions. The assembled $Co_{1-x}S/Co(PO_3)_2$@NC//AC LIC delivers a power density of 504.94 W kg^{-1} and an energy density of 90.47 Wh kg^{-1} within the voltage range of 0–4.0 V. Moreover, they exhibit a high cyclic stability of 86.3% retention after 5000 cycles at 2 A g^{-1}. The facile synthetic method opens new avenues for the fabrication of cost-effective, advanced energy storage devices utilizing Co-based sulfides heterostructures with balanced performance.

Supplementary Materials: The following supporting information can be downloaded at https://www.mdpi.com/article/10.3390/batteries10100346/s1: Figure S1: SEM image of $Co(PO_3)_2$@NC composites; Figure S2: SEM image of $Co_{1-x}S$@NC composites; Figure S3: SEM image of $Co_{1-x}S/Co(PO_3)_2$@NC composites; Figure S4: (a) cycling performance at 0.2 A g^{-1}, (b) rate capability, (c) long-term performance at 1.0 A g^{-1} of $Co_{1\text{-}x}S/Co(PO_3)_2$@NC, $Co_{1-x}S/Co(PO_3)_2$@NC-1v3, and $Co_{1-x}S/Co(PO_3)_2$@NC-1v8 electrodes; Table S1: The LICs performance comparison among Co1-xS/Co(PO3)2@NC and other materials [39–46].

Author Contributions: Conceptualization, J.D. and W.W.; methodology, Y.L. and X.X.; validation, T.W. and H.H.; investigation, Z.W. and F.Z.; writing—original draft preparation, Y.L., X.X. and T.W.; writing—review and editing, Y.L., Z.W. and T.W.; visualization, Y.L. and W.W.; supervision, J.D. and W.W. All authors have read and agreed to the published version of the manuscript.

Funding: The authors gratefully acknowledge the financial support from the Hunan Provincial Natural Science Foundation of China (No. 2024JJ5012), Research Foundation of Education Bureau of Hunan Province (No. 23A0251), Changsha Natural Science Foundation (No. kq2402009).

Data Availability Statement: The data that supported the findings of this study are available from the corresponding author upon reasonable request.

Conflicts of Interest: Authors Xiaopeng Xie and Zhaojia Wu were employed by the company Hunan Datang Xianyi Technology Co., Ltd. Author Fang Zhao was employed by the company Guangdong Power Grid Co., Ltd., Guangzhou Power Supply Bureau. The remaining authors declare that the research was conducted in the absence of any commercial or financial relationships that could be construed as a potential conflict of interest.

References

1. Sun, J.L.; Luo, B.C.; Li, H.X. A Review on the Conventional Capacitors, Supercapacitors, and Emerging Hybrid Ion Capacitors: Past, Present, and Future. *Adv. Energy Sustain. Res.* **2022**, *3*, 2000216–2100191. [CrossRef]
2. Liang, J.; Wang, D.W. Design rationale and device configuration of lithium-ion capacitors. *Adv. Energy Mater.* **2022**, *12*, 2200920. [CrossRef]
3. Wang, L.; Zhang, X.; Li, C.; Sun, X.Z.; Wang, K.W.; Su, F.Y.; Liu, F.Y.; Ma, Y.W. Recent advances in transition metal chalcogenides for lithium-ion capacitors. *Rare Met.* **2022**, *41*, 2971–2984. [CrossRef]
4. Yan, T.; Hu, H.; Duan, J.; Zhu, C.; Wang, Y.; Wen, J.; Li, L.; Xu, Z.; Wen, T.; Yang, P.; et al. Achieving superior sodium storage performance of sulfide heterostructures via copper-driven and electrochemical reconstruction strategy. *Chem. Eng. J.* **2024**, *499*, 155871. [CrossRef]
5. Liang, L.P.; Li, J.C.; Zhu, M.Y.; Li, Y.; Chou, S.L.; Li, W.X. Cobalt Chalcogenides/Cobalt Phosphides/Cobaltates with Hierarchical Nanostructures for Anode Materials of Lithium-Ion Batteries: Improving the Lithiation Environment. *Small* **2021**, *17*, 1903418. [CrossRef]
6. Liu, X.; Zhang, K.; Lei, K.X.; Li, F.J.; Tao, Z.L.; Chen, J. Facile synthesis and electrochemical sodium storage of CoS_2 micro/nano-structures. *Nano Res.* **2016**, *9*, 198–206. [CrossRef]
7. Wang, X.; Chen, Y.; Fang, Y.J.; Zhang, J.T.; Gao, S.Y.; Lou, X.W. Synthesis of cobalt sulfide multi-shelled nanoboxes with precisely controlled two to five shells for sodium-ion batteries. *Angew. Chem. Int. Ed.* **2019**, *58*, 2675–2679. [CrossRef]
8. Xiao, Y.; Hwang, J.Y.; Belharouak, I.; Sun, Y.K. Superior Li/Na-storage capability of a carbon-free hierarchical CoSx hollow nanostructure. *Nano Energy* **2017**, *32*, 320–328. [CrossRef]
9. Zheng, Y.Y.; He, L.; Kong, X.R.; Song, Y.; Zhao, Y. Three-dimensional porous N-doped graphite carbon with embedded CoS_2 nanoparticles as advanced anode for sodium-ion batteries. *Appl. Surf. Sci.* **2022**, *603*, 154481. [CrossRef]
10. Wang, L.; Zhang, X.; Kong, Y.Y.; Li, C.; An, Y.B.; Sun, X.Z.; Wang, K.; Ma, Y.W. Metal-organic framework-derived $CoSe_2$@ N-doped carbon nanocubes for high-performance lithium-ion capacitors. *Rare Met.* **2024**, *43*, 2150–2160. [CrossRef]
11. Li, Q.; Jiao, Q.Z.; Yan, Y.; Li, H.J.; Zhou, W.; Gu, T.T.; Shen, X.R.; Lu, C.X.; Zhao, Y.; Zhang, Y.Y.; et al. Optimized Co-S bonds energy and confinement effect of hollow MXene@CoS_2/NC for enhanced sodium storage kinetics and stability. *Chem. Eng. J.* **2022**, *450*, 137922. [CrossRef]
12. Lei, D.; Gao, Y.; Hou, Z.; Ren, L.; Jiang, M.; Cao, Y.; Zhang, Y.; Wang, J.-G. A Superior Lithium-Ion Capacitor Based on Ultrafine MnO/Dual N-Doped Carbon Anode and Porous Carbon Cathode. *Batteries* **2023**, *9*, 241. [CrossRef]

13. Lin, Y.; Qiu, Z.; Li, D.; Ullah, S.; Hai, Y.; Xin, H.; Liao, W.; Yang, B.; Fan, H.; Xu, J.; et al. NiS_2@CoS_2 nanocrystals encapsulated in N-doped carbon nanocubes for high performance lithium/sodium ion batteries. *Energy Storage Mater.* **2018**, *11*, 67–74. [CrossRef]
14. Liu, J.; Xu, Y.G.; Kong, L.B. Cleverly embedded CoS_2/NiS_2 on two-dimensional graphene nanosheets as high-performance anode material for improved sodium ion batteries and sodium ion capacitors. *J. Mater. Sci. Mater. Electron.* **2020**, *31*, 9946–9959. [CrossRef]
15. Wang, L.; Zhao, S.S.; Zhang, X.; Xu, Y.N.; An, Y.B.; Li, C.; Yi, S.; Liu, C.; Wang, K.; Sun, X.Z.; et al. In Situ Construction of Bimetallic Selenides Heterogeneous Interface on Oxidation-Stable $Ti_3C_2T_x$ MXene Toward Lithium Storage with Ultrafast Charge Transfer Kinetics. *Small* **2024**, 2403078. [CrossRef] [PubMed]
16. Xue, F.F.; Fan, F.F.; Zhu, Z.C.; Zhang, Z.G.; Gu, Y.F.; Li, Q.H. MoS_2/CoS heterostructures grown on carbon cloth as free-standing anodes for high-performance sodium-ion batteries. *Nanoscale* **2023**, *15*, 6822–6829. [CrossRef]
17. Cai, J.M.; Zhou, Y.L.; Tao, S.S.; Liu, Y.C.; Deng, W.T.; Hou, H.H.; Zou, G.Q.; Ji, X.B. Nanocrystalline Heterostructure with Low Voltage Hysteresis for Ultrahigh-Power Sodium-Ion Capacitors. *Energy Storage Mater.* **2024**, *71*, 103582. [CrossRef]
18. Xiao, Y.H.; Kong, Y.; Wang, X.Z.; Luo, H.R.; Yuan, G.Z.; Zhang, S.W.; Zhang, A.Q.; Zhou, J.; Fan, Y.Y.; Xin, L.; et al. Synergetic interface engineering and space-confined effect in $CoSe_2$@$Ti_3C_2T_x$ heterostructure for high power and long life sodium ion capacitors. *J. Colloid Interface Sci.* **2025**, *677*, 577–586. [CrossRef]
19. Dong, C.F.; Guo, L.J.; Li, H.B.; Zhang, B.; Gao, X.; Tian, F.; Qian, Y.T.; Wang, D.B.; Xu, L.Q. Rational fabrication of CoS_2/Co_4S_3@N-doped carbon microspheres as excellent cycling performance anode for half/full sodium ion batteries. *Energy Storage Mater.* **2020**, *25*, 679–686. [CrossRef]
20. Wan, S.Y.; Cheng, M.; Chen, H.Y.; Zhu, H.J.; Liu, Q.M. Nanoconfined bimetallic sulfides (CoSn)S heterostructure in carbon microsphere as a high-performance anode for half/full sodium-ion batteries. *J. Colloid Interface Sci.* **2022**, *609*, 403–413. [CrossRef]
21. Zhao, M.T.; Lu, Q.P.; Ma, Q.L.; Zhang, H. Two-Dimensional Metal-Organic Framework Nanosheets. *Small Methods* **2017**, *1*, 1600030. [CrossRef]
22. Yang, M.; Yan, Z.H.; Zhang, H.; Li, J.W.; Zhu, Z.Q.; Liu, L.; Jiao, L.F. Controllable Synthesis of Sub-10 nm ZnS Nanograins Confined in Micro-Size Carbon Skeleton for Aqueous Zn-S Batteries. *Adv. Funct. Mater.* **2024**, 2406077–2406085. [CrossRef]
23. Wen, F.; Zhu, C.; Li, L.; Zeng, G.; Duan, J.; Chen, Z. Enhanced pseudocapacitive behaviors of Sb-based anodes for lithium ion batteries via dual modification approach of Fe doping combined with double carbon coatings. *J. Alloys Compd.* **2021**, *889*, 161658. [CrossRef]
24. Wu, Y.L.; Zhua, C.; Shu, L.; Duan, J.F.; Wei, D.H.; Xu, J.X.; Zhu, Z.Y.; Li, L.J.; Peng, Z.Y.; Chen, Z.Y. Co_9S_8 confined in bifunctional N/S co-doped carbon/carbon with high electrochemical performance for lithium-ion batteries. *Appl. Surf. Sci.* **2019**, *489*, 528–537. [CrossRef]
25. Yan, T.C.; Wen, F.; Duan, J.F.; Zhu, C.; Wen, J.H.; Wang, Y.X.; Tong, J.T.; Chen, Z.Y. Fabricating tunable metal sulfides embedded with honeycomb-structured N-doped carbon matrices for high-performance lithium-ion capacitors. *Chem. Eng. J.* **2023**, *474*, 145839–145850. [CrossRef]
26. Huang, G.; Hu, M.; Xu, X.T.; Alothman, A.A.; Mushab, M.S.S.; Ma, S.J.; Shen, P.K.; Zhu, J.L.; Yamauchi, Y. Optimizing Heterointerface of Co_2P-Co_xO_y Nanoparticles within a Porous Carbon Network for Deciphering Superior Water Splitting. *Small Struct.* **2023**, *4*, 2200235–2200244. [CrossRef]
27. Tan, L.; Huang, X.; Yin, T.; Guo, Y.; Ning, T.; Mei, Y.; Zou, K.; Li, L.; Ji, X.; Zou, G. A 5 V ultrahigh energy density lithium metal capacitor enabled by the fluorinated electrolyte. *Energy Storage Mater.* **2024**, *71*, 103692. [CrossRef]
28. Cheng, Q.; Liu, X.Z.; Deng, Q.; Chen, C.D.; Zhong, W.T.; Yang, C.H. Heterostructured Ni_3S_4/Co_9S_8 Encapsulated in Nitrogen-Doped Carbon Nanocubes for Advanced Potassium Storage. *Chem. Eng. J.* **2022**, *446*, 136829–136836. [CrossRef]
29. Zhang, J.F.; Sun, C.H.; Qu, S.Q.; Qian, M.M.; Zhan, W.; Su, A.Q.; Zhang, K.; Liu, Q.; Shao, R.W.; Wang, J.; et al. Paradigm metallothermic-sulfidation-carbonization constructing ZIFs-derived TMSs@Graphene/CNx heterostructures for high-capacity and long-life energy storage. *Nano Energy* **2023**, *111*, 108401–108410. [CrossRef]
30. Shen, M.; Ma, H. Metal-organic frameworks (MOFs) and their derivative as electrode materials for lithium-ion batteries, Coordination. *Chem. Rev.* **2022**, *470*, 214715.
31. Shi, X.; Li, G.; Liu, X.; Li, J.; Zhang, X.; Guo, J. Carbon coated $Co(PO_3)_2/CoSe_2$ heterostructure as high performance sodium storage anode. *J. Alloys Compd.* **2023**, *951*, 169989. [CrossRef]
32. Zhong, H.Y.; Lu, X.; Zhong, Y.; Zhao, Y.; Liu, X.M.; Cheng, D.H.; Huang, X.Y.; Du, K.Z.; Wu, X.H. Lithium Storage Performance Boosted via Delocalizing Charge in $Zn_xCo_{1-x}PS_3/CoS_2$ of 2D/3D Heterostructure. *Small* **2022**, *18*, 2104295. [CrossRef]
33. Cheng, W.; Di, H.F.; Shi, Z.; Zhang, D. Synthesis of ZnS/CoS/CoS_2@N-doped carbon nanoparticles derived from metal-organic frameworks via spray pyrolysis as anode for lithium-ion battery. *J. Alloys Compd.* **2020**, *831*, 154607. [CrossRef]
34. Li, Q.; Xu, M.Q.; Wang, T.; Wang, H.J.; Sun, J.W.; Sha, J.Q. Nanohybridization of CoS_2/MoS_2 Heterostructure with Polyoxometalate on Functionalized Reduced Graphene Oxide for High-Performance LIBs. *Chem. A Eur. J.* **2022**, *28*, e202200207. [CrossRef] [PubMed]
35. Nong, Y.T.; Zhang, M.; Li, Q.Q.; Pan, Q.C.; Huang, Y.G.; Wang, H.Q.; Zheng, F.H.; Li, Q.Y. Carbon coated bimetallic sulfides Co_9S_8/ZnS heterostructures microrods as advanced anode materials for lithium ion batteries. *J. Taiwan Inst. Chem. Eng.* **2022**, *141*, 104601. [CrossRef]

36. Zhu, L.; Lu, H.Y.; Xiao, F.P.; Yao, T.H.; Liu, T.; Li, F.; Wang, J.K.; Han, X.G.; Cheng, Y.H.; Wang, H.K. Flower-like Mn/Co Glycerolate-Derived α-MnS/Co_9S_8/Carbon Heterostructures for High-Performance Lithium-Ion Batteries. *ACS Appl. Energy Mater.* **2020**, *3*, 10215. [CrossRef]
37. Hou, J.B.; Shao, Y.Y.; Ellis, M.W.; Moore, R.B.; Yi, B.L. Graphene-based electrochemical energy conversion and storage: Fuel cells, supercapacitors and lithium ion batteries. *Phys. Chem. Chem. Phys.* **2011**, *13*, 15384–15402. [CrossRef]
38. Tao, S.S.; Momen, R.; Luo, Z.; Zhu, Y.R.; Xiao, X.H.; Cao, Z.W.; Xiong, D.Y.; Deng, W.T.; Liu, Y.C.; Hou, H.S.; et al. Trapping Lithium Selenides with Evolving Heterogeneous Interfaces for High-Power Lithium-Ion Capacitors. *Small* **2023**, *19*, 2207975. [CrossRef]
39. Shi, Z.C.; Wei, S.; Zuo, H.; Huang, M.H.; Shi, J.; Wang, H.L. Boosting capacitance and energy density by construction $NiCoO_2$/CoS_2 nanocomposites arrays as pseudocapacitor. *J. Alloys Compd.* **2021**, *881*, 160627. [CrossRef]
40. Wang, S.Q.; Song, Y.P.; Ma, Y.; Zhu, Z.Q.; Zhao, C.H.; Zhao, C.J. Attaining a high energy density of 106 Wh kg^{-1} for aqueous supercapacitor based on VS_4/rGO/CoS_2@Co electrode. *Chem. Eng. J.* **2019**, *365*, 88. [CrossRef]
41. Sonia, Y.K.; Paliwal, M.K.; Meher, S.K. The rational design of hierarchical CoS_2/$CuCo_2S_4$ for three-dimensional all-solid-state hybrid supercapacitors with high energy density, rate efficiency, and operational stability. *Sustain. Energy Energy Fuels* **2021**, *5*, 973. [CrossRef]
42. Li, X.N.; Zhang, W.Y.; Kang, H.W.; Liu, H.L.; Yang, B.C.; Li, Z.J.; Li, Z.K. Self-assembled CoS_2/$NiCo_2S_4$/RGO nanohybrids as advanced electrode for hybrid supercapacitor with enhanced energy density and ultra-long durability. *J. Energy Storage* **2023**, *67*, 107528. [CrossRef]
43. Wang, Y.K.; Liu, M.C.; Cao, J.Y.; Zhang, H.J.; Kong, L.B.; Trudgeon, D.P.; Li, X.H.; Frank, C.W. 3D Hierarchically Structured CoS Nanosheets: Li+ Storage Mechanism and Application of the High-Performance Lithium-Ion Capacitors. *ACS Appl. Mater. Interfaces* **2020**, *12*, 3709. [CrossRef] [PubMed]
44. Wang, H.Y.; Tian, L.H.; Zhao, X.; Ali, M.; Feng, H.M.; Han, S.Y.; Xing, Z.C.; Kumar, S.; Ding, J. Synthesis of MoS_2/CoS composite electrode and its application for supercapacitors. *J. Alloys Compd.* **2023**, *960*, 170835. [CrossRef]
45. Reddy, P.A.K.; Han, H.; Kim, K.C.; Bae, S. Synthesis of ZIF-67-derived CoS_2@graphitic carbon/reduced graphene oxide for supercapacitor application. *Chem. Eng. J.* **2023**, *471*, 144608. [CrossRef]
46. Zhang, K.; Gao, X.; Yao, F.; Xie, Y.Q.; Bai, H.; Sun, Y.J.; Liu, R.R.; Yue, H.Y. Construction of hierarchical MOF-derived CoS_2 microsheet arrays@$NiMo_2S_4$ nanoflakes on Ni foam as a high-performance supercapacitor electrode. *J. Colloid Interface Sci.* **2023**, *650*, 105. [CrossRef]

batteries

MDPI

Review

Recent Advances in High-Performance Carbon-Based Electrodes for Zinc-Ion Hybrid Capacitors

Ying Liu [1,*], Lechun Song [1], Chenze Li [1], Caicheng Song [1] and Xiang Wu [2,*]

[1] SINOPEC Dalian (Fushun) Research Institute of Petroleum and Petrochemicals, Dalian 116045, China; songlechun.fshy@sinopec.com (L.S.); lichenze.fshy@sinopec.com (C.L.); songcaicheng.fshy@sinopec.com (C.S.)
[2] School of Materials Science and Engineering, Shenyang University of Technology, Shenyang 110870, China
[*] Correspondence: liuying.fshy@sinopec.com (Y.L.); wuxiang05@sut.edu.cn (X.W.)

Abstract: Aqueous zinc-ion hybrid capacitors (ZIHCs) have emerged as a promising technology, showing superior energy and power densities, as well as enhanced safety, inexpensive and eco-friendly features. Although ZIHCs possess the advantages of both batteries and supercapacitors, their energy density is still unsatisfactory. Therefore, it is extremely crucial to develop reasonably matched electrode materials. Based on this challenge, a surge of studies has been conducted on the modification of carbon-based electrode materials. Herein, we first summarize the progress of the related research and elucidate the energy storage mechanism associated with carbon-based electrodes for ZIHCs. Then, we investigate the influence of the synthesis routes and modification strategies of the electrode materials on electrochemical stability. Finally, we summarize the current research challenges facing ZIHCs and predict potential future research pathways. In addition, we suggest key scientific questions to focus on and potential directions for further exploration.

Keywords: aqueous zinc-ion hybrid capacitors; carbon-based materials; cathode; energy storage device; electrochemical stability

1. Introduction

With the rapid changes in the energy patterns of the world, the efficient utilization and conversion of fossil fuels is an inevitable trend to achieve high-quality and sustainable energy development [1]. Recently, lithium-ion batteries (LIBs) have occupied a dominant position in the electronics industry, especially in portable electronics and electric vehicles [2]. However, limited Li resources and flammable organic electrolytes cause cost and safety concerns [3]. Thus, aqueous energy storage devices (metal-ion batteries, hybrid capacitors, and supercapacitors) have risen as potential solutions to the existing dilemma due to their high safety [4–9]. Among them, sodium and potassium ions possess ionic radii of 0.95 nm and 1.33 nm, respectively. It leads to slow diffusion kinetics and serious electrode polarization. In contrast, the ion radius of the zinc ion is relatively small (0.74 nm). Also, zinc anodes are characterized by their high theoretical capacity of 820 mAh g^{-1}, economical price, easy availability, and a low redox potential of -0.762 eV relative to the standard hydrogen electrode [10–12]. Nonetheless, the practical application of zinc anodes is limited by the scarcity of matching cathode materials and low power density [13–16]. Energy storage systems with high power densities and extremely long lifetimes can be fully recharged in a short period of time. They are also less susceptible to volume changes during cycling, which meets the needs of society for energy development. Zinc-ion hybrid capacitors (ZIHCs) incorporate their many benefits over traditional zinc-ion batteries. Generally, the device is featured by integrating the properties of a capacitive material with those of a battery-type material in a mild Zn-based electrolyte [17–21]. Due to the different operating potential ranges of these two types, the voltage of the matched device is extended.

As a result, there is an increase in the energy and power density of the devices. This is facilitated by the favorable combination of batteries and supercapacitors [22,23].

Since 2016, Wang and collaborators [24] have designed an aqueous zinc-ion capacitor assembled with oxidized carbon nanotubes and zinc metal as electrodes. It can be repeatedly charged and discharged for 5000 cycles (10 mV s^{-1}) with the working voltage of 0–1.8 V. Then, Kang et al. [25] reported the study of aqueous activated carbon (AC)/Zn capacitors with ultra-long lifetimes. ZIHCs are rapidly growing as a research hotspot [26]. Further, Kang's group [27] constructed a hybrid ion capacitor with MnO_2 and AC as cathode and anode, respectively. The device with Zn^{2+} aqueous solution as electrolyte can output a maximum power density of 13 kW kg^{-1}. During the past decade, carbon-based materials have been exploited as cathode materials owing to their high conductivity and customizable pore structure, including biomass and polymer-derived carbon, metal organic compounds derived carbon, graphene, and carbon nanotubes [28–30]. For example, Alshareef's group [31] prepared hybrid capacitors with oxygen-enriched porous carbon cathodes and carbon-coated zinc anodes. Benefiting from the EDLC of the porous carbon and the pseudocapacitance provided by the oxygen functional groups, the assembled ZIHCs obtain a specific capacity of 179.8 mAh g^{-1}. The energy density is up to 104.8 Wh kg^{-1} (0.1 A g^{-1}) with a voltage window of 0–1.9 V. Fan and co-workers [32] designed honeycomb porous carbon using polyacrylonitrile (PAN) as a precursor through a pre-oxidation and activation process. This abundant pore and interconnected structure facilitate rapid charge transfer and generate numerous ion adsorption sites. The assembled capacitor shows a specific capacity of 238 mAh g^{-1} at 0.1 A g^{-1}. Furthermore, it achieves an energy density of 193.6 Wh kg^{-1}, corresponding to a power density of 76.6 W kg^{-1}. Li et al. [33] fabricated porous carbon rich in pyridine nitrogen (PrN) with Zn and Co bimetallic organic skeletons as precursors. The content of PrN can be controlled to 56% by changing the annealing temperature. This high pyridine N content provides rich reaction sites for the structure of materials. Moreover, the presence of residual cobalt nanoparticles contributes to accelerating electron transfer. Based on this, the assembled ZIHCs deliver a specific capacity of 302 mAh g^{-1} (1 A g^{-1}) and an energy density of 157.6 Wh kg^{-1}.

The energy density of these reported devices is significantly weaker than expected. It can be ascribed to the distinct energy storage mechanisms of these two electrodes. This leads to the dynamic imbalance of ZIHCs, which fails to acquire high energy and power density [34]. This asymmetric device tends to increase the overpotentials of hydrogen and oxygen evolution in aqueous solutions. Its voltage range is generally restricted to 2.0 V [35,36]. Nevertheless, the energy density of aqueous ZIHCs is still far below that of batteries. Therefore, the charge storage capacity and voltage window can be increased by designing the electrode structure, electrolyte, and electrode/electrolyte interface [37].

Herein, we focus on the recent developments of carbon-based materials as electrodes for aqueous ZIHCs. First, we distinguish the different types of ZIHCs according to the properties of electrode materials. Then, we discuss the structure and morphology of carbon-based materials. Their cycling, rate performance, and durability are demonstrated when they are assembled as positive electrodes into capacitors. Further, we highlight the modification strategies of carbon-based materials, including surface modification, morphology and size tuning, and heterogeneous atom doping. We also summarize the energy storage mechanism in conjunction with the electrode structural changes. Finally, we present a conclusion and prospect the future development of ZIHCs.

2. The Bases of Zinc-Ion Capacitors

2.1. The Growth of Energy Storage Technologies

Among the various energy storage systems, supercapacitors and batteries are two highly representative electrochemical energy storage technologies. The former is a promising device with the merits of rapid charge capabilities, longevity, and excellent power density. The latter demonstrates high energy density and voltage window. Research on energy storage devices began in the 1800s (Figure 1). H. I. Becker first discovered electrochemical capacitors with a high farad in 1954. In the following 20 years, Whittingham reported reversible electrochemical embedding reactions of layered TiS_2 with lithium in Li/TiS_2 batteries [38]. However, Li/TiS_2 batteries cannot be developed into commercially promising secondary batteries. It can be attributed to the low open-circuit voltage of the TiS_2 cathode (2.2 V). Goodenough et al. [39] proposed that the layered $LiCoO_2$ materials can be used as the cathodes for LIBs. It presents an open-circuit voltage of 4.0 V, almost twice that of the TiS_2 electrode. In the 21st century, research on various metal-ion capacitors has also become increasingly attractive with the massive growth in energy demand [40].

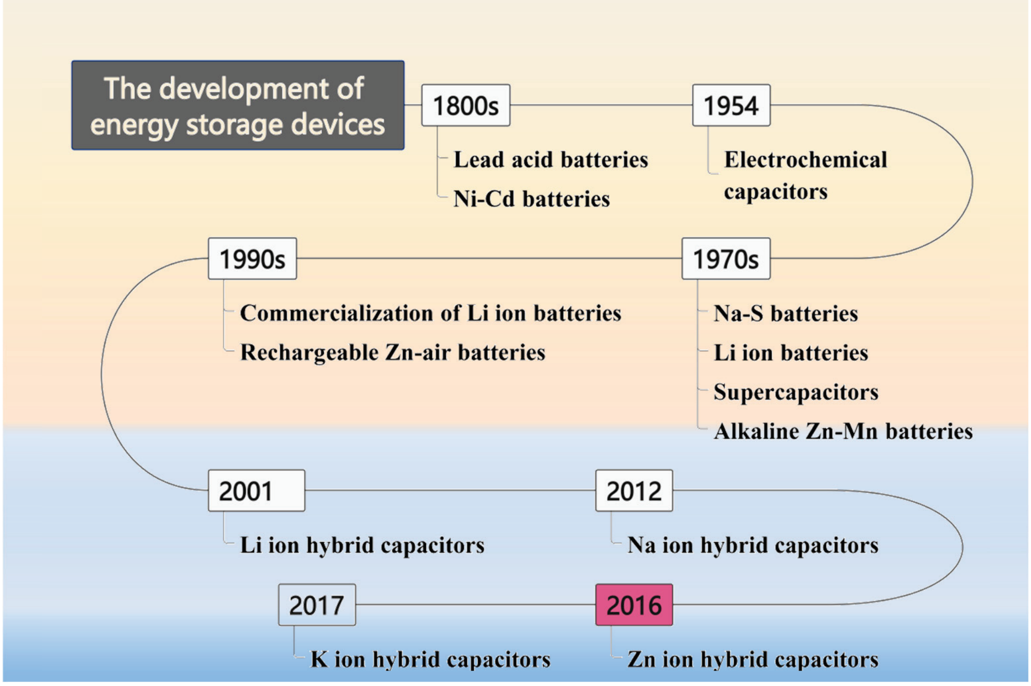

Figure 1. The growth of energy storage technologies.

Supercapacitors are mainly employed in portable electronic devices, rail public transportation, heavy trucks, and backup energy for uninterruptible power supply (UPS) [41]. Based on the principles of charge accumulation, the cathode can be categorized into two main types: double electric layer capacitors (EDLCs) and faradaic electrode materials [42,43]. The former involves the formation of a double layer by electrostatic adsorption of charges at the electrode/electrolyte interface. The latter represents a prompt reversible redox process occurring on/near the surface. The difference between the two is that EDLC is not undergoing a faradaic process [44,45]. The electrode materials for supercapacitors include carbonaceous materials, conducting polymers, and transition metal oxides and hydroxides [46–49]. Notably, carbon-based materials are characterized by abundant resources, inexpensiveness, extensive specific surface area, and superior electrical conductivity [50,51]. During the past few years, a multitude of studies have concentrated on the design of the pore structure of such electrodes to modulate the electrochemical performance of the devices [52]. Liu et al. [53] designed an activated porous carbon material with a specific surface area of 843 $m^2\ g^{-1}$ via rapid high-temperature shock carbonization and the HTS-KOH activation approach. The prepared electrodes are assembled into supercapacitors with an energy density of 25 Wh kg^{-1} and a power density of 582 W kg^{-1}. Prabakar's group [54] synthesized activated carbon nanosheets with a specific surface area up to 2943 $m^2\ g^{-1}$ by one-step activation method. The assembled symmetric supercapacitor achieves a capacitance of 403 F g^{-1} with an energy density of 32.9 Wh kg^{-1} (0.5 A g^{-1}).

2.2. The Types of ZIHCs

Benefiting from the synergistic strengths of supercapacitors and batteries, the novel ZIHCs are regarded as critical candidates for energy storage technologies. This is attributed to their ability to satisfy market requirements for high energy and power density [55]. Among them, electrodes can be divided into capacitor-type and battery-type materials. The former is mainly carbon-based electrodes (derived carbon and graphene-based materials) and pseudocapacitive electrodes (MXene and polymer–carbon materials) [56]. Generally, zinc ion adsorption/desorption reactions occur on their surfaces during charging and discharging. The latter is generally metallic zinc, Mn, and V oxides, which mainly occur in zinc ion insertion/extraction reactions. Based on the unique characteristics of carbon-based electrodes, the cathode and anode materials of ZIHCs can be classified into carbon materials/Zn foils and manganese-based or vanadium-based oxides/carbon materials.

Figure 2 illustrates the dual energy storage mechanisms of ZIHCs. From Figure 2a, carbon-based cathodes utilize the EDLC mechanism to facilitate highly reversible ion adsorption/desorption processes, thus providing excellent power densities. In fact, their total capacitance is contributed by EDLC and pseudocapacitance. Therefore, a redox reaction can occur on the surface or near the surface of a carbon electrode. On the anode side, zinc ions in the electrolyte can be deposited and stripped on the zinc foil with the charging and discharging process to obtain excellent energy density.

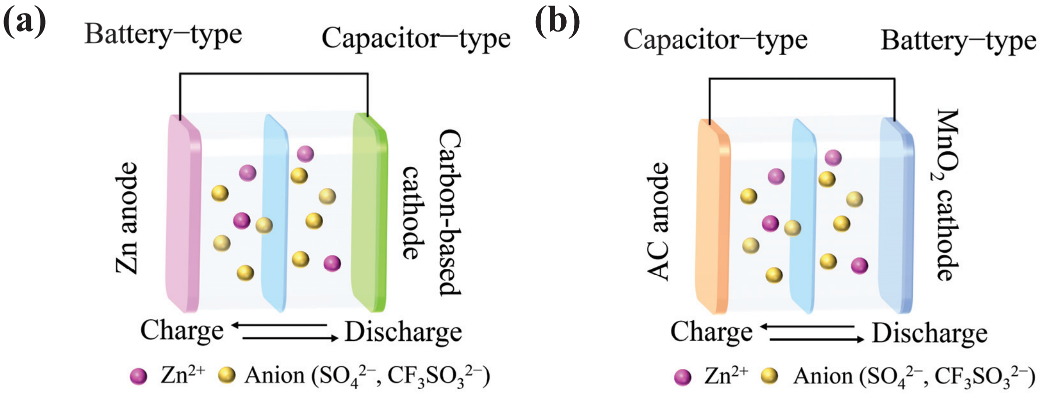

Figure 2. The energy storage mechanism of different electrodes. (**a**) Carbon-based cathode/Zn anode capacitor. (**b**) MnO_2 cathode/AC anode capacitor.

In Figure 2b, a Mn-based oxide/carbon material hybrid capacitor is taken as an example. When charging, zinc ions escape from the battery-type cathode and adhere to the surface of the capacitor-type anode. In the discharge phase, zinc ions are desorbed from the anode and embedded in the structure of the cathode. This reversible transfer of zinc ions contributes to the stable electrochemical performance of ZIHCs.

Compared with the two systems, the capacitive material as the cathode can provide rapid ion adsorption/desorption, thus achieving high power density. However, zinc anode is prone to producing zinc dendrites, which leads to potential safety hazards. The battery material as cathode enables a dendrite-free system. The voltage range of the device can be extended up to 2 V, showing high energy density. However, their electrochemical performance suffers from issues such as low rate capability and cycling stability, which are attributed to the dissolution of the cathode material.

3. Carbon-Based Electrode Materials

Carbon is an indispensable material to promote social development and progress. In the last two decades, carbon materials with various allotropic structures (graphene, diamond, carbon fiber, and carbon nanotubes) have grown rapidly in a wide range of fields. In particular, they stand out in new energy sources owing to their highly theoretically specific surface area and superior electrical conductivity [57]. From Figure 3, carbon-based cathodes mainly include commercial activated carbon (AC), biomass or polymer-derived carbon, metallic organic compound-derived carbon, nanofibers, and other graphite-like carbon materials. This section mainly introduces the structure and morphology of these carbon materials and their corresponding electrochemical performance.

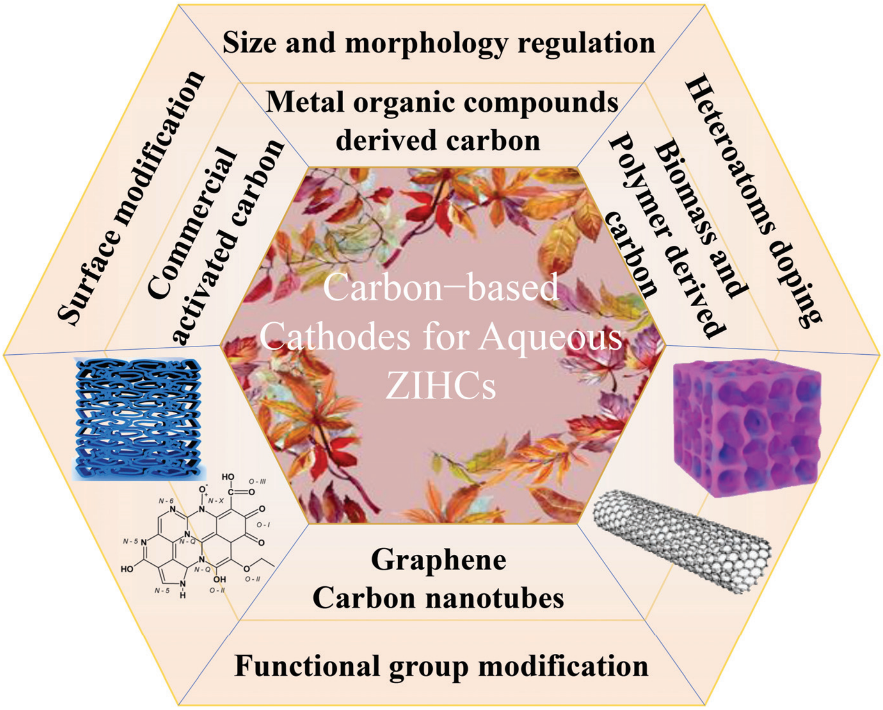

Figure 3. Classification and synthetic approaches of carbon-based cathodes for aqueous ZIHCs.

3.1. Amorphous Carbon Materials

3.1.1. Commercial Activated Carbon

In recent years, AC has attracted great interest as a promising candidate electrode material for ZIHCs because of its specific surface area of 3000 m^2 g^{-1}, rich pore structure, high chemical stability, and wide working potential window. They can usually be prepared from various precursors such as polymers, biomass, coal, organometallic frameworks, and organic salts. However, commercial AC has a specific capacity of only 100–200 mAh g^{-1}. The electrochemical performance of ZIHCs depends on the pore structure, conductivity, and surface properties of carbon-based electrodes. Pore structure is critical for charge storage and diffusion of hydrated Zn^{2+} ions [58]. Strategic designs of pore structures (including pore volume, size distribution, and surface functional group chemistry) are effective approaches to enhance the specific capacitance of electrodes.

Pore size distribution is an important parameter affecting zinc-ion storage. The pore structures in AC are usually categorized into micropores with a size less than 2 nm, mesopores with a size of 2–50 nm, and macropores with a size over 50 nm [59–61]. However, not all pores in the material are beneficial to charge storage. Both micropores and mesopores contribute to the EDLC. However, a part of the micropores prevents the embedding of electrolyte ions because of the distorted pore channel or small pore size. It also deprives their electrochemical activity at high loadings. The solvated $[Zn(H_2O)_6]^{2+}$ and SO_4^{2-} are the main carriers in the charging and discharging process of ZIHCs [62]. Its ion diameters are 0.86 and 0.59 nm, respectively. After solvation, the radius of Zn^{2+} is increased compared with the original one. For carbonaceous materials with pore sizes less than 1 nm, most of the solvated Zn^{2+} ions are limited by the pore structure. This leads to their inability to provide capacitive contributions.

From Figure 4, when there are various pores in the structure of carbon materials, they are prone to diffuse in the one with large pore size. It contributes to enhancing the specific capacitance of the devices. The pore size structure affects the ion diffusion resistance of the electrode. Small pore size enhances the diffusion resistance of electrolyte ions. The presence of mesopores and macropores can shorten the ion migration path and contribute to the rate capacity [63]. Zhang and colleagues [64] systematically compared various samples with similar specific surface areas but distinct pore structures. It is found that the materials with abundant micropore structure (0.6 nm) are generally lower in capacitance and rate performance than those with mesoporous channels. This phenomenon is associated with the partial failure of the microporous structure, which hinders the accommodation and storage of hydrated zinc ions. Hence, it is the key to stabilizing the cycle performance to match the appropriate pore channels.

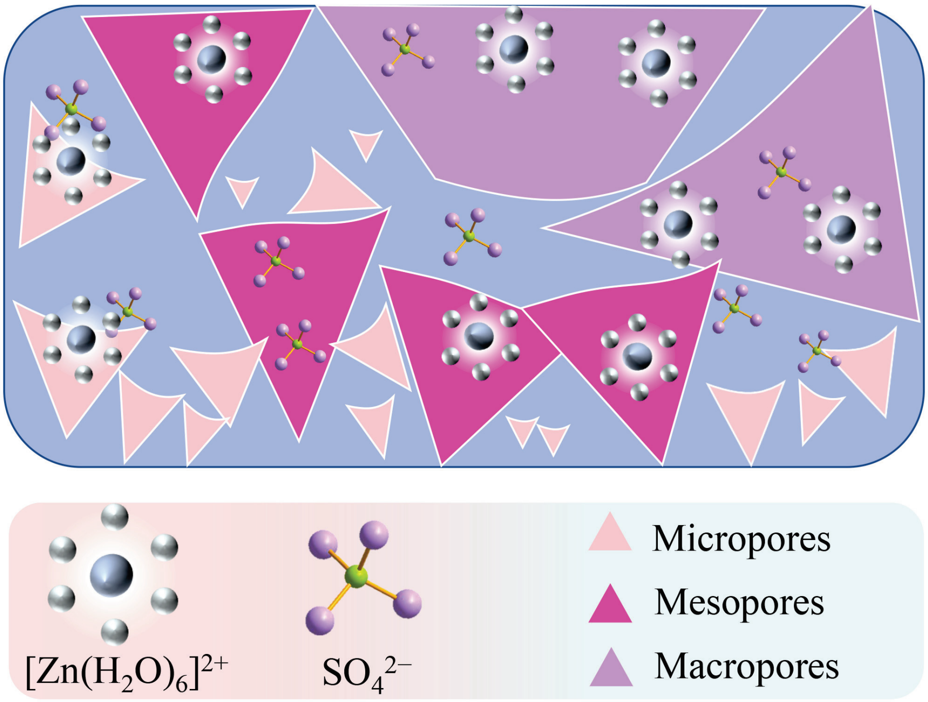

Figure 4. Schematic of charge carriers embedded in various pore structures.

To address the issue of the low specific capacitance of commercial AC, researchers have made many efforts. Dong et al. [25] designed the AC/Zn devices with a capacity of 121 mAh g^{-1} and an energy density of 84 Wh kg^{-1}. In fact, there is still space for improvement in cycle performance. Surface-functionalized AC with reasonable pore size enhances chemical binding with carriers, which contributes to an increase in specific capacity [65]. For instance, An's group [66] prepared the AC material with a mesoporous structure by polymerization PVP dehydrogenation process. This increases the number of oxygen groups on the surface of AC. The modified materials, such as cathodes, show an abundance of electrochemical active sites and rapid ion diffusion and transmission ability. Therefore, the assembled ZIHCs can still deliver a specific capacity of 72 mAh g^{-1} even at a current density of 10 A g^{-1}. In addition, the cycle life can reach 40,000 cycles with a capacity retention rate of 78% (Figure 5a).

The specific capacity of AC electrodes is enhanced based on surface modulation techniques, but there are limited improvements in their conductivity, wettability of the electrode and electrolyte surfaces, and specific surface area. Therefore, researchers have developed some effective modification strategies and superior electrode materials. Heterogeneous atom doping can introduce O-/N-containing functional groups. This offers fast redox reactions for the electrodes and increases the pseudocapacitive contribution to charge storage [67,68]. The construction of novel nanostructures or hierarchically porous carbon materials can effectively increase the adsorption sites. This accelerates ion/electron transport and favors the rate capacity [69]. Further detailed discussions are presented in the subsequent sections.

3.1.2. Metal–Organic Compound Derived Carbon

Metal–organic compounds are converted into nanostructured carbon materials through high-temperature calcination or controlled chemical reactions. This conversion process is conducive to the formation of porous architecture. This hierarchical porous structure facilitates the optimization of electrochemical performance. Zhang and collaborators [70] fabricated ultra-thin layered porous carbon nanoplates (Ca-900 samples) using calcium gluconate precursor by in situ template method. The tuning of calcination temperature can optimize the specific surface area and porosity of carbon materials. The assembled device shows an energy density of 75.22 Wh kg^{-1} and a power density of 879.12 W kg^{-1}. After 4000 times of charge and discharge, the capacitance retention rate is 90.9%.

Metal–organic frameworks (MOFs) constitute a class of crystalline compounds synthesized by coordination of metal ions with organic linkers. MOF-derived carbon materials can possess a wide range of specific surface areas and rich porous structures by high-temperature calcination and etching processes [71]. Li et al. [72] designed a rod-like porous carbon fabricated by pyrolysis of MOF (MIL-88B). Based on the structural features of MOF and the synergistic effect of alkali activation, the carbon rod material possesses a specific surface area (SSA) of 1272.4 m^2 g^{-1}. The assembled device can still show a specific capacity of 73.5 mAh g^{-1} at 50 A g^{-1}. The capacity retention of 96.5% (10 A g^{-1}) is achieved after 10,000 cycles. Our group [20] prepared V metal–organic framework (MOF)-derived porous carbon anodes. The assembled devices present specific capacities of 168 and 140 mAh g^{-1} with a capacity loss of 16.7% at 0.1 and 2 A g^{-1}, respectively. These kinds of materials are often treated by strong acid/alkali etching, which increases the technical difficulty and cost. Therefore, there is an urgent need to design eco-friendly, high-performance carbonaceous materials.

3.1.3. Polymer-Derived Porous Carbon

Polymers are complex structures composed of many macromolecular chains. They possess nanoscale self-assembly ability. Compared with small molecular hydrocarbons, polymers as carbon sources show controllability in structure and doping amount. A variety of porous carbonaceous structures, including spherical particles, fibrous materials, films, or membrane-type materials, can be prepared by matching suitable polymer precursors, such as polyacrylonitrile, polyphenylamine, and conjugated polymers. Due to the unique atomic composition of polymer precursors, non-metallic atoms can be doped by pyrolysis, including N, B, P, and S. These types of atoms are combined into the carbon framework individually or jointly to optimize the energy storage capability of carbon materials [73]. Yang et al. [74] developed a hierarchical porous carbon fiber derived from polyvinylpyrrolidone/polyacrylonitrile (PVP/PAN) by electrospinning. The device assembled with PVP-/PAN-derived porous carbon fibers shows a specific capacity of 208 mAh g^{-1} and a rate retention of 49.5% (0.5~5 A g^{-1}). After 10,000 stable cycles, the capacity maintains 72.25% of the initial capacity. This multi-channel structure is beneficial to the specific capacity and rate performance of ZIHCs. However, the specific surface area obtained by this direct pyrolysis is only 449.05 m^2 g^{-1}. Therefore, its cyclic stability is limited. Liu group's [75] studied the pyrolysis of chitosan aerogels to produce porous carbon with 3D honeycomb lattice. The combination of nitrogen and oxygen realizes the co-doping of carbon materials. However, the specific surface area of carbonized chitosan is only 1000 m^2 g^{-1}, and it lacks essential micropores and mesopores. Combined with the KOH activation strategy, its specific surface area can be increased to 2267 m^2 g^{-1}. Therefore, the capacity retention of the assembled device can remain at 86.3% after 10,000 cycles.

Carbon materials derived from asphalt have garnered extensive research attention for their applications in supercapacitors and LIBs [76–78]. However, the activation of asphalt with complex compositions at high temperatures usually leads to violent volatilizing of light components and polymerization of polycyclic aromatic hydrocarbons [79]. To regulate the pore size during fabrication, Liu and co-workers [80] proposed two steps of carbonization and alkali activation to enhance its structural stability. In Figure 5b, compared with commercial AC, the specific surface area of this material can be increased to 3525 m^2 g^{-1}. The porous structure is composed of micropores and abundant mesopores, which effectively increase the ion occupation sites. The fabricated device achieves a specific capacity of 172.7 mAh g^{-1} at 1 A g^{-1}, and it retains a capacity of 119.4 mAh g^{-1} at 20 A g^{-1} (Figure 5c). Lu and collaborators [81] designed an N-doped asphalt-derived carbon material (NPC) as a cathode. In Figure 5d, incorporating N into the carbon electrode material enhances its electrical conductivity, and the addition of pyridine N effectively increases the electrochemical kinetics. They further proposed a nitrogen redox mechanism. From Figure 5e, the activation energy (E_a2) of the NPC electrode is much superior to that of PC one. This indicates that the addition of N triggers multiple redox processes in favor of increasing the pseudocapacitance. The assembled device possesses a capacity of 136.2 mAh g^{-1}. When the current density increases from 0.3 A g^{-1} to 15 A g^{-1}, the capacity retention rate is 50.8% (Figure 5f). In addition, it only experienced 4.6% self-discharge capacity loss within 24 h.

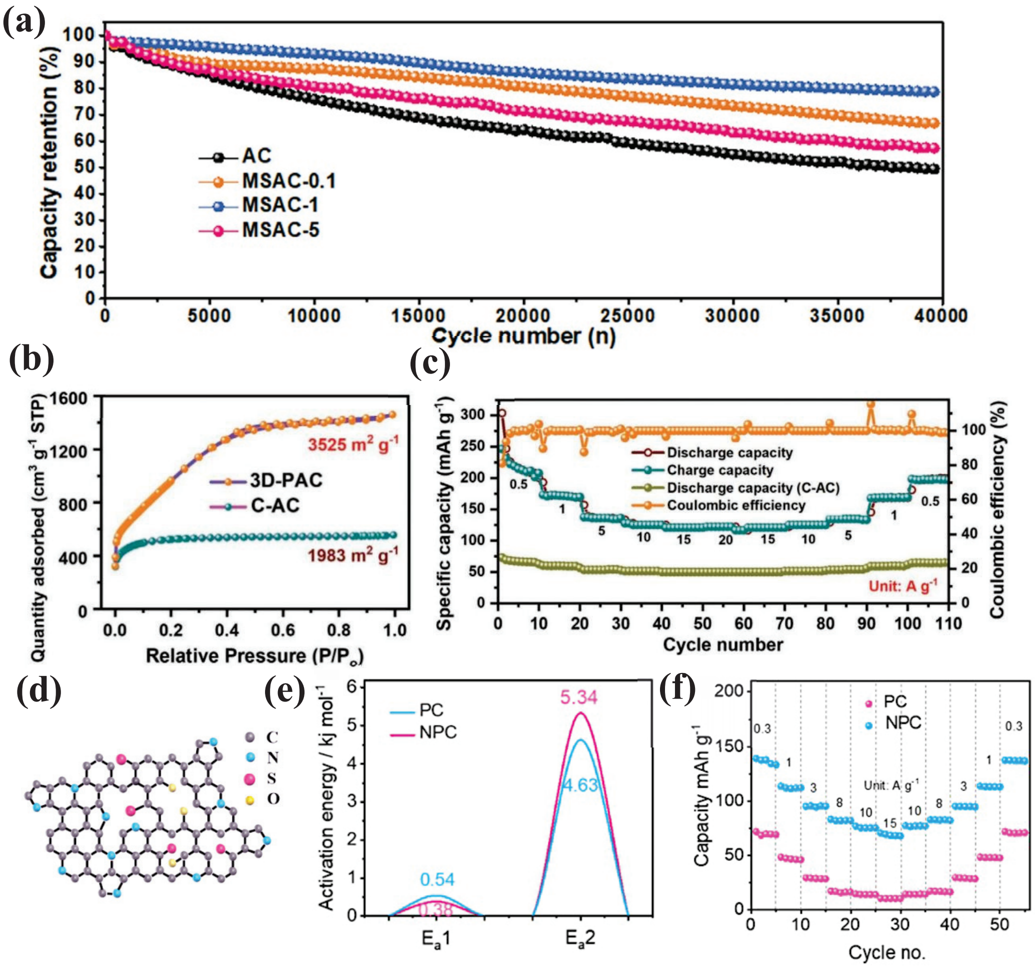

Figure 5. Effect of specific surface area on electrochemical performance of materials (**a**) The capacity retention (10.0 A g^{-1}) for the various electrodes. Reproduced with permission [66], Copyright 2020, Elsevier B.V. (**b**) Nitrogen adsorption–desorption isotherms of the two materials. (**c**) Rate capability of the assembled device. Reproduced with permission [80], Copyright 2020, Wiley-VCH GmbH. (**d**) Schematic structure of NPC. (**e**) The activation energy comparison of PC and NPC. (**f**) Rate performance. Reproduced with permission [81], Copyright 2021, American Chemical Society.

3.1.4. Biomass-Derived Porous Carbon

Biomass-derived porous carbon materials are frequently applied as cathodes for capacitors due to their cost-effectiveness, structural diversity, and preparation convenience [82]. Li and co-workers [83] synthesized pencil shaving-derived carbon materials and obtained optimal PSC-A600 electrodes by adjusting the pyrolysis temperature. This porous structure enables a fast ion transport rate and provides sufficient charge storage space. Therefore, the Zn/PSC-A600 device presents a specific capacity of 183.7 mAh g^{-1}. From Figure 6a, it can perform 10,000 cycles at 10 A g^{-1} and maintain a retention rate of 92.2%. Qiu's group [84] prepared porous carbon positive electrodes (LHPCs) by the self-templating method employing lignin as a carbon precursor. The electrode material demonstrates fast electrochemical kinetic processes. This is due to the rich pore structure and the introduction of carboxyl functional groups. The assembled Zn/LHPCs capacitors obtain an energy density of 135 Wh kg^{-1} at a power density of 101 W kg^{-1}.

However, the impurities and functional groups of biomass carbon-based raw materials accelerate the self-discharge speed of the assembled hybrid capacitor. This is closely related to the pore structure of the carbon cathode. This pore effect exacerbates charge redistribution and carbon oxidation [85]. Li et al. [86] synthesized oxygen-enriched multistage porous carbon by olive pyrolysis through chemical activation. Oxygen-enriched functional groups provide additional capacitance and boost the wettability and conductivity of porous carbon. The as-built devices obtain an energy density of 136.3 Wh kg^{-1} and a self-discharge rate of 2.3 mV h^{-1} (Figure 6b). They can achieve 20,000 charge and discharge cycles at 10 A g^{-1} (Figure 6c).

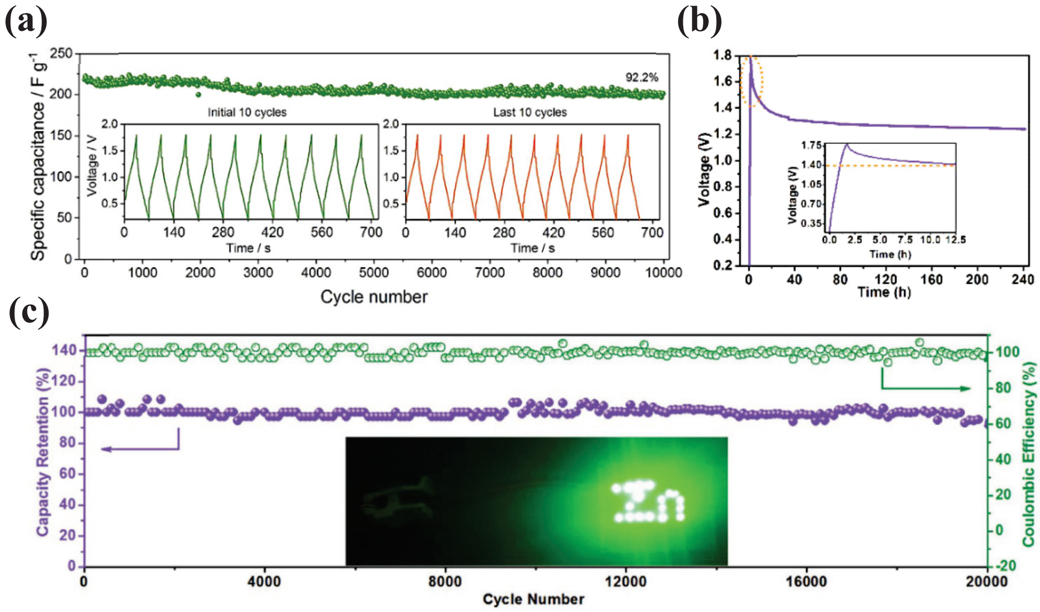

Figure 6. The cycle capability of biomass-derived porous carbon. (**a**) Cycle performance. Reproduced with permission [83], Copyright 2020, Elsevier B.V. (**b**) Self-discharge curves. (**c**) Cycling durability at 10 A g^{-1}. Reproduced with permission [86], Copyright 2023, Wiley-VCH GmbH.

3.2. Carbon Nanofibers

Flexible wearable devices have been a hot research topic. Therefore, there is a demand for the exploitation of flexibility electrodes. Typically, the fabrication of electrodes depends on the support of current collectors and additives in addition to active materials, which can reduce the total energy density. One-dimensional (1D) carbon nanofibers are highly promising for the construction of freestanding cathodes, which is attributed to their favorable flexibility and abundant pore structure. However, their hydrophobicity hinders charge transport at the electrolyte–electrode interface, demonstrating a large interfacial resistance.

Surface modification improves the hydrophilicity of carbon-based materials. For instance, this is a viable approach to enhance the chemisorption of metal ions on electrode materials. Zhang and collaborators [87] synthesized flexible oxygen-enriched carbon fiber films by electrostatic spinning and acid-assisted oxidation. ZIHCs with this carbon fiber cathode show an energy density of 97.7 Wh kg^{-1} and a power density of 9.9 kW kg^{-1}. Also, they maintain long-term cycling stability (81%) of 50,000 cycles. Figure 7a demonstrates the near-zero superhydrophilicity angle. It reduces the interfacial resistance between electrolyte and electrode. The adsorption of zinc ions on the electrode surface is greatly enhanced. Density functional theory (DFT) calculations show the chemisorption relationship between zinc ions and C=O functional groups (Figure 7b). Among them, zinc ions are more easily adsorbed between two carbonyl groups. The adsorption process is shown below:

$$2C{=}O + Zn^{2+} + 2e^{-} \rightarrow C\text{-}O\text{-}Zn\text{-}O\text{-}C, \tag{1}$$

The existence of oxygen-enriched functional groups significantly improves the wettability of carbon fiber and promotes the chemisorption of zinc ions. In addition, these cathodes could operate stably with a loading of 20 mg cm^{-2} and 180° bending. Their specific capacity decreases by 19% (5 A g^{-1}) after 50,000 cycles (Figure 7c).

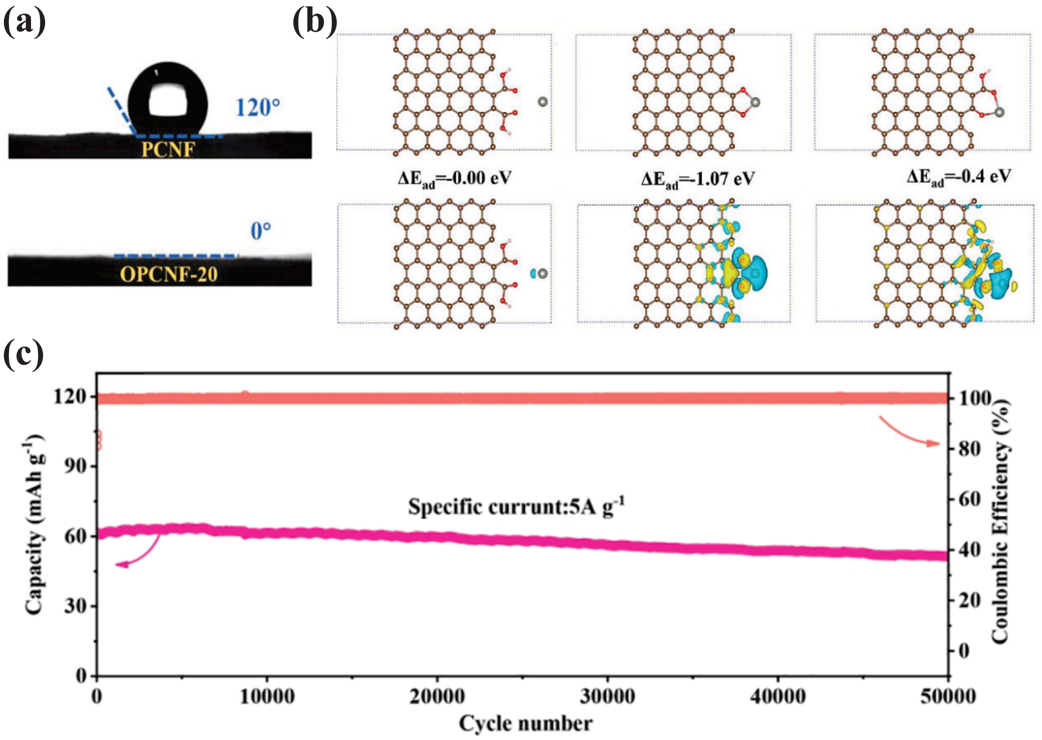

Figure 7. Wetting behavior and cycling stability. (**a**) Contact angles. (**b**) DFT calculations for zinc storage behavior. Red, brown, white and gray balls represent oxygen, carbon, hydrogen and zinc atoms, respectively. The regions indicate the increase (yellow) and decrease (blue) of electron density. (**c**) Long-term cycle at 5 A g^{-1}. The pink and orange curves represent capacity and coulombic efficiency, respectively. Reproduced with permission [87], Copyright 2021, Elsevier B.V.

3.3. Graphite-Type Carbon Materials

This refers to a high-performance material with a graphite-like microcrystalline structure. Representative members include graphene, carbon nanotubes, and carbon fibers [24,88]. These materials are characterized by a layered accumulation of carbon atoms interconnected by van der Waals interactions. This unique layered structure endows graphite-like carbon materials with favorable electrical and thermal properties, as well as excellent chemical stability. Therefore, they show wide application potential in various fields, including energy storage, electronic devices, composite materials, and catalytic technology [89].

3.3.1. Carbon Nanotubes

One-dimensional carbon nanotube (CNT) materials offer unique fast carrier transfer pathways, but the limited specific surface area (less than 500 m^2 g^{-1}) hinders their further development. Previous studies have demonstrated that the introduction of pseudocapacitive active sites on carbon nanotubes can increase the specific capacitance of carbon nanotubes [24,90,91]. Wang's group [24] used oxidized CNT (oCNT) as cathode and revealed the role of oxygen groups in ion storage by electrochemical characterization. As shown in Figure 8a, Zn^{2+} on the oxygen-containing groups of the oCNT electrode undergoes electrochemical adsorption/desorption. The surface-endowed ZICs are confirmed to provide better performance than the pure carbon nanotube cathode.

3.3.2. Graphene

Graphene, featuring a single atom thickness, superior electrical conductivity (10^6 S cm^{-1}), mechanical properties, and a specific surface area of 2630 m^2 g^{-1}, is a suitable positive material for ZIHCs. However, two-dimensional (2D) graphene tends to aggregate. Moreover, there are morphological defects such as holes, edges, cracks, and heteroatoms on the surface of graphene [92]. This greatly limits its properties. Three-dimensional (3D) graphene is a novel class of carbon nanomaterial composed of 2D graphene on a macroscopic scale. When graphene nanosheets are interconnected as building blocks, they can be assembled into 3D structures from the bottom up. Han et al. [93] fabricated a ZIHC based on 3D nanostructures graphene and polyaniline composites as cathodes (Figure 8b). It shows an energy density of 205 Wh kg^{-1} (0.1 A g^{-1}). From Figure 8c, it can still maintain 80.5% of the initial capacity after 6000 cycles of repeated charging and discharging. However, these high-porosity materials always present low bulk density and high weight capacitance. It reduces the volume capacitance and hinders the practical application of the device [88]. Therefore, it is very necessary to develop highly dense structures. Zheng's group [94] prepared a high-density nanoparticle 3D porous graphene (3D-PG-1) through capillary evaporation. The pores formed through the evaporation process provide extensive pathways for the rapid diffusion of Zn^{2+}. It also weakens the strong electrostatic force of Zn^{2+} embedded in the structure. This ensures that the electrode achieves 30,000 stable cycles (Figure 8d).

Recently, graphene-derived 3D network/aerogel structures have been identified to enhance the number of active sites in electrode materials. Compared with conventional graphene films, graphene aerogels feature stable 3D networks and high pore volumes [95]. Okhay et al. [96] synthesized reduced graphene oxide aerogels with optimal properties by tuning the freeze-drying conditions. The graphene oxide composite electrode demonstrates favorable uniformity and surface wettability with a specific capacitance of 129 F g^{-1} at 0.1 A g^{-1}.

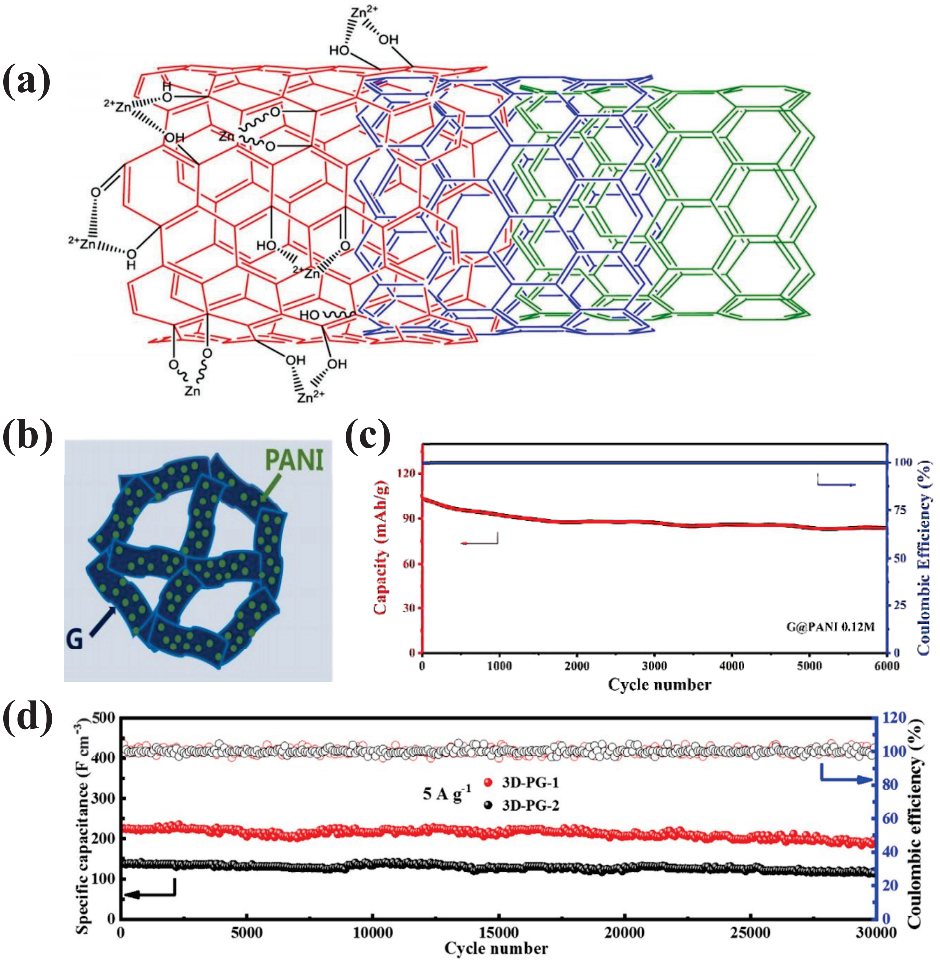

Figure 8. The electrochemical performance of the other carbon electrodes. (**a**) Schematic of zinc ion adsorption on the surface of oCNTs electrode, Reproduced with permission [24], Copyright 2016, Frontiers. (**b**) 3D cross-linked structure of graphene@PANI materials (**c**) The cycle stability of graphene@PANI electrode at 5 A g^{-1}. Reproduced with permission [93], Copyright 2018, Royal Society of Chemistry. (**d**) Long cycle stability at 5 A g^{-1}. Reproduced with permission [94], Copyright 2021, Elsevier Ltd.

4. Modification Strategies

These carbon materials suffer from many issues as electrode materials, including structural instability, poor wettability, and slow electrochemical kinetic. This hinders efficient carrier transport. Therefore, it is essential to modify the carbon-based materials to mitigate these adverse effects. Researchers have proposed several effective strategies, including surface modification, morphology and size tuning, and heterogeneous atom doping.

4.1. Surface Modification

To further improve the cycle stability, it is a feasible method to construct novel carbon-based composites. Xin et al. [97] prepared a poly(4,40-thiodiphenol, TDP)-modified nanoporous AC cathode material. The introduction of this polymer increases the capacitance contribution and broadens the voltage window to 1.9 V through the faraday process. The areal energy density of the device is 1.03 mWh cm^{-2}, and the corresponding power density can reach 0.9 mW cm^{-2}. The increase in voltage is related to their charge storage mechanism. During the charging, Zn^{2+} first extracts from the cathode due to strong electrostatic interaction. Then, H^+ is released from the carbonyl group of poly(4,40-TDP). This continuous extraction leads to a wide voltage window of the device. The interfacial redox reaction is also a viable strategy for increasing the energy density of the device.

Ramanujam's group [98] synthesized a porous AC from chitosan and N, N′-bis(glycinyl) naphthalene diimide (H_2BNDI) composite electrode material. The porous structure can reduce the transmission path of ions to facilitate the rapid transfer of ions. The presence of oxygen functional groups and N-enriched sites on the electrode surface can provide additional pseudocapacitance. Therefore, the fabricated devices deliver a specific capacitance of 500 F g^{-1} with an energy density of 250 Wh kg^{-1} at 0.1 A g^{-1}.

Graphene and CNT materials produce severe agglomeration and re-stacking. This significantly reduces their actual specific surface area and causes a reduction in the specific capacity. To address these drawbacks, it is necessary to fabricate composites with optimal structures. It is a common approach to prevent agglomeration by functionalizing graphene oxide with redox-active organic molecules. For example, Chen's group [99] introduced the p-phenylenediamine (PPD) into the interlayer of the graphene film. This enlarges the interlayer distance and exposes more ion-accessible regions. In addition, the partial reduction of the amino group improves the conductivity of the RGO film. Benefiting from the redox activity of PPD, the RGO@PPD film electrode shows high pseudocapacitance and EDLC for charge storage. Yang et al. [100] prepared a composite electrode of electrochemical graphene oxide (EGO) and polypyrrole (PPy) by one-step electrochemical co-deposition. The Zn-PPy/EGO hybrid capacitor obtains an energy density of 72.1 Wh kg^{-1} at 12.4 kW kg^{-1} and maintains the long-term cycle stability of 81% after 5000 cycles. Compared with chemical graphene oxide (CGO), EGO material possesses strong π-π interaction with PPy due to less structural destruction of graphene [101]. It is beneficial to enhance the conductivity of the composite material.

The lamination issue between 2D nanosheets can be effectively resolved by introducing additional dimensional materials, such as 1D carbon nanotubes [102,103]. Zhang and co-workers [104] developed kapok-derived N- and P-rich 2D thin-walled microporous carbon tiles (CTs). Leveraging the superior conductivity of single-walled carbon nanotubes (SWNTs), they constructed CT/SWNT porous paper cathodes with considerable specific surface area. The uniformly doped thin walled (~700 nm) structure can effectively shorten the ion diffusion path. The submicron layer spacing between the CTs with suitable curvature and carbon nanotubes builds a fast ion/charge transport channel. Based on this synergistic effect, this carbon cathode delivers a specific capacity of 127.6 mAh g^{-1} at 0.1 A g^{-1}. Even at 20 A g^{-1}, its specific capacity can still be kept at 72.4 mAh g^{-1}.

4.2. Morphology Regulation

The microstructure of carbon materials plays a pivotal role in regulating the electrochemical performance of energy storage devices. Carbon materials can be generally categorized into 0D carbon spheres, 1D carbon nanofibers, 2D carbon nanosheets, and 3D porous structures [30]. According to various preparation approaches, carbon spheres can be adjusted into hollow, yolk–shell, and core–shell structures. It possesses favorable conductivity and controllable particle size distribution. The hollow architecture facilitates the rapid transport of carriers and relieves the volume expansion in the long-term cycle [105].

The template method is commonly utilized to prepare hollow structures. Yan's group [106] synthesized mesoporous hollow carbon spheres by the SiO_2 template method. They are used as cathodes and MCHSs-coated Zn foils as anodes to assemble hybrid capacitors in 2M $ZnSO_4$ electrolyte. The nanostructures of MCHSs electrodes provide abundant ion diffusion channels. In addition, the cladding layer inhibits the growth of dendrites/protrusions on the Zn anode surface. Based on the above advantages, the devices show a high energy density of 129.3 Wh kg^{-1} at 266.4 W kg^{-1} and a cycle retention of 96% after 10,000 cycles at 1 A g^{-1}. Further, they found that the capacity of the devices with different mass loadings decayed as the mass of the active substance increased. This is attributed to the sluggish ion and charge transport of thick electrodes. Nonetheless, the device can still achieve a specific capacity of 110 mAh g^{-1} at a high mass loading (20 mg cm^{-2}). Chen et al. [107] reported a copolymer-derived (polyaniline-co-polypyrrole) hollow carbon sphere using surfactant as a soft template. This cavity sphere possesses a high surface area, which facilitates the increase of the active site of the electrode. The hollow structure expands the contact area between electrode and electrolyte. Therefore, the assembled capacitor shows an energy density of 59.7 Wh kg^{-1} and a power density of 447.8 W kg^{-1}. In addition, it can be stably cycled 15,000 times at 1 A g^{-1} with less capacity loss (2%).

4.3. Heteroatom Doping

Carbon materials doped with N, S, P, B, and other heteroatoms are increasingly gaining attention due to their high electron mobility and enhanced energy storage capacity [67,108,109]. The interaction between the heteroatoms and the host material improves the adsorption of electrolyte ions as well as optimizing the surface wettability and conductivity. This promotes rapid charge transfer, which effectively accelerates the point electrochemical kinetics. We mentioned above that the AC cathode suffers from a low practical specific capacity. In addition, it shows weak wettability at the interface with the electrolyte. This constrains the longevity of the device at high current densities [110]. Due to the formation of polar functional groups, the combination of N and O in carbon materials enhances the interaction with electrolytes, thus improving wettability. Wang et al. [111] reported that doping onion-like carbon with N and P elements significantly increased the surface area available for ion adsorption. The assembled N, P-OLC-based devices provide 63% capacity retention at 20 A g^{-1}. Their energy and power densities are 149.5 Wh kg^{-1} and 26.7 kW kg^{-1}. Among them, the doping of N significantly increases the hydrophilicity of the electrode interface, thus optimizing the contact resistance between the electrode and the electrolyte. Also, a nitric acid treatment can provide oxygen-containing functional groups on the surface of porous carbon, which contributes to the improvement of wettability [112]. Therefore, the device can obtain superior rate performance at high current density [113].

Dong's group [114] constructed a fiber-carbon cathode HPCF with a layered porous surface and O/N functional groups. The surface of the electrode contains a large number of micropores to provide high capacity, and the mesopores and macropores can ensure superior rate capability (Figure 9a). The CV curve further reveals that HPCF cathodes store more Zn^{2+} cations and ${SO_4}^{2-}$ anions at high scanning rates. This indicates that most of the stored charge of the cathode comes from ${SO_4}^{2-}$ anion storage. Figure 9b shows the capacitance contribution of the electrode gradually increases with the scanning rate. The reason could be that the rich N/O heteroatoms in HPCF cathode can enhance the interaction between pseudocapacitance behavior and electrolyte ions. The mechanism of charge storage is explored through combining various characterization methods. When the electrode is in the discharge state, $Zn_4SO_4(OH)_6{\cdot}5H_2O$ flakes (BZS) appear. At charging, most of the flakes disappear. This may be due to the following reactions:

$$4Zn^{2+} + 6OH^- + {SO_4}^{2-} + 5H_2O \rightarrow Zn_4SO_4(OH)_6{\cdot}5H_2O\downarrow, \quad (2)$$

In addition, the H+ provided by the acidic electrolyte adsorbs on the electrode surface, which results in an increase in the pH of the electrolyte. This suppresses the hydrogen evolution potential of the electrolyte. Only BZS products are detected in the structure of the HPCF cathode. This further confirms the energy storage mechanism of ion adsorption/desorption occurring at the surface of the electrode. Zheng et al. [69] designed an O-doped 3D porous carbon material. The combination of 3D porous structure and oxygen-containing functional group can endow the electrode with fast ion/electron transport and strong pseudocapacitance. The assembled flexible device can be recharged and discharged 10,000 times at 1.0 A g^{-1} with a capacity retention rate of 87.6%. Zhang's group [115] utilized potassium chloroacetate ($ClCH_2COOK$) as a carbon source and template to form oxygen-enriched porous carbon (ORCs) with an average pore size of 1.95–2.19 nm. This strategy can construct ORCs with high oxygen doping (4.38 atomic%). As a cathode material, it shows high EDLC and pseudocapacitance.

However, excessive oxygen functional groups can diminish the interaction between electrolyte ions and the carbon surface, which induces the aggravation of the self-discharge behavior. This directly inhibits the dynamic process of the device [85]. Yuan et al. [116] modulated the temperature range during their hydrogen thermal reduction process to prepare superior starch-based porous carbon materials. It reveals the structural evolution of the reactive deoxygenation process. The results indicate that the pyrolysis and hydrogenation of oxygen functional groups may occur simultaneously. Among them, the HAC-700 electrode can be maintained for 10 h at an open-circuit voltage of 2.29 V, demonstrating strong resistance to self-discharge (Figure 9c). This may be associated with the suitable pore size in the carbon skeleton and the consumption of instable COOH and R-COOR groups. They can effectively improve the wettability of the electrode and prevent the electrolyte from irreversibly reacting with the unstable oxygen functional groups on the carbon electrode surface.

The addition of N can reduce the energy barrier of C-O interaction with Zn ions [117]. Lu's group [37] constructed capacitors with a lifetime of 100,000 cycles based on nitrogen-doped layered porous carbon (HNPC) as the cathode (Figure 9d). The existence of the N element optimizes the conductivity, electrochemical active surface area (ECSA) of the electrode, and surface wettability. It also improves the efficient transfer of ions/electrons and ensures sufficient storage space for charges. DFT calculation reveals the whole process of zinc ion adsorption and desorption. The adsorption of zinc ions causes the O-H bond to form a C-O-Zn bond, resulting in the release of H^+ ions. In Figure 9e, the reaction of an N-doped HNPC electrode only needs to overcome the energy barrier of 1.25 eV (2.13 eV for an undoped electrode). It effectively promotes the chemical adsorption of Zn ions on the electrode surface.

Biomass-derived porous carbon possesses inherent functional groups, or heteroatoms. It can offer sufficient active sites and surface wettability for the reaction. Therefore, the addition of chemical activators can further increase the specific surface area and optimize the pore structure, which is beneficial to the improvement of electrochemical performance. Wang et al. [118] proposed a novel potassium thioacetate activation technique. The pine needles are pyrolyzed as a carbon source to produce sulfur-doped 3D porous carbon (S-3DPCs). The prepared S-3DPCs material shows a specific surface area of 2336.9 $m^2\ g^{-1}$ and a certain amount of sulfur (0.88–3.60 at%). Therefore, the capacitor assembled with the S-3DPC-800 positive electrode can provide a specific capacity of 203.3 mAh g^{-1} (0.2 A g^{-1}) and 81 mAh g^{-1} (20 A g^{-1}). In addition, it can be recycled 18,000 times at 10 A g^{-1}, and the specific capacity retention reaches 96.8%.

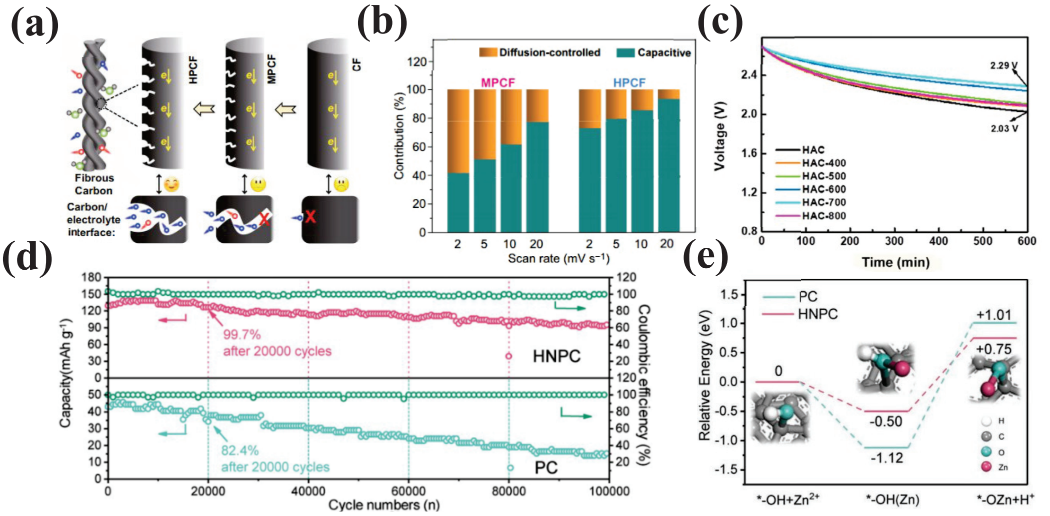

Figure 9. Performance of doped carbon-based materials. (**a**) Schematic of energy storage on cathodes with various surface conditions. (**b**) Contribution ratio of charge storage behavior. Reproduced with permission [114], Copyright 2021, Springer Nature. (**c**) Leakage current curves. Reproduced with permission [116], Copyright 2020, Elsevier B.V. and Science Press. (**d**) Cycling stability. (**e**) The energy profiles.* represents C atom. Reproduced with permission [37], Copyright 2019, Wiley-VCH.

Lu and his collaborators [119] designed the activation mechanism of microporous carbon (DSPCs) derived from sodium alginate through double templates. Highly active micropores (about 0.7–2.0 nm) endow the material with reasonable specific surface area and rich reaction sites. The assembled device shows an energy density of 99.22 Wh kg^{-1} (200 W kg^{-1}). The reversible specific capacity of the electrode is 87.5 mAh g^{-1} at 0.2 A g^{-1}. The capacity of 18.1 mAh g^{-1} can be maintained when the current density rises to 40 A g^{-1}.

In Table 1, we summarize the electrochemical performance of the various carbon-based electrodes. All of these electrode materials can achieve a long cycle life up to more than 10,000 cycles. Among them, the specific capacity of the hierarchical porous material is higher than that of the AC material. Oxygen-rich carbon electrodes can show a cycle life of more than 20,000 cycles. The atom-doped electrode materials demonstrate a long cycle life of up to 60,000 cycles with a capacity retention of 98.9% and a maximum power density of 48.8 kW kg^{-1}.

Table 1. The electrochemical performance of the various electrodes for ZIHCs.

Cathode	Electrolyte	Voltage (V)	Capacity/ Current Density (mAh g^{-1}/A g^{-1})	Capacity Retention/ Current Density/ The Long-Term Cycle (%/A g^{-1}/cycles)	Energy Density (Wh kg^{-1})	Power Density (kW kg^{-1})	Refs.
AC	2M $ZnSO_4$	0.2–1.8	121/0.1	91/10/10,000	30	14.9	[25]
O-rich porous carbon	3 M $Zn(ClO_4)_2$	0–1.9	179.8/0.1	99.2/20/30,000	40.4	48.8	[31]
Mesoporous AC	2M $ZnSO_4$	0.3–1.8	176/0.5	78/10/40,000	77	10.7	[66]
Porous AC	3M $Zn(CF_3SO_3)_2$	0.01–1.8	231/0.5	70/10/18,000	77.5	11.4	[80]
N doped pitch-derived carbon	1 M $ZnSO_4$	0–1.8	136.2/0.3	98.9/10/60,000	81.1	12.8	[81]
Porous carbon	1M $Zn(CF_3SO_3)_2$	0.2–1.8	183.7/0.2	92.2/10/10,000	65.4	15.7	[83]
O-rich porous carbon	2M $ZnSO_4$	0.2–1.8	317.8/0.5	91/10/20,000	136.3	20	[86]
O-enriched carbon fiber	gelatin/$ZnSO_4$ gel	0.2–1.8	136.4/0.1	81/5/50,000	97.7	9.9	[89]
3D graphene@PANI composite	2M $ZnSO_4$	0.3–1.6	154/0.1	80.5/5/6000	205	45.8	[93]
3D graphene	3M $Zn(CF_3SO_3)_2$	0.1–1.8	299 F cm^{-3}/0.1	85/5/30,000	61 Wh/L	23.2 kW/L	[94]
H_2BNDI@Ch-C	2 M $ZnSO_4$	0.1–1.9	500/0.1	80/5/10,000	55	9.5	[98]
PPy/EGO	1 M $ZnCl_2$	0.5–1.5	444.2/0.35	81/5 mA cm^{-2}/5000	72.1	12.4	[100]
Hollow carbon spheres	2M $ZnSO_4$	0.2–1.8	174.7/0.1	96/1/10,000	36.8	13.7	[106]
S-doped 3D porous carbon	2M $ZnSO_4$	0.2–1.8	203.3/0.2	96.8/10/18,000	64.8	16	[118]

5. Summary and Outlook

In summary, carbon-based materials are of interest owing to their structural diversity, superior electrical conductivity, and large specific surface area. These features render them crucial electrode materials in ZIHCs. We concentrate on the research advances of carbon cathode and discuss their energy storage mechanism, electrochemical performance, and electrode material structure optimization strategies. Some progress has been achieved, but there are still challenges in applications, especially in improving the energy power density and specific capacitance. At present, ZIHCs are in the infancy stage of growth, and more efforts are needed to propose new innovations to overcome these problems (Figure 10).

1. It is still difficult to identify the energy storage mechanism of ZIHCs. In the current study, carbon materials are often compounded with some materials for structural optimization in order to increase the specific capacity of electrodes. The pseudocapacitance during charge storage provides a partial contribution rather than simple ion adsorption/desorption. Furthermore, there is no complete clarification about the contribution ratio of the charge storage behavior. The combination of first-principles calculations, electrochemical kinetic analysis, and in situ structural characterization can also illustrate the structural changes of the electrode during charging and discharging and reveal the energy storage mechanism. The effect of by-product generation on electrode performance is still controversial.
2. Carbon-based electrode materials inherently show low specific capacitance and poor energy density. Suitable structural modifications, including heteroatom doping, microstructure modulation, and surface modification, can effectively improve the charge storage capacity of carbon-based materials. However, the constitutive relationship and intrinsic connection between structural improvement and electrochemical performance are still not clearly explained.

3. Commercially available zinc foils are usually the counter electrodes of the devices. Although they present high theoretical capacity, issues such as dendrite growth, corrosion, and HER reactions limit the high performance of ZIHCs. Therefore, it is essential to develop the structural design of anode materials to facilitate their advancement. For example, 3D nanostructured zinc electrodes possess rich active sites and a large electrolyte/electrode contact area. The uniformly distributed electric field can retard the growth of dendrites and promote the diffusion of ions.
4. Fully charged hybrid capacitors often suffer from spontaneous charge loss and voltage drop, resulting in self-discharge. The existence of the self-discharge process limits its market application. For carbon-based electrodes, ash and oxygen-containing functional groups can weaken the interaction between electrolyte ions and the electrode surface and enhance the self-discharge rate. In addition, the pore effect of porous structures leads to the redistribution of charges in carbon materials. We should also focus on the self-discharge behavior of devices in diverse working conditions. The corresponding approach is established to suppress the self-discharge of the device.

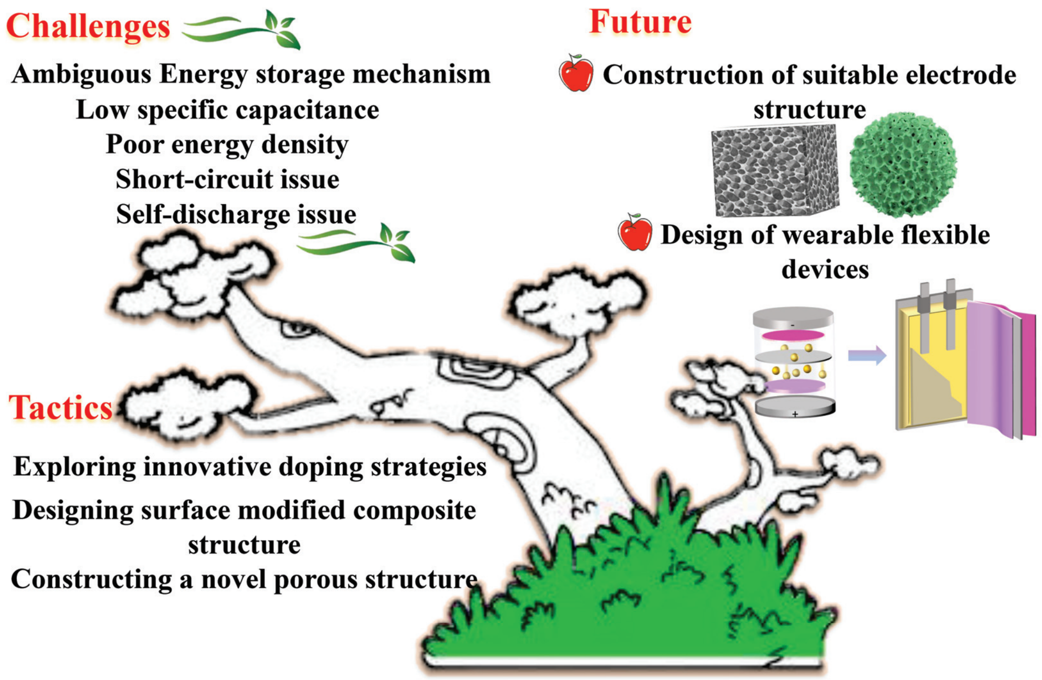

Figure 10. Challenges, tactics, and future goals for carbon-based electrodes of ZIHCs.

In the future, we consider that ZIHCs should concern the following aspects:

1. It is necessary to explore novel electrode material synthesis tactics to obtain porous carbon with favorable pore size and electrolyte ion compatibility. Various carbon-based precursor materials, such as biomass, asphalt, and polymers, possess diverse physical and chemical properties. It is helpful to design reasonable approaches according to their properties to give full play to the characteristics of raw materials and avoid their shortcomings.
2. The development of gel electrolyte is in line with the future development trend. Ordinary diaphragm is easy to be pierced by zinc branches in long-term circulation, resulting in a short circuit. Hydrogel electrolyte shows certain flexibility and mechanical strength, which can effectively slow down the growth of zinc dendrites. In addition, with the development of wearable flexible devices, positive and negative electrodes as well as the matching of the diaphragm are a key concern. The electrodes of flexible capacitors need to meet the characteristics of superior mechanical flexibility, light weight, and high-pressure resistance. For instance, Wu's group [120] prepared a super-folded conductive carbon material based on the bionic design idea of silkworm

spinning–cocooning–reeling, which can withstand 1 million or even unlimited folds without any damage. These structural materials possess superior mechanical properties. Their integration with ZIHCs can greatly improve the durability and life of devices. This synergy can promote the technological innovation of wearable devices.

3. Combining advanced in situ characterization techniques, it allows an intensive investigation into the structure of the electrodes and the dynamic changes in the energy storage process. It is essential for revealing the electrode energy storage process. Also, the structural design of electrode materials combined with theoretical calculation can provide theoretical guidance for structural stability, reaction-free energy, ion adsorption, diffusion, and reaction processes.

Author Contributions: Conceptualization, investigation, and resources, Y.L., L.S. and C.L.; writing—original draft preparation, Y.L. and C.S.; writing—review and editing, Y.L., C.S., L.S., C.L. and X.W.; visualization, Y.L. and C.S.; supervision, Y.L. and X.W. All authors have read and agreed to the published version of the manuscript.

Funding: This research was funded by the Technology Development Contract of Sinopec, grant number: 122013.

Data Availability Statement: All data used for this work are included within the manuscript.

Conflicts of Interest: Authors Ying Liu, Lechun Song, Chenze Li and Caicheng Song were employed by the company SINOPEC Dalian (Fushun) Research Institute of Petroleum and Petrochemicals. The remaining author declare that the research was conducted in the absence of any commercial or financial relationships that could be construed as a potential conflict of interest.

References

1. Huang, Y.; Zhu, M.; Huang, Y.; Pei, Z.; Li, H.; Wang, Z.; Xue, Q.; Zhi, C. Multifunctional Energy Storage and Conversion Devices. *Adv. Mater.* **2016**, *28*, 8344–8364. [CrossRef] [PubMed]
2. Zheng, M.; Tang, H.; Hu, Q.; Zheng, S.; Li, L.; Xu, J.; Pang, H. Tungsten-Based Materials for Lithium-Ion Batteries. *Adv. Funct. Mater.* **2018**, *28*, 1707500. [CrossRef]
3. Ue, M.; Sakaushi, K.; Uosaki, K. Basic knowledge in battery research bridging the gap between academia and industry. *Mater. Horiz.* **2020**, *7*, 1937–1954. [CrossRef]
4. Wang, H.; Zhu, C.; Chao, D.; Yan, Q.; Fan, H.J. Nonaqueous Hybrid Lithium-Ion and Sodium-Ion Capacitors. *Adv. Mater.* **2017**, *29*, 1702093. [CrossRef] [PubMed]
5. Dong, L.; Yang, W.; Yang, W.; Li, Y.; Wu, W.; Wang, G. Multivalent metal ion hybrid capacitors: A review with a focus on zinc-ion hybrid capacitors. *J. Mater. Chem. A* **2019**, *7*, 13810–13832. [CrossRef]
6. Liu, H.; Zhao, D.; Hu, P.; Wu, X. Ternary core-shell structured transition metal chalcogenide for hybrid electrochemical capacitor. *Chin. Chem. Lett.* **2018**, *29*, 1799–1803. [CrossRef]
7. Yang, Y.; Yang, S.; Xue, X.; Zhang, X.; Li, Q.; Yao, Y.; Rui, X.; Pan, H.; Yu, Y. Inorganic All-Solid-State Sodium Batteries: Electrolyte Designing and Interface Engineering. *Adv. Mater.* **2024**, *36*, 2308332. [CrossRef]
8. Sun, J.; Zhang, Q.; Liu, C.; Zhang, A.; Hou, L.; Yuan, C. Conductive Zinc-Based Metal–Organic Framework Nanorods as Cathodes for High-Performance Zn-Ion Capacitors. *Batteries* **2024**, *10*, 222. [CrossRef]
9. Zhou, J.; Hu, H.-Y.; Li, H.-Q.; Chen, Z.-P.; Yuan, C.-Z.; He, X.-J. Advanced carbon-based materials for Na, K, and Zn ion hybrid capacitors. *Rare Met.* **2023**, *42*, 719–739. [CrossRef]
10. Liu, Y.; Liu, Y.; Wu, X.; Cho, Y.-R. Enhanced Electrochemical Performance of Zn/VO_x Batteries by a Carbon-Encapsulation Strategy. *ACS Appl. Mater. Interfaces* **2022**, *14*, 11654–11662. [CrossRef]
11. Zhao, D.; Wang, X.; Zhang, W.; Zhang, Y.; Lei, Y.; Huang, X.; Zhu, Q.; Liu, J. Unlocking the Capacity of Vanadium Oxide by Atomically Thin Graphene-Analogous $V_2O_5{\cdot}nH_2O$ in Aqueous Zinc-Ion Batteries. *Adv. Funct. Mater.* **2023**, *33*, 2211412. [CrossRef]
12. Liu, Y.; Liu, Y.; Wu, X. Rational design of bi-phase CaV_2O_6/NaV_6O_{15} cathode materials for long-life aqueous zinc batteries. *EcoMat* **2023**, *5*, e12409. [CrossRef]
13. Blanc, L.E.; Kundu, D.; Nazar, L.F. Scientific Challenges for the Implementation of Zn-Ion Batteries. *Joule* **2020**, *4*, 771–799. [CrossRef]
14. Liu, Y.; Wu, X. Review of vanadium-based electrode materials for rechargeable aqueous zinc ion batteries. *J. Energy Chem.* **2021**, *56*, 223–237. [CrossRef]
15. Tang, B.; Shan, L.; Liang, S.; Zhou, J. Issues and opportunities facing aqueous zinc-ion batteries. *Energy Environ. Sci.* **2019**, *12*, 3288–3304. [CrossRef]

16. Liu, Y.; Wu, X. High durable aqueous zinc ion batteries by synergistic effect of V_6O_{13}/VO_2 electrode materials. *J. Energy Chem.* **2023**, *87*, 334–341. [CrossRef]
17. Sun, Y.; Liu, B.; Liu, L.; Lang, J.; Qiu, J. A Low-Concentration and High Ionic Conductivity Aqueous Electrolyte toward Ultralow-Temperature Zinc-Ion Hybrid Capacitors. *Small Struct.* **2023**, *4*, 2200345. [CrossRef]
18. Liu, Y.; Zhao, D.; Liu, H.; Umar, A.; Wu, X. High performance hybrid supercapacitor based on hierarchical MoS_2/Ni_3S_2 metal chalcogenide. *Chin. Chem. Lett.* **2019**, *30*, 1105–1110. [CrossRef]
19. Muzaffar, A.; Ahamed, M.B.; Deshmukh, K.; Thirumalai, J. A review on recent advances in hybrid supercapacitors: Design, fabrication and applications. *Renew. Sust. Energy Rev.* **2019**, *101*, 123–145. [CrossRef]
20. Liu, Y.; Umar, A.; Wu, X. Metal-organic framework derived porous cathode materials for hybrid zinc ion capacitor. *Rare Met.* **2022**, *41*, 2985–2991. [CrossRef]
21. Yu, L.; Li, J.; Ahmad, N.; He, X.; Wan, G.; Liu, R.; Ma, X.; Liang, J.; Jiang, Z.; Zhang, G. Recent progress on carbon materials for emerging zinc-ion hybrid capacitors. *J. Mater. Chem. A* **2024**, *12*, 9400–9420. [CrossRef]
22. Miao, L.; Lv, Y.; Zhu, D.; Li, L.; Gan, L.; Liu, M. Recent advances in zinc-ion hybrid energy storage: Coloring high-power capacitors with battery-level energy. *Chin. Chem. Lett.* **2023**, *34*, 107784. [CrossRef]
23. Lal, M.S.; Arjunan, A.; Balasubramanian, V.; Sundara, R. Redox-active polymer hydrogel electrolyte in biowaste-derived microporous carbon-based high capacitance and energy density ultracapacitors. *J. Electroanal. Chem.* **2020**, *870*, 114236. [CrossRef]
24. Tian, Y.; Amal, R.; Wang, D.-W. An Aqueous Metal-Ion Capacitor with Oxidized Carbon Nanotubes and Metallic Zinc Electrodes. *Front. Energy Res.* **2016**, *4*, 34. [CrossRef]
25. Dong, L.; Ma, X.; Li, Y.; Zhao, L.; Liu, W.; Cheng, J.; Xu, C.; Li, B.; Yang, Q.H.; Kang, F. Extremely safe, high-rate and ultralong-life zinc-ion hybrid supercapacitors. *Energy Storage Mater.* **2018**, *13*, 96–102. [CrossRef]
26. Li, Z.; An, Y.; Dong, S.; Chen, C.; Wu, L.; Sun, Y.; Zhang, X. Progress on zinc ion hybrid supercapacitors: Insights and challenges. *Energy Storage Mater.* **2020**, *31*, 252–266. [CrossRef]
27. Ma, X.; Cheng, J.; Dong, L.; Liu, W.; Mou, J.; Zhao, L.; Wang, J.; Ren, D.; Wu, J.; Xu, C.; et al. Multivalent ion storage towards high-performance aqueous zinc-ion hybrid supercapacitors. *Energy Storage Mater.* **2019**, *20*, 335–342. [CrossRef]
28. Sun, Y.; Shi, X.L.; Yang, Y.L.; Suo, G.Q.; Zhang, L.; Lu, S.Y.; Chen, Z.G. Biomass-Derived Carbon for High-Performance Batteries: From Structure to Properties. *Adv. Funct. Mater.* **2022**, *32*, 2201584. [CrossRef]
29. Li, X.; Wei, B.Q. Supercapacitors based on nanostructured carbon. *Nano Energy* **2013**, *2*, 159–173. [CrossRef]
30. Liu, Y.; Wu, L. Recent advances of cathode materials for zinc-ion hybrid capacitors. *Nano Energy* **2023**, *109*, 108290. [CrossRef]
31. Yin, J.; Zhang, W.; Wang, W.; Alhebshi, N.A.; Salah, N.; Alshareef, H.N. Electrochemical Zinc Ion Capacitors Enhanced by Redox Reactions of Porous Carbon Cathodes. *Adv. Energy Mater.* **2020**, *10*, 2001705. [CrossRef]
32. Fan, X.; Liu, P.; Ouyang, B.; Cai, R.; Chen, X.; Liu, X.; Liu, W.; Wang, J.; Liu, K. Polyacrylonitrile Derived Porous Carbon for Zinc-Ion Hybrid Capacitors with High Energy Density. *ChemElectroChem* **2021**, *8*, 3572–3578. [CrossRef]
33. Li, Y.; Lu, P.; Shang, P.; Wu, L.; Wang, X.; Dong, Y.; He, R.; Wu, Z.-S. Pyridinic nitrogen enriched porous carbon derived from bimetal organic frameworks for high capacity zinc ion hybrid capacitors with remarkable rate capability. *J. Energy Chem.* **2021**, *56*, 404–411. [CrossRef]
34. Huang, Z.; Wang, T.; Song, H.; Li, X.; Liang, G.; Wang, D.; Yang, Q.; Chen, Z.; Ma, L.; Liu, Z.; et al. Effects of Anion Carriers on Capacitance and Self-Discharge Behaviors of Zinc Ion Capacitors. *Angew. Chem. Int. Ed.* **2020**, *60*, 1011–1021. [CrossRef]
35. Kühnel, R.-S.; Reber, D.; Battaglia, C. A High-Voltage Aqueous Electrolyte for Sodium-Ion Batteries. *ACS Energy Lett.* **2017**, *2*, 2005–2006. [CrossRef]
36. Tan, J.; Liu, J. Electrolyte Engineering Toward High-Voltage Aqueous Energy Storage Devices. *Energy Environ. Mater.* **2020**, *4*, 302–306. [CrossRef]
37. Zhang, H.; Liu, Q.; Fang, Y.; Teng, C.; Liu, X.; Fang, P.; Tong, Y.; Lu, X. Boosting Zn-Ion Energy Storage Capability of Hierarchically Porous Carbon by Promoting Chemical Adsorption. *Adv. Mater.* **2019**, *31*, 1904948. [CrossRef]
38. Whittingham, M.S.; Siu, C.; Ding, J. Can Multielectron Intercalation Reactions Be the Basis of Next Generation Batteries? *Acc. Chem. Res.* **2018**, *51*, 258–264. [CrossRef]
39. Thomas, M.G.S.R.; Bruce, P.G.; Goodenough, J.B. Lithium Mobility in the Layered Oxide $Li_{1-x}COO_2$. *Solid State Ion.* **1985**, *17*, 13–19. [CrossRef]
40. Amatucci, G.G.; Badway, F.; Pasquier, A.D.; Zheng, T. An Asymmetric Hybrid Nonaqueous Energy Storage Cell. *J. Electrochem. Soc.* **2001**, *148*, A930. [CrossRef]
41. Raza, W.; Ali, F.; Raza, N.; Luo, Y.; Kim, K.-H.; Yang, J.; Kumar, S.; Mehmood, A.; Kwon, E.E. Recent advancements in supercapacitor technology. *Nano Energy* **2018**, *52*, 441–473. [CrossRef]
42. Simon, P.; Gogotsi, Y.; Dunn, B. Where Do Batteries End and Supercapacitors Begin? *Science* **2014**, *343*, 1210–1211. [CrossRef] [PubMed]
43. Zan, G.; Li, S.; Chen, P.; Dong, K.; Wu, Q.; Wu, T. Mesoporous Cubic Nanocages Assembled by Coupled Monolayers With 100% Theoretical Capacity and Robust Cycling. *ACS Cent. Sci.* **2024**, *10*, 1283–1294. [CrossRef] [PubMed]
44. Gui, Q.; Ba, D.; Li, L.; Liu, W.; Li, Y.; Liu, J. Recent advances in materials and device technologies for aqueous hybrid supercapacitors. *Sci. China Mater.* **2021**, *65*, 10–31. [CrossRef]
45. Zuo, W.; Li, R.; Zhou, C.; Li, Y.; Xia, J.; Liu, J. Battery-Supercapacitor Hybrid Devices: Recent Progress and Future Prospects. *Adv Sci* **2017**, *4*, 1600539. [CrossRef]

46. Wu, X.; Yao, S. Flexible electrode materials based on WO_3 nanotube bundles for high performance energy storage devices. *Nano Energy* **2017**, *42*, 143–150. [CrossRef]
47. Yan, J.; Wang, Q.; Wei, T.; Fan, Z. Recent Advances in Design and Fabrication of Electrochemical Supercapacitors with High Energy Densities. *Adv. Energy Mater.* **2014**, *4*, 1300816. [CrossRef]
48. Liu, C.; Wu, X.; Wang, B. Performance modulation of energy storage devices: A case of Ni-Co-S electrode materials. *Chem. Eng. J.* **2020**, *392*, 123651. [CrossRef]
49. Liu, H.; Dai, M.; Zhao, D.; Wu, X.; Wang, B. Realizing Superior Electrochemical Performance of Asymmetric Capacitors through Tailoring Electrode Architectures. *ACS Appl. Energy Mater.* **2020**, *3*, 7004–7010. [CrossRef]
50. Lv, Y.; Zhang, L.; Wei, X.; Qiu, B.; Zhang, W.; Qin, Q.; Jia, D.; He, X.; Liu, Z.; Wei, F. The emerging of zinc-ion hybrid supercapacitors: Advances, challenges, and future perspectives. *Sustain. Mater. Technol.* **2023**, *35*, e00536. [CrossRef]
51. Wang, Y.; Sun, S.; Wu, X.; Liang, H.; Zhang, W. Status and Opportunities of Zinc Ion Hybrid Capacitors: Focus on Carbon Materials, Current Collectors, and Separators. *Nano Micro Lett.* **2023**, *15*, 78. [CrossRef] [PubMed]
52. Sui, D.; Wu, M.; Shi, K.; Li, C.; Lang, J.; Yang, Y.; Zhang, X.; Yan, X.; Chen, Y. Recent progress of cathode materials for aqueous zinc-ion capacitors: Carbon-based materials and beyond. *Carbon* **2021**, *185*, 126–151. [CrossRef]
53. Liu, Z.; Duan, C.; Dou, S.; Yuan, Q.; Xu, J.; Liu, W.D.; Chen, Y. Ultrafast Porous Carbon Activation Promises High-Energy Density Supercapacitors. *Small* **2022**, *18*, 2200954. [CrossRef] [PubMed]
54. Selvaraj, A.R.; Muthusamy, A.; Inho, C.; Kim, H.-J.; Senthil, K.; Prabakar, K. Ultrahigh surface area biomass derived 3D hierarchical porous carbon nanosheet electrodes for high energy density supercapacitors. *Carbon* **2021**, *174*, 463–474. [CrossRef]
55. Liu, Y.; Liu, Y.; Wu, X.; Cho, Y.-R. General Carbon Modification Avenue to Construct Highly Stable V_2O_5 Electrodes for Aqueous Zinc-Ion Batteries. *ACS Sustain. Chem. Eng.* **2023**, *11*, 13298–13305. [CrossRef]
56. Jin, J.; Geng, X.; Chen, Q.; Ren, T.-L. A Better Zn-Ion Storage Device: Recent Progress for Zn-Ion Hybrid Supercapacitors. *Nano Micro Lett.* **2022**, *14*, 64. [CrossRef]
57. Pomerantseva, E.; Bonaccorso, F.; Feng, X.; Cui, Y.; Gogotsi, Y. Energy storage: The future enabled by nanomaterials. *Science* **2019**, *366*, eaan8285. [CrossRef]
58. Borchardt, L.; Leistenschneider, D.; Haase, J.; Dvoyashkin, M. Revising the Concept of Pore Hierarchy for Ionic Transport in Carbon Materials for Supercapacitors. *Adv. Energy Mater.* **2018**, *8*, 1800892. [CrossRef]
59. Lee, J.; Kim, J.; Hyeon, T. Recent Progress in the Synthesis of Porous Carbon Materials. *Adv. Mater.* **2006**, *18*, 2073–2094. [CrossRef]
60. Presser, V.; Heon, M.; Gogotsi, Y. Carbide-Derived Carbons-From Porous Networks to Nanotubes and Graphene. *Adv. Funct. Mater.* **2011**, *21*, 810–833. [CrossRef]
61. Borchardt, L.; Oschatz, M.; Kaskel, S. Tailoring porosity in carbon materials for supercapacitor applications. *Mater. Horiz.* **2014**, *1*, 157–168. [CrossRef]
62. Wang, C.; Pei, Z.; Meng, Q.; Zhang, C.; Sui, X.; Yuan, Z.; Wang, S.; Chen, Y. Toward Flexible Zinc-Ion Hybrid Capacitors with Superhigh Energy Density and Ultralong Cycling Life: The Pivotal Role of $ZnCl_2$ Salt-Based Electrolytes. *Angew. Chem. Int. Ed.* **2020**, *60*, 990–997. [CrossRef] [PubMed]
63. Lv, K.; Zhang, J.; Zhao, X.; Kong, N.; Tao, J.; Zhou, J. Understanding the Effect of Pore Size on Electrochemical Capacitive Performance of MXene Foams. *Small* **2022**, *18*, 2202203. [CrossRef] [PubMed]
64. Jian, W.; Zhang, W.; Wei, X.; Wu, B.; Liang, W.; Wu, Y.; Yin, J.; Lu, K.; Chen, Y.; Alshareef, H.N.; et al. Engineering Pore Nanostructure of Carbon Cathodes for Zinc Ion Hybrid Supercapacitors. *Adv. Funct. Mater.* **2022**, *32*, 2209914. [CrossRef]
65. Hulicova Jurcakova, D.; Seredych, M.; Lu, G.Q.; Bandosz, T.J. Combined Effect of Nitrogen- and Oxygen-Containing Functional Groups of Microporous Activated Carbon on its Electrochemical Performance in Supercapacitors. *Adv. Funct. Mater.* **2009**, *19*, 438–447. [CrossRef]
66. An, G.H. Ultrafast long-life zinc-ion hybrid supercapacitors constructed from mesoporous structured activated carbon. *Appl. Surf. Sci.* **2020**, *530*, 147220. [CrossRef]
67. Liu, Y.; Liu, Y.; Wu, X. Defect engineering of vanadium-based electrode materials for zinc ion battery. *Chin. Chem. Lett.* **2023**, *34*, 107839. [CrossRef]
68. Song, C.; Liu, K.; Wang, T.; Zhao, P.-Y.; Huang, H.; Liu, Y.; Lu, R.; Zhang, S. Spontaneous template approach towards nitrogenous multi-shelled hollow carbon spheres with unique onion-like architecture. *Mater. Today Chem.* **2024**, *40*, 102196. [CrossRef]
69. Zheng, Y.; Zhao, W.; Jia, D.; Liu, Y.; Cui, L.; Wei, D.; Zheng, R.; Liu, J. Porous carbon prepared via combustion and acid treatment as flexible zinc-ion capacitor electrode material. *Chem. Eng. J.* **2020**, *387*, 124161. [CrossRef]
70. Zhang, Y.; Wang, Z.; Li, D.; Sun, Q.; Lai, K.; Li, K.; Yuan, Q.; Liu, X.; Ci, L. Ultrathin carbon nanosheets for highly efficient capacitive K-ion and Zn-ion storage. *J. Mater. Chem. A* **2020**, *8*, 22874–22885. [CrossRef]
71. Deng, S.; Yuan, Z.; Tie, Z.; Wang, C.; Song, L.; Niu, Z. Electrochemically Induced MOF-Derived Amorphous V_2O_5 for Superior Rate Aqueous Zn-Ion Batteries. *Angew Chem. Int. Ed.* **2020**, *59*, 22002. [CrossRef] [PubMed]
72. Li, H.; Liao, Q.; Liu, Y.; Li, Y.; Niu, X.; Zhang, D.; Wang, K. Hierarchically Porous Carbon Rods Derived from Metal-Organic Frameworks for Aqueous Zinc-Ion Hybrid Capacitors. *Small* **2023**, *20*, 2307184. [CrossRef] [PubMed]
73. Wang, H.; Shao, Y.; Mei, S.; Lu, Y.; Zhang, M.; Sun, J.-k.; Matyjaszewski, K.; Antonietti, M.; Yuan, J. Polymer-Derived Heteroatom-Doped Porous Carbon Materials. *Chem. Rev.* **2020**, *120*, 9363–9419. [CrossRef] [PubMed]
74. Yang, S.-H.; Fu, W.-Q.; Cui, Y.-W.; Cao, B.-Q. PVP/PAN-derived porous carbon fiber for zinc-ion hybrid supercapacitors. *Rare Met.* **2024**, *43*, 3066–3073. [CrossRef]

75. Zhang, Y.; Wang, L.; Jia, D.; Yue, L.; Zhang, H.; Liu, J. Hierarchical Porous Doped Carbon Plates Derived from Chitosan Aerogel as Cathode for High Performance Zn-ion Hybrid Capacitor. *ChemElectroChem* **2023**, *10*, e202200972. [CrossRef]
76. Pan, L.; Wang, Y.; Hu, H.; Li, X.; Liu, J.; Guan, L.; Tian, W.; Wang, X.; Li, Y.; Wu, M. 3D self-assembly synthesis of hierarchical porous carbon from petroleum asphalt for supercapacitors. *Carbon* **2018**, *134*, 345–353. [CrossRef]
77. Zhang, M.; Sun, Z.; Zhang, T.; Qin, B.; Sui, D.; Xie, Y.; Ma, Y.; Chen, Y. Porous asphalt/graphene composite for supercapacitors with high energy density at superior power density without added conducting materials. *J. Mater. Chem. A* **2017**, *5*, 21757–21764. [CrossRef]
78. Zhang, X.; Tian, X.; Song, Y.; Wu, J.; Yang, T.; Liu, Z. Boosting Zn-ion storage capacity of pitch coke-based activated carbon via pre-oxidation assisted KOH activation strategy. *Micropor. Mesopor. Mater.* **2022**, *333*, 111721. [CrossRef]
79. Yang, Y.; Li, Z.; Zhao, J.; Qu, S. Structural engineering of pitch-based porous carbon and its application in supercapacitors: A review. *J. Energy Storage* **2023**, *74*, 109334. [CrossRef]
80. Zhou, Z.; Zhou, X.; Zhang, M.; Mu, S.; Liu, Q.; Tang, Y. In Situ Two-Step Activation Strategy Boosting Hierarchical Porous Carbon Cathode for an Aqueous Zn-Based Hybrid Energy Storage Device with High Capacity and Ultra-Long Cycling Life. *Small* **2020**, *16*, 2003174. [CrossRef]
81. Shi, X.; Zhang, H.; Zeng, S.; Wang, J.; Cao, X.; Liu, X.; Lu, X. Pyrrolic-Dominated Nitrogen Redox Enhances Reaction Kinetics of Pitch-Derived Carbon Materials in Aqueous Zinc Ion Hybrid Supercapacitors. *ACS Mater. Lett.* **2021**, *3*, 1291–1299. [CrossRef]
82. Saini, S.; Chand, P.; Joshi, A. Biomass derived carbon for supercapacitor applications: Review. *J. Energy Storage* **2021**, *39*, 102646. [CrossRef]
83. Li, Z.; Chen, D.; An, Y.; Chen, C.; Wu, L.; Chen, Z.; Sun, Y.; Zhang, X. Flexible and anti-freezing quasi-solid-state zinc ion hybrid supercapacitors based on pencil shavings derived porous carbon. *Energy Storage Mater.* **2020**, *28*, 307–314. [CrossRef]
84. Zhao, L.; Jian, W.; Zhang, X.; Wen, F.; Zhu, J.; Huang, S.; Yin, J.; Lu, K.; Zhou, M.; Zhang, W.; et al. Multi-scale self-templating synthesis strategy of lignin-derived hierarchical porous carbons toward high-performance zinc ion hybrid supercapacitors. *J. Energy Storage* **2022**, *53*, 105095. [CrossRef]
85. Liu, K.; Yu, C.; Guo, W.; Ni, L.; Yu, J.; Xie, Y.; Wang, Z.; Ren, Y.; Qiu, J. Recent research advances of self-discharge in supercapacitors: Mechanisms and suppressing strategies. *J. Energy Chem.* **2021**, *58*, 94–109. [CrossRef]
86. Li, H.; Su, P.; Liao, Q.; Liu, Y.; Li, Y.; Niu, X.; Liu, X.; Wang, K. Olive Leaves-Derived Hierarchical Porous Carbon as Cathode Material for Anti-Self-Discharge Zinc-Ion Hybrid Capacitor. *Small* **2023**, *19*, 2304172. [CrossRef]
87. He, H.; Lian, J.; Chen, C.; Xiong, Q.; Zhang, M. Super hydrophilic carbon fiber film for freestanding and flexible cathodes of zinc-ion hybrid supercapacitors. *Chem. Eng. J.* **2021**, *421*, 129786. [CrossRef]
88. Li, Z.; Gadipelli, S.; Li, H.; Howard, C.A.; Brett, D.J.L.; Shearing, P.R.; Guo, Z.; Parkin, I.P.; Li, F. Tuning the interlayer spacing of graphene laminate films for efficient pore utilization towards compact capacitive energy storage. *Nat. Energy* **2020**, *5*, 160–168. [CrossRef]
89. Hu, X.; Bao, X.; Zhang, M.; Fang, S.; Liu, K.; Wang, J.; Liu, R.; Kim, S.H.; Baughman, R.H.; Ding, J. Recent Advances in Carbon Nanotube-Based Energy Harvesting Technologies. *Adv. Mater.* **2023**, *35*, 2303035. [CrossRef]
90. Wei, F.; Wei, Y.; Wang, J.; Han, M.; Lv, Y. N, P dual doped foamy-like carbons with abundant defect sites for zinc ion hybrid capacitors. *Chem. Eng. J.* **2022**, *450*, 137919. [CrossRef]
91. Sun, Y.; Zheng, J.; Tong, Y.; Wu, Y.; Liu, X.; Niu, L.; Li, H. Construction of three-dimensional nitrogen doped porous carbon flake electrodes for advanced potassium-ion hybrid capacitors. *J. Colloid Interface Sci.* **2022**, *606*, 1940–1949. [CrossRef] [PubMed]
92. Fang, X.Y.; Yu, X.X.; Zheng, H.M.; Jin, H.B.; Wang, L.; Cao, M.S. Temperature- and thickness-dependent electrical conductivity of few-layer graphene and graphene nanosheets. *Phys. Lett. A* **2015**, *379*, 2245–2251. [CrossRef]
93. Han, J.; Wang, K.; Liu, W.; Li, C.; Sun, X.; Zhang, X.; An, Y.; Yi, S.; Ma, Y. Rational design of nano-architecture composite hydrogel electrode towards high performance Zn-ion hybrid cell. *Nanoscale* **2018**, *10*, 13083–13091. [CrossRef] [PubMed]
94. Xu, X.; Zhao, X.; Yang, Z.; Lin, Q.; Jian, B.; Li, N.; Zheng, C.; Lv, W. High-density three-dimensional graphene cathode with a tailored pore structure for high volumetric capacity zinc-ion storage. *Carbon* **2022**, *186*, 624–631. [CrossRef]
95. Mao, J.; Iocozzia, J.; Huang, J.; Meng, K.; Lai, Y.; Lin, Z. Graphene aerogels for efficient energy storage and conversion. *Energy Environ. Sci.* **2018**, *11*, 772–799. [CrossRef]
96. Okhay, O.; Tkach, A.; Gallo, M.J.H.; Otero-Irurueta, G.; Mikhalev, S.; Staiti, P.; Lufrano, F. Energy storage of supercapacitor electrodes on carbon cloth enhanced by graphene oxide aerogel reducing conditions. *J. Energy Storage* **2020**, *32*, 101839. [CrossRef]
97. Xin, T.; Wang, Y.; Wang, N.; Zhao, Y.; Li, H.; Zhang, Z.; Liu, J. A high-capacity aqueous Zn-ion hybrid energy storage device using poly(4,4′-thiodiphenol)-modified activated carbon as a cathode material. *J. Mater. Chem. A* **2019**, *7*, 23076–23083. [CrossRef]
98. Potham, S.; Ramanujam, K. A novel hierarchical porous activated carbon-organic composite cathode material for high performance aqueous zinc-ion hybrid supercapacitors. *J. Power Sources* **2023**, *557*, 232551. [CrossRef]
99. Xu, Y.; Chen, X.; Huang, C.; Zhou, Y.; Fan, B.; Li, Y.; Hu, A.; Tang, Q.; Huang, K. Redox-active p-phenylenediamine functionalized reduced graphene oxide film through covalently grafting for ultrahigh areal capacitance Zn-ion hybrid supercapacitor. *J. Power Sources* **2021**, *488*, 229426. [CrossRef]
100. Yang, J.; Cao, J.; Peng, Y.; Bissett, M.; Kinloch, I.A.; Dryfe, R.A.W. Unlocking the energy storage potential of polypyrrole via electrochemical graphene oxide for high performance zinc-ion hybrid supercapacitors. *J. Power Sources* **2021**, *516*, 230663. [CrossRef]

101. Cao, J.; Wang, Y.; Chen, J.; Li, X.; Walsh, F.C.; Ouyang, J.H.; Jia, D.; Zhou, Y. Three-dimensional graphene oxide/polypyrrole composite electrodes fabricated by one-step electrodeposition for high performance supercapacitors. *J. Mater. Chem. A* **2015**, *3*, 14445–14457. [CrossRef]
102. Xu, T.; Yang, D.; Fan, Z.; Li, X.; Liu, Y.; Guo, C.; Zhang, M.; Yu, Z.-Z. Reduced graphene oxide/carbon nanotube hybrid fibers with narrowly distributed mesopores for flexible supercapacitors with high volumetric capacitances and satisfactory durability. *Carbon* **2019**, *152*, 134–143. [CrossRef]
103. Ni, T.; Wang, S.; Shi, J.; Du, X.; Cheng, Q.; Dong, Z.; Ruan, L.; Zeng, W.; Guo, X.; Ren, X.; et al. Highly Flexible and Self-Healable Zinc-Ion Hybrid Supercapacitors Based on MWCNTs-RGO Fibers. *Adv. Mater. Technol.* **2020**, *5*, 2000268. [CrossRef]
104. Cao, Y.; Tang, X.; Liu, M.; Zhang, Y.; Yang, T.; Yang, Z.; Yu, Y.; Li, Y.; Di, J.; Li, Q. Thin-walled porous carbon tile-packed paper for high-rate Zn-ion capacitor cathode. *Chem. Eng. J.* **2022**, *431*, 133241. [CrossRef]
105. Li, J.; Zhang, J.; Yu, L.; Gao, J.; He, X.; Liu, H.; Guo, Y.; Zhang, G. Dual-doped carbon hollow nanospheres achieve boosted pseudocapacitive energy storage for aqueous zinc ion hybrid capacitors. *Energy Storage Mater.* **2021**, *42*, 705–714. [CrossRef]
106. Liu, P.; Liu, W.; Huang, Y.; Li, P.; Yan, J.; Liu, K. Mesoporous hollow carbon spheres boosted, integrated high performance aqueous Zn-Ion energy storage. *Energy Storage Mater.* **2020**, *25*, 858–865. [CrossRef]
107. Chen, S.; Ma, L.; Zhang, K.; Kamruzzaman, M.; Zhi, C.; Zapien, J.A. A flexible solid-state zinc ion hybrid supercapacitors based on copolymer derived hollow carbon spheres. *J. Mater. Chem. A* **2019**, *7*, 7784–7790. [CrossRef]
108. Li, W.; Zhou, M.; Li, H.; Wang, K.; Cheng, S.; Jiang, K. A high performance sulfur-doped disordered carbon anode for sodium ion batteries. *Energy Environ. Sci.* **2015**, *8*, 2916–2921. [CrossRef]
109. Lee, Y.-G.; An, G.-H. Synergistic Effects of Phosphorus and Boron Co-Incorporated Activated Carbon for Ultrafast Zinc-Ion Hybrid Supercapacitors. *ACS Appl. Mater. Interfaces* **2020**, *12*, 41342–41349. [CrossRef]
110. Zhou, H.; Liu, C.; Wu, J.-C.; Liu, M.; Zhang, D.; Song, H.; Zhang, X.; Gao, H.; Yang, J.; Chen, D. Boosting the electrochemical performance through proton transfer for the Zn-ion hybrid supercapacitor with both ionic liquid and organic electrolytes. *J. Mater. Chem. A* **2019**, *7*, 9708–9715. [CrossRef]
111. Wang, H.; Chen, Q.; Xiao, P.; Cao, L. Unlocking Zinc-Ion Energy Storage Performance of Onion-Like Carbon by Promoting Heteroatom Doping Strategy. *ACS Appl. Mater. Interfaces* **2022**, *14*, 9013–9023. [CrossRef] [PubMed]
112. Nian, Y.-R.; Teng, H. Nitric Acid Modification of Activated Carbon Electrodes for Improvement of Electrochemical Capacitance. *J. Electrochem. Soc.* **2002**, *149*, A1008–A1014. [CrossRef]
113. Li, X.; Jiang, Y.; Wang, P.; Mo, Y.; Lai, W.; Li, Z.; Yu, R.; Du, Y.; Zhang, X.; Chen, Y. Effect of the oxygen functional groups of activated carbon on its electrochemical performance for supercapacitors. *New Carbon Mater.* **2020**, *35*, 232–243. [CrossRef]
114. Li, Y.; Yang, W.; Yang, W.; Wang, Z.; Rong, J.; Wang, G.; Xu, C.; Kang, F.; Dong, L. Towards High-Energy and Anti-Self-Discharge Zn-Ion Hybrid Supercapacitors with New Understanding of the Electrochemistry. *Nano Micro Lett.* **2021**, *13*, 95. [CrossRef] [PubMed]
115. Zhao, L.; Jian, W.; Zhu, J.; Zhang, X.; Wen, F.; Fei, X.; Chen, L.; Huang, S.; Yin, J.; Chodankar, N.R.; et al. Molten Salt Self-Template Synthesis Strategy of Oxygen-Rich Porous Carbon Cathodes for Zinc Ion Hybrid Capacitors. *ACS Appl. Mater. Interfaces* **2022**, *14*, 43431–43441. [CrossRef]
116. Yuan, S.; Huang, X.; Wang, H.; Xie, L.; Cheng, J.; Kong, Q.; Sun, G.; Chen, C.-M. Structure evolution of oxygen removal from porous carbon for optimizing supercapacitor performance. *J. Energy Chem.* **2020**, *51*, 396–404. [CrossRef]
117. Lou, G.; Pei, G.; Wu, Y.; Lu, Y.; Wu, Y.; Zhu, X.; Pang, Y.; Shen, Z.; Wu, Q.; Fu, S.; et al. Combustion conversion of wood to N, O co-doped 2D carbon nanosheets for zinc-ion hybrid supercapacitors. *Chem. Eng. J.* **2021**, *413*, 127502. [CrossRef]
118. Wang, D.; Wang, S.; Lu, Z. S-doped 3D porous carbons derived from potassium thioacetate activation strategy for zinc-ion hybrid supercapacitor applications. *Int. J. Energy Res.* **2020**, *45*, 2498–2510. [CrossRef]
119. Lu, Y.; Liu, L.; Zhang, R.; Jiang, Z.; Li, Y.; Sun, Z.; Chen, X.; Song, H. Sodium alginate-derived micropore dominated carbon 3D architectures through dual template engineering for high-performance Zn-ion hybrid capacitors. *Appl. Surf. Sci.* **2022**, *604*, 154631. [CrossRef]
120. Zan, G.; Wu, T.; Zhu, F.; He, P.; Cheng, Y.; Chai, S.; Wang, Y.; Huang, X.; Zhang, W.; Wan, Y.; et al. A biomimetic conductive super-foldable material. *Matter* **2021**, *4*, 3232–3247. [CrossRef]

batteries

Review

Heteroatom Doping Strategy of Advanced Carbon for Alkali Metal-Ion Capacitors

Ti Yin, Yaqin Guo, Xing Huang *, Xinya Yang, Leixin Qin, Tianxiang Ning, Lei Tan, Lingjun Li and Kangyu Zou *

School of Materials Science and Engineering, Changsha University of Science and Technology, Changsha 410114, China; 202228020409@stu.csust.edu.cn (T.Y.); 202228020413@stu.csust.edu.cn (Y.G.); 202328020426@stu.csust.edu.cn (X.Y.); 202328020438@stu.csust.edu.cn (L.Q.); ningtianxiang@csust.edu.cn (T.N.); tanlei@csust.edu.cn (L.T.); lingjun.li@csust.edu.cn (L.L.)

* Correspondence: 22206031250@stu.csust.edu.cn (X.H.); ky-zou@csust.edu.cn (K.Z.)

Abstract: Alkali metal-ion capacitors (AMICs) combine the advantages of the high specific energy of alkali metal-ion batteries (AMIBs) and the high power output of supercapacitors (SCs), which are considered highly promising and efficient energy storage devices. It is found that carbon has been the most widely used electrode material of AMICs due to its advantages of low cost, a large specific surface area, and excellent electrical conductivity. However, the application of carbon is limited by its low specific capacity, finite kinetic performance, and few active sites. Doping heteroatoms in carbon materials is an effective strategy to adjust their microstructures and improve their electrochemical storage performance, which effectively helps to increase the pseudo-capacitance, enhance the wettability, and increase the ionic migration rate. Moreover, an appropriate heteroatom doping strategy can purposefully guide the design of advanced AMICs. Herein, a systematic review of advanced heteroatom (N, S, P, and B)-doped carbon, which has acted as a positrode and negatrode in AMICs (M = Li, Na, and K) in recent years, has been summarized. Moreover, emphasis is placed on the mechanism of single-element doping versus two-element doping for the enhancement in the performance of carbon positrodes and negatrodes, and an introduction to the use of doped carbon in dual-carbon alkali metal-ion capacitors (DC-AMICs) is discussed. Finally, an outlook is given to solve the problems arising when using doped carbon materials in practical applications and future development directions are presented.

Keywords: alkali metal-ion capacitor; carbon material; heteroatom doping; electrochemical performance

1. Introduction

The evolution of energy storage technology has led to increased demands for advanced energy storage devices that offer higher energy and power densities, along with extended lifecycles. Constructing such advanced energy storage devices is crucial for the efficient utilization and storage of sustainable energy sources. Currently, lithium-ion batteries (LIBs) and supercapacitors (SCs) dominate the energy storage market [1]. However, LIBs, characterized by their low specific power, and SCs, characterized by their low specific energy, are increasingly unable to meet the escalating energy demands of the market for energy storage technologies [2–4]. In 2001, Amatucci et al. [5] reported lithium-ion capacitors (LICs) for the first time, which are constructed by an activated carbon (AC) positrode and a $Li_4Ti_5O_{12}$ (LTO) negatrode. Surprisingly, LICs exhibit a specific energy three times greater than that of conventional SCs (20 Wh kg^{-1}), heralding a new era in energy storage systems. LICs combine SC-type positrodes and LIB-type negatrodes [6], achieving high

https://doi.org/10.3390/batteries11020069

specific energy/power and a long lifecycle. Compared to lithium, which is present in low concentrations (0.002wt.%), sodium (2.36wt.%) and potassium (2.09wt.%) are more abundant on Earth and exhibit analogous chemical properties to lithium. They demonstrate significant potential for large-scale storage and cost-effectiveness. Therefore, sodium-ion capacitors (SICs) and potassium-ion capacitors (KICs) exhibit similar mechanisms to LICs, which have become one of the most promising electrochemical energy storage devices. The relationship between the specific energy and specific power of common electrochemical energy storage devices is depicted in Figure 1a [7]. Electrode materials play a crucial role in the electrochemical performance of alkali metal-ion capacitors (AMICs) [8]. Carbon materials, known for their low cost, large specific surface area, and excellent electrical conductivity, are used as electrode materials in AMICs to store energy by absorbing electrolyte ions on the electrode surface, forming an electric double-layer structure. Nevertheless, the application of carbon materials is still constrained due to their low specific capacity, limited kinetic performance, and scarcity of active sites, which result in the inferior specific energy of the assembled devices [9,10].

Heteroatom doping is a rational design method, used in the realm of advanced material development, involving the substitution of certain carbon atoms with other elements [11–14]. This process can alter the electronic structure of the carbon matrix, thereby promoting charge transfer [15]. Additionally, it can increase the number of redox-active sites and defect locations, as well as expand the interlayer distance within the carbon structure. Doping with various heteroatoms can further enhance specific physical and chemical properties of carbon materials, such as electrical conductivity and surface wettability [16,17]. Superior electrical conductivity ensures the swift passage of electrical currents through the material, while excellent surface wettability fosters stronger interactions between the material and its surrounding environment. Figure 1b,c [18] illustrate the comparative positive and negative impacts of different doping atoms in batteries and SCs, respectively. In the context of AMICs, carbon negatrodes and carbon positrodes operate through distinct energy storage mechanisms. For carbon negatrodes, specific heteroatom doping may be essential to bolster stability and energy storage capacity, whereas for carbon positrodes, a different type of heteroatom doping might be necessary to enhance conductivity and reactivity. Consequently, their doping modification strategies and performance enhancement pathways can differ significantly.

Selecting the right dopant atoms is a critical research area for researchers, as it can significantly enhance the electrochemical performance of battery-type carbon negatrodes and capacitor-type carbon positrodes in a targeted manner. This review offers a systematic examination of the recent advancements in the use of advanced heteroatom (N, S, P, and B)-doped carbons as both positrodes and negatrodes in AMICs (M = Li, Na, and K). It concentrates on the application of single-element-doped and double-doped carbons in AMICs, delivering a thorough analysis of the distinct performance benefits offered by various elemental doping strategies and elucidating the mechanisms behind performance enhancement. Furthermore, this discussion tackles the challenges that doped carbon materials face in practical applications and proposes potential avenues for future research and development. The aim is to improve the performance of LICs, SICs, and KICs, and by extension, other MICs. By identifying the unique advantages and mechanisms of different doping elements, researchers can better tailor the design of carbon materials to meet the specific demands of high-performance energy storage devices.

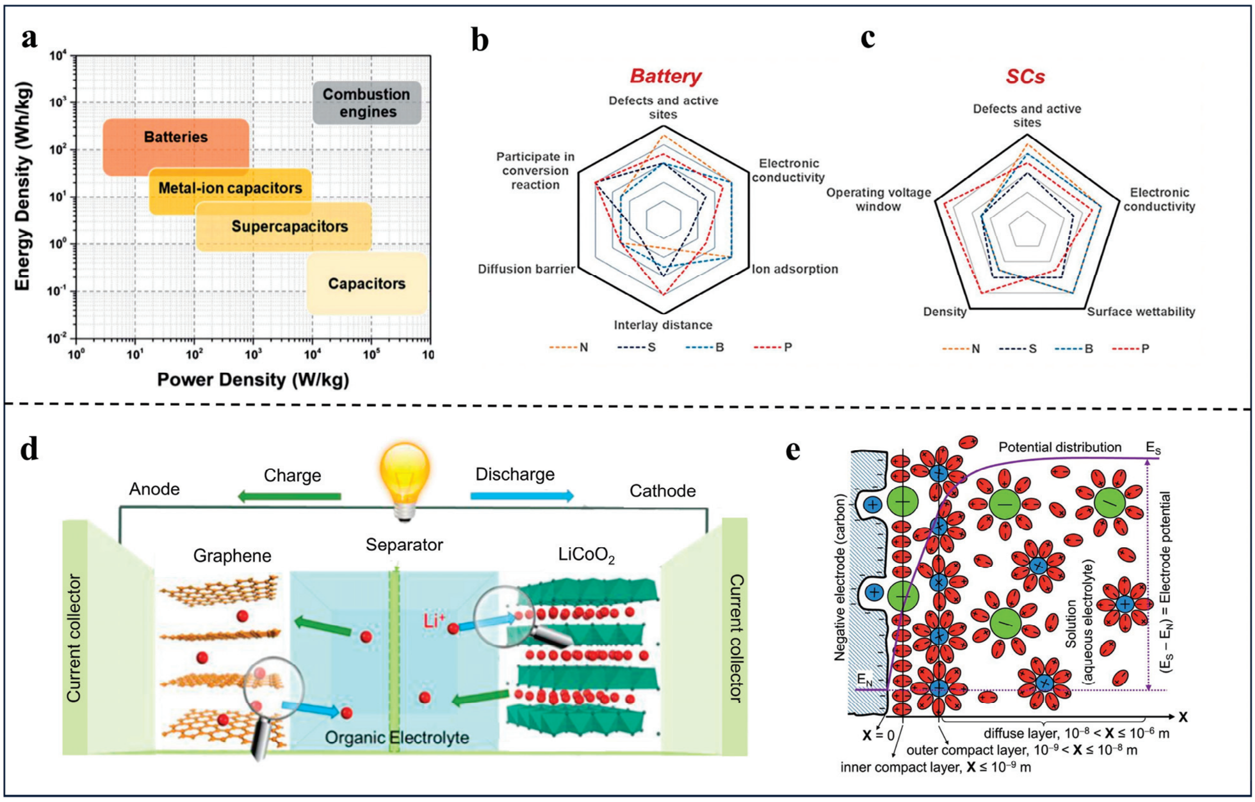

Figure 1. (**a**) A Ragone diagram of the energy storage devices as indicated. Reproduced with permission from Ref. [7]. Copyright 2022, The Royal Society of Chemistry. A comparison of the positive and negative effects of the doping of different heteroatoms in (**b**) batteries and (**c**) SCs. Reproduced with permission from Ref. [18]. Copyright 2021, The Royal Society of Chemistry. (**d**) A schematic of the charging and discharging process in typical MIBs. Reproduced with permission from Ref. [19]. Copyright 2019, Wiley. (**e**) Schematic representations of the EDL structure (cross-section) of the interface between a porous-carbon negative electrode and an aqueous electrolyte. Reproduced with permission from Ref. [20]. Copyright 2017, Taylor & Francis.

2. Energy Storage Mechanisms in Electrochemical Storage Devices

AMICs are hybrid energy storage devices that integrate the energy storage mechanisms of both AMIBs and SCs. Typically, an AMIC comprises a battery-type negatrode and a capacitor-type positrode. The battery-type negatrode supplies sustained power to the device, while the capacitive positrode is designed for the swift absorption and release of energy. MICs are characterized by their high energy and power densities, as well as their extended operational lifetimes. However, there is a kinetic rate mismatch between the Li$^+$ intercalation/de-intercalation of the battery-type negatrode and the ion adsorption/desorption behavior of the capacitor-type negatrode. Thus, it is necessary to understand the two different energy storage mechanisms to ensure the rational engineering of carbon materials for advanced AMICs.

2.1. Embedding–Removal Mechanism of AMIBs

Rechargeable AMIBs have indeed become prominent contenders in the realm of new energy technologies, offering portability, energy efficiency, and environmental sustainability. The energy storage in AMIBs is predicated according to the reversible intercalation/de-intercalation of alkali metal ions (M$^+$) within the electrode materials, a process often referred to as the "rocking chair" mechanism. This mechanism is aptly likened to a magical rocking chair, where M$^+$ oscillates between the negatrode and positrode materials during the charging and discharging cycles.

Let us take lithium-ion batteries (LIBs) as an example. Figure 1d [19] shows the charge–discharge process of a conventional lithium-ion battery. During charging, electrons follow the external circuit from the positive electrode to the negative electrode, while Li^+ located in the lithium layer undergoes removal and enters the electrolyte. Firstly, Li^+ is dissolved by the solvent molecules in the electrolyte, and then migrates across the separator to the negatrode under the action of the electric field to undergo de-solvation behavior and is intercalated in the graphite layer. The discharge process of a lithium-ion battery is opposite to the charging process; electrons flow from the negative electrode to the positive electrode, and Li^+ is removed from the graphite and finally intercalated in the positive electrode.

There exists a significant correlation between the reversible intercalation/de-intercalation properties of AMIBs and their specific energy. If the electrode material possesses a limited number of sites that restrict the quantity of M^+ that can be stored, this limitation diminishes the amount of energy that can be released by the AMIB, resulting in reduced specific energy. Conversely, unfavorable external conditions, such as temperature, pressure, and electrolyte environment, can also impact these reversible intercalation/de-intercalation properties, thereby affecting the specific energy of the battery.

2.2. Electric Double-Layer Capacitors

Electric double-layer capacitors (EDLCs), a subset of supercapacitors, play a critical role in modern energy storage solutions. Based on the electrical double-layer model shown in Figure 1e [20], EDLCs store electrical energy through electrostatic interactions, which facilitate charge separation within the Helmholtz double layer at the interface between the electrode surface and the electrolyte [21–23]. When subjected to an electric field, the positive and negative ions in the electrolyte migrate toward the respective oppositely charged electrodes, creating an electric double layer on the electrode surfaces that enables charge storage [24,25]. During the charging phase, anions migrate to the negatrode, while cations move toward the positrode. Conversely, during the discharging phase, these ions move in the opposite direction, releasing the stored charge.

Table 1 presents a comparison of the primary performance metrics of commercialized AMIBs, SCs, and AMICs. It is evident that EDLCs, a type of SC, exhibit superior specific power and cycling stability in comparison to AMIBs [26,27]. EDLCs store energy through a non-Faradaic process that does not involve electron transfer or redox reactions. This distinct energy storage mechanism endows EDLCs with higher efficiency and stability during both the energy storage and release processes. Consequently, double-layer capacitors can serve as an alternative or supplement to secondary rechargeable batteries in applications where high power transfer or rapid energy harvesting is necessary.

Table 1. Comparison of main properties of commercialized AMIBs, SCs, and AMICs [26,27].

Properties	AMIB	SC	AMIC
Discharging time	0.3–3 h	~30 s	min to h
Charging time	1–5 h	s to min	min to h
Specific energy (Wh kg^{-1})	150–250	20–30	20–200
Specific power (W kg^{-1})	<1000	500–10,000	100–20,000
Cycling efficiency (%)	70–85	85–98	70–95
Lifecycle (Cycles)	<4000	>500,000	>25,000

3. Element Doping for Carbon Negatrode

The carbon negatrode, known for its abundant availability, high conductivity, and stability, is a key component in many energy storage systems. Graphite, the most common negatrode material for lithium-ion batteries, has a theoretical specific capacity of

372 mAh g^{-1}. Since Na^+ has a larger ionic radius than Li^+, it cannot be intercalated or de-intercalated between graphite layers. Consequently, amorphous carbon with significant disorder is employed for its negative electrode [28], among which hard carbon is widely utilized due to its high theoretical specific capacity (>300 mAh g^{-1}) [29]. In contrast, potassium can form intercalation compounds with graphite, allowing graphite to serve as a negatrode material for potassium-ion batteries that exhibit a high theoretical capacity of 279 mAh g^{-1} and demonstrate considerable potassium-embedding capabilities. However, its theoretical capacity, which stands at 372 mAh g^{-1}, and its suboptimal rate performance are limitations that prevent it from meeting the specific energy and specific power demands expected from AMICs. During rapid charging and discharging cycles, carbon negatrodes struggle to respond swiftly to fluctuations in current, further highlighting their inability to fulfill the specific energy and specific power requirements of AMICs. Within the electrochemical energy storage processes of AMICs, there is a significant mismatch between the slow ion diffusion at the negatrode and the rapid electrostatic accumulation at the positrode [30–33], leading to an imbalance in negatrode/positrode kinetics. Therefore, it is necessary to strategically develop carbon negatrodes with high multiplicity performance [34–36], which will increase the specific energy and specific power of AMICs at the same time.

3.1. N Doping

Nitrogen, as the most widely studied doping element, is easier to chemically bond with carbon compared to other elemental doping. The atomic radius of nitrogen is slightly smaller than that of carbon, which means that doping with nitrogen results in minimal disruption to the backbone structure of the carbon material, thereby preserving its stability [37]. Nitrogen atoms tend to form new micropores in the carbon skeleton and increase the specific surface area of the material [38]. In addition, the electronegativity of the nitrogen atoms is high (N is 3.04 and C is 2.55), generating very small lattice distortions [39,40], which gives doped carbon materials excellent electrical conductivity [41].

There are five types of doped N (Figure 2a), namely pyrrolic N, nitroso group, amino group, pyridinic N, and graphitic N [42,43]. Positively charged pyridinic N oxides and graphite N elevate electrical conductivity and facilitate electron transport within the carbon electrode. Negatively charged pyridinic N and pyrrolic N generate pseudo-capacitance and enhance the specific capacity and rate performance of the negatrode carbon material [44]. Despite these benefits, nitrogen doping is not without its drawbacks; for instance, graphitic N can diminish the cycling stability and initial coulombic efficiency (ICE) of doped carbon materials. Thus, the choice of nitrogen doping type and quantity is of paramount importance. Tang et al. [45] developed a method to synthesize high-nitrogen-doped, low-graphitic-N carbons (LGNCs) that exhibit improved ICE by eliminating graphitic nitrogen from graphitic carbon nitride (g-C_3N_4) through a denitrification process. As shown in Figure 2b, the LGNC (C:N = 4:1) has higher pyridinic N and pyrrolic N contents and a lower graphitic N content compared to the other two LGNCs (2:1 and 8:1). Therefore, it shows excellent lithium storage capacity and good cycle stability. By calculating the contribution of LGNC diffusion (intercalation) and capacitance (surface-controlled) at different scanning rates (Figure 2c,d), it is evident that the capacitive contribution of LGNC is directly proportional to the scanning rate.

Incorporating nitrogen into the graphite structure of carbon nanomaterials, such as graphene, carbon nanotubes, and activated carbon, can significantly enhance the atomic and electronic structure of these substrates. This modification not only boosts their electrical conductivity but also introduces a conjugated carbon system with sp2 hybridization. These changes can markedly alter the properties of the material, including its reactivity, mechanical strength, and electrocatalytic performance. Zhao et al. [46] utilized N_2 gas as a dopant to achieve in situ nitrogen doping of carbon substrates. The Raman spectroscopy results indicate a progressive decrease in the intensity ratio (I_D/I_G) of the D-band to the G-band as gaseous N_2 is introduced (Figure 2e). Additionally, a two-dimensional band near 2669 cm^{-1} emerged in the spectra of C-N-30-8 h (introducing N_2 with a flow rate of 30 $mL\cdot min^{-1}$ for 8 h), demonstrating high crystallinity and intensity within the range of 1000–3000 cm^{-1} [47,48]. This suggests that the doping of N atoms enhances the graphitization of the carbon material, which in turn improves the sodium storage capabilities of C-N-30-8h at high rates.

Furthermore, nitrogen doping in carbon negatrodes enhances the anion-exchange capacity [49], creates additional defects and active sites, and bolsters the catalytic activity of redox reactions [50–52], which in turn improves the specific capacitance [53–57]. For instance, the introduction of substantial nitrogen content significantly boosts the pseudocapacitance contribution of reticulated nitrogen-doped carbon nanosheets' negatrode, which stands at 58.5%, compared to the 38.3% contribution from carbon nanosheets' negatrode without nitrogen doping [58]. The researchers [59] induced graphite nanodomains and micro mesopores into N-doped carbon to prepare tubular N-doped porous carbons (NPCs), called As_8Mg. As shown in Figure 2f, As_8Mg exhibits a capacity retention rate of up to 98.7% with close to 100% CE at a specific current of 0.2 A g^{-1}. The cycling performance of As_8Mg is exceptionally outstanding among a variety of NPC negatrodes. Based on As_8Mg, SICs also achieve high specific energy (51 Wh kg^{-1}) and specific power (10,410 W kg^{-1}). This indicates that N-doped As_8Mg has high capacitive energy storage properties and is one of the ideal negatrodes for sodium-ion capacitors.

Nitrogen doping exerts a substantial influence on the storage of metal ions, with a particular emphasis on three forms of doped nitrogen: pyrrolic N, pyridinic N, and graphitic N. Taking Li^+ as an example, Chen et al. [60] prepared nitrogen-doped interconnected carbon networks (INCs) which revealed high reversible capacity and excellent electrochemical kinetics. The prepared INC//AC LIB has high specific energy (172 Wh kg^{-1} at 260 W kg^{-1}) and large specific power (26 kW kg^{-1} at 108 Wh kg^{-1}). The XPS results showed that the N element of the INCs prepared at 800 °C is mainly divided into three components: pyridinic N (N-6, 398.4 eV), pyrrolic N (N-5, 400.2 eV), and graphitic N (N-Q, 401.2 eV) (Figure 2g). Among the N-doped structures, the study concludes that the electronic defects of pyrrolic N (N-5) and pyridinic N (N-6) enhance the adsorption of Li atoms [61,62], while graphitic N doping (N-Q) weakens the adsorption of Li atoms.

3.2. S Doping, P Doping, and B Doping

Owing to the larger atomic radius of sulfur, sulfur doping may occupy a larger space in the pore volume. This causes the expansion of layer spacing and a significant decrease in the specific surface area of the carbon material [63]. Sulfur-doped carbon typically results in larger defects, distortions, and increased interlayer distances within the carbon structure [64–67]. S atoms are often found at the edges or defects of carbon planes, which can offer a greater number of active sites. Using the synthetic strategy of extracting sulfur-doped carbon flakes from softwood (Figure 3a), Casal and co-workers produced S-doped carbon flakes used as negatrodes for SICs [68]. The Galvanostatic charge–discharge (GCD) potential curves in Figure 3b indicate that for S-doped carbon sheets at discharge potentials of 1.2–1.5 V, the curve lengths are proportional to the sulfur content. Meanwhile, the GCD curve of the undoped sheets (Figure 3c) has a potential plateau below 0.1 V. The addition of sulfur doubles the CS-700m (prepared at 700 °C, in the absence of sulfur and subjected as well to a ball milling process) capacity, providing an excellent performance at 420 mAh g^{-1} (403 mAh cm^{-3}, ICE = 69%). At a high rate of 10 A g^{-1} (Figure 3d), the S-doped carbon sheets (55–40 mAh g^{-1}) possess a significantly larger reversible capacity (15 mAh g^{-1}) than the undoped carbon sheet, indicating that the redox reaction brought about by sulfur can still play a significant role at high rates. The above results suggest that sulfur doping provides abundant vacant defect locations for the carbon sheets. Due to the defects, the interlayer spacing of carbon is increased [69], and the resistance to Na^+ diffusion is greatly reduced, accelerating its embedding/removal time.

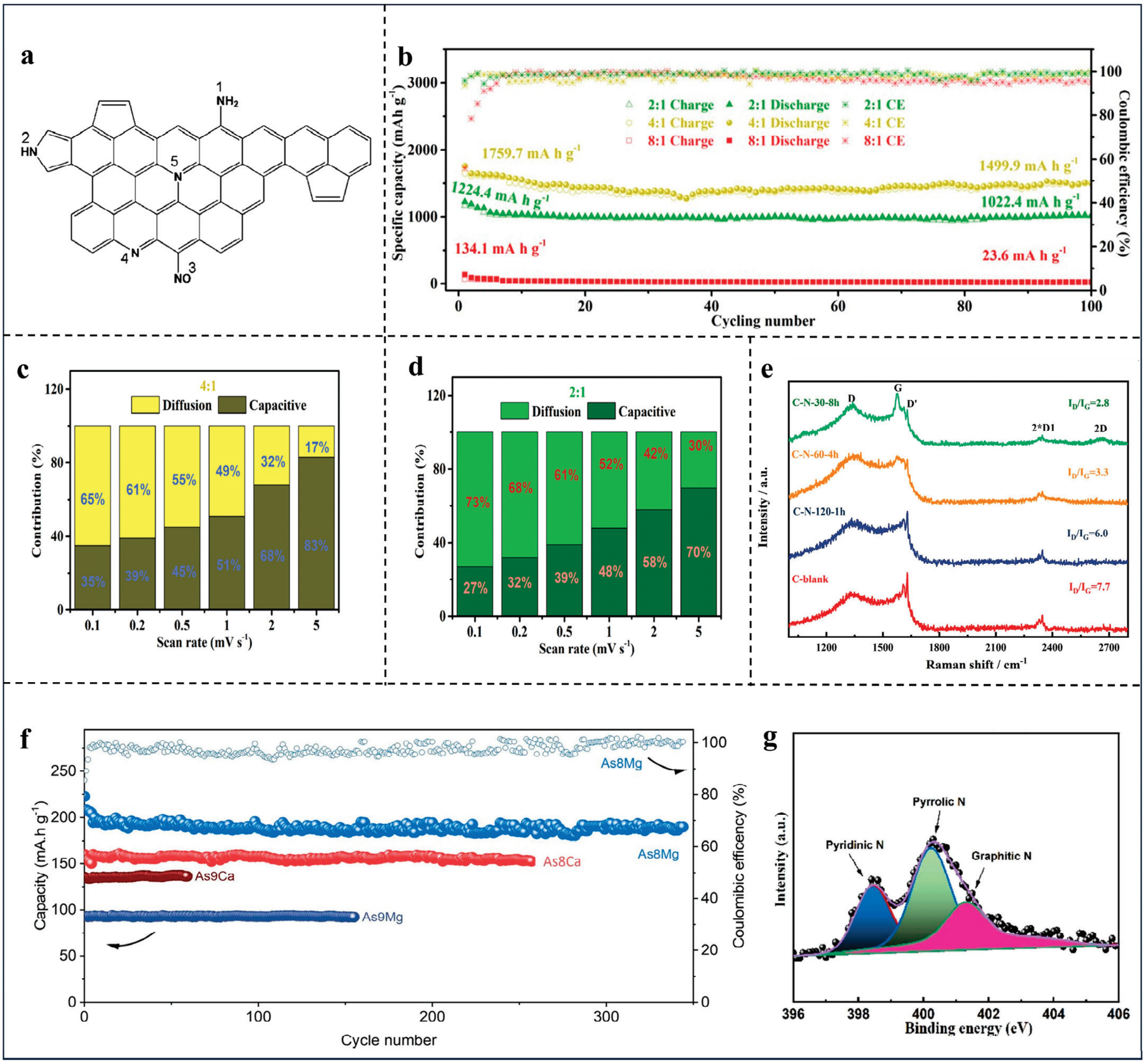

Figure 2. (**a**) Schematic overview of possible N sites of carbon backbone. Reproduced with permission from Ref. [43]. Copyright 2010, The Royal Society of Chemistry. (**b**) Galvanostatic charge/discharge cycling performances. Contribution of capacitive and diffusion-controlled capacity for LGNC at (**c**) 4:1 and (**d**) 2:1. LGNC, low-graphitic-N carbon. Reproduced with permission from Ref. [45]. Copyright 2022, Wiley. (**e**) Raman spectra of C-blank, C-N-120-1h, C-N-60-4h, and C-N-30-8h. Reproduced with permission from Ref. [46]. Copyright 2023, Elsevier. (**f**) Cycling performance of samples with specific current of 0.2 A·g^{-1}. Reproduced with permission from Ref. [59]. Copyright 2024, Wiley. (**g**) High-resolution XPS for N1s of INC prepared at 800 °C. Reproduced with permission from Ref. [60]. Copyright 2023, Elsevier.

Phosphorus (P) atoms are regarded as one of the most promising doping elements. Compared to nitrogen, which shares the same number of valence electrons, P atoms have a larger radius (~0.110 nm). Therefore, phosphorus atoms will cause pore enlargement and increase pore spacing during the doping process [70]. This characteristic endows phosphorus-doped carbon with significant structural distortions and a robust adsorption capacity for M^+ [71–74]. Yang et al. [75] successfully synthesized phosphorus-doped hard carbon (PHC-4), which contains a substantial amount of phosphorus (3.44%), through esterification and carbonation reactions between starch and phytic acid. PHC-4 is based on the phytic acid volume of 4 mL. PHC-4 has three main components. Li_xPC_y with P-C bonds is involved in the electrochemical redox reaction and provides high-capacitance performance [76]; meanwhile, P-O and P=O bonds enhance the adsorption of M^+ by the carbon material [77]. The binding of phosphorus atoms and active sites of carbon increases the chemical stability. Moreover, it is conducive to the insertion/extraction of Li^+, and the presence of P-doped atoms inhibits the oxidation of the carbon materials [78].

Boron (B) doping can significantly alter the characteristics of carbon-based materials in several ways: It disrupts the electroneutrality of these materials, leading to the generation of numerous active sites [79,80], and it also manages the charge distribution, which in turn expedites electron transfer [81,82]. Moreover, B doping can substitute for carbon atoms within the structure of the material, altering its electronic configuration and introducing more micropores into the carbon skeleton [83,84]. These modifications result in improved electrochemical performance for B-doped carbon in supercapacitors. Researchers [85] prepared boron-doped graphene nanosheets (BGNSs) by incorporating B into graphene nanosheets. B doping indispensably boosted the unique lithium storage mechanism and the adsorption properties of microporous capacitive carbon in BGNS. As shown in Figure 3e of the pore size distributions (PSDs), the addition of B prevented the agglomeration of graphene sheets. Moreover, it induced the formation of p-type conductive networks [86,87]. The mesoporous structure of BGNS observed in TEM images (Figure 3f) also supported the above conclusion. Meanwhile, the lithiation/de-lithiation ability of BGNS was greatly enhanced compared to undoped TGNS, as shown in Figure 3g. This enhancement is likely a result of boron doping increasing the disorder within the matrix, which in turn promotes porosity and the creation of Li^+ storage sites.

3.3. N/S Co-Doping

N/S co-doped carbon has seen rapid development in recent years, capitalizing on the synergistic effects between nitrogen and sulfur. The co-doping of N and S atoms enhances the conductivity of carbon materials, increases interlayer distances, and introduces more defect sites within the carbon structure. These changes lead to an improved reversible storage capacity and rate capability, enhancing the overall performance of M^+ ion storage [88–91]. Researchers [92] synthesized an N/S double-doped multistage porous carbon (NSC) with excellent reversibility. Based on this premise, the highly stable LIC (Figure 3h) constructed achieves both high specific energy and high specific power simultaneously. As shown in the XPS spectrum (Figure 3i), the N1 peaks of NSC1–3 include pyridinic N, pyrrolic N, graphitic N, and nitrogen-containing oxides [93,94]. Among these, pyridinic N and pyrrolic N demonstrate strong adsorption properties for M^+, such as Li^+ and Na^+, due to their electron-deficient characteristics [95]. Additionally, S doping enhances the surface wettability of the carbon material and the electrolyte, facilitating rapid charge transfer [96,97]. Moreover, the incorporation of both N and S doping in porous carbon significantly reduces interfacial resistance, thereby improving electron conduction [98,99]. The presence of nitrogen and sulfur heteroatoms contributes to superior sodium-ion storage capabilities, allowing carbon negatrodes doped with N/S to achieve a high reversible capacity and exhibit remarkable cycle stability. As a result, N/S-doped carbon has been widely utilized as a negatrode in SICs [100–106].

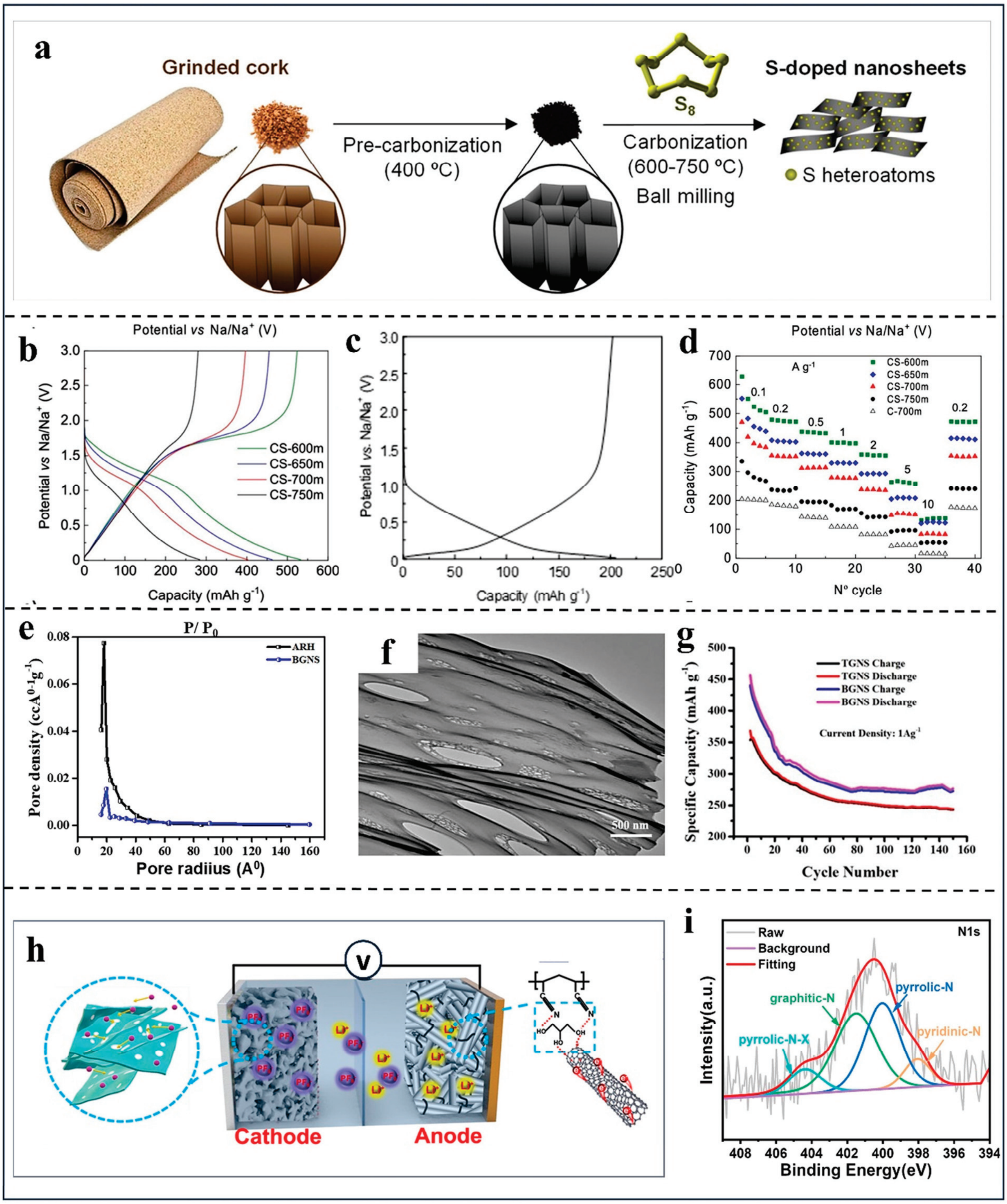

Figure 3. (**a**) An illustration of the synthesis strategy of S-doped carbon sheets from cork. (**b**,**c**) GCD profiles in the third cycle for the different S-doped sheets and un-doped carbon sheets C-700m. (**d**) The rate capability of the different S-doped sheets. Reproduced with permission from Ref. [68]. Copyright 2023, American Chemical Society. (**e**) Pore size distribution plot of BGNSs and ARH. (**f**) TEM images of BGNSs. (**g**) Cycling of BGNSs and TGNSs at a specific current of 1 A g^{-1}. Reproduced with permission from Ref. [85]. Copyright 2022, Elsevier. (**h**) A schematic illustration of LIC (NSC//GPN@CNTs). (**i**) N1s Entire XPS spectra of NSC1–3 carbonized at 800 °C. Reproduced with permission from Ref. [92]. Copyright 2023, Elsevier.

4. Element Doping for Carbon Positrode

The capacitance of metal-ion capacitors is often limited by the properties of the positrode material, making the selection of a suitable positrode material a critical decision. Carbon, being the most prevalent positrode material, is known for its significant capacitance contribution to fast ion storage and its excellent chemical stability, which allows it to maintain its structure and performance across a broad spectrum of electrolyte environments. However, the low specific capacity of carbon can lead to reduced specific energy in devices that incorporate it. Consequently, researchers have dedicated considerable effort to designing positrode carbon materials with enhanced specific capacity. There is an ongoing quest to discover new electrode material structures and preparation techniques aimed at surmounting the challenges related to the low specific capacity of carbon materials. This continuous exploration is essential for advancing the performance and specific energy of AMICs.

4.1. N Doping

To achieve a balance between electrochemical kinetics and specific capacity in the negatrode and positrode of AMICs, Xu and colleagues proposed a preparation method, combining the advantages of elemental doping and nanostructure, and also successfully prepared nitrogen-doped (3.65%) multistage porous carbon sphere (NHPCS) positrodes [107]. Nitrogen doping endows the NHPCS electrode with superior wettability compared to other electrodes, as shown in Figure 4a. This improved wettability is anticipated to reduce interfacial impedance, thereby enhancing the rate performance. Furthermore, Figure 4b illustrates that the synergistic effect of N/O doping markedly enhances the electrochemical performance of the NHPCS. The unique electronic configuration of nitrogen allows N-doped carbon materials to more readily attract ions from the electrolyte [108], which in turn boosts their capacitive characteristics.

4.2. N/S Co-Doping and N/B Co-Doping

The introduction of different dopants into materials can significantly alter their electrochemical properties, leading to substantial changes in both physical and chemical characteristics [109]. Among these dopants, N is the most extensively used and is often co-doped with other elements to achieve synergistic effects, such as in the case of N/S co-doping. Recently, Shi et al. [110] prepared S/N co-doped porous carbon (SNC) by using a simple method. The addition of S and N enhanced the specific capacity and wettability of the SNC samples. The ratio of S to N can be fine-tuned to achieve the optimal synergistic effect, including on the pore structure of the resulting materials. Table 2 confirms the small pore sizes of SNC-3 and SNC-4 micropores. Simultaneously, as can be seen in the CV curves of Figure 4c, all SNC electrodes, particularly SNC-3, exhibit excellent capacitive behavior [111,112]. This is due to the ability of S to significantly enhance the reactivity between the electrode and the electrolyte. However, with an increase in S content and a corresponding decrease in carbon content, the specific capacity of SNC-4 diminishes, preventing the achievement of optimal performance. Therefore, the proportion of non-metallic elements in the doped material can be easily adjusted by modifying the ligand ratio to optimize performance. As depicted in Figure 4d, the LIC using SNC-3 as a positrode and pre-lithiation HC as a negatrode still outperforms others, and it can achieve powerful performance with maximum specific power (6072 W kg^{-1}) and maximum specific energy (52 Wh kg^{-1}).

The electronegativity of carbon lies between that of B and N, which makes it a versatile element for doping. By substituting some carbon atoms with N and B, the surface polarity and electronic structure of the carbon substrate can be synergistically modulated.

Consequently, co-doped carbon materials exhibit greater catalytic and electrochemical activity compared to their singly doped counterparts [113–118]. Zhang et al. [119] utilized N/B co-doped swollen reduced oxidized graphite (NBEG) as a positrode for SICs; the preparation process is shown in Figure 4e. N-containing functional groups are beneficial for increasing the electronic conductivity of carbon-based materials, inducing the creation of unbalanced charged regions in the carbon materials. This action not only enhances electronic conductivity but also provides additional active sites [120], thereby improving the overall electrochemical performance.

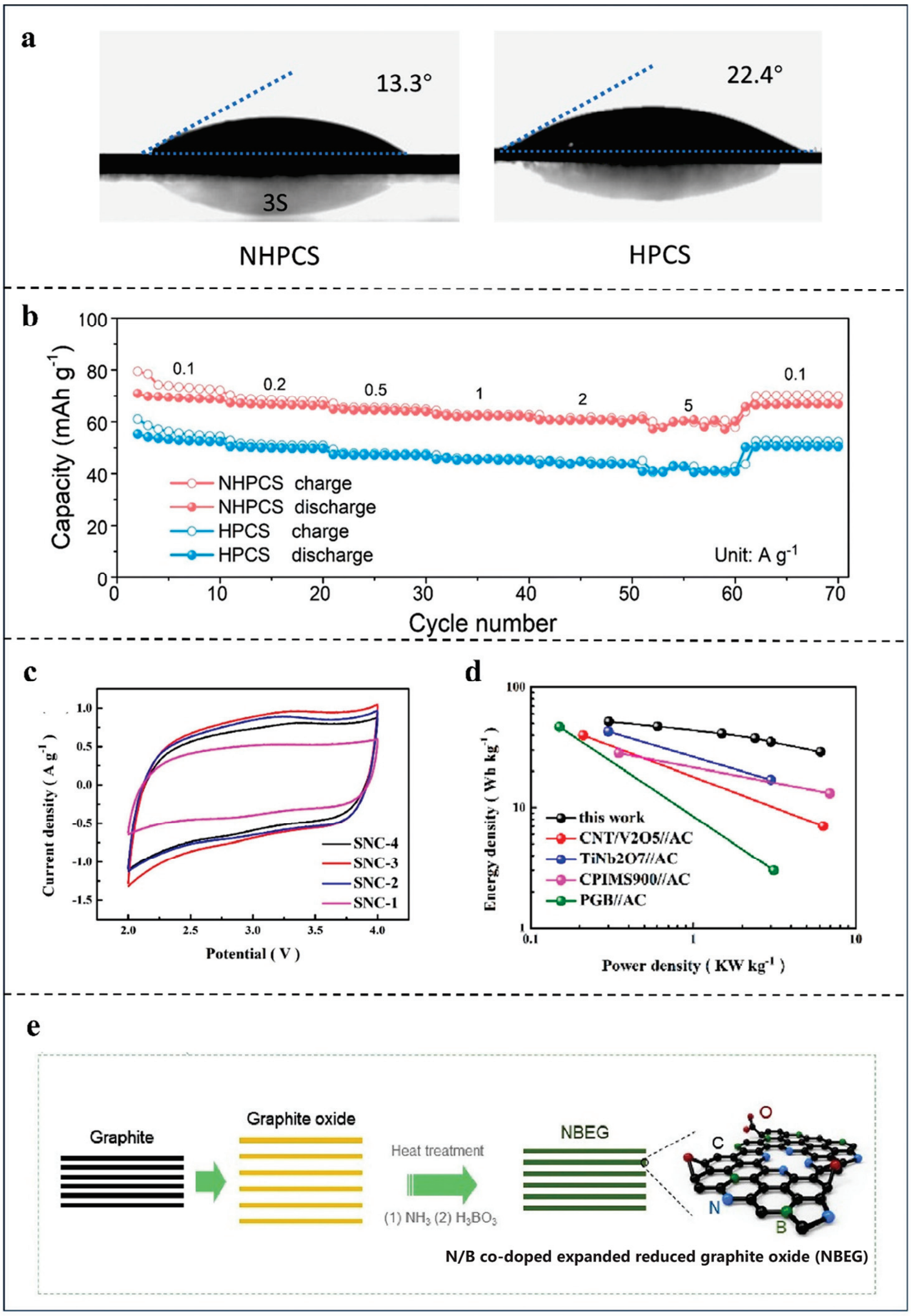

Figure 4. (**a**) The contact angles and (**b**) rate capabilities of the NHPCS and HPCS. Reproduced with permission from Ref. [107]. Copyright 2020, Springer Nature. (**c**) The CV curve of SNC1–4 samples at a scan rate of 10 mV s^{-1}. (**d**) A performance comparison of this LIC with other works. Reproduced with permission from Ref. [110]. Copyright 2023, Elsevier. (**e**) N/B co-doped expanded reduced graphite oxide (NBEG). Reproduced with permission from Ref. [119]. Copyright 2020, Elsevier.

Table 2. Estimated parameters from BET and EDS analysis.

Material	S_{BET} (m^2 g^{-1})	V_{tot} (cm^3 g^{-1})	V_{mic} (cm^3 g^{-1})	D_{DA} (nm)	Elemental Analysis (at%)			
					C1s	N1s	O1s	S2p
SNC-1	547	1.32	0.11	10.91	72.59	12.92	12.7	1.81
SNC-2	619	1.32	0.03	9.68	71.03	11.91	10.52	6.55
SNC-3	616	1.18	0.013	9.72	67.94	7.98	16.67	7.42
SNC-4	514	1.43	0.017	11.58	56.15	5.7	24.62	13.54

S_{BET}: BET surface area. V_{tot}: total volume in pores. V_{mic}: micropore area. D_{DA}: desorption average pore diameter.

5. Element Doping for Dual-Carbon Electrodes

Carbon materials have broad prospects in the field of energy storage due to their large capacity and environmental friendliness [121]. The double-carbon alkali metal-ion capacitor (DC-AMIC), which utilizes carbon materials for both the positrode and negatrode, boasts the benefits of low cost, excellent stability, and adjustable surface compositions and structural morphology. For instance, dual-carbon sodium-ion capacitors (DC-SICs) select similar material systems for their negatrodes and positrodes, addressing the issues of capacity imbalance and kinetic mismatch between the two electrodes. The double-carbon system manifests in two primary forms: one where two distinct carbon materials with different properties serve as the negatrode and positrode, and another where the same carbon material is used for both. The former can fully utilize the advantages of different carbon materials, resulting in a significant improvement in both the capacity and power performance of DC-AMICs. The latter has a lower production cost, which is conducive to mass production and application, while the synergistic effect between the positrode and negatrode in the charging and discharging process will be enhanced.

5.1. Dual Electrodes Made of the Same Carbon Material

5.1.1. LIC

Research has demonstrated that atomic doping can significantly enhance the charge storage capacity of carbon materials. Li et al. [122] prepared a two-dimensional (2D) nitrogen-doped carbon nanosheet (NCN). The high-resolution transmission electron microscopy (HRTEM) image depicted in Figure 5a reveals the lattice stripe extension of the NCN (0.36 nm), providing evidence that the large interlayer distance of the carbon layer contributes to the high electrochemical conductivity of the NCN. This observation is closely associated with the abundant and uniformly distributed nitrogen within the NCN (Figure 5b). Furthermore, the porous structure of the carbon substrate (CNF) endows the NCN positrode with a high specific capacity, enabling excellent pseudo-capacitance storage dynamics even at high current rates. Using an NCN as the negatrode and positrode of the LIC not only reduces the cost but also effectively alleviates the dynamic imbalance, improving the electrochemical performance of the capacitor. The dual-carbon NCN//NCN LIC system can provide a high specific energy of 167 Wh kg^{-1} at a specific power of 240 W kg^{-1}. Moreover, it exhibits good cycling stability (capacity retention of 85.6% for 9000 cycles at 1 A g^{-1}).

Jiang and colleagues have developed coal-based nitrogen-doped porous carbon materials (CNPCs) that feature a folded carbon nanosheet structure [123]. The use of g-C3N4 as both a templating agent and a nitrogen source plays a pivotal role in determining the pore size and nitrogen content of CNPCs, which in turn significantly impacts the electrochemical performance of these materials. In Figure 5c,d, the optimized CNPCs (CTK-1.0) display good pore regulation, high conductivity, and a large specific surface area. Scanning transmission electron microscopy (STEM) and energy-dispersive X-ray spectroscopy (EDS) analyses of CTK-1.0 confirm the uniform distribution of carbon and nitrogen elements within the CNPCs, signifying the successful doping with heteroatomic nitrogen (Figure 5e–g). The nitrogen-doped structures, specifically pyridinic N and pyrrolic N, offer additional active sites for pseudo-capacitance and ion adsorption, thereby enhancing the fast-charging capabilities of the materials. Moreover, ammonium N facilitates electron transfer within the carbon lattice [124], which enhances the capacity of dual-carbon lithium-ion capacitors (DC-LICs). The constructed CTK-1.0//CTK-1.0 LIC achieves a balanced capacity and kinetic balance, with a maximum specific energy of 137.6 Wh kg^{-1} and a long lifetime of 3000 cycles.

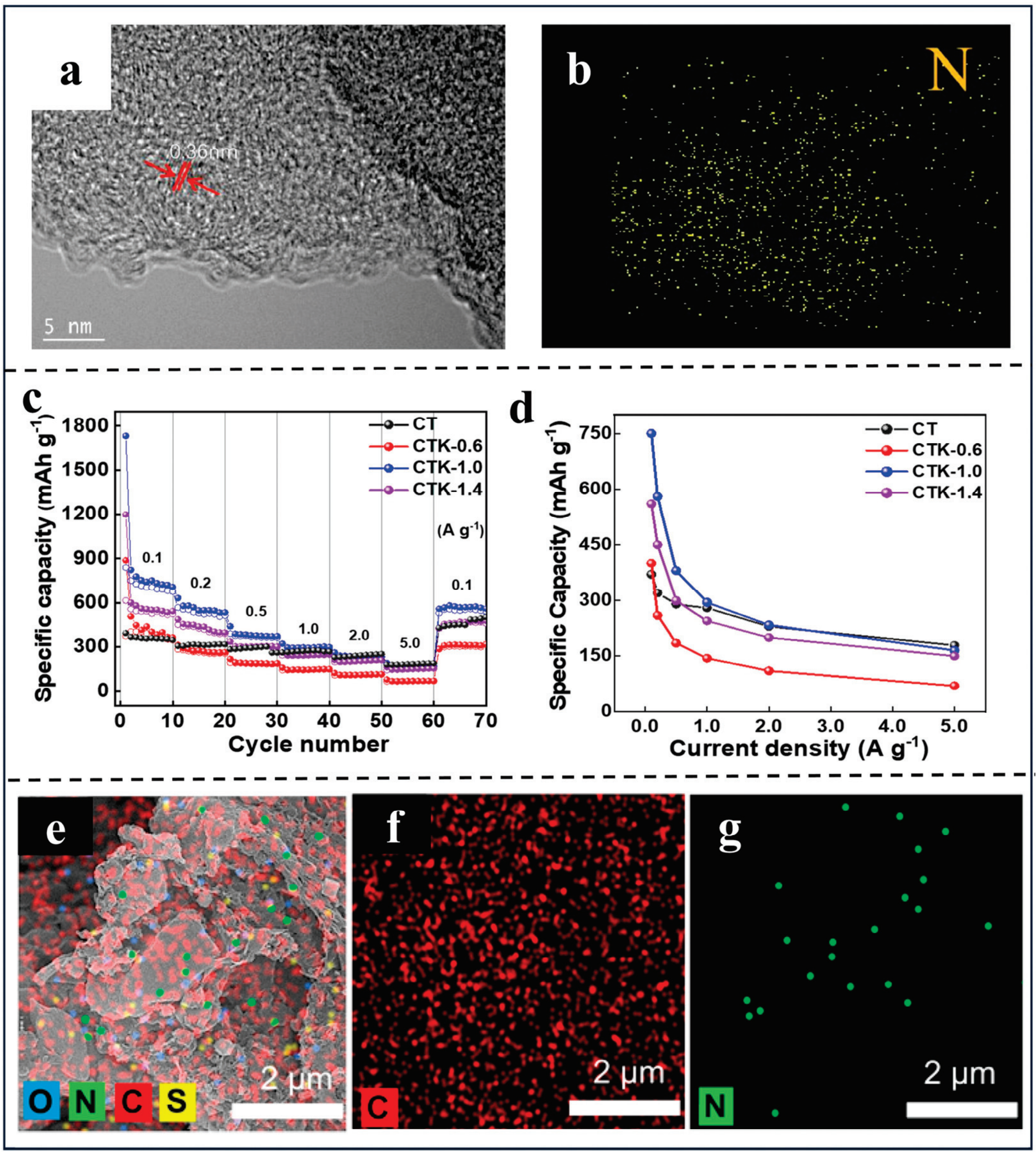

Figure 5. (**a**) HRTEM pictures of the NCN. TEM images (**b**) of the corresponding EDS elemental analysis of the NCN. Reproduced with permission from Ref. [122]. Copyright 2022, Elsevier. (**c**) The rate performance and (**d**) specific capacities at different current densities of CNPCs with different g-C additions. (**e**) STEM images of CTK-1.0 with the corresponding (**f**) C and (**g**) N elemental mappings. Reproduced with permission from Ref. [123]. Copyright 2023, Multidisciplinary Digital Publishing Institute.

Enhancing the low-temperature performance of LICs is a significant challenge in the energy storage industry. At low temperatures, the electrochemical reaction kinetics of capacitors slow down, adversely affecting ion transport and charge transfer, which in turn impedes the normal functioning of LICs. To address this problem, Xiao et al. [125]

prepared S-doped graphene nanocapsules (SGCs) as the negatrode and positrode of LICs. The storage mechanism of the prepared SGCs//SGCs LICs is shown in Figure 6a. As illustrated in Figure 6b, SGCs//SGCs LICs embody a capacity retention rate of more than 83% at −30 °C (10,000 cycles at 5 A g^{-1} and 10 A g^{-1}), revealing excellent ultra-long cryogenic cycle performance. The superior performance of the SGC electrodes is attributed to their stable nanocapsule morphology, abundant pore volume, and S-doped structure. The presence of S contributes to a gradual decrease in the Li^+ migration rate under low-temperature test conditions. As shown in Figure 6c, the Li^+ diffusion coefficients of the SGC negatrode are significantly higher than those of the GC negatrode at −20 and −30 °C. Furthermore, by forming Li-S chemical bonds, the S-doped structure can also facilitate the storage of more Li^+ ions and generate larger pseudo-capacitance, enhancing the overall performance of the LICs under low-temperature conditions.

5.1.2. SIC

Thangavel et al. [126] used graphene hollow nanospheres (GHNSs) doped with double heteroatoms (N and S) for the first time in the fabrication of symmetric DC-SICs. Initially, the NS-GHNSs exhibited a relatively low initial coulombic efficiency of only 36%, which was attributed to the formation of the solid electrolyte interphase (SEI) layer and irreversible reactions between carbon functional groups and sodium ions. However, the NS-GHNSs demonstrated stable performance in subsequent cycles (Figure 6d), achieving a coulombic efficiency of greater than 99% and maintaining a discharge capacity of 264 mAh g^{-1}. This improvement is credited to the presence of nitrogen and sulfur dopants, which enhance the electrical conductivity of the carbon substrate and help mitigate irreversible capacity loss during the initial cycling period. Additionally, there are a large number of heteroatom functional groups on the NS-GHNSs (Figure 6e,f), which have an irreplaceable advantage, for example, providing excellent wettability conducive to the transfer storage of Na^+ [127,128].

5.1.3. KIC

Nitrogen-doped porous carbon nanosheets (NPCNs), serving a dual role, were crafted through a combination of carbonization and self-assembly techniques [129]. In Figure 6g, NPCN-900 shows a type IV curve, and the specific surface area is 1586 m^2 g^{-1}. This suggests that NPCN-900, with its ample pores and expansive surface area, offers swift diffusion channels and adsorption sites for potassium ions (K^+), thereby bolstering its capacitive performance. Similarly, the graphitic N in NPCN-900 can promote the formation of ordered structures, which gives NPCN-900 an ordered graphitic carbon structure [130]. Figure 6h illustrates the remarkable rate capability of NPCN-900, which substantiates its pre-eminent position among negatrode materials [124]. The superior performance can be attributed to three primary factors. The addition of nitrogen not only enriches the active sites on the carbon material, providing more adsorption sites for K^+, but also increases the spacing between the carbon layers, which reduces resistance and deformation during K^+ intercalation/decalcification. Likewise, the abundant pores of the porous carbon nanosheets improve the capacitance performance. The NPCN//NPCN KIC exhibits 128 Wh kg^{-1} with high specific energy and excellent cycling stability (90.8% of the discharge capacity after 9000 cycles at 1.0 A g^{-1}). Notably, the capacity of the KIC shows a trend of decreasing and then increasing. It is shown that a large amount of hidden nitrogen is distributed inside the NPCN electrode, which is gradually activated during the long cycling process, thus releasing more active sites [131,132].

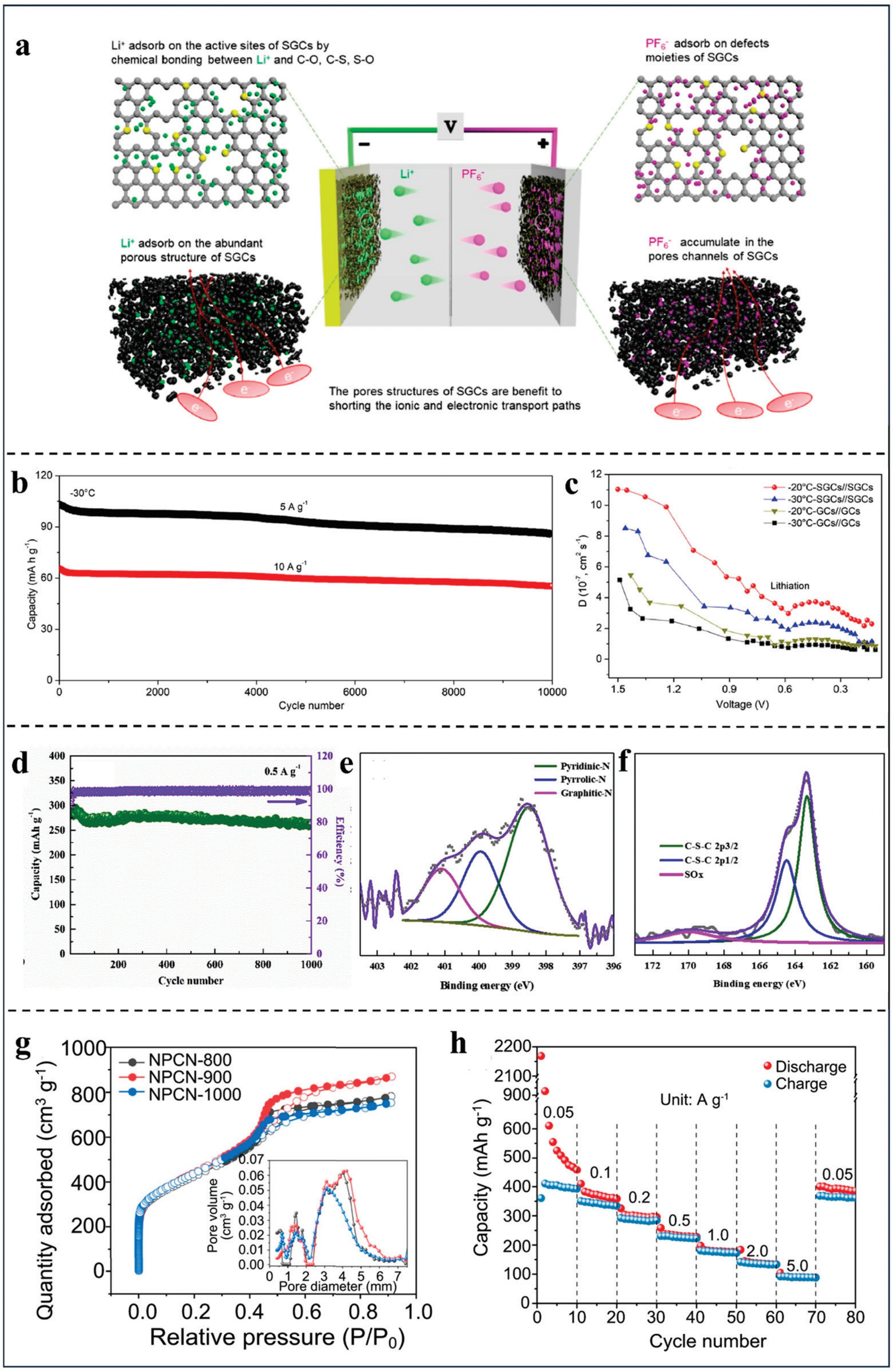

Figure 6. (**a**) A schematic illustration of the entire charge–discharge storage mechanisms of the as-prepared all-graphene symmetric SGCs//SGCs LIC. (**b**) The cycling performance of SGCs//SGCs after 10,000 cycles at −30 °C. (**c**) Li^+ diffusion coefficients of the SGC negatrode compared with GCs at low temperature. Reproduced with permission from Ref. [125]. Copyright 2022, Elsevier. (**d**) The anodic performance of NS-GHNSs, with cycling stability at 0.5 A g^{-1}. XPS survey spectra of NS-GHNSs, and high-resolution deconvoluted XPS spectra of (**e**) N1s, and (**f**) S2p. Reproduced with permission from Ref. [126]. Copyright 2019, Elsevier. (**g**) N_2 adsorption and desorption isotherms of NPCN-T (T = 800, 900, and 1000). (**h**) The rate capability of NPCN-900 as a negatrode for potassium-ion capacitors. Reproduced with permission from Ref. [129]. Copyright 2023, Elsevier.

5.2. Different Carbon Materials as Electrodes

5.2.1. LIC

In AMICs, the selection of negatrode materials with ample layer spacing and rapid kinetics is essential to facilitate the swift embedding/removal of M^+ [133,134]. For the positrode materials, in order to have an outstanding capacitive capacity, abundant active sites and a large specific surface area are necessary [135–137].

Gao et al. [138] synthesized phosphorus-doped activated carbon (PAC-6) by carbonation. Figure 7a shows the manufacturing process of PAC, and the schematic diagram of PHC-4//PAC-6 LIC is shown in Figure 7b. The elemental mapping is shown in Figure 7c, which indicates that P derived from phytic acid (PA) is uniformly doped throughout PAC-6. A higher P content (3.57%) creates active sites for a redox reaction with PAC-6, thus enhancing the capacity of the sample. As a result, the specific capacitance of PAC-6 reaches 147.1 F g^{-1} at 0.05 A g^{-1} with excellent rate capability (90% capacitance retention after 5000 cycles at 1.6 A g^{-1}). Due to the appropriate PA content, the high specific surface area (SSA) and ideal power spectral density (PSD) characteristics of PAC-6 contribute to its superior areal capacitance. The assembled LIC shows excellent energy power characteristics (maximum 122 Wh k g^{-1}, 9775 W k g^{-1}) and operating life.

The electrode kinetics of the negatrode can be significantly constrained by the low conductivity of the electrode material. Fortunately, researchers [139–141] found that S-doped carbon nanotubes (SCNTs) have high conductivity which can improve positrode and negatrode performance. This improvement is attributed to the ability of SCNTs to form a conductive network within the electrodes, thereby accelerating the ion transport rate. Zhao et al. [142] developed an integrated process suitable for sulfur doping in carbon materials, which led to the preparation of sulfur-doped porous carbon (SPC) and sulfur-doped carbon nanotubes (SCNTs). Due to sulfur doping, SPC exhibits an increased energy storage capacity and accelerated electrode kinetics. Then, Li^+ enters the SPC structure by adsorbing on S-containing active sites and inserts into interlayers/pores. The unique hydrophilicity and conductivity of SCNTs enable the construction of a uniformly distributed three-dimensional conductive network within the electrode, significantly enhancing the charge transfer rate and migration speed of Li^+ and PF_6^- during the charging/discharging processes. The constructed AC-SCNTs//SPC-SCNT LIC possesses excellent electrochemical performance (Figure 7d), displaying a specific energy of 169 Wh kg^{-1}, excellent specific power of 1022 W kg^{-1} at 136 Wh kg^{-1}.

5.2.2. SIC

For DC-SIC, doping with heteroatom layers and constructing porous structures are two effective strategies that can significantly enhance the kinetic performance of carbon materials [91,143].

An NHPC-800//NHPAC SIC device was constructed by Zou et al. [144] using nitrogen-doped hierarchical porous carbon (NHPC) as the negatrode and nitrogen-doped hierarchical porous activated carbon (NHPAC) as the positrode. By virtue of the appropriate layer spacing (maximum at 0.42 nm) brought about by N doping and the hierarchical pores. This SIC has excellent specific energy (115 Wh kg^{-1} at 200 W kg^{-1}) and a long lifecycle. Figure 7e demonstrates that the NHPC-800 electrode has the initial charge/discharge capacities of 392.4 mAh g^{-1}/ 536.3 mAh g^{-1}, respectively, with an ICE of 73.2%. Upon activation of NHPC to form NHPAC, both the porosity and specific surface area are enhanced, which is beneficial for the swift adsorption and desorption of anions (ClO_4^-) on the surface. Figure 7f shows the rate performance of the NHPAC electrode at various current densities. The specific capacity of the NHPAC electrode at 0.1 A g^{-1} is 110 mAh g^{-1}, which is much higher than that of commercial activated carbon [145].

While the porous structure of electrode materials is indeed critical for Na^+ storage, pore sizes that are not appropriately tailored can adversely affect the performance of the electrodes.

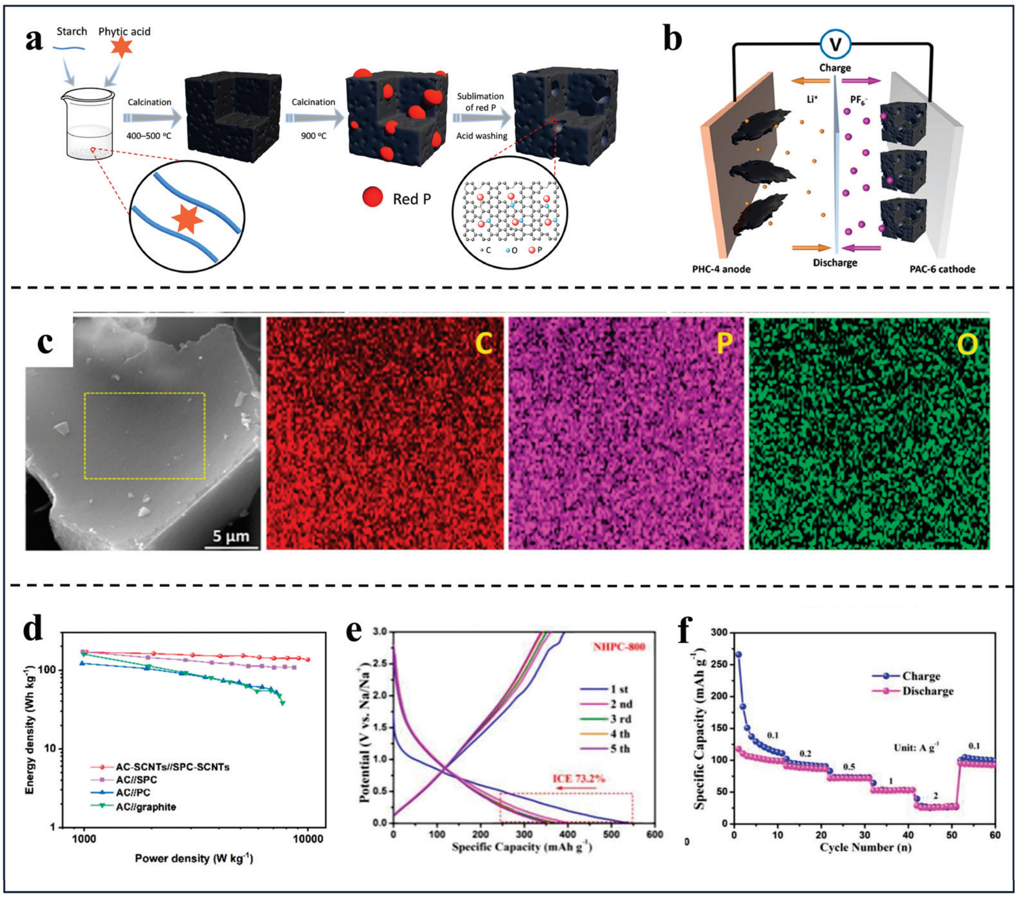

Figure 7. (**a**) Fabrication process for PACs. (**b**) Schematic of fabricated PHC-4//PAC-6 LIC. (**c**) SEM image of PAC-6 and corresponding elemental mapping images. Reproduced with permission from Ref. [138]. Copyright 2021, Elsevier. (**d**) Ragone diagram of assembled two-carbon AC-SCNT//SPC-SCNT LIC. Reproduced with permission from Ref. [142]. Copyright 2022, Elsevier. (**e**) GCD profiles of NHPC-800. (**f**) Rate capability of NHPAC positrode. Reproduced with permission from Ref. [144]. Copyright 2019, The Royal Society of Chemistry.

Wang et al. [146] doped hard carbon (HC) with N/S to enhance SIC performance and specific capacity. The structure of HC bent graphite was tuned by adding thiophene S, which has a characteristic heterocyclic structure, reducing the degree of graphitization and improving the wettability. Introducing more defects and edges during the carbonization process activates the electrochemical potential of the carbon, thereby boosting its electrical conductivity. Furthermore, the incorporation of nitrogen in the form of pyridinic N increases pseudo-capacitance and the capacity of the material. NS-pHC-1.348 (N and S co-doped porous hard carbon with 1.348 g $MgCl_2$ precursor) was prepared to provide reversible capacity, increased rate performance, and excellent cycling stability, which balances the electrochemical kinetics of the positrode and negatrode within the SIC. The NS-pHC-1.348//NPC SIC shows excellent specific power, reaching 92.03 kW kg^{-1} at 5.98 Wh kg^{-1}.

5.2.3. KIC

For KIC, it is important to enhance the K^+ storage capacity to construct a porous carbonaceous negatrode with reasonable-sized defects and abundant active sites.

Liu and colleagues [147] expanded microporous defects while increasing the number of chemisorbed sites, and finally synthesized phosphorus–nitrogen double-doped foamy porous carbon (PN-FPC). The formation process of the PN-FPC material is shown in Figure 8a. P/N double doping constructs a defect-rich structure in PN-FPC, facilitating the reversible adsorption/desorption behaviors of K^+. The rich mesoporous structure and fine size of

PN-FPC forms an inter-connection structure between the carbon bubbles (Figure 8b,c), which allows K^+ to move fast. As the scanning rate increases, the capacitance contribution of the PN-FPC electrode gradually increases, demonstrating that the synergy between P/N co-doping and the carbon matrix results in excellent enhancement in reaction kinetics. Meanwhile, by observing the P-C (133.5 eV) and P-O (132.5 eV) peaks in the P 2p spectra (Figure 8g), it is demonstrated that the P-O functional group could improve the wettability of PN-FPC, shortening the charge transfer process of K^+ [148]. Figure 8d illustrates that PN-FAPC, used as the positrode, maintains a reversible capacity of 110.2 mAh g^{-1} at a high rate of 5 A g^{-1}, showcasing its excellent structural stability. It exhibits a long-term lifecycle of 86.3% capacity retention over 1000 charge/discharge cycles (Figure 8e). The PN-FPC//PN-FAPC KIC shows ultra-high specific energy (155.6 Wh kg^{-1}), specific power (17,000 W kg^{-1}), and an ultra-long lifetime (90.9% capacity retention after 10,000 cycles), as shown in Figure 8f.

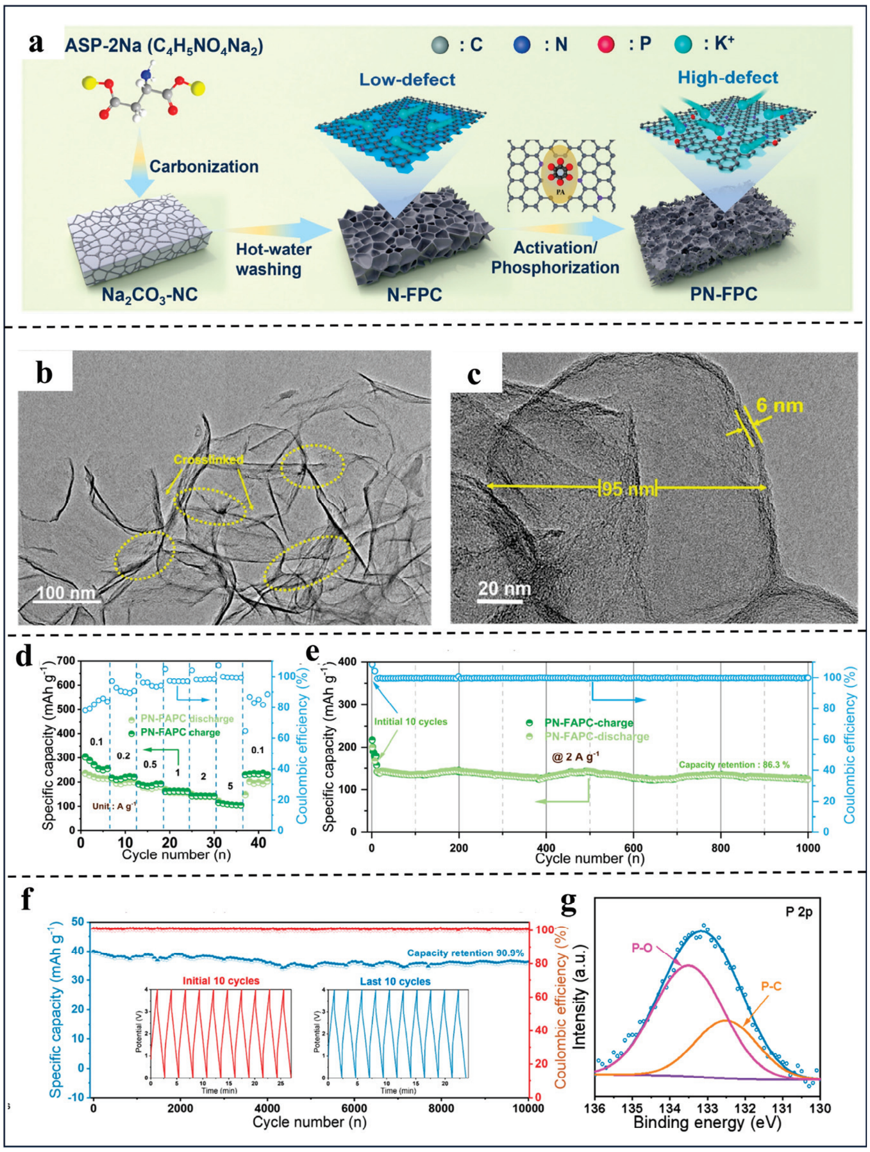

Figure 8. (**a**) A schematic illustration of the formation process of PN-FPC. (**b**,**c**) TEM images of PN-FPC. Half-cell performance of the PN-FAPC electrode tested between 1.5 and 4.2 V vs. K. (**d**) The rate performance and (**e**) lifecycle performance of the PN-FPC positrode (initial 10 cycles worked at 0.1 A g^{-1}). (**f**) The long-term cycling performance of the PN-FPC//PN-FAPC KIC at 2 A g^{-1} in full-cell configuration. (The inset shows GCD curves for the first 10 cycles and the last 10 cycles.) (**g**) The high-resolution XPS spectrum of PN-FPC of P 2p and its deconvolution. Reproduced with permission from Ref. [147]. Copyright 2024, Elsevier.

6. Discussion and Conclusions

This review has systematically summarized the recent advancements in doped carbon materials for alkali metal-ion capacitors (AMICs) with M = Li, Na, and K, as well as the mechanisms by which doping atoms such as nitrogen (N), sulfur (S), phosphorus (P), and boron (B) influence the properties of AMICs. Table 3 reports a summary of the synthesis methods and electrochemical performance of heteroatom co-doped carbon-based materials. By employing diverse synthesis strategies and combining unique precursors with dopants, carbon substrates have been crafted into a variety of electrode materials with superior characteristics. These include single-element-doped carbons (N-, S-, P-, and B-doped) and materials with double-element doping. While there has been a surge in research on heteroatom doping in carbon materials in recent years, leading to significant progress, numerous challenges remain in the practical application of these doped carbon materials as electrode materials for AMICs.

Table 3. A summary of the synthesis methods and electrochemical performance of heteroatom co-doped carbon-based materials.

Materials	Synthesis Method	Heteroatom Content%	Electrochemical System	Working Window	Cycling Data [a]	Rate Capacity [b]	Ref.
LGNC (4:1)	The denitrification and carbonization	N: 23.1at%	LIB	0.01–3.0 V	1499/100	1556/1	[45]
C-N-30-8h	molten salt method	N: 1–2at%	SIB	0.01–3.0 V	179/500	179/1	[46]
As_8Mg	Template-assisted synthesis	N: 17wt.%	SIC	0.01–2.0 V	192/600	159/1	[59]
INC	calcination	N: 5.63wt.%	LIC	0.01–3.0 V	280/3000	316/1	[60]
CS-700m	Ball milling process	S: 19.8wt.%	SIC	0.01–3.0 V	370/200	280/1	[68]
PHC-4	Esterification and carbonation reactions	P: 3.44at%	LIC	0.01–3.0 V	84.7%/5000	770.4/0.1	[75]
BGNS	Thermal reduction	B: 3.01wt.%	LIC	1.9–4.0 V	404/1000	800/0.1	[85]
NSC	Molten salt method and carbonization	N: 5.6wt.% S: 2.3wt.%	LIC	2.0–4.5 V	91.5%/10,000	81/1	[92]
NHPCS	Template-assisted methods	N: 3.65at%		2.0–4.3 V	88.7%/10,000	74/0.1	[107]
NBEG	Calcination (purify by heating)		SIC	1.5–4.2 V		328/0.5	[119]
SNC-3	Template-assisted methods	S: 7.42at% N: 7.98at%	LIC	2.0–4.0 V	90%/5000	78/0.1	[110]
NCN	Template-assisted methods	N: 7.98at%	LIC	Negatrode: 0.01–3.0 V Positrode: 0.5–4.3 V	Negatrode: 620/1000 Positrode: 110/1000	Negatrode: 1129/0.1 Positrode: 110/1.0	[122]
CTK-1.0	Carbonization in argon atmosphere	N: 3.03at%	LIC	0.01–3.0 V	97%/800	750/0.1	[123]
SGCs	Chemical Vapor Deposition (CVD) methods	S: 3.3at%	LIC	Negatrode: 0–1.5V Positrode: 1.5–4.5V	Negatrode: 98.8%/10,000 Positrode: 89.1%/10,000	Negatrode: 336/0.1 Positrode: 1668/0.1	[125]
NS-GHNS		N: 3.34wt.% S: 1.82wt.%	SIC	Negatrode: 0.01–3.0 V Positrode: 2.5–4.2 V	Negatrode: 86%/10,000 Positrode: 92%/10,000	Negatrode: 630/0.1 Positrode: 52/0.2	[126]
NPCNs	Carbonation Self-Assembly method	N: 6.60wt.%	PIC	0.01–3.0 V 0.01–4.0 V		176/1.0 82.8/0.1	[129]
PAC-6	Esterification and carbonation reactions	P: 3.57wt.%	LIC	0.01–3.0 V	90%/10,000	147.1/0.05	[138]
SPC-SCNTs	Template-assisted methods	S: 17.3wt.%	LIC	0.01–1.5 V		348/0.5	[142]
NHPC-800	Pyrolysis	N: 10.4wt.%	SIC	0.01–3.0 V		392.4/0.1	[144]
AC-SCNTs	Activation method	N: 2.1wt.%	SIC	2.0–4.5 V		110/0.1	[144]
NS-pHC-1.348	Carbonization and pickling	S: 7.77wt.%	SIC	0.01–2.5 V		383.9/0.05	[146]
PN-FPC	One-pot activation and phosphatization	N: 7.2wt.% P: 1.9wt.%	PIC	0.01–3.0 V	88.9%/1000	201.1/5	[147]
PN-FAPC	Carbonation	N: 5.1wt.%	PIC	1.5–4.2 V	86.3%/1000	110.2/5	[147]

[a] The cycling data are summarized as capacity (mAh g^{-1})/corresponding cycle numbers. [b] The rate capacity is summarized as capacity (mAh g^{-1}) at a specific current (A g^{-1}).

(1) The incorporation of various doping elements can enhance distinct chemical properties of carbon materials. For instance, the concentration of B doping is pivotal to

altering the electronic mobility within B-containing carbon and the mobility of metal ions. Similarly, different forms of nitrogen doping, such as pyrrolic N and pyridinic N, exert specific influences on the chemical properties of the carbon material. In the case of double-element-doped carbon, selecting the appropriate elements and the optimal doping ratio is crucial for achieving a better balance between the negatrode and positrode. It is important to note that while doping elements are effective in enhancing the properties of carbon materials, suitable doping levels and precise doping locations require extensive and in-depth investigation.

(2) Carbon materials from different groups possess distinct structural features, and these variations can markedly influence how doping elements affect their properties. For instance, the two-dimensional planar structure of graphene endows it with a high specific surface area and superior electrical conductivity. N doping can further enhance its electron transport capacity, thereby improving the overall electrical conductivity of the material. This makes graphene particularly suitable for applications that necessitate swift charge transfer. On the other hand, activated carbon, known for its rich pore structure, experiences an increase in surface active sites and improved ion adsorption capacity when doped with elemental phosphorus. This enhancement bolsters its capacitive performance, making it an effective electrode material. At present, due to the limitations in our research understanding, further exploration and investigation are needed to uncover how the structure of carbon materials can enhance specific chemical properties. Advanced characterization techniques and theoretical calculations can provide a deeper understanding of the interaction mechanisms between doping elements and the structure of carbon substrates.

(3) Doped carbon materials with a high specific surface area indeed offer a greater number of active sites, which enhances the adsorption and storage capabilities for M^+. However, an excessively large specific surface area can lead to excessive consumption of the electrolyte in the initial cycle. The numerous active sites can interact strongly with the electrolyte, leading to the formation of a thick solid electrolyte interphase (SEI) film on the electrode surface. This SEI film formation consumes a significant amount of Li^+, causing substantial energy loss for the electrochemical device. Additionally, the overconsumption of the electrolyte results in a large amount of Li^+ being irreversibly intercalated into the electrode material during the first charge/discharge process, thereby reducing the initial coulombic efficiency (ICE). Therefore, designing doped carbon with an appropriate specific surface area is essential to strike a balance between achieving high capacity and maintaining high ICE.

In summary, the key to the design of doped carbon materials with excellent performance lies in mastering the type of doping atoms, the choice of concentration, and the design of a suitable specific surface area. At present, the practical application of doped carbon materials in AMICs has shown some potential but is still immature. Future research should continue to explore optimization strategies of doped carbon materials to overcome the current challenges and to promote the overall performance of AMICs for wider and more efficient applications in the field of energy storage.

Author Contributions: Conceptualization, K.Z.; methodology, T.Y. and X.H.; software, X.Y.; validation, X.H.; formal analysis, Y.G. and T.N.; investigation, Y.G. and L.Q.; resources, K.Z. and L.T.; data curation, T.Y.; writing—original draft preparation, T.Y. and Y.G.; writing—review and editing, X.H.; visualization, T.Y.; supervision, K.Z. and X.H.; project administration, L.L.; funding acquisition, K.Z. and L.L. All authors have read and agreed to the published version of the manuscript.

Funding: This work was supported by the National Natural Science Foundation of China (52374299, 52304320, and 52204306), the Outstanding Youth Foundation of Hunan Province (2023JJ10044), the

Scientific Research Fund of Hunan Provincial Department of Education (24B0295), the Natural Science Foundation of Hunan Province (2023JJ40014), and the Innovation and Entrepreneurship Training Program of Hunan Province (S202310536164).

Conflicts of Interest: The author declares no conflicts of interest.

References

1. Liu, Z.; Wang, J.; Lu, B. Plum pudding model inspired $KVPO_4F$@3DC as high-voltage and hyperstable cathode for potassium ion batteries. *Sci. Bull.* **2020**, *65*, 1242–1251. [CrossRef]
2. Zou, K.; Jiang, M.; Ning, T.; Tan, L.; Zheng, J.; Wang, J.; Ji, X.; Li, L. Thermodynamics-directed bulk/grain-boundary engineering for superior electrochemical durability of Ni-rich cathode. *J. Energy Chem.* **2024**, *97*, 321–331. [CrossRef]
3. Zhang, X.; Wang, L.; Liu, W.; Li, C.; Wang, K.; Ma, Y. Recent advances in MXenes for lithium-ion capacitors. *ACS Omega* **2020**, *5*, 75–82. [CrossRef] [PubMed]
4. Dai, M.; Zhao, D.; Wu, X. Research progress on transition metal oxide based electrode materials for asymmetric hybrid capacitors. *Chin. Chem. Lett.* **2020**, *31*, 2177–2188. [CrossRef]
5. Amatucci, G.G.; Badway, F.; Pasquier, D.A.; Zheng, T. An asymmetric hybrid nonaqueous energy storage cell. *J. Electrochem. Soc.* **2001**, *148*, A930–A939. [CrossRef]
6. Soltani, M.; Beheshti, S.H. A comprehensive review of lithium ion capacitor: Development, modelling, thermal management and applications. *J. Energy Storage* **2021**, *34*, 102019. [CrossRef]
7. Nagamuthu, S.; Zhang, Y.; Xu, Y.; Sun, J.; Zhang, Y.; Zaman, F.; Denis, D.; Hou, L.; Yuan, C. Non-lithium-based metal ion capacitors: Recent advances and perspectives. *J. Mater. Chem. A* **2022**, *10*, 357–378. [CrossRef]
8. Liu, W.; Zhang, X.; Li, C.; Wang, K.; Sun, X.; Ma, Y. Carbon-coated Li_3VO_4 with optimized structure as high capacity anode material for lithium-ion capacitors. *Chin. Chem. Lett.* **2020**, *31*, 2225–2229. [CrossRef]
9. Cao, L.; Li, H.; Liu, X.; Liu, S.; Zhang, L.; Xu, W.; Yang, H.; Hou, H.; He, S.; Zhao, Y.; et al. Nitrogen, sulfur co-doped hierarchical carbon encapsulated in graphene with "sphere-in-layer" interconnection for high-performance supercapacitor. *J. Colloid Interface Sci.* **2021**, *599*, 443–452. [CrossRef]
10. Ma, X.; Gao, D. High capacitive storage performance of sulfur and nitrogen codoped mesoporous graphene. *ChemSusChem* **2018**, *11*, 1048–1055. [CrossRef] [PubMed]
11. Jiang, M.; Wang, P.; Chen, Q.; Zhang, Y.; Wu, Q.; Tan, L.; Ning, T.; Li, L.; Zou, K. Enabling the Nb/Ti co-doping strategy for improving structure stability and rate capability of Ni-rich cathode. *Chin. Chem. Lett.* **2024**, *35*, 110040. [CrossRef]
12. Wang, B.; Gao, X.; Xu, L.; Zou, K.; Cai, P.; Deng, X.; Yang, L.; Hou, H.; Zou, G.; Ji, X. Advanced carbon materials for sodium-ion capacitors. *Batter. Supercaps* **2021**, *4*, 538–553. [CrossRef]
13. Zhou, J.; Hu, H.; Li, H.; Chen, Z.; Yuan, C.; He, X. Advanced carbon-based materials for Na, K, and Zn ion hybrid capacitors. *Rare Met.* **2023**, *42*, 719–739. [CrossRef]
14. Li, L.; Chen, Q.; Jiang, M.; Ning, T.; Tan, L.; Zhang, X.; Zheng, J.; Wang, J.; Wu, Q.; Ji, X.; et al. Uncovering mechanism behind tungsten bulk/grain-boundary modification of Ni-rich cathode. *Energy Storage Mater.* **2025**, *75*, 104016. [CrossRef]
15. Peng, Y.; Bai, Y.; Liu, C.; Cao, S.; Kong, Q.; Pang, H. Applications of metal-organic framework-derived N, P, S doped materials in electrochemical energy conversion and storage. *Coord. Chem. Rev.* **2022**, *466*, 214602. [CrossRef]
16. Zhang, J.; Fang, J.; Han, J.; Yan, T.; Shi, L.; Zhang, D. N, P, S co-doped hollow carbon polyhedra derived from MOF-based core-shell nanocomposites for capacitive deionization. *J. Mater. Chem. A* **2018**, *6*, 15245–15252. [CrossRef]
17. Zou, K.; Xie, S.; Jiang, M.; Wang, P.; Ning, T.; Tan, L.; Li, H.; Zhou, Y.; Wang, W.; Li, L. Insights into the precursor specific surface area for engineering Co-free Ni-rich cathodes with tailorable properties. *Chem. Eng. J.* **2024**, *483*, 149189. [CrossRef]
18. Feng, X.; Bai, Y.; Liu, M.; Li, Y.; Yang, H.; Wang, X.; Wu, C. Untangling the respective effects of heteroatom-doped carbon materials in batteries, supercapacitors and the ORR to design high performance materials. *Energy Environ. Sci.* **2021**, *14*, 2036–2089. [CrossRef]
19. Shao, T.; Liu, C.; Deng, W.; Li, C.; Wang, X.; Xue, M.; Li, R. Recent research on strategies to improve ion conduction in alkali metal-ion batteries. *Batter. Supercaps* **2019**, *2*, 403–427. [CrossRef]
20. Chen, Z. Supercapacitor and supercapattery as emerging electrochemical energy stores. *Int. Mater. Rev.* **2017**, *62*, 173–202. [CrossRef]
21. Shao, H.; Wu, Y.; Lin, Z.; Taberna, P.; Simon, P. Nanoporous carbon for electrochemical capacitive energy storage. *Chem. Soc. Rev.* **2020**, *49*, 3005–3039. [CrossRef] [PubMed]
22. Mirzaeian, M.; Abbas, Q.; Gibson, D.; Mazur, M. Effect of nitrogen doping on the electrochemical performance of resorcinol-formaldehyde based carbon aerogels as electrode material for supercapacitor applications. *Energy* **2019**, *173*, 809–819. [CrossRef]
23. Rudra, S.; Seo, H.; Sarker, S.; Kim, D. Supercapatteries as hybrid electrochemical energy storage devices: Current status and future prospect. *Molecules* **2024**, *29*, 243. [CrossRef] [PubMed]

24. Sun, Y.; Wang, H.; Wei, W.; Zheng, Y.; Tao, L.; Wang, Y.; Huang, M.; Shi, J.; Shi, Z.; Mitlin, D. Sulfur-rich graphene nanoboxes with ultra-high potassiation capacity at fast charge: Storage mechanisms and device performance. *ACS Nano* **2021**, *15*, 1652–1665. [CrossRef] [PubMed]
25. Zou, K.; Jiang, M.; Zhao, Z.; Xie, S.; Ning, T.; Tan, L.; Li, H.; Zhou, Y.; Wang, W.; Wu, X.; et al. Mechanistic insights into suppressing microcracks by regulating grain size of precursor for high-performance Ni-rich cathodes. *Chem. Eng. J.* **2023**, *476*, 146793. [CrossRef]
26. González, A.; Goikolea, E.; Barrena, J.A.; Mysyk, R. Review on supercapacitors: Technologies and materials. *Renew. Sustain. Energy Rev.* **2016**, *58*, 1189–1206. [CrossRef]
27. Wu, M.; Hu, X.; Zheng, W.; Chen, L.; Zhang, Q. Recent advances in porous carbon nanosheets for high-performance metal-ion capacitors. *Chem. Eng. J.* **2023**, *466*, 143077. [CrossRef]
28. Cao, B.; Li, X. Recent progress on carbon-based anode materials for Na-ion batteries. *Acta Phys.-Chim. Sin.* **2020**, *36*, 1905003. [CrossRef]
29. Zhao, C.; Wei, Y.; Pan, Y.; Chen, C. A novel strategy for capacity judgement of hard carbon in sodium-ion batteries: Ensuring the consistency of the available anode capacity between half-cell and full-cell. *Solid State Ion.* **2024**, *412*, 116586. [CrossRef]
30. Han, P.; Xu, G.; Han, X.; Zhao, J.; Zhou, X.; Cui, G. Lithium ion capacitors in organic electrolyte system: Scientific problems, material development, and key technologies. *Adv. Energy Mater.* **2018**, *8*, 1801243. [CrossRef]
31. Li, B.; Zhen, J.; Zhang, H.; Jin, L.; Yang, D.; Lv, H.; Shen, C.; Shellikeri, A.; Zheng, Y.; Gong, R.; et al. Electrode materials, electrolytes, and challenges in nonaqueous lithium-ion capacitors. *Adv. Mater.* **2018**, *30*, 1705670. [CrossRef]
32. Wei, Q.; Liu, J.; Feng, W.; Sheng, J.; Tian, X.; He, L.; An, Q.; Mai, L. Hydrated vanadium pentoxide with superior sodium storage capacity. *J. Mater. Chem. A* **2015**, *3*, 8070–8075. [CrossRef]
33. Wang, H.; Zhu, C.; Chao, D.; Yan, Q.; Fan, H. Nonaqueous hybrid lithium-ion and sodium-ion capacitors. *Adv. Mater.* **2017**, *29*, 1702093. [CrossRef] [PubMed]
34. Shi, R.; Han, C.; Li, H.; Xu, L.; Zhang, T.; Li, J.; Lin, Z.; Wong, C.; Kang, F.; Li, B. NaCl-templated synthesis of hierarchical porous carbon with extremely large specific surface area and improved graphitization degree for high energy density lithium ion capacitors. *J. Mater. Chem. A* **2018**, *6*, 17057–17066. [CrossRef]
35. Li, N.; Du, X.; Shi, J.; Zhang, X.; Fan, W.; Wang, J.; Zhao, S.; Liu, Y.; Xu, W.; Li, M.; et al. Graphene@hierarchical meso-/microporous carbon for ultrahigh energy density lithium-ion capacitors. *Electrochim. Acta* **2018**, *281*, 459–465. [CrossRef]
36. Ma, H.; Geng, H.; Yao, B.; Wu, M.; Li, C.; Zhang, M.; Chi, F.; Qu, L. Highly ordered graphene solid: An efficient platform for capacitive sodium-ion storage with ultrahigh volumetric capacity and superior rate capability. *ACS Nano* **2019**, *13*, 9161–9170. [CrossRef]
37. Cao, Y.; Mao, S.; Li, M.; Chen, Y.; Wang, Y. Metal/porous carbon composites for heterogeneous catalysis: Old catalysts with improved performance promoted by N-doping. *ACS Catal.* **2017**, *7*, 8090–8112. [CrossRef]
38. Inagaki, M.; Toyoda, M.; Soneda, Y.; Morishita, T. Nitrogen-doped carbon materials. *Carbon* **2018**, *132*, 104–140. [CrossRef]
39. Du, J.; Liu, L.; Yu, Y.; Zhang, Y.; Lv, H.; Chen, A. N-doped ordered mesoporous carbon spheres derived by confined pyrolysis for high supercapacitor performance. *J. Mater. Sci. Technol.* **2019**, *35*, 2178–2186. [CrossRef]
40. Lv, Q.; Si, W.; He, J.; Sun, L.; Zhang, C.; Wang, N.; Yang, Z.; Li, X.; Wang, X.; Deng, W.; et al. Selectively nitrogen-doped carbon materials as superior metal-free catalysts for oxygen reduction. *Nat. Commun.* **2018**, *9*, 3376. [CrossRef]
41. Tan, H.; Tang, J.; Kim, J.; Kaneti, Y.; Kang, Y.; Sugahara, Y.; Yamauchi, Y. Rational design and construction of nanoporous iron- and nitrogen-doped carbon electrocatalysts for oxygen reduction reaction. *J. Mater. Chem. A* **2019**, *7*, 1380–1393. [CrossRef]
42. Wang, X.; Li, X.; Zhang, L.; Yoon, Y.; Weber, P.; Wang, H.; Guo, J.; Dai, H. N-doping of graphene through electrothermal reactions with ammonia. *Science* **2009**, *324*, 768–771. [CrossRef]
43. Paraknowitsch, P.; Thomas, A.; Antonietti, M. A detailed view on the polycondensation of ionic liquid monomers towards nitrogen doped carbon materials. *J. Mater. Chem.* **2010**, *20*, 6746–6758. [CrossRef]
44. Seredych, M.; Hulicova-Jurcakova, D.; Lu, G.; Bandosz, T. Surface functional groups of carbons and the effects of their chemical character, density and accessibility to ions on electrochemical performance. *Carbon* **2008**, *46*, 1475–1488. [CrossRef]
45. Tang, Y.; Chen, J.; Mao, Z.; Roth, C.; Wang, D. Highly N-doped carbon with low graphitic-N content as anode material for enhanced initial coulombic efficiency of lithium-ion batteries. *Carbon Energy* **2022**, *5*, e257. [CrossRef]
46. Zhao, J.; Song, Q.; Zhao, H.; Xie, H.; Ning, Z.; Yu, K. Molten salt splitting of CO_2 with CaC_2 and in-situ nitrogen doping for carbon anode of lithium/sodium-ion batteries. *J. Electroanal. Chem.* **2023**, *950*, 117845. [CrossRef]
47. Zhang, C.; Zhong, X.; Chen, P.; Sun, S.; Jiang, Y.; Yan, X. Facile synthesis of porous graphite by calcium carbide and nitrogen gas for lithium-ion batteries. *J. Energy Storage* **2023**, *66*, 107386. [CrossRef]
48. Sadezky, A.; Muckenhuber, H.; Grothe, H.; Niessner, R.; Pöschl, U. Raman microspectroscopy of soot and related carbonaceous materials: Spectral analysis and structural information. *Carbon* **2005**, *43*, 1731–1742. [CrossRef]
49. Rivera–Utrilla, J.; Ferro–García, M.A. Effect of carbon-oxygen and carbon-nitrogen surface complexes on the adsorption of cations by activated carbons. *Adsorpt. Sci. Technol.* **1986**, *3*, 293–302. [CrossRef]

50. Keegel, F.; Suruda, A.; Schwob, C. The catalytic properties of charcoal. III. A comparison of the oxidative properties of various charcoals. The effect of charcoal hydrosols on hydrogen peroxide and oxygen. *J. Am. Chem. Soc.* **1938**, *60*, 2483–2486. [CrossRef]
51. Stöhr, B.; Boehm, H.; Schlögl, R. Enhancement of the catalytic activity of activated carbons in oxidation reactions by thermal treatment with ammonia or hydrogen cyanide and observation of a superoxide species as a possible intermediate. *Carbon* **1991**, *29*, 707–720. [CrossRef]
52. Boehm, H. Catalytic properties of nitrogen-containing carbons. *Carbon Mater. Catal.* **2008**, *7*, 219–265. [CrossRef]
53. Fu, W.; Zhang, K.; Chen, M.; Zhang, M.; Shen, Z. One-pot synthesis of N-doped hierarchical porous carbon for high-performance aqueous capacitors in a wide pH range. *J. Power Sources* **2021**, *491*, 229587. [CrossRef]
54. Luo, X.; Yang, Q.; Dong, Y.; Huang, X.; Kong, D.; Wang, B.; Liu, H.; Xiao, Z.; Zhi, L. Maximizing pore and heteroatom utilization within N, P-co-doped polypyrrole-derived carbon nanotubes for high-performance supercapacitors. *J. Mater. Chem. A* **2020**, *8*, 17558–17567. [CrossRef]
55. Xu, Y.; Zhang, C.; Zhou, M.; Fu, Q.; Zhao, C.; Wu, M.; Lei, Y. Highly nitrogen doped carbon nanofibers with superior rate capability and cyclability for potassium ion batterie. *Nat. Commun.* **2018**, *9*, 1720. [CrossRef]
56. Chen, Z.; Zhao, S.; Zhou, Y.; Yu, C.; Zhong, W.; Yang, W. Nacre-like laminate nitrogen-doped porous carbon/carbon nanotubes/graphene composite for excellent comprehensive performance supercapacitors. *Nanoscale* **2018**, *10*, 15229–15237. [CrossRef]
57. Sanchez-Sanchez, A.; Izquierdo, M.; Mathieu, S.; González-Álvarez, J.; Celzard, A.; Fierro, V. Outstanding electrochemical performance of highly N- and O-doped carbons derived from pine tannin. *Green Chem.* **2017**, *19*, 2653–2665. [CrossRef]
58. Li, Z.; Cao, L.; Chen, W.; Huang, Z.; Liu, H. Mesh-like carbon nanosheets with high-level nitrogen doping for high-energy dual-carbon lithium-ion capacitors. *Small* **2019**, *15*, e1805173. [CrossRef] [PubMed]
59. Li, C.; Song, Z.; Liu, M.; Lepre, E.; Antonietti, M.; Zhu, J.; Liu, J.; Fu, Y.; López-Salas, N. Template-induced graphitic nanodomains in nitrogen-doped carbons enable high-performance sodium-ion capacitors. *Energy Environ. Mater.* **2024**, *7*, e12695. [CrossRef]
60. Chen, J.; Zhu, Y.; Luo, D.; Ma, G.; Zhao, Y.; Liu, B.; Yang, B.; Li, Y. Interconnected N-doped carbon network as high-performance anode material for superior lithium ion hybrid capacitor. *Mater. Today Commun.* **2023**, *34*, 105142. [CrossRef]
61. Ma, C.; Shao, X.; Cao, D. Nitrogen-doped graphene nanosheets as anode materials for lithium ion batteries: A first-principles study. *J. Mater. Chem.* **2012**, *22*, 8911–8915. [CrossRef]
62. Lu, Z.; Gao, D.; Yi, D.; Yang, Y.; Wang, X.; Yao, J. sp^2/sp^3 hybridized carbon as an anode with extra Li-ion storage capacity: Construction and origin. *ACS Cent. Sci.* **2020**, *6*, 1451–1459. [CrossRef]
63. Yan, J.; Li, W.; Feng, P.; Wang, R.; Jiang, M.; Han, J.; Cao, S.; Wang, K.; Jiang, K. Enhanced Na^+ pseudocapacitance in a P, S co-doped carbon anode arising from the surface modification by sulfur and phosphorus with C-S-P coupling. *J. Mater. Chem. A* **2020**, *8*, 422–432. [CrossRef]
64. Gopalakrishnan, A.; Raju, D.; Badhulika, S. Green synthesis of nitrogen, sulfur-co-doped worm-like hierarchical porous carbon derived from ginger for outstanding supercapacitor performance. *Carbon* **2020**, *168*, 209–219. [CrossRef]
65. Li, G.; Mao, K.; Liu, M.; Yan, M.; Zhao, J.; Zeng, Y.; Yang, L.; Wu, Q.; Wang, X.; Hu, Z. Achieving ultrahigh volumetric energy storage by compressing nitrogen and sulfur dual-doped carbon nanocages via capillarity. *Adv. Mater.* **2020**, *32*, 2004632. [CrossRef] [PubMed]
66. Zhao, G.; Yu, D.; Zhang, H.; Sun, F.; Li, J.; Zhu, L.; Sun, L.; Yu, M.; Besenbacher, F.; Sun, Y. Sulphur-doped carbon nanosheets derived from biomass as high-performance anode materials for sodium-ion batteries. *Nano Energy* **2020**, *67*, 104219. [CrossRef]
67. Li, D.; Chang, G.; Zong, L.; Xue, P.; Wang, Y.; Xia, Y.; Lai, C.; Yang, D. From double-helix structured seaweed to S-doped carbon aerogel with ultra-high surface area for energy storage. *Energy Storage Mater.* **2018**, *17*, 22–30. [CrossRef]
68. Casal, M.; Díez, N.; Payá, S.; Sevilla, M. Cork-derived carbon sheets for high-performance Na-ion capacitors. *ACS Appl. Energy Mater.* **2023**, *6*, 8120–8131. [CrossRef] [PubMed]
69. Hong, Z.; Zhen, Y.; Ruan, Y.; Kang, M.; Zhou, K.; Zhang, J.; Huang, Z.; Wei, M. Rational design and general synthesis of S-Doped hard carbon with tunable doping sites toward excellent Na-ion storage performance. *Adv. Mater.* **2018**, *30*, 1802035. [CrossRef]
70. Liu, F.; Niu, J.; Chuan, X.; Zhao, Y. Nitrogen and phosphorus co-doped porous carbon: Dopant, synthesis, performance enhancement mechanism and versatile applications. *J. Power Sources* **2024**, *601*, 234308. [CrossRef]
71. Wang, H.; Chen, H.; Chen, C.; Li, M.; Xie, Y.; Zhang, X.; Wu, X.; Zhang, Q.; Lu, C. Tea-derived carbon materials as anode for high-performance sodium ion batteries. *Chin. Chem. Lett.* **2023**, *34*, 107465. [CrossRef]
72. Liu, H.; Wang, M.; Zhai, D.; Chen, X.; Zhang, Z. Design and theoretical study of carbon-based supercapacitors especially exhibiting superior rate capability by the synergistic effect of nitrogen and phosphor dopants. *Carbon* **2019**, *155*, 223–232. [CrossRef]
73. Wang, X.; Hou, M.; Shi, Z.; Liu, X.; Mizota, I.; Lou, H.; Wang, B.; Hou, X. Regulate phosphorus configuration in high P-doped hard carbon as a superanode for sodium storage. *ACS Appl. Mater. Interfaces* **2021**, *13*, 12059–12068. [CrossRef]
74. Guo, J.; Xu, X.; Hill, J.; Wang, L.; Dang, J.; Kang, Y.; Li, Y.; Guan, W.; Yamauchi, Y. Graphene-carbon 2D heterostructures with hierarchically-porous P, N-doped layered architecture for capacitive deionizatio. *Chem. Sci.* **2021**, *12*, 10334–10340. [CrossRef]
75. Yang, Z.; Gao, Y.; Zhao, Z.; Wang, Y.; Wu, Y.; Wang, X. Phytic acid assisted formation of P-doped hard carbon anode with enhanced capacity and rate capability for lithium ion capacitors. *J. Power Sources* **2020**, *474*, 228500. [CrossRef]

76. Qian, Y.; Jiang, S.; Li, Y.; Yi, Z.; Zhou, J.; Li, T.; Han, Y.; Wang, Y.; Tian, J.; Lin, N.; et al. In situ revealing the electroactivity of P-O and P-C bonds in hard carbon for high-capacity and long-life Li/K-ion batteries. *Adv. Energy Mater.* **2019**, *9*, 1901676. [CrossRef]
77. Li, Y.; Yuan, Y.; Bai, Y.; Liu, Y.; Wang, Z.; Li, L.; Wu, F.; Amine, K.; Wu, C.; Lu, J. Insights into the Na^+ storage mechanism of phosphorus-functionalized hard carbon as ultrahigh capacity anodes. *Adv. Energy Mater.* **2018**, *8*, 1702781. [CrossRef]
78. McKee, D. Oxidation protection of carbon materials. In *Chemistry & Physics of Carbon*; CRC Press: Boca Raton, FL, USA, 2021; pp. 173–232. [CrossRef]
79. Yao, J.; Li, F.; Zhou, R.; Guo, C.; Liu, X.; Zhu, Y. Phosphorous-doped carbon nanotube/reduced graphene oxide aerogel cathode enabled by pseudocapacitance for high energy and power zinc-ion hybrid capacitors. *Chin. Chem. Lett.* **2024**, *35*, 108354. [CrossRef]
80. Zhao, Y.; Yang, L.; Chen, S.; Wang, X.; Ma, Y.; Wu, Q.; Jiang, Y.; Qian, W.; Hu, Z. Can boron and nitrogen co-doping improve oxygen reduction reaction activity of carbon nanotubes? *J. Am. Chem. Soc.* **2013**, *135*, 1201–1204. [CrossRef]
81. Kim, Y.; Fujisawa, K.; Muramatsu, H.; Hayashi, T.; Endo, M.; Fujimori, T.; Kaneko, K.; Terrones, M.; Behrends, J.; Eckmann, A.; et al. Raman spectroscopy of boron-doped single-layer graphene. *ACS Nano* **2012**, *6*, 6293–6300. [CrossRef]
82. Zhang, Y.; Zuo, L.; Zhang, L.; Yan, J.; Lu, H.; Fan, W.; Liu, T. Immobilization of NiS nanoparticles on N-doped carbon fiber aerogels as advanced electrode materials for supercapacitors. *Nano Res.* **2016**, *9*, 2747–2759. [CrossRef]
83. Han, J.; Zhang, L.; Lee, S.; Oh, J.; Lee, K.; Potts, J.; Ji, J.; Zhao, X.; Ruoff, R.; Park, S. Generation of B-doped graphene nanoplatelets using a solution process and their supercapacitor application. *ACS Nano* **2013**, *7*, 19–26. [CrossRef]
84. Panchakarla, S.; Subrahmanyam, S.; Saha, K.; Govindaraj, A.; Krishnamurthy, R.; Waghmare, V.; Rao, R. Synthesis, structure, and properties of boron- and nitrogen-doped graphene. *Adv. Mater.* **2009**, *21*, 4726–4730. [CrossRef]
85. Bhattacharjee, U.; Bhowmik, S.; Ghosh, S.; Vangapally, N.; Martha, S. Boron-doped graphene anode coupled with microporous activated carbon cathode for lithium-ion ultracapacitors. *Chem. Eng. J.* **2022**, *430*, 132835. [CrossRef]
86. Wang, X.; Sun, G.; Routh, P.; Kim, D.; Huang, W.; Chen, P. Heteroatom-doped graphene materials: Syntheses, properties and applications. *Chem. Soc. Rev.* **2014**, *43*, 7067–7098. [CrossRef] [PubMed]
87. Naresh, V.; Bhattacharjee, U.; Martha, K. Boron doped graphene nanosheets as negative electrode additive for high-performance lead-acid batteries and ultracapacitors. *J. Alloys Compd.* **2019**, *797*, 595–605. [CrossRef]
88. Miao, X.; Sun, D.; Zhou, X.; Lei, Z. Designed formation of nitrogen and sulfur dual-doped hierarchically porous carbon for long-life lithium and sodium ion batteries. *Chem. Eng. J.* **2019**, *364*, 208–216. [CrossRef]
89. Ruan, J.; Zhao, Y.; Luo, S.; Yuan, T.; Yang, J.; Sun, D.; Zheng, S. Fast and stable potassium-ion storage achieved by in situ molecular self-assembling N/O dual-doped carbon network. *Energy Storage Mater.* **2019**, *23*, 46–54. [CrossRef]
90. Zou, G.; Hou, H.; Foster, C.; Banks, C.; Guo, T.; Jiang, Y.; Zhang, Y.; Ji, X. Advanced hierarchical vesicular carbon co-doped with S, P, N for high-rate sodium storage. *Adv. Sci.* **2018**, *5*, 1800241. [CrossRef]
91. Huang, R.; Cao, Y.; Qin, S.; Ren, Y.; Lan, R.; Zhang, L.; Yu, Z.; Yang, H. Ultra-high N-doped open hollow carbon nano-cage with excellent Na^+ and K^+ storage performances. *Mater. Today Nano* **2022**, *18*, 100217. [CrossRef]
92. Hu, S.; Ge, Z.; Tan, J.; Lai, H.; Feng, T.; Zhang, S.; Xu, Z.; Zhou, H.; Cao, X.; Zhu, G.; et al. Dual-functionally modified N/S doped hierarchical porous carbon and glycerol-engineered polyacrylonitrile carbon nanofibers combine for high-performance lithium-ion capacitors. *J. Power Sources* **2023**, *558*, 232624. [CrossRef]
93. Guan, L.; Pan, L.; Peng, T.; Gao, C.; Zhao, W.; Yang, Z.; Hu, H.; Wu, M. Synthesis of biomass-derived nitrogen-doped porous carbon nanosheests for high-performance supercapacitors. *ACS Sustain. Chem. Eng.* **2019**, *7*, 8405–8412. [CrossRef]
94. Pei, Z.; Li, H.; Huang, Y.; Xue, Q.; Huang, Y.; Zhu, M.; Wang, Z.; Zhi, C. Texturing in situ: N, S-enriched hierarchically porous carbon as a highly active reversible oxygen electrocatalyst. *Energy Environ. Sci.* **2017**, *10*, 742–749. [CrossRef]
95. Ghosh, S.; Barg, S.; Jeong, S.; Ostrikov, K. Heteroatom-doped and oxygen-functionalized nanocarbons for high-performance supercapacitors. *Adv. Energy Mater.* **2020**, *10*, 2001239. [CrossRef]
96. Chen, M.; Le, T.; Zhou, Y.; Kang, F.; Yang, Y. Thiourea-induced N/S dual-doped hierarchical porous carbon nanofibers for high-performance lithium-ion capacitors. *ACS Appl. Energy Mater.* **2020**, *3*, 1653–1664. [CrossRef]
97. Hu, L.; Hou, J.; Ma, Y.; Li, H.; Zhai, T. Multi-heteroatom self-doped porous carbon derived from swim bladders for large capacitance supercapacitors. *J. Mater. Chem. A* **2016**, *4*, 15006–15014. [CrossRef]
98. Wang, J.; Liu, H.; Zhang, X.; Shao, M.; Wei, B. Elaborate construction of N/S-co-doped carbon nanobowls for ultrahigh-power supercapacitors. *J. Mater. Chem. A* **2018**, *6*, 17653–17661. [CrossRef]
99. Xu, F.; Tang, Z.; Huang, S.; Chen, L.; Liang, Y.; Mai, W.; Zhong, H.; Fu, R.; Wu, D. Facile synthesis of ultrahigh-surface-area hollow carbon nanospheres for enhanced adsorption and energy storage. *Nat. Commun.* **2015**, *6*, 7221. [CrossRef] [PubMed]
100. Xu, D.; Chen, C.; Xie, J.; Zhang, B.; Miao, L.; Cai, J.; Huang, Y.; Zhang, L. A hierarchical N/S-codoped carbon anode fabricated facilely from cellulose/polyaniline microspheres for high-performance sodium-ion batterie. *Adv. Energy Mater.* **2016**, *6*, 1501929. [CrossRef]
101. Ye, J.; Zang, J.; Tian, Z.; Zheng, M.; Dong, Q. Sulfur and nitrogen co-doped hollow carbon spheres for sodium-ion batteries with superior cyclic and rate performance. *J. Mater. Chem. A* **2016**, *4*, 13223–13227. [CrossRef]

102. Chen, C.; Li, G.; Zhu, J.; Lu, Y.; Jiang, M.; Hu, Y.; Shen, Z.; Zhang, X. In-situ formation of tin-antimony sulfide in nitrogen-sulfur co-doped carbon nanofibers as high performance anode materials for sodium-ion batteries. *Carbon* **2017**, *120*, 380–391. [CrossRef]
103. Sheng, J.; Yang, L.; Zhu, Y.; Li, F.; Zhang, Y.; Zhou, Z. Oriented SnS nanoflakes bound on S-doped N-rich carbon nanosheets with a rapid pseudocapacitive response as high-rate anodes for sodium-ion batteries. *J. Mater. Chem. A* **2017**, *5*, 19745–19751. [CrossRef]
104. Zou, L.; Lai, Y.; Hu, H.; Wang, M.; Zhang, K.; Zhang, P.; Fang, J.; Li, J. N/S Co-doped 3D porous carbon nanosheet networks enhancing anode performance of sodium-ion batteries. *Chem. A Eur. J.* **2017**, *23*, 14261–14266. [CrossRef]
105. Ruan, J.; Yuan, T.; Pang, Y.; Luo, S.; Peng, C.; Yang, J.; Zheng, S. Nitrogen and sulfur dual-doped carbon films as flexible free-standing anodes for Li-ion and Na-ion batteries. *Carbon* **2018**, *126*, 9–16. [CrossRef]
106. Yang, J.; Zhou, X.; Wu, D.; Zhao, X.; Zhou, Z. S-doped N-rich carbon nanosheets with expanded interlayer distance as anode materials for sodium-ion batteries. *Adv. Mater.* **2017**, *29*, 1604108. [CrossRef]
107. Xu, Y.; Jiang, J.; Li, Z.; Yang, Z.; Zhang, Y.; An, Y.; Zhu, Q.; Dou, H.; Zhang, X. Aerosol-assisted preparation of N-doped hierarchical porous carbon spheres cathodes toward high-stable lithium-ion capacitors. *J. Mater. Sci.* **2020**, *55*, 13127–13140. [CrossRef]
108. Sun, L.; Zhou, H.; Yao, Y.; Qu, H.; Zhang, C.; Liu, S.; Zhou, Y. Double soft-template synthesis of nitrogen/sulfur-codoped hierarchically porous carbon materials derived from protic ionic liquid for supercapacitor. *ACS Appl. Mater. Interfaces* **2017**, *9*, 26088–26095. [CrossRef] [PubMed]
109. Deng, X.; Zou, K.; Momen, R.; Cai, P.; Chen, J.; Hou, H.; Zou, G.; Ji, X. High content anion (S/Se/P) doping assisted by defect engineering with fast charge transfer kinetics for high-performance sodium ion capacitors. *Sci. Bull.* **2021**, *66*, 1858–1868. [CrossRef] [PubMed]
110. Shi, L.; Zeng, Q.; Liu, J.; Yang, Y. S, N co-doped porous carbon derived from metal-organic frameworks as cathode for lithium-ion capacitor. *J. Electroanal. Chem.* **2023**, *944*, 117675. [CrossRef]
111. Bhagwan, J.; Nagaraju, G.; Ramulu, B.; Sekhar, S.; Yu, J. Rapid synthesis of hexagonal $NiCo_2O_4$ nanostructures for high-performance asymmetric supercapacitors. *Electrochim. Acta* **2019**, *299*, 509–517. [CrossRef]
112. Gu, J.; Sun, L.; Zhang, Y.; Zhang, Q.; Li, X.; Si, H.; Shi, Y.; Sun, C.; Gong, Y.; Zhang, Y. MOF-derived Ni-doped CoP@C grown on CNTs for high-performance supercapacitors. *Chem. Eng. J.* **2020**, *385*, 123454. [CrossRef]
113. Zou, K.; Deng, W.; Silvester, D.S.; Zou, G.; Hou, H.; Banks, C.E.; Li, L.; Hu, J.; Ji, X. Carbonyl chemistry for advanced electrochemical energy storage systems. *ACS Nano* **2024**, *18*, 19950–20000. [CrossRef]
114. Hu, Y.; Tang, C.; Li, H.; Du, A.; Luo, W.; Wu, M.; Zhang, H. B-incorporated, N-doped hierarchically porous carbon nanosheets as anodes for boosted potassium storage capability. *Chin. Chem. Lett.* **2022**, *33*, 480–485. [CrossRef]
115. Choi, C.H.; Park, S.H.; Woo, S.I. Binary and ternary doping of nitrogen, boron, and phosphorus into carbon for enhancing electrochemical oxygen reduction activity. *ACS Nano* **2012**, *6*, 7084–7091. [CrossRef]
116. Wang, S.; Iyyamperumal, E.; Roy, A.; Xue, Y.; Yu, D.; Dai, L. Vertically aligned BCN nanotubes as efficient metal-free electrocatalysts for the oxygen reduction reaction: A synergetic effect by co-doping with boron and nitrogen. *Angew. Chem. Int. Ed.* **2011**, *50*, 11756–11760. [CrossRef]
117. Zheng, Y.; Jiao, Y.; Ge, L.; Jaroniec, M.; Qiao, S. Two-step boron and nitrogen doping in graphene for enhanced synergistic catalysis. *Angew. Chem. Int. Ed.* **2013**, *52*, 3110–3116. [CrossRef] [PubMed]
118. Wu, Z.; Winter, A.; Chen, L.; Sun, Y.; Turchanin, A.; Feng, X.; Müllen, K. Three-dimensional nitrogen and boron co-doped graphene for high-performance all-solid-state supercapacitors. *Adv. Mater.* **2012**, *24*, 5130–5135. [CrossRef]
119. Zhang, H.; Hu, M.; Huang, Z.; Kang, F.; Lv, R. Sodium-ion capacitors with superior energy-power performance by using carbon-based materials in both electrodes. *Prog. Nat. Sci. Mater. Int.* **2020**, *30*, 13–19. [CrossRef]
120. Putri, K.; Ong, W.; Chang, S.; Chai, S. Heteroatom doped graphene in photocatalysis: A review. *Appl. Surf. Sci.* **2015**, *358*, 2–14. [CrossRef]
121. Subramanyan, K.; Divya, M.; Aravindan, V. Dual-carbon Na-ion capacitors: Progress and future prospects. *J. Mater. Chem. A* **2021**, *9*, 9431–9450. [CrossRef]
122. Li, S.; Liu, P.; Zheng, X.; Wu, M. High-performance dual carbon lithium-ion capacitors based on nitrogen-doped 2D carbon nanosheets as both anode and cathode. *Electrochim. Acta* **2022**, *428*, 140921. [CrossRef]
123. Jiang, J.; Shen, Q.; Chen, Z.; Wang, S. Nitrogen-doped porous carbon derived from coal for high-performance dual-carbon lithium-ion capacitors. *Nanomaterials* **2023**, *13*, 2525. [CrossRef] [PubMed]
124. Jiang, J.; Zhang, Y.; An, Y.; Wu, L.; Zhu, Q.; Dou, H.; Zhang, X. Engineering ultrathin MoS_2 nanosheets anchored on N-doped carbon microspheres with pseudocapacitive properties for high-performance lithium-ion capacitors. *Small Methods* **2019**, *3*, 1900081. [CrossRef]
125. Xiao, Z.; Yu, Z.; Gao, Z.; Li, B.; Zhang, M.; Xu, C. S-doped graphene nano-capsules toward excellent low-temperature performance in Li-ion capacitors. *J. Power Sources* **2022**, *535*, 231404. [CrossRef]
126. Thangavel, R.; Kannan, G.; Ponraj, R.; Yoon, G.; Aravindan, V.; Kim, D.; Kang, K.; Yoon, W.; Lee, Y. Surface enriched graphene hollow spheres towards building ultra-high power sodium-ion capacitor with long durability. *Energy Storage Mater.* **2019**, *25*, 702–713. [CrossRef]

127. Zou, G.; Hou, H.; Zhao, G.; Huang, Z.; Ge, P.; Ji, X. Preparation of S/N-codoped carbon nanosheets with tunable interlayer distance for high-rate sodium-ion batteries. *Green Chem.* **2017**, *19*, 4622–4632. [CrossRef]
128. Dong, S.; Xu, Y.; Wu, L.; Dou, H.; Zhang, X. Surface-functionalized graphene-based quasi-solid-state Na-ion hybrid capacitors with excellent performance. *Energy Storage Mater.* **2018**, *11*, 8–15. [CrossRef]
129. Du, Q.; Zhao, Y.; Chen, Y.; Liu, J.; Li, H.; Bai, G.; Zhou, K.; Wang, J. Nitrogen-doped porous carbon nanosheets as both anode and cathode for advanced potassium-ion hybrid capacitors. *Green Energy Environ.* **2023**, *8*, 579–588. [CrossRef]
130. Zhang, W.; Yin, J.; Sun, M.; Wang, W.; Chen, C.; Altunkaya, M.; Emwas, A.; Han, Y.; Schwingenschlögl, U.; Alshareef, H. Direct pyrolysis of supermolecules: An ultrahigh edge-nitrogen doping strategy of carbon anodes for potassium-ion batteries. *Adv. Mater.* **2020**, *32*, 2000732. [CrossRef] [PubMed]
131. Pham, H.; Mahale, K.; Hoang, T.; Mundree, S.; Gomez-Romero, P.; Dubal, D. Dual carbon potassium-ion capacitors: Biomass-derived graphene-like carbon nanosheet cathodes. *ACS Appl. Mater. Interfaces* **2020**, *12*, 48518–48525. [CrossRef]
132. Hu, X.; Liu, Y.; Chen, J.; Yi, L.; Zhan, H.; Wen, Z. Fast redox kinetics in Bi-heteroatom doped 3D porous carbon nanosheets for high-performance hybrid potassium-ion battery capacitors. *Adv. Energy Mater.* **2019**, *9*, 1901533. [CrossRef]
133. Chang, X.; Zhou, X.; Ou, X.; Lee, C.; Zhou, J.; Tang, Y. Ultrahigh nitrogen doping of carbon nanosheets for high capacity and long cycling potassium ion storage. *Adv. Energy Mater.* **2019**, *9*, 1902672. [CrossRef]
134. Tai, Z.; Liu, Y.; Zhang, Q.; Zhou, T.; Guo, Z.; Liu, H.K.; Dou, S.X. Ultra-light and flexible pencil-trace anode for high performance potassium-ion and lithium-ion batteries. *Green Energy Environ.* **2017**, *2*, 278–284. [CrossRef]
135. Tan, L.; Huang, X.; Yin, T.; Guo, Y.; Ning, T.; Mei, Y.; Zou, K.; Li, L.; Ji, X.; Zou, G. A 5 V ultrahigh energy density lithium metal capacitor enabled by the fluorinated electrolyte. *Energy Storage Mater.* **2024**, *71*, 103692. [CrossRef]
136. Cao, J.; Xu, H.; Zhong, J.; Li, X.; Li, S.; Wang, Y.; Zhang, M.; Deng, H.; Wang, Y.; Cui, C.; et al. Dual-carbon electrode-based high-energy-density potassium-ion hybrid capacitor. *ACS Appl. Mater. Interfaces* **2021**, *13*, 8497–8506. [CrossRef] [PubMed]
137. Cui, Y.; Liu, W.; Wang, X.; Li, J.; Zhang, Y.; Du, Y.; Liu, S.; Wang, H.; Feng, W.; Chen, M. Bioinspired mineralization under freezing conditions: An approach to fabricate porous carbons with complicated architecture and superior K^+ storage performance. *ACS Nano* **2019**, *13*, 11582–11592. [CrossRef] [PubMed]
138. Gao, Y.; Yang, Z.; Wang, Y.; Wang, X. Boosting capacitive storage of cathode for lithium-ion capacitors: Combining pore structure with P-doping. *Electrochim. Acta* **2021**, *368*, 137646. [CrossRef]
139. Huynh, N.; Tran, D.; Nguyen, A.; Nguyen, T.; Tran, M.; Grag, A.; Le, P. Carbon-coated $LiFePO_4$-carbon nanotube electrodes for high-rate Li-ion battery. *J. Solid State Electrochem.* **2018**, *22*, 2247–2254. [CrossRef]
140. Shah, A.; Zahid, A.; Subhan, H.; Munir, A.; Iftikhar, F.; Akbar, M. Heteroatom-doped carbonaceous electrode materials for high performance energy storage devices. *Sustain. Energy Fuels* **2018**, *2*, 1398–1429. [CrossRef]
141. Qi, C.; Ma, X.; Ning, G.; Song, X.; Chen, B.; Lan, X.; Li, Y.; Zhang, X.; Gao, J. Aqueous slurry of S-doped carbon nanotubes as conductive additive for lithium ion batteries. *Carbon* **2015**, *92*, 245–253. [CrossRef]
142. Zhao, L.; Sun, D.; Cao, Q.; Xiao, Z.; Yu, Z.; Qi, C.; Li, X.; Ning, G.; Ma, X.; Peng, C.; et al. Green and universal sulfur doping technique coupled with construction of conductive network for enhanced kinetics of Li-ion capacitors. *Chem. Eng. Sci.* **2022**, *258*, 117749. [CrossRef]
143. Yang, C.; Xiong, J.; Ou, X.; Wu, C.; Xiong, X.; Wang, J.; Huang, K.; Liu, M. A renewable natural cotton derived and nitrogen/sulfur co-doped carbon as a high-performance sodium ion battery anode. *Mater. Today Energy* **2018**, *8*, 37–44. [CrossRef]
144. Zou, K.; Cai, P.; Liu, C.; Li, J.; Gao, X.; Xu, L.; Zou, G.; Hou, H.; Liu, Z.; Ji, X. A kinetically well-matched full-carbon sodium-ion capacitor. *J. Mater. Chem. A* **2019**, *7*, 13540–13549. [CrossRef]
145. Que, L.; Yu, F.; He, K.; Wang, Z.; Gu, D. Robust and conductive $Na_2Ti_2O_{5-x}$ nanowire arrays for high-performance flexible sodium-ion capacitor. *Chem. Mater.* **2017**, *29*, 9133–9141. [CrossRef]
146. Wang, C.; Zhao, N.; Li, B.; Yu, Q.; Shen, W.; Kang, F.; Lv, R.; Huang, Z. Pseudocapacitive porous hard carbon anode with controllable pyridinic nitrogen and thiophene sulfur co-doping for high-power dual-carbon sodium ion hybrid capacitors. *J. Mater. Chem. A* **2021**, *9*, 20483–20492. [CrossRef]
147. Liu, Z.; Peng, H.; Xie, X.; Wang, X.; Hou, W.; Miao, W.; Tao, B.; Ma, G.; Lei, Z. Coupling of reasonable micro-defect structure and multiple chemisorption sites for boosting the K^+ storage capacity in dual-carbon potassium ion hybrid capacitors. *Energy Storage Mater.* **2024**, *65*, 103100. [CrossRef]
148. Peng, Z.; Bannov, G.; Li, S.; Huang, Y.; Tang, L.; Tan, L.; Chen, Y. Coupling uniform pore size and multi-chemisorption sites: Hierarchically ordered porous carbon for ultra-fast and large zinc ion storage. *Adv. Funct. Mater.* **2023**, *33*, 2303205. [CrossRef]

batteries

MDPI

Article

Construction of $CoNi_2S_4@Ni(OH)_2$ Nanosheet Structures for Asymmetric Supercapacitors with Excellent Performance

Yongli Tong [1,*], Baoqian Chi [1], Yu Jiang [1] and Xiang Wu [2,*]

[1] School of Science, Shenyang Ligong University, Shenyang 110159, China; baoqianchi@sylu.edu.cn (B.C.); jiangyu@sylu.edu.cn (Y.J.)
[2] School of Materials Science and Engineering, Shenyang University of Technology, Shenyang 110870, China
* Correspondence: tongyongli@sylu.edu.cn (Y.T.); wuxiang05@sut.edu.cn (X.W.)

Abstract: It is crucial for energy storage devices to construct electrode materials with excellent performance. However, enhancing energy density and cycling stability for supercapacitors is a significant challenge. We successfully synthesized $CoNi_2S_4@Ni(OH)_2$ nanosheets on the surface of Ni foam substrate by a two-step hydrothermal approach. The obtained products exhibit a remarkable areal capacitance of 1534 F g^{-1} at a current density of 1 A g^{-1}. Moreover, even after 10,000 cycles, the specific capacitance remains 90% of its initial value, highlighting the exceptional long-term stability and durability. Furthermore, an asymmetric supercapacitor (ASC) device incorporating the $CoNi_2S_4@Ni(OH)_2$ material shows remarkable electrochemical performance. It delivers an energy density of 58.5 mW h g^{-1} at a power density of 2700 W kg^{-1}. The outstanding performance mainly arises from the selection of materials, the design of the structure, and the synergistic interaction between the materials. The result suggests that this material holds great potential as an energy storage material.

Keywords: supercapacitors; $CoNi_2S_4@Ni(OH)_2$; energy density; composite structure; specific capacity

1. Introduction

The world is currently facing significant environmental and energy challenges [1–3]. These issues pose a serious threat to both human life and wildlife. To mitigate these problems, the development of green renewable energy sources has become essential [4–6]. Investing in green energy can help to reduce carbon footprints, create jobs, and promote energy independence, while preserving natural resources for future generations. Supercapacitors have garnered considerable interest due to their outstanding advantages over traditional batteries. Unlike conventional batteries, supercapacitors offer extremely fast charge/discharge rates, which make them an excellent choice for applications that demand rapid bursts of energy. Additionally, supercapacitors have an extended cycle life, which can endure hundreds of thousands to millions of cycles without significant degradation. Supercapacitors feature high power density, enabling them to deliver large amounts of power in a short time [7–10]. Moreover, supercapacitors are more environmentally friendly and have fewer safety concerns. Based on the charge storage mechanism, asymmetric supercapacitors are classified into two types. One is a double-layer capacitor, which stores energy by electrostatically adsorbing charges between the electrolyte and the interface of the electrode. During this process, ions gather on the surface of electrode, creating a double electric layer that facilitates energy storage. The other is a pseudocapacitor, where energy is stored through fast surface redox reactions, involving electron transfer between

Batteries **2025**, *11*, 83 https://doi.org/10.3390/batteries11030083

the electrolyte and the electrode material. The material type is essential in determining the charge storage capacity. The advancement of these supercapacitors is crucial for meeting the increasing need for energy storage solutions. They are not only environmentally sustainable, but also efficient [11–14].

Transition metal sulfides, like Co_3S_4 and $CoNi_2S_4$, have already been extensively studied as electrode materials, due to their outstanding electrochemical properties [15–17]. Among these, $CoNi_2S_4$ has been extensively researched. This material exhibits a high specific capacitance, primarily due to its extensive surface area, which allows for greater charge storage. Additionally, it can undergo reversible redox reactions when the charge–discharge reaction is repeated. This contributes to its high capacitance. These reactions, which involve the transfer of electrons between the electrolyte and the electrode, provide an additional mechanism for charge storage beyond just physical adsorption. Furthermore, the material's relatively high electrical conductivity is essential for boosting its performance. This enhanced conductivity facilitates the efficient movement of charge. Good conductivity improves the flow of charge, leading to a better rate capability. This means that the material can charge and discharge more quickly without significant loss of efficiency, which makes it ideal for high-power applications [18]. Li et al. [19] report the creation of r-$CoNi_2S_4$ nanosheets in transition metal dichalcogenides though a moderate-reduction method. The material demonstrated a remarkable improvement in conductivity and an increased number of active sites, which were mainly attributed to the abundant sulfur vacancies that were deliberately introduced. These vacancies are key to improving the electrochemical properties of the material, leading to better charge storage and faster electron transfer. The r-$CoNi_2S_4$ nanosheets, in particular, demonstrated a considerably higher specific capacitance, reaching 1117 C g^{-1} at 2 A g^{-1}. In addition, the device utilizing these nanosheets achieved an outstanding energy density of 55.4 Wh kg^{-1} at a power density of 8 kW kg^{-1}, along with 80% capacitance retention after 10,000 cycles. However, like many transition metal sulfides, $CoNi_2S_4$ experiences volume expansion during cycling, which can lead to mechanical stress and degradation of the material, reducing its long-term performance.

To improve this drawback, a composite structure has been designed. When transition metal sulfides are combined with other components, the composite structure can provide better mechanical stability, reducing the effects of volume changes and improving cycling performance. Additionally, by combining these materials with conductive materials, the resulting composite improves the overall electrical conductivity, facilitating better electron transport and faster charge/discharge rates [20,21]. The combination of different materials can lead to a synergistic effect, where the properties of the individual components complement each other [22–24]. Thus, composites can be specifically engineered to improve multiple aspects of supercapacitor performance, making them a highly versatile and effective solution. In this work, a hybrid $CoNi_2S_4$@$Ni(OH)_2$ electrode is fabricated on the surface of nickel foam through a two-step hydrothermal approach. The composite material exhibits outstanding electrochemical performance. The assembled device also possesses excellent power density and energy density.

2. Experimental Section

2.1. Preparation of Materials

Cobalt nitrate, nickel nitrate, ammonium fluoride, urea, and nickel foam were sourced from Aladdin. All chemical reagents were used without any modifications. Before the experiment, a piece of Ni foam (4 × 4 × 0.3 cm) was immersed in a 1 M hydrochloric acid solution for half an hour to remove surface impurities, then rinsed three times with ethanol and deionized (DI) water, respectively. Finally, it was placed in an oven to dry at 60 °C overnight.

Total volumes of 60 mL DI water, 3 mmol NH_4F, 2 mmol $Co(NO_3)_2{\cdot}6H_2O$, 7 mmol urea, and 1 mmol $Ni(NO_3)_2{\cdot}6H_2O$ were placed in a beaker, followed by magnetic stirring. When the solution became clear at room temperature, stirring was stopped. The prepared mixture was subsequently introduced into an autoclave of 100 mL, to which prepared Ni foam was added. The autoclave was heated at 120 °C for 6 h in an oven, to facilitate the reaction. After the heating process was complete, the product was left to cool to room temperature. The product was then washed thoroughly with ethanol and DI water multiple times to eliminate any remaining impurities, resulting in the formation of the cobalt–nickel precursor.

After that, 0.40 g Na_2S and the as-prepared sample above, along with 40 mL DI water, were transferred to an autoclave, where they were heated at 120 °C for 4 h. The sample was dried according to the steps mentioned above, to obtain the $CoNi_2S_4$ product. Finally, 0.12 g of urea, 0.29 g of $Ni(NO_3)_2{\cdot}6H_2O$, and 60 mL of DI water were mixed thoroughly to obtain clear solution. The prepared $CoNi_2S_4$ sample was then immersed in the mixture and heated at 100 °C for 8 h. $CoNi_2S_4$@$Ni(OH)_2$ samples were successfully obtained. The average mass loading on the nickel foam was approximately 2.32 mg cm^{-2}.

2.2. Morphology and Structure Characterization

The structural features of the products were analyzed through scanning electron microscopy (SEM, Sigma500 field emission, ZEISS, Oberkochen, Germany). X-ray diffraction (XRD) was performed with a BRUKER D8 X-ray diffractometer(BRUKER, Karlsruhe, Germany), utilizing Cu Kα radiation (λ = 1.5406 Å). The elemental composition and structural details were examined through X-ray photoelectron spectroscopy (XPS, ESCALAB250, Thermo Fisher Scientific, Waltham, MA, USA).

2.3. Fabrication of ASC Device

A mixture of activated carbon, acetylene black, and polytetrafluoroethylene (PTFE), in a mass ratio of 7:2:1, was applied to the surface of the treated nickel foam with a diameter of 1 cm, followed by heating at 80 °C for 24 h. The carbon electrode obtained as described above was used as the cathode of the ASC, and the $CoNi_2S_4$@$Ni(OH)_2$ product served as the cathode. The electrolyte was bended by first heating 50 mL of deionized (DI) water to 95 °C. Then, 5 mg of PVA and 5 g of KOH were added gradually. The solution was stirred until it became clear. A piece of NKK paper was used to separate the anode and cathode to form a sandwich structure. The mass ratio of the anode and cathode can be determined using the following formula, based on charge balance [25]:

$$m^+/m^- = C_- \times V_-/C_+ \times V_+ \tag{1}$$

2.4. Electrochemical Characterization

A range of electrochemical tests were carried out on an electrochemical workstation (Shanghai Chenhua CHI660e, Shanghai Chenhua Instrument Co., Ltd., Shanghai, China) to characterize the material's performance. They included Galvanostatic Charge–Discharge (GCD) tests, Electrochemical Impedance Spectroscopy (EIS) and Cyclic Voltammetry (CV). Specific capacitance (C_s) was obtained using the following formula [26,27]:

$$C_s = I\Delta t/mV \tag{2}$$

The energy density (E) and power density (P) of the ASC were constructed by the following formula:

$$E = 1/2C_s(\Delta V)^2 \tag{3}$$

$$P = 3600E/t \tag{4}$$

in which I serves as current density, and m stands for the mass of the electrode.

3. Results and Discussion

The phase component of the $CoNi_2S_4@Ni(OH)_2$ sample was analyzed by XRD; the results are shown in Figure 1a. The diffraction peaks at 44.5°, 51.8°, and 76.4° correspond to those characteristic of nickel foam (JCPDS no. 04-0850). These peaks indicate that the structure of the material is consistent with the well-established crystallographic patterns of nickel foam. The peaks at 38.2 °, 47.2 °, 50.3 °, 55.1 °, and 68.9 ° correspond well to the (400), (422), (511), (440), and (444) planes of $CoNi_2S_4$ (JCPDS no. 86–2247). The peaks observed at 33.2°, 38.6°, 52.1°, 59.3°, and 73.0° are attributed to the specific crystallographic planes of $Ni(OH)_2$, namely the (100), (011), (012), (110), and (201) planes, respectively. These peaks serve as clear indicators of the presence of $Ni(OH)_2$ within the material, confirming its formation and crystallinity. Each of these diffraction angles corresponds to a distinct plane in the crystal structure of $Ni(OH)_2$, providing valuable information about its phase and orientation.

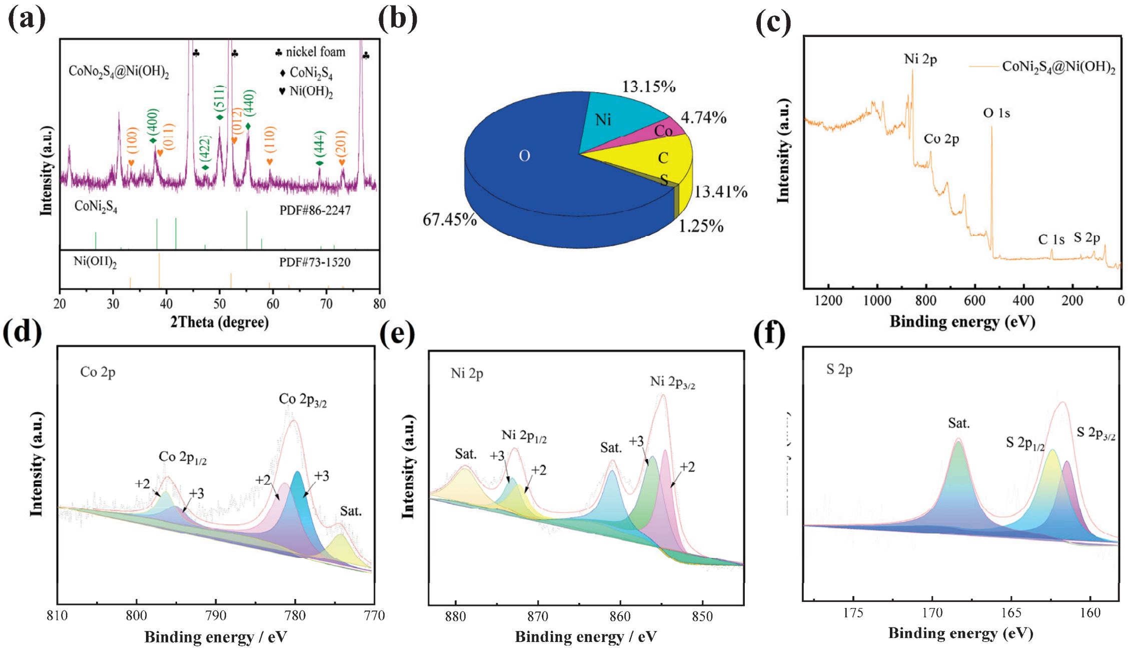

Figure 1. (**a**) XRD patterns of $CoNi_2S_4@Ni(OH)_2$. (**b**) Element content pie chart. (**c**) XPS survey. (**d**) Co 2p. (**e**) Ni 2p. (**f**) S 2p.

The surface chemical states of the $CoNi_2S_4@Ni(OH)_2$ sample were determined by XPS. Figure 1b shows the proportions of the five elements, as follows: O—67.45%, Ni—13.15%, Co—4.74%, C—13.41%, and S—1.25%. The survey spectrum in Figure 1c indeed confirms the presence of these elements. As shown in Figure 1d, the spectra exhibit two characteristic spin–orbit doublet peaks, which correspond to Co $2p_{3/2}$ and Co $2p_{1/2}$, with binding energies of 796.1 eV and 780.2 eV, respectively. These peaks suggest the presence of cobalt in its characteristic oxidation states, with the measured binding energies closely matching expectations for Co 2p electron states in cobalt-containing compounds. The spin–orbit splitting value is approximately 15.9 eV, which is attributed to the presence of Co^{3+} and Co^{2+} ionic states [28,29]. The energies at 778.2 and 792.6 eV are attributed to Co^{3+}, while the energies at 796.4 and 780.9 eV are associated with Co^{2+}.

The Ni 2p spectra (Figure 1e) exhibit four peaks, at 855.4, 873.4, 857.1, and 875.6 eV, corresponding to Ni^{2+} and Ni^{3+} [30,31]. Additionally, two satellite peaks at 862.1 and 880.4 eV can be attributed to the higher oxidation state. Among the four peaks shown on the Ni spectra, the two energies of 872.8 eV and 854.9 eV are the orbital peaks, while the energies at 862.1 and 880.4 eV are satellite peaks. The peaks at 855.4 and 873.4 eV are attributed to Ni^{2+}, while the energies at 857.3 and 875.7 eV correspond to Ni^{3+}. The S 2p spectra display two orbital peaks, at 156.6 eV and 157.2 eV, corresponding to S $2p_{3/2}$ and S $2p_{1/2}$, respectively.

The morphology of the prepared samples is illustrated in Figure 2. It can be seen that the nanosheets evenly cover the whole surface of the Ni foam (Figure 2a). From the high-magnification SEM image in Figure 2b, it can be seen that the thickness of the $CoNi_2S_4$ product is approximately 20 nm, and nanowires grow uniformly at the edges of the nanosheets. This means that the sample has a larger specific surface area compared to pure sheets. Figure 2c,d show the uniform morphology of $Ni(OH)_2$ directly grown on Ni foam. The average thickness of its nanosheets is around 10 nm. Figure 2e,f show how the $Ni(OH)_2$ nanosheets are uniformly attached to the surface of the $CoNi_2S_4$ material. The $CoNi_2S_4$@ $Ni(OH)_2$ nanosheets reinforce the electrode structure and exhibit a large specific surface area, suggesting excellent electrochemical performance.

The electrochemical data of the prepared products were evaluated though a traditional three-electrode system, with a 3 M potassium hydroxide solution serving as the electrolyte. Figure 3a shows the CV curves of the three samples, $Ni(OH)_2$, $CoNi_2S_4$, and $CoNi_2S_4$@$Ni(OH)_2$, obtained at 50 mV s^{-1}. The clearly defined redox peaks suggest that the materials exhibit battery-type behavior. The $CoNi_2S_4$@$Ni(OH)_2$ samples show the largest area among the three materials, which suggests a significant improvement in capacitance following the formation of the composite. This improvement can be attributed to the shortening of the electron and ion transport pathways, as well as the increase in specific surface area following the formation of the composite material. The large surface area provides abundant active sites, allowing for more efficient electrochemical reactions during charge and discharge cycles. With more available sites, the material can accommodate a greater number of ions, enhancing its overall capacitance. Additionally, the shorter transport pathways facilitate faster electron and ion movement, which allow for more efficient electron and ion movement. This combination enhances the material's overall electrochemical performance, leading to better charge storage capacity, faster charge–discharge rates, and improved energy efficiency.

Figure 3b exhibits the GCD curves of the $CoNi_2S_4$@$Ni(OH)_2$, $CoNi_2S_4$, and $Ni(OH)_2$ materials at 1 A g^{-1}. The curves show distinct plateaus, which correspond to the charge–discharge redox processes of the electrode, consistently with the CV curves. The $CoNi_2S_4$@$Ni(OH)_2$ material possesses the longest discharge time, suggesting that it has the highest capacitance. Therefore, it shows significant improvement compared to the $CoNi_2S_4$ and $Ni(OH)_2$ materials. This suggests that the composite material is more efficient at storing and releasing charge.

Nyquist plots of three electrodes were created to further assess the kinetic performance, as shown in Figure 3c. The linear segment indicates the rate at which ions are transported between the electrolyte and the electrode surface. A greater slope of the line signifies a more rapid ion transport rate. The figure shows that the $CoNi_2S_4$@$Ni(OH)_2$ material possesses a faster rate compared to the other two materials. The equivalent resistance of the $CoNi_2S_4$@$Ni(OH)_2$ sample at the intersection with the x-axis is approximately 0.65 Ω, which is smaller than that of the other two materials.

CV curves were created to further assess the performance of the $CoNi_2S_4$@$Ni(OH)_2$ sample at various scan rates, as shown in Figure 3d. As the scan rate increases, the general shape of the curve stays largely unchanged, suggesting that the material maintains a stable electrochemical behavior and can function effectively across a range of operating conditions. Moreover, with an increase in scan rate, the redox peaks display a slight shift in both directions. This shift is often attributed to limitations in ion diffusion at higher scan rates, where the material may experience slight delays in the movement of ions to the active sites.

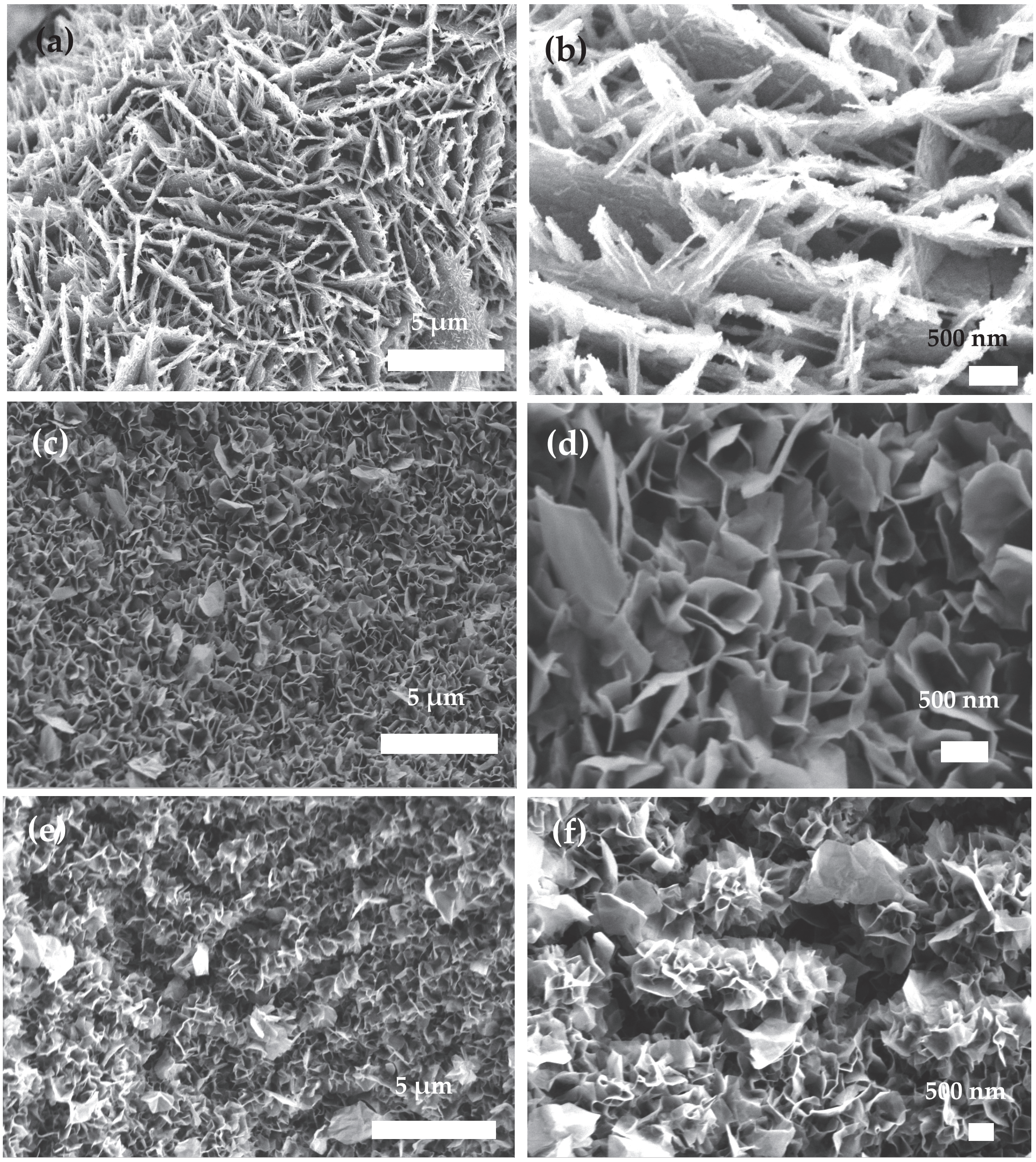

Figure 2. SEM images of samples: (**a**,**b**) $CoNi_2S_4$ material; (**c**,**d**) $Ni(OH)_2$ sample; (**e**,**f**) $CoNi_2S_4@Ni(OH)_2$ sample.

From these CV curves, the charge–discharge mechanism is further revealed in Figure 3e. CV curves serve as a powerful method for analyzing the reaction kinetics of the as-prepared samples. The equation for this is presented below:

$$i = av^b \tag{5}$$

In this equation, i serves as the current, v stands for scan rate, and b indicates the reaction kinetics speed.

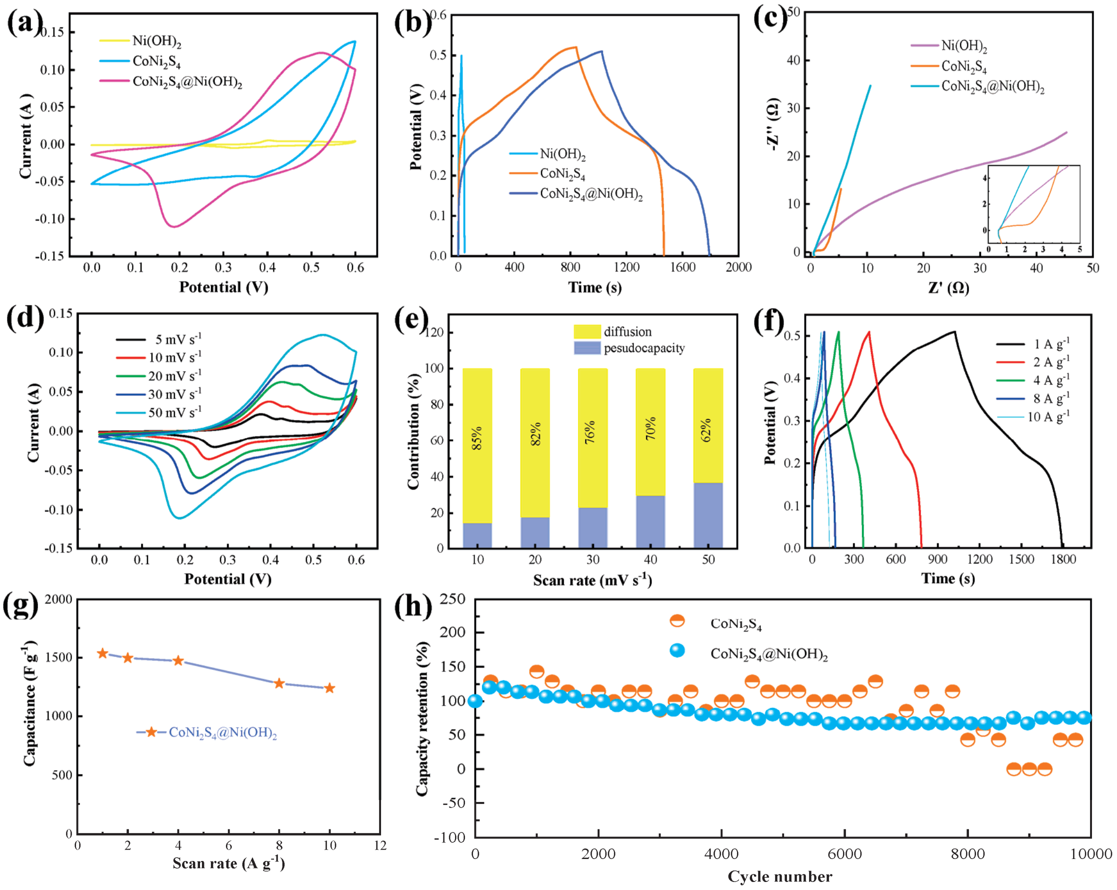

Figure 3. Electrochemical performance: (**a**) CV curves of prepared samples at scan rate of 50 mV/s. (**b**) GCD curves of prepared samples at 1 A g^{-1}. (**c**) Nyquist plots of prepared samples. (**d**) CV curves at different scan rates. (**e**) Contribution ratio. (**f**) GCD curves at different current densities. (**g**) Capacitance at different scan rates. (**h**) Cycling performance.

To explore the proportional contribution of the two charge storage mechanisms, surface capacitance and diffusion capacitance, the following formula is used:

$$i = k_1 v + k_2 v^{1/2} \quad (6)$$

where the values of k_1 and k_2 can be determined from the CV curves. The charge storage caused by diffusion reaches 85% at 10 mV s^{-1}, and decreases continuously when the scan rate increases. The charge storage caused by pseudocapacitance increases continuously with an increase in scan rate.

The charging and discharging portions of the GCD curves are basically symmetrical, indicating that the material has high recoverability. According to Equation (2), the specific capacitance is calculated to be 1534 F g^{-1}, based on the discharge time at 1 A g^{-1} (Figure 3f). The material maintains a capacitance retention rate of up to 80%, even at a high current density of 10 A g^{-1}, which indicates that the phenomenon of polarization of the material is not significant. As observed from Figure 3g, the curve drops gently. This indicates that the specific capacitance gradually decreases with an increase in current density. This demonstrates the material's excellent ability to withstand rapid charge and discharge cycles.

The stability and durability of the $CoNi_2S_4$@Ni(OH)$_2$ electrode material were explored through long-cycle testing, as shown in Figure 3h. As the number of cycles increases, the curve shows an upward trend, reaching a maximum value at approximately 200 cycles. This indicates the activation process of the material. The electrode material continuously absorbs the electrolyte, leading to an increase in active sites, more particles participating in the reaction, and a rise in specific capacitance. Subsequently, the curve shows a downward trend, which is due to the repeated adsorption/desorption of the material, causing volume expansion or collapse, and even convergence in some cases. This leads to a gradual reduction in reaction sites. After 10,000 cycles, the specific capacitance retains 90% of its original value, demonstrating impressive cycling stability. This excellent retention indicates that the material undergoes minimal degradation during the repeated redox process, which is a key factor for long-term performance. After the composite formation, it is evident that the material's stability is significantly improved. This is because sulfides have poor stability. By coating them with a layer of $Ni(OH)_2$ material, this can alleviate issues, such as volume expansion and material collapse, caused by the repeated reversible redox process.

To explore the applicability of the $CoNi_2S_4@Ni(OH)_2$ electrode material, a device was assembled. As shown in Figure 4a, the shape of the curves remains largely unchanged when the operating voltage varies from 1.2 to 1.6 V. This indicates that the device functions normally. Meanwhile, the shape of the curve remains largely unchanged when the scan rate varies between 10 and 100 mV s^{-1} (Figure 4b). This suggests that the material possesses a low polarization rate and excellent electrochemical performance [32,33].

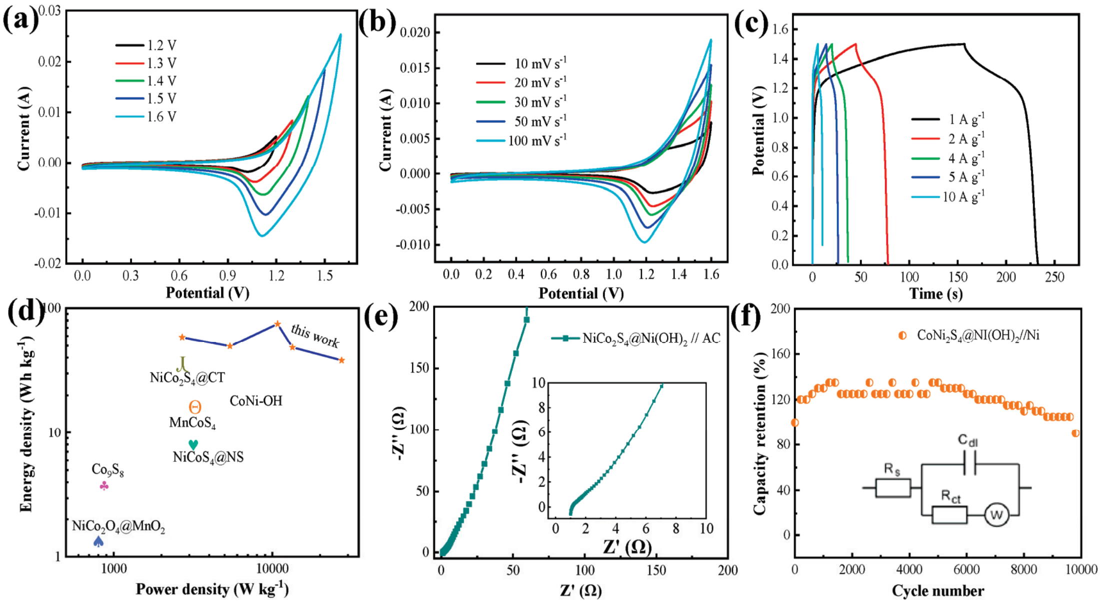

Figure 4. Electrochemical performance of device: (**a**) CV curves at different scan rates. (**b**) CV curves at 50 mV/s. (**c**) GCD curves at different current densities. (**d**) Nyquist plots. (**e**) Ragone plot. (**f**) Cycling performance.

It can be observed that the GCD curve shows some deviation in the charge and discharge times, which means lower Coulombic efficiency. This may be caused by the following factors: 1. Charge leakage and electrode polarization; 2. Inconsistent electrochemical kinetics between the anode and cathode. The kinetic rate of the $CoNi_2S_4@Ni(OH)_2$ material is slower than that of the carbon material used for the cathode; 3. The use of a separator and binder during the device assembly process increases the resistance of the electrode and hinders the transfer of electrons and charge; 4. At high potentials, the ion transport rate in the electrolyte slows down, requiring a longer time for charge accumulation. The specific capacitance of the device is determined to be 52.4 F g^{-1} at 1 A g^{-1}, according to Figure 4c. To further assess the device's performance, its energy density and power density were calculated by Equations (2) and (3). The energy density of the device is calculated to be 58.5 Wh kg^{-1}, while the power density reaches 2700 W kg^{-1}. These calculations highlight the material's ability in terms of storing and delivering energy efficiently, making it a match in terms of both high power output and substantial energy storage. As shown in Figure 4d, the values for these are higher in this work than in some previously reported data [34–39]. Table 1 shows a data comparison between this sample and other materials. Figure 4e shows that the equivalent resistance of the device is about 1 Ω. The results of EIS and inset in Figure 4e show that the device possesses a small equivalent resistance and a fast transmission speed. The cyclic characteristic of the device is also an important indicator. The device can still maintain a specific capacitance that equals 90% of the initial capacitance after 10,000 cycles, which reveals its outstanding electrochemical properties.

Table 1. A comparison of the current device with previously reported electrode materials.

Materials	Energy Density ($Wh\cdot kg^{-1}$)	Power Density ($W\cdot kg^{-1}$)	Capacitance ($F\ g^{-1}$)	Stability	Refs.
$NiCo_2S_4$@CT	36.1	798	59.2	89.2% (3000 cycles)	[34]
$NiCo_2S_4$@NS	25.5	334	71.6	85.6% (4000 cycles)	[35]
$MnCo_2S_4$	31.3	800	41.2	89% (5000 cycles)	[36]
Co_9S_8	13.3	1110	48.4	73% (4000 cycles)	[37]
$NiCo_2O_4$@MnO_2	5.8	175	31.3	93% (3000 cycles)	[38]
CoNi-OH	34.2	800	62.5	70% (6000 cycles)	[39]
$CoNi_2S_4$@$Ni(OH)_2$	58.5	2700	52.4	90% (10,000 cycles)	This work

4. Conclusions

In summary, we prepared $CoNi_2S_4$@$Ni(OH)_2$ samples using a straightforward hydrothermal synthesis method. $Ni(OH)_2$ nanosheets are interspersedly grown on the surface of $CoNi_2S_4$ nanosheets, significantly enhancing the material's electrochemical performance. This approach not only simplifies the production process, but also yields a material with exceptional electrochemical performance, exhibiting a specific capacitance of 1534 F g^{-1}. The assembled device still retains 90% of the initial specific capacitance after 10,000 cycles, and it can achieve an energy density of 58.5 Wh kg^{-1} at 2700 W kg^{-1}. Through this innovative design, this method not only effectively enhances the material's specific surface area and shortens the reaction path, but also strengthens the surface strength of the sulfide, greatly improving cycling performance.

Author Contributions: Conceptualization, Y.T., B.C., Y.J. and X.W.; Software, B.C. and Y.J.; Validation, B.C.; Formal analysis, Y.T. and X.W.; Investigation, B.C.; Resources, X.W.; Data curation, Y.T. and Y.J.; Writing—original draft, Y.T.; Writing—review & editing, X.W.; Project administration, Y.T. and X.W.; Funding acquisition, Y.T. All authors have read and agreed to the published version of the manuscript.

Funding: The work is supported by the Special Fund of Basic scientific Research Business expenses of undergraduate universities in Liaoning Province (LJ212410144004) from Liaoning Provincial Department of Education, and the College student innovation and entrepreneurship project of Shenyang Ligong University (X202410144013) from Shenyang Ligong University.

Data Availability Statement: Data are contained within the article.

Conflicts of Interest: The authors declare no conflicts of interest.

References

1. Zhang, Y.; Chen, Y.; Liang, K.; Zhang, Y.; Wang, D.; Wang, W.; Wang, J.; Mitsuzaki, N.; Chen, Z. Synthesis of nickel cobalt sulfide electrode materials for high-performance asymmetric supercapacitors. *J. Energy Storage* **2025**, *109*, 115176. [CrossRef]
2. Iqbal, M.; Saykar, N.G.; Alegaonkar, P.S.; Mahapatra, S.K. Synergistically modified WS_2@PANI binary nanocomposite-based all-solid-state symmetric supercapacitor with high energy density. *New J. Chem.* **2022**, *46*, 7043–7054. [CrossRef]
3. Yao, S.Y.; Jiao, Y.; Lv, C.D.; Kong, Y.; Ramakrishna, S.; Chen, G. Lattice-strain engineering of CoOOH induced by NiMn-MOF for high-efficiency supercapacitor and water oxidation electrocatalysis. *J. Colloid Interf. Sci.* **2022**, *623*, 1111–1121. [CrossRef]
4. De Adhikari, A.; Shauloff, N.; Turkulets, Y.; Shalish, I.; Jelinek, R. Tungsten-Disulfide/Polyaniline High Frequency Supercapacitors. *Adv. Electron. Mater.* **2021**, *7*, 2100025. [CrossRef]
5. Crisci, M.; Boll, F.; Merola, L.; Pflug, J.J.; Liu, Z.M.; Gallego, J.; Lamberti, F.; Gatti, T. Nanostructured 2D WS_2@PANI nanohybrids for electrochemical energy storage. *Front. Chem.* **2022**, *10*, 1000910. [CrossRef]
6. Tong, Y.; Liu, X.; Qi, D.; Chi, B. Constructing high performance supercapacitor electrode through PPy decorated Co_3O_4@$CoMoO_4$ sandwich structure. *J. Energy Storage* **2024**, *97*, 112798. [CrossRef]
7. Shi, C.; Wang, Y.; Kulaots, I.; Zhu, H.; Sheldon, B. Water-in-Salt Battery Electrolyte for High-Voltage Supercapacitors: A Fundamental Study on Biomass and Carbon Fiber Electrodes. *J. Electrochem. Soc.* **2024**, *171*, 110526. [CrossRef]
8. Yao, S.Y.; Jiao, Y.; Sun, S.F.; Wang, L.X.; Li, P.Y.; Chen, G. Vertically Co-oriented Mn-Metal−Organic Framework grown on 2D cation-intercalated manganese oxide via a self-sacrificing template process for a high-performance asymmetric supercapacitor. *ACS Sustain. Chem. Eng.* **2020**, *8*, 3191–3199. [CrossRef]
9. Li, R.Y.; Xu, S.L.; Ai, Z.Q.; Qi, J.G.; Wu, F.F.; Zhao, R.D.; Zhao, D.P. Interface Engineering Accelerated Surface Reconstruction for Electrocatalytic Water Splitting and Energy Storage Device through Hybrid Structured $ZnCo_2O_4$@NiCo-LDH Nanocomposite. *Int. J. Hydrog. Energy* **2024**, *91*, 867–876. [CrossRef]
10. Li, R.Y.; Shen, X.Y.; Li, J.; Zhao, D.P.; Zhao, R.D.; Wu, F.F. Enhanced Electrochemical Performance of NiCo-Layered Double Hydroxides: Optimal Synthesis Conditions and Supercapacitor Applications. *Adv. Sustain. Syst.* **2024**, 2400753.
11. Yao, S.Y.; Ramakrishna, S.; Chen, G. Recent advances in metal–organic frameworks based on electrospinning for energy storage. *Adv. Fiber Mater.* **2023**, *5*, 1592–1617. [CrossRef]
12. Dhandapani, E.; Thangarasu, S.; Ramesh, S.; Ramesh, K.; Vasudevan, R.; Duraisamy, N. Recent development and prospective of carbonaceous material, conducting polymer and their composite electrode materials for supercapacitor—A review. *J. Energy Storage* **2022**, *52*, 104937. [CrossRef]
13. Zhag, M.; Du, H.; Wei, Z.; Zhang, X.; Wang, R. Ultrafast microwave synthesis of nickel-cobalt sulfide/graphene hybrid electrodes for high-performance asymmetrical supercapacitors. *ACS Appl. Energy Mater.* **2021**, *4*, 8262–8274.
14. Zhu, J.; Wu, Q.; Li, J. Review and prospect of Mn_3O_4-based composite materials for supercapacitor electrodes. *ChemistrySelect* **2020**, *5*, 10407–10423. [CrossRef]
15. Chen, L.; Wan, J.f.; Fan, L.; Wei, Y.; Zou, J.l. Construction of $CoNi_2S_4$ hollow cube structures for excellent performance asymmetric supercapacitors. *Appl. Surf. Sci.* **2021**, *570*, 151174. [CrossRef]
16. Aisha, S.; Nagaraju, D.H.; Mahesh, P. High-energy-density asymmetric supercapacitor based on layered-double-hydroxide-derived $CoNi_2S_4$ and eco-friendly biomass-derived activated carbon. *Energy Fuels* **2022**, *36*, 13286–13295.
17. Zhu, J.; Han, C.; Song, X. Facile synthesis of novel $CoNi_2S_4$/carbon nanofibers composite for high-performance supercapacitor. *Mater. Chem. Phys.* **2022**, *283*, 126038. [CrossRef]
18. Patil, S.J.; Kim, J.H.; Lee, D.W. Self-assembled Ni_3S_2//$CoNi_2S_4$ nanoarrays for ultra high-performance supercapacitor. *Chem. Eng. J.* **2017**, *322*, 498–509. [CrossRef]
19. Li, Z.; Zhao, D.; Xu, C.; Ning, J.; Zhong, Y.; Zhang, Z.; Wang, Y.; Hu, Y. Reduced $CoNi_2S_4$ nanosheets with enhanced conductivity for high-performance supercapacitors. *Electrochim. Acta* **2018**, *278*, 33–41. [CrossRef]
20. Visakh, C.; Mohan, V.; Rakhi, R.B. WS_2/Conducting polymer nanocomposite-based flexible and binder-free electrodes for high-performance supercapacitors. *Electrochim. Acta* **2024**, *498*, 144657.
21. Wang, J.; Zheng, F.; Yu, Y.; Hu, P.; Li, M.; Wang, J.; Fu, J.; Zhen, Q.; Bashir, S.; Liu, J.L. Symmetric supercapacitors composed of ternary metal oxides ($NiO/V_2O_5/MnO_2$) nanoribbon electrodes with high energy storage performance. *Chem. Eng. J.* **2021**, *426*, 131804. [CrossRef]
22. Chevulamaddi, H.; Kalagadda, V.R. The improved electrochemical performance of MnO_2 nanorods decorated with polyaniline as efficient electrode towards high performance supercapacitors. *J. Mater. Sci. Mater. Electron.* **2024**, *35*, 2273. [CrossRef]
23. Yue, T.; Shen, B.; Gao, P. Carbon material/MnO_2 as conductive skeleton for supercapacitor electrode material: A review. *Renew. Sustain. Energy Rev.* **2022**, *158*, 112131. [CrossRef]
24. Song, M.; Zhou, Y.; Ren, X.; Wan, J.; Du, Y.; Wu, G.; Ma, F. Biowaste-based porous carbon for supercapacitor: The influence of preparation processes on structure and performance. *J. Colloid Interface Sci.* **2019**, *535*, 276–286. [CrossRef] [PubMed]
25. Agyapong, A.D.; Cooley, K.A.; Mohney, S.E. Reactivity of contact metals on monolayer WS_2. *J. Appl. Phys.* **2020**, *128*, 055306. [CrossRef]

26. Zubairi, H.; Lu, Z.; Zhu, Y.; Reaney, I.M.; Wang, G. Current development, optimisation strategies and future perspectives for lead-free dielectric ceramics in high field and high energy density capacitors. *Chem. Soc. Rev.* **2024**, *53*, 10761–10790. [CrossRef]
27. Yang, W.; Wang, P.; Tu, Z.; Hou, L.; Yan, L.; Jiang, B.; Zhang, C.; Huang, G.; Yang, F.; Li, Y. Heteroatoms-doped hierarchical porous carbon with multi-scale structure derived from petroleum asphalt for high-performance supercapacitors. *Carbon* **2022**, *187*, 338–348. [CrossRef]
28. Zhang, M.; Du, H.; Wei, Z.; Zhang, X.; Wang, R. Facile electrodeposition of Mn-CoP nanosheets on Ni foam as high-rate and ultrastable electrodes for supercapacitors. *ACS Appl. Energy Mater.* **2022**, *5*, 186–195. [CrossRef]
29. Luo, L.; Lan, Y.; Zhang, Q.; Deng, J.; Luo, L.; Zeng, Q.; Gao, H.; Zhao, W. A review on biomass-derived activated carbon as electrode materials for energy storage supercapacitors. *J. Energy Storage* **2022**, *55*, 105839. [CrossRef]
30. Shah, S.S. Biomass-Derived Carbon Materials for Advanced Metal-Ion Hybrid Supercapacitors: A Step Towards More Sustainable Energy. *Batteries* **2024**, *10*, 168. [CrossRef]
31. Sun, L.; Zhuo, K.; Chen, Y.; Du, Q.; Zhang, S.; Wang, J. Ionic Liquid-Based Redox Active Electrolytes for Supercapacitors. *Adv. Funct. Mater.* **2022**, *32*, 2203611. [CrossRef]
32. Liu, R.; Wang, J.-X.; Yang, W.-D. Hierarchical Porous Heteroatoms—Co-Doped Activated Carbon Synthesized from Coconut Shell and Its Application for Supercapacitors. *Nanomaterials* **2022**, *12*, 3504. [CrossRef] [PubMed]
33. Li, Y.; Zhang, D.; Zhang, Y.; He, J.; Wang, Y.; Wang, K.; Xu, Y.; Li, H.; Wang, Y. Biomass-derived microporous carbon with large micropore size for high-performance supercapacitors. *J. Power Sources* **2020**, *448*, 227396. [CrossRef]
34. Hao, L.; Shen, L.; Wang, J.; Xu, Y.; Zhang, X. Hollow $NiCo_2S_4$ nanotube arrays grown on carbon textile as a self-supported electrode for asymmetric supercapacitors. *RSC Adv.* **2016**, *6*, 9950–9957. [CrossRef]
35. Wu, Z.; Pu, X.; Ji, X.; Zhu, Y.; Jing, M.; Chen, Q.; Jiao, F. High energy density asymmetric supercapacitors from mesoporous $NiCo_2$S4 nanosheets. *Electrochim. Acta* **2015**, *174*, 238–245. [CrossRef]
36. Liu, S.; Jun, S. Hierarchical manganese cobalt sulfide core–shell nanostructures for high-performance asymmetric supercapacitors. *J. Power Sources* **2017**, *342*, 629–637. [CrossRef]
37. Mao, X.; Wang, Z.; Kong, W.; Wang, W. Nickel foam supported hierarchical Co_9S_8 nanostructures for asymmetric supercapacitors. *New J. Chem.* **2017**, *41*, 1142–1148. [CrossRef]
38. Kuang, M.; Wen, Z.; Guo, X.; Zhang, S.; Zhang, Y. Engineering firecracker-like beta-manganese dioxides@spinel nickel cobaltates nanostructures for high-performance supercapacitors. *J. Power Sources* **2014**, *270*, 426–433. [CrossRef]
39. Tang, Y.; Liu, Y.; Yu, S.; Guo, W.; Mu, S.; Wang, H.; Zhao, Y.; Hou, L.; Fan, Y.; Gao, F. Template-free hydrothermal synthesis of nickel cobalt hydroxide nanoflowers with high performance for asymmetric supercapacitor. *Electrochim. Acta* **2015**, *161*, 279–289. [CrossRef]

batteries

MDPI

Review

One Stone, Three Birds: Innovations and Challenges of Layered Double Hydroxides in Batteries, Supercapacitors, and Hydrogen Production

Syed Shaheen Shah *, Manisha Das and Takaya Ogawa *

Socio-Environmental Energy Science Department, Graduate School of Energy Science, Kyoto University, Yoshida-Honmachi, Sakyo-Ku, Kyoto 606-8501, Japan; nisha.ma.25s@st.kyoto-u.ac.jp
* Correspondence: shah.syedshaheen.3d@kyoto-u.ac.jp (S.S.S.); ogawa.takaya.8s@kyoto-u.ac.jp (T.O.)

Abstract: Layered double hydroxides (LDHs), notable for their unique two-dimensional layered structures, have attracted significant research attention due to their exceptional versatility and promising performance in energy storage and conversion applications. This comprehensive review systematically addresses the fundamentals and diverse synthesis strategies for LDHs, including co-precipitation, hydrothermal synthesis, electrochemical deposition, sol-gel processes, ultrasonication, and exfoliation techniques. The synthesis methods profoundly influence the physicochemical properties, morphology, and electrochemical performance of LDHs, necessitating a detailed understanding to optimize their applications. In this paper, the role of LDHs in batteries, supercapacitors, and hydrogen production is critically evaluated. We discuss their incorporation in various battery systems, such as lithium-ion, lithium–sulfur, sodium-ion, chloride-ion, zinc-ion, and zinc–air batteries, highlighting their structural and electrochemical advantages. Additionally, the superior pseudocapacitive behavior and high energy densities offered by LDHs in supercapacitors are elucidated. The effectiveness of LDHs in hydrogen production, particularly through electrocatalytic water splitting, underscores their significance in renewable energy systems. This review paper uniquely integrates these three pivotal energy technologies, outlining current innovations and challenges, thus fulfilling a critical need for the scientific community by providing consolidated insights and guiding future research directions.

Keywords: layered double hydroxides; energy storage and conversion; batteries and supercapacitors; hydrogen evolution reaction; sustainable energy materials

1. Introduction

Layered double hydroxides (LDHs), known as hydrotalcite-like compounds or anionic clays, represent a versatile class of two-dimensional nanostructured materials characterized by their unique layered architecture and compositional tunability [1–4]. Structurally, LDHs are composed of positively charged metal hydroxide layers balanced by interlayer anions and water molecules, forming a stacked, sandwich-like configuration. The general chemical formula of LDHs is expressed as $[M(II)_{1-x}M(III)_x(OH)_2]^{x+}(A^{n-})_{x/n}\cdot mH_2O$, where M(II) and M(III) denote divalent and trivalent metal cations, respectively, and A^{n-} represents exchangeable interlayer anions [5]. This intrinsic flexibility in structure and composition has made LDHs attractive candidates for various scientific and industrial applications, especially in energy storage, conversion, and environmental remediation.

The urgent global demand for efficient, sustainable energy technologies has intensified research into materials that enhance performance in batteries, supercapacitors, and hydro-

https://doi.org/10.3390/batteries11050193

gen production systems [4,6]. LDHs have emerged as promising materials due to their advantageous properties, including high specific surface area, tunable interlayer chemistry, rich redox-active sites, and robust electrochemical stability [7]. These features improve ion mobility, energy storage capacity, and catalytic efficiency. In battery technologies, especially those supporting electric vehicles and large-scale energy storage, materials with high energy density, long cycle life, and stable charge/discharge behavior are essential [8]. LDHs have demonstrated substantial potential to meet these requirements. Their layered structure facilitates efficient ion transport, while their ability to accommodate multiple metal cations and interlayer species enables tailored electrochemical properties. Moreover, the hybridization of LDHs with carbon-based materials such as graphene and carbon nanotubes (CNTs) further enhances electrical conductivity and structural integrity, thereby extending their practical utility in lithium-ion batteries (LIBs) and other emerging battery systems [9,10]. In addition to LIBs, LDHs have been applied in different battery chemistries, including lithium–sulfur batteries (LSBs), sodium-ion batteries (NIBs), chloride-ion batteries (CIBs), zinc-ion batteries (ZIBs), and zinc–air batteries (ZABs) [11–16]. In LSBs, LDHs help mitigate the polysulfide shuttle effect by effectively adsorbing and immobilizing dissolved polysulfides. Their high surface area and interlayer spacing also enhance sodium-ion diffusion in NIBs, which is critical for their energy storage performance. Furthermore, their incorporation into aqueous batteries, such as ZIB and ZAB systems, has improved rate capability and cyclic stability. LDHs also offer compelling advantages in supercapacitor applications, particularly due to their pseudocapacitive behavior [17]. Their electrochemical performance stems from fast and reversible surface redox reactions facilitated by the layered architecture that supports rapid ion transport. Consequently, LDHs exhibit high capacitance, fast charge/discharge rates, and long cycle life, making them suitable for high-power applications. Developing hybrid LDH materials, especially those combined with conductive polymers or carbon nanomaterials, has led to further energy and power density enhancements, expanding their practical viability in real-world devices [18,19]. Parallel to their electrochemical applications, LDHs have gained increasing recognition in hydrogen production, particularly through electrocatalytic water splitting [20]. Efficient and sustainable hydrogen generation depends on active, stable, and cost-effective catalysts for the hydrogen evolution reaction (HER) and oxygen evolution reaction (OER). LDHs, owing to their tunable composition and catalytic activity, have proven to be excellent candidates. Their performance can be further optimized by compositional modifications or integration with nanoparticles, semiconductors, or metal–organic frameworks (MOFs) to enhance electronic conductivity and surface reactivity [21–26].

The synthesis route plays a vital role in tailoring the physicochemical and electrochemical properties of LDHs. Conventional methods such as co-precipitation and hydrothermal synthesis have been widely adopted for their scalability and simplicity. Co-precipitation enables precise control over metal cation ratios and particle morphology, while hydrothermal methods offer improved crystallinity and uniform particle distribution [27]. Other advanced techniques, including electrochemical deposition, sol-gel processing, ultrasonication-assisted synthesis, and exfoliation, have shown promise in producing LDHs with higher surface areas, controlled nanoscale morphologies, and enhanced electrochemical behavior [28]. Furthermore, successfully doping various metal cations into LDH frameworks allows for the rational design of materials that address specific challenges in energy applications, such as conductivity limitations and ion diffusion barriers [29,30]. This adaptability highlights the strategic importance of synthesis optimization in maximizing LDH performance for targeted functionalities.

Beyond energy applications, LDHs also exhibit strong potential in environmental remediation due to their anion exchange capabilities and high chemical reactivity [31]. Recent advancements demonstrate that LDHs are pivotal in advancing circular economy principles and sustainable material practices. Researchers have significantly reduced environmental burdens while creating high-value functional materials by utilizing industrial by-products such as red mud, slag, and fly ash for LDH synthesis [32,33]. Waste-derived LDHs, particularly Ni-based variants, have shown remarkable efficiency in electrocatalysis for oxygen evolution reactions, simultaneously addressing waste valorization and promoting green hydrogen production [34]. In carbon capture, LDH-based photocatalysts facilitate CO_2 reduction to value-added chemicals under solar irradiation, supporting carbon circularity strategies [35]. Moreover, LDHs have been successfully applied in agriculture for controlled-release fertilizers, enhancing nutrient efficiency and minimizing environmental runoff [36]. These examples underscore the growing importance of LDHs in enabling resource recovery, pollution mitigation, and sustainable energy solutions, making them crucial materials in the transition toward greener technologies and closed-loop material systems. These characteristics make them effective in adsorbing pollutants, such as heavy metals and organic contaminants, from aqueous solutions. The dual functionality of LDHs as both energy materials and environmental agents underscores their relevance in supporting sustainability goals and circular economy models. In recent advancements, LDH-derived composite materials, especially those integrated with MOFs, have shown exceptional improvements in surface area, electron/ion transport pathways, and structural robustness [37]. These composites combine the best properties of both components, opening up new directions for multifunctional material systems capable of simultaneously addressing energy and environmental challenges.

LDHs have witnessed a significant surge in global research interest over the past decade due to their structural versatility and broad application potential. As of 2023, the global LDH market was valued at approximately USD 30.57 billion and is projected to reach USD 47.91 billion by 2032, growing at a compound annual growth rate (CAGR) of 5.12%. Research trends show that LDHs are extensively explored in biomedical fields (e.g., drug delivery, cancer therapy, and biosensors), environmental remediation (such as selenium and heavy metal removal from water), energy storage (as precursors for battery and supercapacitor electrodes), and catalytic applications. In the biomedical sector alone, there has been an average annual increase of ~8% in LDH-related publications between 2018 and 2024 [38]. Environmental applications are also expanding, with LDH-based materials achieving over 90% removal efficiencies for specific contaminants like selenium [39]. Research publications in LDH-based energy applications increased by over 250% between 2017 and 2023 (Scopus database). NiFe-LDHs are leading candidates for water splitting in electrocatalysis and hydrogen production with doping strategies (e.g., Co, Mn, Cr) and interlayer anion modifications significantly boosting activity and stability [40]. LDHs are also increasingly explored in supercapacitors, where their pseudocapacitive behavior and fast ion diffusion are enhanced through hybridization with graphene and carbon nanotubes; this field has seen a CAGR of approximately 10% in publications over the past five years. In photocatalysis, LDH-based heterostructures such as LDH/TiO_2 and LDH/g-C_3N_4 composites are under intense study for solar-driven water splitting and CO_2 reduction, with key focus areas including bandgap tuning and charge carrier separation [41]. Furthermore, due to their high surface area and redox-active sites, calcined LDH-derived mixed metal oxides are increasingly used for Li-ion and Zn–air batteries [42]. Novel research also advances LDHs as hosts for anion intercalation batteries and fuel cell electrocatalysts for the ORR [43]. LDHs are at the center of next-generation energy technologies, driven by their structural flexibility, high activity, and earth-abundant composition. Future research directions focus on designing magnetic or structurally modified LDHs for easier recovery and enhanced performance, aiming to expand their role in advanced catalysis, CO_2 capture, and sustainable technologies.

Despite the vast promise of LDHs, several challenges hinder their widespread application. These include their relatively low intrinsic electronic conductivity, structural degradation under prolonged electrochemical cycling, and difficulties scaling up industrial synthesis techniques. To overcome these limitations, continued efforts are required to understand the fundamental relationships between LDH structure, composition, and electrochemical performance. Addressing these gaps will be crucial to unlocking the full potential of LDHs across diverse energy technologies. This review provides a comprehensive overview of the recent progress and emerging trends in applying LDHs in energy-related fields. By systematically discussing the role of LDHs in batteries, supercapacitors, and hydrogen production, alongside synthesis strategies and hybrid material developments, this work aims to consolidate fragmented research findings and provide an integrated perspective. Although several recent reviews have discussed the role of LDHs in electrochemical applications [44–49], most have focused on individual systems or narrowly defined topics. This review uniquely integrates the applications of LDHs across batteries, supercapacitors, and hydrogen production within a single framework, offering a comprehensive and comparative analysis that highlights interconnections, emerging challenges, and future research opportunities. The focus on batteries, supercapacitors, and hydrogen production as application areas for LDHs stems from their central role in advancing clean energy technologies. These three domains, although distinct, share critical commonalities in their underlying electrochemical processes, including charge storage, ion transport, and surface redox reactions, processes where LDHs exhibit remarkable properties such as tunable composition, high surface area, and excellent ion exchange capabilities. The synergy among them is evident via the advancements in LDH-based electrode materials for batteries, which often directly inform the design strategies for supercapacitors, given the need for high conductivity and cycling stability. Similarly, the catalytic properties of LDHs that enhance HER are closely tied to the electron and ion mobility mechanisms essential for energy storage devices. Thus, studying these three applications together allows a more integrated understanding of how LDH structural tuning can optimize performance across multiple energy technologies, paving the way for multifunctional materials that can simultaneously address storage and generation needs. The review also identifies existing challenges and future research directions, offering valuable insights for advancing LDH-based technologies toward scalable and sustainable energy solutions.

2. Fundamentals of LDHs

LDHs, often called anionic clays or hydrotalcite-like materials, represent a unique class of compounds characterized by their layered structure and variable ionic composition. These materials have attracted considerable attention across various fields, including catalysis, energy storage, and environmental remediation, owing to their distinctive properties and potential applications [23,50–52]. LDHs adopt a general structural formula of $[M_{1-x}{}^{2+}M_x{}^{3+}(OH)_2]^{x+}(A^{n-})_{x/n}\cdot mH_2O$, where M^{2+} and M^{3+} are metal cations (i.e., divalent (e.g., Fe^{2+}, Mg^{2+}, Ni^{2+}) and trivalent (e.g., Al^{3+}, Fe^{3+}, Cr^{3+}), while A^{n-} denotes interlayer anions (such as $CO_3{}^{2-}$, $NO_3{}^{-}$, or Cl^{-}) [5,40,50,53,54]. The schematic representation for LDH basic structures is shown in Figure 1a,b. The octahedral sheets formed by metal hydroxides create anionic layers that house exchangeable anions and water molecules within their interlayer spaces [51,52]. This unique structural arrangement provides a large surface area for adsorption and allows for easy intercalation of various anions, making LDHs versatile for numerous applications. LDHs can form various morphologies, the most prominent being flower-like structures [55], as illustrated in Figure 1c. Different types of LDHs have been synthesized, including those based on magnesium–aluminum (MgAl), nickel–aluminum (NiAl), nickel–cobalt (NiCo), and zinc–aluminum (ZnAl) combinations. The versatility of LDHs is primarily attributed to the variety of cations that can exist in the mixed metal sheets, leading to a diverse range of properties and functionalities. For instance, the intercalation of anionic species can significantly affect the catalytic activity, thermal stability, and solubility of LDHs, tailoring their usability in specific applications [56–58]. One notable property of LDHs is their hydrophilic nature, which enhances their interaction with water and biological systems, making them suitable for drug delivery and biocompatibility applications [58,59]. Furthermore, LDHs exhibit excellent acid–base characteristics, which can be optimized for processes such as CO_2 capture and adsorption of pollutants from aqueous solutions [60,61]. For example, studies have shown that LDHs can effectively remove azo dyes and other organic contaminants from water through adsorption mechanisms [57,62,63]. In energy storage applications, LDHs have emerged as promising candidates for electrode materials in supercapacitors and batteries. Their layered structure allows for easy ion diffusion, essential for charge/discharge processes [64,65]. Research has demonstrated that LDH-based composites incorporating materials such as graphene can significantly enhance the performance and efficiency of energy storage devices [56,66]. This dual functionality as ion storage matrices and conductive frameworks bolsters their application relevance in renewable energy systems. Another significant aspect of LDHs is their utility in hydrogen production, particularly in catalysis. LDHs, when modified with transition metals such as nickel or cobalt, can serve as highly efficient electrocatalysts for water splitting, an essential reaction to produce hydrogen [67,68]. Incorporating these metals into the LDH framework improves catalytic activity due to increased surface area and enhanced electronic properties. Studies have revealed that such modified LDHs can maintain stability and activity over prolonged periods, making them suitable candidates for industrial applications [66,69]. Several examples highlight the utility and properties of specific LDHs. The MgAl-LDH, often synthesized through coprecipitation methods, has shown remarkable adsorption capabilities for various pollutants due to its high surface area and effective ion exchange properties [70,71]. Similarly, ZnAl-LDH composites have been used for effective dye removal owing to their favorable ion exchange capacities and adsorptive kinetics, demonstrating high removal rates in wastewater treatments [72,73]. Additionally, NiFe-LDHs have been utilized as electrocatalysts for HER, achieving commendable efficiencies and stability in alkaline electrolytes [67,68]. LDHs are a vital material with extensive applications in various fields, such as water purification, energy storage, and catalysis. Their unique structural and compositional characteristics allow for adaptable performance based on specific application requirements. This adaptability, coupled with ongoing research to optimize their properties, ensures continued advancements in the functionality and applicability of LDHs in enhancing environmental sustainability and energy efficiency [74–76].

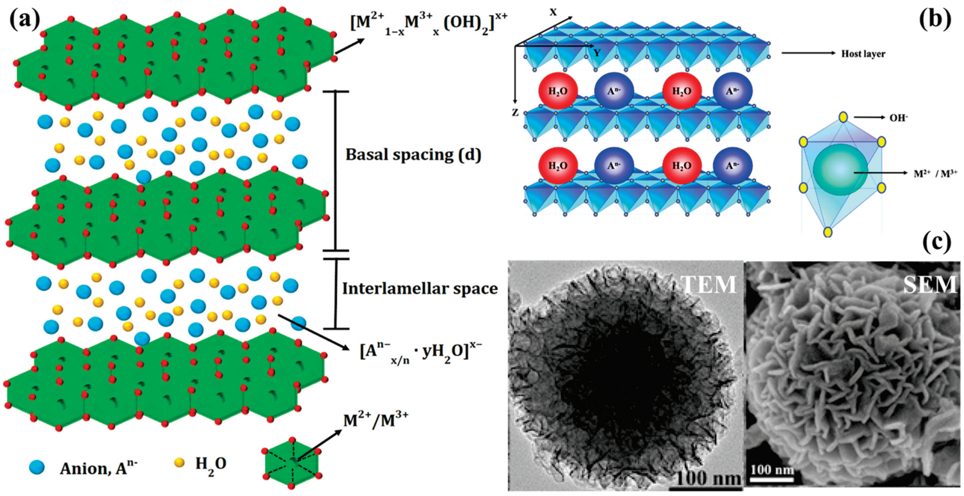

Figure 1. (**a**,**b**) Schematic representation for LDH structures. Reproduced with permission [77,78]. (**c**) TEM and FESEM images of LDH. Reproduced with permission [55].

The deployment of LDHs in practical applications faces several significant challenges, particularly when scaling up synthesis methods, ensuring stability during long-term operation, and addressing low intrinsic conductivity. These issues must be thoroughly examined and mitigated through ongoing research to realize the full potential of LDH-based materials in large-scale systems. One of the critical hurdles in deploying LDHs at scale is the synthesis methods employed. Traditional synthesis techniques often lack the efficiency required for large production. However, recent advancements, such as the "on-the-fly" synthesis method demonstrated by Mattera et al., utilize controlled microfluidic reaction/diffusion conditions to rapidly produce self-supported LDH hollow structures [79]. This technique not only enhances the scalability of production but also maintains the unique structural characteristics of LDHs, potentially overcoming current limitations in synthesis yields and uniformity. Furthermore, the separate nucleation and aging steps method has been explored, providing additional strategies for scalable synthesis while maintaining the structural integrity and performance of the resulting LDHs [80]. Stability under operational conditions represents another significant concern for the practical application of LDHs. The structural integrity of LDH materials can degrade over time in various environments, particularly in aqueous solutions, where traditional LDH configurations may disintegrate [81]. Research focusing on hybrid materials that combine LDHs with conductive carbon matrices has shown promising results. Integrating LDHs with conductive materials significantly enhances their electrochemical performance and stability over extended periods [82]. Moreover, innovative designs, such as incorporating porous structures into LDH composites, exhibit improved performance metrics, addressing the inherent limitations of LDHs regarding durability and efficiency [83]. The intrinsic low conductivity of LDHs is a well-documented limitation that impedes their performance in many electrochemical applications. Recent studies indicate that hybrid LDH composites, such as those combined with conductive polymers or carbon-based materials, can ameliorate these issues [84,85]. The enhancement of electric conductivity through these composites and the careful design of the pore structure allow for better electrolyte penetration and lower charge transfer resistance, significantly boosting the electrochemical activity of LDH-based systems [86]. Hybrid LDH–polymer membranes have also demonstrated substantial improvements in permeability and selectivity for CO_2 separation, showcasing their potential for real-world applications while addressing the conductivity concerns inherent to traditional LDH materials [87]. Significant strides have been made in addressing the challenges of deploying LDH-based materials. Innovations in synthesis techniques, material design, and stability enhancements are crucial to overcoming these barriers. Continued research will be essential to refine these approaches further and ensure that LDHs can fulfil their promise in large-scale applications.

3. Synthesis Methods of LDHs

LDHs can be synthesized through various methods, each significantly influencing their structural, morphological, and functional properties. Common synthesis techniques include the co-precipitation method [88], valued for its simplicity and scalability, typically producing LDHs with uniform morphology and high purity; hydrothermal synthesis [89], favored for precise control over crystallinity and particle size, resulting in materials with enhanced thermal stability; and electrochemical deposition [90], advantageous for fabricating thin films with controllable thickness and adherence. Advanced techniques such as sol-gel, ultrasonication, and exfoliation offer further control over LDH structures; the sol-gel approach produces highly homogeneous and porous LDHs, ultrasonication facilitates smaller particle sizes and improved dispersion, while exfoliation allows isolation of single-layer nanosheets with exceptional surface activity [23]. Figure 2 depicts the structural framework of LDHs, highlighting common synthesis methods and their wide-ranging applications. Overall, the choice of synthesis method profoundly affects LDHs' properties, including crystallinity, surface area, porosity, interlayer spacing, and electrochemical performance, thus determining their suitability for diverse applications like batteries, supercapacitors, and catalysis.

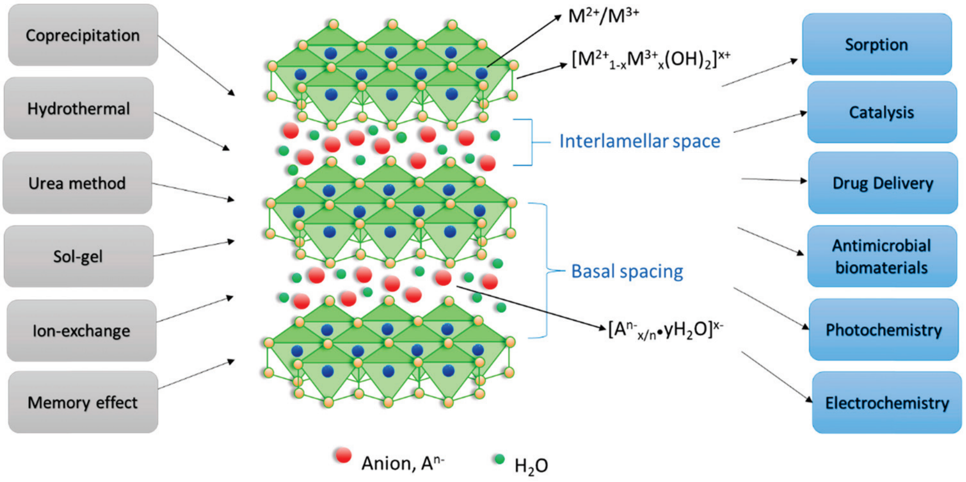

Figure 2. Schematic illustration of the synthesis methods, layered structure, and diverse applications of LDHs. Reproduced with permission [91].

3.1. Co-Precipitation

The co-precipitation method is a widely utilized synthesis technique for LDHs. This method involves the simultaneous precipitation of two or more metal salts from an aqueous solution in a specific pH-controlled environment. The goal is to create a solid precipitate comprising cations with differing oxidation states that can form a layered structure upon aging and further processing. The co-precipitation approach offers advantages such as simplicity, cost-efficiency, and the capability of producing homogeneous materials [92,93]. The fundamental mechanism underlying the co-precipitation of LDHs includes the generation of hydroxides by reacting an alkaline solution (e.g., sodium hydroxide) with metal salt solutions. When mixed, metal ions, typically divalent metals (M^{2+}) and trivalent metals (M^{3+}), condense to form brucite-like sheets, a precursor structure of LDHs. The excess positive charge of the brucite-like layers is balanced by the intercalation of anions within the interlayer spacing, such as carbonate, nitrate, or organic molecules [94,95]. Thus, the co-precipitation method is fundamental for synthesizing LDHs with diverse properties suitable for various applications, including catalysis, ion exchange, and drug delivery systems [96,97].

Recent advancements in solid-state reactions have revealed numerous strategies for improving the structural and morphological qualities of LDHs synthesized via the co-precipitation method. For instance, a meticulous study by Wijitwongwan et al. [98] demonstrated that varying layer charge densities effectively alter the microstructure and performance of NiFe-LDH. Similarly, Zhang et al. [99] expounded on the preparation of chromium-modified ultrathin CoFe-LDH, noting that enhanced electrocatalytic performance can be attributed to its nanosheet structure, achieved efficiently through the co-precipitation route. Additionally, other research has indicated the potential for co-precipitation in the fabrication of ZnAl-LDH, particularly in enhancing the corrosion protection of steel-reinforced concrete. This study determined that the layering structure includes intercalated organic anions, which augment the protective qualities of the resulting material [88,98]. Their findings emphasize the importance of co-precipitation in producing multifunctional layered structures designed for specific engineering applications. In the domain of catalysis, the co-precipitation method allows for creating various catalytic layered materials with particular properties tailored for high activity. For example, NiAl-LDHs synthesized via the co-precipitation method exhibited significant electrochemical activity and stability, making them suitable candidates for application in batteries and supercapacitors [96,99]. The correlation between the morphology of LDHs and their catalytic behaviors has been systematically reviewed, indicating that factors such as particle size, crystallinity, and layering impact performance significantly [92,100]. Furthermore, approaches involving the hybridization of various LDH materials have emerged, expanding the range of applications and performance metrics of these materials. For instance, research has explored Co–Ni–Fe oxyhydroxide composites synthesized via co-precipitation, modifying their catalytic capabilities for various reactions [101]. These hybrid systems demonstrate that co-precipitation can yield single-component LDHs and complex multi-component systems with advanced functionality [97]. Ongoing studies focus on optimizing synthesis parameters to enhance performance metrics. Key considerations include the concentration of metal salts, pH level, temperature, and stirring conditions during synthesis. Attempts to generate various forms of zinc–Al LDHs have shown that altering these conditions can lead to significant variations in structural integrity and interlayer spacing, characterized through advanced spectroscopy techniques [93,102]. The versatility of the co-precipitation method is evident in its application; in a recent study exploring hybrid nanoparticles, the uniformity and dispersion of mesoporous ZnAl-LDHs were ensured by carefully controlling synthesis parameters [93,103]. Innovative adaptations of the co-precipitation method, including using surfactants and polymers as structure-directing agents, have progressively unlocked pathways for producing new LDH varieties with tailored layer spacing and enhanced chemical reactivity [96,104].

Thorough examinations have also been directed at using co-precipitation to produce nanostructured materials like mesoporous catalysts. For example, Zhang et al. [99] elucidated the synthesis of cobalt-LDH nanostructures displaying significant efficacy in HER. The nanosheet morphology achieved through co-precipitation allows for higher surface area and better catalytic performance than bulk materials [99,105]. The emergence of LDHs as effective adsorbents for environmental remediation has garnered considerable attention, with co-precipitation playing a critical role. Various authors have demonstrated the removal of toxic anionic contaminants such as fluoride and heavy metals using LDHs synthesized through this method [104,106]. The selective adsorption capabilities are primarily attributed to the structural characteristics of LDHs, wherein the intercalated anions can be exchanged with environmental pollutants, applying this functionality in wastewater treatment [96,98]. The co-precipitation method is not limited to traditional LDH compositions; recent works have shown its viability in synthesizing more complex layered materials that integrate organic and inorganic components. Such multifunctional materials can effectively combine properties, enabling application in fields ranging from nanotechnology to biochemistry and medicine [107,108]. The co-precipitation method remains a powerful and versatile technique for synthesizing LDHs, allowing significant control over their structure and properties. The evolution and innovation in this methodology reflect ongoing academic and industrial pursuits toward developing sophisticated materials capable of addressing contemporary challenges in catalysis, energy storage, and environmental sustainability.

Flower-like NiCo-LDH nanoparticles were synthesized via the co-precipitation method using triethanolamine as the alkali source and hydrogen peroxide (H_2O_2) as the size-controlling reagent [109]. A subsequent heat treatment step (at 200 °C) was implemented to create a nanocrystal@amorphousness core/shell structure. This precise temperature-controlled process effectively induced amorphization at the surface of LDH crystals, significantly refining the grain size. As illustrated in Figure 3a, the LDH structure transforms with increasing temperature in an inert (Ar) atmosphere, leading to increased amorphous content and improved Li^+ diffusion channels due to the formation of disordered regions. Figure 3b presents the nitrogen adsorption/desorption isotherms of LDH samples treated at different temperatures. It can be observed that surface area increases significantly with temperature, reaching up to 178.9 m^2/g for LDH. In Figure 3c, the pore size distribution reveals that higher temperatures increase pore volume and broader pore distribution, which benefits ion transport and electrochemical performance. FESEM and TEM analyses revealed flower-like nanoparticles (~100 nm diameter) composed of small nanosheets (~20 nm × 5 nm), forming a unique nanocrystal@amorphous core/shell structure. The BET surface area measurement indicated a mesoporous structure with a specific surface area of approximately 76.6 m^2/g, conducive to efficient electrolyte interaction and lithium-ion diffusion. The LDH amorphous-crystalline core/shell structure and enhanced surface area promote rapid lithium-ion transport, making it highly suitable for high-performance LIBs anodes.

The MgAl-LDH was synthesized via a straightforward co-precipitation method and incorporated with CNTs to form a hybrid composite [110]. This LDH@CNT hybrid was subsequently employed to create a sulfur composite cathode. The resulting material exhibited a well-dispersed morphology with nanoscale features and layered structure, a large surface area, and strong polysulfide adsorption characteristics. These features make the LDH highly suitable for LSB applications by effectively mediating polysulfide conversion and suppressing the shuttle effect. In another study, NiFe-NO_3 LDH was synthesized via a one-pot co-precipitation method by titrating a mixed nitrate solution of Ni and Fe with NaOH under an inert atmosphere, then aging at 70 °C for three days [111]. The obtained product was filtered, washed, dried, and ground to obtain the final LDH powder. The material revealed a typical hexagonal LDH structure with low crystallinity, turbostratic stacking, and a nanostructured surface. These structural features, combined with the high theoretical capacity (477 mAh/g) and dual redox/active metal centers (Ni^{2+}/Fe^{3+}), make the LDH highly suitable as an anode for NIB applications. The $Ni_3Mn_{0.7}Fe_{0.3}$-LDH was synthesized via a co-precipitation method and subsequently activated electrochemically to introduce hydrogen vacancies, resulting in the Hv-$Ni_3Mn_{0.7}Fe_{0.3}$-LDH [16]. The activation process involved CV in 1 M KOH to generate hydrogen-deficient lamellae that enhance zinc-ion accommodation. The reported LDH structure is highly suitable for ZIB applications due to its exposed terminal-O active sites and reduced Zn^{2+} diffusion barriers. NiFe

LDH nanosheets with varying interlayer spacings were synthesized through a simple co-precipitation method by intercalating different anionic species (Cl^-, $C_7H_5O_3^-$, and $C_{17}H_{25}O_3^-$) into the interlayer space [112]. The interlayer spacing was tuned from 7.695 Å to 24.114 Å by substituting the interlayer anions. The materials exhibited layered sheet-like morphology, preserved crystallinity, distinct interlayer anion fingerprints, uniform elemental distribution, consistent oxidation states, and enhanced interlayer water retention, all indicative of structural integrity and ion transport capacity. The expanded interlayer spacing and water facilitate rapid chloride ion diffusion, making these LDH materials highly suitable as cathodes in CIBs.

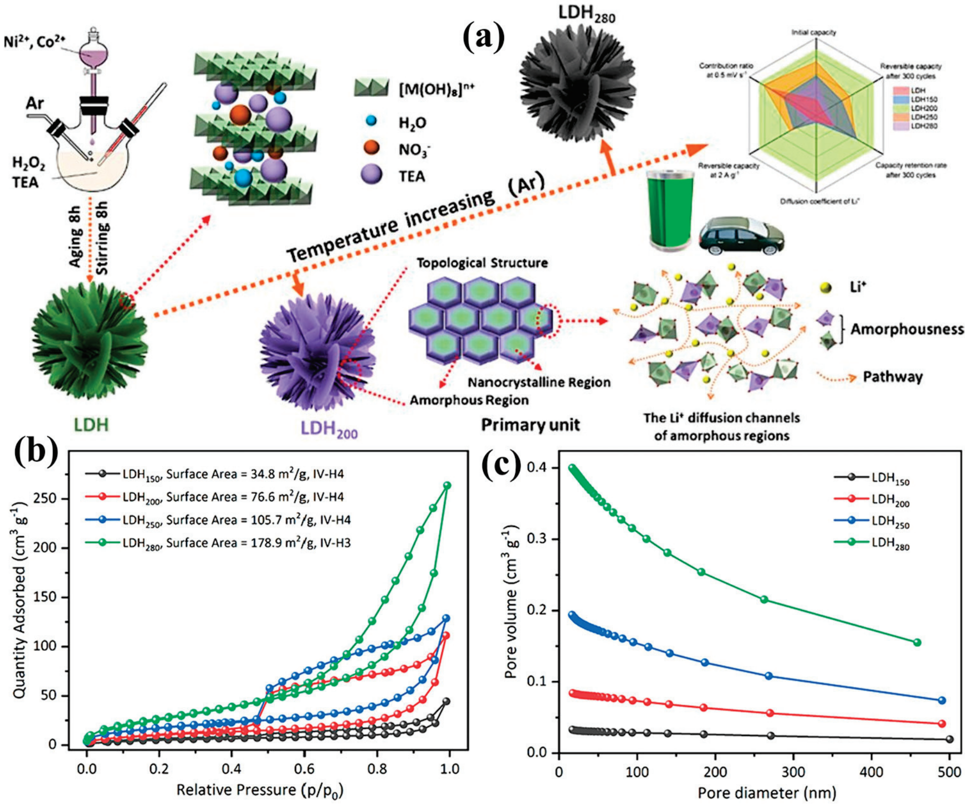

Figure 3. (**a**) Illustration of the synthesis pathway of temperature-regulated LDH and its transformation into an amorphous structure through thermal treatment. (**b**) Nitrogen adsorption/desorption curves and (**c**) pore size distribution profiles corresponding to the prepared samples. Reproduced with permission [109].

The NiMn-Cl LDH was synthesized via a co-precipitation method involving grafting NiMn-LDH nanosheets with chloride ion intercalation onto a CNT framework [113]. This process yielded a cross-linked network with a core/shell structure, enhancing ion transport and mechanical stability. These features make the material highly suitable for reversible chloride-ion storage in CIB applications. Similarly, Ni_5Ti-Cl LDH was synthesized via a simple co-precipitation method using a high nickel-to-titanium molar ratio (5:1), followed by an anion exchange process in HCl/NaCl solution to replace interlayer carbonate with chloride ions [114]. This resulted in successful Cl^- intercalation, evidenced by XRD peak shifts and IR spectra indicating carbonate removal. Figure 4 highlights the structural and chemical characteristics of Ni_5Ti-Cl LDH, designed to improve stability during cycling and enhance chloride ion adsorption. As seen in Figure 4a, the XRD analysis confirms the well-ordered layered structure. The FTIR results in Figure 4b show carbonate replacement with chloride, indicating successful ion exchange. Figure 4c presents a model structure of the LDH, showing expanded interlayer spacing favorable for Cl^- ion interaction. The TEM image and elemental maps in Figure 4d reveal a uniform distribution of key elements and confirm nanosheet morphology. Figure 4e displays XPS spectra, verifying the oxidation states of Ni and Ti and supporting the material's chemical composition and structure. The high redox activity (Ni^{2+}/Ni^{3+} and Ti^{3+}/Ti^{4+}) and excellent structural integrity with minimal volume change (~1.006%) make this LDH suitable for reversible chloride-ion intercalation in CIBs. The LDH was synthesized via a two-step method where ZIF-67 was first formed and then partially converted into Co-Fe-LDH by ion exchange and structural transformation under hydrothermal treatment at 80 °C for 48 h [115]. This Co-Fe-LDH was further hybridized with Fe-MOF and subsequently pyrolyzed at 900 °C under an argon atmosphere to yield the final CoFe/Fe_3C@CN heterojunction catalyst. The material possessed a nanosphere morphology with well-dispersed metal nanoparticles encapsulated by graphitic carbon layers, a high BET surface area of 247 m^2/g, abundant mesoporosity, and a heterojunction structure. The resulting structure exhibits high surface area, abundant oxygen vacancies, and fast electron transfer, making it highly suitable as a bifunctional cathode catalyst in ZABs. Fe/Co LDH was synthesized via a simple in situ co-precipitation reaction over a cobalt-rich nitrogen-doped carbon framework (Co/N–C) derived by annealing ZIF-67 [116]. The resulting composite (CoL 2:1) was formed by varying mass ratios of LDH and Co/N–C precursors to optimize bifunctional catalytic performance. The material reveals a flaky LDH morphology on a porous carbon matrix with a high specific surface area of 230 m^2/g and a meso/microporous structure. This structure enhances the availability of catalytic sites and is highly suitable for ZAB applications due to its excellent bifunctionality and electrochemical stability.

3.2. Hydrothermal Synthesis

Hydrothermal synthesis is a versatile method involving aqueous reactions at elevated temperatures and pressures, promoting controlled nucleation, dissolution/recrystallization, and growth of crystalline LDHs. This approach enables precise size, morphology, composition, and crystallinity tuning, making it highly effective for fabricating LDHs with tailored properties suitable for various applications, including catalysis and environmental remediation. Hydrothermal synthesis of LDHs typically involves an initial co-precipitation of metal salts with a base, followed by treatment under controlled temperature and pressure within an autoclave to enhance crystallinity and phase purity [117]. During hydrothermal processing, diffusion-controlled nucleation and growth mechanisms facilitate the oriented assembly of metal hydroxide layers and the systematic intercalation of anions, resulting in highly ordered and defect-minimized structures [118,119]. The precise regulation of synthesis parameters such as temperature, pressure, reaction time, and precursor concentration enables fine-tuning of LDH composition, morphology, and functional properties, optimizing them for catalytic, ion exchange, and environmental remediation applications [120,121]. The hydrothermal synthesis of LDHs involves an intricate balance between nucleation and growth, beginning with rapidly forming a gelatinous, disordered metal hydroxide precipitate. Under hydrothermal conditions, this initial phase undergoes a dissolution/reprecipitation cycle driven by thermodynamic stability, resulting in a well-ordered, defect-free lamellar structure through controlled alignment and stacking of hydroxide layers [122]. Furthermore, hydrothermal synthesis uniquely facilitates the incorporation of multiple metal cations into LDH frameworks, enabling the development of multi-cationic or high-entropy LDHs with distinct electronic and structural attributes [77]. These high-entropy LDHs exhibit superior electrocatalytic properties due to synergistic interactions among diverse cationic species, making them highly promising for advanced applications such as CO_2 methanation and other catalytic processes [123,124].

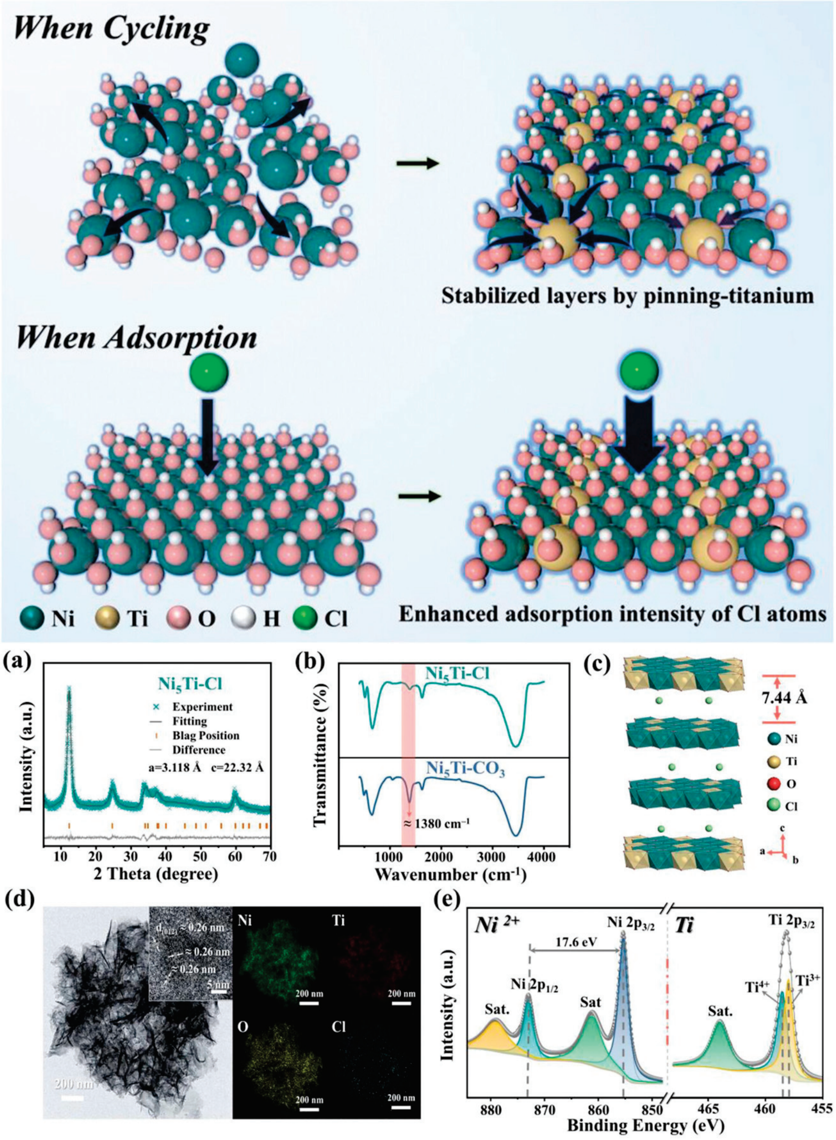

Figure 4. Demonstration of the structural stabilization and improved Cl adsorption in Ni_5Ti-Cl LDH. (**a**) XRD pattern refined using the Rietveld method for Ni_5Ti-Cl LDH. (**b**) FTIR spectra compare the Ni_5Ti-Cl LDH and its carbonate-based precursor (Ni_5Ti-CO_3 LDH). (**c**) Structural model illustrating the layer arrangement in Ni_5Ti-Cl LDH. (**d**) TEM image with SAED inset and elemental mapping showing distributions of Ni, Ti, O, and Cl. (**e**) Ni and Ti XPS profiles, confirming the oxidation states present in Ni_5Ti-Cl LDH. Reproduced with permission [114].

Hydrothermal synthesis provides precise control over morphology, particle size, and structural ordering of LDHs, enabling the tailored formation of uniform nanosheets, nanorods, hierarchical architectures, and ultrathin nanosheets with large surface areas beneficial for catalytic, adsorption, and energy-related applications [125]. This method facilitates controlled intercalation of anions, defect healing through ion migration, incorporation of multiple cations, and utilization of structure-directing additives or surfactants, enhancing LDH crystallinity, phase purity, ion exchange capacities, and electrochemical performance [126]. Additionally, the adaptability and scalability of hydrothermal synthesis make it environmentally attractive and economically viable for industrial-scale production of multifunctional LDHs optimized for diverse applications, including catalysis, environmental remediation, sensors, and energy storage systems [127]. Recent advancements in hydrothermal synthesis have enabled the fabrication of compositionally complex and highly crystalline LDHs with tunable properties for advanced applications [128].

By precisely controlling parameters such as temperature, pressure, pH, and precursor composition, this method facilitates the formation of defect-minimized, high-surface-area materials with tailored morphology, ion distribution, and interlayer characteristics [129]. High-entropy LDHs, multi-metallic composites, and nitrogen-doped structures synthesized hydrothermally demonstrate enhanced catalytic, adsorption, and electrochemical performance, particularly in environmental remediation and energy storage. The technique's scalability, energy efficiency, and use of water as a benign solvent further highlight its potential as a sustainable and industrially viable approach for producing multifunctional LDHs with minimal environmental impact [130]. Hydrothermal synthesis offers a highly versatile and controllable route for fabricating LDHs with tailored morphology, interlayer spacing, crystallinity, and multi-metal compositions [131]. Fine-tuning reaction parameters such as temperature, pressure, pH, and precursor concentration produces defect-minimized, thermally and chemically stable LDHs with enhanced ion exchange, catalytic, and electrochemical properties. The process supports in situ functionalization, hybridization with organic or carbonaceous materials, and integrating bulky anions or multiple cations [132]. It is ideal for diverse applications in catalysis, energy storage, environmental remediation, and advanced composites. Its scalability, reproducibility, and use of water as a benign solvent further establish hydrothermal synthesis as a sustainable and industrially viable strategy for developing high-performance, multifunctional LDH-based materials [133].

ZIF-67@NiCo-LDH heterostructures were synthesized using a straightforward one-pot hydrothermal method involving the reaction of cobalt and nickel nitrate precursors with 2-methylimidazole in methanol at 90 °C for 11 h [134]. This synthesis resulted in the formation of unique flower-shaped structures composed of ZIF-67 MOF cores uniformly decorated with NiCo-LDH nanosheets. The controlled reaction time allowed morphology tuning and ensured good dispersion and stability of the composite materials. Characterizations confirmed the heterostructures' flower-like morphology, high crystallinity, and uniform elemental distribution of Ni, Co, O, C, and N. The resulting porous structure exhibited enhanced electrolyte accessibility and improved electrical conductivity compared to the pristine LDH. The flower-shaped morphology and porous structure of ZIF-67@NiCo-LDH enhance ionic and electronic conductivity, making it suitable for LIB anode applications. $NiFe_2O_4$@NiCo-LDH was synthesized using a two-step hydrothermal process [135]. Initially, NiFe-MOF precursors were hydrothermally treated and annealed to obtain hollow $NiFe_2O_4$ nanocubes. Subsequently, NiCo-LDH nanosheets were hydrothermally grown onto the surface of these nanocubes, creating a hierarchical $NiFe_2O_4$@NiCo-LDH structure. The $NiFe_2O_4$@NiCo-LDH composite featured hollow hierarchical nanocubes with uniformly distributed NiCo-LDH nanosheets grown on $NiFe_2O_4$ surfaces. XRD and BET analyses revealed a crystalline structure with enhanced surface area (58.4 m^2/g) and mesoporous characteristics (pore size 2–3 nm), advantageous for electrochemical reactions. Due to its hierarchical hollow structure, high surface area, and mesoporosity, the $NiFe_2O_4$@NiCo-LDH is highly suitable for batteries, facilitating rapid electron and ion transport and alleviating volumetric expansion during cycling. NiZn-LDH intercalated with dodecyl sulfate anions was synthesized using a facile hydrothermal method [136]. Nickel nitrate and zinc nitrate precursors were dissolved under an inert atmosphere, followed by a controlled addition of sodium dodecyl sulfate and sodium hydroxide solution. The mixture was then subjected to hydrothermal treatment at 100 °C for 4 h, centrifuged, washed, and freeze-dried. The synthesized LDH exhibited ultra-thin nanosheet morphology with significantly expanded interlayer spacing due to the intercalation of dodecyl sulfate anions. BET analysis revealed a mesoporous structure with a specific surface area of around 53.4 m^2/g, indicating good accessibility and interaction sites for lithium ions. Due to its expanded interlayer spacing, ultra-thin nanosheet morphology, and favorable surface area, the synthesized NiZn-LDH provides effective diffusion pathways for lithium ions, thus making it suitable for battery applications.

LDH was synthesized initially through a solvothermal process, creating NiFe glyceric acid precursors using $Ni(NO_3)_2 \cdot 6H_2O$ and $Fe(NO_3)_3 \cdot 9H_2O$ in glycerol/isopropanol solution [137]. These precursors were then coated with polydopamine and subjected to high-temperature carbonization and vulcanization, forming NiS_2/FeS_2@NC structures. Finally, NiFe LDH/FeO(OH) nanosheets were grown on these structures via a hydrothermal reaction, resulting in hollow yolk/shell NiS_2/FeS_2@NC@NiFe LDH/FeO(OH) microspheres. The synthesized LDH exhibited a hollow yolk/shell structure with nanoflower morphology. The LDH's porous hollow yolk/shell structure and high specific surface area enable efficient ion transport and structural stability, making it highly suitable for battery applications. NiCo-LDH nanowires were synthesized using a simple one-step hydrothermal method [138]. Initially, MXene nanosheets were prepared by etching and delaminating Ti_3AlC_2. Subsequently, NiCo-LDH nanowires were uniformly grown in situ onto MXene nanosheets, forming a hierarchical 1D/2D heterostructure [139]. The composite exhibited a 1D nanowire-on-2D nanosheet morphology with increased specific surface area (14.50 m^2/g) and enhanced structural stability. The NiCo-LDH/MXene composite, with its hierarchical structure and enhanced conductivity, is highly suitable for battery applications as it ensures rapid lithium-ion diffusion and stable electrochemical cycling. MgAl LDH (Mg_2Al_1–CO_3-LDH) was synthesized using a simple hydrothermal method [140]. Carbonate ions ($CO_3{}^{2-}$) were intercalated within Mg and Al layers as interlayer anions. The synthesized LDH exhibited a typical hexagonal flake-like morphology with uniform elemental distribution. The Mg_2Al_1–CO_3-LDH reveals a well-defined hexagonal layered structure, a flake-like morphology, homogeneous elemental dispersion, and an interlamellar spacing of 7.45 Å. These analyses confirmed its composition as $[Mg_{0.68}Al_{0.32}(OH)_2](CO_3{}^{2-})_{0.16} \cdot 0.66H_2O$ with a high structural integrity. The Mg_2Al_1–CO_3-LDH demonstrates suitable properties such as high specific surface area, structural stability, and active interlayer spaces, making it a promising candidate as an anode material for LIBs. The NiCo-LDH nanoflowers were synthesized via a hydrothermal method using nickel nitrate, cobalt nitrate, and CTAB, with in situ growth on either nickel foam (NF) or jute-derived AC (JAC-2) as substrates [89]. The optimal composite, NiCoLDH-1@JAC-2, was prepared by hydrothermally treating a mixture of Ni/Co in a 1:1 molar ratio with JAC-2 at 180 °C for 12 h. Figure 5a,b presents the synthetic routes for preparing JAC and the subsequent in situ formation of NiCo-LDH@JAC nanoflowers. The resulting NiCoLDH nanostructures exhibit a hierarchical nanoflower morphology composed of ultrathin nanosheets (~10 nm) with high crystallinity and a well-defined layered structure confirmed by XRD and HRTEM. JAC-2 support contributed significantly with its nanosheet structure, high surface area (~2600 m^2/g), and rich micro/mesoporous texture, enhancing ion transport. These structural and morphological features make the composite highly suitable for supercapacitor applications by maximizing active surface area and minimizing ion diffusion resistance.

The CoLa-LDH (CL) was synthesized via a hydrothermal method followed by a second hydrothermal step to grow NiCoOOH (NC) onto the CL, forming a hierarchical NiCoOOH@CoLa-LDH (NC@CL) heterostructure [141]. The NC was tightly coated over the CL nanosheets, yielding a flower-like 3D nanosheet architecture. Morphologically, the NC@CL exhibited interconnected ultrathin nanosheets with a high BET surface area of 316.4 m^2/g and mesoporous features (mainly 2–10 nm pores). Structural characterizations confirmed successful heterojunction formation and lattice deformation beneficial for ion/electron transport. The NC@CL structure provides abundant active sites and excellent electron/ion kinetics, making it highly suitable for ZIB applications. The NiCoMo LDH was initially synthesized via a hydrothermal method, followed by an anion exchange reaction to replace interlayer carbonate ions with chloride ions [142]. Subsequent temperature-differential phosphorus doping using NaH_2PO_2 vapor at different controlled temperatures introduced P heteroatoms into the LDH structure. Morphologically, the LDH retained a sea urchin-like microsphere architecture composed of nanowires, while XRD, TEM, and XPS confirmed structural integrity and successful P-doping, with increased oxygen vacancies and enhanced electronic properties. These features collectively support its application in CIBs by improving conductivity and diffusion kinetics.

Figure 5. (**a**) Illustration of the JAC fabrication process involving a two-step pyrolysis method, and (**b**) detailed schematic of the in situ synthesis approach for growing NiCoLDH@JAC nanoflower structures. Reproduced with permission [89].

The NiAl-LDH was synthesized by first depositing Al_2O_3 on graphene using atomic layer deposition (ALD), followed by a hydrothermal transformation into NiAl-LDH@G [143]. This two-step process enabled the vertical growth of ultrathin LDH nanosheets on graphene, forming a nanoarray architecture. Characterization revealed a well-defined mesoporous structure with vertical LDH nanosheets (~3 nm thick), high surface area (230.44 m^2/g), and a uniform elemental distribution. This architecture enhances electron/ion transport and structural stability, making it ideal for CIB cathode applications.

The NiCo-based LDH was synthesized via a hydrothermal method, and chloride ions were introduced through a post-synthesis ion exchange process by treating the carbonate-intercalated LDH with an NaCl/HCl solution [144]. This treatment replaced CO_3^{2-} ions with Cl^- in the interlayer, enabling its function as a chloride host. The Mo-doped NiCo LDH exhibited a well-defined sea urchin-like morphology composed of ultrafine nanowires, with increased BET surface area (74.6 m^2/g), preserved LDH structure confirmed by XRD, and homogenous elemental distribution. This structural configuration provides enhanced active surface area and diffusion pathways, making the material highly suitable as a CIB cathode. The CoFe–Cl-LDH/CNT composite was synthesized via a modified co-precipitation method followed by hydrothermal treatment under N_2 protection [145]. The process involved the preparation of a Co/Fe/CNT precursor solution, pH adjustment, and hydrothermal aging at 130 °C, followed by Cl^- intercalation in NaCl/HCl solution. Characterizations revealed nanoflake-like LDH morphology with high crystallinity, uniform Cl^- intercalation, and improved conductivity due to CNTs. The material's layered structure, reversible Cl^- storage, and enhanced electrochemical performance make it suitable as an anode for CIBs. NiFe-LDH was synthesized on electrospun carbon nanofibers (CNFs) via hydrothermal treatment, followed by the in situ growth of conductive Ni-CAT nanorods using nickel acetate and HHTP at 85 °C for 12 h [146]. This hierarchical assembly yielded a 3D Ni-CAT/NiFe-LDH/CNFs composite. The morphology revealed interconnected nanosheets and nanorods forming a porous architecture, while XRD and XPS verified structural and chemical composition. The BET surface area of Ni-CAT/NiFe-LDH/CNFs was significantly high at 258.84 m^2/g. This structure ensures high conductivity, active site exposure, and porosity, making it highly suitable for ZAB applications.

Using a two-step hydrothermal process, the NiMn-LDH was synthesized over a $ZnCo_2O_4$ (ZCO) nanowire array pre-grown on nickel foam [147]. The first step involved forming ZCO nanowires, followed by hydrothermal deposition of NiMn-LDH nanosheets with varied Ni/Mn precursor ratios, optimized at 2:1. Characterization revealed that the LDH formed a uniform core/shell structure with high crystallinity, a flower-like morphology, and a large surface area (BET: 57.91 m^2/g), along with favorable pore distribution, layered structure, and high electrochemical surface area. This tailored architecture with synergistic interactions and abundant electroactive sites renders the LDH ideal for use as an efficient air cathode catalyst in ZABs. The NiCo-LDH/NCM@NF catalyst was synthesized through a two-step process [148]. First, nitrogen-doped carbon nanosheets (NCMs) were formed via self-assembly and calcination of perylene tetracarboxylic dianhydride and dicyandiamide under hydrothermal conditions; subsequently, NiCo-LDH nanoplates were grown in situ on these NCM-modified nickel foam substrates using hydrothermal treatment. The incorporation of NCMs during LDH growth modulated the morphology into rough-edged, ultrathin nanoflakes and enhanced nucleation and dispersion. Characterization revealed a 2D flake morphology, enlarged interlayer spacing, a high BET surface area (235.6 m^2/g for NiCo-LDH/NCM vs. 140.3 m^2/g for pristine NiCo-LDH), uniform elemental distribution, and rich oxygen vacancies. This LDH architecture ensures enhanced electron transport and more exposed catalytic sites, making it highly suitable for ZAB applications.

First, Co_9S_8 nanospheres synthesized NiFe-LDH@Co_9S_8 via hydrothermal treatment, were grown, followed by in situ growth of NiFe-LDH nanosheets on their surface [149]. Pt nanoparticles were then anchored onto the NiFe-LDH nanoflakes through a spontaneous redox reaction, exploiting cation vacancies in the LDH. NiFe-LDH nanosheet flowers were synthesized via a hydrothermal route [150], and two modified versions, CoNiFe-LDH (via one-step hydrothermal doping) and Co@NiFe-LDH (via two-step heterostructure formation with $Co(OH)_2$ nanoarrays) were developed. The morphology was characterized by FESEM and TEM, revealing spherical structures with smooth or flocculated surfaces; XRD, XPS, and SAED provided structural confirmation, while BET analysis showed Co@NiFe-LDH had the highest surface area (34.14 m^2/g) and hierarchical porosity. These structural and surface properties make the LDH, particularly Co@NiFe-LDH, well-suited for ZAB air cathode applications due to enhanced active site availability and electronic conductivity.

NiCo-LDH was synthesized via a one-step hydrothermal method by optimizing reaction temperature, time, and Ni/Co molar ratio, as shown in Figure 6a [119]. The resulting LDH showed a uniform sheet-like morphology with high porosity, well-defined crystalline structure, and the presence of Ni^{2+}/Ni^{3+} and Co^{2+}/Co^{3+} redox states, while FESEM revealed high surface area features favoring electrolyte diffusion and charge transport. Due to enhanced electron conductivity and electrochemical activity, these structural attributes make it an ideal candidate for supercapacitor applications. NiCo-LDH nanosheets were synthesized on nickel foam using a one-pot hydrothermal method involving nickel and cobalt nitrate precursors in the presence of HMTA at 110 °C [151]. As shown in Figure 6b, the basic structure of an LDH comprises stacked layers with positively charged metal hydroxides, separated by interlayer anions and water molecules. This layered structure is essential for the material's chemical and physical properties. Meanwhile, Figure 6c presents the hydrothermal synthesis approach for preparing NiCo-LDH nanosheets. It highlights how the morphology and structure of the nanosheets evolve depending on the duration of the hydrothermal treatment. Different reaction times can change sheet thickness, uniformity, and surface characteristics, significantly affecting the material's performance in various applications. The resulting LDH exhibited a binder-less, ultrathin, porous nanosheet morphology with high crystallinity and a large specific surface area of 46.8 m^2/g (for the optimized sample). These structural and morphological features facilitated rapid ion transport and abundant electroactive sites, rendering the material highly suitable for supercapacitor applications. The CoLa-LDH (CL) was synthesized via a hydrothermal method, followed by a secondary hydrothermal deposition of NiCoOOH (NC) to form the hierarchical NC@CL heterostructure [141]. As seen in Figure 6d, the process involves two hydrothermal steps. First, the CL nanosheets are synthesized at 120 °C for 5 h. Then, a second hydrothermal treatment at the same temperature for 3 h enables the formation of NC@CL, where a second layer is formed on top of the initial CL structure. Figure 6e–g presents FESEM images of the as-prepared CL nanosheets at different magnifications. These images reveal a highly porous, interconnected sheet-like structure that facilitates ion and electron transport. In comparison, Figure 6h–j displays the FESEM images of the NC@CL nanosheet arrays. The surface becomes more complex and flower-like, indicating the successful growth of the secondary NC layer. This hierarchical structure can enhance surface area and active sites, making it beneficial for energy storage or catalysis applications. The resulting NC@CL nanosheets displayed a 3D hierarchical flower-like morphology with a high BET surface area (316.4 m^2/g), mesoporous structure, and uniform elemental distribution; XRD and XPS analyses confirmed the formation of a mixed-phase structure with strong electronic interactions and lattice distortions beneficial for charge transport. These characteristics render the NC@CL heterostructure particularly advantageous for supercapacitor applications due to enhanced ion/electron transport and abundant electroactive sites.

The Ni_2Co-LDH was synthesized via a simple co-precipitation method, where nickel and cobalt chloride precursors reacted with hexamethylenetetramine under reflux conditions at 80 °C for 8 h [152]. Expanded graphite (EG) was separately synthesized by rapid microwave irradiation of expandable graphite powder. Subsequently, Ni_2Co-LDH/EG composites were prepared through an in situ growth technique, anchoring Ni_2Co-LDH nanosheets onto the surface of EG. Structural and morphological characterizations revealed layered, crystalline nanosheets of Ni_2Co-LDH anchored uniformly onto EG surfaces, with lattice spacings consistent with Ni_2Co-LDH. BET analysis indicated enhanced surface area from 26.1 m^2/g for pure LDH to 30.3 m^2/g for the composite, confirming effective integration with EG. The enhanced surface area and stable layered morphology confirmed by characterizations facilitate improved ionic and electronic transport, making Ni_2Co-LDH/EG composites suitable for battery electrode applications. NiAl LDH was synthesized via a one-pot hydrothermal reaction using nickel nitrate, aluminum nitrate, and urea dissolved in deionized water [153]. The solution was transferred to a Teflon-lined autoclave and heated at 100 °C for 24 h. The high surface area, porous nano-lamellar morphology, and structural stability of the synthesized NiAl LDH make it a promising candidate for LIB anodes. The CoNi-LDH/C composite was synthesized by first preparing ZIF-67 polyhedrons, which were then subjected to laser-induced carbonization to obtain porous Co/C structures [154]. These carbonized materials were reacted with $Ni(NO_3)_2 \cdot 6H_2O$ in ethanol under hydrothermal conditions at 90 °C to form the final CoNi-LDH/C composite. This process was optimized to retain polyhedral morphology while introducing amorphous carbon and catalytic metal sites. The resulting material exhibited a mesoporous structure with a high specific surface area ($24.5\ m^2/g$), tubular morphology, and crystalline CoNi-LDH domains enclosed by conductive carbon layers. Due to increased carbon content, structural characterizations confirmed the uniform distribution of Co/Ni, porous architecture, and enhanced conductivity. This hierarchical and conductive CoNi-LDH/C framework provides abundant active sites for LiPS adsorption and conversion, making it highly suitable for LSB cathodes. Li-Al LDH was synthesized via hydrothermal $Al(OH)_3$ and LiCl treatment at 90 °C for 24 h [155]. The LDH was exfoliated in formamide and reassembled with varying amounts of polystyrene sulfonate (PSS) to form LDH@PSS. The optimal composition (LDH/PSS = 1:1.5) was obtained through self-assembly under N_2 atmosphere and centrifugation. The notable structural and electrochemical properties render LDH@PSS highly suitable for stabilizing Li metal anodes in LSBs by suppressing polysulfide shuttling and dendrite formation.

The FeNi-LDH was synthesized hydrothermally by mixing $NiCl_2 \cdot 6H_2O$, $FeCl_2 \cdot 6H_2O$, and L-cysteine in water/ethanol, followed by ammonia addition, then heating in a Teflon-lined autoclave at 180 °C for 12 h [156]. The resulting cysteine-functionalized FeNi-LDH (Cys/FeNi-LDH) was further reacted with $NaVO_3$ in methanol under reflux to yield the ternary V_2O_5/Cys/FeNi-LDH (VCFN) composite. This process ensured the uniform decoration of V_2O_5 nanoparticles on the LDH disks through strong coordination with cysteine functional groups. This LDH-based composite, with its synergistic combination of polysulfide adsorption, catalytic conversion capability, and mesoporous framework, is highly suitable for suppressing the shuttle effect and enhancing sulfur redox kinetics in LSBs. The NiFe-LDH, NiAl-LDH, and ZnAl-LDH were synthesized via a hydrothermal method by co-dissolving respective metal nitrates and urea in deionized water, followed by heating under controlled temperatures for different durations [157]. Sulfur was incorporated into the LDHs using the classical melt/impregnation method at 155 °C, achieving ~75% sulfur loading. Characterization revealed that the LDHs had nanoflake morphology with a 3D network-like architecture, uniform sulfur distribution, and surface areas ranging from 52.6 to $54.8\ m^2/g$. This structure with high surface area and interlayer spacing enabled strong interaction with polysulfides, making the LDHs suitable sulfur hosts for LSBs. NiCoAl-LDH nanosheets were synthesized on carbon cloth (CC) via a hydrothermal method [158]. Subsequently, vertical graphene was grown on the LDH/CC surface using plasma-enhanced chemical vapor deposition (PECVD), forming a 3D interconnected structure. The morphology showed uniformly distributed nanosheets and vertically aligned graphene, with lattice spacings confirming NiCo alloy and graphite planes. This nanocomposite offers strong polysulfide adsorption and fast redox kinetics, making it a suitable host for LSBs. The NiCr-Cl LDH/rGO composite was synthesized via a one-step hydrothermal method to produce NiCr-CO_3 LDH/rGO, followed by ion exchange in a NaCl/HCl solution to replace CO_3^{2-} with Cl^- ions [159]. This approach involved urea-assisted hydrothermal reaction at 150 °C for 24 h, forming a well-dispersed LDH on GO sheets. Morphological and structural characterizations revealed flower-like nanosheet morphology, increased interlayer spacing after Cl^- exchange, and intense interaction between LDH and rGO; the BET surface area of the NiCr-CO_3 LDH/rGO composite was 170.44 m^2/g, supporting good electrochemical performance. The resulting LDH composite demonstrated enhanced suitability for NIB applications due to its improved conductivity, mesoporous structure, and structural stability.

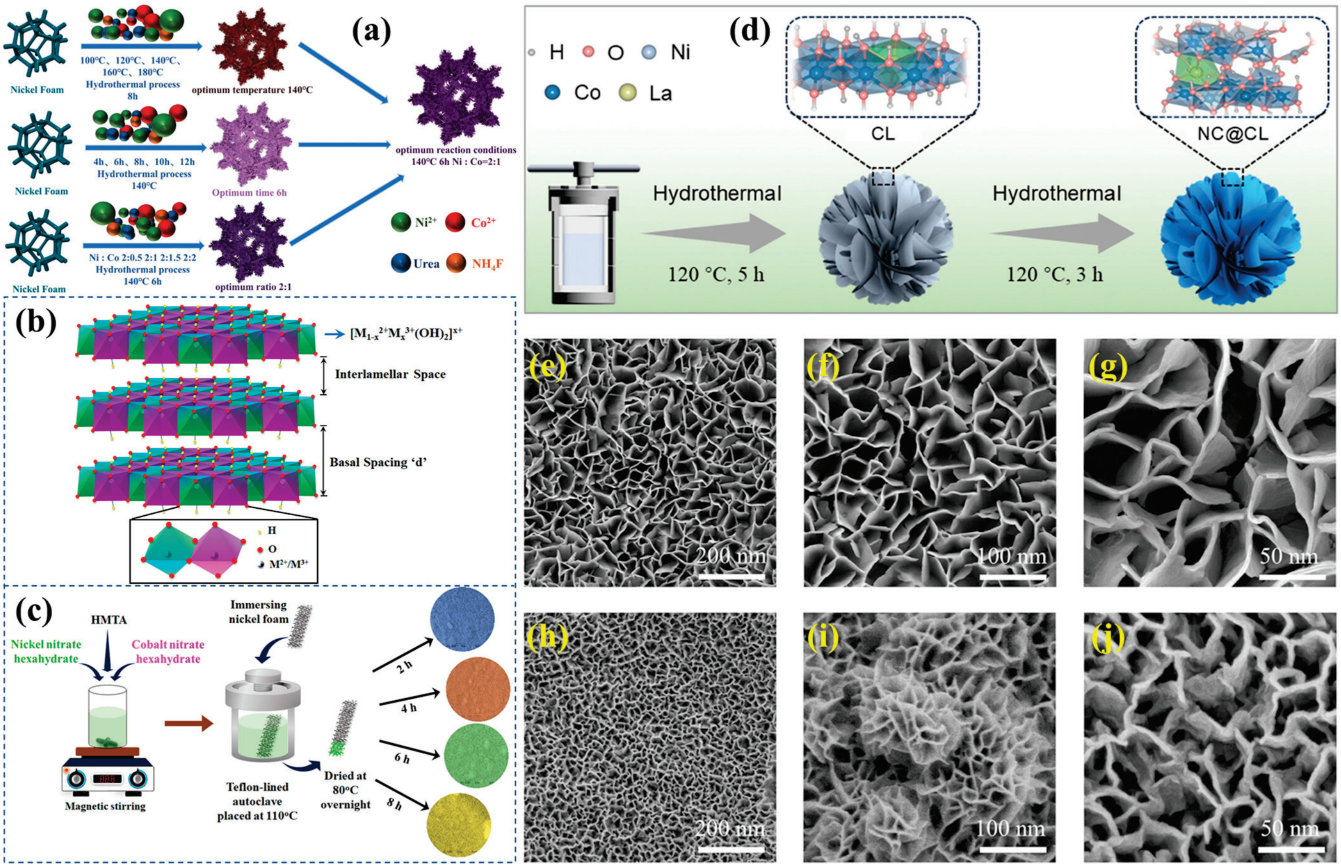

Figure 6. (**a**) Schematic representation for the NiCo-LDH synthesis. Reproduced with permission [119]. (**b**) Illustration showing the structural layout of an LDH material, and (**c**) diagram depicting the hydrothermal synthesis process of Ni-Co LDH nanosheets at various time intervals. Reproduced with permission [151]. (**d**) Conceptual diagram outlining the stepwise hydrothermal synthesis of NC@CL nanosheet arrays, beginning with CL formation and followed by growth of the NC layer. (**e**–**g**) FESEM images showing the surface morphology of the CL nanosheets at increasing magnifications. (**h**–**j**) FESEM images displaying the detailed nanostructure of the NC@CL hierarchical flower-like nanosheet arrays. Reproduced with permission [141].

The NiCo-LDH was synthesized via a hydrothermal method by immersing pre-treated sulfide-hollow ZIF-67 structures into a solution of $Ni(NO_3)_2$, $Co(NO_3)_2$, and hexamethylenetetramine at 90 °C for 24 h [160]. The resulting LDH featured a nanoflower-like morphology, layered structure, and a BET surface area of 266.76 m^2/g with a mesoporous architecture, enhancing electron/ion transport and active surface sites. Due to its superior redox activity and efficient charge storage capability, these characteristics render the NiCo-LDH highly suitable for high-performance supercapacitor applications. NiFe-LDH/$MnCO_3$/MXene (NFMM) ternary composite was synthesized via a hydrothermal method by reacting Ni, Fe, and Mn nitrates with urea in the presence of MXene [161]. The resulting NFMM exhibited a layered and granular sandwich-like structure with uniformly distributed $MnCO_3$ and NiFe-LDH on MXene, showing a high BET surface area of 32.62 m^2/g and a hierarchical mesoporous network with improved electronic conductivity. These properties make NFMM an ideal candidate for supercapacitor electrodes due to its enhanced ion/electron transport and abundant active sites. The FeCoNi-LDH nanosheets were synthesized via a secondary hydrothermal reaction onto pre-formed $MnCo_2O_4$ nanowires anchored on CC [162]. The resulting $MnCo_2O_4$@FeCoNi-LDH exhibited a nanoflower-like, hierarchical morphology with high crystallinity, uniform nanosheet distribution, and a mesoporous structure, showing a specific surface area of 33.9 m^2/g and distinct XRD and XPS signatures confirming multi-metal synergy. Figure 7 displays the synthesis steps and morphology changes of MnCo before and after FCN coating on CC, highlighting structural differences observed under SEM. This architecture enhances ion diffusion and redox activity, making it highly suitable for high-performance supercapacitor applications.

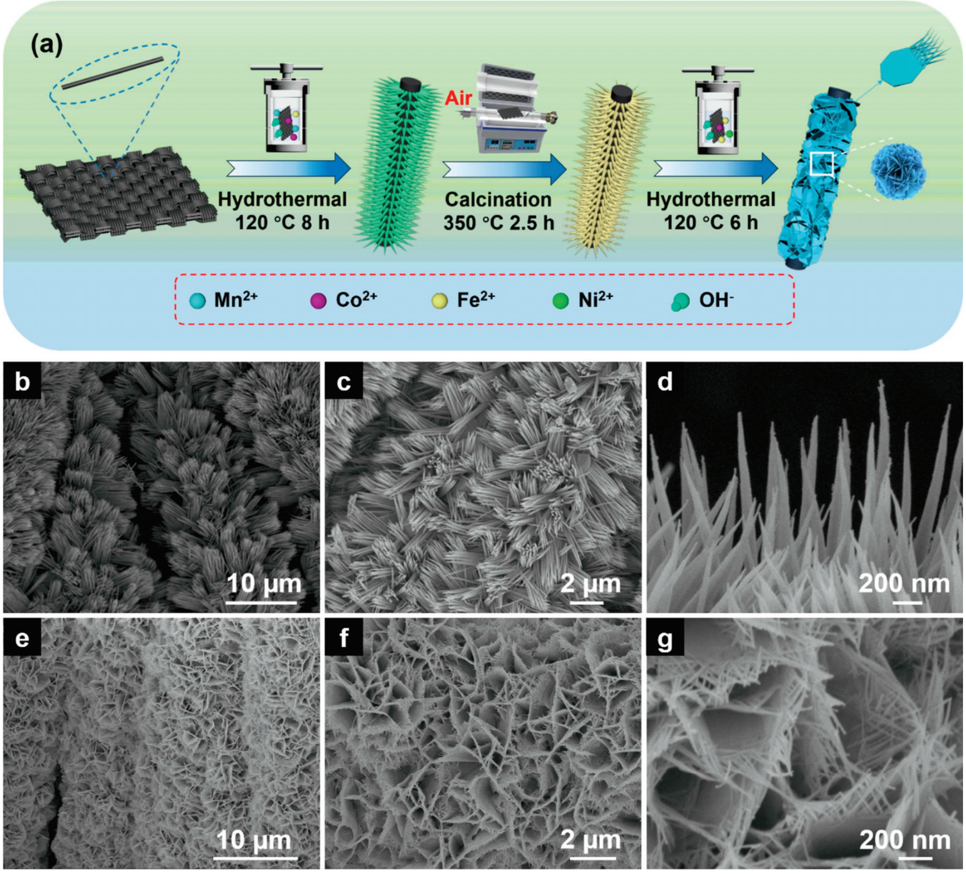

Figure 7. (**a**) Illustration of the step-by-step process to make MnCo@FCN on CC via hydrothermal synthesis. (**b**–**d**) FESEM images showing the surface of MnCo on CC at various zoom levels. (**e**–**g**) FESEM images of MnCo@FCN coated on CC under different magnifications. Reproduced with permission [162].

CoMo-LDH was synthesized via hydrothermal treatment of cobalt nitrate and sodium molybdate in the presence of urea, followed by coating with polydopamine (PDA) through a polymerization process and subsequent carbonization at 800 °C to form CoMoLDH@C-PDA composites [163]. The duration of the hydrothermal and polymerization steps was optimized to achieve controlled morphology and appropriate carbon layer thickness. The carbon-coated CoMoLDH is considered suitable as an anode material for NIBs due to enhanced conductivity, structural stability, and sodium-ion diffusion. Co-Co LDH was synthesized via a hydrothermal method using ZIF-67 as the precursor and grown onto nitrogen-doped hollow carbon nanospheres (NHCNS) [164]. The resultant Co-Co LDH@NHCNS was then selenized and coated with a carbon shell to obtain the final NHCNS@$CoSe_2$@C composite. The composite exhibited a nanoflower-like morphology with uniformly distributed $CoSe_2$ nanoparticles on the NHCNS surface. XRD validated the successful transformation to $CoSe_2$; XPS and Raman revealed the chemical states and defect structures, and TGA estimated a carbon content of 43.4%. This unique sandwich structure offers enhanced conductivity, stability, and sodium storage capability, making it highly suitable for NIB applications. The CoNi-LDH was synthesized via a two-step hydrothermal method, where cobalt phosphate (CP) was first grown on nickel foam, followed by in situ growth of molybdate-intercalated CoNi-LDH (MCN-LDH) on the CP surface [165]. Incorporating molybdate ions was achieved using urea and ammonium fluoride as structure-directing agents. The prepared LDH exhibited interconnected nanosheets on microsheets; XRD confirmed phase structure; BET analysis showed a surface area of 212.68 m^2/g; Raman and XPS confirmed successful $MoO_4{}^{2-}$ intercalation. These structural and textural improvements make the MCN-LDH highly suitable for high-performance ZIB cathode applications. ZnCo-LDH was synthesized via a hydrothermal process by dissolving $CoCl_2 \cdot 6H_2O$, $ZnCl_2$, urea, and PVP in deionized water, then heating at 120 °C for 12 h [166]. The resulting product was collected, washed, and dried to obtain ZnCo-LDH microspheres. BET measurements showed a surface area of 37.1 m^2/g with mesopores averaging 28.2 nm in diameter. These structural features, including high surface area and mesoporosity, make the material highly suitable for electrochemical applications in ZIBs.

NiAl LDH was synthesized using a one-step hydrothermal method [167]. The resulting LDH exhibited a porous nanosheet morphology with oxygen vacancies, high crystallinity, hierarchical nanostructures, and a BET surface area of up to 300 m^2/g, promoting efficient ion transport and electron transfer. These features make it a suitable candidate for supercapacitor applications due to its enhanced redox activity, mechanical integrity, and electrochemical performance. MoB@NiCo-LDH was synthesized via a hydrothermal process by growing NiCo-LDH nanosheets on layered MoB templates derived from NaOH-etched MoAlB; subsequent phosphorization and $NaBH_4$ treatment introduced phosphorus vacancies, resulting in MP2 material [168]. The synthesized LDH exhibits an amorphous structure with a nanosheet-to-nanoparticle morphological transition, a layered architecture, uniform elemental distribution, enhanced electrical conductivity, and abundant surface-active sites due to phosphorus vacancies. These features contribute to fast charge transport, high redox activity, and structural stability, making the LDH ideal for supercapacitor applications.

The Te-doped NiMn LDH was synthesized via hydrothermal growth on CTAB-modified MXene-coated nickel foam, followed by tellurium doping through immersion in $TeCl_4$ ethanol solution [169]. The step-by-step design strategy and structural characterization of the Te-doped NiMn LDH system are illustrated in Figure 8. The CTAB-modified MXene coating on nickel foam (C-MXene/NF) is shown in Figure 8, which offers a rough, layered texture that supports better growth of the active material. Figure 8a,b shows the FESEM image of NiMn LDH directly grown on bare nickel foam, revealing a relatively smoother and flatter structure. With the addition of the MXene layer, Figure 8c shows that the NiMn LDH forms a more clustered, 3D nanostructure on C-MXene/NF, offering increased surface area and potential active sites. Figure 8d displays the final morphology after tellurium doping, which results in a highly porous, flower-like structure. This modification enhances electrochemical activity by introducing more redox-active centers and improving conductivity. XRD confirms the structural phases of the different samples in Figure 8e, where distinct peaks are observed for NiMn LDH/NF, NiMn LDH/C-MXene/NF, and Te-NiMn LDH/C-MXene/NF. Reference patterns for $Ni(OH)_2$ and $Mn(OH)_2$ are also compared, confirming the successful formation of the LDH phases and the influence of doping and substrate modification. The prepared LDH displayed vertically aligned, nanosheet-like morphology with enhanced crystallinity, a significantly expanded interlayer spacing, increased surface roughness, and higher electrochemical surface area; BET analysis confirmed elevated surface area due to CTAB intercalation. Such morphological and structural characteristics, combined with improved conductivity from Te doping and MXene support, make this LDH ideal for high-performance supercapacitor applications.

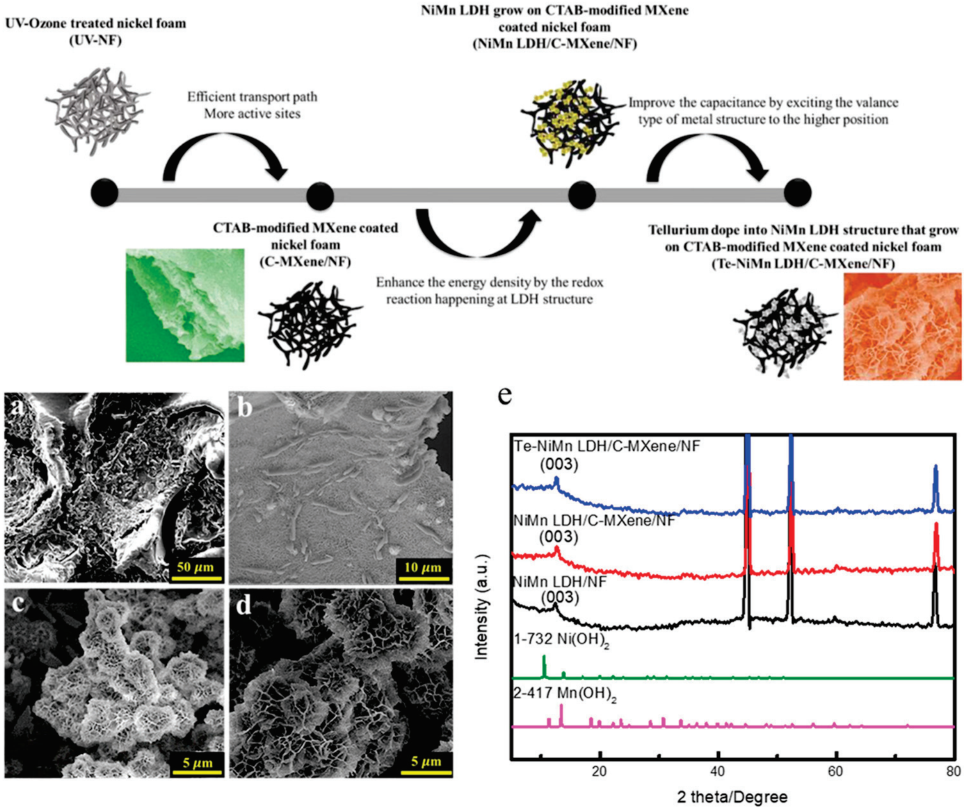

Figure 8. Overview of the synthesis process for Te-doped NiMn LDH on CTAB-modified MXene-coated nickel foam. FESEM images showing surface morphologies at various stages: (**a**) C-MXene/NF, (**b**) NiMn LDH on bare NF, (**c**) NiMn LDH on C-MXene/NF, and (**d**) Te-doped NiMn LDH on C-MXene/NF. (**e**) XRD patterns comparing NiMn LDH/NF, NiMn LDH/C-MXene/NF, and Te-NiMn LDH/C-MXene/NF, with standard reference peaks of $Ni(OH)_2$ and $Mn(OH)_2$ included for comparison. Reproduced with permission [169].

3.3. Electrochemical Deposition

Electrochemical deposition reduces metal ions from a solution with the potential to generate thin lamellar films on substrates for LDHs. Binders and post-treatment are unnecessary with this method [170–172]. Faradaic interactions at the electrode/electrolyte interface generate localized hydroxide ions, which combine with metal cations in solution to precipitate LDHs' layered structure [92,173]. This approach directly synthesizes LDHs with controlled composition and form by changing electrochemical parameters, making it a strong functional material creation tool. Electrochemical environments improve deposition kinetics, enabling fast nucleation for nanostructured coatings with high surface areas. Environmental friendliness and operational simplicity approach a viable alternative to existing chemical precipitation procedures. Electrochemical deposition for LDH synthesis reduces oxygen-containing species at the cathode, quickly raising local pH and forming metal hydroxide layers. Metal hydroxide layers form a lamellar structure held together by intercalated anions like carbonates or nitrates. The water reduction rate and hydroxide ion supply for LDH production rely on the applied voltage. Current density and deposition duration can often change the LDHs' deposit shape and crystallinity. Researchers can tune LDH film performance for catalysis and energy storage.

Water electrolysis raises local hydroxide concentrations, which react with divalent and trivalent metal cations to synthesize LDHs by electrochemical deposition [174]. Metal hydroxide layers form in situ and stack into an organized array. The interaction between nucleation and growth controls deposition, ensuring uniform deposition across the electrode surface with controlled current or potential. The mechanism is complicated since deposition kinetics and ion transport compete to determine film structure. Understanding and regulating these parameters is necessary for making high-quality LDH films with desirable qualities. LDH film shape and crystallinity depend on electrodeposition parameters such as applied voltage, current density, and deposition time. Researchers can optimize these settings to create LDH deposits with consistent thickness and well-defined platelets [174]. Changing the electrolyte composition and pH controls LDH nanofilm deposition kinetics and structural evolution. These optimized conditions give synthesized films excellent electrochemical performance, which is helpful for catalytic applications and energy storage devices. Extensive parameter optimization is necessary to synthesize materials with specific functional properties [175]. Electrochemical deposition of LDHs commonly has hexagonal platelet-like formations after alkaline treatment, as documented in the literature [176]. Reorientation and crystallization of amorphous deposits under alkaline circumstances create an ordered lamellar pattern. Ion concentration and water decrease support platelet formation. Morphological aspects directly affect functional properties like ion intercalation and film catalytic activity. Optimizing LDH-based electrode performance requires precise control over deposition and post-treatment. Alternating metal hydroxide layers and intercalated anions or water molecules give LDHs their lamellar structure. Recent research confirms this tendency [93]. The systematic stacking of LDHs is caused by metal cations reacting with hydroxide ions during electrochemical deposition. Interlayer anions balance the positive charge of metal hydroxide layers and improve structural stability and functionality. The deposition environment can also be modified to these intercalated species, further controlling material characteristics. The deposition method naturally forms highly structured, anion-rich structures, enabling rapid ion exchange and high specific surface areas.

When comparing electrodeposition with traditional synthesis methods, such as co-precipitation or hydrothermal techniques, it becomes evident that electrochemical deposition offers significant advantages for the fabrication of LDHs [177]. This technique enables the direct deposition of LDHs onto conductive substrates, thereby eliminating the need for binder agents and enhancing electron transfer efficiency. In addition, the in situ formation of hydroxide films during electrodeposition leads to rapid synthesis and improved uniformity relative to conventional methods. Such direct synthesis is crucial in applications where interface quality between the active material and the substrate determines overall device performance. Consequently, electrochemical deposition has become a preferred method for preparing LDH films in many high-performance electrochemical systems. Electrochemical deposition presents several notable advantages, including precise control over film thickness, composition, and morphology, which are critical factors for optimizing the properties of LDHs [174,177]. This approach may change reactant concentration and deposition rate by carefully adjusting the applied voltage and current. This control guarantees uniform nucleation density across the substrate, decreasing flaws and improving electrode performance. Electrodeposition also makes LDH integration on metal foams and carbon-based electrodes easy. These tunable characteristics allow researchers to customize LDHs' physical and chemical features for energy storage and electrocatalysis applications. Recent studies have exemplified the successful application of electrodeposition in synthesizing NiCo-LDH films directly onto nickel foam substrates, a configuration that significantly enhances electrocatalytic performance [174,178]. Direct development of LDHs on structured substrates provides excellent electrical connection and a high electrochemically active surface area for effective catalytic reactions. Interconnected nanosheets in the hierarchical microstructure enable quick charge transfer and mechanical stability under operational conditions. The substrate/active LDH material synergy boosts device performance, making them attractive for water splitting and supercapacitor electrodes. Electrodeposition helps synthesize improved composite electrodes for energy conversion and storage. Pulse electrodeposition, a variant of the traditional electrochemical deposition technique, involves applying cyclic pulses of current or potential, which are sometimes interspersed with reverse pulses [179]. Incorporating pauses between deposition pulses alleviates the local depletion of metal ions, thereby allowing a more uniform ion concentration to be maintained across the deposition zone. This technique effectively enhances the morphological quality of the deposited LDH films, leading to more homogeneous structures with reduced defects. Additionally, reverse pulses can help remove undesirable surface charges that may otherwise impede further deposition or lead to non-uniform film growth. As a result, pulse electrodeposition is a valuable method for fine-tuning the properties of LDH films in various electrochemical applications.

Recent research using in situ techniques, such as atomic force microscopy, has revealed the dynamic morphological evolution of Co-based LDH nanosheets during electrodeposition [180]. These studies have shown that the initial nucleation step is critical in establishing the eventual sheet-like structure and that subsequent growth is susceptible to the applied deposition parameters. The evolution process is characterized by the formation of nanoscale features that promote efficient charge transport and ion diffusion. Moreover, the real-time observation of the growth process has provided critical insights into the nucleation and growth mechanisms, enabling further optimization of deposition protocols. This understanding is vital for designing LDHs with enhanced electrocatalytic or supercapacitive properties, as the nanosheet structure is key to their high surface area and functionality. The impact of deposition time and current density is well documented, with studies demonstrating that prolonged deposition or increased current can significantly enhance the crystallinity and overall quality of LDH films [181]. Longer deposition times allow for gradually reorganising initially amorphous deposits into highly ordered, crystalline platelets suitable for various electrochemical applications. Similarly, higher current densities can accelerate hydroxide ion generation, boosting nucleation rates and leading to finer nanostructures. However, excessive current may also lead to inhomogeneities; thus, optimizing these parameters is crucial to maintaining the lattice structure. Therefore, systematic studies that vary these factors are essential for mapping the optimal conditions that yield LDHs with superior structural and electrochemical characteristics.

A significant body of work has centered on the electrochemical deposition of NiFe and NiCo LDHs, which have been shown to provide high performance for water oxidation and other electrocatalytic reactions [182,183]. In these systems, the deposition process is optimized to ensure the formation of ultrathin nanosheets, whose abundant active sites contribute to enhanced catalytic activity. The simultaneous incorporation of two types of metal ions in the LDH structure is particularly beneficial, as it facilitates synergistic effects that lower overpotentials and improve reaction kinetics. Moreover, such bimetallic systems benefit from the tunability offered by electrodeposition, allowing researchers to balance the composition and morphology for maximum efficiency. These studies provide compelling evidence that electrodeposited LDHs can meet the rigorous demands of modern electrocatalytic applications.

In another compelling example, the synthesis of CoNi-LDH films via electrodeposition onto copper substrates has been reported for high-performance supercapacitor applications [184]. Direct deposition promotes strong adhesion between the active material and substrate, improving device stability and charge/discharge cycling. Hierarchical nanostructures created by electrodeposition improve accessible surface area, boosting pseudocapacitive performance, according to researchers. Active sites are evenly distributed over the electrode surface, enabling fast ion transport and energy storage. According to such studies, electrodeposition methods are widely applicable and work well in LDH-based energy storage devices. The pulsed deposition methods, as discussed earlier, also play a critical role in refining LDH film morphology by allowing for periodic replenishment of metal ions and the removal of excessive surface charge [179]. This controlled deposition method produces uniform, defect-free coatings with outstanding adhesion and electrochemical characteristics. The intermittent deposition approach slows reactant depletion near the cathode, assuring film growth. Such methods benefit complex multimetal systems that require homogeneous distribution for desirable electrical properties. Thus, pulse electrodeposition provides a versatile and practical approach for synthesizing improved LDH materials.

Electrochemical deposition has also been extended to synthesizing CoFe and CoNi LDH catalysts, which show superior OER performance owing to their enhanced conductivity and abundant active sites [177,185]. In these studies, precise control over the deposition conditions results in ultrathin films that maximize the exposure of catalytically active sites while maintaining excellent adherence to the substrate. The voltage and current parameters are optimized to balance the nucleation and growth processes, ensuring the resulting film is uniform and highly porous. Such optimization is key to reducing the overpotential required for OER and enhancing overall catalytic efficiency. The resulting electrode architectures, therefore, present a promising route for developing cost-effective and efficient water splitting systems. Consistent with the critical role of processing parameters, numerous experimental studies have underscored that the nucleation rate and the growth kinetics during electrodeposition are pivotal in determining the overall quality of LDH films [174]. Optimal equilibrium between these elements ensures continuous, defect-free, nanostructured deposited layers. Furthermore, systematic modification of deposition time and applied voltage has greatly affected film shape and crystallinity. Finely tailored deposition techniques increase electrochemical performance and reproducibility across substrate materials. Optimizing the electrodeposition process is necessary to produce high-quality LDH films for advanced energy and catalytic applications.

The versatility of electrodeposition has allowed for the synthesis of LDH films on various substrates, including metal alloys and conductive carbon materials, thereby broadening the scope of potential applications [186,187]. Growth on substrates like titanium and aluminum alloys has been demonstrated to improve corrosion resistance and enhance the material’s durability in aggressive environments. Similarly, deposition on carbon-based substrates offers benefits such as improved conductivity and flexibility, which are crucial for fabricating next-generation electrodes. The inherent adaptability of the electrochemical deposition process accommodates modifications to suit various substrate types while retaining high film quality and consistency. Thus, the method’s applicability to various substrates significantly expands potential applications for LDH-based materials. The electrodeposition method inherently facilitates the formation of binder-free LDH films, thereby eliminating potential interference from insulating binders and enhancing electrical connectivity between the active material and the substrate [188,189]. This direct deposition onto conductive substrates results in improved electron transfer and overall device performance, which is particularly beneficial in electrochemical sensing and energy storage devices. Without additional processing steps, the simplicity and efficiency of the process are markedly enhanced, leading to lower production costs and higher material uniformity. Moreover, the direct interface formed by binder-free deposition ensures intimate contact between the catalyst and the electrode, a crucial factor for high-performance devices. Therefore, electrodeposition is an efficient route to achieving high-quality, binder-free LDH films with optimized properties.

The fundamental mechanism driving the electrochemical deposition of LDHs pivots on the local generation of hydroxide ions from water reduction, which quickly interact with dissolved metal cations to create precipitated hydroxide layers [175]. This process is initiated at the cathode and progresses by the continuous supply of hydroxide ions, resulting in sustained growth of the layered structure as long as the applied potential is maintained. The reaction environment is finely tuned so that the concentration gradients created during deposition facilitate the uniform nucleation of the LDH phase across the electrode surface. Additionally, the ease of ion migration and fluid dynamics within the electrolyte further contributes to the modernization of the deposition front. Thus, the coupling between electrochemical reactions and diffusive transport is essential in establishing the layered architecture characteristic of LDHs. Under optimized electrochemical deposition conditions, it is possible to generate LDH films exhibiting diverse morphologies, including nanosheets, nanoframes, and porous networks [180,183]. Deposition parameters, including current density, pulse duration, and electrolyte composition, can be adjusted to control these morphological differences to match the application. Rapid nucleation and anisotropic growth in the substrate plane produce ultrathin nanosheets with excellent lateral connectivity. Slower deposition rates and higher ion diffusion can create a more porous network, which is helpful for quick ion transport applications. Thus, controlling the deposition environment allows researchers to construct LDH films with unique morphologies for specific functional tasks.

The deposition process is susceptible to external parameters like pH and temperature, which influence the reaction kinetics and the structural outcome of the synthesized LDH films [190]. High pH levels enhance nucleation by increasing hydroxide ion concentration, forming hydroxide layers that assemble into lamellar structures quickly. Temperature also helps constituent ions move, enabling rearrangement to create a crystal lattice. This sensitivity to deposition circumstances requires rigorous experimental control because even small variations might impact material characteristics. The interaction between pH, temperature, and applied voltage is crucial for regulated deposition and high-quality LDH films. The overall synthesis of LDHs by electrodeposition has been widely employed in developing electrocatalysis and energy storage device catalysts [181,182]. The layered structure of LDHs, alternating metal hydroxide sheets intercalated with anions, provides many active sites and improved ion transport routes in various applications. These functional applications require accurate film thickness and composition control, which the deposition process offers. Electrodeposited LDHs adhere well to substrates, making them stable under high-current or long-term operation. In addition to being a straightforward synthetic pathway, the technology allows the integration of high-performance LDH materials in innovative technological applications [191]. Structural and electrochemical analyses have indicated that the LDH films produced through electrodeposition feature a unique lamellar morphology and highly porous structure, essential for rapid ion transport and high surface reactivity [177,192]. These materials have large interlayer spacing because the deposition process creates loosely packed layers intercalated by anions or solvent molecules. Electrocatalysis and supercapacitors require rapid ion diffusion and high charge storage capacities, making porousness favorable. The films' wide pore channels minimize ion transport resistance, improving electrochemical performance. The structure of electrodeposited LDHs allows for adequate charge storage and robust catalytic processes.

Recent examples in the literature have demonstrated that strategic modulation of the pulse deposition sequence, by incorporating rest periods and reverse pulses, can significantly enhance the quality of LDH films [174,179]. Incorporating pauses between active deposition pulses allows for the equilibrium re-establishment of metal ion concentration near the electrode surface, thereby avoiding depletion effects and promoting uniform growth. Furthermore, reverse pulses help remove excess charge accumulation on the surface, which can otherwise lead to undesirable side reactions or film defects. The precise control over these deposition parameters enables the creation of LDH films with highly uniform thicknesses and minimized defect densities, both of which are crucial for ensuring high electrochemical performance. Therefore, advanced pulse modulation strategies have emerged as indispensable tools in the electrodeposition synthesis of high-quality LDH materials.

Certain studies have highlighted the deposition of MnCo-based films, where incorporating cobalt into the electrodeposited film significantly affected the electrocatalytic performance of OERs [175,193]. This research demonstrated that by varying the deposition parameters, the crystallinity and morphology of the LDH films could be tailored to enhance their catalytic activity. In these cases, the presence of cobalt was shown to improve the films' electronic conductivity and redox capabilities, thereby reducing the overpotential required for catalysis. Additionally, the synergistic effect of the mixed metal composition resulted in enhanced nucleation rates and more uniform film formation during deposition. These findings underscore the importance of compositional tuning in the electrodeposition process to optimize the functional properties of LDHs [175,193].

The transformation of precursor materials such as MOFs into LDHs via electrochemical deposition is another emerging avenue that broadens the synthesis strategies available for these materials [190,194]. In this approach, the MOF serves as a sacrificial template, which, upon exposure to an alkaline environment and an applied potential, is converted into an LDH. This method offers the advantage of controlling the porosity and morphology of the final product by precisely tuning the conversion process. The reconstruction of MOFs into LDH structures simplifies the synthetic steps and results in materials with enhanced catalytic and electrochemical properties. As a result, this technique has garnered attention as a promising strategy for producing advanced LDHs with tailored features for diverse applications. In a related innovation, the reconstruction of Prussian blue analogs into thin LDHs has been meticulously demonstrated, offering a pathway toward synthesizing efficient electrocatalysts [194,195]. One of the foremost benefits of electrodeposition is the direct integration of LDH films onto conductive substrates, eliminating the need for non-conductive binders that might hinder electron transport [177,196]. The resulting electrodes exhibit excellent electrical connectivity and reduced interfacial resistance by depositing LDHs directly onto substrates such as titanium carbide or nickel foam. This direct synthesis approach enhances electrochemical performance, particularly in applications requiring high-rate charge transport, such as supercapacitors and electrolysis cells. Moreover, the robust interface formed through electrodeposition contributes significantly to the devices' mechanical stability and operational longevity. Consequently, the method provides a streamlined route to high-performance electrodes by ensuring that the active material is directly and intimately connected with the current collector.

The inherent precision of the electrodeposition method allows for exceptional tunability in the thickness, composition, and morphology of the resulting LDH films, which is essential for correlating structure with performance [174,177]. Researchers have effectively exploited this precision to fabricate films optimized for specific applications, whether enhanced catalytic activity or improved storage capacity. By adjusting parameters such as deposition potential and electrolyte concentration, the process can be customized to yield films with distinct microstructures ranging from smooth continuous layers to highly porous networks. This level of control is particularly beneficial in energy-related applications, where the surface area and active site accessibility largely dictate the device's performance. Therefore, electrodeposition remains a desirable method due to its flexibility and effectiveness in producing high-quality LDH films tailored to meet specific performance criteria. In addition to conventional electrodeposition, recent advancements have illustrated how integrated deposition strategies can further enhance the functional properties of LDH films [197,198]. During LDH electrodeposition, nanostructured carbon materials can increase the composite electrode's electrical conductivity and surface area. This synergistic combination creates an electrode with better charge transport and effective capacitance, which is ideal for energy storage. Dual nanocarbon supports ensure structural integrity and excellent catalytic reactivity of deposited LDHs. Such hybrid structures emphasize the need for multifarious deposition techniques to generate integrated materials with improved performance.

Advanced methodologies also include the in situ formation of NiAl-LDHs within confined microreactor environments, where tunable interlayer spacing can be achieved by adjusting the impinging jet parameters during deposition [186]. Microreactor-assisted electrodeposition enables precise nanoscale control of LDH structures, enhancing their electrochemical performance for energy applications. The unique design of deposition setups, including pauses between deposition pulses, further ensures the uniform regeneration of metal ion concentrations near the electrode surface [173,179]. Pulse-controlled electrodeposition enhances LDH film uniformity and structural order, yielding high-performance electrodes with reduced defects and improved interlayer connectivity.

Electrodeposition techniques have also been highly effective in synthesizing uniformly mixed LDH films incorporating multimetal systems, such as NiCo-LDH, which are critical for high-performance electrocatalysis [174,196]. Electrodeposition enables uniform multimetal integration in LDH films, enhancing conductivity, redox activity, and catalytic performance for advanced energy applications. Detailed interfacial analyses have shown that the layer-by-layer growth achieved during the electrodeposition of LDHs results in exceptional interfaces crucial for efficient electron transport and ion accessibility [183,192]. The well-organized lamellar structure in these systems ensures that charge carriers can traverse the electrode with minimal impedance due to the abundant and organized active sites. The formation of these homogeneous interfaces is critical in reducing the electrode's internal resistance and enhancing the overall electrochemical performance. Furthermore, the intimate contact facilitated by the direct deposition method minimizes potential interfacial delamination issues, thereby contributing to the longevity and robustness of the device. Consequently, the layer-by-layer growth mechanism achieved through electrodeposition is a key feature that reinforces the practical viability of LDHs in complex electrochemical applications.

The electrodeposition synthesis strategy is strongly influenced by the competition between nucleation and growth processes, which are both sensitive to the deposition parameters set during the process [193]. A higher applied potential can increase the nucleation rate, leading to a greater density of small nuclei, which eventually merge to form a continuous film. However, if the growth process is not carefully managed, rapid nucleation can lead to the formation of overly rough and non-uniform surfaces. Therefore, selecting the appropriate deposition conditions, such as current density and pulse duration, is essential to achieve the desired balance between nucleation and growth.

This delicate balance is fundamental for synthesizing high-quality LDH films with optimal microstructural characteristics [181,193].

Among the innovative examples in recent literature are ternary LDH composites that have been synthesized via electrodeposition, demonstrating significantly improved OER performance [199,200]. The introduction of a third metal component not only enhances the electronic structure of the LDH but also introduces a new level of active sites that facilitate more efficient catalytic processes. Detailed electrochemical studies have revealed that such ternary systems lower the overpotential required for OER and improve reaction kinetics due to the synergistic interactions among the incorporated metal species. Moreover, these composite materials were obtained by adjusting the deposition parameters to ensure uniformity and high dispersion of the active species across the electrode. Therefore, the evolution of electrodeposition techniques to include multimetal systems represents a significant advancement toward developing next-generation catalysts for clean energy applications.

An intriguing dimension of electrodeposition is its adaptability in fabricating flexible energy storage devices. LDH films are deposited onto flexible substrates to yield electrodes with outstanding mechanical integrity and high capacitance [189,201]. Such flexible electrodes not only sustain large mechanical deformations but also maintain excellent electrochemical performance during long-term cycling. The direct growth of LDHs onto flexible substrates ensures that the interface is robust and the ion transport channels remain unimpeded despite mechanical bending or stretching. In addition, the combination of electrodeposited LDHs with flexible conductive materials opens up new possibilities for wearable energy storage devices and portable electronics. This innovative approach underscores the versatility of electrochemical deposition in producing advanced electrodes that combine mechanical flexibility with exceptional electrochemical properties.

The careful selection of deposition parameters, such as electrolyte composition and deposition time, is essential to unlocking the theoretical structural advantages of LDHs, including high surface areas, accessible interlayer spaces, and controlled redox properties [196,202]. For instance, tuning the electrolyte composition can promote the selective intercalation of specific anions, thereby optimizing the interlayer spacing and significantly enhancing the electrochemical performance. Similarly, adjusting the deposition time allows for precise control over film thickness, directly impacting the electron and ion transport kinetics within the LDH film. These controlled modifications enable the synthesis of LDHs that exhibit tailored properties for applications ranging from water splitting to supercapacitors. In this context, the electrodeposition technique stands out for its flexibility and effectiveness in producing materials with finely tuned structural and functional characteristics.

Numerous studies have demonstrated the advantages of pulsed electrodeposition, wherein reverse pulses are utilized to mitigate the accumulation of surface charges and to ensure a steady state of deposition ion concentration [174]. By carefully calibrating the pulse duration and the intervals between pulses, the deposition process can be optimized to yield smoother, more uniform LDH films with reduced defect densities. This method also minimizes undesirable side reactions, thereby enhancing the deposited materials' chemical integrity and electrochemical stability. The resulting improvement in uniformity is directly related to improved device performance, as fewer defects translate to fewer pathways for unwanted charge recombination or degradation. As such, pulsed electrodeposition represents a sophisticated synthesis strategy well-suited for preparing high-quality LDHs for advanced electrochemical applications.

The high degree of tunability in electrodeposition also permits the fabrication of LDH films with diverse morphologies, ranging from densely packed continuous layers to highly porous, exfoliated nanosheets [180,183]. By systematically adjusting deposition conditions, researchers have induced a controlled exfoliation of the layered structure, thereby exposing more active sites and increasing the effective surface area. These morphological features are particularly beneficial for supercapacitors and electrocatalysts, where rapid ion diffusion and extensive charge storage are critical. Moreover, synthesizing distinct nanostructures within a single processing technique allows for integrating materials with complementary properties, further enhancing device performance. Consequently, the tunability of the electrodeposition process serves as a key advantage in the strategic design and synthesis of advanced LDH-based materials.

Complementary to the direct electrodeposition approach, in situ reconstruction methodologies have emerged as powerful strategies to convert existing compounds into LDH structures with desired morphologies and enhanced functionalities [92,194]. Such methods involve transforming precursor materials under the influence of applied potential and alkaline conditions, leading to the formation of LDH structures from an initially non-layered phase. This reconstruction process streamlines the overall synthesis and results in LDH materials with improved crystallinity and increased active surface areas. Integrating reconstruction techniques with electrodeposition offers additional control over the deposition kinetics and final structure. As a result, these coupled strategies enable the fabrication of high-performance LDH-based electrodes suitable for an array of advanced applications [92].

These advanced synthesis strategies have been further refined by incorporating design templates that direct the formation of hierarchical LDH structures with enhanced catalytic and energy storage properties [178,197]. Whether sacrificial or permanent, templates allow the growth of LDH films with controlled porosity, uniform layer thickness, and precisely engineered interlayer distances. Such templated electrodeposition enhances the material's electrochemical performance by increasing the effective surface area, improving ion transport, and imparting mechanical robustness to the composite electrode. Moreover, the templating approach facilitates the formation of multidimensional architectures tailored to specific functional requirements. Consequently, these design strategies underscore the critical role of electrodeposition in synthesizing advanced LDH materials with tailored structure/property relationships for various applications. The electrochemical deposition and synthesis mechanism for LDHs embodies a multifaceted process that leverages controlled faradaic reactions to generate well-defined, nanostructured films with tunable compositions and morphologies [173,181,193]. By meticulously adjusting parameters such as deposition potential, current density, ionic concentration, and pulse duration, researchers can achieve high-quality LDH films that are directly integrated with conductive substrates, making them readily applicable in electrocatalysis, energy storage, and corrosion protection [177,184,196]. Recent advances have further demonstrated that innovative approaches, ranging from pulsed electrodeposition to reconstruction of precursor materials, significantly enhance the performance attributes of LDH films by optimizing the exposure of active sites and ensuring efficient ion transport. The versatility and scalability of the electrochemical deposition technique promise to further advance the field of nanostructured material synthesis and are expected to play a pivotal role in developing next-generation devices. Thus, this synthesis process's robust and adaptable nature ultimately underscores its importance and potential for future applications in various scientific and technological domains.

NiCo LDH was synthesized via an electrodeposition method, enhanced by incorporating $Ti_3C_2T_x$ MXene on the nickel foam (NF) substrate and in the plating solution [203]. This dual role of MXene improved interfacial contact and conductivity, facilitating the deposition of ultrathin LDH nanosheets with high areal loading (~65 mg/cm^2). Characterization revealed a porous nanosheet morphology, polycrystalline hexagonal structure via HRTEM, uniform Ni and Co distribution, and MXene confirmed through XRD and XPS analyses. These features collectively make the MXene-enhanced LDH electrode highly suitable for high-performance ZIB cathodes. The CoNi-LDH was synthesized on flexible CC via in situ electrochemical deposition from a Co^{2+}/Ni^{2+} precursor, followed by electrochemical activation (ECA) in aqueous KOH to induce H-vacancy formation, resulting in CoNi-LDH(v) [204]. Figure 9a outlines the two-step process used to create the CoNi-LDH electrode. First, CoNi-LDH is deposited onto CC via electrochemical deposition, then it undergoes electrochemical activation to introduce hydrogen vacancies, forming CoNi-LDH(v)@CC. As shown in Figure 9b, the deposition occurs in a solution containing Co^{2+}, Ni^{2+}, and OH^- ions. The corresponding CV curve shows redox behavior, and the resulting material has a layered crystal structure with nitrate ions. Figure 9c illustrates the activation step, where CoNi-LDH is treated under an applied voltage to create hydrogen vacancies. The CV plot shows enhanced electrochemical activity after activation, and the structure model confirms the formation of H vacancies that improve the material's electrochemical properties. The morphology revealed vertically aligned nanosheets forming a porous 3D network; structural analysis via XRD and TEM confirmed partial amorphization and reduced interlayer spacing due to NO_3^- extravasation. BET surface area was not directly stated, but the induced H vacancies and 2D open channels significantly increased the active surface and conductivity. These features enhanced Zn^{2+} diffusion and intercalation, making the LDH highly suitable for Zn-ion battery applications.

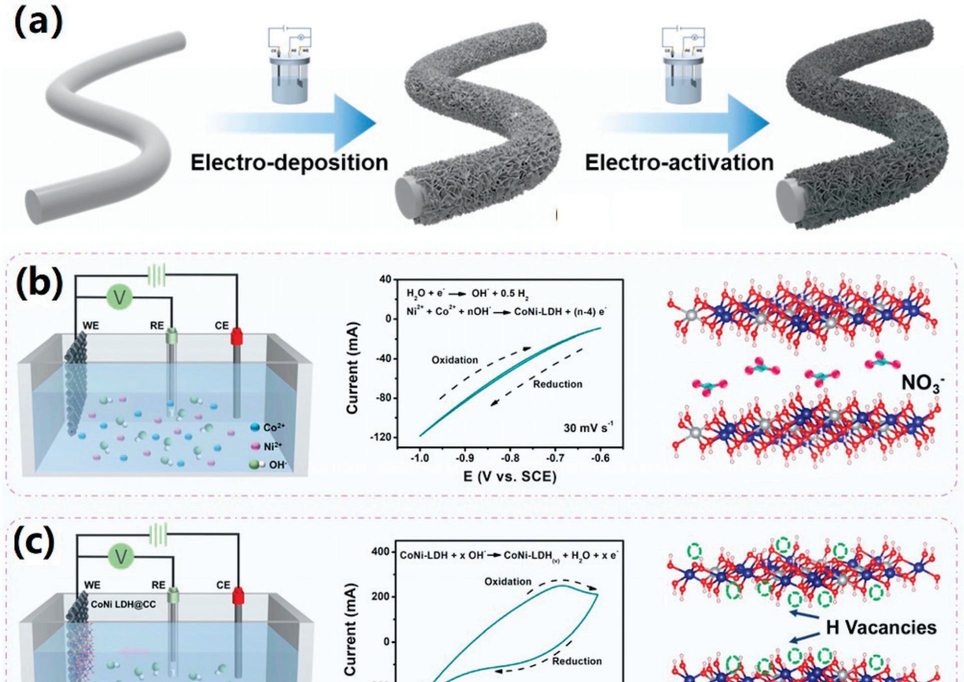

Figure 9. (**a**) Illustration of the fabrication steps involving electrochemical deposition of CoNi-LDH on CC (CoNi-LDH@CC), followed by electrochemical activation to generate hydrogen-deficient CoNi-LDH(v)@CC. (**b**) Diagram of the deposition setup (left), corresponding CV curve (middle), and the crystal structure of the as-prepared CoNi-LDH (right). (**c**) Electrochemical activation process (left), CV curve under optimized activation conditions (middle), and structural model showing hydrogen vacancies in CoNi-LDH(v) (right). Reproduced with permission [204].

A novel synthesis pathway involves the reconstruction of MOFs or Prussian blue analogs into LDHs, which can also be achieved through an electrochemical deposition process [190,194]. This approach uses the structural change of a precursor molecule in an alkaline environment under an applied voltage to create an LDH. The reconstruction method simplifies synthesis and increases product surface area and reactivity. Using MOFs as sacrificial templates also allows fine control over the LDH structure's porosity and shape. This comprehensive technique shows how electrochemical deposition can synthesize customized LDHs with enhanced functional characteristics. Adjusting the deposition parameters enables the production of ultrathin LDH films with exceptional surface area and catalytic activity, which are crucial for their application in sensors and energy devices. By fine-tuning factors such as ionic strength, deposition time, and pulse frequency, researchers can achieve controlled growth that yields films with homogeneous thickness and low defect densities [173]. The resulting LDHs exhibit enhanced electron mobility and rapid ion diffusion, vital for high-performance catalytic and supercapacitor applications. Furthermore, the deposition technique provides a direct route to engineering the film architecture, which supports efficient charge storage and transfer. As a result, the method stands out for its ability to customize nanostructured films for a wide range of electrochemical applications.

The formation of hexagonal platelets, a hallmark of well-crystallized LDHs, is significantly influenced by the alkaline treatment following electrodeposition, during which an initial disordered film is reorganized into an ordered lamellar structure [93]. This transition is attributed to the enhanced mobility of constituent ions within the deposit, which facilitates the rearrangement into a thermodynamically favorable configuration. The development of hexagonal platelets indicates high crystallinity and correlates with improved functional properties, such as ion exchange capacity and catalytic performance. Therefore, the post-deposition treatment must be carefully controlled to maximize these desirable features. Consequently, combining electrodeposition with subsequent alkaline treatment forms a robust strategy for synthesizing ordered and functional LDH films. Control over interlayer composition during the synthesis of LDHs via electrodeposition can be effectively achieved by modulating the electrolyte composition and deposition parameters [190]. Selecting electrolyte anions affects LDH charge balance, interlayer spacing, and structural stability. This process is useful when improved conductivity or selective adsorption is needed. The deposition potential also affects intercalating species production and integration, fine-tuning the final layered structure [186]. Thus, deliberate control over the ionic environment during deposition is essential for crafting LDHs with tailored interlayer characteristics and optimized performance. Co-deposition techniques have been effectively employed in more complex systems to synthesize hierarchical LDH structures by concurrently depositing multiple metal ions, which leads to synergistic enhancements in electrocatalytic performance [182,205]. The simultaneous incorporation of different metal species into the LDH framework generates a material with a multifaceted electronic structure that supports rapid redox kinetics. This hierarchical organization improves not only the catalytic activity but also the mechanical stability of the electrode under rigorous operational conditions. The co-deposition strategy thus enables fine control over the relative concentrations and spatial distribution of the metal ions, ensuring that each contributes efficiently to the overall performance. Such advanced synthesis techniques highlight the power of electrodeposition in crafting multifunctional LDH catalysts tailored for high-demand electrochemical processes.

The ZnAl-LDH coating layer was synthesized on commercial Zn foil using a galvanostatic electrochemical deposition method in a nitrate aqueous solution [172]. Optimized parameters included a current density of 3 mA/cm^2 for 2 min and a Zn^{2+}/Al^{3+} molar ratio of 2:1. The LDH layer exhibited a smooth and uniform morphology with a hydrotalcite-like structure. The coating had a thickness of ~1.5 μm and displayed excellent wettability (contact angle ~5.96°) and strong zincophilicity, indicating its suitability as an artificial interfacial layer. This tailored ZnAl-LDH effectively stabilizes Zn plating/stripping and inhibits dendrite growth, making it highly suitable for ZIB anode protection. Figure 10a–c illustrates the critical balance between zincophilicity and zincophobicity in stabilizing Zn anodes [206], a concept highly relevant to LDH-based strategies where their tunable surface chemistry and layered structures can be engineered to regulate Zn^{2+} deposition and electrolyte interactions in both ZIBs and ZABs. The CoNi LDH was synthesized via in situ electrochemical deposition on an exfoliated graphite (EG) substrate, followed by CV-based electrochemical activation in KOH to introduce hydrogen vacancies [207]. During activation, interlayer anions (NO_3^-) were removed, and O–H bonds in the hydroxide lattice were cleaved to form a defect-rich CoNi LDH(v) structure. The resulting material exhibited ultrathin mesoporous nanosheets (∼5 nm thick), a hierarchically porous architecture, increased surface area (from 28.3 to 40.7 m^2/g), and good elemental distribution and crystallinity. These structural and surface properties make this LDH well-suited for Zn-ion battery cathode applications due to enhanced ion accessibility, conductivity, and defect-driven cation adsorption.

The synthesis of NiCo-LDH involved a two-step process [208]. Initially, NiCoS nanotubes were formed on nickel foam using hydrothermal sulfidation, followed by constant potential electrodeposition of ultrathin NiCo-LDH nanosheets to construct a core/shell heterostructure. Characterization through FESEM and TEM confirmed a 3D nanotube@nanosheet architecture, XRD and Raman verified phase composition, and XPS analyzed valence states; the morphology provided abundant active sites and fast ion/electron pathways. This architecture is particularly suitable for ZIB cathodes due to its enhanced conductivity and electrochemical kinetics. The LDH-based composite was synthesized by first hydrothermally growing Ni_3S_2/NiS hetero-nanowire arrays on nickel foam, followed by electrodeposition of NiCo-LDH nanosheets to form a hierarchical core/shell structure [209]. This two-step process enables intimate interfacial contact between the conductive sulfide core and the active LDH shell. The resulting composite exhibited a 3D nanoarray morphology and chemical states characterized by XPS. The uniform architecture and rich surface functionalities render this LDH ideal for rapid ion/electron transport and structural stability, making it highly suitable for ZIB applications.

NiFe LDH was synthesized via a multi-step electrochemical approach where $Cu(OH)_2$ nanowires were first electroplated onto Cu foam, converted to CuO by annealing, reduced to Cu nanowires, and, finally, used as a scaffold for the electrochemical deposition of NiFe LDH nanosheets [210]. This process formed a 3D hierarchical core/shell structure of Cu@Cu NWs@LDH. The morphology presents uniform vertical nanosheet growth; XRD verified the crystalline structure, and XPS confirmed the elemental composition and valence states. The high surface area, strong bonding, and excellent electron conductivity make this LDH suitable for ZAB applications. CuCo LDH was synthesized by potentiostatic electrodeposition on nickel foam, followed by CV-based electrodeposition of Ni_3S_2 to form the CuCo LDH@Ni_3S_2 composite [211]. The resulting composite featured a tremella-like interconnected nanosheet morphology, exhibited a layered LDH structure confirmed by XRD, weak crystallinity with abundant active sites, and had a high electrochemical double-layer capacitance (Cdl = 2.74 mF/cm^2), indicating excellent charge storage potential. This unique architecture provided enhanced conductivity, lower diffusion resistance, and increased redox sites, making it highly suitable for high-performance supercapacitor applications.

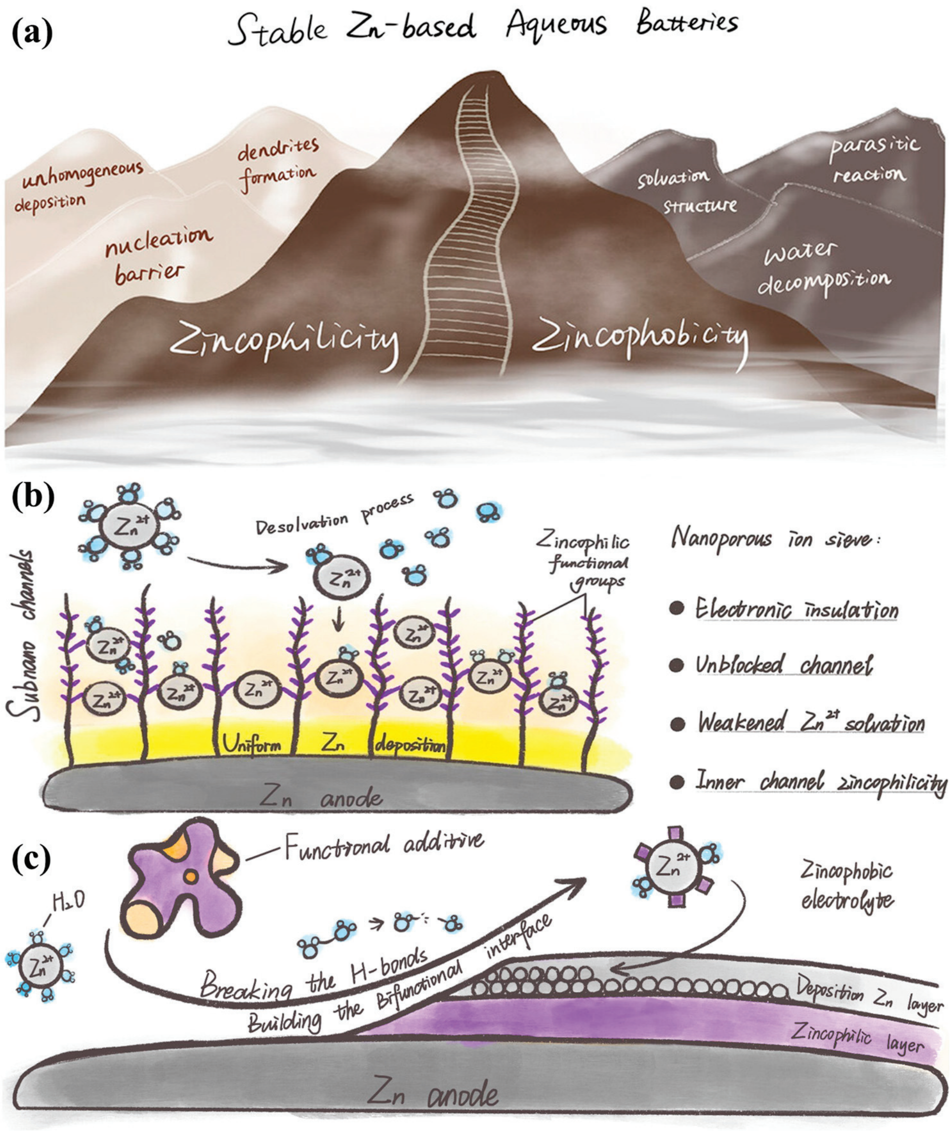

Figure 10. (**a**) Schematic illustration of the trade-off between zincophilicity and zincophobicity in achieving stable Zn-based aqueous batteries. (**b**) Design of a nanoporous ion sieve with zincophilic functional groups to enable uniform Zn deposition through controlled Zn^{2+} desolvation and selective ion transport. (**c**) Formation of a bifunctional interface using functional additives to simultaneously break water hydrogen bonds and construct zincophilic/zincophobic regions on the Zn anode. Reproduced with permission [206].

NiCo-LDH was synthesized via a simple electrochemical deposition process onto CC, followed by CV activation at various scan rates to induce hydrogen vacancies [212]. The as-prepared LDH retained its nanosheet morphology with a polycrystalline layered structure, showed reduced interlayer spacing (from 0.71 to 0.60 nm), preserved elemental homogeneity (Ni, Co, O), and exhibited enhanced M–O bonding indicative of H vacancy formation. These structural features, particularly the vacancy-rich domains, significantly improved the redox kinetics and ion diffusion, making this LDH highly suitable for supercapacitor applications. Khalafallah et al. [213] presented a low-cost, binder-free Zn-doped cobalt/lanthanum LDH (Zn/CoLa LDH) nanoarray-on-nanoarray electrode fabricated via a two-step electrodeposition method (Figure 11a), demonstrating superior electrochemical performance and durability for high-energy, high-power supercapacitor applications. NiAl-LDH was synthesized by a single-step electrochemical deposition on AC cloth using a chronoamperometry method at −1.0 V for 15 min [214]. Figure 11b depicts the stepwise electrochemical strategy to grow NiAl-LDH nanosheets on a CC substrate. The resulting NiAl-LDH@CC composite exhibited a porous, vertically aligned nanosheet array structure with a high BET surface area of 437.5 m^2/g, crystalline hydrotalcite-like layered structure, well-distributed elements (Ni, Al, O), and uniform coating thickness of ~1.11 μm. This combination of high surface area, structural integrity, and improved electron/ion transport characteristics renders the LDH highly suitable for supercapacitor applications. LDH was synthesized via in situ electrochemical deposition of nickel and cobalt nitrates onto carbon felt at -1 V for 10 min using a chronoamperometry technique [215]. The prepared NiCo-LDH formed a coral reef-inspired ultrathin mesoporous nanosheet architecture vertically aligned on the carbon felt, displaying a high BET surface area of 14.56 m^2/g and a narrow average pore diameter of 5.52 nm, with enhanced structural features confirmed by SEM, FTIR, and XRD analyses. This morphology, porosity, and strong electronic interaction between Ni and Co make the LDH ideal for efficient ion diffusion and redox kinetics, which is suitable for high-performance supercapacitor applications.

3.4. Other Advanced Synthesis Techniques (e.g., Sol-Gel, Ultrasonication, Exfoliation)

Various other methods have been reported for synthesizing LDHs, which are anionic materials characterized by a unique layered structure of hydroxides intercalated with anions. Among these methods, sol-gel synthesis, ultrasonication, and exfoliation stand out due to their distinct advantages in producing LDHs with controlled morphology and composition. The sol-gel method is a widely employed technique for synthesizing LDHs because of its ability to control the chemical composition, morphology, and crystallinity of the resultant materials. This method involves the hydrolysis and polycondensation of metal alkoxides or salts, forming a gel that can then be converted into an oxide or hydroxide material upon thermal treatment. For instance, Klydziute et al. [216] highlighted the capacity of the sol-gel approach to yield MgAl-LDHs with tunable properties, emphasizing its versatility across different metal compositions and operating conditions. Additionally, Valente et al. [217] reported that the sol-gel method allows for precise control over parameters such as pH and temperature during synthesis, which facilitates particle size and distribution adjustments, making it suitable for various applications in catalysis and environmental remediation. Ultrasonication is another promising synthesis technique that has gained popularity for preparing LDHs due to its ability to enhance reaction rates and promote homogeneous nucleation. This method employs high-frequency sound waves to create cavitation bubbles, which, upon collapsing, generate localized high temperatures and pressures conducive to the chemical reactions needed to form LDHs. Mallakpour et al. [218] demonstrated that using ultrasonic waves shortened reaction times and improved the characteristics of the synthesized LDHs. Further, Sokol et al. [219] showcased that ultrasonication could accelerate the formation of Mg–Al–phosphate LDHs, signifying the method's effectiveness in synthesizing complex layered structures. Exfoliation refers to methods to produce nanosheets or dispersed layers from bulk LDH materials, enhancing their surface area and accessibility for various applications. This technique often involves delining layered structures in suitable solvents or via chemical treatments. According to Ibrahimova [92], several methods, including exfoliation, can alter the interlayer spacing of LDHs, facilitating the intercalation of functional anions. Additionally, Butenko et al. [220] provided evidence for the potential of exfoliated LDHs as effective adsorbents for environmental contaminants like phenols, thereby highlighting the practical implications of such synthesized materials. Specific examples of LDH synthesis using these advanced techniques are abundant in the literature. For instance, research by Mahjoubi et al. [221] employed sol-gel synthesis to produce ZnAl-LDHs intercalated with various anionic species, affirming the method's capability in tailoring materials for specific functionalities such as dye removal. In the context of ultrasonication, the study by Mallakpour [218] emphasized the synthesis of bioactive intercalated LDHs with accelerated reaction rates and enhanced functional properties, which can significantly improve material performance in biomedical applications. Furthermore, the application of exfoliation in generating high-surface-area LDHs has been validated in environmental science, where these materials demonstrated promising performances in adsorbing toxic pollutants [220]. Sol-gel synthesis, ultrasonication, and exfoliation represent significant advancements in producing LDHs, allowing for tailored properties and functionalities. Each method contributes unique benefits that enhance the applicability of LDHs in diverse fields such as catalysis, environmental remediation, and materials science, leading to growing interest and research in this area.

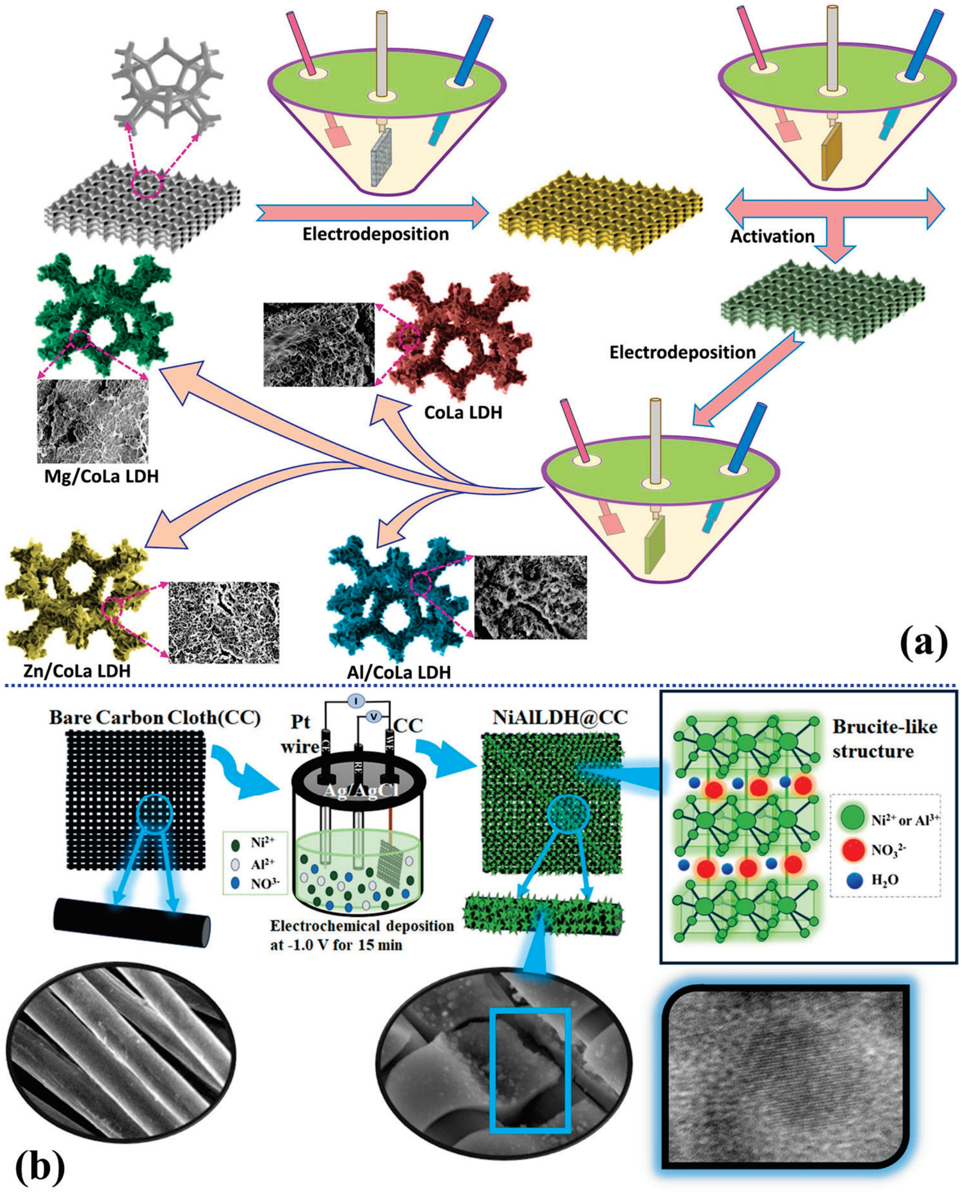

Figure 11. (**a**) Schematic illustration of the electrodeposition-based synthesis of binder-free CoLa LDH nanoarray-on-nanoarray networks doped with Zn^{2+}, Mg^{2+}, and Al^{3+} ions. Reproduced with permission [213]. (**b**) Illustration of the electrochemical synthesis procedure for fabricating NiAl-LDH nanosheets directly on CC (NiAl-LDH@CC). Reproduced with permission [214].

The nickel microwire aerogel (NMWAs) was synthesized via a sol-gel method under a magnetic field, followed by vacuum drying to obtain a porous and flexible aerogel structure [222]. Subsequently, ultrathin NiCo-LDH nanosheets were grown in situ on the NMWAs surface via a solvothermal route, resulting in a core/shell NMWAs@NiCo-LDH architecture. The sulfur was then infused into the composite to form NMWAs@NiCo-LDH/S via a melt/diffusion method. Characterization revealed a 3D porous network of aligned nickel microwires coated with ultrathin LDH nanosheets (~6.8 nm thick). BET analysis showed mesopores (4–10 nm) and high surface area, while XRD, Raman, and XPS confirmed the phase purity and the presence of active functional groups like hydroxyls. This core/shell structure with high porosity, hydrophilicity, and strong chemical affinity for polysulfides makes it highly suitable for LSB applications by enhancing electrolyte access, trapping LiPSs, and promoting redox kinetics.

NiCo-LDHs were synthesized via a self-growth aging method in the presence of Ti_3C_2-MXene [156]. Initially, few-layered MXene nanosheets were prepared through LiF/HCl etching of Ti_3AlC_2, followed by ultrasonic exfoliation. These MXene sheets then served as substrates for the in situ growth of NiCo-LDHs through the reaction of Ni^{2+} and Co^{2+} with $NH_3 \cdot H_2O$ under an inert atmosphere, resulting in Vo-LDHs-MXenes with abundant oxygen vacancies. Morphologically, TEM and FESEM revealed a homogeneous 2D nanosheet structure, while BET analysis showed a high surface area (35.22 m^2/g) with mesoporosity, ideal for electrolyte access and sulfur redox reaction sites. XRD, XPS, and EPR further confirmed structural integration, oxygen vacancies, and electronic synergy between LDHs and MXenes. These features collectively enhance the immobilization of polysulfides and facilitate faster redox kinetics, making Vo-LDHs-MXenes highly suitable for LSB applications.

The NiCo-LDH was first synthesized by refluxing a mixed aqueous solution of $Ni(NO_3)_2 \cdot 6H_2O$, $Co(NO_3)_2 \cdot 6H_2O$, hexamethylenetetramine, and oxalic acid at 100 °C for 6 h [223]. This precursor was then converted into NiCo–MOF/LDH nanorods through a solvothermal reaction with 2,5-dihydroxyterephthalic acid (DHTA) in a DMF/ethanol/water mixture at 140 °C for 24 h. The synthesized NiCo–MOF/LDH nanorods exhibit a rod-like morphology with homogeneous elemental distribution, a high surface area (512.3 m^2/g), meso/microporosity, and coexisting crystalline (NiCo–MOF) and amorphous (NiCo–LDH) phases. These features make the material ideal for LSB applications by combining strong polysulfide adsorption and electrocatalytic conversion properties.

NiCo-LDH was synthesized by etching ZIF-67 nanocrystals using $Ni(NO_3)_2 \cdot 6H_2O$ in ethanol at elevated temperature, which led to the formation of hollow NiCo-LDH nanostructures [224]. Sulfur was subsequently incorporated into the LDH via a melt/diffusion process. The composite exhibited a hollow polyhedral morphology, confirmed by SEM/TEM, with a high BET surface area of 76.089 m^2/g, mesoporosity (2–8 nm), and phase purity validated by XRD and XPS. This structural design, featuring abundant active sites and high sulfur content (~71.9%), is highly beneficial for Li–S batteries due to enhanced polysulfide confinement and catalytic redox behavior.

Ni-Co LDH was synthesized by ion-exchanging Co from ZIF-67 nanocubes with Ni^{2+} ions in ethanol, forming ZIF-67@LDH nanoboxes [225]. These were subsequently carbonized and sulfided at 400 °C to form $NiCo_2S_4$-NiS_2 nano-heterostructures embedded in hollow carbon boxes. Characterization using SEM, TEM, and XRD confirmed well-maintained nanobox morphology, distinct lattice spacings for $NiCo_2S_4$ and NiS_2, and uniform elemental distribution; BET analysis showed a high surface area of 111.5 m^2/g. The resulting LDH-derived nano-heterostructure offers abundant catalytic sites and strong lithium polysulfide (LiPS) adsorption capabilities, making it ideal for LSB applications. The CuCo-LDH was synthesized via a chemical etching strategy, where ZIF-67 (a cobalt-based MOF) acted as a sacrificial template and was treated with $Cu(NO_3)_2 \cdot 3H_2O$ in ethanol to form a hollow and hierarchical structure composed of vertically aligned LDH nanosheets [226]. Figure 12 shows the synthesis process and morphological evolution of CuCo-LDH materials used in lithium–sulfur batteries. The structure is derived from ZIF-67 by introducing copper nitrate, forming a CuCo-LDH composite that enhances sulfur redox kinetics and polysulfide adsorption. FESEM images in Figure 12A–G reveal how particle morphology changes with different Co/Cu ratios. As the Co content decreases, the structure becomes less defined and more fragmented, indicating that the metal ratio significantly influences the material's architecture, which, in turn, may affect its electrochemical performance. The optimal Co/Cu ratio (0.7) facilitated complete etching and formation of well-defined CuCo-LDH polyhedrons. Characterization results revealed that the synthesized LDH has a hollow dodecahedral morphology, layered nanosheet microstructure, mesoporous texture (BET surface area: 104.1 m^2/g), and a mixed Cu^{2+}/Co^{3+} oxidation state. CuCo-LDH is highly suitable for LSBs due to its strong polysulfide anchoring capability and catalytic activity.

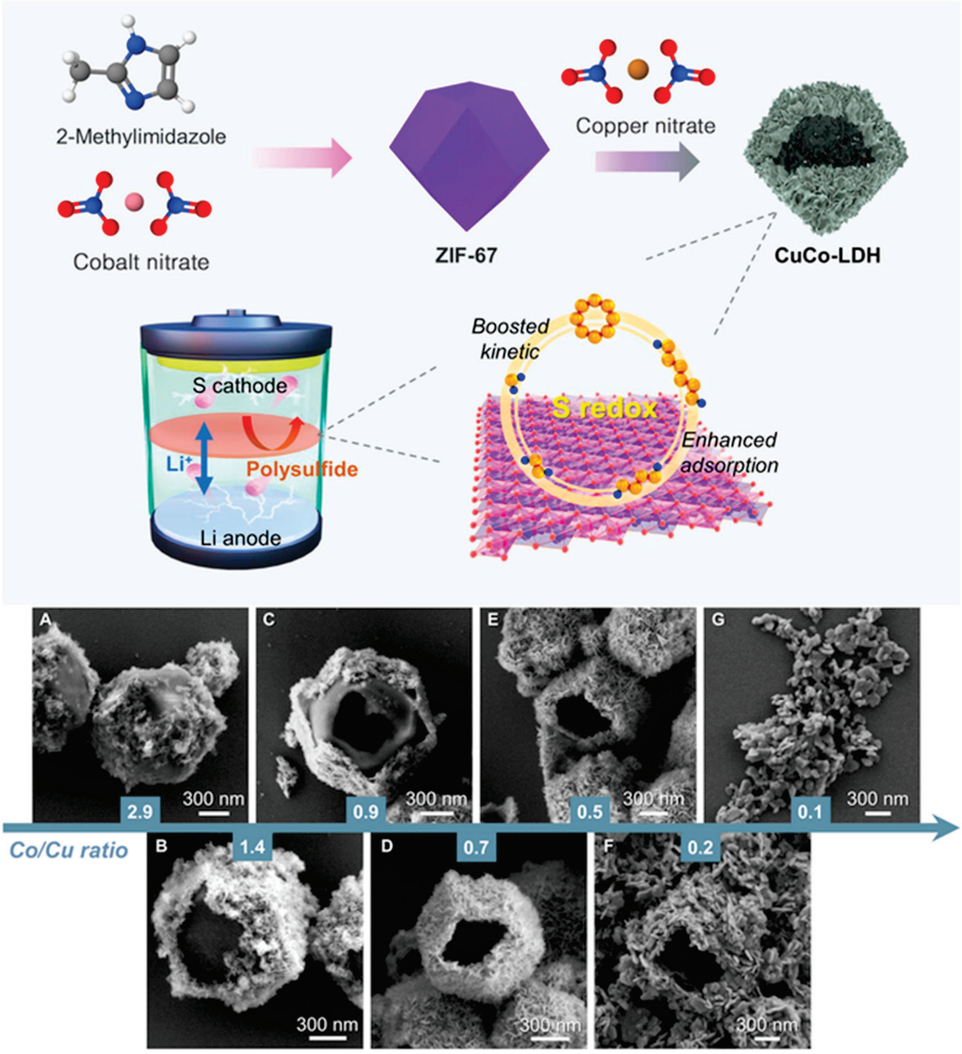

Figure 12. Schematic representation of the synthesis route for CuCo-LDH derived from ZIF-67 and its role in LSBs, highlighting its ability to accelerate redox reactions and trap polysulfides. FESEM images show the morphology of CuCo-LDH synthesized at various Co/Cu molar ratios: (**A**) 2.9, (**B**) 1.4, (**C**) 0.9, (**D**) 0.7, (**E**) 0.5, (**F**) 0.2, and (**G**) 0.1. Reproduced with permission [226].

The synthesis of PPy@LDH-S involved a multi-step process beginning with the formation of ZIF-67 nanocrystals, which were then transformed into hollow NiCo-LDH through a nickel ion exchange process [227]. Subsequently, sulfur was infiltrated via the solid-state melting method, and finally, a thin polypyrrole (PPy) film was polymerized onto the LDH-S composite. BET analysis showed a progressive reduction in surface area from 135.4 m^2/g (LDH) to 3.3 m^2/g (PPy@LDH-S) due to sulfur loading. The structural and chemical features—such as strong polysulfide adsorption, mesoporosity, and catalytic activity—make PPy@LDH-S a highly effective sulfur host for LSBs. The $NixCa_{2-x}Al$-Cl LDH and $CoyCa_{2-\gamma}Al$-Cl LDH were synthesized through a simple one-step ion exchange method, using Ca_2Al-Cl LDH derived from chlorine-containing wastewater as a precursor [228]. Ni^{2+} and Co^{2+} ions replaced Ca^{2+} ions under ambient conditions with stirring and sonication, followed by filtration and drying. The resulting LDHs exhibited a thin, porous, tunnel-like morphology with abundant surface folds; XRD confirmed the layered structure, BET indicated high surface area (∼4× compared to the precursor), and XPS verified successful Ni^{2+}/Co^{2+} substitution. Due to improved conductivity, active sites, and ion diffusion kinetics, this structural and electronic modification makes the LDHs highly suitable as anode materials for NIBs. CoSn-LDH@MXene nanocomposites were synthesized via a one-step solvothermal process where $Co(NO_3)_2{\cdot}6H_2O$ and $SnCl_2{\cdot}2H_2O$ were reacted in a mixture of isopropanol and glycerol at 180 °C, followed by ultrasonic treatment with few-layer Ti_3C_2 MXene in ethanol [229]. The CoSn-LDH microspheres self-assembled and anchored onto the MXene nanosheets through hydrogen bonding and electrostatic interactions, forming a uniform hybrid structure. BET analysis showed a high surface area (44.15 m^2/g) and mesoporous structure, and XPS confirmed successful chemical integration. This architecture facilitates electron/ion transport and suppresses agglomeration, making it well-suited for Na-ion battery applications. Ni_3Ti-CO_3 LDH was synthesized via a urea precipitation method, whereas Ni_3Cr-CO_3 LDH was prepared using a conventional hydrothermal method [230]. Both were further converted into Cl^--intercalated LDHs through an anion exchange process using HCl/NaCl solution. The developed LDHs exhibit high Cl^- insertion capacity and structural integrity, making them well-suited for CIB applications.

The CoMn-LDH/NPGA was synthesized via a combined cross-linking gelation, hydrothermal self-assembly, and freeze-drying process [231]. Vertically grown CoMn-LDH nanosheets were anchored onto a 3D hierarchical porous N,P co-doped graphene aerogel framework (NPGA). Characterizations revealed a lamellar morphology, well-defined crystalline structure, mesoporous nature with a BET surface area of 105.8 m^2/g, and a high degree of N,P doping. This configuration provides high surface area, exposed active sites, and effective charge/mass transport, making it well-suited for ZAB applications. CoNi LDH nanoflowers (NFs) and nanosheets (NSs) were synthesized via a simple solvothermal method using a mixed solvent of deionized water and ethylene glycol in varying ratios [232]. The nanoflowers exhibited a hierarchical flower-like morphology with high crystallinity, a mesoporous structure, and a large BET surface area of 101.28 m^2/g (vs. 38.54 m^2/g for NSs), with XRD confirming α-phase $Co(OH)_2$ and $Ni(OH)_2$, and XPS revealing mixed oxidation states of Co^{2+}/Co^{3+} and Ni^{2+}. These structural and surface characteristics endow the CoNi LDH, especially the NFs, with abundant active sites, good charge transport properties, and superior suitability for high-performance supercapacitor applications. NiCo-MOF@LDH hybrid nanosheets were synthesized via a one-step solvothermal method using 1,4-terephthalic acid and urea [233]. The resulting material displayed ultrathin, interconnected nanosheet morphology with high porosity, alongside the presence of Ni, Co, O, and C through EDS and XPS; the XRD patterns confirmed a hybrid structure of NiCo-MOF and LDH, and the sample exhibited high surface area and abundant active sites. These structural features enhance ion diffusion and electron transfer, making the material highly suitable for supercapacitor applications.

NiCo-LDH nanosheets were synthesized by transforming Co-based MOFs on AC cloth (ACC) using a simple room-temperature ion exchange method in a mixed water and ethylene glycol solution [234]. The resulting material exhibited vertically aligned ultrathin amorphous nanosheets interconnected in a 3D mesoporous network, with a surface area of 25.8 m^2/g and a pore diameter of 3.9 nm. This unique structure and amorphous nature facilitate high electrochemical activity and ion transport, making it highly suitable for high-performance supercapacitor applications. Co-Ni LDH was synthesized through a facile cation exchange reaction between $Mg(OH)_2$ and Co^{2+}/Ni^{2+} ions, followed by a controlled anion exchange sulfurization using Na_2S [235]. The resulting CoNi LDH displayed a nanosheet morphology, layered crystal structure, and a BET surface area of 58 m^2/g, progressively decreasing with sulfurization. These structural and chemical features, coupled with improved conductivity due to sulfur incorporation, make the material well-suited for high-performance supercapacitor applications. $NiCo_2S_4$@CoAl-LDH (NCS@CA) heterojunction nanosheets were synthesized on nickel foam using a two-step solvothermal process [236]. The resulting material exhibited a unique flower-like core/shell nanosheet morphology with high crystallinity and a well-defined layered structure; it also showed enhanced light absorption (bandgap ~2.23 eV) and high redox-active surface area ideal for electrochemical applications. This rationally designed nanostructure facilitates fast ion diffusion and superior redox activity, making it highly suitable for supercapacitor applications. The NiCo-LDH was synthesized via a one-step microwave hydrothermal co-assembly method using tannin-derived carbon microspheres as a substrate [237]. The resulting LDH exhibited a well-defined sea urchin-like morphology with a core/shell nanostructure composed of uniformly distributed NiCo-LDH nanoneedles anchored on smooth carbon microspheres, possessing mesoporous features and a BET surface area of 56 m^2/g. This structured design provides a high active surface area and improved charge transport, making it highly suitable for supercapacitor applications.

3.5. Impact of Synthesis Methods on LDH Properties

The synthesis methods employed significantly influence the structural, morphological, and functional characteristics of LDHs, directly impacting their performance in batteries, supercapacitors, and hydrogen production applications. Co-precipitation, a widely adopted synthesis method, excels due to its simplicity, scalability, and cost-efficiency. It typically results in LDHs with uniform morphology, high purity, and controllable interlayer spacing. These attributes are particularly beneficial in battery applications, where homogeneity and controlled particle size ensure efficient ion diffusion and high electrochemical stability. Recent advancements, such as incorporating surfactants, polymers, and organic anions during co-precipitation, have enabled further refinement of LDHs, enhancing their corrosion protection capabilities in reinforced concrete, boosting electrochemical activity, and improving stability in NIB and LIB systems. Furthermore, co-precipitated LDHs demonstrate remarkable adsorption characteristics, making them suitable for environmental remediation, a critical supplementary property in battery and supercapacitor electrodes where impurity management is crucial.

Hydrothermal synthesis, characterized by elevated temperatures and pressures, provides precise control over the crystallinity, particle size, and hierarchical architectures of LDHs, yielding materials with enhanced thermal stability and defect-free structures. This technique is particularly advantageous in synthesizing high-entropy LDHs and multimetallic systems, where synergistic interactions among multiple cationic species significantly improve electrocatalytic performance. Hydrothermally synthesized LDHs display superior catalytic activities for hydrogen production applications due to their high surface area, controlled porosity, and finely tuned morphology, collectively facilitating efficient HER. Hybridization approaches combining LDHs with MOFs or carbonaceous substrates via hydrothermal methods further enhance their suitability for energy storage and catalytic processes by improving conductivity, structural integrity, and electrolyte accessibility.

Electrochemical deposition offers direct, binder-free growth of LDH films onto conductive substrates, thereby improving electron transport, adherence, and structural stability crucial for high-performance supercapacitors and catalytic electrodes. The tunability of electrochemical parameters enables precise control over film thickness, crystallinity, and porosity, directly correlating with enhanced electrochemical and catalytic performance. Techniques such as pulsed electrodeposition provide superior morphological control, reducing defects and optimizing the exposure of catalytic active sites, which is significantly beneficial for hydrogen production and supercapacitor applications.

Advanced synthesis methods such as sol-gel, ultrasonication, and exfoliation further expand the potential of LDHs. Sol-gel synthesis enables highly homogeneous and porous structures with tailored compositions, significantly enhancing electrode performance in supercapacitors and batteries due to improved ion transport pathways and increased active sites. Ultrasonication accelerates LDH formation, yielding finer particle sizes and improved dispersion, which critically benefits applications requiring rapid charge/discharge capabilities and high surface reactivity. Exfoliation methods generate ultrathin LDH nanosheets with exceptional surface area, which is crucial for enhancing catalytic activities in hydrogen production by maximizing exposed active sites and facilitating efficient electron transfer. Collectively, the meticulous selection and optimization of LDH synthesis methodologies are essential for tailoring materials with targeted functional properties, ensuring optimal performance across energy storage and catalytic applications.

LDHs are a class of materials characterized by a unique double-layered structure formed by two distinct metallic cations and an interlayer of anions, typically hydroxides or organic moieties. They exhibit properties that make them suitable for energy storage and hydrogen production applications. This response categorizes LDHs based on structural composition, defect engineering, and their composites, examining their properties relevant to energy applications. LDHs can be broadly classified based on their cationic composition. Common cations include transition metals such as nickel, cobalt, magnesium, aluminum, and iron, which can form various configurations [44,238]. Synthesis methods, such as hydrothermal and co-precipitation techniques, can induce defects like vacancies and irregular stacking, significantly influencing their electrochemical properties [239,240]. For instance, NiFe-LDHs exhibit enhanced OER activity when defects are strategically engineered, allowing for improved electronic conductivity and catalytic performance [241,242]. Structural modifications enable tailoring LDHs for specific application requirements. For example, engineering heterostructures, combining LDHs with other materials (such as carbon or metal oxides), can enhance catalytic activity and stability for water-splitting applications [242,243]. Using pulsed laser ablation or ion intercalation can produce nanosheets that provide a larger surface area for ion exchange, which is crucial for efficient energy storage systems like supercapacitors [244,245].

LDHs can also be integrated into composite matrices, enhancing their performance in energy applications. For instance, composites of LDHs with conductive polymers or carbonaceous materials show improved capacitance and energy density relative to their standalone counterparts [243,246]. The synergistic effects observed in such composites lead to enhanced electrochemical performance, making them suitable candidates for hybrid supercapacitors and batteries [247].

LDHs stand out due to their impressive electrochemical properties relevant to energy storage and hydrogen production. LDHs demonstrate significant catalytic activity toward the OER and HER due to their tunable electronic structures and high specific surface areas [248–250]. The presence of transition metals in their structure allows them to participate actively in redox reactions, enhancing their functionality as electrocatalysts [241,251]. The layered structure of LDHs contributes to their stability under operational conditions. They can maintain structural integrity during cycling in energy devices, making them reliable choices for applications in supercapacitors and batteries [240,252]. Furthermore, proper intercalation and defect engineering can improve their ionic conductivity and structural resilience, leading to a prolonged lifespan and consistent performance [251,253]. The unique interlayer space in LDHs permits the exchange of various anions to enhance energy storage capabilities. For instance, LDHs can be intercalated with anions suited for specific electrochemical applications, improving overall electrochemical properties [40,254]. The classification of LDHs into structural categories, the strategic use of defects and engineering approaches, and the development of composite materials are pivotal in leveraging their properties for enhanced energy storage and hydrogen production. Ongoing research continues to explore this fascinating class of materials, further unlocking their potential across various applications.

Among various synthesis strategies for LDHs, hydrothermal synthesis has emerged as the most widely employed method, particularly for energy-related applications. The hydrothermal route allows for precise control over crystallinity, morphology, and composition, enabling the fabrication of highly ordered LDH nanostructures with tailored porosity and surface area, properties that are critical for high-performance battery electrodes, supercapacitors, and electrocatalysts for water splitting and CO_2 reduction. Co-precipitation methods remain popular for producing LDHs at large scales, especially for supercapacitor electrodes and lithium-ion batteries, due to their simplicity and compositional flexibility. Electrodeposition techniques are increasingly favored for directly growing LDH thin films on conductive substrates, particularly in water-splitting electrocatalysis and flexible energy devices, where strong substrate adhesion and tunable thickness are desirable. Emerging methods such as spray pyrolysis, microemulsion synthesis, and mechanochemical activation are being explored for large-scale production of LDH-derived oxides for HER and carbon dioxide reduction reactions (CO_2RR). Ultimately, the choice of synthesis method critically influences the structural features, ion transport properties, and overall electrochemical performance of LDHs, thereby determining their suitability for specific energy storage and conversion applications. Figure 13 highlights the key advantages of various synthesis methods for LDHs, emphasizing how each technique offers unique benefits such as compositional flexibility, controlled morphology, high purity, and structural tailoring.

Figure 13. Schematic illustration of the advantages associated with different synthesis methods for LDHs.

4. LDHs in Batteries

LDHs have garnered significant interest in recent years due to their unique structural properties and wide-ranging applications, particularly in batteries. Composed of positively charged metal hydroxide layers interleaved with charge-compensating anions, LDHs can host a variety of cations and anions, which endow them with tunable electrochemical properties essential for battery technologies. Optimizing LDH materials for battery applications involves enhancing their structural integrity, electrochemical performance, and conductivity. Several strategies have emerged in recent studies. Incorporating high-valence metal ions, such as molybdenum, into LDH structures can stimulate lattice oxygen and improve stability and performance in applications such as CIBs [144]. Adjusting the metal/ion ratio within LDHs can optimize charge storage capabilities and reduce phase instability, enhancing electrochemical properties [255]. Research has also shown that hybridizing LDHs with conductive materials, such as graphene or carbon nanotubes, further enhances electrical conductivity and facilitates electron transport, providing superior performance in high-capacity batteries [256]. Furthermore, computational models for high-throughput screening of LDHs enable the identification of optimal stoichiometric ratios and structures, streamlining the development process [230]. Collectively, these strategies represent a multifaceted approach to optimizing LDH materials for next-generation battery technologies.

4.1. Lithium-Ion Batteries

In LIBs, LDHs exhibit promising behavior as cathode materials. For instance, nickel–cobalt LDHs have been shown to provide higher capacity and stability than conventional materials. Research by Bai et al. [257] highlights that these LDHs achieve about 160 mAh/g capacities at high current densities, showcasing excellent rate capability and cycling stability, which are crucial for practical applications. Furthermore, the study emphasizes how the layered structure and the ability to intercalate lithium ions enhance ionic conductivity and electron transport, improving overall battery performance. ZIF-67@NiCo-LDH was utilized as an anode material in LIBs, displaying high electrochemical performance [134]. Initially, the composite delivered a high discharge capacity of 1997.1 mAh/g at 100 mA/g and maintained a stable reversible capacity of 807.9 mAh/g after 100 cycles. It demonstrated excellent rate capability, achieving capacities of approximately 1303.9, 931.5, 601.3, and 445.0 mAh/g at current densities of 100, 200, 500, and 1000 mA/g, respectively. The excellent cyclic stability, high specific capacity, and superior rate performance were attributed to the synergistic effect between ZIF-67 MOF and NiCo-LDH nanosheets and the unique heterostructure morphology's enhanced conductivity and structural integrity. $NiFe_2O_4$@NiCo-LDH was utilized as an anode in LIBs [135], exhibiting superior electrochemical performance characterized by a high specific capacity of 636.9 mAh/g after 100 cycles at 0.3 A/g, along with high coulombic efficiency (~98%). The composite anode demonstrated good rate performance, maintaining stable capacities at various current densities and temperatures (−10 °C, 25 °C, 50 °C), thus confirming its robustness. Electrochemical impedance and galvanostatic intermittent titration techniques indicated that the $NiFe_2O_4$@NiCo-LDH possessed significantly lower internal resistance and higher conductivity, resulting in efficient ion/electron transfer and improved cyclic stability compared to pristine $NiFe_2O_4$. The synthesized NiZn-LDH, intercalated with DS− anions, was employed as an anode material for LIBs [136]. Specifically, the optimized LDH (NZDS-20) demonstrated superior electrochemical performance, delivering a high specific capacity of 850 mAh/g at a current density of 0.5 A/g, which remained stable after 400 cycles. Furthermore, the material showed excellent rate capability, maintaining a capacity of approximately 473.5 mAh/g at a higher current density of 3 A/g. EIS and galvanostatic intermittent titration technique (GITT) measurements further confirmed improved lithium-ion diffusivity and reduced reaction resistance, highlighting the beneficial effects of DS− intercalation. Moreover, a significant pseudocapacitance contribution was observed, underscoring rapid reaction kinetics and enhanced electrochemical stability. The hollow yolk/shell NiS_2/FeS_2@NC@NiFe LDH/FeO(OH) microspheres were utilized as an anode in LIBs, demonstrating excellent electrochemical performance [137]. At 0.2 A/g, the LDH electrode delivered a specific 709.9 mAh/g capacity after 200 cycles, highlighting robust cycling stability. Furthermore, at a higher current density (1.0 A/g), it maintained a capacity of 403.3 mAh/g even after 500 cycles, showcasing superior cyclic and rate stability compared to individual NiS_2/FeS_2 or NiFe LDH/FeO(OH) electrodes. The improved performance is attributed to the hollow yolk/shell structure, N-doped carbon layer, and enhanced conductivity and stability. The NiCo-LDH/MXene composite was used as an anode material for LIBs, showing excellent electrochemical performance [138]. It achieved a high specific capacity of 1081 mAh/g after 100 cycles at 100 mA/g and demonstrated outstanding rate capability, retaining 439 mAh/g even at a high current density of 1000 mA/g. Additionally, the material exhibited superior cycling stability, with minimal capacity fading, demonstrating the effectiveness of the 1D/2D structure in enhancing battery performance. Mg_2Al_1–CO_3-LDH was utilized as an anode in LIBs [140], exhibiting an impressive initial discharge-specific capacity of 814 mAh/g at a current density of 200 mA/g. Despite initial capacity fading, the material recovered significantly, stabilizing at 203.8 mAh/g after 300 cycles. Additionally, it demonstrated reasonable rate capabilities (up to 61.3 mAh/g at 2000 mA/g), attributing electrochemical performance primarily to reversible Li^+ storage through valence change of Mg and conversion reactions involving LiOH and LiH/Li_2O.

An LDH material (LDH200) was employed as an anode material for LIBs, demonstrating exceptional electrochemical properties [109]. Specifically, the LDH anode delivered a high specific capacity of 1821.3 mAh/g at a current density of 0.1 A/g. Impressively, the material maintained a robust cyclic stability, retaining a reversible capacity of about 687.7 mAh/g after 500 cycles at 0.5 A/g, corresponding to a very low capacity attrition rate of 0.092%. Figure 14A shows the CV curves of LDH200, where the redox peaks remain stable after the first few cycles, indicating good electrochemical reversibility. In Figure 14B, the charge/discharge profiles of LDH200 over various cycles at 0.5 A/g show consistent voltage plateaus, demonstrating stable cycling behavior. Figure 14C compares the long-term cycling performance of LDH200 with other samples. LDH200 shows the highest capacity retention and coulombic efficiency over 500 cycles. Figure 14D presents rate performance data, where LDH200 retains superior capacity across different current densities compared to the other LDH samples. Figure 14E provides a radar plot comparing all electrode types across six performance parameters. LDH200 shows balanced and enhanced electrochemical behavior, confirming it as the most promising candidate among the studied materials. Additionally, this material exhibited a significantly improved lithium-ion diffusion coefficient of approximately 4.08×10^{-11} cm^2/s, indicative of its excellent rate capability and suitability for practical high-performance battery applications.

The synthesized Ni_2Co-LDH/EG composite served as an anode material for LIBs [152], demonstrating superior electrochemical performance compared to pristine Ni_2Co-LDH. It exhibited a high specific capacity of 1880 mAh/g at 0.05 A/g and maintained an excellent specific capacity of 919 mAh/g at a high current density of 1 A/g. Additionally, it showed remarkable cyclic stability with minimal capacity fading, retaining a specific capacity of approximately 973 mAh/g after 100 cycles at 1 A/g. The integration of expanded graphite significantly enhanced electronic conductivity and effectively suppressed volume expansion during the lithiation/delithiation process, supported by reduced charge transfer resistance measured through EIS. NiAl-LDH was used as a negative electrode (anode) material for LIBs and tested with two types of binders: sodium alginate (SA) and PVDF [153]. The SA-based electrode exhibited a remarkable initial discharge capacity of 2586 mAh/g at 0.05 A/g with a reversible 1578 mAh/g capacity. After 400 cycles at 0.5 A/g, the capacity retained was 697 mAh/g (42.2%), and at 1.0 A/g, it remained 388 mAh/g after 1400 cycles (27.6% retention). In contrast, the PVDF-based electrode showed significantly lower retention, indicating the superior performance of the SA binder. The conversion-type mechanism involving Ni^{2+} to Ni^0 and forming a stable SEI layer (rich in Li_2O and LiOH) contributed to the enhanced cycling stability and rate capability.

4.2. Lithium–Sulfur Batteries

In LSBs, utilizing LDHs helps mitigate the polysulfide dissolution issue, which is crucial for improving cycling stability [258]. Bai et al. [257] demonstrated that a NiCo-LDH-based cathode effectively retains capacity over 500 cycles, outperforming conventional sulfur cathodes. The LDH structure helps configure polysulfide species, thus facilitating a more stable electrochemical reaction environment during charge/discharge cycles, addressing a significant challenge in LSBs [202]. LDH@PSS was applied as an artificial solid electrolyte interphase (ASEI) on lithium metal anodes in LSBs [155]. The composite SEI was fabricated via spin-coating, providing mechanical robustness and ionic selectivity. Li||Li symmetric cells with LDH@PSS-Li electrodes demonstrated an ultra-long cycle life of over 3100 h at 1 mA/cm^2 with significantly reduced overpotential. When paired with sulfur cathodes, the full Li–S cells showed excellent performance: an initial specific capacity of 1247.2 mAh/g and a reversible capacity of 1032.6 mAh/g after 200 cycles at 0.2 C, with a minimal capacity decay of 0.086% per cycle. At higher rates (1 C), the cell retained 65.2% of its capacity after 1000 cycles. Additionally, the system exhibited suppressed shuttle currents, lower self-discharge, enhanced Li^+ transference numbers ($tLi^+ = 0.81$), and improved charge transfer kinetics, highlighting its potential for stable, high-performance LSBs.

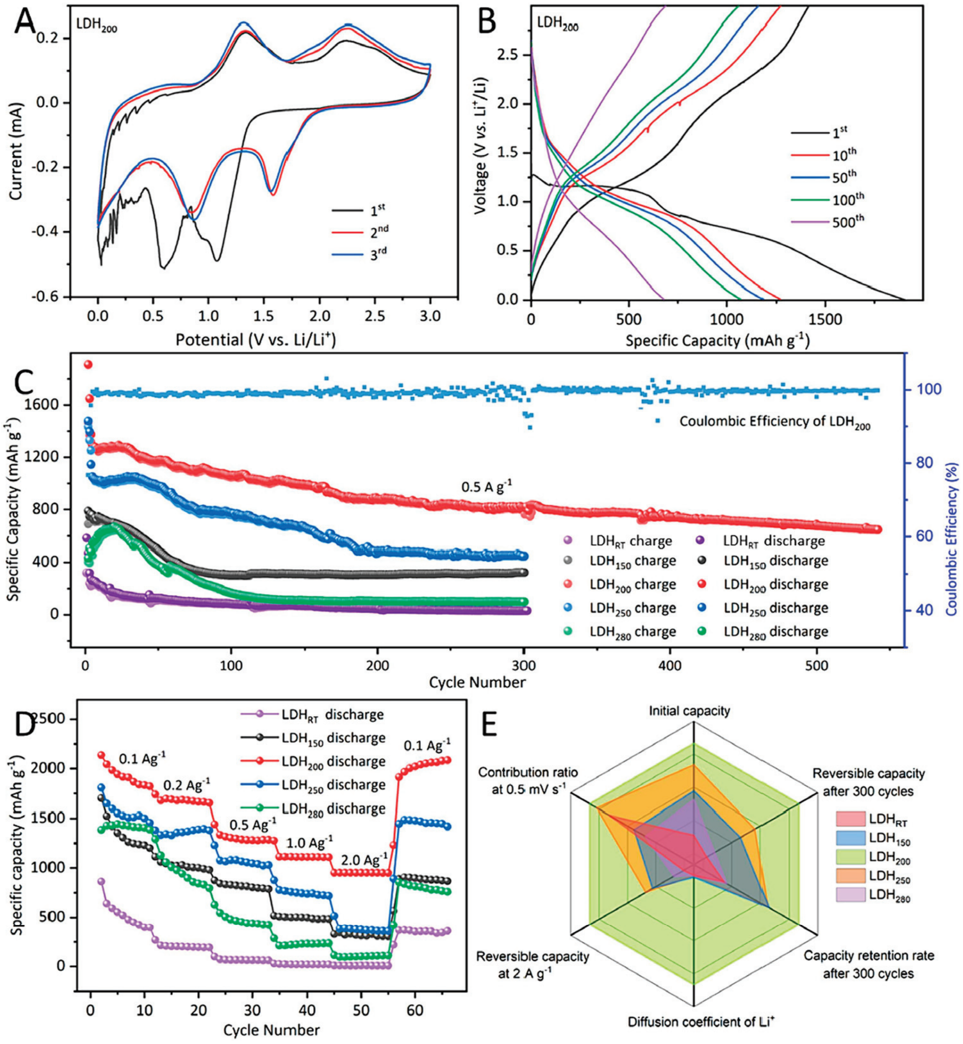

Figure 14. (**A**) CV curves of the LDH sample recorded at 0.1 mV/s within a voltage range of 0.01–3.0 V vs. Li/Li^+. (**B**) Charge/discharge voltage profiles of LDH at a current density of 0.5 A/g over multiple cycles. (**C**) Long-term cycling performance and coulombic efficiency of LDH200 compared to other LDH-based electrodes at 0.5 A/g. (**D**) Rate capability comparison for different samples under various current densities. (**E**) The radar chart displays normalized electrochemical metrics, including initial capacity, rate performance, and capacity retention, for all LDH variants. Reproduced with permission [109].

NiCo-LDH-based material was used as a freestanding cathode (NMWAs@NiCo-LDH/S) in LSBs [222]. It demonstrated exceptional electrochemical performance, with an initial specific capacity of 1238.4 mAh/g at 0.1 C, and 805.8 mAh/g at 5.0 C, reflecting excellent rate capability. Over 700 cycles at 5.0 C, it retained 647.1 mAh/g with a minimal capacity decay rate of 0.018% per cycle. The unique structure facilitated effective sulfur confinement, rapid Li^+ diffusion, and robust redox kinetics while alleviating volume expansion and suppressing the polysulfide shuttle effect. This makes NMWAs@NiCo-LDH/S a competitive candidate for high-rate and long-life LSB cathodes. The Vo-LDHs-MXenes were employed as a functional separator coating in LSBs [156]. The heterostructure significantly improved the electrochemical performance through enhanced adsorption and catalytic conversion of lithium polysulfides. The assembled LSBs exhibited an initial specific capacity of 1549 mAh/g at 0.1 C and retained 701 mAh/g after 300 cycles at 1.0 C, with a minimal capacity decay rate of 0.084% per cycle. Under high sulfur loading (6.7 mg/cm^2) and a low electrolyte/sulfur ratio (6 µL/mg), the areal capacity reached 6.09 mAh/cm^2. The cell demonstrated superior rate capability, ranging from 1530 to 342.9 mAh/g across 0.1 C to 3.0 C. These results underscore the effectiveness of the Vo-LDHs-MXenes in suppressing shuttle effects and enhancing redox kinetics in LSBs.

A VCFN composite was employed not as a cathode or anode material but as a separator modification layer (VCFN/SP/PVDF) on a glass fiber (GF) separator in LSBs [156]. The modified separator enabled superior polysulfide confinement and redox kinetics due to the synergistic effects of V_2O_5 catalysis, LDH's high surface area, and cysteine's functional linkage. The battery exhibited a high initial specific capacity of 1035.2 mAh/g at 0.5 C and retained 920.1 mAh/g after 300 cycles, demonstrating excellent cycling stability with a minimal capacity decay of 0.039% per cycle. Even at elevated sulfur loadings (up to 4.5 mg/cm^2), the system maintained stable capacities above 900 mAh/g, highlighting its scalability. Moreover, the cell exhibited improved Li-ion diffusion, reduced charge/transfer resistance (15.3 Ω), high ionic conductivity (4.1×10^{-2} S/cm), and minimized polarization, underlining the role of the VCFN-modified separator in promoting efficient electrochemical performance.

In LSBs, NiCo–MOF/LDH was applied as a functional interlayer between the sulfur cathode and separator [223]. The cell delivered remarkable electrochemical performance when used with a sulfur cathode composed of sulfur-encapsulated nitrogen-doped carbon nanocages (S@hNCNC). Specifically, it exhibited a high specific capacity of 950 mAh/g after 200 cycles at 1 C with a minimal capacity decay of 0.033% per cycle. It also maintained 982 mAh/g at 0.5 C after 200 cycles and 633 mAh/g over 1000 cycles at 1 C. The rate capability was also excellent, achieving 640 mAh/g at 5 C and returning to 1103 mAh/g when the current returned to 0.1 C. The interlayer significantly reduced polarization and enhanced polysulfide conversion, which was further validated by CV, Tafel plots, and EIS. These enhancements are attributed to the synergistic effect of NiCo-LDH's strong chemisorption and NiCo–MOF's catalytic activity.

In LSBs, the synthesized NiCo-LDH was used as a cathode host after sulfur loading [224]. The S/NiCo-LDH cathode delivered a high initial specific capacity of 1540 mAh/g at 0.1 C and retained 485 mAh/g even at 5 C, showing excellent rate performance. At 0.2 C, the electrode retained a stable 650 mAh/g capacity over 100 cycles with nearly 100% coulombic efficiency. Most notably, after 500 cycles at 1 C, the capacity remained at 475 mAh/g with 78% retention, indicating robust cycling stability. The synergistic effect of strong chemical polysulfide adsorption and catalytic activity of NiCo-LDH significantly improved the redox kinetics and suppressed shuttle effects, validating its potential as a high-performance cathode host in LSB systems.

The synthesized L-CoNi-LDH/C was employed as a sulfur host in the cathode (S@L-CoNi-LDH/C) of LiSB [154]. The composite enabled high sulfur loading (~66.4 wt.%) and delivered a high initial discharge capacity of 1574 mAh/g, retaining 1097 mAh/g after 100 cycles at 0.1 C with nearly 100% coulombic efficiency. At a high rate of 2 C, the electrode exhibited a stable capacity of 503 mAh/g after 200 cycles. Additionally, it showed excellent rate capability, sustaining 486 mAh/g at 5 C and recovering to 730 mAh/g when returned to 0.2 C. Figure 15 highlights the electrochemical performance and mechanism of the S@L-CoNi-LDH/C cathode for LSBs. As shown in Figure 15a, the charge/discharge profiles at 0.1 C indicate that the S@L-CoNi-LDH/C electrode delivers a higher capacity than the

S@CoNi-LDH/C, confirming enhanced redox activity and sulfur utilization. Figure 15b demonstrates the superior cycling stability of S@L-CoNi-LDH/C at 0.1 C, while Figure 15c shows its high capacity retention even at 2 C, along with excellent coulombic efficiency. The performance at various current densities is displayed in Figure 15d, and the rate capability in Figure 15e confirms the electrode's ability to recover its capacity when the current is returned to a lower value. Figure 15f presents EIS measurements at different voltages, illustrating the charge transfer behavior and confirming the effective catalytic role of the CoNi-LDH/C framework in promoting polysulfide conversion. This performance is attributed to the enhanced catalytic activity, conductivity, and strong LiPS confinement offered by the L-CoNi-LDH/C composite. In applying LSBs, the $NiCo_2S_4$-NiS_2 nanoheterostructure was used as a sulfur host in the cathode [225]. The designed cathode exhibited an outstanding initial specific capacity of 1207 mAh/g at 0.2 C and excellent rate capability with 766 mAh/g at 2 C. Under high sulfur loading conditions (5.0 mg/cm^2) and lean electrolyte usage (E/S ratio of 8.0 mL/g), the system achieved a high areal capacity of 6.09 mAh/cm^2. Long-term cycling at 1 C showed a capacity retention of 60.23% after 450 cycles (fading rate of 0.089% per cycle), and further tests confirmed suppression of LiPS shuttle and lithium dendrite formation, validating its superior electrochemical stability and catalytic effect. CuCo-LDH was utilized as a separator modifier rather than a direct cathode or anode material [226]. Its hollow, mesoporous architecture provided a strong barrier against polysulfide shuttle and enhanced sulfur redox kinetics via metal–sulfur interactions. As a result, the CuCo-LDH-modified separator enabled high reversible specific capacities (~1262.8 mAh/g initially at 0.2 C and ~697.0 mAh/g after 500 cycles at 1 C), excellent rate capability up to 5 C, and an extremely low capacity decay of 0.049% per cycle over 500 cycles. Under practical conditions with high sulfur loading (4.2 mg/cm^2) and lean electrolyte (E/S = 6 mL/g), a remarkable areal capacity of 4.39 mAh/cm^2 was achieved and retained 3.42 mAh/cm^2 after 200 cycles. These results highlight its dual-functionality as a physical barrier and a chemical catalyst in improving LSB performance. MgAl-LDH@CNT was utilized as a cathode component in Li–S batteries, combined with sulfur to form a composite cathode and paired with a dual-functional graphene/PP/Al_2O_3 (DF-GPA) separator [110]. This system significantly enhanced the electrocatalytic conversion of polysulfides and stabilized the redox kinetics. As a result, the Li–S cell delivered a high specific capacity and showed excellent cycling performance with minimal capacity decay over 200 cycles at 1 C. With a high sulfur loading of 4.0 mg/cm^2, the battery exhibited stable operation and high coulombic efficiency, making it a promising design for high-energy-density sulfur cathodes in practical applications.

LDHs were used as sulfur host materials in the cathode [157]. Among the variants, NiFe-LDH@S demonstrated superior electrochemical performance due to the stronger coordination between Ni/Fe sites and lithium polysulfides, facilitating better adsorption and catalytic conversion. It delivered an initial 676 mAh/g capacity at 0.2 C and maintained 503 mAh/g after 100 cycles. At a higher rate of 2 C, it still retained 386 mAh/g after 500 cycles. In contrast, NiAl-LDH@S and ZnAl-LDH@S showed poorer capacity retention and higher polarization, highlighting the critical role of transition metal composition in tuning LDH performance. Moreover, NiFe-LDH@S exhibited the lowest charge transfer resistance (4.9 Ω) and the highest polysulfide adsorption capacity, reinforcing its effectiveness as a high-performance sulfur host.

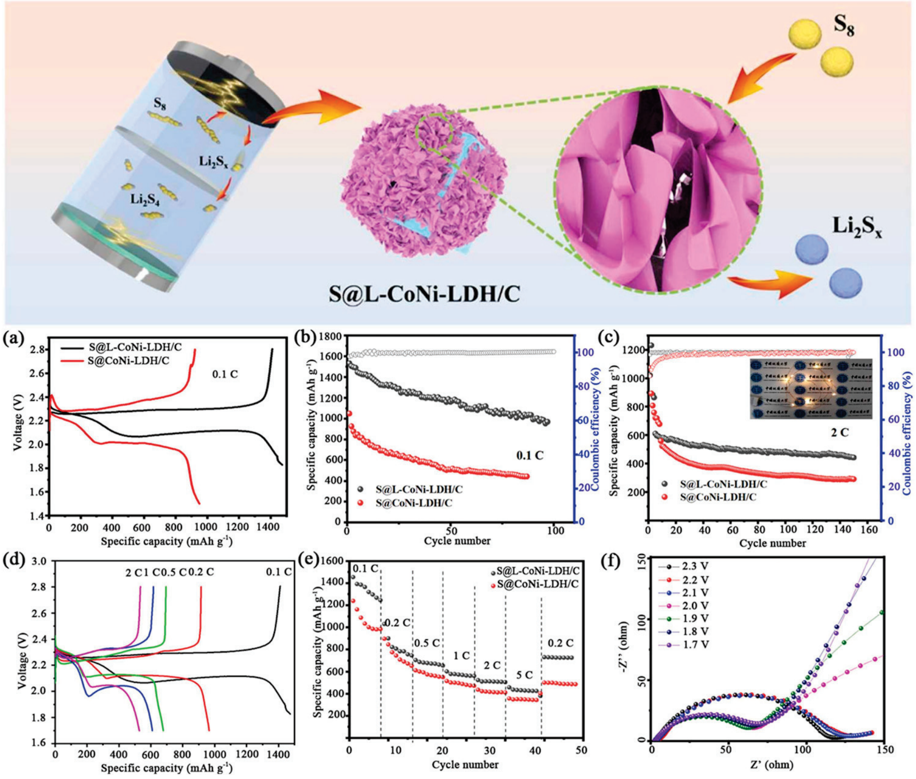

Figure 15. Illustration showing the role of S@CoNi-LDH/C in enhancing polysulfide adsorption and catalytic conversion. (**a**) Charge/discharge voltage profiles of S@L-CoNi-LDH/C and S@CoNi-LDH/C electrodes tested at 0.1 C. (**b**) Cycling stability at 0.1 C and (**c**) high-rate cycling at 2 C for both cathodes, including coulombic efficiency. (**d**) GCD curves at various current rates, and (**e**) corresponding rate capability of S@L-CoNi-LDH/C. (**f**) Nyquist plots of S@L-CoNi-LDH/C cathode collected at different voltage stages. Reproduced with permission [154].

The PPy@LDH-S was employed as a cathode in LSBs [227], demonstrating superior performance due to its unique multi-functional architecture. The composite cathode delivered a high initial discharge capacity of 907.2 mAh/g at 1 C. It retained 633.4 mAh/g after 500 cycles with a minimal fading rate of 0.06% per cycle, maintaining ~99% coulombic efficiency. At various rates from 0.2 C to 5 C, the electrode exhibited excellent rate capability and reversible capacity up to 983.2 mAh/g when returned to 0.2 C. It also achieved a reversible areal capacity of 535.7 mAh/g (3.5 mg/cm^2 sulfur loading) and 416.9 mAh/g (5.2 mg/cm^2) after 500 cycles. The flexible pouch cell configuration further validated its mechanical robustness and suitability for wearable electronics, maintaining functionality under bending and twisting conditions. In the LSB configuration, the VG@LDH/CC composite was used as a sulfur host for the cathode [158]. This structure provides both physical confinement and chemical adsorption of polysulfides, minimizing shuttle effects and improving reaction kinetics. The battery delivered a high specific capacity of 1182.4 mAh/g at 0.1 C, and retained 441.3 mAh/g after 750 cycles at 0.5 C, with a very low capacity decay rate of 0.0755% per cycle. The rate performance was also excellent, sustaining 780.8 mAh/g at 3 C, and maintaining capacity recovery upon returning to lower rates. The design supports high-rate and high-capacity operation, even under high sulfur loading conditions (e.g., 547.7 mAh/g after 300 cycles at 3.5 mg/cm^2 loading at 1 C).

4.3. Sodium-Ion Batteries

For NIBs, LDHs have shown notable electrochemical performance. Research indicates that ZnAl-LDHs can be effective anode materials, exhibiting around 200 mAh/g capacities with good cycling stability over extended periods [102]. The ability to intercalate sodium ions while maintaining structural integrity enhances energy storage capabilities. The intrinsic layered structure also allows for efficient ion diffusion and electron transport, leading to faster charge/discharge rates than traditional anode materials. The synthesized NiCr-Cl LDH/rGO was utilized as an anode material in NIBs [159]. Electrochemical tests revealed a high initial discharge capacity of 632 mAh/g, with a reversible capacity of 218 mAh/g after 200 cycles at 100 mA/g, indicating good cyclic stability. Moreover, it delivered 219 mAh/g at a high rate of 2 A/g, highlighting its excellent rate capability. The improved electrochemical performance is attributed to the expanded interlayer spacing, enhancing Na^+ ion diffusion, and the rGO matrix, which boosts conductivity and buffers volume changes. EIS confirmed the lowest charge transfer resistance among the compared samples, supporting fast kinetics. Capacitive contribution analysis showed dominant pseudocapacitive behavior, with 55.1% capacitive contribution at 0.2 mV/s, confirming its favorable kinetic profile for high-rate applications.

The CoMoLDH@C-PDA material was evaluated as an anode in NIBs [163]. The composite synthesized with 6-h PDA polymerization (CoMoLDH-24@C-PDA-6) exhibited superior electrochemical performance among various samples. This anode delivered an initial specific capacity of 779.9 mAh/g at 0.05 A/g and maintained 310.9 mAh/g after 100 cycles at 0.1 A/g, with a 70% capacity retention. High rate capability and long-term stability were attributed to the formation of α-$CoMoO_4$ and conductive carbon coating, which improved Na^+ diffusion and minimized charge transfer resistance. Figure 16a presents the fabrication steps for CoMoLDH-based materials with and without carbon and PDA modifications. The composite CoMoLDH-24@C-PDA-6 is prepared by combining polymerized dopamine with carbonized CoMoLDH. The electrochemical behavior of these electrodes is shown in Figure 16b,c. The CoMoLDH-24@C-PDA-6 electrode exhibits more stable and extended charge/discharge profiles, indicating enhanced capacity and reaction reversibility. In Figure 16d, cycling performance over 100 cycles at 0.1 A/g shows that CoMoLDH-24@C-PDA-6 retains 70% of its capacity, significantly outperforming the unmodified CoMoLDH-24 (43.7%). Nyquist plots in Figure 16e,f demonstrate reduced charge transfer resistance for the modified electrode, both before and after cycling, confirming improved conductivity and electrochemical stability. Further, EIS and GITT analysis confirmed a lower R_{ct} and higher Na^+ diffusion coefficient for the coated material, reinforcing its viability for high-performance NIB applications.

In NIB applications, both $Ni_{0.8}Ca_{1.2}Al$-Cl LDH and $Co_{0.6}Ca_{1.4}Al$-Cl LDH were evaluated as anode materials in CR2032 coin-type cells [228]. These materials demonstrated promising electrochemical properties, with initial discharge capacities of 819.2 and 746.6 mAh/g and coulombic efficiencies of 65.2% and 56.8%, respectively. $Ni_{0{\cdot}8}Ca_{1{\cdot}2}Al$-Cl LDH delivered a stable specific capacity of 256.9 mAh/g, and $Co_{0.6}Ca_{1.4}Al$-Cl LDH achieved 292.8 mAh/g at 0.2 A/g after 200 cycles. Notably, they maintained 102 and 118.1 mAh/g after 600 cycles at 2 A/g, demonstrating excellent cycling stability. Both materials exhibited enhanced rate capability and reduced impedance, attributable to the porous structure and bimetallic synergies, and their performance was comparable to that of conventional hard carbon. The sodium storage mechanism involved both diffusion-controlled intercalation and surface capacitive effects, supported by ex situ XRD and XPS analyses. NHCNS@$CoSe_2$@C was employed as an anode material. It demonstrated an initial discharge capacity of 465.6 mAh/g at 0.1 A/g, and retained 373.8 mAh/g after 100 cycles, with a coulombic efficiency of 59.7% in the first cycle [164]. Even at a high current density of 5 A/g, the electrode retained a specific capacity of 314.2 mAh/g, reflecting outstanding rate capability. Additionally, long-term cycling at 0.5 A/g for 1000 cycles showed stabilized performance at 325 mAh/g, despite some capacity fade due to volume expansion. The hybrid's superior performance is attributed to its high conductivity, abundant active sites, and structural robustness against sodium insertion/extraction.

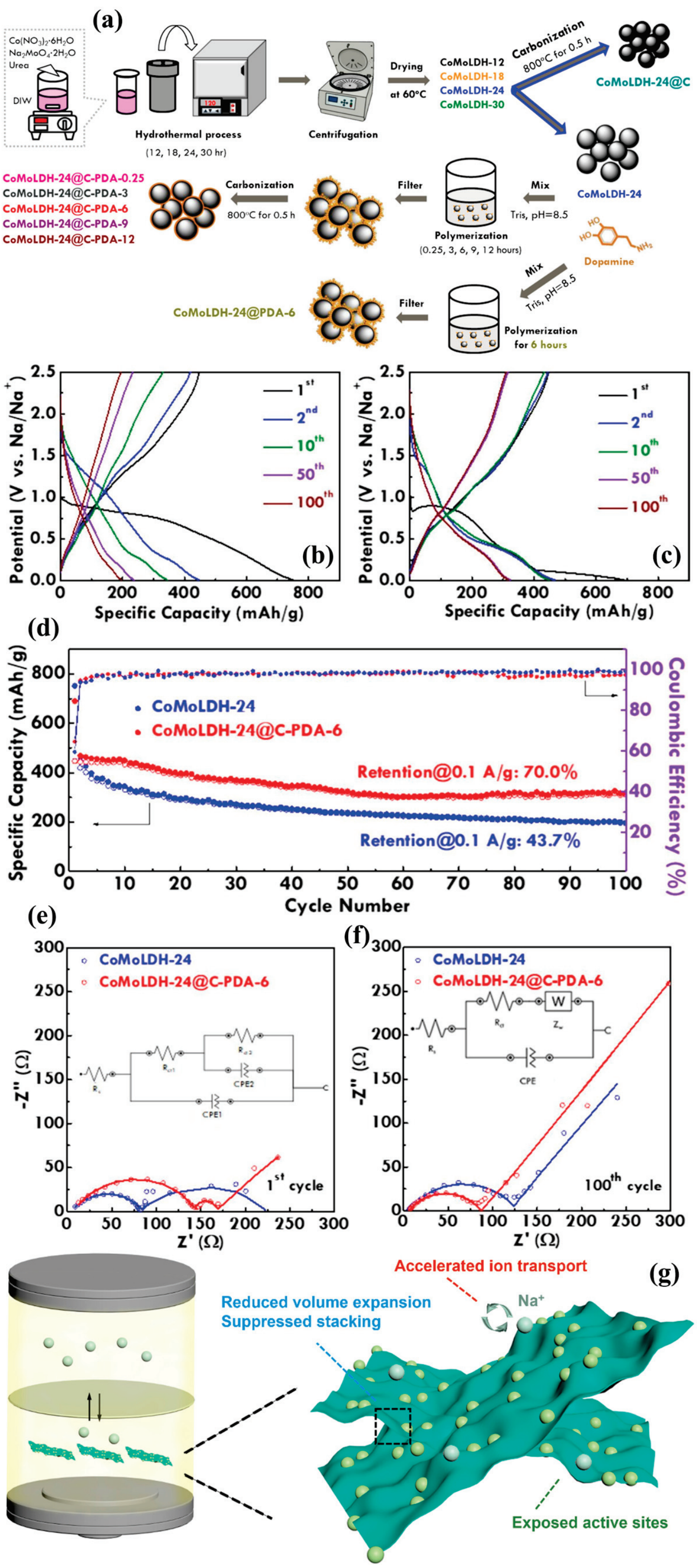

Figure 16. (**a**) Schematic of the synthesis procedure for CoMoLDH, CoMoLDH-24@C, CoMoLDH-24@PDA-6, and CoMoLDH-24@C-PDA composites. (**b**,**c**) GCD profiles of CoMoLDH-24 and CoMoLDH-24@C-PDA-6 electrodes, respectively. (**d**) Cycling performance comparison at 0.1 A/g over 100 cycles for both electrodes. (**e**,**f**) Nyquist plots obtained before cycling and after 100 cycles. Reproduced with permission [163]. (**g**) Diagram illustrating how the electrode design enhances sodium-ion storage by improving ion transport, limiting volume expansion, and increasing active site exposure. Reproduced with permission [229].

NiFe-NO_3 LDH was employed as a conversion-type anode material in a sodium metal half-cell configuration [111]. During electrochemical testing, the electrode demonstrated an impressive initial sodiation capacity of ~972 mAh/g, though with a significant first-cycle irreversibility (~60% coulombic efficiency). Upon cycling at 50 mA/g, it stabilized at ~388 mAh/g after 60 cycles, maintaining over 95% coulombic efficiency. High-rate cycling (500 mA/g) over 500 cycles yielded a final capacity of 122 mAh/g. Rate capability studies showed the electrode retained a reversible capacity of 430 mAh/g when the current returned to 50 mA/g after high-rate steps. Operando XAS and magnetic measurements revealed a hybrid intercalation–conversion mechanism, with Fe^{3+} reducing to Fe^{2+} and forming Fe_3O_4, while Ni partially transitions to NiO_x. This complex, partially reversible mechanism contributed to the sustained capacity despite an initial irreversible structural transformation.

CoSn-LDH@MXene was employed as an anode material in 2032-type coin cells [229]. The hybrid electrode demonstrated remarkable sodium storage performance due to its synergistic structure combining redox-active CoSn-LDH and highly conductive MXene. At a current density of 0.1 A/g, the material delivered an initial specific capacity of 976.1 mAh/g and retained 504 mAh/g after 100 cycles with 97.29% retention. At a higher current density of 0.5 A/g, it maintained 387.4 mAh/g after 100 cycles and still showed 419.3 mAh/g after 1000 cycles, highlighting excellent long-term stability. Rate capability was outstanding, with capacities ranging from 532.2 to 187.1 mAh/g across 0.05–5 A/g. The electrode exhibited strong pseudocapacitive behavior (up to 95% at high scan rates), excellent reversibility, and low charge/transfer resistance (574.5 Ω), positioning it among the top-performing LDH-based anodes for SIBs. Figure 16g visually summarizes the key functional advantages of the electrode structure, such as faster Na^+ ion transport, reduced stacking, enhanced structural integrity, and greater exposure to active sites.

4.4. Chloride-Ion Batteries

Though less explored, the application of LDHs in CIBs presents exciting opportunities. Research indicates that chloride-intercalated LDHs can exhibit promising electrochemical behavior, including good cycling stability and capacity retention [102]. The favorable ion exchange capacity of LDHs facilitates chloride ion intercalation, opening pathways for improved conductivity and performance in battery applications. The ability of these materials to accommodate diverse anions while maintaining structural stability makes them suitable candidates for next-generation battery technologies. NiFe LDH nanosheets with different interlayer spacings were used as cathode materials in Li-based CIBs, where Li sheets served as the anode and 0.5 M 1-butyl 1-methylpyrrolidinium chloride (Bpy14Cl) in propylene carbonate as the electrolyte [112]. Among the three samples, the NiFe-$C_{17}H_{25}O_3$ LDH with the most significant interlayer spacing (24.114 Å) demonstrated superior electrochemical performance, delivering a specific discharge capacity of 64.2 mAh/g after 200 cycles at 300 mA/g, and maintaining 52.4 mAh/g even at 1 A/g. The electrode exhibited a high diffusion coefficient (~10^{-10} cm^2/s), significantly reduced charge transfer resistance (48.9 Ω), and enhanced redox activity of Ni^{2+}/Ni^{3+} and Fe^{2+}/Fe^{3+} couples during Cl^- intercalation. These features enabled improved rate capability, cycling stability, and ion transport kinetics, establishing the interlayer-engineered NiFe LDH as a promising high-rate cathode for CIBs. Ni_3Ti-Cl and Ni_3Cr-Cl LDHs were employed as cathodes in CIBs paired with lithium metal anodes [230]. The Ni_3Ti-Cl LDH delivered a high initial discharge capacity of 346.4 mAh/g and retained a stable reversible capacity of ~131.8 mAh/g over 200 cycles at a current density of 200 mA/g, showcasing excellent cycling stability and coulombic efficiency (~100%). Ni_3Cr-Cl LDH, exhibiting a slightly lower maximum capacity of 182.6 mAh/g, maintained a competitive capacity of 111.3

mAh/g after 200 cycles. The performance validates theoretical predictions, highlighting Ni_3Ti-Cl LDH as a superior cathode material due to its high specific capacity, excellent cyclic stability, and favorable Cl^- insertion dynamics.

Phosphorus-doped NiCoMo-P150 LDH was employed as the cathode material in a CIB configuration with a lithium metal anode and ionic liquid electrolyte [142]. This cathode delivered a high initial discharge capacity of 363.4 mAh/g and maintained a stable 150.2 mAh/g capacity over 800 cycles at 300 mA/g. It exhibited superior cycling stability and coulombic efficiency (~100%), with enhanced Cl^- diffusion coefficients (~10^{-10}–10^{-12} cm^2/s). The redox activity of Ni, Co, and Mo across multiple oxidation states ($Ni^0/^{2+}/^{3+}$, $Co^0/^{2+}/^{3+}$, $Mo^{4+}/^{6+}$) facilitated efficient chloride ion intercalation and de-intercalation, resulting in high energy and power performance metrics suitable for long-cycle chloride-ion storage.

In the CIB application, the Mo-doped $NiCo_2$-Cl LDH was employed as a cathode material [144]. Among various Mo doping levels, $Mo_{0.3}NiCo_2Cl$ LDH exhibited optimal performance. This material delivered an initial specific capacity of 278.5 mAh/g and maintained a reversible discharge capacity of 159.7 mAh/g after 300 cycles at 150 mA/g, demonstrating remarkable cyclic stability. The electrode also showed enhanced chloride-ion diffusion coefficients (10^{-11}–10^{-12} cm^2/s), and its energy storage involved multiple reversible redox couples ($Ni^0/Ni^{2+}/Ni^{3+}$, $Co^0/Co^{2+}/Co^{3+}$, and Mo^{4+}/Mo^{6+}). The material's high performance is attributed to Mo-induced oxygen vacancies and reduced bandgap, promoting superior electronic conductivity, fast Cl^- transport, and low-strain structural stability (volume change <3%). These features result in high energy density and power capability, outperforming many previously reported CIB cathodes.

NiMn-Cl LDH/CNT was employed as a cathode material in the CIB application [113]. The hybrid architecture facilitated efficient chloride-ion intercalation and deintercalation during cycling. The composite electrode delivered a stable specific capacity of approximately 130 mAh/g over 150 cycles, demonstrating good cyclic durability. The enhanced structure ensured prolonged operational performance and mitigated degradation, key metrics for practical CIB deployment. Ni_5Ti-Cl LDH was employed as a cathode material, exhibiting remarkable electrochemical performance in CIB applications [114]. At 300 mA/g, it delivered an initial discharge capacity of 374.6 mAh/g and retained 193.3 mAh/g after 200 cycles. Notably, even under a high current density of 1000 mA/g, it maintained a stable reversible capacity of 127.9 mAh/g over 1000 cycles, showcasing excellent long-term cycling stability. The Ni_5Ti-Cl LDH also demonstrated high-rate capabilities with capacities of 264.9 to 104 mAh/g across increasing current densities (100–1000 mA/g), with capacity recovering when the rate was lowered again. EIS confirmed low charge/transfer resistance (37.44 Ω), and diffusion coefficients ranged from 10^{-10} to 10^{-13} cm^2/s. Figure 17a shows the charge/discharge behavior of the Ni_5Ti-Cl LDH electrode. Structural evolution during cycling is captured by the XRD data in Figure 17b, with a detailed view of the (003) peak in Figure 17c and related volume changes in Figure 17d. Chemical states of Ni and Ti are analyzed through XPS in Figure 17e,f, while Figure 17g,h displays the corresponding oxidation state ratio shifts with voltage. Figure 17i illustrates the Cl^- transport mechanism across the battery. Additionally, density functional theory (DFT) calculations revealed favorable Cl^- adsorption energies and low diffusion barriers (0.045–0.091 eV), correlating with high-rate performance and fast Cl^- transport kinetics. These attributes make the Ni_5Ti-Cl LDH cathode one of the most promising candidates for next-generation CIBs. In the CIB application, CoFe–Cl-LDH/CNT was utilized as the anode, paired with an AgCl/CNT cathode in a neutral aqueous NaCl electrolyte [145]. The cell exhibited an impressive initial capacity of ~190 mAh/g at 200 mA/g and maintained ~125 mAh/g after 200 cycles, highlighting excellent cyclic stability. At higher current densities (400 mA/g), the capacity remained around 120 mAh/g, demonstrating robust rate capability. The energy density reached 165 Wh/kg and power density up to 140 W/kg depending on the current rate and voltage range. The outstanding performance is attributed to reversible Cl^- intercalation/deintercalation, stable layered structure, and enhanced electron transfer facilitated by CNTs, making it a promising anode for aqueous CIBs.

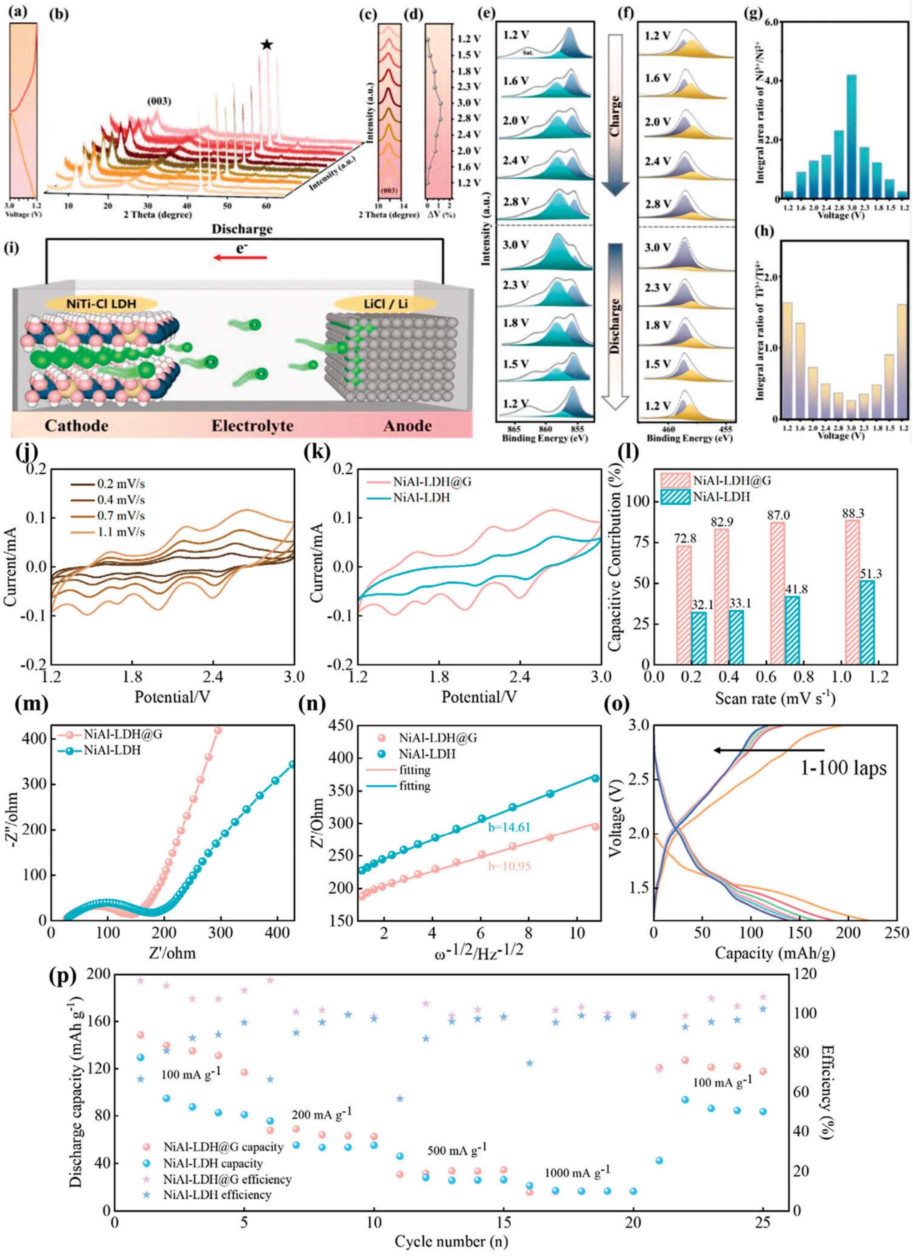

Figure 17. (**a**) Charge/discharge profiles of Ni_5Ti-Cl LDH. (**b**) In situ XRD patterns during full cycling, showing structural changes; the peak at 2θ = 43.17° corresponds to the current collector. (**c**) Enlarged view of the (003) reflection peak. (**d**) Volume variation across charge/discharge states. (**e**,**f**) Ex situ XPS spectra of Ni 2p and Ti 2p regions during different stages of the cycle. (**g**,**h**) Peak area ratio changes of Ni^{3+}/Ni^{2+} and Ti^{3+}/Ti^{4+} with voltage. (**i**) Schematic of Cl^- ion transport mechanism in Li||Ni_5Ti-Cl LDH battery. Reproduced with permission [114]. (**j**) CV curves at various scan rates for NiAl-LDH@G electrode. (**k**) CV comparison of NiAl-LDH and NiAl-LDH@G at 1.1 mV/s. (**l**) Capacitance contribution at different scan rates. (**m**,**n**) Nyquist plots and low-frequency Z′ vs. $\omega^{-1/2}$ plots for NiAl-LDH and NiAl-LDH@G. (**o**) Charge/discharge voltage curves over 100 cycles. (**p**) Rate performance of NiAl-LDH and NiAl-LDH@G at various current densities. Reproduced with permission [143].

NiAl-LDH@G was employed as a cathode material in CIBs. Compared to pure NiAl-LDH, the NiAl-LDH@G cathode demonstrated significantly enhanced electrochemical performance [143]. It delivered a high specific capacity of 223.3 mAh/g during the first discharge and a stable reversible capacity of 107 mAh/g over 500 cycles at 100 mA/g with a coulombic efficiency of ~96%. It also retained 72 mAh/g after 120 days, indicating low self-discharge and excellent long-term stability. The composite exhibited good rate capability with capacities of 148.5, 67.8, 30.9, and 15.9 mAh/g at increasing current densities, recovering to 120.8 mAh/g when returned to 100 mA/g. EIS showed reduced charge transfer resistance and higher chloride ion diffusion coefficients (up to 3.22×10^{-12} cm^2/s), confirming improved conductivity and ion mobility. Electrochemical properties of NiAl-LDH@G are shown in Figure 17j to Figure 17n, with CV and impedance tests confirming improved charge storage and ion diffusion compared to NiAl-LDH. Long-term cycling behavior is presented in Figure 17o, and rate capability at different current densities is plotted in Figure 17p, showing the superior performance of the NiAl-LDH@G composite. These results underscore the superiority of the nanoarray structure in facilitating fast redox kinetics and durable performance in CIBs.

4.5. Zinc-Ion Batteries

ZIBs also benefit from LDH incorporation. Studies have shown that LDH compounds like Zn–Al serve as structural promoters and improve charge storage capabilities, achieving specific capacities upward of 300 mAh/g [259]. Furthermore, their layered structure contributes to the selective intercalation of zinc ions, which further optimizes battery performance and longevity [260]. This characteristic is particularly advantageous in developing versatile and efficient energy storage solutions. Hv-$Ni_3Mn_{0.7}Fe_{0.3}$-LDH was employed as a cathode material in aqueous ZIBs (AZIBs) [16]. The modified LDH displayed exceptional performance, delivering a high specific capacity of 328 mAh/g at 50 mA/g and maintaining 122 mAh/g over 500 cycles at 1 A/g with 85% capacity retention. The enhanced electrochemical behavior stems from introducing hydrogen vacancies that expose terminal oxygen atoms, promoting Zn^{2+} intercalation and diffusion. The material also exhibited robust rate capability and reversible Zn^{2+}/H^+ intercalation mechanism. The synergy among Ni, Mn, and Fe contributed to conductivity and redox activity and effectively suppressed Jahn–Teller distortion, ensuring structural stability during long-term cycling. The Ragone plot revealed competitive energy and power densities, positioning this LDH among the top-performing ZIB cathodes.

The synthesized NiCo LDH, supported with MXene and electrodeposited on nickel foam, served as a high-performance cathode in alkaline Zn||NiCo batteries [203]. The battery exhibited a remarkable areal specific capacity of 20.2 mAh/cm^2 (equivalent to 311.7 mAh/g), with exceptional rate capabilities maintaining 9.6 mAh/cm^2 at 120 mA/cm^2 (148 mAh/g). It also delivered ultrahigh areal and gravimetric energy densities of 31.2 mWh/cm^2 and 465 Wh/kg, respectively, alongside a peak power density of 80 mW/cm^2 (2752 W/kg). The electrode retained 88.6% of its capacity after 10,000 cycles, demonstrating outstanding long-term cycling stability, fast kinetics, and high ion diffusion coefficients due to the unique MXene-assisted structure. MCN-LDH@CP was used as the cathode in an aqueous CoNi//Zn battery [165]. The hybrid electrode exhibited a high areal specific capacity of 1.74 mAh/cm^2, an areal energy density of 2.89 mWh/cm^2, and a peak power density of 111.22 mW/cm^2. It demonstrated excellent cycling stability, maintaining 97.8% capacity retention after 7000 cycles at 40 mA/cm^2. These superior performances are attributed to the molybdate-induced increase in surface area, interlayer spacing, and improved diffusion kinetics. The battery also showed outstanding mechanical resilience and safety in quasi-solid-state form, maintaining functionality under physical damage.

The ZnCo-LDH was employed as a cathode material in Zn-ZnCo batteries, using Ni foam as the current collector and a 6 M KOH + 0.2 M $Zn(CH_3COO)_2$ electrolyte [166]. The batteries exhibited a linear increase in specific capacity with increased ZnCo-LDH loading, reaching up to 2.5 mAh/cm^2 at a 60 mg/cm^2 loading. Remarkable rate performance was maintained across various current densities, with over 75% capacity retention at high rates and full recovery upon returning to lower current densities. The ZnCo-LDH cathode demonstrated exceptional cycling stability, retaining 86% of its capacity after 5000 cycles at 30 mg/cm^2 loading. Additionally, hybrid Zn batteries incorporating an air-accessible Pt/C-coated gas diffusion layer alongside ZnCo-LDH delivered dual-stage voltage plateaus, enabling a combination of Zn–ZnCo and Zn–air functionalities. The hybrid cell exhibited stable cycling over 270 cycles and enhanced Zn–ZnCo segment capacity due to improved electrode wettability.

The H-vacancy-rich CoNi-LDH(v) was used as a cathode in aqueous and flexible solid-state Zn-ion batteries (ZIBs), paired with Zn@CC as the anode [204]. The aqueous CoNi-LDH(v)@CC//Zn@CC battery delivered a high specific capacity of 225 mAh/g at 0.5 A/g, with energy and power densities of 353.62 Wh/kg and 3056.51 W/kg, respectively. It retained 53.9% capacity after 900 cycles, significantly outperforming the non-activated CoNi-LDH. Figure 18a shows the layered structure of the flexible CoNi-LDH(v)@CC//Zn@CC solid-state battery. Electrochemical behavior is displayed in Figure 18b, where the GCD curves demonstrate good performance at different current rates. The corresponding specific capacity and coulombic efficiency over cycling are shown in Figure 18c. Figure 18d presents the cycling stability, with the battery maintaining 47.22% of its capacity after 1000 cycles. Mechanical flexibility is evaluated in Figure 18e, where the battery retains over 85% capacity even when bent at 150°. Figure 18f shows it remains functional after 100 bending cycles with 74.82% capacity retention. Figure 18g–i visually demonstrates the battery's robustness: it powers a digital device while bent, continues operating even after being cut, and maintains output for over 80 h in an open environment. Moreover, a flexible, solid-state version of the battery demonstrated excellent deformability and stability under mechanical stress and sustained operation over 80 h without encapsulation, underlining its promise for wearable electronics.

ZnAl-LDH was applied as an artificial interface layer on Zn anodes (SZ/LDH@Zn) to enhance the performance of aqueous ZIBs [172]. The SZ/LDH@Zn||SZ/LDH@Zn symmetric cell delivered an ultra-long cycling lifespan of 5500 h at 1 mA/cm^2 with low voltage hysteresis (16.4 mV). In asymmetric Zn||Cu cells, it achieved a high average coulombic efficiency of 99.85% over 3800 cycles, outperforming bare Zn and ZnAl-LDH@Zn. Furthermore, in an entire cell with $NaV_3O_8 \cdot xH_2O$ cathode and a low N/P ratio of 3.62, the SZ/LDH@Zn||NVOH cell exhibited a specific capacity of 251.45 mAh/g, an areal capacity of 5.36 mAh/cm^2, and stable cycling over 1500 cycles at 1 A/g. These results confirm the superior reversibility, capacity retention, and anti-corrosion performance of SZ/LDH@Zn in practical ZIB systems.

H-vacancy-enriched CoNi LDH (denoted as CoNi LDH(v)) was employed as a cathode material for aqueous ZIBs in a mild $ZnSO_4$ electrolyte (pH $\approx$ 4) [207]. The electrode demonstrated a high specific capacity of 185 mAh/g at 1.2 A/g, with an average discharge voltage of 1.6 V (vs. Zn^{2+}/Zn), leading to an excellent energy density of 296.2 Wh/kg at a power density of 1894 W/kg. Even at a high current density of 12 A/g, it maintained a 103 mAh/g capacity, indicating good rate performance. Furthermore, the electrode showed impressive cyclic stability with 80% capacity retention over 1000 cycles at 6 A/g. The superior performance was attributed to the Zn^{2+}/H^+ co-intercalation mechanism enabled by the introduced hydrogen vacancies, which improved ion diffusion and electronic conductivity.

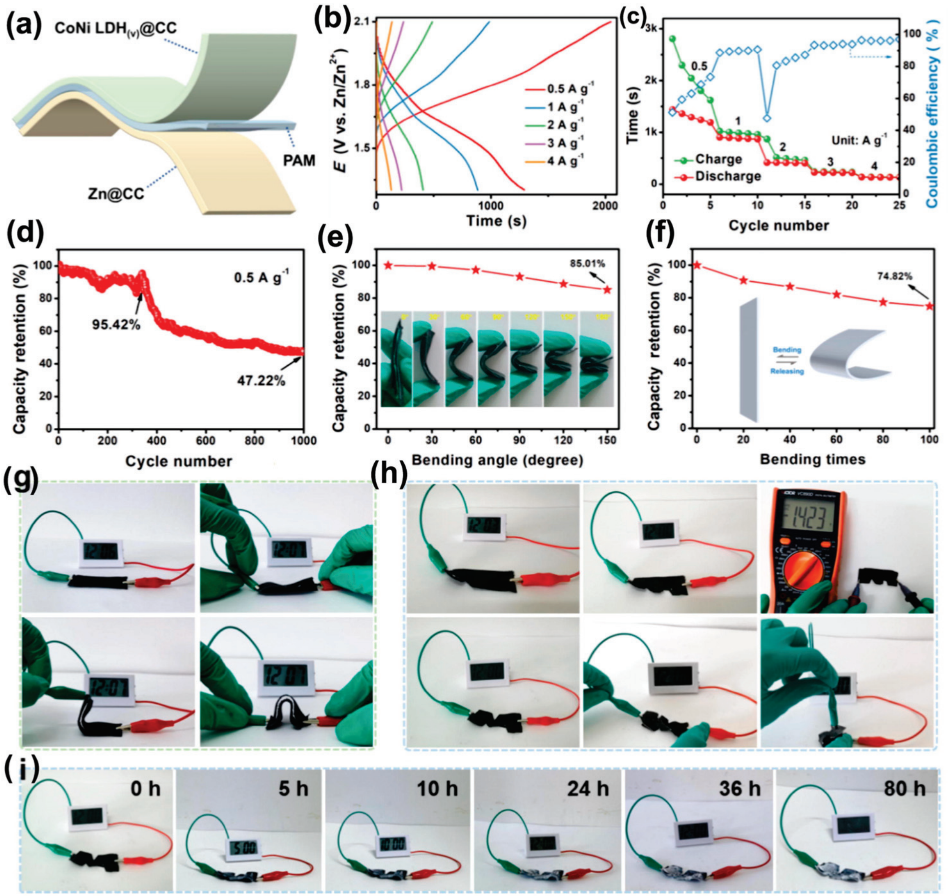

Figure 18. Design and performance of a flexible solid-state battery based on a CoNi-LDH(v)@CC//Zn@CC layered configuration. (**a**) Schematic of the battery's structural composition. (**b**) Charge/discharge profiles at various current densities. (**c**) Specific capacity and coulombic efficiency during charge/discharge cycling. (**d**) Long-term cycling performance at 0.5 A/g. (**e**) Capacity retention under different bending angles. (**f**) Capacity retention after multiple bending cycles. (**g**) Photographs showing operation under various bending and twisting states. (**h**) Device functionality after being cut. (**i**) Duration of continuous power output to a digital watch in open-air conditions. Reproduced with permission [204].

In the alkaline ZIB configuration, NC@CL was employed as the cathode against a Zn anode in an aqueous electrolyte (1 M KOH + 5 mM ZnO) [141]. The NC@CL//Zn battery demonstrated outstanding electrochemical performance with a high specific capacity of 381.1 mAh/g at 0.5 A/g, maintaining 243.4 mAh/g even at 10 A/g, confirming excellent rate capability. The device showed a robust energy density of 66.56 Wh/kg and power density of 15,375 W/kg, with superior cyclic stability—retaining 98% capacity over 2000 cycles at 5 A/g. These performances are attributed to the hierarchical nanosheet morphology, heterostructure-induced interfacial charge redistribution, and enhanced OH^- adsorption facilitated by La-doping and NC–CL synergism. The synthesized NiCoS@NiCo-LDH was utilized as the cathode in aqueous alkaline zinc-based batteries (AAZBs), assembled in a full cell with zinc foil as the anode [208]. The device delivered an impressive specific capacity of 312 mAh/g at 2 mA/cm^2. Moreover, it achieved a high energy density of 435.3 Wh/kg at a power density of 4.1 kW/kg, maintaining 95.9% capacity retention over 3000 cycles at 20 mA/cm^2. These values highlight excellent rate capability and stability and surpass the performance of many previously reported nickel-based cathode materials, showcasing its potential for high-performance, long-life ZIBs.

The synthesized NF\Ni_3S_2/NiS@NiCo-LDH was employed as the cathode in an aqueous alkaline Ni–Zn battery, paired with a zinc anode and a mixed KOH/$Zn(CH_3COO)_2$

electrolyte [209]. The battery delivered a high specific capacity of 434.5 mAh/g at 3 mA/cm^2, showcasing excellent rate performance with capacities ranging from 317.9 to 100.3 mAh/g across 2–15 A/g. The device achieved a maximum energy density of 556.3 Wh/kg and a peak power density of 26.3 kW/kg. The cycling stability was outstanding, retaining 116.7% of its original capacity after 5000 cycles at 60 mA/cm^2, highlighting its activation behavior and robust long-term performance.

4.6. Zinc–Air Batteries

In the context of ZABs, LDHs demonstrate exceptional catalytic activity for OER. Yan et al. [261] highlighted the efficiency of Ni-Fe LDHs as bifunctional electrocatalysts, achieving low overpotentials that significantly enhance the performance of ZABs. Their superior activity can be attributed to the highly active sites the layered structure provides, which facilitate oxygen reduction and evolution reactions. Consequently, integrating LDHs in air battery systems can lead to enhanced energy densities and improved operational lifetimes. In the ZAB application, Co@NiFe-LDH was employed as the air cathode catalyst, while a zinc plate was used as the anode [150]. The battery demonstrated outstanding performance metrics, surpassing even Pt/C + RuO_2-based systems. Specifically, Co@NiFe-LDH achieved a specific capacity of 652 mAh/g, power density of 165 mW/cm^2, and an open circuit voltage of 1.44 V. It exhibited excellent cyclic stability over 90 h of continuous GCD cycling with a minor voltage gap increase (from 0.78 V to 0.80 V), maintaining about 59.5% round-trip efficiency. These results confirm Co@NiFe-LDH's promise as a cost-effective and efficient catalyst for rechargeable ZABs.

The Pt-anchored NiFe-LDH@Co_9S_8 was used as a bifunctional air cathode catalyst in both liquid-state and flexible quasi-solid ZABs [149]. The catalyst demonstrated superior electrocatalytic performance with a high specific capacity of 796.6 mAh/g and a 164.3 mW/cm^2 peak power density in liquid-state ZABs. It also exhibited an energy density of 76.4 Wh/kg and excellent cyclic stability, maintaining performance over 240 cycles (80 h) in flexible ZABs. Figure 19a presents the structural design of the flexible ZAB, which includes an air cathode and a NiFe-LDH@Co_9S_8 electrocatalyst that supports both OER and ORR processes. Figure 19b compares the impedance of three different polymer electrolytes, showing that the PANa-CMC-IL hydrogel offers the lowest resistance. Figure 19c confirms its superior water retention over time, supporting stable operation. The practical application of the battery is shown in Figure 19d, where it successfully powers an LED display. The discharge and power density performance are detailed in Figure 19e, showing a peak power density of 78.4 mW/cm^2. Figure 19f illustrates the battery's ability to maintain high capacities across different current densities, and Figure 19g confirms cycling durability through stable voltage over repeated charge/discharge cycles. Figure 19h demonstrates excellent mechanical flexibility, as the device retains stable output after multiple bending cycles. The catalyst outperformed commercial Pt/C and RuO_2 references, attributed to its synergistic core/shell architecture, high electrochemical surface area (28.2 mF/cm^2), and enhanced ORR/OER activity. The NiCo-LDH/NCM@NF was employed as a bifunctional air cathode in ZABs [148]. It demonstrated a high open-circuit voltage (1.374 V), a peak power density of 158 mW/cm^2, and a specific capacity of 685 mAh/g at 10 mA/cm^2, outperforming commercial Pt/C + IrO_2 catalysts. The catalyst also showed excellent cycling stability, maintaining consistent charge/discharge voltage profiles over 500 cycles and sustaining high round-trip efficiency (~62%) with minimal voltage gap increase. The four-electron ORR pathway, high ECSA (194 cm^2), and low OER overpotential (0.352 V at 50 mA/cm^2) contribute to its robust and durable ZAB performance, attributed to the synergistic integration of NCM and LDH structures enriched with oxygen vacancies.

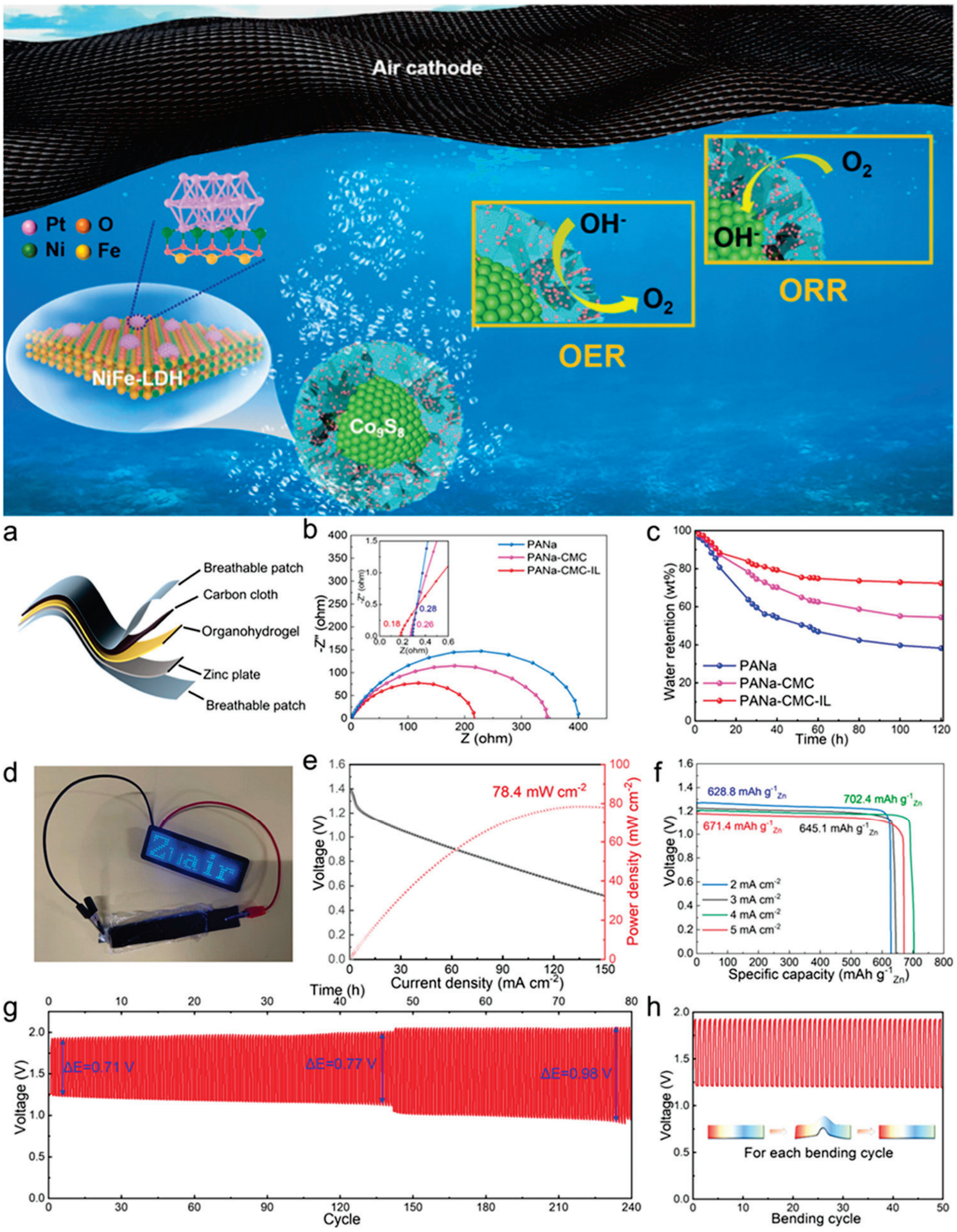

Figure 19. Design and performance of a flexible quasi-solid ZAB using NiFe-LDH@Co_9S_8 nanoflowers with Pt nanocrystals as bifunctional electrocatalysts. (**a**) Schematic of the overall FZAB configuration and its air cathode mechanism involving OER and ORR. (**b**) Nyquist plots comparing PANa, PANa-CMC, and PANa-CMC-IL hydrogels. (**c**) Water retention characteristics over time for each hydrogel type. (**d**) Photograph showing the FZAB powering an LED panel. (**e**) Discharge polarization curve and power density output of the battery. (**f**) Discharge profiles of the device at varying current densities. (**g**) Charge/discharge cycling stability at 2 mA/cm^2. (**h**) Charge/discharge behavior after repeated bending cycles, highlighting mechanical flexibility. Reproduced with permission [149].

In the ZAB application, the synthesized $ZnCo_2O_4$@NiMn-LDH (2:1) was employed as the air cathode [147]. It demonstrated a significantly lower overpotential of 390 mV at a current density of 50 mA/cm^2, outperforming pristine $ZnCo_2O_4$. The battery exhibited a peak power density of 43 mW/cm^2 and delivered a high specific capacity of 639 mAh/g. Notably, it maintained excellent stability, operating continuously for up to 200 h under repeated charge/discharge cycling. These results highlight the material's suitability for long-term and efficient OER catalysis in ZABs. The optimized Fe/CoLDH-based composite (CoL 2:1) was employed as a bifunctional cathode catalyst in a rechargeable ZAB [116].

The assembled battery exhibited a high open-circuit voltage (OCV) of 1.503 V and delivered a peak power density of 161 mW/cm^2. It achieved a specific discharge capacity of 804 mAh/gZn at 5 mA/cm^2 and a calculated energy density of 965 Wh/kg. Notably, the device maintained stable operation over 200 h with a minimal voltage gap of 0.76 V at 10 mA/cm^2, corresponding to a high voltage efficiency of 96%. Even under high current densities (up to 50 mA/cm^2), the system exhibited remarkable rate capability and durability, highlighting the catalyst's robustness and practical viability in real-world ZAB systems.

In application, the CoFe/Fe$_3$C@CN-900 served as the air cathode catalyst in both aqueous and all-solid-state ZABs [115]. The aqueous ZAB delivered a specific 795 mAh/g capacity, an energy density of 982 Wh/kg, and a maximum power density of 190 mW/cm^2, outperforming the benchmark Pt/C + RuO$_2$ catalyst. Additionally, it retained 96.5% current after 10 h in stability tests and displayed excellent charge/discharge cycling performance with minimal voltage hysteresis at 5 and 10 mA/cm^2. Solid-state ZABs also demonstrated competitive performance, with a specific capacity of 750 mAh/g and energy density of 929 Wh/kg, along with robust cycling stability, confirming their strong potential for practical applications. The Ni-CAT/NiFe-LDH/CNFs composite was used as a bifunctional catalyst at the air cathode of both liquid and solid-state ZABs [146]. Liquid ZABs demonstrated a high peak power density of 292.1 mW/cm^2, with an open-circuit voltage of 1.407 V, and superior cyclic stability up to 66 h with a low voltage gap. In solid-state flexible ZABs, it retained structural integrity under bending. It showed even better performance, reaching a power density of 299.48 mW/cm^2 and a cycle life of 30 h at a current density of 1 mA/cm^2. These results highlight its promising bifunctional catalytic activity and robust mechanical flexibility for advanced energy storage systems.

In applying ZABs, the Cu@Cu NWs@LDH composite was employed as the air cathode [210]. The assembled battery exhibited a high open-circuit potential of 1.336 V and achieved a peak power density of 179.3 mW/cm^2. It showed superior charge/discharge performance with a low potential gap of 0.852 V at 50 mA/cm^2. The battery maintained stable cycling performance for over 250 h at 10 mA/cm^2 with negligible voltage decay. The NiFe LDH coating on Cu nanowires offered high catalytic activity for OER and ORR, attributed to its enhanced surface area, conductivity, and corrosion resistance. The synthesized CoMn-LDH/NPGA was used as the air cathode in a rechargeable liquid ZAB, where it demonstrated outstanding bifunctional catalytic activity for both ORR and OER [231]. The ZAB showed an open-circuit voltage of 1.514 V and delivered a maximum power density of 206 mW/cm^2 at 226 mA/cm^2, surpassing the performance of Pt/C + IrO$_2$. It also achieved a high energy density and excellent rate capability, maintaining a discharge voltage of ~1.37 V across varied current densities. Impressively, it exhibited exceptional cycling stability over 72 h (432 cycles) with minimal voltage decay, attributed to the structural robustness of the 3D NPGA framework and uniform CoMn-LDH dispersion.

LDHs have emerged as highly versatile and tunable materials across a wide spectrum of battery chemistries, including LIBs, LSBs, NIBs, CIBs, ZIBs, and ZABs. Their unique 2D lamellar structures, high surface area, compositional flexibility, and anion exchange capacity enable exceptional electrochemical performance through enhanced ion diffusion, redox activity, and structural integrity. In LIBs and NIBs, LDH-based electrodes exhibit high specific capacities, excellent rate performance, and long-term cycling stability due to their ability to accommodate lithium or sodium ions via intercalation and conversion mechanisms. In LSBs, LDHs serve as cathode hosts, interlayers, and separator coatings, effectively suppressing polysulfide shuttling and catalyzing redox reactions, leading to outstanding capacity retention and coulombic efficiency. Their role in CIBs is expanding, with interlayer-engineered LDHs showing promising Cl$^-$ transport properties and structural robustness. Similarly, in ZIBs, LDHs contribute to superior zinc ion intercalation kinetics, energy density, and mechanical resilience, particularly in flexible and high-loading configurations. Moreover, in ZABs, LDHs, often combined with conductive or catalytic materials, act as efficient bifunctional electrocatalysts for oxygen evolution and reduction, offering low overpotentials, high power densities, and extended cycle life. Collectively, the multifunctional role of LDHs across these systems underscores their transformative potential in advancing next-generation, high-performance, and sustainable energy storage technologies. A comprehensive comparison of LDH-based materials in diverse battery systems, including their synthesis methods and electrochemical performance, is presented in Table 1.

Table 1. Summary of various LDH-based electrode materials, their synthesis methods, and electrochemical performance parameters for battery applications.

LDH Name	**Synthesis Procedure**	**Battery Type**	**Electrolyte**	**Specific Capacity (mAh/g)**	**Stability**	**Ref.**
Hv-Ni$_3$Mn$_{0.7}$Fe$_{0.3}$-LDH	Co-precipitation + Electrochemical Activation	ZIB	0.2 M ZnSO$_4$	328	85% capacity retention over 500 cycles at 1 A/g	[16]
NiCo-LDH nanocrystal@amorphousness core/shell structure (LDH200)	Co-precipitation followed by heat treatment at 200 °C	LIB	1.0 M LiPF$_6$	1821.3 (0.1 A/g)	~687.7 mAh/g at 0.5 A/g after 500 cycles (attrition rate: 0.092%)	[109]
MgAl-LDH@CNT	Co-precipitation	LSB	Li$_6$PS$_5$Cl	. . .	Stable over 200 cycles at 1 C with 4.0 mg/cm^2 S loading	[110]
NiFe-NO$_3$ LDH	Co-precipitation	NIB	1 M NaClO$_4$	972 (initial); 388 (60 cycles at 50 mA/g); 122 (500 cycles at 500 mA/g)	388 mAh/g after 60 cycles; 122 mAh/g after 500 cycles	[111]
NiFe-Cl LDH	Co-precipitation	CIB	0.5 M Bpy$_{14}$Cl/PC	27.1	64.2mAh/g after 200 cycles	[112]
Ni$_5$Ti-Cl LDH	Co-precipitation + anion exchange	CIB	0.5 M Bpy$_{14}$Cl	257.8	127.9 mAh/g after 1000 cycles @1 A/g	[114]
CoFe/Fe$_3$C@CN-900	MOF-derived + Co-precipitation	ZAB	0.1 M KOH	795	96.5% current retention after 10 h discharge	[115]
Fe/Co LDH (CoL 2:1)	Co-precipitation	ZAB	0.1 M KOH	804	200 h (307 cycles)	[116]
ZIF-67@NiCo-LDH	One-pot hydrothermal synthesis	LIB	1 M LiPF$_6$	1997.1 (initial), 807.9 (after 100 cycles)	Stable up to 100 cycles, excellent rate capability	[134]
NiFe2O4@NiCo-LDH	Two-step hydrothermal method (MOF-derived)	LIB	1 M LiPF$_6$	636.9	Stable after 100 cycles (636.9 mAh/g at 0.3 A/g), coulombic efficiency ~98%	[135]
Ni-Zn LDH intercalated with DS$^-$	Hydrothermal synthesis	LIB	1 M LiPF$_6$	850 at 0.5 A/g	850 mAh/g over 400 cycles	[136]
NiS$_2$/FeS$_2$@NC@NiFe LDH/FeO(OH)	Solvothermal followed by hydrothermal synthesis	LIB	1 M LiPF$_6$	709.9	709.9 mAh/g at 0.2 A/g after 200 cycles; 403.3 mAh/g at 1.0 A/g after 500 cycles	[137]
NiCo-LDH/MXene	Hydrothermal	LIB	1 M LiPF$_6$	1081 (at 100 mA/g)	100 cycles at 0.1 A/g with excellent capacity retention	[138]
Mg$_2$Al$_1$–CO$_3$-LDH	Hydrothermal synthesis	LIB	1 M LiPF$_6$	814	203.8 mAh/g after 300 cycles	[140]
NiCoOOH@CoLa-LDH (NC@CL)	Hydrothermal synthesis (2-step)	ZIB	1 M KOH + 5 mM ZnO	381.1	98% capacity retention after 2000 cycles	[141]

Table 1. *Cont.*

LDH Name	Synthesis Procedure	Battery Type	Electrolyte	Specific Capacity (mAh/g)	Stability	Ref.
NiCoMo-P150 LDH	Hydrothermal + Anion exchange + Temperature-differential phosphorus doping	CIB	0.5 M Bpy14Cl	363.4 (initial), 150.2 (stable)	800 cycles at 300 mA/g	[142]
NiAl-LDH@G	Atomic layer deposition + Hydrothermal	CIB	0.5 M Bpy14Cl	223.3	107 mAh/g after 500 cycles; 72 mAh/g after 120 days	[143]
$Mo_{0.3}NiCo_2$-Cl LDH	Hydrothermal synthesis + Ion exchange	CIB	0.5 M Bpy14Cl	352.5	159.7 mAh/g (after 300 cycles)	[144]
CoFe–Cl-LDH/CNT	Co-precipitation + Hydrothermal synthesis	CIB	1.0 M NaCl	190	125 mAh/g after 200 cycles	[145]
Ni-CAT/NiFe-LDH/CNFs	Hydrothermal synthesis + in situ MOF growth	ZAB	6 M KOH	. . .	66 h (liquid)/30 h (solid)	[146]
$ZnCo_2O_4$@NiMn-LDH (2:1)	Two-step hydrothermal	ZAB	6 M KOH	639	200 h cycling	[147]
NiCo-LDH/NCM@NF	Hydrothermal synthesis	ZAB	1 M KOH	685	Stable over 500 cycles	[148]
Pt-NiFe-LDH@Co_9S_8	Hydrothermal + Spontaneous-redox strategy	ZAB	6.0 M KOH/ 0.2 M $Zn(OAc)_2$	796.6	240 cycles (80 h, flex)	[149]
Co@NiFe-LDH	Two-step hydrothermal	ZAB	0.2 M $Zn(OAC)_2$ + 6 M KOH	652	90 h cycling with minor degradation	[150]
Ni_2Co-LDH/EG composites	Co-precipitation and Microwave irradiation	LIB	1 M $LiPF_6$	1880 (0.05 A/g); 919 (1 A/g)	~973 mAh/g after 100 cycles at 1 A/g	[152]
NiAl LDH	Hydrothermal	LIB	1 M $LiPF_6$	2586 (initial), 697 (400th cycle @ 0.5 A/g)	27.6% after 1400 cycles @ 1.0 A/g	[153]
L-CoNi-LDH/C	Laser-induced + Hydrothermal synthesis	LSB	1.0 M LiTFSI	1574 (initial), 1097 (100th)	503 mAh/g after 200 cycles @ 2 C	[154]
LDH@PSS (1:1.5)	Hydrothermal + Exfoliation + Self-assembly	LSB	1 M LiTFSI	1247.2 (initial), 1032.6 (after 200 cycles @ 0.2 C)	0.086% capacity decay per cycle over 200 cycles (0.2 C); 65.2% retention after 1000 cycles (1 C)	[155]
Vo-LDHs-MXenes	Self-growth aging	LSB	1.0 M LiTFSI	1549 (initial), 701 (after 300 cycles at 1 C)	300 cycles at 1.0 C, 0.084% decay/cycle	[156]
V_2O_5/Cys/FeNi-LDH	Hydrothermal + Reflux	LSB	1.0 M LiTFSI	1035.2 (initial), 920.1 (after 300 cycles)	88.9% retention after 300 cycles; 0.039% decay per cycle	[156]
NiFe-LDH@S	Hydrothermal	LSB	1 M LiTFSI	676 (initial), 386 (after 500 cycles at 2 C)	386 mAh/g after 500 cycles @2 C	[157]
NiAl-LDH@S	Hydrothermal	LSB	1 M LiTFSI	432 (initial), 238 (after 500 cycles at 2 C)	238 mAh/g after 500 cycles @2 C	[157]
ZnAl-LDH@S	Hydrothermal	LSB	1 M LiTFSI	357 (initial), 198 (after 500 cycles at 2 C)	198 mAh/g after 500 cycles @2 C	[157]

Table 1. *Cont.*

LDH Name	Synthesis Procedure	Battery Type	Electrolyte	Specific Capacity (mAh/g)	Stability	Ref.
NiCoAl-LDH	Hydrothermal + PECVD (for VG growth)	LSB	1.0 M LiTFSI with 1 wt.% $LiNO_3$	1182.4 (initial), 441.3 (after 750 cycles at 0.5 C)	0.0755% capacity decay per cycle (750 cycles at 0.5 C)	[158]
NiCr-Cl LDH/rGO	Hydrothermal + Ion Exchange	NIB	1 M $NaCF_3SO_3$	218 (200 cycles @ 100 mA/g)	34.5% capacity retention after 200 cycles	[159]
CoMoLDH@C-PDA-6	Hydrothermal + Polymerization + Carbonization	NIB	1 M $NaClO_4$	779.9 (initial); 310.9 (after 100 cycles)	70% retention after 100 cycles at 0.1 A/g	[163]
Co-Co LDH-derived $CoSe_2$@NHCNS@C	Hydrothermal synthesis + selenization + carbon coating	NIB	1 M $NaClO_4$	465.6 (initial), 373.8 (after 100 cycles)	373.8 mAh/g after 100 cycles; 325 mAh/g after 1000 cycles at 0.5 A/g	[164]
MCN-LDH@CP	Two-step hydrothermal	ZIB	3.0 M KOH	1.74 mAh/cm^2	97.8% @ 7000 cycles	[165]
ZnCo-LDH	Hydrothermal	Zn-ZnCo/Hybrid Zn	6 M KOH + 0.2 M $Zn(AC)_2$	2.5 mAh/cm^2	86% after 5000 cycles	[166]
NiCo LDH/MXene@NF	Electrodeposition	ZIB	1 M KOH	311.7	capacity retention of 88.6% after 10,000 cycles at 2 A/g	[203]
CoNi-LDH(v)	Electrochemical deposition + Electrochemical activation (ECA)	Aqueous and Solid-state ZIB	3 M $ZnSO_4$	225	53.9% after 900 cycles (aqueous); 47.22% after 1000 cycles (solid-state)	[204]
ZnAl-LDH@Zn	Electrochemical deposition	ZIB	3 M $ZnSO_4$	251.45	Stable after 1500 cycles	[172]
CoNi LDH(v)	Electrochemical deposition + CV activation	ZIB	1 M $ZnSO_4$	185	80% retention after 1000 cycles	[207]
NiCoS@NiCo-LDH	Hydrothermal + Electrodeposition	ZIB	6 M KOH	312	95.9% after 3000 cycles @ 20 mA/cm^2	[208]
Ni_3S_2/NiS@NiCo-LDH	Hydrothermal + Electrochemical deposition	ZIB	6 M KOH	434.5	116.7% after 5000 cycles	[209]
NiFe LDH on Cu NWs	Electrochemical deposition	ZAB	6 M KOH and 0.2 M zinc acetate	...	>250 h @ 10 mA/cm^2	[210]
NiCo-LDH	Sol–gel (Ni aerogel) + Solvothermal	LSB	1.0 M LITFSI	1238.4 (0.1 C); 805.8 (5.0 C)	647.1 mAh/g after 700 cycles at 5.0 C (0.018% decay/cycle)	[222]
NiCo–MOF/LDH	Solvothermal synthesis	LSB	1 M LITFSI	950 (after 200 cycles @ 1 C)	0.033% capacity decay per cycle; 633 mAh/g after 1000 cycles @ 1 C	[223]
NiCo-LDH	ZIF-67 template etching + melt-diffusion with sulfur	LSB	1.0 M LiTFSI	1540 @ 0.1 C, 485 @ 5 C	475 mAh/g after 500 cycles @ 1 C (78%)	[224]
$NiCo_2S_4$–NiS_2 NH@C	Ion exchange + in situ transformation	LSB	5 mM Li_2S_6	1207 at 0.2 C; 766 at 2 C	60.23% retention after 450 cycles at 1 C; 6.09 mAh/cm^2 at 5 mg/cm^2 sulfur loading	[225]
CuCo-LDH	Chemical etching (ZIF-67 template)	LSB	1 M LiTFSI	1262.8 (initial), 697.0 (after 500 cycles at 1 C)	500 cycles, 0.049% capacity decay per cycle	[226]
PPy@LDH-S	Ion exchange + solid-state melting + polymerization	LSB	1 M LiTFSI with 1% $LiNO_3$	907.2 (initial, 1 C); 633.4 after 500 cycles	0.06% capacity fading per cycle over 500 cycles	[227]

Table 1. *Cont.*

LDH Name	Synthesis Procedure	Battery Type	Electrolyte	Specific Capacity (mAh/g)	Stability	Ref.
$Ni_{0.8}Ca_{1.2}$Al-Cl LDH	Ion exchange	NIB	1.0 M $NaPF_6$	256.9 (200 cycles at 0.2 A/g)	102 mAh/g after 600 cycles at 2 A/g	[228]
$Co_{0.6}Ca_{1.4}$Al-Cl LDH	Ion exchange	NIB	1.0 M $NaPF_6$	292.8 (200 cycles at 0.2 A/g)	118.1 mAh/g after 600 cycles at 2 A/g	[228]
CoSn-LDH@MXene	Solvothermal + Ultrasonic	NIB	1 M $NaClO_4$	976.1 (0.1 A/g)	87.6% retention after 1000 cycles	[229]
Ni_3Ti-Cl LDH	Urea precipitation + anion exchange	CIB	0.5 M $PP_{14}Cl$	346.4	131.8 mAh/g over 200 cycles	[230]
CoMn-LDH/NPGA	Cross-linking gelation + Hydrothermal self-assembly + Freeze drying	ZAB	1 M KOH	…	72 h (~432 cycles) stable operation	[231]

5. LDHs in Supercapacitors

LDHs have attracted significant attention in electrochemical energy storage, particularly as electrode materials in supercapacitors, owing to their tunable chemical composition, two-dimensional layered structure, and abundant redox-active sites [18,182]. The distinctive crystal structure of LDHs features divalent and trivalent metal cations coordinated by hydroxyl groups with intercalated anions and water molecules. This architecture offers multiple pathways for charge storage through both surface redox reactions (pseudocapacitance) and ion intercalation mechanisms, as well as enabling the formation of the electric double layer (EDLC) at the electrode/electrolyte interface [262]. In particular, the exchangeable interlayer anions and the expansive interlayer spacing facilitate rapid diffusion of electrolyte ions, which is critical for achieving high-rate capabilities in supercapacitor applications. Structural modifications and composite strategies have been extensively exploited to enhance the electrochemical performance of LDH-based electrodes. Chemical modifications, such as doping with different metal ions (e.g., Ni, Co, Al, Mn) and anion intercalation, allow precise tuning of the redox properties and electrical conductivity [18,263]. For example, constructing NiCo-LDH microspheres derived from MOFs (Ni-MOFs) has significantly enhanced ion transport kinetics, reduced the charge transfer resistance, and increased the accessible electroactive surface area. Moreover, the integration of LDHs with conductive carbonaceous materials (e.g., graphene, CNTs) or conductive polymers has emerged as a promising strategy to overcome the intrinsic low electronic conductivity of LDHs, thereby improving the overall charge storage efficiency and cycling durability [264,265]. These composite strategies involve synergistic effects whereby the carbon matrix provides an effective conductive network while the LDH component contributes high pseudocapacitance from its Faradaic reactions [18,266].

Electrochemical performance metrics such as capacitance, cycling stability, and rate capability have been a primary focus in assessing the viability of LDH-based supercapacitors. High specific capacitances have been achieved by designing nanostructured LDH architectures that maximize ion diffusion and electron transfer; for example, ultrathin LDH nanosheets demonstrate significantly enhanced pseudocapacitive behavior due to the exposure to a high density of active sites [267]. The cycling stability of these materials is also improved by engineering composite structures that mitigate the typically observed volume changes and agglomeration during charge/discharge cycles [268,269]. Additionally, the rate capability, crucial for high-power applications, is enhanced when LDHs are integrated with conductive scaffolds, resulting in faster charge/transfer kinetics and high capacitance retention at increased current densities [263,266].

Hybrid LDH-based supercapacitors represent a sophisticated approach to delivering high energy and power density by synergistically combining materials that exhibit EDLC and pseudocapacitive behaviors. In hybrid devices, incorporating LDHs as pseudocapacitive components in conjunction with high-conductivity materials (such as MXenes, CNTs, or metal tellurides) has demonstrated promising improvements in energy and power performance [270,271]. For instance, the fabrication of hybrid architectures involving CuCo LDHs coated on conductive substrates, as well as the assembly of molecular-level heterostructures between titanium carbide MXene and Ni-Co-Al-LDH nanosheets, has led to devices capable of delivering rapid charge/discharge cycles while maintaining high specific capacitance and excellent cyclic stability [271,272]. These hybrid systems effectively leverage the ultrafast redox reactions of LDHs and the robust electrical conductivity of the secondary phases, making them attractive for applications in portable electronics and electric vehicles where both high energy and power demands are critical [270,271].

The application of LDHs in supercapacitors is underpinned by their unique layered structures that facilitate efficient charge storage via EDLC and pseudocapacitive mechanisms. The evolution of structural modifications and composite strategies, including the integration with conductive carbonaceous materials and the formation of hybrid heterostructures, has advanced the electrochemical performance of LDH-based devices in terms of high capacitance, improved cycling stability, and superior rate capability. These innovations pave the way for the next generation of high-energy and high-power supercapacitors. Shah et al. [89] reported that NiCoLDH-1@JAC-2 served as the positive electrode, while JAC-2 was employed as the negative electrode in an all-solid-state asymmetric HSC, using a PVA/KOH gel as the solid electrolyte. Figure 20a,b outlines the design and assembly of both symmetric and ASC devices based on JAC and NiCoLDH@JAC materials. The device demonstrated a specific capacitance of 750 F/g, with a specific capacity of 209 mAh/g at a current density of 0.5 A/g. Figure 20c–f demonstrates the electrochemical behavior of the NiCoLDH-1@JAC-2//JAC-2 HSC under different scan rates, potential windows, and current densities. It achieved a maximum energy density of 100 Wh/kg at a power density of 250 W/kg, significantly outperforming many conventional systems. The supercapacitor maintained excellent cyclic stability, with negligible performance degradation over repeated cycles. The synergistic interaction between the high surface area carbon scaffold and the electroactive LDH nanoflowers contributed to the remarkable electrochemical behavior.

The synthesized NiCo-LDH was employed as the positive electrode in an ASC with AC as the negative electrode, using PVA-KOH gel as the electrolyte [119]. Under optimal conditions (140 °C, 6 h, Ni/Co = 2:1), the device demonstrated a high specific capacitance of 400.2 C/g at 1 A/g. The ASC exhibited a maximum energy density of 51.59 μWh/cm^2 at a power density of 1.125 mW/cm^2. GCD profiles were highly symmetric, and impedance analysis revealed low internal resistance (0.861–0.915 Ω), indicating efficient charge transport. Furthermore, the device maintained 70% of its initial capacitance after 10,000 cycles, highlighting excellent cycling stability and long-term operational reliability. The CoNi LDH materials were employed as positive electrodes in HSC devices, with AC as the negative electrode and 2 M KOH as the electrolyte [232]. The CoNi LDH nanoflowers (NFs) demonstrated superior performance, delivering a specific capacity of 768.3 C/g at 1 A/g and maintaining 643.1 C/g at 10 A/g, compared to 669.3 C/g for nanosheets (NSs). The HSC assembled with CoNi LDH NFs//AC exhibited a high energy density of 37.1 Wh/kg at a power density of 748.0 W/kg while retaining 21.6 Wh/kg even at 7.12 kW/kg. Both HSCs showed excellent long-term cyclic stability, maintaining over 93% capacity retention after 4000 cycles at 10 A/g, demonstrating their strong potential as advanced battery-type materials in energy storage devices.

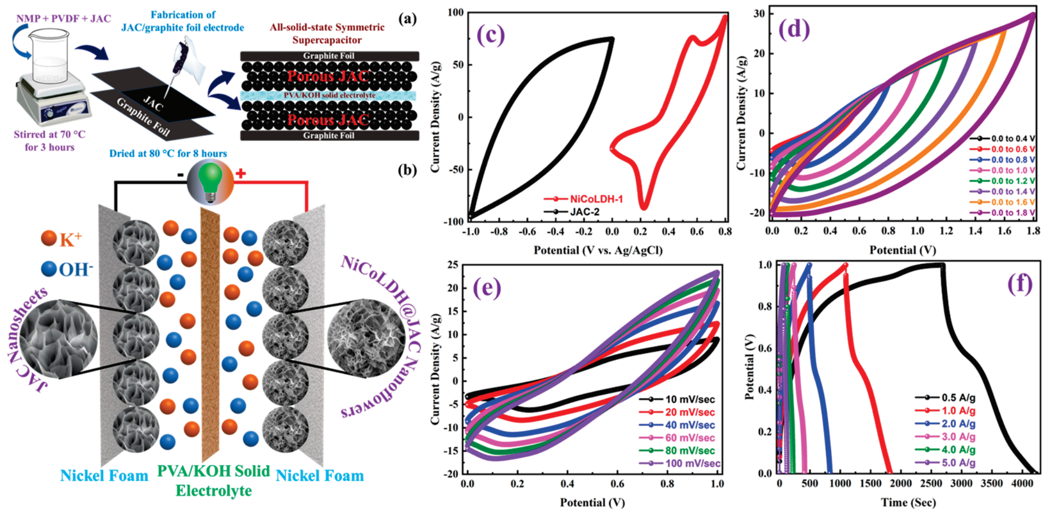

Figure 20. (**a**) Schematic overview of the fabrication process for JAC-based electrodes and assembly of the corresponding all-solid-state symmetric supercapacitor. (**b**) Diagram illustrating the configuration of the asymmetric HSC constructed using NiCoLDH@JAC and JAC electrodes. (**c**) CV curves of JAC-2 and NiCoLDH-1 electrodes measured in a three-electrode setup at a scan rate of 50 mV/s, (**d**) CV responses of the NiCoLDH-1@JAC-2//JAC-2 HSC at different operating potential windows (OPWs) at 50 mV/s, (**e**) CV curves of the same HSC recorded at various scan rates, and (**f**) GCD profiles of the HSC at different current densities. Reproduced with permission [89].

The electrochemical performance of the synthesized NiCo-LDH/NF (NCL3 for the optimized 6 h synthesis) was assessed in three-electrode and asymmetric two-electrode configurations [151]. In the three-electrode system with 1 M KOH, the NiCo-LDH served as the positive electrode, demonstrating a high specific capacitance of 1577 F/g at 1 mA/cm^2, with an energy density of 107.34 Wh/kg and a power density of 159.09 W/kg. Excellent cyclic stability was observed, with 96.17% retention after 5000 cycles. For the asymmetric device (NiCo-LDH/NF as positive and AC as negative electrode), the assembled AHSC device delivered an energy density of 38 Wh/kg and a power density of 1702 W/kg, retaining 76% capacitance after 2000 cycles, highlighting its practical viability for high-performance supercapacitor applications.

The synthesized NiCo-MOF@LDH-2 was employed as the positive electrode in an ASC device, with AC serving as the negative electrode and 2 M KOH as the electrolyte [233]. Electrochemical tests revealed excellent pseudocapacitive behavior with a high specific capacitance of 1873.9 F/g at 0.5 A/g and a maintained capacitance of 694.5 F/g at 20 A/g, indicating good rate capability. The ASC device (NiCo-MOF@LDH-2//AC) delivered an energy density of 49.8 Wh/kg at a power density of 422.4 W/kg and retained 21 Wh/kg even at 9318 W/kg, demonstrating superior energy/power performance. Furthermore, the device exhibited impressive cyclic stability with 83% capacitance retention after 10,000 cycles at 5 A/g, and coulombic efficiency of 99.3%, confirming its durability and practical viability. The synthesized NiCo-LDH/ACC composite was employed as a bifunctional electrode (cathode and anode) in a symmetric aqueous supercapacitor configuration with 1 M KOH as the electrolyte [234]. As a cathode, it achieved a high areal capacitance of 3770 mF/cm^2 at 1 mA/cm^2 and retained 79.5% of its capacity at 50 mA/cm^2 with 88% capacitance retention after 5000 cycles. As an anode, the electrode showed 1480 mF/cm^2 at 1 mA/cm^2, retaining 80% at 50 mA/cm^2 and demonstrating 100% stability after 10,000 cycles. The symmetric device delivered a high areal energy density of 0.352 mWh/cm^2 and a volumetric energy density of 5.61 mWh/cm^3, with a maximum power density of 559.5 mW cm^{-3}, maintaining performance over 15,000 cycles, indicating exceptional durability and fast ion/electron transport due to the amorphous, ultrathin architecture.

The synthesized NiCo-LDH-based heterostructure (S-NCCO) was employed as the positive electrode in an ASC, paired with AC as the negative electrode and PVA/KOH gel as the solid-state electrolyte [160]. The ASC device, configured as S-NCCO//AC, demonstrated exceptional performance, achieving a high specific capacitance of 3744.4 F/g at 1 A/g. It delivered an energy density of 92.3 Wh/kg and a power density of 750 W/kg, significantly outperforming comparable materials. Moreover, the device retained 87% of its capacitance after 5000 cycles at 10 A/g, indicating excellent long-term cycling stability and practical viability in energy storage applications. In supercapacitor applications, the CuCo LDH@Ni_3S_2 composite (specifically the CCNS-15 sample) was used as the positive electrode, while AC served as the negative electrode in an ASC configuration [211]. The device demonstrated exceptional areal capacitance (11.24 F/cm^2 at 5 mA/cm^2), an impressive energy density of 0.62 mWh/cm^2, and a power density of 8 mW/cm^2. Even after 6000 charge/discharge cycles, the ASC retained 72.2% of its initial capacitance, highlighting excellent cyclic stability. The superior electrochemical behavior was attributed to the composite's tremella-like structure and the synergistic interaction between CuCo LDH and Ni_3S_2, which enhanced charge transfer and ion diffusion pathways.

In the application section, the NFMM composite was used as a positive electrode in an ASC, paired with AC as the negative electrode and 6 M KOH as the electrolyte [161]. The device exhibited battery-type behavior with a remarkable specific capacitance of 2079.6 F/g at 1 A/g, and retained 85% of its capacitance after 5000 cycles. The assembled NFMM//AC ASC delivered a high energy density of 67.3 Wh/kg at a power density of 750.9 W/kg, and maintained 89% capacitance retention after 5000 cycles, showcasing excellent cycling stability. The synergistic interaction between NiFe-LDH, $MnCO_3$, and MXene enhanced conductivity, charge storage, and structural stability, affirming NFMM's suitability for high-performance supercapacitor applications. The $MnCo_2O_4$@FeCoNi-LDH/CC was used as the positive electrode and AC/CC as the negative electrode in an all-solid-state ASC device, with a PVA/KOH gel as the electrolyte [162]. The device exhibited exceptional electrochemical performance with a high specific capacitance of 145.2 F/g at 1 A/g, an energy density of 51.66 Wh/kg at a power density of 890.81 W/kg, and outstanding cyclic stability, retaining 90.3% capacitance after 10,000 charge/discharge cycles. Figure 21 demonstrates the electrochemical performance and practical application of the MnCo@FCN-LDH/CC//AC/CC ASC device, including stability, energy storage capability, and its ability to power an LED. These results highlight the material's potential in flexible and high-energy-density supercapacitor applications.

The vacancy-rich NiCo-LDH (designated as AL-LDH) was employed as the positive electrode in a magnesium-ion HSC (Mg-HSC), with VS_2 as the negative electrode and $MgSO_4$ as the electrolyte [212]. The AL-LDH electrode delivered a specific capacitance of 47.70 mAh/g (≈238.5 F/g) at 1 A/g in a two-electrode setup. The device achieved a high energy density of 48.44 Wh/kg and a power density of 937.49 W/kg, demonstrating excellent rate capability by retaining 4 mAh/g at 20 A/g. After 500 cycles, the device retained ~42% of its capacity, indicating moderate stability. These results highlight the effectiveness of defect engineering (via H vacancy formation) in boosting charge storage and delivery performance in LDH-based supercapacitor systems. The electrochemical performance of NiAl-LDH was explored by constructing an ASC with NiAl-LDH@CC as the positive electrode and AC cloth as the negative electrode, using 1 M KOH as the electrolyte [214]. The ASC exhibited excellent pseudocapacitive behavior with a high specific capacitance of 310 mF/cm^2, corresponding to an energy density of 51.67 μWh/cm^2 and a power density of 913.84 μW/cm^2 at a current density of 0.2 mA/cm^2, maintaining a stable operating voltage of 1.6 V. The device demonstrated outstanding long-term durability with 90% capacitance retention over 10,000 cycles and an average coulombic efficiency of 98.9%, emphasizing the suitability of NiAl-LDH@CC for high-performance, flexible energy storage systems. NiAl LDH was employed as the positive electrode in an ASC configuration, paired with AC or graphene as the negative electrode [167]. The ASC devices demonstrated excellent performance, such as a specific capacitance of 214.4 F/g, energy density of up to 76.23 Wh/kg, and power density of 1127.03 W/kg, depending on the configuration. These devices maintained outstanding cycling stability, retaining 91.4% to 95.84% of their original capacitance after 5000–10,000 cycles at high current densities, showcasing the LDH's potential for long-term energy storage applications.

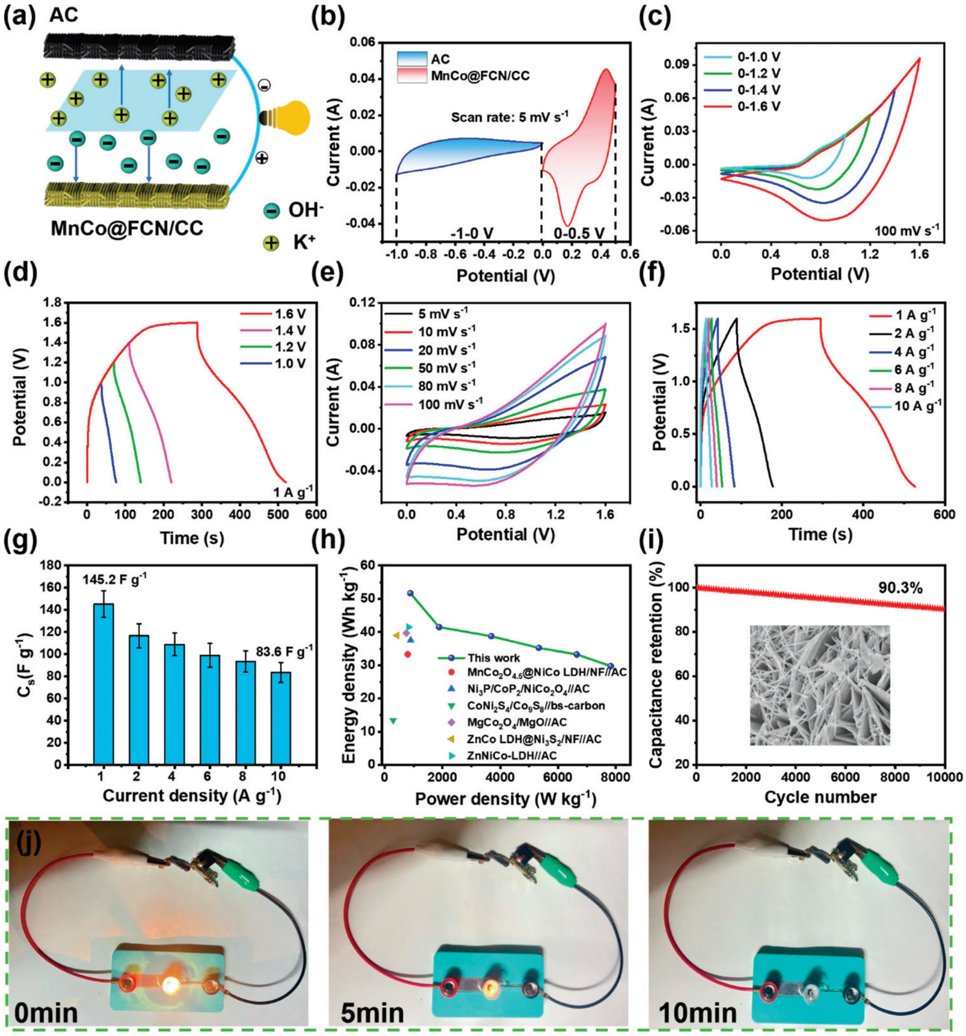

Figure 21. (**a**) Illustration of the MnCo@FCN-LDH/CC//AC/CC ASC setup. (**b**) CV comparison of AC and MnCo@FCN-LDH/CC electrodes at 5 mV/s. (**c**) CV curves of the ASC device at various voltages from 0–1.0 V to 0–1.6 V at 100 mV/s. (**d**) GCD curves at 1 A/g under the same voltage range. (**e**,**f**) CV and GCD performance of the device at 0–1.6 V. (**g**) Specific capacitance at different current densities. (**h**) Ragone plot comparing energy and power density with previous reports. (**i**) Cycling stability over 10,000 cycles at 1 A/g. (**j**) Digital photographs showing the device powering an LED for different durations. Reproduced with permission [162].

The optimized MP2 material, phosphorized MoB@NiCo-LDH with phosphorus vacancies, was employed as the positive electrode in an ASC device, with AC used as the negative electrode and 3 M KOH as the electrolyte [168]. The device exhibited outstanding electrochemical performance, including a high specific capacitance of 112.52 F/g at 1 A/g (two-electrode configuration), a maximum energy density of 39.91 Wh/kg at a power density of 948.25 W/kg, and an excellent power density of 7876.76 W/kg at 20.62 Wh/kg.

Furthermore, the device maintained 78.76% of its capacitance after 5000 cycles, demonstrating excellent cycling stability. These results highlight the synergistic effect of heterojunction formation and phosphorus vacancy engineering in enhancing charge transport kinetics and redox reactivity, thereby boosting the practical application potential of LDH-based electrodes in advanced energy storage systems. The NCS@CA heterojunction was employed as the positive electrode in a light-assisted ASC, with AC as the negative electrode and 3 M KOH as the electrolyte [236]. Under illumination, the device exhibited a remarkable specific capacitance of 112.2 F/g, a high energy density of 35.1 Wh/kg at a power density of 751.2 W/kg, and maintained 97.7% of its initial capacitance after 10,000 cycles, demonstrating excellent cyclic stability. Due to the semiconductor nature of NCS and LDH, the synergistic photoelectrochemical effect further enhanced charge separation and electrochemical kinetics, leading to substantial performance improvement over non-illuminated conditions.

In supercapacitor applications, the synthesized Te-NiMn LDH was employed as the positive electrode in a hybrid device, with AC as the negative electrode [169]. The resulting Te-NiMn LDH/C-MXene/NF//AC device achieved an impressive specific capacitance of 202.6 F/g at 2 A/g in a two-electrode configuration, along with a high energy density of 52.3 Wh/kg and a maximum power density of 6452 W/kg. Long-term cycling stability tests demonstrated excellent performance, with 77.3% capacitance retention after 10,000 cycles. The electrochemical performance of the Te-NiMn LDH/C-MXene/NF//AC device is illustrated in Figure 22. As shown in Figure 22a, the CV curves reveal that the Te-NiMn LDH/C-MXene/NF electrode exhibits a significantly higher current response than the AC electrode, indicating better electrochemical activity. Figure 22b presents CV measurements under different voltage ranges, showing that the area under the curve increases with higher potential windows, which reflects enhanced energy storage capacity. Figure 22c shows CV curves at various scan rates (5 to 50 mV/s) for a fixed voltage window of 1.5 V. The shapes of the curves remain consistent, suggesting good rate capability and reversibility. Figure 22d shows the GCD curves at different current densities, where the discharge time decreases with increasing current, typical of pseudocapacitive behavior. Long-term cycling performance is assessed in Figure 22e, with the device retaining 77.3% of its initial capacitance after 10,000 cycles at 5 A/g, indicating excellent stability. Finally, Figure 22f compares GCD curves before and after cycling. The slight change in shape further confirms the material's durability over extended use. These results highlight the synergistic enhancement due to CTAB-modified MXene conductivity and Te doping, which collectively facilitate improved redox kinetics, higher charge storage, and structural integrity over prolonged cycling.

The NC@CL nanosheet electrode was employed as the positive electrode in an ASC with AC as the negative electrode in a 2 M KOH electrolyte [141]. The NC@CL electrode delivered a high specific capacitance of 213 F/g at 0.2 A/g in the two-electrode device configuration, showcasing superior electrochemical performance due to its hierarchical nanostructure. The device achieved an energy density of 66.56 Wh/kg at a power density of 148.83 W/kg, maintaining 88.1% capacitance retention over 20,000 cycles, indicating excellent stability and reversibility. The enhanced performance is attributed to the synergistic interaction between NC and CL, large surface area, and efficient ion diffusion through the mesoporous framework.

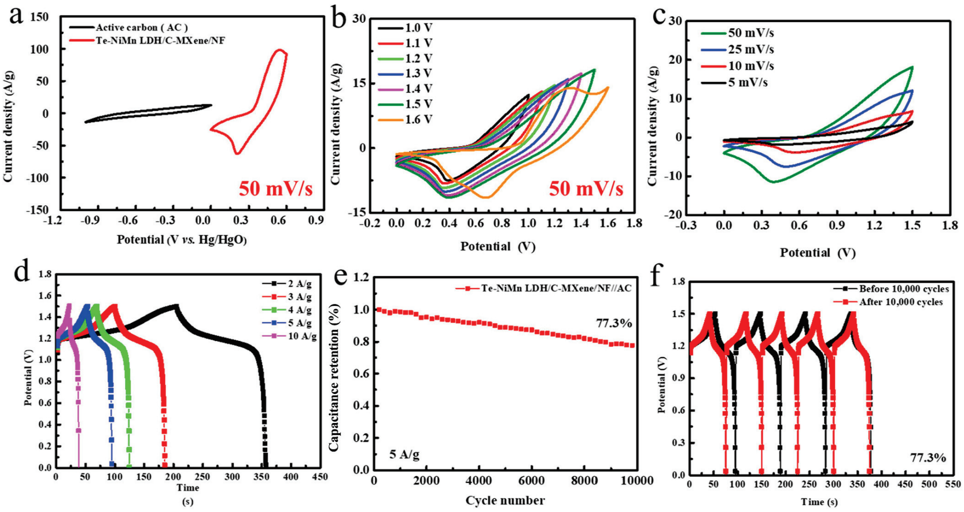

Figure 22. (**a**) CV comparison of Te-NiMn LDH/C-MXene/NF and AC electrodes at a scan rate of 50 mV/s. (**b**) CV profiles of Te-NiMn LDH/C-MXene/NF//AC device recorded under varying potential windows. (**c**) CV curves at different scan rates within a fixed voltage range of 1.5 V. (**d**) GCD curves at multiple current densities. (**e**) Cycling stability test showing capacitance retention after 10,000 cycles at 5 A/g. (**f**) GCD comparison before and after 10,000 charge/discharge cycles to evaluate long-term durability. Reproduced with permission [169].

The synthesized CF/CRBI-NiCo-LDH was employed as the positive electrode, while AC-coated carbon felt (CF/AC) was the negative electrode in an ASC [215]. The device utilized a cellulose separator and 6 M KOH aqueous electrolyte. In a two-electrode configuration, the supercapacitor achieved an impressive specific capacitance of 167.85 F/g at 0.5 A/g, with a high energy density of 57.2 Wh/kg and power density of 820 W/kg. Furthermore, the device retained 89% of its capacitance after 3000 cycles, highlighting excellent cycling stability and mechanical integrity. Figure 23a illustrates the coral reef-inspired structure of the CF/CRBI-NiCo-LDH electrode, promoting strong binding and fast redox transitions. CV curves (Figure 23b) confirm pseudocapacitive behavior with good rate capability, while GCD profiles (Figure 23c) show high coulombic efficiency across current densities. The specific capacitance trend (Figure 23d) indicates excellent rate performance, and the Ragone plot (Figure 23e) highlights the device's superior energy and power densities. The vertically grown nanoflake structure enhanced the charge storage through efficient ion transport and minimal resistance, confirmed by EIS and CV.

In the application as a supercapacitor, NiCo-LDH@TAC600-0 composite was used as the positive electrode, and tannin-derived AC (TAC600-2) served as the negative electrode in an ASC configuration with 6 M KOH as the electrolyte [237]. The device achieved a specific capacitance of 1250 F/g (three-electrode) and excellent performance in a two-electrode system, delivering a maximum energy density of 30.8 Wh/kg at a power density of 800 W/kg. Moreover, it demonstrated a stable cycle life with 72.5% capacitance retention after 5000 cycles at a high current density of 10 A/g. The sea urchin-like morphology contributed to a high rate of performance (82.8%) and facilitated fast ion/electron transport, validating its effectiveness in high-performance energy storage devices. In ASC configuration, CoNi LDH and its sulfurized derivatives were used as the positive electrode, while commercial AC was the negative electrode [235]. Figure 24a presents the synthesis and performance of the CoNiS-50-based electrode, highlighting its formation via sequential cation and anion exchange reactions to produce a flower-like CoNiS nanostructure. Among the synthesized materials, CoNiS-50 exhibited the most promising electrochemical performance, achieving a high specific capacitance of 150 F/g in the two-electrode configuration. The device delivered a maximum energy density of 37.8 Wh/kg at a power density of

750 W/kg. Furthermore, as shown in Figure 24a, the CoNiS-50-based ASC demonstrated excellent cycling stability, retaining 92.2% of its initial capacitance after 10,000 cycles at 10 A/g, attributed to the stabilized microstructure facilitated by residual $Mg(OH)_2$ and improved intrinsic conductivity from sulfur doping. Jia et al. [273] engineered NiCo-LDH/$NiCo_2S_4$ nanotube arrays modified with BPQDs, achieving an ultra-high specific capacitance of 2938.2 F/g, energy density of 133.7 Wh/kg at 800 W/kg, and 76.5% retention after 10,000 cycles. Figure 24b provides a visual overview of the energy storage mechanism. It outlines how charge is stored and transferred during electrochemical reactions, typically involving a combination of surface adsorption, redox reactions, and ion diffusion. This mechanism plays a key role in determining the overall performance of the electrode material, including its capacity, rate capability, and cycling stability. Figure 24c presents the design of the NiCo-LDH/$NiCo_2S_4$/BPQD//AC ASC. The electrochemical behavior of each electrode is shown in Figure 24d, where the CV curves confirm that the positive electrode has significantly higher redox activity than the AC negative electrode. Figure 24e displays CV curves at various voltage windows, indicating the device can operate stably up to 1.7 V. Figure 24f shows how the CV shape changes with increasing scan rates, suggesting good rate capability. The GCD curves in Figure 24g confirm that the device delivers longer discharge times at lower current densities. Finally, Figure 24h shows that the specific capacitance decreases as the current density increases, which is a typical trend in supercapacitor behavior.

Khalafallah et al. [213] developed Zn/CoLa LDH nanoarray-on-nanoarray electrodes using electrodeposition, achieving a specific capacitance of 269.4 F/g, an energy density of 59.9 Wh/kg at 800 W/kg, and a stability of 86.4% over 12,000 cycles in an ASC device. Liu et al. [162] synthesized $MnCo_2O_4$@FeCoNi-LDH on CC, achieving a high specific capacitance of 2235 F/g, an energy density of 51.66 Wh/kg at 890.81 W/kg, and 92.9% retention after 10,000 cycles in an ASC device. Luo et al. [274] prepared N-doped ZnNi-LDH via one-step hydrothermal synthesis, demonstrating a specific capacitance of 1265.7 C/g (~351.6 F/g), energy density of 64.6 Wh/kg at 850 W/kg, and excellent long-term cycle life when used with AC. Wei et al. [275] developed BPQD-embedded NiCoCu-LDH with a porous structure, reaching a specific capacitance of 1810.6 F/g, an outstanding energy density of 202.2 Wh/kg at 800 W/kg, and retained 81.4% capacity after 10,000 cycles. Moradi et al. [276] created a partially sulfurized CoMn-LDH/CoMn-S heterostructure, showing a capacity of 792.4 C/g (~220 F/g), energy density of 82.63 Wh/kg, power density up to 10,998 W/kg, and 94% stability over 6000 cycles. Wang et al. [277] introduced Ce into NiCo LDH@PBAs multi-core/shell structure, yielding a specific capacitance of 1847 F/g, energy density of 99.8 Wh/kg at 1283 W/kg, and 95.7% stability over 10,000 cycles.

Optimization strategies for LDH cathode materials in supercapacitors involve several synergistic approaches. Firstly, element doping, such as scandium doping, has promoted a superlong activation process and enhanced cycling durability while modifying the intrinsic electronic properties [278]. Secondly, tailoring the synthesis conditions to control the nanoscale morphology, including the design of hollow and quantum-layered structures, significantly improves ion diffusion and charge storage capability [119,243]. Modifying the intercalated anions and integrating LDHs with conductive substrates further optimizes electron transfer and overall capacitance performance [119,279]. These optimization methods, thus, address the challenges of moderate energy density and rate capability by enhancing both the redox activity and structural stability of LDH cathodes, ensuring improved electrochemical outcomes for supercapacitor applications [243,279].

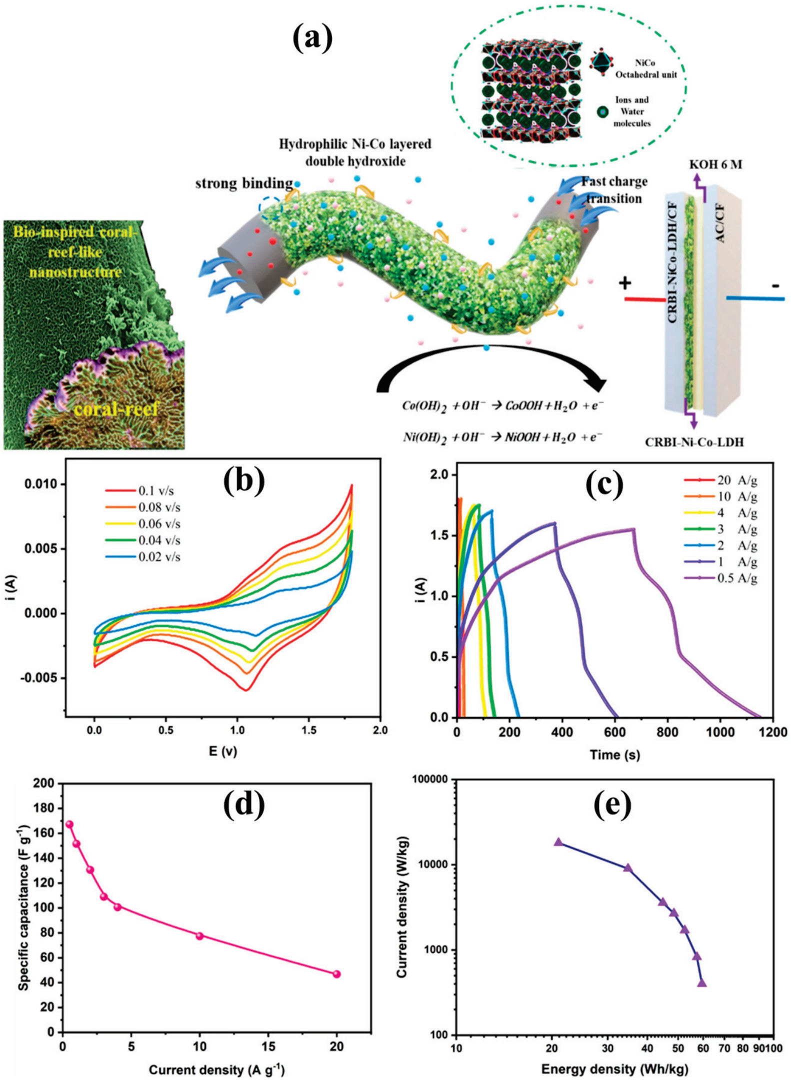

Figure 23. (**a**) Schematic illustration of the enhanced electrochemical charge storage mechanism in the electrosynthesized CF/CRBI-NiCo-LDH electrode, featuring a coral reef-inspired nanostructure that promotes strong binding, fast charge transfer, and redox reactions of Ni and Co hydroxides. (**b**) CV curves and (**c**) GCD profiles of the CF/CRBI-NiCo-LDH||CF/AC HSC at various scan rates and current densities. (**d**) Specific capacitance as a function of current density, and (**e**) Ragone plot comparing energy and power densities of the hybrid device. Reproduced with permission [215].

LDHs have emerged as highly effective electrode materials for supercapacitors, owing to their unique two-dimensional structure, tunable composition, and abundance of electroactive redox sites that support both pseudocapacitive and electric double-layer charge storage mechanisms. Their exceptional electrochemical behavior is attributed to the synergistic effects of compositional tailoring, such as metal-ion doping and anion intercalation, and advanced structural engineering, including nanosheet design, hierarchical porosity, and vacancy modulation. Integration with conductive matrices like carbon nanotubes, graphene, MXenes, and conductive polymers has been pivotal in mitigating LDHs' intrinsic low conductivity while enhancing rate capability, specific capacitance, and cycling durability. Particularly in asymmetric and hybrid supercapacitor configurations, LDHs paired with carbon-based or sulfide materials have demonstrated remarkable energy and power densities, extended cycle life, and mechanical robustness. Recent innovations such as heterostructures, phosphorization, photoelectrochemical enhancement, and defect engineering have pushed LDH-based devices toward practical viability in flexible, wearable, and high-performance energy storage systems. The continued development of LDH-based composites is central to advancing next-generation supercapacitors with superior energy density, fast charge/discharge kinetics, and long-term stability. A detailed summary of LDH-based materials applied in supercapacitor devices, highlighting their fabrication methods, device architecture, and electrochemical performance, is provided in Table 2.

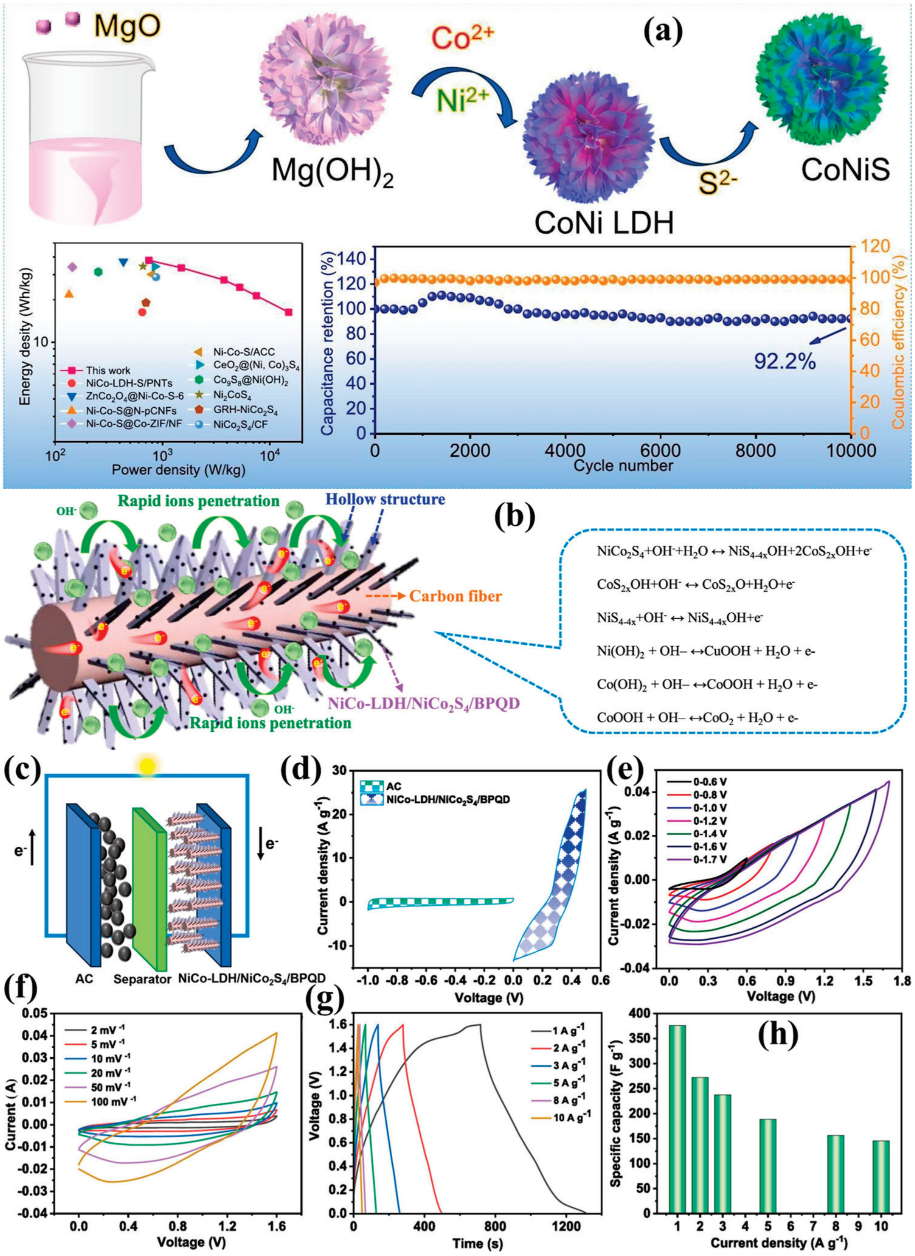

Figure 24. (**a**) An illustration shows the stepwise synthesis of CoNiS via combined cation and anion exchange, along with the energy and power density comparison of the CoNiS-50-based ASC and its cycling performance at 10 A/g. Reproduced with permission [235]. (**b**) Schematic representation illustrating the energy storage mechanism involved in the electrochemical process. (**c**) Schematic representation of the assembled NiCo-LDH/$NiCo_2S_4$/BPQD//AC ASC device. (**d**) CV curves of the NiCo-LDH/$NiCo_2S_4$/BPQD positive electrode and AC negative electrode measured at 2 mV/s. (**e**) CV profiles of the full device at varying voltage windows recorded at 100 mV/s. (**f**) CV curves at different scan rates ranging from 2 to 100 mV/s. (**g**) GCD curves at different current densities. (**h**) Specific capacitance values derived from the GCD results at various current densities. Reproduced with permission [273].

Table 2. Overview of LDH-based supercapacitor electrode materials with corresponding synthesis techniques, electrode configurations, and electrochemical performance metrics.

LDH Synthesis Procedure	Positive Electrode	Negative Electrode	Electrolyte	Specific Capacitance (F/g)	Energy Density (Wh/kg)	Power Density (W/kg)	Stability (%, No. of Cycles)	Ref.
Hydrothermal synthesis	NiCoLDH-1@JAC-2	JAC-2	PVA/KOH	750	100	250	95%, 10,000	[89]
Hydrothermal synthesis	NC@CL nanosheets	AC	1 M KOH	213	66.56	148.83	88%, 20,000	[141]
Hydrothermal synthesis	NiCo-LDH	AC	PVA/KOH	400.2 C/g	51.59 μWh/cm^2	1.125 mW/cm^2	70%, 10,000	[119]
Hydrothermal synthesis	Ni–Co LDH/NF (NCL3)	AC	1 M KOH	107	38	1702	76%, 2000	[151]
Hydrothermal + TA etching + sulfurization	S-NCCO (NiCo-LDH on S-ZIF-67)	AC	PVA/KOH	295	92.3	750	87%, 5000	[160]
Hydrothermal	NiFe-LDH/MnCO$_3$/MXene	AC	6 M KOH	215	67.3	750.9	89%, 5000	[161]
Hydrothermal synthesis	MnCo$_2$O$_4$@FeCoNi-LDH/CC	AC/CC	6 M KOH	145.2	51.66	890.81	90.3%, 10,000	[162]
Electrodeposition	NiAl LDH-rGO	Fe$_2$O$_3$-rGO	2 M KOH	214.4	76.23	800	95%, 5000	[167]
Hydrothermal synthesis + Phosphorization + NaBH$_4$ reduction	MP2 (MoB@NiCoP)	AC	3 M KOH	112.52	39.91	948.25	78.76%, 5000	[168]
Hydrothermal + Te soaking	Te-NiMn LDH/C-MXene/NF	AC	6 M KOH	202.6	52.3	6452	77.3%, 10,000	[169]
Two-step electrodeposition	CuCo LDH@Ni$_3$S$_2$	AC	3 M KOH	11.24 F/cm^2	0.62 mWh/cm^2	8 mW/cm^2	72.2%, 6000	[211]
Electrodeposition + Electrochemical Activation	Hv-rich NiCo-LDH	VS$_2$	1 M KOH	238.5 F/g	48.44	937.49	42%, 500	[212]
Electrodeposition of CoLa LDH nanoarrays followed by Zn^{2+} doping	Zn/CoLa LDH	AC	3 M KOH	269.4	59.9	800	86.4%, 12,000	[213]
Electrochemical deposition	NiAl-LDH@CC	CC	1 M KOH	310	51.67	913.84	90%, 10,000	[214]
Electrochemical deposition	CF/CRBI-NiCo-LDH	CF/AC	6 M KOH	167.85	57.2	820	89%, 3000	[215]
Solvothermal synthesis	CoNi LDH nanoflowers	AC	2 M KOH	768.3 C/g @ 1 A/g	37.1	748.0	93.7%, 4000	[232]
Solvothermal	NiCo-MOF@LDH-2 nanosheets	AC	2 M KOH	1873.9	49.8	422.4	83%, 10,000	[233]
Ion exchange	NiCo-LDH/ACC	NiCo-LDH/ACC	3 M KOH	876 mF/cm^2	0.352 mWh/cm^2	559.5 mW/cm^3	94.9%, 15,000	[234]
Cation/anion exchange	CoNiS-50	AC	6 M KOH	150	37.8	750	92.2%, 10,000	[235]
Two-step solvothermal	NCS@CoAl-LDH	AC	3 M KOH	112.2	35.1	751.2	97.7%, 10,000	[236]
Microwave hydrothermal synthesis	NiCo-LDH@TAC600-0	TAC600-2	6 M KOH	1250 (3-electrode)	30.8	800	72.5%, 5000	[237]

Table 2. *Cont.*

LDH Synthesis Procedure	Positive Electrode	Negative Electrode	Electrolyte	Specific Capacitance (F/g)	Energy Density (Wh/kg)	Power Density (W/kg)	Stability (%, No. of Cycles)	Ref.
Solvothermal synthesis followed by BPQD modification and hydrothermal sulfidation	NiCo-LDH/NiCo2S4/BPQD	AC	6 M KOH	376.1	133.7	800	76.5%, 10,000	[273]
Hydrothermal synthesis using 2-methylimidazole for N-doping	N-doped ZnNi-LDH	AC	3 M KOH	351.6	64.6	850	85.6%, 10,000	[274]
Precipitation and hydrothermal method with BPQD anchoring on CC	NiCoCu-LDH/BPQD	AC	6 M KOH	568.7	202.2	800	81.4%, 10,000	[275]
Electrochemical deposition followed by partial hydrothermal sulfidation	CoMn-LDH/CoMn-S	AC	3 M KOH	201	82.63	985	94%, 6000	[276]
Core/shell formation using Ce bridging between NiCo LDH and PBAs	NiCo-Ce@PBAs	AC	1 M KOH	222.3	99.8	1283	95.7%, 10,000	[277]

6. LDHs in Electrochemical Hydrogen Production

Hydrogen is a key clean energy carrier in the shift toward sustainable, low-carbon systems due to its high energy density, zero-emission profile, and broad applicability across sectors [280]. Efficient and affordable hydrogen production, particularly via water electrolysis, relies on effective catalysts for the HER and OER [281]. While noble metals like Pt, RuO_2, and IrO_2 offer excellent performance, their cost and scarcity limit widespread use [282]. LDHs have emerged as promising alternatives, thanks to their tunable brucite-like layered structure, high surface area, and rich active sites [283]. Their general formula, $[M^{2+}{}_{1-x}M^{3+}{}_{x}(OH)_2]^{x+}(A^{n-})_{x/n}\cdot yH_2O$, reflects their compositional flexibility, allowing precise control over layer charge, interlayer spacing, and anion content. LDHs also exhibit favorable redox behavior and surface characteristics, while modifications such as metal doping or hybridization with conductive materials can overcome their low intrinsic conductivity [284]. These properties make LDHs strong candidates for next-generation electrocatalysts in hydrogen production.

Pt-based catalysts are widely regarded as the benchmark for HER due to their exceptionally low overpotentials and high exchange current densities across a broad pH range. However, advanced LDH-based catalysts, particularly NiFe-LDH and CoFe-LDH, have emerged as competitive alternatives, especially under alkaline conditions. These LDHs can achieve overpotentials within 50–100 mV of Pt/C at a current density of 10 mA/cm^2, showcasing promising catalytic efficiency at a significantly reduced material cost [20,285,286]. In terms of stability, LDH catalysts exhibit excellent durability in alkaline electrolytes, maintaining over 90% of their initial performance after extended testing periods exceeding 50–100 h, whereas Pt-based catalysts, although stable in acidic environments, are prone to degradation in alkaline media. Furthermore, the use of earth-abundant and low-cost transition metals in LDHs provides a major economic advantage over expensive and scarce platinum. Nevertheless, LDHs still face limitations such as relatively lower electrical conductivity and reduced HER kinetics in acidic media, which currently limit their direct application in proton exchange membrane (PEM) electrolyzers [287]. Various strategies, including hybridization with conductive materials and defect engineering, are actively being explored to overcome these challenges [288].

6.1. Fundamentals of Electrochemical Hydrogen Production

Hydrogen production via water electrolysis involves passing an electric current through electrodes immersed in an electrolyte, triggering two key half-reactions: the HER at the cathode and the OER at the anode. Thermodynamically, water splitting requires a minimum of 1.23 V at standard conditions (25 °C, 1 atm), but in practice, a higher voltage (typically 1.8–2.0 V) is needed due to kinetic barriers and system resistances [289,290]. This additional energy input is known as the overpotential (η), caused by factors like charge transfer resistance, bubble formation, and ion diffusion limitations. Lowering η is critical for enhancing efficiency, often achieved by using advanced electrocatalysts that optimize interactions with H^+ or H_2O molecules. HER is a multi-step, pH-dependent process influenced by electrolyte type. In acidic media, H^+ ions are reduced via the Volmer (adsorption), Heyrovsky (electrochemical desorption), or Tafel (recombination) steps. In basic conditions, water molecules act as proton sources, undergoing similar steps but with a higher energy barrier due to stronger H–O bonds [291]. The general HER mechanism is described by Equations (1)–(6) and illustrated in Figure 25.

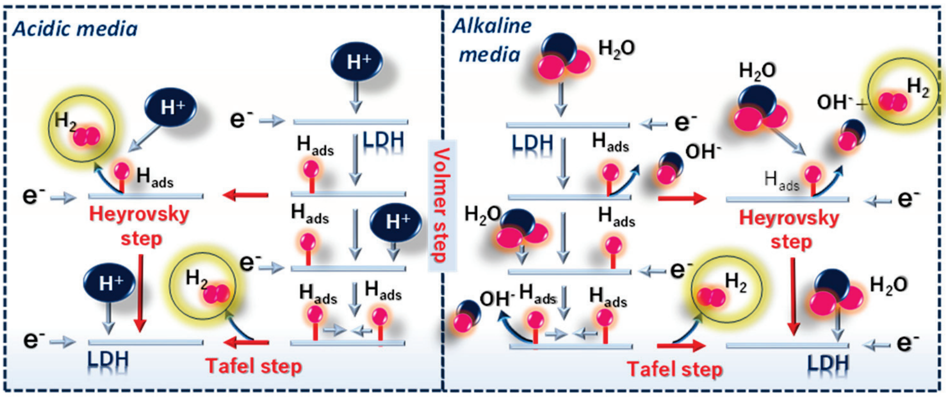

Figure 25. Schematic illustration of Volmer, Tafel, and Heyrovsky steps for HER in acidic and alkaline media.

Acidic HER:

$$H^+ + e^- \rightarrow H^* \text{ (Volmer)} \tag{1}$$

$$H^* + H^+ + e^- \rightarrow H_2 \text{ (Heyrovsky)} \tag{2}$$

$$H^* + H^* \rightarrow H_2 \text{ (Tafel)} \tag{3}$$

Alkaline HER:

$$H_2O + e^- \rightarrow H^* + OH^- \text{ (Volmer)} \tag{4}$$

$$H^* + H_2O + e^- \rightarrow H_2 + OH^- \text{ (Heyrovsky)} \tag{5}$$

$$H^* + H^* \rightarrow H_2 \text{ (Tafel)} \tag{6}$$

Due to slower kinetics in alkaline media, developing efficient electrocatalysts, such as composition/doping/interfacial engineering, etc., in LDHs is vital to lower overpotentials and enhance reaction rates, especially under non-acidic conditions [284,292]. Consequently, extensive research has turned toward low-cost, earth-abundant alternatives. Strategies such as carbon integration have improved conductivity and charge transfer, enhancing HER performance. Non-noble metal-based materials, including phosphides, sulfides, nitrides, borides, oxides, hydroxides, and especially LDHs, have gained prominence as bifunctional catalysts. Tailoring the composition, morphology, and electronic structure of LDHs through doping, defect engineering, and heterostructure construction has proven highly effective in enhancing their intrinsic activity and charge transfer efficiency for HER.

6.2. Mechanistic Role of LDHs Catalysts in Electrochemical HER

LDHs play a critical mechanistic role in HER due to their unique lamellar structure and tuneable composition. The brucite-like layers composed of divalent and trivalent metal cations create a high density of active sites and favorable charge environments that facilitate proton adsorption and electron transfer during HER. The metal composition significantly influences the catalytic behavior; for instance, incorporating transition metals like Ni, Co, or Fe enhances redox activity and electron conductivity, while synergistic interactions between metal centers modulate the hydrogen binding energy. Additionally, the interlayer anions and hydration layers contribute to ion transport and surface reactivity. HER performance of LDHs is strongly pH-dependent. In acidic media, LDHs often face stability challenges but can support HER through proton reduction if properly engineered. In neutral or alkaline environments, LDHs exhibit better structural durability, and the HER mechanism proceeds via water dissociation, making the Volmer step rate-limiting. Modifying the metal layers or coupling with conductive supports improves activity across all pH ranges. Among various electrocatalysts developed for water splitting, LDHs have gained considerable attention due to their tuneable composition, abundant active sites, and structural versatility [7]. While traditionally more active toward OER, several LDH systems have been tailored to exhibit excellent HER performance, especially in alkaline media [293,294]. Binary LDHs such as NiCo-LDH, NiMn-LDH, and CoMn-LDH have shown promising HER activity due to their redox flexibility and enhanced conductivity [295–297]. NiFe-LDH, though more renowned for OER, can be modified to support HER when integrated with conductive or catalytically active phases [298]. Ternary and doped LDHs, including NiCoFe-LDH, NiFeMn-LDH, and NiMo/NiFe-LDH, further enhance HER performance through synergistic electronic effects and optimized adsorption of intermediates [299–301]. Doping with elements like Cu, Mo, and W modulates the electronic structure, increases conductivity, and facilitates water dissociation [302–304]. Additionally, heterostructures such as NiFe-LDH@NiCoP, NiFe-LDH/NiS_2/VS_2, and LDH hybrids with MXene or graphene provide an ideal platform by coupling HER-active phases with conductive supports, promoting rapid charge transfer and improved stability [185,305,306]. These tailored LDH-based materials collectively demonstrate strong potential as noble metal-free HER electrocatalysts for efficient and scalable hydrogen production.

Another effective strategy involves combining LDHs with carbon-based materials such as graphene, CNTs, or reduced graphene oxide through the intercalation/exfoliation method. These LDH/carbon hybrids not only improve electrical conductivity but also provide a high surface area scaffold that prevents layer restacking and promotes better dispersion of active sites. The conductive carbon matrix facilitates rapid charge transport and enhances overall electrocatalytic kinetics. Exfoliation and intercalation of bulk NiFe LDHs into ultrathin nanosheets have proven to be powerful strategies for improving HER activity, primarily by enlarging surface area, enhancing charge transport, and exposing more active sites. Several advanced techniques, such as ultrasonic exfoliation, laser irradiation, and solid-phase assembly, have been employed to tailor their structure and electrochemical properties. For instance, Yao et al. fabricated a NiFe LDH nanosheet–defective graphene hybrid (NiFe LDH-NS@DG10) [307]. The synthesis of NiFe LDH@DG nanocomposite is successfully achieved through a straightforward electrostatic assembly of positively charged exfoliated NiFe LDH nanosheets with negatively charged defective graphene

(Figure 26a). Structural analyses confirm the formation of a well-dispersed hybrid architecture. XRD and AFM results validate the effective exfoliation into single-layer nanosheets (Figure 26b–e), while TEM and SAED demonstrate the preservation of crystallinity and uniform anchoring on the graphene support (Figure 26f,g). The EDS and HAADF mapping further confirm the homogeneous distribution of key elements, underscoring the intimate coupling between the LDH and DG components, as depicted in Figure 26h. This layered heterostructure achieved outstanding bifunctional performance with HER and OER overpotentials of 115 mV and 210 mV, respectively, at 10 mA/cm^2. This approach allows the coupling of diverse catalytic materials, creating junctions that foster synergistic interactions and facilitate more efficient charge transport. Such tailored interfaces can significantly lower the energy barriers for intermediate species and improve their adsorption behavior, thereby addressing the performance limitations typically observed in single-phase catalysts.

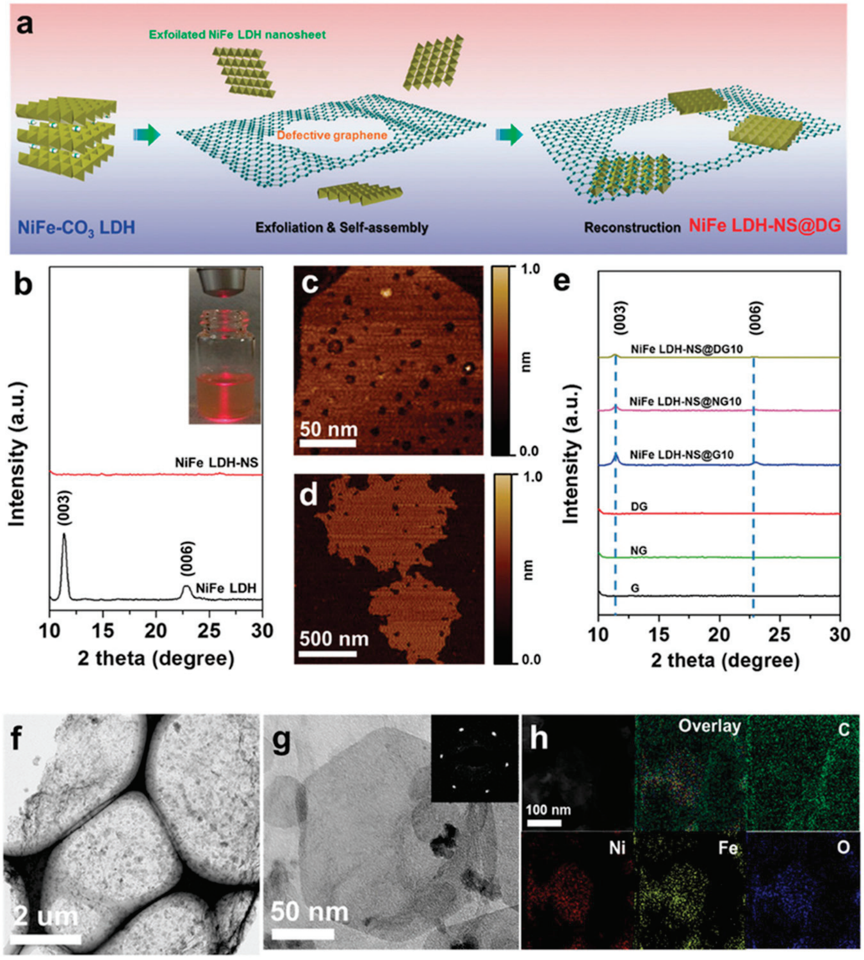

Figure 26. (**a**) Schematic depicting the synthesis pathway for the NiFe LDH-NS@DG hybrid, starting from bulk NiFe–CO$_3$ LDH, followed by exfoliation and integration with defective graphene, leading to the reconstructed nanocomposite. (**b**) XRD profiles comparing the bulk NiFe LDH and its exfoliated nanosheet form. (**c**,**d**) Atomic force microscopy (AFM) images showing the morphology of the exfoliated NiFe LDH nanosheets and defective graphene sheets, respectively. (**e**) XRD patterns of NiFe LDH nanosheets combined with various graphene types, including defective (DG), nitrogen-doped (NG), and pristine graphene (G). (**f**) Low-magnification TEM image displaying the overall morphology of the NiFe LDH-NS@DG10 composite. (**g**) High-resolution TEM highlighting the anchoring of NiFe LDH nanosheets on defective graphene, with the corresponding SAED pattern shown in the inset. (**h**) Elemental mapping via STEM-HAADF and EDS, confirming the uniform distribution of Ni, Fe, O, and C within the hybrid structure. Reproduced with permission [307].

LDH–metal composites, particularly those incorporating transition metals like Ni or Co, exhibit improved electron transfer and catalytic activity due to strong metal/metal interactions and enhanced redox behavior. These bimetallic or multimetallic systems often benefit from synergistic effects that optimize hydrogen adsorption and lower activation energy barriers. For example, Yao et al. developed a hierarchical heterostructured electrocatalyst, NiTe@CoFe LDH, by coupling conductive NiTe nanorods with amorphous CoFe-LDH via hydrothermal synthesis followed by electrodeposition [308]. This 3D architecture promotes rapid electron transfer, enhanced mass diffusion, and abundant active sites due to its large surface area and synergistic interfacial interactions. As a result, the catalyst exhibits excellent HER performance in alkaline media, requiring an overpotential of only 103 mV for HER at a current density of 10 mA/cm^2. The catalyst also demonstrates remarkable durability, maintaining stable performance for over 50 h. When used as both anode and cathode in a two-electrode configuration, the NiTe@CoFe LDH system achieves efficient overall water splitting at a low cell voltage of 1.56 V at 10 mA/cm^2, with admirable stability, indicating its strong potential for practical hydrogen production applications, as shown in Figure 27a–e. In addition, NiCo LDHs are promising electrocatalysts for hydrogen production due to their tunable redox properties, hydrophilicity, and structural flexibility. However, their HER performance is limited by poor conductivity and sluggish water dissociation kinetics. To address this, Xia et al. developed a hierarchical heterostructure comprising Cu-doped NiCo LDH grown on NiCo alloy (Cu-NiCo LDH/NiCo@CC) via a two-step electrodeposition process as shown in Figure 27f [285]. The NiCo alloy substrate enhanced conductivity, while Cu doping introduced oxygen vacancies and modulated the electronic structure. This optimized architecture delivered superior HER performance, achieving an overpotential of just 73 mV at 10 mA/cm^2 and a Tafel slope of 78.5 mV/dec in 1.0 M KOH. Electrochemical impedance spectroscopy showed a low charge transfer resistance of 1.48 Ω, and the catalyst also exhibited high surface capacitance (C_{dl} = 10.3 mF/cm^2) and excellent long-term stability. DFT calculations confirmed that Cu doping and interface effects enhanced water adsorption and charge transport, making this a promising strategy for efficient alkaline hydrogen evolution. Wang et al. developed a CoNiN@NiFe LDH hybrid electrocatalyst by electrodepositing NiFe-LDH onto NH_3-treated CoNiN grown on CC [309]. This structure combines the high conductivity of CoNiN with the catalytic activity of NiFe-LDH, enhancing charge transfer and active site exposure. In 1.0 M KOH, it delivered a low HER overpotential of 150 mV at 10 mA/cm^2, a Tafel slope of 169 mV/dec, and a charge/transfer resistance of 1.5 Ω, with excellent stability over 50 h. The synergy between components makes it a promising bifunctional catalyst for alkaline water splitting.

Furthermore, hybrid systems LDH with MOFs have shown great promise. MOFs offer a porous structure and high surface area that can be leveraged to host LDHs, creating hierarchical architectures with tailored pore channels and improved mass transport. For example, Huo et al. developed a novel strategy to fabricate monodispersed platinum (Pt) sites supported on NiFe-LDH via a targeted-anchoring and spontaneous-redox approach [286]. By engineering a MOF/LDH heterostructure, they introduced abundant defect sites that enabled the uniform dispersion and stabilization of Pt atoms. The synthesis of Pt@LDH-4h involves a stepwise strategy beginning with the formation of Fe-soc-MOF nanocubes, which serve as a structural scaffold, as shown in Figure 28a,b. Through urea-assisted hydrolysis in the presence of Ni^{2+} ions, a partial transformation occurs, generating a NiFe-LDH layer on the MOF surface and forming a MOF/LDH heterostructure rich in interfacial defects. These defects act as anchoring sites for Pt^{2+} ions introduced via K_2PtCl_4. A spontaneous redox reaction between Fe^{2+} in the MOF and Pt^{2+} leads to the in situ reduction of Pt to a lower valence state (~+0.96), resulting in the formation of monodispersed Pt sites, including both single atoms and nanoparticles (~4–5 nm). This process not only stabilizes the Pt species but also enhances electron transfer and active site exposure. The resulting Pt@LDH-4h catalyst demonstrated remarkable bifunctional activity for overall water splitting in alkaline media, achieving an impressively low overpotential of 58 mV for HER at 10 mA/cm^2. Among various LDH-based materials, NiAl-LDHs are attractive for their structural stability and tunable composition, and recent strategies have explored noble metal incorporation to enhance their catalytic performance. In this context, Kalusulingam et al. synthesized Pd-integrated NiAl-LDH nanosheets via a simple coprecipitation method, where Pd^{2+} was embedded into the brucite layer of NiAl-LDH to enhance electronic interactions and surface activity [310]. Pd-NiAl-LDH exhibited significantly improved HER performance in 1.0 M KOH, delivering an overpotential of 189 mV at 10 mA/cm^2 and a Tafel slope of 133.2 mV/dec, outperforming the pristine NiAl-LDH (258 mV, 137.4 mV/dec). The catalyst also showed a TOF of 40.37 s^{-1} at -0.4 V, indicating high intrinsic activity as depicted in Figure 29a–f. Moreover, the Pd-NiAl-LDH retained stability over 48 h of continuous HER operation, confirming its potential as a durable and efficient bifunctional catalyst for alkaline water electrolysis. The remarkable HER performance of Pd-NiAl-LDH in 1.0 M KOH is primarily attributed to its facilitation of the Volmer–Heyrovsky mechanism, enabling efficient hydrogen generation at reduced overpotentials, as shown in Figure 29g.

Transition metal compounds such as phosphides, oxides, and hydroxides are widely studied for water splitting, with phosphides like Ni_2P showing excellent HER activity due to their high conductivity and strong hydrogen affinity [311–313]. Coupling phosphides with LDHs enhances HER kinetics by improving water adsorption and proton transfer [185,314]. Ge et al. synthesized a Ni_2P/NiFe-LDH heterostructure featuring p–d orbital coupling P–Fe heterosites, which promoted O–H bond cleavage and improved charge transfer [315]. The catalyst achieved an HER overpotential of 230 mV at 100 mA/cm^2 and a Tafel slope of 47.43 mV/dec in 1.0 M KOH. DFT calculations revealed a significantly reduced Gibbs free energy (0.55 eV) for H_2O dissociation at the interface, confirming the synergistic effect of the heterostructure.

Zheng et al. developed a series of hybrid crystalline/amorphous electrocatalysts by decorating amorphous CoM LDHs (M = Mn, Fe, Ni, Cu, Zn) with crystalline CoMP nanostructures directly on nickel foam through partial dehydroxylation and phosphidation [316]. Among the variants, c-CoMnP/a-CoMn LDH/NF exhibited the best HER activity in 1.0 M KOH, requiring overpotentials of 170.3 mV and 254.9 mV to reach current densities of 100 and 500 mA/cm^2, respectively, with an onset potential of –0.134 V vs. RHE and a Tafel slope of 73.7 mV/dec. The enhanced performance was attributed to the synergistic effects between crystalline CoP domains and the amorphous LDH matrix, which increased active site density and improved charge transfer. The catalyst also demonstrated excellent stability over 60 h of continuous operation, positioning it as a promising candidate for high-rate alkaline hydrogen evolution.

Optimization of LDH cathode materials for hydrogen production focuses on tailoring composition, morphology, and surface properties to boost HER. Recent strategies include engineering 2D structures such as nanosheets or nanosheet arrays to increase the active surface area and thereby enhance charge transfer [317]. Additionally, compositional modifications, such as doping with transition metals or atomic platinum deposition, can tune the electronic structure, reduce reaction barriers, and promote efficient hydrogen adsorption [318]. Structural modulation via controlled annealing or anisotropic strain has also been shown to optimize phase evolution and lower water dissociation energy barriers, which further accelerates the HER kinetics [319,320]. Finally, surfactant-assisted exfoliation techniques help to overcome intrinsic conductivity limitations by exposing internal active sites and facilitating electron mobility [321]. These collective approaches contribute to the design of high-performance, stable, and cost-effective LDH cathodes for sustainable hydrogen production.

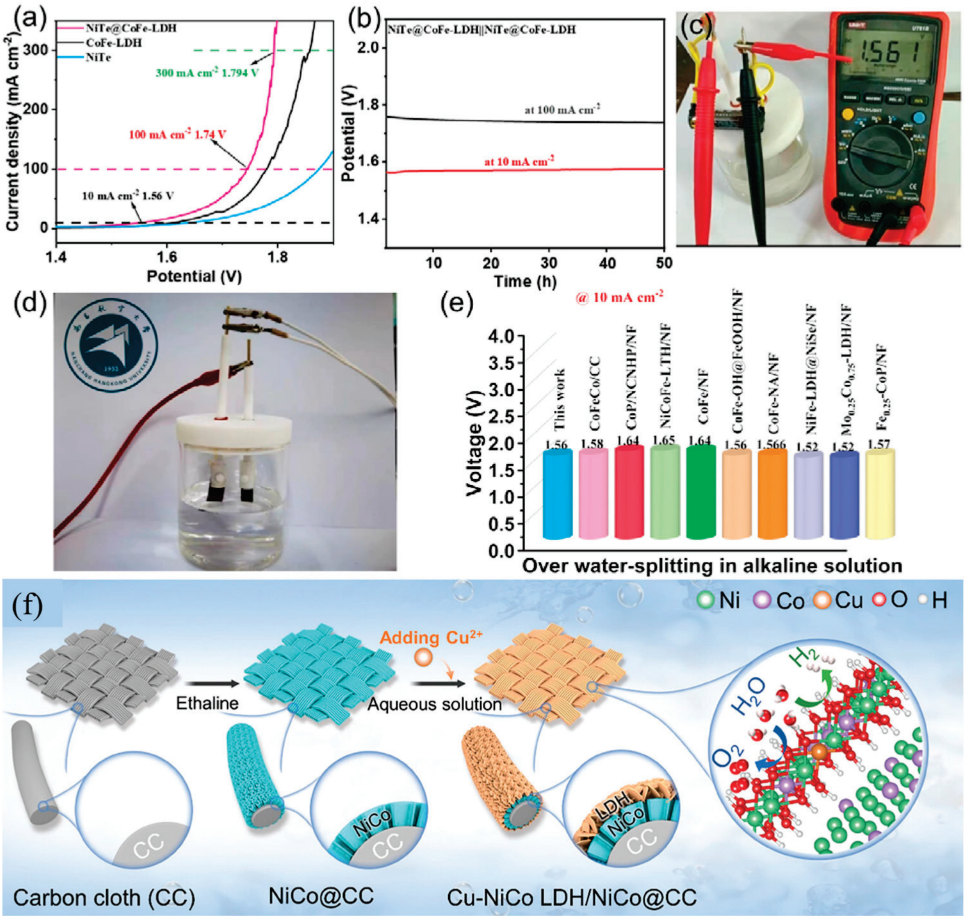

Figure 27. (**a**) Polarization curves of different electrocatalysts for overall water splitting recorded in 1.0 M KOH using a two-electrode setup at a scan rate of 1 mV/s. (**b**) Durability evaluation of NiTe@CoFe-LDH electrodes operated at current densities of 10 and 100 mA/cm^2 over a 50-h period. (**c**) Visual representation of the water-splitting device powered by a single battery, with a digital voltmeter showing the applied cell voltage. (**d**) Photograph of the assembled full-cell system under operation. (**e**) Comparative analysis of the cell voltages at 10 mA/cm^2 for NiTe@CoFe-LDH and other recently reported bifunctional catalysts in alkaline conditions. Reproduced with permission [308]. (**f**) Illustration of the synthetic strategy for constructing 3D hierarchical Cu-doped NiCo LDH nanosheets on NiCo alloy substrate and their deployment in overall water splitting applications. Reproduced with permission [285].

Integrating LDHs with MXenes significantly enhances catalytic performance by improving conductivity, preventing aggregation, and increasing exposure of active metal sites. This synergy accelerates gas evolution kinetics and boosts redox efficiency [306,322]. MXenes also offer corrosion resistance and mechanical reinforcement, improving overall catalyst durability. Though still emerging, LDH–MXene hybrids show great promise for water splitting applications. Xi et al. reported a CoFe-LDH-based catalyst synthesized via a partial in situ transformation of Co-MOF on a modified 3D MXene substrate (N-MXene), followed by the introduction of cationic vacancy defects to boost electrocatalytic activity [323]. The modified MXene provided a porous, conductive scaffold, while the vacancies tuned the electronic structure and enhanced active site exposure. The resulting hybrid, d-MLN (MOF-d-CoFe LDH@N-MXene), delivered excellent HER performance, requiring an overpotential of only 206 mV at 10 mA/cm^2 in 1 M KOH. It also showed a Tafel slope of 113 mV/dec, high electrochemical surface area (C_{dl} = 13.07 mF/cm^2), and charge transfer resistance as low as 1.72 Ω, confirming its fast kinetics and efficient electron transfer. Stability tests revealed minimal performance degradation over 60 h, highlighting its practical potential for sustainable hydrogen production. In one study, Shen et al. designed a 3D interwoven architecture combining $Ti_3C_2T_x$ MXene, reduced graphene oxide (RGO), and NiFe-LDH nanosheets via a hydrothermal co-assembly method. This structure, denoted as LDH (60%)/MX-RGO, featured a meso/macroporous network with a large BET surface area of 254.7 m^2/g, enhanced charge transfer, and strong electronic interactions among components. The optimized composite exhibited outstanding HER performance in 1 M KOH, with an overpotential of only 326 mV at 10 mA/cm^2 and a Tafel slope of 100 mV/dec. It also showed a high electrochemical double-layer capacitance (C_{dl} = 8.3 mF/cm^2) and a low charge/transfer resistance (2.7 Ω), indicating improved intrinsic activity and conductivity. The catalyst maintained excellent stability over 40 h of continuous operation and 2000 CV cycles, establishing its robustness and practical potential in alkaline HER systems. Table 3 presents a comparative overview of recent LDH-based HER electrocatalysts, highlighting the diversity in synthesis approaches and their corresponding electrocatalytic performances, including overpotential, stability, and Tafel slope.

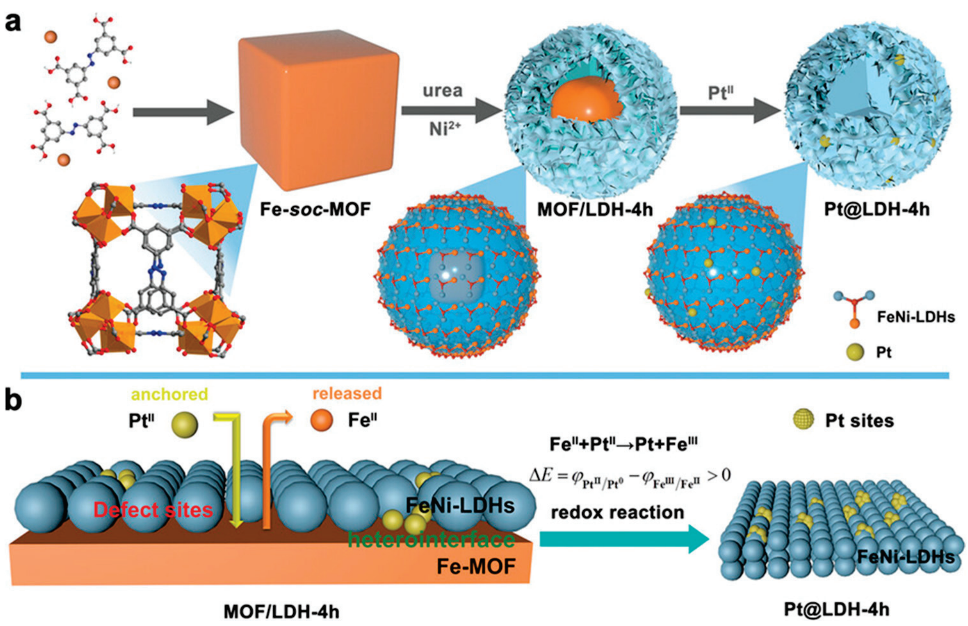

Figure 28. (**a**,**b**) Schematic representation of the strategic stepwise synthesis of Pt@LDH-4h catalysts tailored for efficient overall water splitting. Reproduced with permission [286].

Table 3. Summary of various LDH-based electrocatalysts for HER.

LDH Name	Synthesis Procedure	Electrolyte	HER Overpotential (η/mV, *j*/mA/cm^2)	Stability (Retention/%, Time/h)	Tafel Slope (mV/dec), FE (%)	Ref.
NiFe LDH-NS@DG10	Exfoliation method	1 M KOH	115, 10	~100%, 5.5 h	110, 97.3%	[307]
NiTe@CoFe-LDH	Hydrothermal and electrodeposition	1 M KOH	103, 10	~100%, 50 h	20, 100%	[308]
Cu-NiCo LDH/NiCo@CC	Electrodeposition process	1 M KOH	73, 10	. . ., 100 h	78.5, . . .	[285]
CoNiN@NiFe	Co-deposition	1 M KOH	150, 10	. . ., 60 h	167, 100%	[309]

Table 3. *Cont.*

LDH Name	Synthesis Procedure	Electrolyte	HER Overpotential (η/mV, *j*/mA/cm^2)	Stability (Retention/%, Time/h)	Tafel Slope (mV/dec), FE (%)	Ref.
Pt@LDH-4h	Hydrolysis reaction	1 M KOH	58, 10	~100%, 24 h	43.6, 95%	[286]
Pd-NiAl-LDH	Chemical precipitation	1 M KOH	189, 10	~100%, 48 h	133.2, . . .	[310]
Ni_2P/NiFe-LDH	Hydrothermal	1 M KOH	230, 100	~100%, 32 h	47.43, . . .	[315]
c-CoMnP/a-CoMn LDH/NF	Chemical and thermal route	1 M KOH	170, 100	99%, 60 h	73.7, . . .	[316]
MOF-d-CoFe LDH@N-MXene	Hydrothermal and electrophoretic deposition	1 M KOH	206, 10	. . ., 60 h	113, 93%	[323]
LDH(60%)/MX-RGO	Hydrothermal co-assembly	1 M KOH	326, 10	. . ., 40 h	100, . . .	[324]

LDH: Layered double hydroxide, HER: Hydrogen evolution reaction, FE: Faradaic efficiency

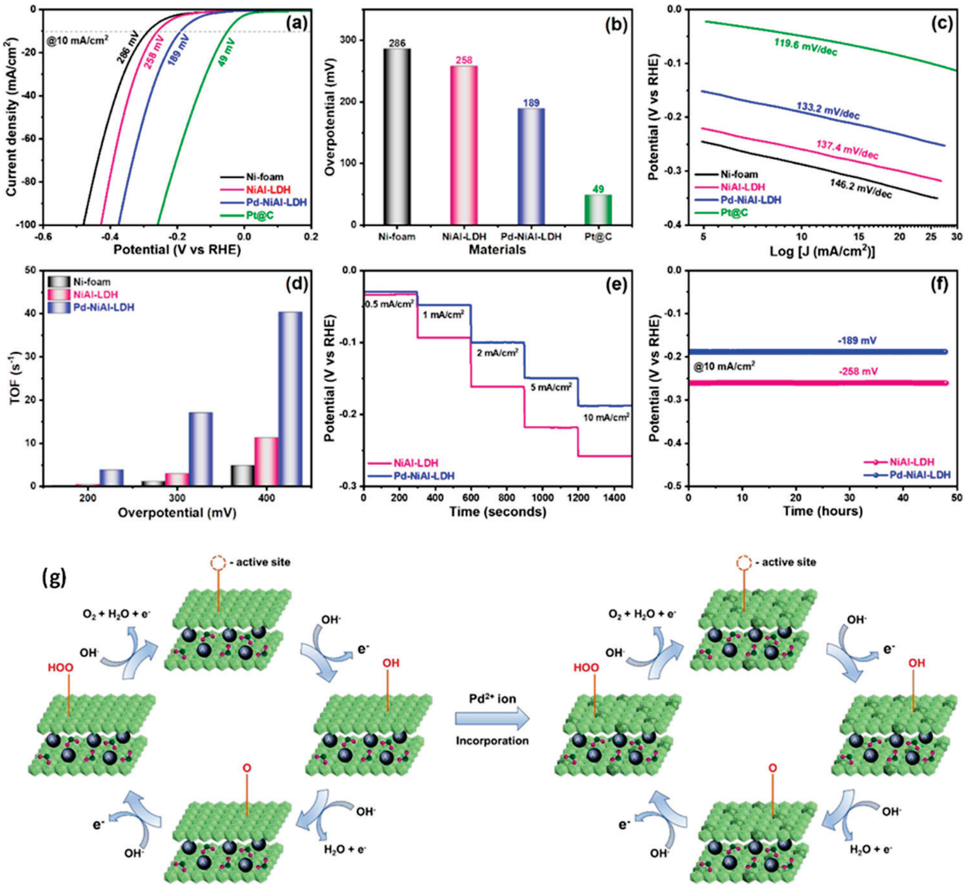

Figure 29. Evaluation of hydrogen evolution performance in 1.0 M KOH for NiAl-LDH, Pd-NiAl-LDH, Pt@C, and bare nickel foam: (**a**) Linear sweep voltammetry (LSV) profiles without iR compensation, (**b**) comparative HER overpotentials at 10 mA/cm^2, (**c**) Tafel plots indicating reaction kinetics, (**d**) TOF analysis, (**e**) stepwise chronopotentiometry tests across current densities from 0.5 to 10 mA/cm^2 with 300-s intervals for NiAl-LDH and Pd-NiAl-LDH, and (**f**) long-term stability test of Pd-NiAl-LDH at a constant current density of 10 mA/cm^2 over 48 h. (**g**) Illustration of the HER pathway involving two-electron transfer steps on NiAl-LDH and Pd-NiAl-LDH surfaces. Reproduced with permission [310].

6.3. Challenges in Catalytic Activity, Stability, and Practical Deployment

Despite their considerable promise, LDH-based electrocatalysts face several challenges that limit their widespread deployment in practical hydrogen production systems. A primary issue is their relatively modest intrinsic catalytic activity compared to noble metals, which stems from suboptimal hydrogen binding energies and sluggish electron transfer kinetics. While compositional tuning, doping, and heterostructure engineering have improved activity, achieving a balance between stability, conductivity, and catalytic efficiency remains complex. Durability under continuous operation is another major concern. Prolonged electrolysis can lead to structural disintegration, metal ion leaching, and the collapse of layered architectures, particularly under acidic or high-current conditions. These degradation mechanisms compromise long-term performance and hinder reliability. Scalability also presents significant hurdles. Many advanced LDH synthesis routes, such as hydrothermal growth, exfoliation, or electrodeposition, are challenging to scale due to batch limitations, material inconsistency, and the need for controlled environments. Moreover, integrating LDH materials into commercial electrolyzers and ensuring compatibility with system architectures and operational demands requires further development. To address these limitations, future efforts should focus on developing scalable and green synthesis methods that allow precise control over morphology and composition and enhancing interfacial engineering strategies, such as LDH–MXene, LDH–MOF, or LDH–graphene composites, to improve stability and charge transfer, in situ/operando characterization to uncover dynamic structural and electronic transformations under reaction conditions, and computational screening and machine learning approaches to accelerate the discovery of optimized compositions and architectures. Ultimately, advancing LDH-based electrocatalysts will require interdisciplinary strategies combining materials science, electrochemistry, and engineering design to bridge the gap from laboratory innovation to commercial application.

The utilization of LDHs in electrochemical hydrogen production presents several notable challenges related to their catalytic activity, stability, and practical deployment. This delves into these challenges, emphasizing the current understanding shaped by multiple academic explorations. One of the primary challenges in leveraging LDHs for electrochemical hydrogen production is their catalytic activity. Despite demonstrated potential, the efficiency of LDHs as electrocatalysts for HER remains limited when compared to noble metal counterparts. Transition metal-based LDHs exhibit favorable properties such as tunable composition and layered structures, yet often show inferior electrocatalytic efficiency. For instance, Wang et al. state that the catalytic performance is significantly influenced by the crystallographic phase and morphology of LDHs, where variations can lead to diverse electrochemical activities under identical conditions [314]. Luo et al. emphasize the necessity for adequately designed LDHs to provide more active sites while reducing reaction energy barriers [325]. Moreover, specific LDH compositions reveal limitations in their electrocatalytic performance; for instance, NiFe-based LDHs have been recognized as effective but still face challenges regarding the balance of active sites and reaction kinetics [326]. Optimizing the density of active sites while managing charge transfer efficiency is critical. Research by Liu et al. articulates that enhancing the uniform distribution of catalytic sites is vital for improving overall catalytic performance [327]. Ultimately, the ability of LDHs to function under diverse electrochemical conditions remains an area demanding further exploration and innovation.

In addition to catalytic activity, stability is a crucial concern regarding the performance of LDHs in practical applications. The intrinsic structure of LDHs is often susceptible to degradation under harsh electrochemical conditions, leading to a diminished operational lifetime [328]. For instance, during prolonged electrolysis, corrosion can occur, particularly in saline environments, resulting in the dissolution of components and loss of functionality. Research has demonstrated that specific compositions, such as $CoCO_3$/CoFe LDHs, show improved electrochemical stability, yet widespread stability challenges remain. Furthermore, Zhao highlights that ion leaching and structural collapse under continuous operational stress compromise the sustainable use of LDHs [329]. This instability limits their practical applications, especially in environments subjected to varying pH and current densities. Thus, integrating robust structural mechanisms capable of withstanding electrochemical stress while maintaining active sites is crucial for the successful deployment of LDHs in hydrogen evolution technologies.

In considering the practical deployment of LDHs in industry, several logistical and economic factors arise. The synthesis of LDHs must strike a balance between cost, scalability, and reproducibility. Current methods for producing LDHs, such as coprecipitation and hydrothermal techniques, may not be sufficiently scalable for industrial application, which is underscored by Chen et al., who point to the need for more efficient synthesis protocols that minimize costs and resource usage [330]. Additionally, the integration of LDHs into existing systems presents challenges regarding compatibility with associated materials, such as electrodes and supporting substrates [331]. Adjusting the physical and chemical properties of LDHs to facilitate optimal interaction with other components of electrochemical cells is critical [332]. The demand for multifunctional applications frames LDHs not merely as catalysts but as composite materials requiring structural and functional harmonization with other energy storage technologies. Moreover, environmental considerations, regulatory compliance, and societal acceptance play vital roles in deploying LDHs within commercial settings. As the push toward sustainable energy production intensifies, the environmental footprint of LDH processes must be carefully evaluated. Balancing lifecycle impacts while achieving functional deployment is an ongoing challenge faced by researchers and engineers [13].

Addressing the challenges of catalytic activity, stability, and deployment of LDHs in hydrogen production processes necessitates innovative strategies. Incorporating advanced synthesis methodologies can enhance the uniformity and availability of active sites within LDHs, as supported by various studies highlighting the effectiveness of nanosheet morphologies [314,333]. Additionally, engineering techniques such as doping and structural modification can enhance both the electrocatalytic performance and stability of LDHs [334]. Promising advancements include integrating LDHs with conductive substrates or hybrid materials that leverage the beneficial properties of both materials, thereby improving charge transfer and catalyst stability [89,335]. Achieving a harmonious integration of LDHs with materials such as MXenes or incorporating them into composite structures may offer pathways to overcome existing challenges [332]. Moreover, ongoing research focused on tailoring LDH compositions to optimize their electrochemical characteristics, stability, and economic viability is crucial. A deeper understanding of structure/performance relationships is fundamental to innovating LDH-based systems for hydrogen production applications. While LDHs present promising opportunities as electrocatalysts for hydrogen production, their utility is tempered by considerable challenges in catalytic activity, stability, and practical deployment. Addressing these concerns through innovative research and development is essential to realizing the potential of LDHs in contributing to sustainable hydrogen energy solutions.

7. Conclusions and Future Prospects

LDHs have emerged prominently as versatile and promising 2D materials for a wide array of energy applications, including batteries, supercapacitors, and hydrogen production. This review systematically outlines the foundational principles, synthesis methodologies, and application-specific advantages of LDHs, offering a comprehensive reference for researchers within this domain. In battery-related applications, LDHs demonstrate significant potential driven by their remarkable structural stability, chemically adjustable composition, and advantageous electrochemical properties. Specifically, in LIBs, LDHs have been shown to enhance electrode performance through stabilization of electrode/electrolyte interfaces, mitigation of volumetric expansion, and improvement in electrical conductivity. LSBs benefit substantially from the inherent capability of LDHs to adsorb polysulfides, effectively reducing the shuttle effect, thereby enhancing cycle stability and capacity retention. Similarly, NIBs leverage LDHs' expanded interlayer spacing, facilitating efficient diffusion of larger sodium ions, which directly addresses critical challenges in electrode kinetics and rate capability. Beyond conventional systems, LDHs hold significant promise in emerging battery technologies, including LIBs, CIBs, ZIBs, LSBs, and ZABs. They provide innovative solutions to longstanding challenges, such as corrosion resistance, dendritic growth prevention, and enhancement of sluggish ion diffusion processes.

In supercapacitor technologies, LDHs offer a compelling combination of high specific capacitance, excellent pseudocapacitive behavior, and robust electrochemical stability. Their layered structures provide abundant active sites and pathways conducive to rapid ion transport and electron mobility, positioning LDHs as exceptionally suitable electrode materials. Further optimization through doping and composite formation allows tailored improvements in energy density and power output. Nevertheless, considerable challenges remain, including their inherently low electrical conductivity and mechanical instability during extended cycling, necessitating innovative synthetic strategies or composite structures to overcome these limitations. Regarding catalytic hydrogen production, LDHs have exhibited substantial promise, especially in electrocatalytic water splitting processes. Their adjustable layer compositions and diverse elemental combinations enable precise tuning of catalytic properties, significantly boosting both HER and OER. Despite these advances, achieving industrial-level efficiency and durability poses substantial challenges, primarily due to insufficient intrinsic conductivity, limited specific surface areas of bulk forms, and operational durability under prolonged and harsh conditions.

Addressing these challenges requires strategic and innovative approaches. Future research should explicitly focus on precise control and reproducibility of LDH morphologies and electrochemical properties through meticulous optimization of synthesis parameters. Advanced synthesis techniques such as exfoliation into ultrathin nanosheets, integration with conductive substrates, or hybridization with complementary catalysts must be systematically developed and standardized to enhance material performance consistently. One of the most pressing challenges is the scalable and economically feasible production of LDHs. Current advanced synthesis methods, such as exfoliation, sol-gel processes, or hydrothermal treatments, are typically complex, expensive, and challenging to scale. Future research must prioritize the development of simplified, cost-effective, and scalable manufacturing techniques. Techniques such as continuous-flow reactors, microwave-assisted synthesis, and scalable hydrothermal reactors warrant intensive exploration due to their potential to deliver LDHs on a commercially viable scale. Integration into commercial energy systems demands attention to the practical aspects of LDHs, including long-term cycling stability in energy storage applications and durability under harsh catalytic conditions. Detailed investigations into degradation mechanisms, especially under realistic operational scenarios, will be crucial. For instance, comprehensive studies addressing the interfacial stability of LDHs within electrode structures under extensive cycling are necessary to design robust materials for commercial applications. Furthermore, understanding and optimizing complex interactions within composite structures incorporating LDHs is another critical area requiring in-depth study. This includes evaluating the interfacial chemistry between LDHs and conductive additives like carbon nanotubes, graphene, and conductive polymers.

Advanced analytical and characterization techniques, including in situ microscopy and spectroscopy, are needed to elucidate interfacial phenomena and interactions at the atomic scale, facilitating targeted optimization of composite performance.

To expedite and streamline the development of advanced LDH materials, computational modeling and simulation represent potent tools for predicting optimal material compositions and structures. Employing DFT, molecular dynamics, and machine learning algorithms can dramatically reduce experimental iterations, guide synthetic strategies, and facilitate the rapid design of optimized LDH-based materials. Exploration of novel and hybrid battery chemistries involving LDHs, such as hybrid supercapacitors and dual-ion batteries, could further expand their applications, potentially delivering high-performance and safer energy storage solutions. This requires systematic exploration and validation of LDHs within these novel battery architectures to assess performance, reliability, and safety comprehensively. In hydrogen production, future research directions must center on enhancing intrinsic catalytic activities, addressing conductivity and stability constraints. Hybrid electrocatalysts, combining LDHs with high-conductivity materials such as graphene, carbon nanotubes, or conductive polymers, present promising pathways for significant enhancements in electron transport and catalytic efficiency. Research must also focus on developing novel support structures and protective coatings to improve catalyst durability under industrially relevant operating conditions.

While LDHs have been extensively explored in conventional liquid electrolyte-based batteries, their application in solid-state batteries (SSBs) remains largely untapped, presenting a promising future direction. SSBs, offering enhanced safety, higher energy density, and broader operating temperature ranges, require materials with excellent ionic conductivity, chemical stability, and favorable interfacial properties. The unique layered structure of LDHs, combined with their tunable composition and ion exchange capability, suggests their potential use as solid electrolytes, interfacial layers, or electrode additives in SSBs. For instance, modifying LDHs to create highly conductive, defect-rich structures or composite materials could help facilitate ion transport across solid interfaces, a critical bottleneck in current SSB technologies. Moreover, their intrinsic ability to incorporate various metal cations could be exploited to engineer multifunctional interfaces that enhance both mechanical stability and electrochemical performance. Therefore, future research focused on tailoring the structure, conductivity, and interface compatibility of LDHs could open new pathways for their integration into solid-state battery systems, contributing significantly to the next generation of safe and high-performance energy storage devices.

Critically, researchers should adopt a pragmatic approach to LDH development, balancing theoretical performance enhancements against practical economic and industrial constraints. This includes comprehensive lifecycle assessments, economic viability studies, and scalability analyses to align research trajectories closely with industry requirements and commercial realities. LDHs exhibit immense potential in addressing pivotal challenges across energy storage and conversion technologies. Nevertheless, realizing their commercial and practical utility demands targeted research efforts addressing synthesis reproducibility, scalability, material stability, and interfacial interactions within composites. By leveraging advanced computational techniques, innovative synthesis methods, and rigorous practical assessments, LDHs can significantly impact future energy technologies. This review provides a robust foundation, clearly identifying critical areas requiring deeper exploration and establishing a structured path toward innovative, efficient, and sustainable LDH-based solutions.

Funding: This research received no external funding.

Acknowledgments: The authors acknowledge the support from the Graduate School of Energy Science, Kyoto University, Japan.

Conflicts of Interest: The authors declare no conflict of interest.

References

1. Chen, S.; Zhuo, Y.; Wang, X.; Li, S.; Lu, J.; Liu, D.; Pan, H.; Wang, Z. Advances of Layered Double Hydroxide Electrocatalysts for High-Current-Density Alkaline Water/Seawater Splitting. *Coord. Chem. Rev.* **2024**, *510*, 215832. [CrossRef]
2. Long, X.; Wang, Z.; Xiao, S.; An, Y.; Yang, S. Transition Metal Based Layered Double Hydroxides Tailored for Energy Conversion and Storage. *Mater. Today* **2016**, *19*, 213–226. [CrossRef]
3. Lin, Q.; Wang, L. Layered Double Hydroxides as Electrode Materials for Flexible Energy Storage Devices. *J. Semicond.* **2023**, *44*, 041601. [CrossRef]
4. Yu, W.; Deng, N.; Cheng, K.; Yan, J.; Cheng, B.; Kang, W. Advances in Preparation Methods and Mechanism Analysis of Layered Double Hydroxide for Lithium-Ion Batteries and Lithium-Sulfur Batteries. *J. Energy Chem.* **2021**, *58*, 472–499. [CrossRef]
5. Sahoo, D.P.; Das, K.K.; Mansingh, S.; Sultana, S.; Parida, K. Recent Progress in First Row Transition Metal Layered Double Hydroxide (LDH) Based Electrocatalysts towards Water Splitting: A Review with Insights on Synthesis. *Coord. Chem. Rev.* **2022**, *469*, 214666. [CrossRef]
6. Hu, X.; Zheng, W.; Wu, M.; He, Q.; Zhan, F.; Chen, L. Ternary Layered Double Hydroxide Cathode Materials for Electrochemical Energy Storage: A Review and Perspective. *Sustain. Energy Fuels* **2022**, *6*, 4551–4581. [CrossRef]
7. Zhou, D.; Li, P.; Lin, X.; McKinley, A.; Kuang, Y.; Liu, W.; Lin, W.F.; Sun, X.; Duan, X. Layered Double Hydroxide-Based Electrocatalysts for the Oxygen Evolution Reaction: Identification and Tailoring of Active Sites, and Superaerophobic Nanoarray Electrode Assembly. *Chem. Soc. Rev.* **2021**, *50*, 8790–8817. [CrossRef]
8. Jing, C.; Tao, S.; Fu, B.; Yao, L.; Ling, F.; Hu, X.; Zhang, Y. Layered Double Hydroxide-Based Nanomaterials for Supercapacitors and Batteries: Strategies and Mechanisms. *Prog. Mater. Sci.* **2024**, *150*, 101410. [CrossRef]
9. Zhang, D.; Guo, X.; Tong, X.; Chen, Y.; Duan, M.; Shi, J.; Jiang, C.; Hu, L.; Kong, Q.; Zhang, J. High-Performance Battery-Type Supercapacitor Based on Porous Biocarbon and Biocarbon Supported Ni–Co Layered Double Hydroxide. *J. Alloys Compd.* **2020**, *837*, 155529. [CrossRef]
10. Antil, B.; Olhan, S.; Vander Wal, R.L. Production of Graphitic Carbon from Renewable Lignocellulosic Biomass Source. *Minerals* **2025**, *15*, 262. [CrossRef]
11. Chaudhuri, H.; Yun, Y.S. A Critical Review on the Properties and Energy Storage Applications of Graphene Oxide/Layered Double Hydroxides and Graphene Oxide/MXenes. *J. Power Sources* **2023**, *564*, 232870. [CrossRef]
12. Tomboc, G.M.; Kim, J.; Wang, Y.; Son, Y.; Li, J.; Kim, J.Y.; Lee, K. Hybrid Layered Double Hydroxides as Multifunctional Nanomaterials for Overall Water Splitting and Supercapacitor Applications. *J. Mater. Chem. A Mater.* **2021**, *9*, 4528–4557. [CrossRef]
13. Fan, K.; Xu, P.; Li, Z.; Shao, M.; Duan, X. Layered Double Hydroxides: Next Promising Materials for Energy Storage and Conversion. *Next Mater.* **2023**, *1*, 100040. [CrossRef]
14. Sherryna, A.; Tahir, M. Recent Developments in Layered Double Hydroxide Structures with Their Role in Promoting Photocatalytic Hydrogen Production: A Comprehensive Review. *Int. J. Energy Res.* **2022**, *46*, 2093–2140. [CrossRef]
15. Mohanty, U.A.; Sahoo, D.P.; Paramanik, L.; Parida, K. A Critical Review on Layered Double Hydroxide (LDH)-Derived Functional Nanomaterials as Potential and Sustainable Photocatalysts. *Sustain. Energy Fuels* **2023**, *7*, 1145–1186. [CrossRef]
16. Zhao, Y.; Zhang, P.; Liang, J.; Xia, X.; Ren, L.; Song, L.; Liu, W.; Sun, X. Unlocking Layered Double Hydroxide as a High-Performance Cathode Material for Aqueous Zinc-Ion Batteries. *Adv. Mater.* **2022**, *34*, 2204320. [CrossRef] [PubMed]
17. Aziz, M.A.; Shah, S.S.; Mahnashi, Y.A.; Mahfoz, W.; Alzahrani, A.S.; Hakeem, A.S.; Shaikh, M.N. A High-Energy Asymmetric Supercapacitor Based on Tomato-Leaf-Derived Hierarchical Porous Activated Carbon and Electrochemically Deposited Polyaniline Electrodes for Battery-Free Heart-Pulse-Rate Monitoring. *Small* **2023**, *19*, 2300258. [CrossRef]
18. Jing, C.; Dong, B.; Zhang, Y. Chemical Modifications of Layered Double Hydroxides in the Supercapacitor. *Energy Environ. Mater.* **2020**, *3*, 346–379. [CrossRef]
19. Antil, B.; Elkasabi, Y.; Strahan, G.D.; Vander Wal, R.L. Development of Graphitic and Non-Graphitic Carbons Using Different Grade Biopitch Sources. *Carbon* **2025**, *232*, 119770. [CrossRef]
20. Yuan, Z.; Bak, S.M.; Li, P.; Jia, Y.; Zheng, L.; Zhou, Y.; Bai, L.; Hu, E.; Yang, X.Q.; Cai, Z.; et al. Activating Layered Double Hydroxide with Multivacancies by Memory Effect for Energy-Efficient Hydrogen Production at Neutral pH. *ACS Energy Lett.* **2019**, *4*, 1412–1418. [CrossRef]
21. Khorshidi, M.; Asadpour, S.; Sarmast, N.; Dinari, M. A Review of the Synthesis Methods, Properties, and Applications of Layered Double Hydroxides/Carbon Nanocomposites. *J. Mol. Liq.* **2022**, *348*, 118399. [CrossRef]

22. Riaz, S.; Rehman, A.; Akhter, Z.; Najam, T.; Hossain, I.; Karim, M.R.; Assiri, M.A.; Shah, S.S.A.; Nazir, M.A. Recent Advancement in Synthesis and Applications of Layered Double Hydroxides (LDHs) Composites. *Mater. Today Sustain.* **2024**, *27*, 100897. [CrossRef]
23. Jijoe, P.S.; Yashas, S.R.; Shivaraju, H.P. Fundamentals, Synthesis, Characterization and Environmental Applications of Layered Double Hydroxides: A Review. *Environ. Chem. Lett.* **2021**, *19*, 2643–2661. [CrossRef]
24. Ali Khan, A.; Tahir, M.; Khan, N. Recent Developments in Titanium Carbide (Ti_3C_2)-Based Layered Double Hydroxide (LDH) Nanocomposites for Energy Storage and Conversion Applications: A Minireview and Perspectives. *Energy Fuels* **2022**, *36*, 9821–9843. [CrossRef]
25. Parsapour, F.; Moradi, M.; Bahadoran, A. Metal-Organic Frameworks-Derived Layered Double Hydroxides: From Controllable Synthesis to Various Electrochemical Energy Storage/Conversion Applications. *Adv. Colloid. Interface Sci.* **2023**, *313*, 102865. [CrossRef] [PubMed]
26. Li, C.; Zhao, J.; Xie, L.; Wu, J.; Ren, Q.; Wang, Y.; Li, G. Surface-Adsorbed Carboxylate Ligands on Layered Double Hydroxides/Metal–Organic Frameworks Promote the Electrocatalytic Oxygen Evolution Reaction. *Angew. Chem.* **2021**, *133*, 18277–18285. [CrossRef]
27. Bukhtiyarova, M.V. A Review on Effect of Synthesis Conditions on the Formation of Layered Double Hydroxides. *J. Solid. State Chem.* **2019**, *269*, 494–506. [CrossRef]
28. Wang, Q.; Ohare, D. Recent Advances in the Synthesis and Application of Layered Double Hydroxide (LDH) Nanosheets. *Chem. Rev.* **2012**, *112*, 4124–4155. [CrossRef]
29. Li, F.; Zhang, L.; Evans, D.G.; Duan, X. Structure and Surface Chemistry of Manganese-Doped Copper-Based Mixed Metal Oxides Derived from Layered Double Hydroxides. *Colloids Surf. A Physicochem. Eng. Asp.* **2004**, *244*, 169–177. [CrossRef]
30. Xu, J.; Liu, X.; Zhou, Z.; Deng, L.; Liu, L.; Xu, M. Surface Defects Introduced by Metal Doping into Layered Double Hydroxide for CO_2 Photoreduction: The Effect of Metal Species in Light Absorption, Charge Transfer and CO_2 Reduction. *Chem. Eng. J.* **2022**, *442*, 136148. [CrossRef]
31. Forano, C. Environmental Remediation Involving Layered Double Hydroxides. In *Interface Science and Technology*; Elsevier: Amsterdam, The Netherlands, 2004; Volume 1, pp. 425–458.
32. Perera-Solis, D.D.; Pimlott, M.; Fidment, E.; Whiting, A.; Greenwell, H.C. Adding Value to Waste Minerals in a Circular Economy Framework: Ochre-Derived Layered Double Hydroxide Catalysts in Fatty Acid Ketonisation. *Minerals* **2019**, *9*, 681. [CrossRef]
33. Roy Chowdhury, P.; Medhi, H.; Bhattacharyya, K.G.; Mustansar Hussain, C. Layered Double Hydroxides Derived from Waste for Highly Efficient Electrocatalytic Water Splitting: Challenges and Implications towards Circular Economy Driven Green Energy. *Coord. Chem. Rev.* **2024**, *501*, 215547. [CrossRef]
34. Chowdhury, P.R.; Medhi, H.; Bhattacharyya, K.G.; Hussain, C.M. Recent Developments in Ni-Based Layered Double Hydroxides Extracted from Waste for Oxygen Evolution Reactions: A Review on the Pursuit for Sustainable Green Hydrogen. *Sustain. Energy Fuels* **2025**, *9*, 1447–1463. [CrossRef]
35. Jerome, M.P.; Alahmad, F.A.; Salem, M.T.; Tahir, M. Layered Double Hydroxide (LDH) Nanomaterials with Engineering Aspects for Photocatalytic CO_2 Conversion to Energy Efficient Fuels: Fundamentals, Recent Advances, and Challenges. *J. Environ. Chem. Eng.* **2022**, *10*, 108151. [CrossRef]
36. Singha Roy, A.; Kesavan Pillai, S.; Ray, S.S. Layered Double Hydroxides for Sustainable Agriculture and Environment: An Overview. *ACS Omega* **2022**, *7*, 20428–20440. [CrossRef]
37. Zubair, M.; Daud, M.; McKay, G.; Shehzad, F.; Al-Harthi, M.A. Recent Progress in Layered Double Hydroxides (LDH)-Containing Hybrids as Adsorbents for Water Remediation. *Appl. Clay Sci.* **2017**, *143*, 279–292. [CrossRef]
38. Li, L.; Soyhan, I.; Warszawik, E.; van Rijn, P. Layered Double Hydroxides: Recent Progress and Promising Perspectives Toward Biomedical Applications. *Adv. Sci.* **2024**, *11*, 2306035. [CrossRef]
39. Nemček, L.; Hagarová, I.; Matúš, P. Layered Double Hydroxides as Next-Generation Adsorbents for the Removal of Selenium from Water. *Appl. Sci.* **2024**, *14*, 8513. [CrossRef]
40. Altalhi, A.A.; Mohamed, E.A.; Negm, N.A. Recent Advances in Layered Double Hydroxide (LDH)-Based Materials: Fabrication, Modification Strategies, Characterization, Promising Environmental Catalytic Applications, and Prospective Aspects. *Energy Adv.* **2024**, *3*, 2136–2151. [CrossRef]
41. Li, C.; Jing, H.; Wu, Z.; Jiang, D. Layered Double Hydroxides for Photo(Electro)Catalytic Applications: A Mini Review. *Nanomaterials* **2022**, *12*, 3525. [CrossRef]
42. Gao, J.; Jin, B.; Shao, M. Layered Double Hydroxides Functionalization toward Rechargeable Batteries. *Particuology* **2024**, *91*, 138–154. [CrossRef]
43. Lu, L.; Zheng, Y.; Yang, R.; Kakimov, A.; Li, X. Recent Advances of Layered Double Hydroxides–Based Bifunctional Electrocatalysts for ORR and OER. *Mater. Today Chem.* **2021**, *21*, 100488. [CrossRef]
44. Gaur, A.; Sharma, J.; Lim, D.; Lee, H.I.; Han, H. Recent Advances in Electronic Structure Modifications of Layered Double Hydroxide (LDH) for the Water Splitting Application. *ChemCatChem* **2025**, *17*, e202401584. [CrossRef]

45. Lin, Z.; Li, X.; Zhang, H.; Xu, B.B.; Wasnik, P.; Li, H.; Singh, M.V.; Ma, Y.; Li, T.; Guo, Z. Research Progress of MXenes and Layered Double Hydroxides for Supercapacitors. *Inorg. Chem. Front.* **2023**, *10*, 4358–4392. [CrossRef]
46. Li, X.; Ren, J.; Sridhar, D.; Xu, B.B.; Algadi, H.; El-Bahy, Z.M.; Ma, Y.; Li, T.; Guo, Z. Progress of Layered Double Hydroxide-Based Materials for Supercapacitors. *Mater. Chem. Front.* **2023**, *7*, 1520–1561. [CrossRef]
47. Luo, F.; San, X.; Wang, Y.; Meng, D.; Tao, K. Layered Double Hydroxide-Based Electrode Materials Derived from Metal–Organic Frameworks: Synthesis and Applications in Supercapacitors. *Dalton Trans.* **2024**, *53*, 10403–10415. [CrossRef] [PubMed]
48. Jafari, M.; Ganjali, F.; Eivazzadeh-Keihan, R.; Maleki, A.; Geranmayeh, S. Recent Advances in Applications of Graphene-Layered Double Hydroxide Nanocomposites in Supercapacitors and Batteries. *FlatChem* **2024**, *45*, 100658. [CrossRef]
49. Aman, M.; Konduparty, P.; Sharma, S.; Srivastava, R.P.; Bhattacharyya, S.; Sharma, V.; Balani, K.; Jha, S.K.; Omar, S. Layered Double Hydroxide Based Composites for Energy Storage Applications: Insights into Supercapacitors and Batteries. *J. Energy Storage* **2025**, *116*, 116093. [CrossRef]
50. Fan, G.; Li, F.; Evans, D.G.; Duan, X. Catalytic Applications of Layered Double Hydroxides: Recent Advances and Perspectives. *Chem. Soc. Rev.* **2014**, *43*, 7040–7066. [CrossRef]
51. Cardinale, A.M.; Carbone, C.; Consani, S.; Fortunato, M.; Parodi, N. Layered Double Hydroxides for Remediation of Industrial Wastewater from a Galvanic Plant. *Crystals* **2020**, *10*, 443. [CrossRef]
52. Tsuneishi, T.; Sakamoto, H.; Hayashi, K.; Kawamura, G.; Muto, H.; Matsuda, A. Preparation of Hydroxide Ion Conductive KOH–Layered Double Hydroxide Electrolytes for an All-Solid-State Iron–Air Secondary Battery. *J. Asian Ceram. Soc.* **2014**, *2*, 165–168. [CrossRef]
53. Leung, D.W.J.; Laney, K.R.; Kenyon, P.; Rees, N.H.; Buffet, J.-C.; Chen, C.; O'Hare, D. Optimising the Acid–Base Ratio of Mg–Al Layered Double Oxides to Enhance CO_2 Capture Performance: The Critical Role of Calcination Conditions. *Dalton Trans.* **2024**, *53*, 6200–6206. [CrossRef] [PubMed]
54. Xu, S.-M.; Zhu, Y.-Q.; Chen, Z.-R.; Yang, J.-R.; Chen, X.; Yan, H. Theoretical Prediction of the Carrier Mobilities for $M^{II}{}_2M^{III}$-Cl-Layered Double Hydroxides in Three-Dimensional Directions. *J. Mater. Chem. C Mater.* **2022**, *10*, 9573–9585. [CrossRef]
55. Xu, J.; Deng, H.; Song, J.; Zhao, J.; Zhang, L.; Hou, W. Synthesis of Hierarchical Flower-like Mg_2Al-Cl Layered Double Hydroxide in a Surfactant-Free Reverse Microemulsion. *J. Colloid. Interface Sci.* **2017**, *505*, 816–823. [CrossRef] [PubMed]
56. Memon, J.; Sun, J.; Meng, D.; Ouyang, W.; Memon, M.A.; Huang, Y.; Yan, S.; Geng, J. Synthesis of Graphene/Ni–Al Layered Double Hydroxide Nanowires and Their Application as an Electrode Material for Supercapacitors. *J. Mater. Chem. A Mater.* **2014**, *2*, 5060–5067. [CrossRef]
57. Palapa, N.R.; Taher, T.; Mohadi, R.; Lesbani, A. Removal of Anionic Direct Dye Using Zn/Al, Zn/Fe and Zn/Cr Layered Double Hydroxides Toward Interlayer Distance. *Sci. Technol. Indones.* **2019**, *4*, 70–76. [CrossRef]
58. Ibrahimova, K.A.; Azizov, A.A.; Balayeva, O.O.; Alosmanov, R.M.; Abbasov, M.H. The sonochemical synthesis of PVA/Mg-Al-OH layered double hydroxide nanocomposite film. *Azerbaijan Chem. J.* **2023**, *1*, 141–148. [CrossRef]
59. Harada, K.; Nguyen, T.K.N.; Matsui, Y.; Fujii, K.; Grasset, F.; Ohashi, N.; Matsuda, M.; Uchikoshi, T. Observation of Stacking Faults and Photoluminescence of Laurate Ion Intercalated Zn/Al Layered Double Hydroxide. *Mater. Lett.* **2018**, *213*, 323–325. [CrossRef]
60. Kahl, M.; Golden, T.D. Corrosion Resistance of Electrochemically Synthesized Modified Zaccagnaite LDH-Type Films on Steel Substrates. *Materials* **2021**, *14*, 7389. [CrossRef]
61. Sun, X.; Neuperger, E.; Dey, S.K. Insights into the Synthesis of Layered Double Hydroxide (LDH) Nanoparticles: Part 1. Optimization and Controlled Synthesis of Chloride-Intercalated LDH. *J. Colloid. Interface Sci.* **2015**, *459*, 264–272. [CrossRef]
62. Geng, D.G. Removal of Nitrophenol from Water by Dodecyl Sulfate Modified Layered Double Hydroxides. *Asian J. Chem.* **2014**, *26*, 447–450. [CrossRef]
63. Mohadi, R.; Amri, A.; Badaruddin, M.; Ahmad, N.; Lesbani, A. Adsorption of Phenol from Aqueous Solution Using Zn/Al Layered Double Hydroxides-Cellulose Composite. *Sci. Technol. Indones.* **2023**, *8*, 123–128. [CrossRef]
64. Smalenskaite, A.; Sen, S.; Salak, A.N.; Ferreira, M.G.S.; Skaudzius, R.; Katelnikovas, A.; Kareiva, A. Sol-Gel Synthesis and Characterization of Non-Substituted and Europium- Substituted Layered Double Hydroxides $Mg_3/Al_{1-x}Eu_x$. *Curr. Inorg. Chem.* **2017**, *6*, 149–154. [CrossRef]
65. George, G.; Saravanakumar, M.P. Synthesising Methods of Layered Double Hydroxides and Its Use in the Fabrication of Dye Sensitised Solar Cell (DSSC): A Short Review. *IOP Conf. Ser. Mater. Sci. Eng.* **2017**, *263*, 032020. [CrossRef]
66. Yang, B.; Yang, Z.; Wang, R.; Feng, Z. Silver Nanoparticle Deposited Layered Double Hydroxide Nanosheets as a Novel and High-Performing Anode Material for Enhanced Ni–Zn Secondary Batteries. *J. Mater. Chem. A* **2014**, *2*, 785–791. [CrossRef]
67. Gong, M.; Li, Y.; Wang, H.; Liang, Y.; Wu, J.Z.; Zhou, J.; Wang, J.; Regier, T.; Wei, F.; Dai, H. An Advanced Ni–Fe Layered Double Hydroxide Electrocatalyst for Water Oxidation. *J. Am. Chem. Soc.* **2013**, *135*, 8452–8455. [CrossRef]
68. Shao, M.; Ning, F.; Zhao, J.; Wei, M.; Evans, D.G.; Duan, X. Hierarchical Layered Double Hydroxide Microspheres with Largely Enhanced Performance for Ethanol Electrooxidation. *Adv. Funct. Mater.* **2013**, *23*, 3513–3518. [CrossRef]

69. Jia, Z.; Wang, Y.; Qi, T. Hierarchical Ni–Fe Layered Double Hydroxide/MnO_2 Sphere Architecture as an Efficient Noble Metal-Free Electrocatalyst for Ethanol Electro-Oxidation in Alkaline Solution. *RSC Adv.* **2015**, *5*, 83314–83319. [CrossRef]
70. Gao, X.; Lei, L.; Chen, L.; Wang, Y.; He, L.; Lian, Y. Synthesis and Controlled Release of Vitamin C Intercalated Zn/Al Layered Double Hydroxide. *Asian J. Chem.* **2014**, *26*, 3471–3476. [CrossRef]
71. Iqbal, M.A.; Sun, L.; Fedel, M. Synthesis of Novel Cone-Shaped CaAl-LDH Directly on Aluminum Alloy by a Facile Urea Hydrolysis Method. *SN Appl. Sci.* **2019**, *1*, 1415. [CrossRef]
72. Liu, X.L. Chiral Recognition of Lysine by Cyclodextrin Intercalated Layered Double Hydroxides. *Asian J. Chem.* **2013**, *25*, 10277–10282. [CrossRef]
73. ABD MALEK, A.H.; YASIN, Y. Use of Layered Double Hydroxides to Remove Sunset Yellow FCF Dye from Aqueous Solution. *Chem. Sci. Trans.* **2012**, *1*, 194–200. [CrossRef]
74. Hanifa, Y.; Rahayu Palapa, N. Mg/Al Double Layer Hydroxides: Intercalation with $H_3[\alpha\text{-}PW_{12}O_{40}]\bullet nH_2O$. *Sci. Technol. Indones.* **2016**, *1*, 16–19. [CrossRef]
75. Rasouli, N. Application of a Novel, Efficient and Recyclable Photo Redox Catalyst (Zn–Al Layered Double Hydroxide/Eosin) for the Synthesis of Substituted Pyridine Derivatives under Visible Light Irradiation. *Appl. Organomet. Chem.* **2018**, *32*, e4585. [CrossRef]
76. Imron, M.; Said, M. Adsorption of Procion Red Using Layer Double Hydroxide Mg/Al. *Sci. Technol. Indones.* **2017**, *2*, 64–67. [CrossRef]
77. Mishra, G.; Dash, B.; Pandey, S. Layered Double Hydroxides: A Brief Review from Fundamentals to Application as Evolving Biomaterials. *Appl. Clay Sci.* **2018**, *153*, 172–186. [CrossRef]
78. Shin, J.; Kim, K.; Hong, J. Zn-Al Layered Double Hydroxide Thin Film Fabricated by the Sputtering Method and Aqueous Solution Treatment. *Coatings* **2020**, *10*, 669. [CrossRef]
79. Mattera, M.; Sorrenti, A.; De Gregorio Perpiñá, L.; Oestreicher, V.; Sevim, S.; Arteaga, O.; Chen, X.; Pané, S.; Abellán, G.; Puigmartí-Luis, J. "On-The-Fly" Synthesis of Self-Supported LDH Hollow Structures Through Controlled Microfluidic Reaction-Diffusion Conditions. *Small* **2024**, *20*, 2307621. [CrossRef]
80. Wang, C.; Xu, J.; Zhou, Z. A Mini-Review on CO_2 Photoreduction by MgAl-LDH Based Materials. *Energies* **2022**, *15*, 8117. [CrossRef]
81. Wang, L.; Yuan, Z.; Zhang, Y.; Guo, W.; Sun, X.; Duan, X. Sandwich Layered Double Hydroxides with Graphene Oxide for Enhanced Water Desalination. *Sci. China Mater.* **2022**, *65*, 803–810. [CrossRef]
82. Jaramillo-Hernández, C.; Oestreicher, V.; Mizrahi, M.; Abellán, G. Upscaling the Urea Method Synthesis of CoAl Layered Double Hydroxides. *Beilstein J. Nanotechnol.* **2023**, *14*, 927–938. [CrossRef] [PubMed]
83. Rosaiah, P.; Vadivel, S.; Prakash, N.G.; Dhananjaya, M.; Al-Asbahi, B.A.; Roy, S.; Chalapathi, U.; Park, S.-H. Fabrication of Porous Ni-Co LDH Nanocomposites as Efficient Electrodes for Supercapacitors. *Int. J. Energy Res.* **2023**, *2023*, 5793868. [CrossRef]
84. Cao, Y.; Zheng, D.; Li, X.; Lin, J.; Wang, C.; Dong, S.; Lin, C. Enhanced Corrosion Resistance of Superhydrophobic Layered Double Hydroxide Films with Long-Term Stability on Al Substrate. *ACS Appl. Mater. Interfaces* **2018**, *10*, 15150–15162. [CrossRef]
85. Kim, A.; Varga, I.; Adhikari, A.; Patel, R. Recent Advances in Layered Double Hydroxide-Based Electrochemical and Optical Sensors. *Nanomaterials* **2021**, *11*, 2809. [CrossRef] [PubMed]
86. Li, X.; Chen, F.; Zhao, B.; Zhang, S.; Zheng, X.; Wang, Y.; Jin, X.; Dai, C.; Wang, J.; Xie, J.; et al. Ultrafast Synthesis of Metal-Layered Hydroxides in a Dozen Seconds for High-Performance Aqueous Zn (Micro-) Battery. *Nanomicro Lett.* **2023**, *15*, 32. [CrossRef] [PubMed]
87. Xu, X.; Wang, J.; Zhou, A.; Dong, S.; Shi, K.; Li, B.; Han, J.; O'Hare, D. High-Efficiency CO_2 Separation Using Hybrid LDH-Polymer Membranes. *Nat. Commun.* **2021**, *12*, 3069. [CrossRef]
88. Belskaya, O.B.; Terekhova, E.N.; Gorbunova, O.V.; Muromtsev, I.V.; Trenikhin, M.V.; Salanov, A.N.; Likholobov, V.A. Synthesis of CuAl-LDHs by Co-Precipitation and Mechanochemical Methods and Selective Hydrogenation Catalysts Based on Them. *Inorganics* **2023**, *11*, 247. [CrossRef]
89. Shah, S.S.; Aziz, M.A.; Ali, M.; Hakeem, A.S.; Yamani, Z.H. Advanced High-Energy All-Solid-State Hybrid Supercapacitor with Nickel-Cobalt-Layered Double Hydroxide Nanoflowers Supported on Jute Stick-Derived Activated Carbon Nanosheets. *Small* **2024**, *20*, 2306665. [CrossRef]
90. Wu, F.; Liang, J.; Peng, Z.; Liu, B. Electrochemical Deposition and Characterization of Zn-Al Layered Double Hydroxides (LDHs) Films on Magnesium Alloy. *Appl. Surf. Sci.* **2014**, *313*, 834–840. [CrossRef]
91. Johnston, A.L.; Lester, E.; Williams, O.; Gomes, R.L. Understanding Layered Double Hydroxide Properties as Sorbent Materials for Removing Organic Pollutants from Environmental Waters. *J. Environ. Chem. Eng.* **2021**, *9*, 105197. [CrossRef]
92. Ibrahimova, K.A. The synthesis methods and applications of layered double hydroxides—A brief review. *NNC RK Bull.* **2022**, *4*, 16–29. [CrossRef]
93. Palapa, N.R.; Saria, Y.; Taher, T.; Mohadi, R.; Lesbani, A. Synthesis and Characterization of Zn/Al, Zn/Fe, and Zn/Cr Layered Double Hydroxides: Effect of M^{3+} Ions Toward Layer Formation. *Sci. Technol. Indones.* **2019**, *4*, 36–39. [CrossRef]

94. Huang, X.; Yang, X.; Li, G.; Ezeh, C.I.; Sun, C.; Snape, C. Hybrid Two-Step Preparation of Nanosized MgAl Layered Double Hydroxides for CO_2 Adsorption. In *Sorption in 2020s*; IntechOpen: Rijeka, Croatia, 2020.
95. G.Fouad, H.; Sayed Amin, A.; S.Ahmed, I.; A.Ali, A. Zinc-Aluminium Layered Double Hydroxides: Fabrication, Study and Adsorption Application for Removal Organic Dye from Aqueous Media. *Benha J. Appl. Sci.* **2022**, *7*, 53–61. [CrossRef]
96. Smalenskaite, A.; Kaba, M.M.; Grigoraviciute-Puroniene, I.; Mikoliunaite, L.; Zarkov, A.; Ramanauskas, R.; Morkan, I.A.; Kareiva, A. Sol–Gel Synthesis and Characterization of Coatings of Mg-Al Layered Double Hydroxides. *Materials* **2019**, *12*, 3738. [CrossRef]
97. Xu, Y.; Liu, T.; Li, Y.; Liu, Y.; Ge, F. Nanostructure Design and Catalytic Performance of Mo/ZnAl-LDH in Cationic Orchid X-BL Removal. *Materials* **2018**, *11*, 2390. [CrossRef]
98. Wijitwongwan, R.P.; Saothayanun, T.K.; Ogawa, M. Synthesis of NiFe Layered Double Hydroxides with Varied Layer Charge Densities: The Templating Effect of Dioctyl Sulfosuccinate. *Dalton Trans.* **2023**, *52*, 4692–4699. [CrossRef]
99. Zhang, J.-J.; Li, M.-Y.; Li, X.; Bao, W.-W.; Jin, C.-Q.; Feng, X.-H.; Liu, G.; Yang, C.-M.; Zhang, N.-N. Chromium-Modified Ultrathin CoFe LDH as High-Efficiency Electrode for Hydrogen Evolution Reaction. *Nanomaterials* **2022**, *12*, 1227. [CrossRef] [PubMed]
100. Cao, Y.; Zheng, D.; Luo, J.; Zhang, F.; Dong, S.; Pan, J.; Lin, C. Insight into the Fabrication of ZnAl Layered Double Hydroxides Intercalated with Organic Anions and Their Corrosion Protection of Steel Reinforced Concrete. *J. Electrochem. Soc.* **2019**, *166*, C617–C623. [CrossRef]
101. Fang, S.; Chen, K.; Yao, H.; Cao, Y.; Guo, S.; Wang, L.; Wang, Y.; Yu, S.; Wang, N. Preparation of Gallic Acid Intercalated Layered Double Hydroxide for Enhanced Corrosion Protection of Epoxy Coatings. *Coatings* **2023**, *13*, 128. [CrossRef]
102. Bani Hashemi, A.; Kasiri, G.; Glenneberg, J.; Langer, F.; Kun, R.; La Mantia, F. Electrochemical and Morphological Characterization of Zn−Al−Cu Layered Double Hydroxides as a Negative Electrode in Aqueous Zinc-Ion Batteries. *ChemElectroChem* **2018**, *5*, 2073–2079. [CrossRef]
103. Neethu, P.P.; Venkatachalam, G.; Venkatesha, N.J.; Joseph, D.; Sakthivel, A. Cobalt-Based Hydrotalcite: A Potential Non-Noble Metal-Based Heterogeneous Catalyst for Selective Hydrogenation of Aromatic Aldehydes. *Ind. Eng. Chem. Res.* **2023**, *62*, 4976–4986. [CrossRef]
104. Kitano, S.; Sato, Y.; Tagusari, R.; Zhu, R.; Kowalski, D.; Aoki, Y.; Habazaki, H. Facile Synthesis Approach of Bifunctional Co–Ni–Fe Oxyhydroxide and Spinel Oxide Composite Electrocatalysts from Hydroxide and Layered Double Hydroxide Composite Precursors. *RSC Adv.* **2023**, *13*, 10681–10692. [CrossRef]
105. Huang, L.; Megías-Sayago, C.; Bingre, R.; Zheng, Q.; Wang, Q.; Louis, B. Catalytic Performance of Layered Double Hydroxides (LDHs) Derived Materials in Gas-Solid and Liquid-Solid Phase Reactions. *ChemCatChem* **2019**, *11*, 3279–3286. [CrossRef]
106. Kovalenko, V.; Borysenko, A.; Kotok, V.; Nafeev, R.; Verbitskiy, V.; Melnyk, O. Determination of the Dependence of the Structure of Zn-Al Layered Double Hydroxides, as a Matrix for Functional Anions Intercalation, on Synthesis Conditions. *East.-Eur. J. Enterp. Technol.* **2022**, *1*, 12–20. [CrossRef]
107. Nyaba, L.; Munonde, T.S.; Mpupa, A.; Nomngongo, P.N. Magnetic Fe_3O_4@Mg/Al-Layered Double Hydroxide Adsorbent for Preconcentration of Trace Metals in Water Matrices. *Sci. Rep.* **2021**, *11*, 2302. [CrossRef] [PubMed]
108. Liu, J.; Yue, X.; Lu, X.; Guo, Y. Uptake Fluoride from Water by Starch Stabilized Layered Double Hydroxides. *Water* **2018**, *10*, 745. [CrossRef]
109. Yang, K.; Huang, Y.; Wang, P.; Tang, Y.; Zhu, Y.; Zhu, X.; Xu, Y.; Jiang, W.; Pan, L.; Li, Q.; et al. LDH Nanocrystal@amorphousness Core–Shell Structure Derived from LDH→LDO Transformation: Synergistically Enhanced Energy Stored for LIBs Anode. *Chem. Eng. J.* **2024**, *486*, 150416. [CrossRef]
110. Hwang, J.Y.; Park, H.; Kim, H.; Kansara, S.; Sun, Y.K. Advanced Cathodes for Practical Lithium-Sulfur Batteries. *Acc. Mater. Res.* **2025**, *6*, 245–258. [CrossRef]
111. Fortunato, M.; Sarapulova, A.; Schwarz, B.; Cardinale, A.M.; Dsoke, S. NiFe-NO_3 Layered Double Hydroxide as a Novel Anode for Sodium Ion Batteries. *Batter. Supercaps* **2024**, *8*, 2400451. [CrossRef]
112. Wu, Y.; Yuan, Q.; Wu, Z.; Zhao, Z.; Yin, Q.; Han, J. Interlayer-Spacing Regulation of NiFe LDH Nanosheets Cathode with High Rate Performance for Chloride Ion Battery. *J. Ind. Eng. Chem.* **2024**, *143*, 176–183. [CrossRef]
113. Li, J.; Li, M.; Xu, S.; Weng, H. Chloride Ion Batteries-Excellent Candidates for New Energy Storage Batteries Following Lithium-Ion Batteries. *Ionics* **2024**, *30*, 27–38. [CrossRef]
114. Song, Z.; Yin, Q.; Yang, S.; Miao, Y.; Wu, Y.; Li, Y.Z.; Ren, Y.; Sui, Y.; Qi, J.; Han, J. A High-Nickel Layered Double Hydroxides Cathode Boosting the Rate Capability for Chloride Ion Batteries with Ultralong Cycling Life. *Small* **2023**, *19*, 2302896. [CrossRef]
115. Chen, K.; Chen, C.; Long, J.; Zhou, G. MOF/LDH Cross Composites Derived Heterojunction Nanospheres as Highly Efficient Catalysts for ORR-OER and Rechargeable Zn-Air Batteries. *Appl. Surf. Sci.* **2024**, *657*, 159803. [CrossRef]
116. Allwyn, N.; Gokulnath, S.; Sathish, M. In-Situ Nanoarchitectonics of Fe/Co LDH over Cobalt-Enriched N-Doped Carbon Cookies as Facile Oxygen Redox Electrocatalysts for High-Rate Rechargeable Zinc–Air Batteries. *ACS Appl. Mater. Interfaces* **2024**, *16*, 20360–20374. [CrossRef] [PubMed]
117. Ogawa, M.; Asai, S. Hydrothermal Synthesis of Layered Double Hydroxide-Deoxycholate Intercalation Compounds. *Chem. Mater.* **2000**, *12*, 3253–3255. [CrossRef]

118. Jiang, F.; Xie, Y.; Zhang, H.; Zhang, L.; Gao, X.; Bai, H.; Yao, F.; Yue, H. Hierarchical Core-Shelled CoMo Layered Double Hydroxide@$CuCo_2S_4$ Nanowire Arrays/Nickel Foam for Advanced Hybrid Supercapacitors. *J. Colloid. Interface Sci.* **2025**, *677*, 150–157. [CrossRef]
119. Li, R.Y.; Shen, X.Y.; Li, J.; Zhao, D.P.; Zhao, R.D.; Wu, F.F. Enhanced Electrochemical Performance of NiCo-Layered Double Hydroxides: Optimal Synthesis Conditions and Supercapacitor Applications. *Adv. Sustain. Syst.* **2024**, *9*, 2400753. [CrossRef]
120. Zhi, P.X.; Guo, Q.L. Hydrothermal Synthesis of Layered Double Hydroxides (LDHs) from Mixed MgO and Al_2O_3: LDH Formation Mechanism. *Chem. Mater.* **2005**, *17*, 1055–1062. [CrossRef]
121. Ai, L.; Zhang, C.; Meng, L. Adsorption of Methyl Orange from Aqueous Solution on Hydrothermal Synthesized Mg-Al Layered Double Hydroxide. *J. Chem. Eng. Data* **2011**, *56*, 4217–4225. [CrossRef]
122. Knorpp, A.J.; Zawisza, A.; Huangfu, S.; Borzì, A.; Clark, A.H.; Kata, D.; Graule, T.; Stuer, M. Hydrothermal Synthesis of Multi-Cationic High-Entropy Layered Double Hydroxides. *RSC Adv.* **2022**, *12*, 26362–26371. [CrossRef]
123. Rybka, K.; Matusik, J. Exploring Synthesis Approaches, Properties and Applications of Layered Double Hydroxides Derived from Alternative Sources: A Comprehensive Review. *J. Clean. Prod.* **2025**, *498*, 145215. [CrossRef]
124. Sakai, M.; Imagawa, H.; Baba, N. Layered-Double-Hydroxide-Based Ni Catalyst for CO_2 Capture and Methanation. *Appl. Catal. A Gen.* **2022**, *647*, 118904. [CrossRef]
125. Liao, L.; Zhao, N.; Xia, Z. Hydrothermal Synthesis of Mg-Al Layered Double Hydroxides (LDHs) from Natural Brucite and $Al(OH)_3$. *Mater. Res. Bull.* **2012**, *47*, 3897–3901. [CrossRef]
126. Pan, Y.; Li, L.; Liu, D.; Wang, F.; Xia, M.; Wang, F. Macroscale Structures of Layered Double Hydroxides: A Review of Formation Strategies and Applications in Water Treatment. *J. Environ. Chem. Eng.* **2025**, *13*, 115284. [CrossRef]
127. Cheng, X.; Zhang, L.; Li, L.; Wu, H.; Zheng, J.; Sun, J.; Li, G. One-Step Hydrothermal Synthesis of Glucose-Induced Low Crystallinity NiCo-Based Layered Double Hydroxides for High-Performance Asymmetric Supercapacitors. *Chem. Eur. J.* **2024**, *31*, e202403439. [CrossRef]
128. Zhao, Y.; Xiao, F.; Jiao, Q. Hydrothermal Synthesis of Ni/Al Layered Double Hydroxide Nanorods. *J. Nanotechnol.* **2011**, *2011*, 646409. [CrossRef]
129. Zhang, F.; Du, N.; Song, S.; Liu, J.; Hou, W. Mechano-Hydrothermal Synthesis of Mg_2Al-NO_3 Layered Double Hydroxides. *J. Solid. State Chem.* **2013**, *206*, 45–50. [CrossRef]
130. Clark, I.; Dunne, P.W.; Gomes, R.L.; Lester, E. Continuous Hydrothermal Synthesis of Ca_2Al-NO_3 Layered Double Hydroxides: The Impact of Reactor Temperature, Pressure and NaOH Concentration on Crystal Characteristics. *J. Colloid. Interface Sci.* **2017**, *504*, 492–499. [CrossRef] [PubMed]
131. Wang, W.; Zhou, J.; Achari, G.; Yu, J.; Cai, W. Cr(VI) Removal from Aqueous Solutions by Hydrothermal Synthetic Layered Double Hydroxides: Adsorption Performance, Coexisting Anions and Regeneration Studies. *Colloids Surf. A Physicochem. Eng. Asp.* **2014**, *457*, 33–40. [CrossRef]
132. Tung, N.Q.; Van, D.T.C.; Thang, D.X.; An, N.T.K.; Trang, T.T.; Nhi, B.D.; Thao, N.P.; Son, L.T.; Huy, N.N.; Dung, N.T. Hydrothermal Synthesis of CuCoFe Layered Double Hydroxide and Its Performance in the Degradation of Antibiotics: Influencing Factors, Degradation Pathways, and Reaction Mechanism. *J. Environ. Chem. Eng.* **2023**, *11*, 110127. [CrossRef]
133. Prevot, V.; Caperaa, N.; Taviot-Guého, C.; Forano, C. Glycine-Assisted Hydrothermal Synthesis of NiAl-Layered Double Hydroxide Nanostructures. *Cryst. Growth Des.* **2009**, *9*, 3646–3654. [CrossRef]
134. Xiong, Q.; Li, X.; Zhou, M.; Chen, R.; Sun, C.; Zhou, Y.; Wang, S.; Qiu, X.; Song, M.; Wei, T. One-Pot Hydrothermal Synthesis of Flower-Shaped Zif-67@NiCo-LDH Heterostructure as Anode Materials for Lithium-Ion Batteries. *Ionics* **2023**, *29*, 1741–1749. [CrossRef]
135. Zhu, L.; Han, T.; Ding, Y.; Long, J.; Lin, X.; Liu, J. A Metal–Organic-Framework Derived $NiFe_2O_4$@NiCo-LDH Nanocube as High-Performance Lithium-Ion Battery Anode under Different Temperatures. *Appl. Surf. Sci.* **2022**, *599*, 153953. [CrossRef]
136. Luo, K.; Li, Y.; Yao, J.; Huang, B.; Zhu, Q.; Yang, J. Boosting the Lithium Storage Property of Nickel-Zinc Layered Double Hydroxides by Intercalation with Dodecyl Sulfate Anions. *Appl. Surf. Sci.* **2023**, *620*, 156850. [CrossRef]
137. Liu, Y.; Zhou, X.; Chen, P.; Cao, X.; Liu, D.; Wang, R. Properties of Hollow Yolk-Shell NiS_2/FeS_2@NC@NiFe LDH/FeO(OH) Nanoflower Microspheres as Anode Materials for Lithium-Ion Batteries. *J. Electroanal. Chem.* **2023**, *943*, 117606. [CrossRef]
138. Yang, T.; Zhang, Z.; Ma, P.; Li, H. Constructing 1D/2D NiCo-LDH Nanowire/MXene Composites for Efficient and Stable Lithium Storage. *Adv. Mater. Interfaces* **2024**, *11*, 2300962. [CrossRef]
139. Shah, S.S.; Aziz, M.A.; Rasool, P.I.; Mohmand, N.Z.K.; Khan, A.J.; Ullah, H.; Feng, X.; Oyama, M. Electrochemical Synergy and Future Prospects: Advancements and Challenges in MXene and MOFs Composites for Hybrid Supercapacitors. *Sustain. Mater. Technol.* **2024**, *39*, e00814. [CrossRef]
140. Yuan, Q.; Zhang, J.; Li, B.; Wu, Y.; Wu, Z.; Dou, Y.; Yin, Q.; Han, J. An MgAl Layered Double Hydroxide as a New Transition Metal-Free Anode for Lithium-Ion Batteries. *Chem. Commun.* **2023**, *59*, 13903–13906. [CrossRef]
141. Zhang, D.; Hua, Y.; Fu, X.; Cheng, C.; Kong, D.; Zhang, M.; Lei, B.; Liu, Z. Hierarchical Flower Array NiCoOOH@CoLa-LDH Nanosheets for High-Performance Supercapacitor and Alkaline Zn Battery. *Adv. Funct. Mater.* **2025**, *35*, e202414686. [CrossRef]

142. Yin, Q.; Song, Z.; Yang, S.; Zhao, Z.; Yuan, Q.; Qi, J.; Sui, Y.; Han, J. Heteroatoms Introduction via Temperature-Differential Doping Strategy Achieves Long-Cycle-Life NiCoMo-P LDH Cathode for Rechargeable Chloride-Ion Battery. *J. Electroanal. Chem.* **2023**, *951*, 117924. [CrossRef]
143. Zhao, G.; Deng, Z.; Wan, G.; Zhao, J.; Wang, G. Array Structured NiAl-Layered Double Hydroxides Grown on Graphene by Atomic Layer Deposition as Chloride-Ion Battery Cathode. *DeCarbon* **2025**, *8*, 100106. [CrossRef]
144. Yang, S.; Yin, Q.; Song, Z.; Xu, F.; Xie, Z.; Wu, Y.; Xu, S.; Li, Y.Z.; Zhao, D.; Xiao, B.; et al. Introducing High-Valence Molybdenum to Stimulate Lattice Oxygen in a NiCo LDH Cathode for Chloride Ion Batteries. *Mater. Horiz.* **2023**, *10*, 3429–3437. [CrossRef] [PubMed]
145. Wu, Z.; Wu, Y.; Yuan, Q.; Zhang, J.; Dou, Y.; Han, J. Aqueous Chloride-Ion Battery within a Neutral Electrolyte Based on a CoFe-Cl Layered Double Hydroxide Anode. *ACS Appl. Mater. Interfaces* **2023**, *15*, 38540–38549. [CrossRef]
146. Li, J.; Qin, Y.; Bai, Z.; Li, S.; Li, L.; Ouyang, B.; Kan, E.; Zhang, W. Investigating the Role of 3D Hierarchical Ni-CAT/NiFe-LDH/CNFs in Enhancing the Oxygen Evolution Reaction and Zn-Air Battery Performance. *Appl. Surf. Sci.* **2024**, *648*, 159080. [CrossRef]
147. Bhanuse, G.B.; Kumar, S.; Yu, C.C.; Fu, Y.P. Nanostructured $ZnCo_2O_4$@NiMn-LDH Electrodes for Supercapacitor and Zinc-Air Battery Application. *ACS Appl. Nano Mater.* **2024**, *7*, 13649–13663. [CrossRef]
148. Jia, Z.; Shang, J.; Xue, K.; Yang, X.; Wang, S.; Xu, C.; Wang, Q. N-doped Nanocarbon Inserted NiCo-LDH Nanoplates on NF with High OER/ORR Performances for Zinc-Air Battery. *ChemCatChem* **2023**, *15*, e202201469. [CrossRef]
149. Chen, J.; Liu, Z.; Liu, Y.; Cheng, Z.; Zhang, J.; Zhang, Q.; Li, Y.; Hou, C.; Li, K.; Wang, H. Efficient Bifunctional NiFe-LDH@Co_9S_8 Nanoflower Electrocatalysts Anchored with Pt Nanocrystal for Flexible Quasi-Solid Rechargeable Zinc Air Battery. *Energy Fuels* **2024**, *38*, 10264–10274. [CrossRef]
150. Liu, S.; Wan, R.; Lin, Z.; Liu, Z.; Liu, Y.; Tian, Y.; Qin, D.-D.; Tang, Z. Probing the Co Role in Promoting the OER and Zn–Air Battery Performance of NiFe-LDH: A Combined Experimental and Theoretical Study. *J. Mater. Chem. A Mater.* **2022**, *10*, 5244–5254. [CrossRef]
151. Dighe, P.S.; Redekar, R.S.; Tarwal, N.L.; Sarawade, P.B. Design and Development of the High-Performance Aqueous Asymmetric Supercapacitor Based on the Hydrothermally Grown Binder-Less Ni-Co LDH Nanosheets. *J. Energy Storage* **2024**, *88*, 111467. [CrossRef]
152. Chandra Sahoo, R.; Moolayadukkam, S.; Seok, J.H.; Lee, S.U.; Matte, H.S.S.R. Enhanced Charge Storage Capacity and High Rate Capabilities of Ni_2Co-Layered Double Hydroxides/Expanded-Graphite Composites as Anodes for Li-Ion Batteries. *J. Mater. Chem. A Mater.* **2023**, *11*, 7142–7151. [CrossRef]
153. Li, X.; Fortunato, M.; Cardinale, A.M.; Sarapulova, A.; Njel, C.; Dsoke, S. Electrochemical Study on Nickel Aluminum Layered Double Hydroxides as High-Performance Electrode Material for Lithium-Ion Batteries Based on Sodium Alginate Binder. *J. Solid. State Electrochem.* **2022**, *26*, 49–61. [CrossRef]
154. Du, P.; Xi, W.; Zhang, Y.; Wang, R.; Gong, Y.; He, B.; Wang, H.; Jin, J. Laser Induction of Hierarchically Micro/Nanostructured CoNi-LDH/C Composite for High-Performance Lithium-Sulfur Batteries. *J. Alloys Compd.* **2024**, *985*, 174043. [CrossRef]
155. Ye, Z.; Zhai, S.; Liu, R.; Liu, M.; Xu, Y.; Li, C.; Wang, X.; Mei, T. Sulfonate-Rich Polymer Intercalated LDH Artificial SEI Film to Enable High-Stability Li-S Batteries. *Chem. Eng. J.* **2024**, *479*, 147847. [CrossRef]
156. Zhen, M.; Meng, X.; Wang, X.; Zhang, Z.; Guo, S.-Q.; Hu, Z.; Shen, B. Layered Double Hydroxides-MXene Heterointerfaces with Abundant Anion Vacancies Expediting Sulfur Redox Kinetics for High-Performance Lithium–Sulfur Batteries. *Chem. Eng. J.* **2024**, *489*, 151285. [CrossRef]
157. Liu, Q.; Zhang, Y.; Zhou, Y.; Wang, M.; Li, R.; Yue, W. Layered Double Hydroxides Used as the Sulfur Hosts for Lithium-Sulfur Batteries and the Influence of Metal Composition on Their Performance. *J. Solid. State Electrochem.* **2023**, *27*, 797–807. [CrossRef]
158. Wang, H.Y.; Dai, Y.K.; Liao, K.M.; Deng, S.; Dai, G.P. Vertical Graphene Growth on LDH Nanosheets and Carbon Cloth Nanofibers with NiCo Nanoparticles as a Freestanding Host for High-Performance Lithium-Sulfur Batteries. *J. Phys. Chem. Lett.* **2025**, *16*, 1103–1113. [CrossRef]
159. Zhang, Y.; Zhang, Y.; Ma, L.; Yang, M.; Zhao, X. NiCr-Cl LDH/RGO Composite as Anode Material for Sodium-Ion Batteries. *J. Electron. Mater.* **2022**, *51*, 6067–6075. [CrossRef]
160. Li, B.; Li, J.; Li, P.; Zhang, N.; Shang, H.; Zhang, B. Sulfide Hollow ZIF-67 and NiCo-LDH Heterostructure for Superior Asymmetric Supercapacitors. *J. Alloys Compd.* **2025**, *1017*, 179128. [CrossRef]
161. He, L.; Cai, P.; Lai, H.; Lu, K.; Xu, Z.; Zeng, R.; Hao, C.; Wang, Z.; Gan, W. Sandwich-like NiFe-LDH/$MnCO_3$/MXene Ternary Nanocomposites Serve as Battery-Type Electrode for High-Performance Asymmetric Supercapacitor. *Chem. Eng. J.* **2025**, *504*, 159149. [CrossRef]
162. Liu, Y.; Wang, C.; Sun, H.; Duan, L.; Yang, Z.; Wang, X.; Liu, J. Construction of Flexible $MnCo_2O_4$@FeCoNi-LDH Electrode Materials with Nanoflower-like and Hierarchical Structure for High-Performance Asymmetric Supercapacitor. *J. Colloid. Interface Sci.* **2025**, *682*, 1051–1061. [CrossRef]

163. Tai, P.C.; Chung, R.J.; Wang, G.B.; Kongvarhodom, C.; Husain, S.; Yougbaré, S.; Chen, H.M.; Wu, Y.F.; Lin, L.Y. Polydopamine Derived Carbon Coated Cobalt Molybdenum Layered Double Hydroxide as Highly Stable Anode Materials of Sodium-Ion Battery. *J. Energy Storage* **2024**, *101*, 113961. [CrossRef]
164. Lin, Q.; Yuan, Z.; Wang, D.; Wei, W.; Wang, X.; Han, W.; Wang, L. Co-Co LDH-Derived $CoSe_2$ Anchored on N-Doped Carbon Nanospheres as High-Performance Anodes for Sodium-Ion Batteries. *Electrochim. Acta* **2022**, *432*, 141012. [CrossRef]
165. Ma, X.; Zhou, L.; Chen, T.; Sun, P.; Lv, X.; Yu, H.; Sun, X.; Leo Liu, T. High-Performance Aqueous Rechargeable NiCo//Zn Battery with Molybdate Anion Intercalated CoNi-LDH@CP Bilayered Cathode. *J. Colloid. Interface Sci.* **2024**, *658*, 728–738. [CrossRef]
166. Wang, C.; Han, L.; Yang, S.; Liu, Z.; Liu, M.; Li, B. Nanosheet-Structured ZnCo-LDH Microsphere as Active Material for Rechargeable Zinc Batteries. *J. Colloid. Interface Sci.* **2024**, *659*, 119–126. [CrossRef] [PubMed]
167. Zhang, Y.; Hu, S.; Li, C.; Yan, X.; Zhang, Y.; Yin, R.; Wei, Y.; Gao, K.; Gao, H. Advanced Strategies for Enhancing Electrochemical Performance of NiAl LDH Electrodes in Supercapacitors. *Coord. Chem. Rev.* **2025**, *531*, 216497. [CrossRef]
168. Jing, C.; Huang, L.; Tao, S.; Chen, Y.; Zhang, S.; Dong, W.; Ling, F.; Tang, X.; Li, Y.; Feng, L.; et al. Construction of MoB@LDH Heterojunction and Its Derivates through Phase and Interface Engineering for Advanced Supercapacitor Applications. *J. Colloid. Interface Sci.* **2024**, *660*, 10–20. [CrossRef]
169. Tai, P.-Y.; Sakthivel, M.; Peng, Y.-J.; Kubendhiran, S.; Lin, L.-Y.; Ho, K.-C. In Situ Growing Te-Doped Ni–Mn Layered Double Hydroxide on a Cetyltrimethylammonium Bromide-Modified MXene Conductive Layer for Binder-Free Supercapacitors. *ACS Appl. Energy Mater.* **2025**, *8*, 4122–4133. [CrossRef]
170. Han, X.; Li, J.; Lu, J.; Luo, S.; Wan, J.; Li, B.; Hu, C.; Cheng, X. High Mass-Loading NiCo-LDH Nanosheet Arrays Grown on Carbon Cloth by Electrodeposition for Excellent Electrochemical Energy Storage. *Nano Energy* **2021**, *86*, 106079. [CrossRef]
171. He, T.-L.; Zhang, X.-R.; Ma, Q.-L.; Hua, W.-M.; Xiong, H.-M. Positive Carbon Dots Induced Electrodeposition of NiCo-LDH Nanosheets for High-Performance Supercapacitors. *ACS Appl. Energy Mater.* **2024**, *7*, 5508–5516. [CrossRef]
172. Niu, Y.; Chang, L.; Huang, Y.; Sun, Q.; Lu, X.; Cheng, H. Electrochemical Constructing Versatile ZnAl-LDH Artificial Interface Layer Coated (002)-Textured Zn for Highly Reversible Zinc Anodes. *Chem. Eng. J.* **2024**, *499*, 155813. [CrossRef]
173. Lashgari, M.; Yamini, Y. Fiber-in-tube Solid-phase Microextraction of Caffeine as a Molecular Tracer in Wastewater by Electrochemically Deposited Layered Double Hydroxide. *J. Sep. Sci.* **2018**, *41*, 2393–2400. [CrossRef]
174. Seumo Tchekwagep, P.M.; Banks, C.E.; Crapnell, R.D.; Farsak, M.; Kardaş, G. Electrochemical Synthesis of NiCo Layered Double Hydroxides on Nickel-Coated Graphite for Water Splitting: Understanding the Electrochemical Experimental Parameters. *RSC Adv.* **2025**, *15*, 3969–3978. [CrossRef] [PubMed]
175. Cysewska, K.; Zając, M.; Łapiński, M.; Karczewski, J.; Rybarczyk, M.K.; Kamecki, B.; Jasiński, P.; Molin, S. The Effect of Cobalt Incorporation into Nickel–Iron Oxide/(oxy)Hydroxide Catalyst on Electrocatalytic Performance Toward Oxygen Evolution Reaction. *Energy Technol.* **2021**, *9*, 2100688. [CrossRef]
176. Wu, Q.; Li, F.; Sheng, H.; Qi, Y.; Yuan, J.; Bi, H.; Li, W.; Xie, E.; Lan, W. In Situ Fabrication of Hierarchical CuO@CoNi-LDH Composite Structures for High-Performance Supercapacitors. *ACS Appl. Mater. Interfaces* **2024**, *16*, 23241–23252. [CrossRef]
177. Kim, Y.; Jun, S.E.; Lee, G.; Nam, S.; Jang, H.W.; Park, S.H.; Kwon, K.C. Recent Advances in Water-Splitting Electrocatalysts Based on Electrodeposition. *Materials* **2023**, *16*, 3044. [CrossRef] [PubMed]
178. Pawar, S.A.; Yu, S.; Ju, E.; Seo, H.; Yeu, J.; Kim, J.; Patil, D.S.; Shin, J.C. Zinc Cobalt Layered Double Hydroxide Electrode for High-Performance Supercapacitor. *Appl. Sci. Converg. Technol.* **2019**, *28*, 164–168. [CrossRef]
179. Arbenin, A.Y.; Zemtsova, E.G.; Orekhov, E.V.; Sokolova, D.N.; Baburova, P.I.; Petrov, A.A.; Gaĭshun, V.E.; Smirnov, V.M. Features of Fabrication of Titanium Dioxide Based Coatings for Non-Lithographic Template Electrochemical Synthesis of Micron Metal Particle Arrays. *Gels* **2021**, *7*, 202. [CrossRef] [PubMed]
180. Guo, H.; Guan, Y.; Zhang, M.; Qin, J.; Guo, X.; Li, Z.; Zhang, B.; Tang, J. Dynamic Morphological Evolution of Co-Based Layered Double Hydroxide Nanosheets Investigated by In Situ Electrochemical-Atomic Force Microscopy. *J. Phys. Chem. C* **2023**, *127*, 5219–5229. [CrossRef]
181. Wang, T.; Wang, W.; Shao, W.; Bai, M.; Zhou, M.; Li, S.; Ma, T.; Ma, L.; Cheng, C.; Liu, X. Synthesis and Electronic Modulation of Nanostructured Layered Double Hydroxides for Efficient Electrochemical Oxygen Evolution. *ChemSusChem* **2021**, *14*, 5112–5134. [CrossRef]
182. Ramachandran, R.; Lan, Y.; Xu, Z.X.; Wang, F. Construction of NiCo-Layered Double Hydroxide Microspheres from Ni-MOFs for High-Performance Asymmetric Supercapacitors. *ACS Appl. Energy Mater.* **2020**, *3*, 6633–6643. [CrossRef]
183. Shahid, N.F.; Jamal, A.; Haq, G.; Javed, M.; Saifullah, M.; Anjum, M.A.R. Cobalt–Iron Layered Double Hydroxide Nanosheet-Wrapped Nitrogen-Doped Graphite Felt as an Oxygen-Evolving Electrode. *Energy Adv.* **2023**, *2*, 2109–2118. [CrossRef]
184. Ren, B.; Zhang, B.Y.; Zhang, H.; Jiang, X.; Yi, Q.; Xu, K.; Yu, H.; Hu, Z.; Jeerapan, I.; Ou, J.Z. CoNi Layered Double Hydroxide Nanosheets Vertically Grown on Electrodeposited Dendritic Copper Substrates for Supercapacitor Applications. *ACS Appl. Nano Mater.* **2022**, *5*, 2395–2404. [CrossRef]

185. Zhang, H.; Li, X.; Hähnel, A.; Naumann, V.; Lin, C.; Azimi, S.; Schweizer, S.L.; Maijenburg, A.W.; Wehrspohn, R.B. Bifunctional Heterostructure Assembly of NiFe LDH Nanosheets on NiCoP Nanowires for Highly Efficient and Stable Overall Water Splitting. *Adv. Funct. Mater.* **2018**, *28*, 1706847. [CrossRef]
186. Iqbal, M.A.; Sun, L.; LaChance, A.M.; Ding, H.; Fedel, M. In Situ Growth of a CaAl-NO_3^- -Layered Double Hydroxide Film Directly on an Aluminum Alloy for Corrosion Resistance. *Dalton Trans.* **2020**, *49*, 3956–3964. [CrossRef] [PubMed]
187. Gualandi, I.; Vlamidis, Y.; Mazzei, L.; Musella, E.; Giorgetti, M.; Christian, M.; Morandi, V.; Scavetta, E.; Tonelli, D. Ni/Al Layered Double Hydroxide and Carbon Nanomaterial Composites for Glucose Sensing. *ACS Appl. Nano Mater.* **2019**, *2*, 143–155. [CrossRef]
188. Alsaç, E.P.; Zhou, K.; Rong, W.; Salamon, S.; Landers, J.; Wende, H.; Smith, R.D.L. Identification of Non-Traditional Coordination Environments for Iron Ions in Nickel Hydroxide Lattices. *Energy Environ. Sci.* **2022**, *15*, 2638–2652. [CrossRef]
189. Shi, Z.; Yuan, Y.; Xiao, Q.; Li, Z.; Zhu, J. Carbonate Doped NiCo-LDH Modified with PANI for High Performance Asymmetric Supercapacitors. *CrystEngComm* **2022**, *24*, 3546–3555. [CrossRef]
190. Tan, Z.; Luo, X.; Wei, T.; Zhang, F.; Lv, Y.; Chen, L.; Shi, Y. In Situ Formation of NiAl-Layered Double Hydroxide with a Tunable Interlayer Spacing in a Confined Impinging Jet Microreactor. *Energy Fuels* **2020**, *34*, 8939–8946. [CrossRef]
191. Yan, Z.; Sun, H.; Chen, X.; Liu, H.; Zhao, Y.; Li, H.; Xie, W.; Cheng, F.; Chen, J. Anion Insertion Enhanced Electrodeposition of Robust Metal Hydroxide/Oxide Electrodes for Oxygen Evolution. *Nat. Commun.* **2018**, *9*, 2373. [CrossRef]
192. Ghadimi, A.M.; Ghasemi, S.; Omrani, A.; Mousavi, F. Nickel Cobalt LDH/Graphene Film on Nickel-Foam-Supported Ternary Transition Metal Oxides for Supercapacitor Applications. *Energy Fuels* **2023**, *37*, 3121–3133. [CrossRef]
193. Cysewska, K.; Rybarczyk, M.K.; Cempura, G.; Karczewski, J.; Łapiński, M.; Jasinski, P.; Molin, S. The Influence of the Electrodeposition Parameters on the Properties of Mn-Co-Based Nanofilms as Anode Materials for Alkaline Electrolysers. *Materials* **2020**, *13*, 2662. [CrossRef] [PubMed]
194. Kumar, M.; Singh, R.P. Transforming Prussian Blue Analogues: The Future-Centric Pathway to Rise of Thin Layered Double Hydroxides for Superior Water Oxidation: An Overview. *Int. J. Multidiscip. Res.* **2024**, *6*, 240529213. [CrossRef]
195. Yang, Q.; Wang, Q.; Long, Y.; Wang, F.; Wu, L.; Pan, J.; Han, J.; Lei, Y.; Shi, W.; Song, S. In Situ Formation of Co_9S_8 Quantum Dots in MOF-Derived Ternary Metal Layered Double Hydroxide Nanoarrays for High-Performance Hybrid Supercapacitors. *Adv. Energy Mater.* **2020**, *10*, 1903193. [CrossRef]
196. Li, Z.; Han, F.; Li, C.; Jiao, X.; Chen, D. Multi-Anion Intercalated Layered Double Hydroxide Nanosheet-Assembled Hollow Nanoprisms with Improved Pseudocapacitive and Electrocatalytic Properties. *Chem. Asian J.* **2018**, *13*, 1129–1137. [CrossRef]
197. Li, S.; Mo, T.; Chen, L.; Zhang, F.; Jamil, S.; Lu, Y.; Cai, Q. Hierarchical MgAl-Layered Double Hydroxide Growth on Porous MgO Template for Pollution Removal. *Environ. Prog. Sustain. Energy* **2022**, *41*, e13907. [CrossRef]
198. Wei, M.; Huang, Q.; Zhou, Y.; Peng, Z.; Chu, W. Ultrathin Nanosheets of Cobalt-Nickel Hydroxides Hetero-Structure via Electrodeposition and Precursor Adjustment with Excellent Performance for Supercapacitor. *J. Energy Chem.* **2018**, *27*, 591–599. [CrossRef]
199. Chavan, H.S.; Lee, C.H.; Inamdar, A.I.; Han, J.; Park, S.; Cho, S.; Shreshta, N.K.; Lee, S.U.; Hou, B.; Im, H.; et al. Designing and Tuning the Electronic Structure of Nickel–Vanadium Layered Double Hydroxides for Highly Efficient Oxygen Evolution Electrocatalysis. *ACS Catal.* **2022**, *12*, 3821–3831. [CrossRef]
200. Zhai, P.; Xia, M.; Wu, Y.; Zhang, G.; Gao, J.; Zhang, B.; Cao, S.; Zhang, Y.; Li, Z.; Fan, Z.; et al. Engineering Single-Atomic Ruthenium Catalytic Sites on Defective Nickel-Iron Layered Double Hydroxide for Overall Water Splitting. *Nat. Commun.* **2021**, *12*, 4587. [CrossRef]
201. Wang, G.; Liu, G.; Jin, Z. In Situ Coupled Nickel-Based Layered Double Hydroxides with MXene to Enhance Supercapacitor Performance. *J. Mater. Chem. C Mater.* **2023**, *11*, 10547–10561. [CrossRef]
202. Laipan, M.; Yu, J.; Zhu, R.; Zhu, J.; Smith, A.T.; He, H.; O'Hare, D.; Sun, L. Functionalized Layered Double Hydroxides for Innovative Applications. *Mater. Horiz.* **2020**, *7*, 715–745. [CrossRef]
203. Chen, Z.; Zhu, J.; Yang, S.; Wei, Z.; Wang, Y.; Chen, A.; Huang, Z.; Zhi, C. MXene Supported Electrodeposition Engineering of Layer Double Hydroxide for Alkaline Zinc Batteries. *Angew. Chem. Int. Ed.* **2024**, *63*, e202411443. [CrossRef]
204. Cheng, X.; Wu, D.; Gao, H.; Wang, Q.; Lv, P.; Yoon, S.S.; Wei, Q. A Mild, Configurable, Flexible CoNi-LDH(v)/Zn Battery Based on H-Vacancy-Induced Reversible Zn^{2+} Intercalation. *J. Energy Chem.* **2025**, *100*, 498–508. [CrossRef]
205. Inamdar, A.I.; Chavan, H.S.; Jo, Y.; Im, H.; Kim, H. Nonprecious Bimetallic NiFe-layered Hydroxide Nanosheets as a Catalyst for Highly Efficient Electrochemical Water Splitting. *Int. J. Energy Res.* **2021**, *45*, 16963–16972. [CrossRef]
206. Li, H.; Zhao, R.; Zhou, W.; Wang, L.; Li, W.; Zhao, D.; Chao, D. Trade-off between Zincophilicity and Zincophobicity: Toward Stable Zn-Based Aqueous Batteries. *JACS Au* **2023**, *3*, 2107–2116. [CrossRef]
207. Meng, J.; Song, Y.; Qin, Z.; Wang, Z.; Mu, X.; Wang, J.; Liu, X.X. Cobalt–Nickel Double Hydroxide toward Mild Aqueous Zinc-Ion Batteries. *Adv. Funct. Mater.* **2022**, *32*, 2204026. [CrossRef]

208. Dai, L.; Peng, S.; Wang, X.; Chen, B.; Wu, Y.; Xie, Q.; Ruan, Y. Three-Dimensional NiCoS Nanotubes@NiCo-LDH Nanosheets Core–Shell Heterostructure for High-Rate Capability Alkaline Zinc-Based Batteries. *RSC Adv.* **2024**, *14*, 7999–8006. [CrossRef] [PubMed]
209. Zhou, K.; Wang, S.; Zhong, G.; Chen, J.; Bao, Y.; Niu, L. Hierarchical Heterostructure Engineering of Layered Double Hydroxides on Nickel Sulfides Heteronanowire Arrays as Efficient Cathode for Alkaline Aqueous Zinc Batteries. *Small* **2022**, *18*, 2202799. [CrossRef]
210. Cai, X.; Jiang, T.; Wu, M. Confined Growth of NiFe LDH with Hierarchical Structures on Copper Nanowires for Long-Term Stable Rechargeable Zn-Air Batteries. *Appl. Surf. Sci.* **2022**, *577*, 151911. [CrossRef]
211. Zhou, P.; Ji, Y.; Zhang, B.; Zhang, P.; Zhang, S.; Wang, S. Rational Construction of Tremella-like CuCo LDH@Ni_3S_2 Nanocomposites as High-Performance Supercapacitor Electrode Materials. *J. Alloys Compd.* **2025**, *1021*, 179586. [CrossRef]
212. Xing, H.; Deng, X.; Wang, X. Alkaline Capacity Decay Induced Vacancy-Rich LDH for High-Performance Magnesium Ions Hybrid Supercapacitor. *J. Colloid. Interface Sci.* **2025**, *679*, 43–53. [CrossRef]
213. Khalafallah, D.; Ibrahim, M.A.; Hou, H.; Wang, J.; Liu, C.; Zhang, Q. Configuring Cations–Doped Cobalt Lanthanum LDH Nanoarray-on-Nanoarray Platforms for Supercapacitors. *Sustain. Mater. Technol.* **2025**, *43*, e01286. [CrossRef]
214. Duddi, R.; Shivani; Dhiman, S.; Kumar Singh, A.; Kamboj, N.; Kumar, S. Superior Cycle Stability and Enhanced Pseudocapacitive Performance of NiAl-LDH Decorated Carbon Cloth for Supercapacitor Application. *Appl. Surf. Sci.* **2025**, *679*, 161298. [CrossRef]
215. Mazloum-Ardakani, M.; Mozaffari, S.A.; Rasche, B.; Ebrahimi, F. Bio-Inspired Coral Reef-like NiCo-LDH Nanostructure Fabricated on Carbon Felt for High Performance Flexible Supercapacitor. *Sci. Rep.* **2025**, *15*, 10542. [CrossRef] [PubMed]
216. Klydziute, G.; Gliaudyte, L.; Sokol, D.; Vasiliauskiene, D.; Yang, T.C.-K.; Kareiva, A. Layered Double Hydroxides: Sol-Gel Synthesis, Characterization and Application. *Preprint* **2024**. [CrossRef]
217. Valente, J.S.; Lima, E.; Toledo-Antonio, J.A.; Cortes-Jacome, M.A.; Lartundo-Rojas, L.; Montiel, R.; Prince, J. Comprehending the Thermal Decomposition and Reconstruction Process of Sol−Gel MgAl Layered Double Hydroxides. *J. Phys. Chem. C* **2010**, *114*, 2089–2099. [CrossRef]
218. Mallakpour, S.; Dinari, M.; Behranvand, V. Ultrasonic-Assisted Synthesis and Characterization of Layered Double Hydroxides Intercalated with Bioactive N,N′-(Pyromellitoyl)-Bis-$_{\text{L}}$-α-Amino Acids. *RSC Adv.* **2013**, *3*, 23303–23308. [CrossRef]
219. Sokol, D.; Vieira, D.E.L.; Zarkov, A.; Ferreira, M.G.S.; Beganskiene, A.; Rubanik, V.V.; Shilin, A.D.; Kareiva, A.; Salak, A.N. Sonication Accelerated Formation of Mg-Al-Phosphate Layered Double Hydroxide via Sol-Gel Prepared Mixed Metal Oxides. *Sci. Rep.* **2019**, *9*, 10419. [CrossRef]
220. Butenko, E.; Malyshev, A.; Kapustin, A. LDHs as Adsorbents of Phenol and Their Environmental Applications. *Am. J. Environ. Prot.* **2014**, *2*, 11–15. [CrossRef]
221. Mahjoubi, F.Z.; Khalidi, A.; Abdennouri, M.; Barka, N. Zn–Al Layered Double Hydroxides Intercalated with Carbonate, Nitrate, Chloride and Sulphate Ions: Synthesis, Characterisation and Dye Removal Properties. *J. Taibah Univ. Sci.* **2017**, *11*, 90–100. [CrossRef]
222. Shan, X.; Guo, Z.; Zhang, C.; Wang, W.; Zhao, L. Nickel Aerogel @ Ultra-Thin NiCo-LDH Nanosheets Integrated Freestanding Film as a Collaborative Adsorption and Accelerated Conversion Cathode to Improve the Rate Performance of Lithium Sulfur Batteries. *Chem. Eng. J.* **2024**, *488*, 151105. [CrossRef]
223. Yang, Y.; Ma, S.; Xia, M.; Guo, Y.; Zhang, Y.; Liu, L.; Zhou, C.; Chen, G.; Wang, X.; Wu, Q.; et al. Elaborately Converting Hierarchical NiCo–LDH to Rod–like LDH–Decorated MOF as Interlayer for High–Performance Lithium–Sulfur Battery. *Mater. Today Phys.* **2023**, *35*, 101112. [CrossRef]
224. Li, J.; Qiu, W.; Liu, X.; Zhang, Y.; Zhao, Y. NiCo-Layered Double Hydroxide to Composite with Sulfur as Cathodes for High-Performance Lithium-Sulfur Batteries. *ChemElectroChem* **2022**, *9*, e202101211. [CrossRef]
225. Chen, Q.; Zhou, J.; Zhu, Y.; Jin, C.; Zhang, J.; Wu, Y.; Tang, W. In Situ Transformation of LDH into $NiCo_2S_4$-NiS_2 Nano-Heterostructures on Hollow Carbon Boxes to Promote Sulfur Electrochemistry for High-Performance Lithium-Sulfur Batteries. *Energy Fuels* **2023**, *37*, 4711–4719. [CrossRef]
226. Li, M.; Li, Y.; Cu, Q.; Li, Y.; Li, H.; Li, Z.; Li, M.; Liao, H.; Li, G.; Li, G.; et al. Hollow and Hierarchical CuCo-LDH Nanocatalyst for Boosting Sulfur Electrochemistry in Li-S Batteries. *Energy Mater. Adv.* **2023**, *4*, 0032. [CrossRef]
227. Dong, H.; Qi, S.; Wang, L.; Chen, X.; Xiao, Y.; Wang, Y.; Sun, B.; Wang, G.; Chen, S. Conductive Polymer Coated Layered Double Hydroxide as a Novel Sulfur Reservoir for Flexible Lithium-Sulfur Batteries. *Small* **2023**, *19*, 2300843. [CrossRef]
228. Wu, Y.; Yang, S.; Liu, K.; Li, Q.; Wang, H.; Jiang, J. New Anode Materials for Sodium-Ion Batteries: $Ni_xCa_{2\text{-}x}$Al-Cl LDH and $Co_yCa_{2\text{-}y}$Al-Cl LDH Prepared from Dechlorination Wastes. *J. Energy Storage* **2024**, *101*, 113991. [CrossRef]
229. Li, Y.; Xu, C.; Li, D.; Zhang, Y.; Ni, G.; Xu, S.; Liu, B.; Huo, P. Sodium-Ion Batteries Enabled by CoSn-LDH Microspheres Anchored on Few-Layer Ti_3C_2 MXene. *ACS Appl. Nano Mater.* **2024**, *7*, 20598–20608. [CrossRef]
230. Yin, Q.; Wang, T.; Song, Z.; Yang, S.; Miao, Y.; Wu, Y.; Sui, Y.; Qi, J.; Li, Y.; Zhao, D.; et al. Computational High-Throughput Screening of Layered Double Hydroxides as Cathodes for Chloride Ion Batteries. *Chem. Eng. J.* **2023**, *459*, 141545. [CrossRef]

231. Zhang, G.; Xing, J.; Zhao, Y.; Yang, F. Hierarchical N,P Co-Doped Graphene Aerogels Framework Assembling Vertically Grown CoMn-LDH Nanosheets as Efficient Bifunctional Electrocatalyst for Rechargeable Zinc-Air Battery. *J. Colloid. Interface Sci.* **2021**, *590*, 476–486. [CrossRef]
232. Bao, E.; Ren, X.; Wang, Y.; Zhang, Z.; Luo, C.; Liu, X.; Xu, C.; Chen, H. Advanced Hybrid Supercapacitors Assembled with CoNi LDH Nanoflowers and Nanosheets as High-Performance Cathode Materials. *J. Energy Storage* **2024**, *82*, 110535. [CrossRef]
233. Wu, S.; Cai, D.; Tian, Z.; Guo, L.; Wang, Y. One-Step Synthesis of NiCo-MOF@LDH Hybrid Nanosheets for High-Performance Supercapacitor. *J. Energy Storage* **2024**, *89*, 111670. [CrossRef]
234. Owusu, K.A.; Wang, Z.; Saad, A.; Boakye, F.O.; Mushtaq, M.A.; Tahir, M.; Yasin, G.; Liu, D.; Peng, Z.; Cai, X. Room Temperature Synthesis of Vertically Aligned Amorphous Ultrathin NiCo-LDH Nanosheets Bifunctional Flexible Supercapacitor Electrodes. *Energy Environ. Mater.* **2024**, *7*, e12545. [CrossRef]
235. Zhang, Y.; Yao, Y.; Ye, H.; Chen, J.; Wan, L.; Du, C.; Zhang, Y.; Xie, M. Gradually Sulfurized Co-Ni LDH as Electrode for Highly-Stable Asymmetric Supercapacitor. *J. Energy Storage* **2024**, *91*, 112117. [CrossRef]
236. Hu, J.; Pan, Y.; Zhang, Q.; Dong, Z.; Han, S. Constructing Flower-Shaped $NiCo_2S_4$ @CoAl-LDH Heterojunction Nanosheets Exhibits Extraordinary Electrochemical Behavior for a Light-Assisted Asymmetric Supercapacitor. *Energy Fuels* **2024**, *38*, 6459–6470. [CrossRef]
237. Zhao, W.; Deng, J.; Li, M.; Du, G.; Fan, M.; Gao, H.; Yuan, Z. Rational Synthesis of Sea Urchin-like NiCo-LDH/Tannin Carbon Microsphere Composites Using Microwave Hydrothermal Technique for High-Performance Asymmetric Supercapacitor. *Adv. Compos. Hybrid. Mater.* **2025**, *8*, 215. [CrossRef]
238. Kovalenko, V.; Kotok, V.; Murashevych, B. Layered Double Hydroxides as the Unique Product of Target Ionic Construction for Energy, Chemical, Foods, Cosmetics, Medicine and Ecology Applications. *Chem. Rec.* **2024**, *24*, e202300260. [CrossRef] [PubMed]
239. Luo, Y.; Yang, Y.; Tian, Y.; Wu, Q.; Lin, W.-F.; Wen, M. Collaborative Reconstruction of FeOOH/FeNiCo-LDH Heterogeneous Nanosheets for Enhancing Anion Exchange Membrane Seawater Electrolysis. *J. Mater. Chem. A Mater.* **2025**, *13*, 7136–7148. [CrossRef]
240. Yang, L.; Lin, Q.; Guo, D.; Wu, L.; Guan, Z.; Jin, H.; Fang, G.; Chen, X.; Wang, S. Nitrogen Plasma Activates CoMn-Layered Double Hydroxides for Superior Electrochemical Oxygen Evolution. *Inorg. Chem.* **2023**, *62*, 17565–17574. [CrossRef]
241. Shankar Naik, S.; Theerthagiri, J.; Nogueira, F.S.; Lee, S.J.; Min, A.; Kim, G.-A.; Maia, G.; Pinto, L.M.C.; Choi, M.Y. Dual-Cation-Coordinated CoFe-Layered Double-Hydroxide Nanosheets Using the Pulsed Laser Ablation Technique for Efficient Electrochemical Water Splitting: Mechanistic Screening by In Situ/Operando Raman and Density Functional Theory Calculations. *ACS Catal.* **2023**, *13*, 1477–1491. [CrossRef]
242. Wu, K.; Shi, L.; Wang, Z.; Zhu, Y.; Tong, X.; He, W.; Wang, J.; Zheng, L.; Kang, Y.; Shan, W.; et al. A General Strategy to Generate Oxygen Vacancies in Bimetallic Layered Double Hydroxides for Water Oxidation. *Chem. Commun.* **2023**, *59*, 3138–3141. [CrossRef]
243. Zhou, J.; Wang, Y.; Chen, L.; Zhao, W.; Han, L. Precise Design and in Situ Synthesis of Hollow Co_9S_8 @CoNi-LDH Heterostructure for High-Performance Supercapacitors. *Dalton Trans.* **2023**, *52*, 12978–12987. [CrossRef] [PubMed]
244. Li, N.; Yang, T.; Huang, L.; Jiang, H.; Xiao, J.; Ma, X.; Lou, H.; Xie, C.; Yang, Y. Interfacial Coupling Engineering Boosting Electrocatalytic Performance of CoFe Layered Double Hydroxide Assembled on N-Doped Porous Carbon Nanosheets for Water Splitting and Flexible Zinc-Air Batteries. *ACS Appl. Mater. Interfaces* **2023**, *15*, 52530–52541. [CrossRef] [PubMed]
245. Jiang, H.; Ke, Q.; Qiu, X.; Chen, J.; Chen, P.; Wang, S.; Luo, X.; Rao, B. NiCo Layered Double Hydroxide Nanocages for High-Performance Asymmetric Supercapacitors. *Inorg. Chem. Front.* **2023**, *10*, 2154–2164. [CrossRef]
246. Zhai, H.; Wu, L.; Yu, L.; Li, L.; Wan, G.; Zhang, Y.; Yuan, X.; Wang, J.; Wang, G. Polypyrrole/NiFe-Layered Double Hydroxide Composite as an Anticorrosive Microwave Absorber. *J. Mater. Chem. C Mater.* **2024**, *12*, 11001–11011. [CrossRef]
247. Zhang, W.; Zhang, B.; Wang, Y.; Cao, X.; Wang, J.; Lu, W.; Guo, Y. Gelatin-Based Hydrogel Functionalized with Dopamine and Layered Double Hydroxide for Wound Healing. *Gels* **2024**, *10*, 318. [CrossRef] [PubMed]
248. Mohammadi Zardkhoshoui, A.; Arian, R.; Hosseiny Davarani, S.S. Tunable Construction of CuS Nanosheets@flower-like ZnCo-Layered Double Hydroxide Nanostructures for Hybrid Supercapacitors. *Ind. Chem. Mater.* **2023**, *1*, 443–457. [CrossRef]
249. Wang, L.; Li, J.; Meng, Q.; Xiao, M.; Liu, C.; Xing, W.; Zhu, J. Facilitating Active NiOOH Formation via Mo Doping towards High-Efficiency Oxygen Evolution. *Catal. Sci. Technol.* **2024**, *14*, 4166–4173. [CrossRef]
250. Lin, X.; Wang, Z.; Cao, S.; Hu, Y.; Liu, S.; Chen, X.; Chen, H.; Zhang, X.; Wei, S.; Xu, H.; et al. Bioinspired Trimesic Acid Anchored Electrocatalysts with Unique Static and Dynamic Compatibility for Enhanced Water Oxidation. *Nat. Commun.* **2023**, *14*, 6714. [CrossRef]
251. Das, J.P.; Nardekar, S.S.; Kesavan, D.; Bhunia, K.; Ravichandran, V.; Kim, S.-J. Unveiling the Effect of Growth Time on Bifunctional Layered Hydroxide Electrodes for High-Performance Energy Storage and Green Energy Conversion. *J. Mater. Chem. A Mater.* **2024**, *12*, 20179–20190. [CrossRef]
252. Chen, S.; Zheng, Z.; Li, Q.; Wan, H.; Chen, G.; Zhang, N.; Liu, X.; Ma, R. Boosting Electrocatalytic Water Oxidation of NiFe Layered Double Hydroxide via the Synergy of 3d–4f Electron Interaction and Citrate Intercalation. *J. Mater. Chem. A Mater.* **2023**, *11*, 1944–1953. [CrossRef]

253. Matsuda, K.; Okuda, A.; Kawashimo, M.; Fukuzaki, R.; Iio, N.; Tarutani, N.; Katagiri, K.; Inumaru, K. Molecular-Level Pictures of Chemical and Structural Transformations of Mg–Al Layered Double Hydroxide Crystals (Mg/Al = 2) at Elevated Temperatures. *J. Phys. Chem. C* **2023**, *127*, 12599–12605. [CrossRef]
254. Dillenburger, J.D.; Schulte, L.; Mahale, P.; Suleiman, M.; Mallouk, T.E. Anion-Dependent Structure, Dehydration, and Hydroxide Ion Conductivity of Magnesium Aluminum Layered Double Hydroxides. *Chem. Mater.* **2023**, *35*, 6437–6446. [CrossRef]
255. Fang, J.; Wen, D.; Zhang, Z.; Zheng, D.; Meng, A.; Su, Y.; Zhou, S. CoNiMn-Layered Double Hydroxide/$Ti_3C_2T_x$ Nanosheet Composites for Enhanced Pseudocapacitive Performance. *J. Phys. Conf. Ser.* **2023**, *2566*, 012004. [CrossRef]
256. Zou, L.; Sun, S.; Zhang, C.; Zhao, X. NiTi-Layered Double Hydroxide@Carbon Nanotube as a Cathode Material for Chloride-Ion Batteries. *Nanomaterials* **2023**, *13*, 2779. [CrossRef] [PubMed]
257. Bai, X.; Liu, Q.; Lu, Z.; Liu, J.; Chen, R.; Li, R.; Song, D.; Jing, X.; Liu, P.; Wang, J. Rational Design of Sandwiched Ni-Co Layered Double Hydroxides Hollow Nanocages/Graphene Derived from Metal-Organic Framework for Sustainable Energy Storage. *ACS Sustain. Chem. Eng.* **2017**, *5*, 9923–9934. [CrossRef]
258. Xu, J.; Tang, R.; Liu, M.; Xie, S.; Zhang, D.; Kong, X.; Jin, S.; Ji, H.; Zhang, T. Enhancing the Catalytic Activity of Layered Double Hydroxide Supported on Graphene for Lithium–Sulfur Redox Reactions. *Batteries* **2022**, *8*, 200. [CrossRef]
259. Hu, J.; Yuan, C.; Zhi, L.; Zhang, H.; Yuan, Z.; Li, X. In Situ Defect-Free Vertically Aligned Layered Double Hydroxide Composite Membrane for High Areal Capacity and Long-Cycle Zinc-Based Flow Battery. *Adv. Funct. Mater.* **2021**, *31*, 2102167. [CrossRef]
260. Zhang, D.; Cao, J.; Zhang, X.; Insin, N.; Wang, S.; Han, J.; Zhao, Y.; Qin, J.; Huang, Y. Inhibition of Manganese Dissolution in Mn_2O_3 Cathode with Controllable Ni^{2+} Incorporation for High-Performance Zinc Ion Battery. *Adv. Funct. Mater.* **2021**, *31*, 2009412. [CrossRef]
261. Yan, Z.; Wang, E.; Gao, J.; Yang, J.; Wu, C.; Jiang, L.; Zhu, M.; Sun, G. An Exceptionally Facile Synthesis of Highly Efficient Oxygen Evolution Electrodes for Zinc-Oxygen Batteries. *ChemElectroChem* **2017**, *4*, 2190–2195. [CrossRef]
262. Gao, Z.; Wang, J.; Li, Z.; Yang, W.; Wang, B.; Hou, M.; He, Y.; Liu, Q.; Mann, T.; Yang, P.; et al. Graphene Nanosheet/Ni^{2+}/Al^{3+} Layered Double-Hydroxide Composite as a Novel Electrode for a Supercapacitor. *Chem. Mater.* **2011**, *23*, 3509–3516. [CrossRef]
263. Zhang, D.; Cao, J.; Zhang, X.; Zeng, Z.; Insin, N.; Qin, J.; Huang, Y. Modification Strategies of Layered Double Hydroxides for Superior Supercapacitors. *Adv. Energy Sustain. Res.* **2022**, *3*, 2100183. [CrossRef]
264. Malak-Polaczyk, A.; Vix-Guterl, C.; Frackowiak, E. Carbon/Layered Double Hydroxide (LDH) Composites for Supercapacitor Application. *Energy Fuels* **2010**, *24*, 3346–3351. [CrossRef]
265. Zhang, C.; Zhu, Z.; Zhang, Y.; Shao, W.; Wu, D.; Peng, G.; Liu, Z. Introduction of Bimetallic Oxide-Modified Carbon Nanotubes for Boosting the Energy Storage Performance of NiCo-LDH Based in-Plane Micro-Supercapacitors on Paper. *Chem. Eng. J.* **2024**, *494*, 153242. [CrossRef]
266. Wang, J.; Ding, Q.; Bai, C.; Wang, F.; Sun, S.; Xu, Y.; Li, H. Synthesis of CNTs/CoNiFe-LDH Nanocomposite with High Specific Surface Area for Asymmetric Supercapacitor. *Nanomaterials* **2021**, *11*, 2155. [CrossRef] [PubMed]
267. Chen, H.; Hu, L.; Chen, M.; Yan, Y.; Wu, L. Nickel–Cobalt Layered Double Hydroxide Nanosheets for High-performance Supercapacitor Electrode Materials. *Adv. Funct. Mater.* **2014**, *24*, 934–942. [CrossRef]
268. Li, L.; Hui, K.S.; Hui, K.N.; Xia, Q.; Fu, J.; Cho, Y.-R. Facile Synthesis of NiAl Layered Double Hydroxide Nanoplates for High-Performance Asymmetric Supercapacitor. *J. Alloys Compd.* **2017**, *721*, 803–812. [CrossRef]
269. Shah, S.S. Biomass-Derived Carbon Materials for Advanced Metal-Ion Hybrid Supercapacitors: A Step Towards More Sustainable Energy. *Batteries* **2024**, *10*, 168. [CrossRef]
270. Jayababu, N.; Kim, D. CuCo LDHs Coated CuCoTe Honeycomb-Like Nanosheets as a Novel Anode Material for Hybrid Supercapacitors. *Small* **2021**, *17*, 2102369. [CrossRef]
271. Zhao, R.; Wang, M.; Zhao, D.; Li, H.; Wang, C.; Yin, L. Molecular-Level Heterostructures Assembled from Titanium Carbide MXene and Ni–Co–Al Layered Double-Hydroxide Nanosheets for All-Solid-State Flexible Asymmetric High-Energy Supercapacitors. *ACS Energy Lett.* **2018**, *3*, 132–140. [CrossRef]
272. Yang, J.; Yu, C.; Fan, X.; Qiu, J. 3D Architecture Materials Made of NiCoAl-LDH Nanoplates Coupled with NiCo-Carbonate Hydroxide Nanowires Grown on Flexible Graphite Paper for Asymmetric Supercapacitors. *Adv. Energy Mater.* **2014**, *4*, 1400761. [CrossRef]
273. Jia, H.; Wang, M.; Feng, M.; Li, G.; Li, L.; Liu, Y. Synergistic Enhancement of Supercapacitor Performance: Modish Designation of BPQD Modified NiCo-LDH/$NiCo_2S_4$ Hybrid Nanotube Arrays with Improved Conductivity and OH^- Adsorption. *Chem. Eng. J.* **2024**, *484*, 149591. [CrossRef]
274. Luo, C.-W.W.; Zhang, K.; Zeng, H.-Y.Y.; Yan, W.; Lv, S.-B.B.; Wu, G.-Z.Z. Engineering ZnNi-LDH with Improved Wettability by N-Direct-Doping for High-Performance Supercapacitor. *J. Alloys Compd.* **2025**, *1010*, 177406. [CrossRef]
275. Wei, X.; Li, M.; Li, L.; Feng, W.; Wu, H. Black Phosphorus Quantum Dots Embedded NiCoCu-LDH with Porous Structure for High-Performance Hybrid Supercapacitor. *Appl. Surf. Sci.* **2025**, *686*, 162203. [CrossRef]

276. Moradi, M.; Afkhami, A.; Madrakian, T.; Moazami, H.R.; Tirandaz, A. Partial Hydrothermal Sulfidation of Electrosynthesized Co-Mn Layered-Double-Hydroxide as an Active Material for Supercapacitor Applications. *J. Power Sources* **2025**, *629*, 235993. [CrossRef]
277. Wang, J.; Li, J.; Wang, F.; Zhang, X.; Wu, X.; Zhang, J.; Niu, S.; Chen, L. Introducing Ce into the Interface of NiCo LDH@PBAs to Build Multi Core–Shell Electrode with Superior Stability of Supercapacitor. *Chem. Eng. J.* **2024**, *488*, 150932. [CrossRef]
278. Hu, W.; Hu, B.; Wu, Z.; Zuo, M.; Song, Y.; Zheng, Q.; Shan, G.; Du, M. Exceeding 50 000 Cycle Durability of Layered Hydroxide-Based Hybrid Supercapacitor Through Scandium Doping-Induced Superlong Activation Process. *Small Struct.* **2024**, *5*, 2300574. [CrossRef]
279. Chen, R.X.; Cheng, L. Preparation of Flower-Like Layered Double Hydroxides Supercapacitor Cathode Based on Biomineralization Strategy. *Key Eng. Mater.* **2024**, *993*, 3–8. [CrossRef]
280. Bhandari, R.; Shah, R.R. Hydrogen as Energy Carrier: Techno-Economic Assessment of Decentralized Hydrogen Production in Germany. *Renew. Energy* **2021**, *177*, 915–931. [CrossRef]
281. Terlouw, T.; Bauer, C.; McKenna, R.; Mazzotti, M. Large-Scale Hydrogen Production via Water Electrolysis: A Techno-Economic and Environmental Assessment. *Energy Environ. Sci.* **2022**, *15*, 3583–3602. [CrossRef]
282. Haque, M.A.; Kawawaki, T.; Negishi, Y. Navigating Challenges and Possibilities for Improving Polymer Electrolyte Membrane Fuel Cells via Pt Electrocatalyst, Support and Ionomer Advancements. *Int. J. Hydrogen Energy* **2024**, *85*, 30–47. [CrossRef]
283. Zhang, B.; Ma, C.; Wang, J.; Zhang, X.; Tu, J. Layered Hydroxides as Electrocatalysts for Water Splitting. In *Metal Oxides and Related Solids for Electrocatalytic Water Splitting*; Elsevier: Amsterdam, The Netherlands, 2022; pp. 241–272, ISBN 9780323857352.
284. Ye, S.; Xu, Y.; Bai, X.; Liang, Z.; Liu, Q.; Wei, Q.; Yang, D.; Yang, W.; Gao, F.; Shi, Q. Efficient Bifunctional Water Splitting Catalysts Enabled by Crystalline-Amorphous Ni_xS_y@NiFe LDH Heterojunctions. *J. Mater. Chem. A Mater.* **2025**. [CrossRef]
285. Xia, X.; Wang, S.; Liu, D.; Wang, F.; Zhang, X.; Zhang, H.; Yu, X.; Pang, Z.; Li, G.; Chen, C.; et al. Electronic Modulation in Cu Doped NiCo LDH/NiCo Heterostructure for Highly Efficient Overall Water Splitting. *Small* **2024**, *20*, 2311182. [CrossRef]
286. Huo, J.M.; Ma, Z.L.; Wang, Y.; Cao, Y.J.; Jiang, Y.C.; Li, S.N.; Chen, Y.; Hu, M.C.; Zhai, Q.G. Monodispersed Pt Sites Supported on NiFe-LDH from Synchronous Anchoring and Reduction for High Efficiency Overall Water Splitting. *Small* **2023**, *19*, 2207044. [CrossRef] [PubMed]
287. Tucker-Quiñónez, A.M.; Rivadeneira-Mendoza, B.F.; Gorozabel-Mendoza, M.L.; Pérez-Almeida, I.B.; García-Guerrero, A.J.; Dueñas-Rivadeneira, A.A.; Yadav, K.K.; Zambrano-Intriago, L.A.; Rodríguez-Díaz, J.M. Challenges and Potential of Layered Double Hydroxides as Electrocatalytic Materials for Hydrogen Production from Water: A Review of Recent Advances and Applications. *Energy Nexus* **2025**, *17*, 100399. [CrossRef]
288. He, H.; Xiao, J.; Liu, Z.; Yang, B.; Wang, D.; Peng, X.; Zeng, L.; Li, Z.; Lei, L.; Qiu, M.; et al. Boosting the Hydrogen Evolution of Layered Double Hydroxide by Optimizing the Electronic Structure and Accelerating the Water Dissociation Kinetics. *Chem. Eng. J.* **2023**, *453*, 139751. [CrossRef]
289. Jia, Q.; Liu, E.; Jiao, L.; Li, J.; Mukerjee, S. Current Understandings of the Sluggish Kinetics of the Hydrogen Evolution and Oxidation Reactions in Base. *Curr. Opin. Electrochem.* **2018**, *12*, 209–217. [CrossRef]
290. Wang, S.; Lu, A.; Zhong, C.J. Hydrogen Production from Water Electrolysis: Role of Catalysts. *Nano Converg.* **2021**, *8*, 4. [CrossRef]
291. de Chialvo, M.R.G.; Chialvo, A.C. Hydrogen Evolution Reaction: Analysis of the Volmer-Heyrovsky-Tafel Mechanism with a Generalized Adsorption Model. *J. Electroanal. Chem.* **1994**, *372*, 209–223. [CrossRef]
292. You, H.; Wu, D.; Si, D.; Cao, M.; Sun, F.; Zhang, H.; Wang, H.M.; Liu, T.F.; Cao, R. Monolayer NiIr-Layered Double Hydroxide as a Long-Lived Efficient Oxygen Evolution Catalyst for Seawater Splitting. *J. Am. Chem. Soc.* **2022**, *144*, 9254–9263. [CrossRef]
293. Jadhav, H.S.; Roy, A.; Desalegan, B.Z.; Seo, J.G. An Advanced and Highly Efficient Ce Assisted NiFe-LDH Electrocatalyst for Overall Water Splitting. *Sustain. Energy Fuels* **2019**, *4*, 312–323. [CrossRef]
294. Shivakumar, P.; Monika, M.N.; Deepu, M.; Manjunatha Kumara, K.S.; Budagumpi, S.; Nagaraju, D.H. Amorphous and Crystalline Heterostructure $MoSe_2$/NiFe-LDH through p-n Junction Formation for Electrochemical Water Splitting-Synergistic Back Bonding Effect. *Int. J. Hydrogen Energy* **2024**, *65*, 74–82. [CrossRef]
295. Liu, G.; Huang, C.; Yang, Z.; Su, J.; Zhang, W. Ultrathin NiMn-LDH Nanosheet Structured Electrocatalyst for Enhanced Electrocatalytic Urea Oxidation. *Appl. Catal. A Gen.* **2021**, *614*, 118049. [CrossRef]
296. Cao, H.; Liu, B.; Bai, J.; Li, C.; Xu, G. Interfacial Engineering of Hierarchical Ultra-Thin NiCo-LDH Nanosheet Superstructures Nanofiber for Water Cracking Electrocatalysis. *J. Alloys Compd.* **2025**, *1010*, 178041. [CrossRef]
297. Yan, F.; Guo, D.; Kang, J.; Liu, L.; Zhu, C.; Gao, P.; Zhang, X.; Chen, Y. Fast Fabrication of Ultrathin CoMn LDH Nanoarray as Flexible Electrode for Water Oxidation. *Electrochim. Acta* **2018**, *283*, 755–763. [CrossRef]
298. Bodhankar, P.M.; Sarawade, P.B.; Singh, G.; Vinu, A.; Dhawale, D.S. Recent Advances in Highly Active Nanostructured NiFe LDH Catalyst for Electrochemical Water Splitting. *J. Mater. Chem. A Mater.* **2021**, *9*, 3180–3208. [CrossRef]
299. Fu, X.; Liao, H.; Zhang, Z.; Zheng, Y.; Lu, J.; Cheng, S.; Jiang, Y.; Gao, Y. Medium-Entropy Heterostructure of Crystalline NiCoFeP @ Amorphous NiCoFe-LDH for Industrial-Current Density and Ultrastable Overall Water Splitting. *Chem. Eng. J.* **2025**, *505*, 159520. [CrossRef]

300. Hong, C.; Ji, J.; Huang, J.; Zhang, Y.; Li, L. NiMo/NiFe-LDH Heterostructured Electrocatalyst for Hydrogen Production from Water Electrolysis. *Mater. Lett.* **2025**, *379*, 137664. [CrossRef]
301. Hou, Y.; Lu, Q.; Guo, Z.; Zhang, Y.; Zhang, Y.; Wan, X.; Lei, L. One-Step Electrodeposition Synthesis of Composites of NiFeMn Alloy and Its Hydroxide as an Efficient Bifunctional Water Splitting Catalyst. *J. Solid. State Chem.* **2025**, *348*, 125356. [CrossRef]
302. Ye, Z.; Wang, P.; Zhong, W.; Zheng, X.; Cai, W. Active-Site-Enriched Cu-Doped Ni-Fe Layered Double Hydroxide Nanosheets for Boosting the Oxygen Evolution Reaction. *New J. Chem.* **2023**, *47*, 9536–9539. [CrossRef]
303. Guo, J.; Wang, K.; Zhang, H.; Zhang, H. Enhanced Electrocatalytic Activity of Mo-Doped NiFe Layered Double Hydroxide Nanosheet Arrays for the Hydrogen Evolution Reaction. *ACS Appl. Nano Mater.* **2023**, *6*, 379–389. [CrossRef]
304. Ding, L.; Li, K.; Xie, Z.; Yang, G.; Yu, S.; Wang, W.; Cullen, D.A.; Yu, H.; Zhang, F.Y. W-Induced Morphological Modification of NiFe Layered Double Hydroxides as Efficient Electrocatalysts for Overall Water Splitting. *Electrochim. Acta* **2021**, *395*, 139199. [CrossRef]
305. Wang, T.; Zhang, X.; Yu, X.; Li, J.; Wang, K.; Niu, J. Interfacial Interaction in NiFe LDH/NiS_2/VS_2 for Enhanced Electrocatalytic Water Splitting. *Molecules* **2024**, *29*, 951. [CrossRef] [PubMed]
306. Udayakumar, A.; Dhandapani, P.; Ramasamy, S.; Angaiah, S. Layered Double Hydroxide (LDH)—MXene Nanocomposite for Electrocatalytic Water Splitting: Current Status and Perspective. *ES Energy Environ.* **2023**, *20*, 902. [CrossRef]
307. Jia, Y.; Zhang, L.; Gao, G.; Chen, H.; Wang, B.; Zhou, J.; Soo, M.T.; Hong, M.; Yan, X.; Qian, G.; et al. A Heterostructure Coupling of Exfoliated Ni–Fe Hydroxide Nanosheet and Defective Graphene as a Bifunctional Electrocatalyst for Overall Water Splitting. *Adv. Mater.* **2017**, *29*, 1700017. [CrossRef]
308. Yao, L.; Li, R.; Zhang, H.; Humayun, M.; Xu, X.; Fu, Y.; Nikiforov, A.; Wang, C. Interface Engineering of NiTe@CoFe LDH for Highly Efficient Overall Water-Splitting. *Int. J. Hydrogen Energy* **2022**, *47*, 32394–32404. [CrossRef]
309. Wang, J.; Lv, G.; Wang, C. A Highly Efficient and Robust Hybrid Structure of CoNiN@NiFe LDH for Overall Water Splitting by Accelerating Hydrogen Evolution Kinetics on NiFe LDH. *Appl. Surf. Sci.* **2021**, *570*, 151182. [CrossRef]
310. Kalusulingam, R.; Mariyaselvakumar, M.; Antonyraj, C.A.; Mathi, S.; Mikhailova, T.S.; Khubezhov, S.A.; Pankov, I.V.; Srinivasan, K.; Myasoedova, T.N. Highly Efficient Water Splitting with Pd-Integrated NiAl-LDH Nanosheets as Bifunctional Electrocatalysts. *Energy Fuels* **2023**, *37*, 13319–13330. [CrossRef]
311. Zhai, P.; Zhang, Y.; Wu, Y.; Gao, J.; Zhang, B.; Cao, S.; Zhang, Y.; Li, Z.; Sun, L.; Hou, J. Engineering Active Sites on Hierarchical Transition Bimetal Oxides/Sulfides Heterostructure Array Enabling Robust Overall Water Splitting. *Nat. Commun.* **2020**, *11*, 5462. [CrossRef]
312. Das, M.; Khan, Z.B.; Biswas, A.; Dey, R.S. Inter-Electronic Interaction between Ni and Mo in Electrodeposited Ni-Mo-P on 3D Copper Foam Enables Hydrogen Evolution Reaction at Low Overpotential. *Inorg. Chem.* **2022**, *61*, 18253–18259. [CrossRef]
313. Govind Rajan, A.; Carter, E.A. Microkinetic Model for pH- And Potential-Dependent Oxygen Evolution during Water Splitting on Fe-Doped β-NiOOH. *Energy Environ. Sci.* **2020**, *13*, 4962–4976. [CrossRef]
314. Wang, Y.; Zhang, M.; Liu, Y.; Zheng, Z.; Liu, B.; Chen, M.; Guan, G.; Yan, K. Recent Advances on Transition-Metal-Based Layered Double Hydroxides Nanosheets for Electrocatalytic Energy Conversion. *Adv. Sci.* **2023**, *10*, 2207519. [CrossRef] [PubMed]
315. Ge, Z.Q.; Li, J.; Zhang, H.J.; Liu, C.; Che, G.; Liu, Z.Q. p–d Orbitals Coupling Heterosites of Ni_2P/NiFe-LDH Interface Enable O–H Cleavage for Water Splitting. *Adv. Funct. Mater.* **2024**, *34*, 2411024. [CrossRef]
316. Zheng, K.; Ren, J.; Li, X.; Li, G.; Jiao, L.; Xu, C. Engineering Crystalline CoMP-Decorated (M = Mn, Fe, Ni, Cu, Zn) Amorphous CoM LDH for High-Rate Alkaline Water Splitting. *Chem. Eng. J.* **2022**, *441*, 136031. [CrossRef]
317. Feng, Y.; Smith, R.L.; Shen, F.; Qi, X. Structure-Oriented Electrochemical Synthesis of Layered Double Hydroxide Electrocatalytic Materials for 5-Hydroxymethylfurfural Oxidation. *ACS Sustain. Chem. Eng.* **2024**, *12*, 16905–16913. [CrossRef]
318. Yi, W.; Yu, R.; Jiang, H.; Wu, J.; Cheng, G.J. Unveiling the Synergistic Potential of Laser Chemical Solid-Phase Deposition of Atomic Platinum-Metal Layer on 2D Materials for Bifunctional Catalysts. *Adv. Funct. Mater.* **2024**, *34*, 2308575. [CrossRef]
319. Xiong, T.; Zhu, Z.; He, Y.; Balogun, M.-S.; Huang, Y. Phase Evolution on the Hydrogen Adsorption Kinetics of NiFe-Based Heterogeneous Catalysts for Efficient Water Electrolysis. *Small Methods* **2023**, *7*, 2201472. [CrossRef]
320. Zhai, Z.; Li, H.; Zhou, C.; Zheng, H.; Liu, Y.; Yan, W.; Zhang, J. Anisotropic Strain Boosted Hydrogen Evolution Reaction Activity of F-NiCoMo LDH for Overall Water Splitting. *J. Electrochem. Soc.* **2023**, *170*, 036509. [CrossRef]
321. Rosely, C.V.S.; John, H. Role of Surfactants on Electrocatalytic Activity of Co/Al Layered Double Hydroxides for Hydrogen and Oxygen Generation. *ChemCatChem* **2025**, *17*, 2401377. [CrossRef]
322. Wang, J.; Wei, X.; Song, W.; Shi, X.; Wang, X.; Zhong, W.; Wang, M.; Ju, J.; Tang, Y. Plasmonic Enhancement in Water Splitting Performance for NiFe Layered Double Hydroxide-N_{10}TC MXene Heterojunction. *ChemSusChem* **2021**, *14*, 1948–1954. [CrossRef]
323. Xi, C.; Ding, W.; Jiang, J.; Wang, Y.; Wang, S.; Zhang, Z.; Han, S. Unveiling the CoFe LDH Generated by Partial in Situ Conversion Strategy: Synergistic Effect of Modified MXene and Cationic Vacancies for Overall Water Splitting. *Fuel* **2024**, *370*, 131844. [CrossRef]
324. Shen, B.; Huang, H.; Jiang, Y.; Xue, Y.; He, H. 3D Interweaving MXene–Graphene Network–Confined Ni–Fe Layered Double Hydroxide Nanosheets for Enhanced Hydrogen Evolution. *Electrochim. Acta* **2022**, *407*, 139913. [CrossRef]

325. Luo, H.; Liu, C.; Chen, N.; Xue, K.; Yu, L.; Zhu, H.; Zhang, Y. Metal-Organic Frameworks Derived NiFe-Hydroxides for Efficient Electrocatalytic Hydrogen Evolution. *Adv. Comput. Mater. Sci. Res.* **2024**, *1*, 192. [CrossRef]
326. Lee, E.; Jeong, S.; Jeong, Y.; Kim, B.; Lee, K. Nanoscale-Confined Synthesis of 2D Metal Compounds for Electrochemical Applications. *Small Methods* **2025**, *9*, 2301782. [CrossRef] [PubMed]
327. Liu, J.; Zheng, K.; Hua, Y.; Peng, L.; Meng, X.; Zhang, C.; Su, R.; Tao, X.; Hu, H.; Guo, Y.; et al. LDHs and Their Derivatives for Electrochemical Energy Storage and Conversion Systems: Design, Insights and Applications. *ChemElectroChem* **2024**, *11*, e202400156. [CrossRef]
328. Yao, Y.; Zou, C.; Sun, S.; Guo, Y.; Hong, S.; Cai, Z.; Yang, C.; Zhuang, W.; Luo, F.; Hamdy, M.S.; et al. Ultrastable Seawater Oxidation at Ampere-level Current Densities with Corrosion-resistant $CoCO_3$/CoFe Layered Double Hydroxide Electrocatalyst. *Small* **2025**, *21*, 2409627. [CrossRef]
329. Ding, L.; Shen, Z.; Pan, H.; Chen, Y.; Hu, Y.; Zhao, G.; Hai, G.; Huang, X. Regulating Intermediate Adsorption and Promoting Charge Transfer of CoCr-LDHs by Ce Doping for Enhancing Electrooxidation of 5-Hydroxymethylfurfural. *Small* **2025**, *21*, 2409343. [CrossRef]
330. Chen, Y.; Zhang, Y.; Bai, X.; Zhao, J.; Yang, L.; Wang, X.; Wu, Q.; Hu, Z. Interlayer Engineering of Layered Double Hydroxides for Advanced Energy Storage and Conversion. *FlatChem* **2024**, *48*, 100775. [CrossRef]
331. Wang, Y.; Ying, Z.; Gao, Y.; Shi, L. Layered Double Hydroxide Nanosheets: Synthesis Strategies and Applications in the Field of Energy Conversion. *Chem. Eur. J.* **2024**, *30*, e202303025. [CrossRef]
332. Zhou, X.; Hou, Z.; Zhang, H.-Y.; Yu, J. Synergistic Coupling of NiVAl-Layered Double Hydroxide with Few-Layered $Ti_3C_2T_x$–MXene Nanosheets for Superior Asymmetric Supercapacitor Performance. *J. Mater. Chem. C Mater.* **2023**, *11*, 15571–15580. [CrossRef]
333. Jaramillo Hernández, C.; Oestreicher, V.; Mizrahi, M.; Abellán, G. An In-Situ Study of the Transformation of Hybrid Layered Hydroxides into Metallic Nanocomposites with Interest in Energy Storage Systems. In Proceedings of the ECS Meeting Abstracts 2023, Boston, MA, USA, 28 May–2 June 2023; Volume MA2023-01, p. 1322. [CrossRef]
334. Sun, X.; Chen, H.; Li, Y.; Zeng, D.; Qiu, P.; Zeng, H.; Ji, X.; Chen, L.; Shi, X. Efficient Harvesting Waste Heat by Zn-Ion Battery Under Thermally Regenerative Electrochemical Cycles. *Adv. Mater.* **2025**, *37*, 2418482. [CrossRef]
335. Abu Nayem, S.M.; Hardianto, Y.P.; Shuaibu, A.D.; Shah, S.S.; Islam, S.; Jafar Mazumder, M.A.; Aziz, M.A.; Saleh Ahammad, A.J. Biomass Derived Amino Acid Assisted Synthesis of FeNi Layered Double Hydroxide for Efficient Oxygen Evolution Reaction. *Inorg. Chem. Commun.* **2025**, *171*, 113574. [CrossRef]

MDPI AG
Grosspeteranlage 5
4052 Basel
Switzerland
Tel.: +41 61 683 77 34

Batteries Editorial Office
E-mail: batteries@mdpi.com
www.mdpi.com/journal/batteries

MDPI

Academic Open
Access Publishing

mdpi.com

ISBN 978-3-7258-6196-5